RIDE DYNAMICS OF HIGH MOBILITY WHEELED/TRACKED OFF-ROAD VEHICLES: COMPUTER SIMULATION WITH FIELD VALIDATION

Anil Dhir

A Thesis

in

The Department

of

Mechanical Engineering

Presented in Partial Fulfillment of the Requirements
of the Degree of Doctor of Philosophy at
Concordia University
Montreal, Quebec
Canada

November 1993

© Anil Dhir, 1993

Dedicated to my parents,

the late Balbir Chand & Kailash Rani Dhir

ABSTRACT

RIDE DYNAMICS OF HIGH MOBILITY WHEELED/TRACKED OFF-ROAD VEHICLES: COMPUTER SIMULATION WITH FIELD VALIDATION

Anil Dhir, Ph.D.
Concordia University, 1993

This thesis deals with the ride dynamic aspects of high mobility wheeled/tracked off-road vehicles through comprehensive computer modeling of the vehicle-terrain dynamical system and field validation of the computer model predictions. A multi-purpose ride dynamic simulation model (RIDSIM) is developed and proposed as an effective and precise tool to study and improve the ride comfort and safety, and thus the performance of wheeled/tracked off-road vehicles.

The development of RIDSIM is primarily based on the modeling strategies adopted for the ride model formulation of a typical high-speed multi-wheeled tracked vehicle (an armoured personnel carrier: M113 APC), which was selected as a candidate vehicle for this study. Consequently, this study has largely focused on the analytical and experimental ride investigations of the candidate vehicle. An extensive field testing of the candidate vehicle was carried out. Field test data were recorded for a variety of test conditions (i.e. vehicle configurations, field courses, vehicle speeds), and conditioned/reduced for ride quality assessment and computer model validation.

The candidate vehicle ride model is conceived based on three formalism of varying complexities: MODEL I, MODEL II, and MODEL III. These are time-domain simulation models developed assuming an in-plane representation of the vehicle negotiating an arbitrary rigid terrain profile at constant forward speed. These models incorporate nonlinear

suspension characteristics, a continuous radial spring and an equivalent damper model of the wheel/track-terrain interaction, and dynamic track loads computed considering kinematic constraining effects of the track belt loop. Effective computational algorithms are developed to establish wheel-terrain and track-terrain contact patches, and wheel-track connectivity. The equations of motion are written with respect to the vehicle's zero-force reference in order to simulate the vehicle-terrain contact loss. Computational procedures are devised to establish the zero-force and static equilibrium configurations of the vehicle.

The ride response predictions of the candidate vehicle are evaluated using all three models, and directly compared against field measurements in order to assess the relative performance of these models. The ride predictions obtained using MODEL I show generally good agreement with field measurements. However, the agreement between measured and predicted ride response is considerably improved through refinements of the ride dynamic model (MODEL II and MODEL III). The wheel and track sub-models proposed in this study are also compared with those reported in the literature, and shown to yield relatively accurate ride predictions while requiring less computational time.

A parametric sensitivity analysis is carried out using MODEL III to study the influence of suspension design parameters on the ride dynamics of the candidate vehicle. In addition, the ride performance potentials of an alternate hydrogas suspension system exclusively developed for application with the candidate vehicle are investigated. The hydrogas suspension system is found to reduce the ride acceleration levels, however, at the expense of relatively high displacement magnitude especially due to the vehicle pitch.

ACKNOWLEDGEMENTS

The author is sincerely grateful to his supervisor, Dr. S. Sankar, for initiating this project, and for his guidance and encouragement throughout the course of this research and during the preparation of this thesis.

The author also wishes to thank members of the faculty and staff of CONCAVE (Concordia Computer-Aided Vehicle Engineering) Research Centre, Department of Mechanical Engineering, Concordia University, for their time and assistance during the progression of this work.

Financial support provided through DRES (Defence Research Establishment Suffield, Alberta), and IRSST (Institut de Recherche en Santé et en Sécurité du Travail du Québec, Montréal, Québec) is gratefully acknowledged.

The author would like to thank LETE (Land Engineering Test Establishment, Ottawa, Ontario) for carrying out the field testing, and Dr. V.S. Shankhla (Senior Research Scientist, DRES) for his advice and assistance during the course of this research.

The author wishes to thank his wife, Karen, for her love, encouragement, patience, and many sacrifices, which made this work possible. This thesis is also dedicated to her and their twins, Kailash and Sanjay.

TABLE OF CONTENTS

LIST OF FIGURES

LIST OF FIGURES (continued)

LIST OF FIGURES (continued)

LIST OF FIGURES (continued)

LIST OF FIGURES (continued)

LIST OF FIGURES (continued)

LIST OF FIGURES (continued)

LIST OF FIGURES (continued)

LIST OF FIGURES (continued)

LIST OF FIGURES (continued)

LIST OF TABLES

LIST OF TABLES (continued)

NOMENCLATURE

a_{hk}, b_{hk}	Location of k^{th} hull wheel centre w.r.t. hull c.g. (m)
a_i, b_i	Location of i^{th} suspension-hull connection w.r.t. hull c.g. (m)
a_o, b_o	Location of seat base w.r.t. hull c.g. (m)
a_{si}, b_{si}	Location of i^{th} shock absorber-hull connection w.r.t. hull c.g. (m)
a_{wi}, b_{wi}	Location of i^{th} road wheel center w.r.t. hull c.g. (m)
a_o, a_1, a_2	Constants of quadratic polynomial approximating hanging track
b_o, b_1, b_2	Constants of quadratic polynomial approximating track sag
c^i_{rw}, c^i_{rw}	Uniformally distributed discrete viscous damping coefficient for i^{th} road wheel (N.s/m)
C^i_{rw}	Equivalent viscous damping coefficients for i^{th} road wheel (N.s/m)
C_θ	$\cos(\theta_h)$
C^i_θ	$\cos(\theta_{wi})$
d	Length of the line adjoining tops of sprocket and idler (m)
d_{max}	Maximum horizontal travel distance (m)
F^k_{hn}	Net footprint force acting at k^{th} hull wheel (N)
F^k_{hx}, F^k_{hy}	Net horizontal and vertical forces acting at k^{th} hull wheel (N)
$\mathbb{F}^k_{hx}, \mathbb{F}^k_{hy}$	Horizontal and vertical components of net foot-print force acting at k^{th} hull wheel (N)
$F^i_{r\ell}$	Foot-print force acting along ℓ^{th} radial segment of i^{th} wheel (N)
F_{si}, F_{di}	Spring and damping forces due to i^{th} primary suspension (N/m)
F_{so}, F_{do}	Spring and damping forces due to seat suspension (N/m)
F^i_S	Spring/damping force due to i^{th} inclined suspension unit (N)
F^i_{wn}	Net footprint force acting at i^{th} road wheel (N)
F^i_{wx}, F^i_{wy}	Net horizontal and vertical forces acting at i^{th} road wheel (N)

F^i_{wx}, F^i_{wy}	Horizontal and vertical components of net foot-print force acting at i^{th} road wheel (N)
$\{ F \}$	Generalized dynamic force vector
$\{ F_a \}$	Generalized static force vector
g	gravity term (9.81 m/s^2)
h_{cg}	Height of the hull c.g. (m)
h_{wi}	Height of the i^{th} road wheel centre (m)
I_h	Half of hull pitch mass moment of inertia ($kg.m^2$)
I_{wi}	Mass moment of inertia of i^{th} road wheel assembly or walking/ bogie suspension beam ($kg.m^2$)
I^i_{ra}	Mass moment of inertia of i^{th} road arm ($kg.m^2$)
K_i, K_o, K_{wi}	Local Spring constant of i^{th} primary suspension, secondary suspension, and i^{th} road wheel (N/m)
k^j_f	Spring constant for track front (j=1)/rear (j=N+1) feeler (N/m)
k^j_t	Vertical spring constant of j^{th} intermediate track segment (N/m)
k^i_{rw}, k^i_{rw}	Uniformally distributed discrete spring constant for i^{th} road wheel (N/m)
K^i_{rw}	Equivalent spring constant for i^{th} road wheel (N/m)
K^i_{rw}	Continuous radial spring constant for i^{th} road wheel (N/m/rad)
K_{tr}	Longitudinal stiffness of track (N/m)
K_{Ti}	Torsional spring constant for i^{th} suspension unit (N.m/rad)
K^U_{Ti}, K^L_{Ti}	Equivalent torsional spring constants for upper and lower bump stops (N.m/rad)
$[K]$	Stiffness matrix
l_{1i}, l_{2i}	Dimensions of i^{th} walking/bogie beam (m)
l_{s1i}, l_{s2i}	Dimensions of i^{th} walking beam (m)
ℓ	Half of track hanging length (m)
L_j	Length of j^{th} track segment between adjacent wheels (m)
L_h	Length of track segment supported on drive sprocket and idler (m)

L_{tr}	Length of track from top of drive sprocket, around road wheels, and up to top of idler (m)
L_{tr}	Overall track length (m)
m_h, m_o, m_{wi}	Half of hull (sprung) mass, suspended mass of driver and seat, and unsprung mass of i^{th} road wheel assembly (only for one side of the vehicle) (kg)
m^i_{rw}, m^i_{ra}	masses of i^{th} road wheel and road arm (m)
M	Number of hull wheels
M_a	Static moment about sprung mass c.g. (N.m)
M^i_T	Resistive moment due to i^{th} suspension unit (N.m)
[M]	Mass/inertia matrix
N	Number of road wheels
N_f	Number of discrete radial segments within instantaneous wheel-terrain contact patch
N_S	Number of terrain profile points within the horizontal diametrical range or shadow of wheel circle
N_I	Number of terrain profile points inside the wheel circle
NU	Number of unsprung/rigid suspensions
NI	Number of independent suspensions
NT	Number of torsion bar/trailing arm suspensions
NW	Number of walking beam suspensions
NB	Number of bogie suspensions
P_{CG}, P_{wi}, P_{hk}	Position vectors indicating sprung mass c.g., i^{th} road wheel centre, k^{th} hull wheel centre w.r.t. the global frame.
{ q }	Generalized coordinate vector
Q_i	Generalized force/moment i (N or N.m)
r_i, r_o	Relative displacement across i^{th} primary suspension, and secondary suspension (m)
R_{ai}	Length of i^{th} road arm (m)

R_{hk}, R_{wi}	Radius of k^{th} hull wheel, and i^{th} road wheel (m)
S_{ai}	Overhang length of i^{th} road arm (m)
S_T	Track sag (m)
S_θ	$\sin(\theta_h)$
S_θ^i	$\sin(\theta_{wi})$
t	Time (s)
t_{max}	Maximum simulation time (s)
T	Maximum track tension at top of hull wheels (N)
$\mathbf{T}$	Kinetic energy (N.m)
$\mathbb{T}_{CG}$	Transformation matrix describing the central body-fixed frame w.r.t. to the fixed/global frame
${}^{c}\mathbb{T}_{CG}$	Transformation matrix describing torsion bar-fixed frame w.r.t. central body-fixed frame
T_A, T_B	Magnitude of track tension at top of idler and sprocket (N)
T_j	Tension in track feeler (front: j=1 ; rear: j=N+1) (N)
T_o	Minimum or horizontal tension of hanging track (N)
T_0	Reference tension for track stretching (N)
T_{tr}	Overall track tension (N)
T_{hx}^k, T_{hy}^k	Horizontal and vertical components of T_{tr} acting at k^{th} hull wheel (N)
T_{wx}^i, T_{wy}^i	Horizontal and vertical components of T_{tr} acting at i^{th} road wheel (N)
$\mathbf{U}$	Potential energy (N.m)
V_x	Vehicle speed (m/s)
w_s	Track belt weight per unit length (N/m)
W_h, W_o, W_{wi}	Half of hull (sprung) weight, suspended weight of driver/seat, and unsprung weight of i^{th} road wheel assembly (on one side of vehicle)
X_A, Y_A	Cartesian coordinates of end point of hanging track at idler (m)

X_B, Y_B	Cartesian coordinates of end point of hanging track at sprocket (m)
X_{cg}, Y_{cg}	Cartesian coordinates of hull c.g. (m)
X_{hk}, Y_{hk}	Cartesian coordinates of k^{th} hull wheel centre (m)
X_{wi}, Y_{wi}	Cartesian coordinates of i^{th} road wheel centre (m)
y_h, y_o, y_{wi}	Vertical displacement of hull c.g., driver/seat, and i^{th} road wheel (m)
α_{hk}, α_{wi}	Half of wheel-terrain contact patch angle of k^{th} hull wheel, and i^{th} road wheel (rad)
$\delta_h, \delta_o, \delta_{wi}$	Static vertical displacement of hull c.g., driver/seat, and i^{th} road wheel center
$\Delta_i, \Delta_o, \Delta_{wi}$	Static relative displacement across i^{th} primary suspension, secondary suspension, and i^{th} road wheel
δ^j_{max}	Maximum deflection of track feeler (front: j=1 ; rear: j=N+1) (m)
δ_{rk}	Displacement of k^{th} radial segment of a wheel (m)
$\varepsilon^j_1, \varepsilon^j_2$	Horizontal inclinations of j^{th} track segment at its ends (rad)
ϕ_{hk}, ϕ_i	Track wrap angle around k^{th} hull wheel, and i^{th} road wheel (rad)
γ_{hk}, γ_i	Vertical inclination of net footprint force acting at k^{th} hull wheel, and i^{th} road wheel (rad)
γ_{Pi}	Local slope angle of terrain profile at i^{th} radial segment (rad)
ψ_i	Vertical inclination of i^{th} radial segment of a wheel (rad)
λ^j_1, λ^j_2	End angles of deflected track feeler with respect to undeflected feeler (front: j=1 ; rear: j=N+1) (rad)
θ_h	Hull pitch angle (rad)
θ_{wi}	Angle of i^{th} road arm w.r.t. hull frame or horizontal inclination of i^{th} walking/bogie suspension beam (rad)
$\theta^U_{wi}, \theta^L_{wi}$	Angles indicating locations of upper and lower bump stops (rad)
Θ_1, Θ_2	Horizontal inclinations of the front and rear track feelers (rad)

θ_A, θ_B Horizontal inclinations of hanging track at top of idler and sprocket (rad)

θ_h Slope angle of the line adjoining tops of idler and sprocket (rad)

ξ_i Overhang angle of i^{th} road arm (rad)

ζ_{ni} Angles indicating horizontal inclinations of shock absorbers associated with i^{th} suspension unit (rad)

Chapter 1

INTRODUCTION, LITERATURE SURVEY, AND OBJECTIVES

1.1 GENERAL INTRODUCTION

Computer simulation has become an important and essential component of research and development in almost all fields of science and engineering. It is a convenient and economical tool to effectively study the problem of interest, and provide guidelines for the solution without resorting to the expensive and time-consuming process of repeated testing. Computer simulation involves mathematical modelling of a given physical system based on certain assumptions and then solving the governing equations on a digital computer. Modelling is a creative and intuitive process which usually involves a *modular* or *building-block approach* to build a mathematical analogy of the actual system. Since it is impossible to model the world, one must recognize, isolate and idealize principal components of the system in view of the specific objectives of study. The model, thus evolved, provides a simplified yet credible mathematical formulation of the system.

Computer simulation in the field of ground vehicle system dynamics is no exception. As vehicles have become more sophisticated and hence expensive, vehicle dynamicists and designers are turning more to computer simulation techniques in an effort to study the vehicle dynamic behaviour, to obtain optimal design parameters, and to predict and quantify the effects of proposed changes in the vehicle parameters. Computer simulations can, however, only be beneficial if the analytical model reflects accurately the dynamic behaviour of the vehicle. Appropriate field and/or laboratory testing of the physical system to

validate the computer simulation model, thus becomes absolutely essential in order to establish confidence in the predicted results.

A number of general-purpose simulation softwares for dynamic analysis of mechanical systems are commercially available. These softwares including IMP, DADS, ADAMS, DRAM, etc., are *self-formulating* programs developed based on the theory of multi-body dynamics, and are largely suited for kinematic and dynamic analysis of machine mechanisms, and spacecraft structures [1]. Application of these softwares for the study of vehicle system dynamics has, however, been limited primarily in view of following factors [1]:

- Modelling strategies employed in these programs generate a large number of differential equations for the multibody system. Thus, full vehicle dynamics may include hundreds of differential equations and may take an hour or more of main frame CPU time for a single second of vehicle simulation.
- Because of the complexity of the vehicle model generated, little physical insight can be gained into the effects of various components.
- The task of preparing input-data is tedious, and becomes quite demanding if the user wishes to introduce modifications in the design parameters. These softwares assume that the user is well versed in simulation techniques and many other specialized fields and syntax.
- Formulation for vehicle-terrain can be very tedious since these softwares model mechanical systems as spatial mechanisms with constraint equations for each joint.

Consequently, general-purpose softwares are very costly and inconvenient option for performing preliminary design surveys, routine

and repeated simulation runs, and for conducting parametric studies. It is usually recommended that these softwares should only be used for critical event simulation to validate the results and findings of other more flexible and specialized programs. Because of these factors, the majority of previous studies in the area of vehicle dynamics have developed and employed their own simulation models without resorting to general-purpose softwares.

The field of ground vehicle system dynamics incorporates three major areas of study [2]:

- *Ride*: study of the terrain-induced vibration environment and its effects on passenger and goods.
- *Handling*: study of the vehicle response to driver's command and external disturbances (e.g. aerodynamic forces).
- *Performance*: study of vehicle's ability to accelerate/decelerate, to develop drawbar pull, and to overcome obstacles.

Although ultimate objectives of the above-mentioned studies may be different, a common first step usually involves developing an analytical model of vehicle-terrain dynamical system with basic components illustrated in Figure 1.1. Over the years, a number of analytical model of varying complexities have been developed to represent each of the subsystems of the basic vehicle-terrain system illustrated in Figure 1.1. The normal selection process consists of choosing the appropriate subsystem model through tradeoff between analytical complexity (cost) and simulation realism.

The scope of the current research program is limited to the area of *ride dynamic* study of ground vehicle systems, and the general objectives are:

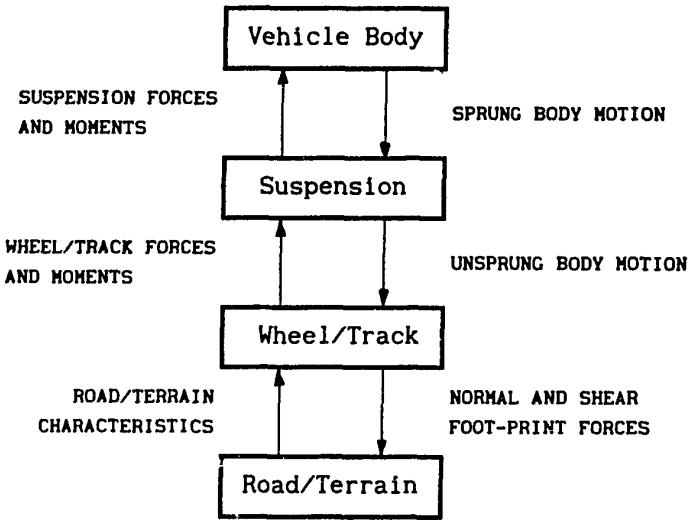

Figure 1.1. Basic vehicle-terrain simulation model.

(a) to develop a comprehensive time-domain ride dynamic simulation model for wheeled/tracked vehicles primarily employed for high speed off-road operations,

(b) to carry out field testing of a typical wheeled/tracked vehicle for a variety of test conditions, and

(c) to validate and refine the ride simulation model.

The computer simulation model, thus evolved, would be an effective and precise tool to understand and improve the off-road vehicle ride dynamic behaviour.

1.2 STATE OF THE ART AND LITERATURE SURVEY

In this section, a general summary of off-road vehicle types and their ride dynamic behaviour is presented. Computer ride simulation models developed over the last two decades are briefly reviewed. A summary of various ride vibration standards and tolerance criteria for ground vehicles is presented.

1.2.1 Off-Road Vehicles and Ride Dynamics

Off-road vehicles are categorized into two types according to their running gear: *wheeled* or *tracked* vehicles. Figure 1.2 shows examples of a few wheeled and tracked off-road vehicles employed for different applications. The design of off-road vehicles varies dramatically with the type of use: agricultural, earthmoving or military. Wheeled vehicles, which are generally fitted with pneumatic tires, are usually designed for both on- and off-road use, whereas tracked vehicles are generally unsuitable for road use. Off-road vehicles, whether wheeled or tracked, are either low speed *non-suspended* vehicles (e.g. agricultural tractors, bulldozers, earthmovers) designed to produce high tractive efforts or *suspended* vehicles (e.g. tanks, cross country utility vehicles) capable

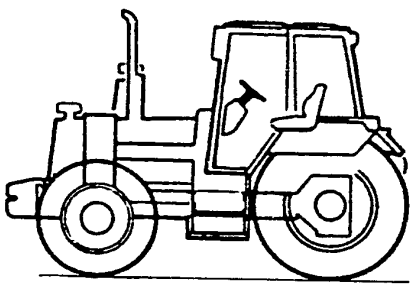

Agricultural Tractor

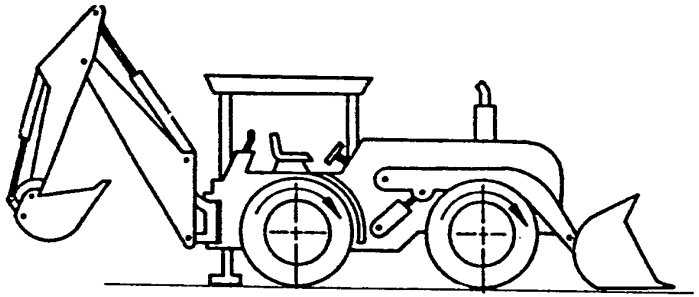

Earthmover

(a) *Typical Non-Suspended Off-Road Vehicles.*

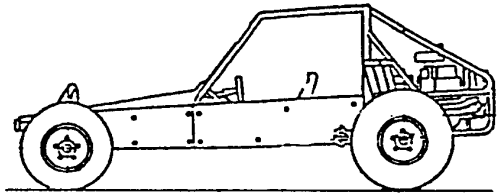

Cross-Country Utility Vehicle

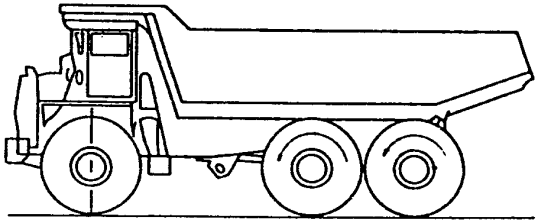

Dump Truck

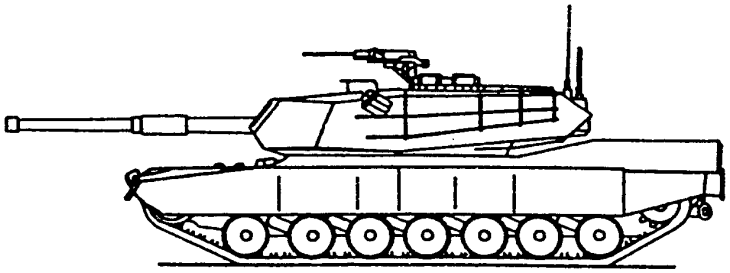

Main Battle Tank

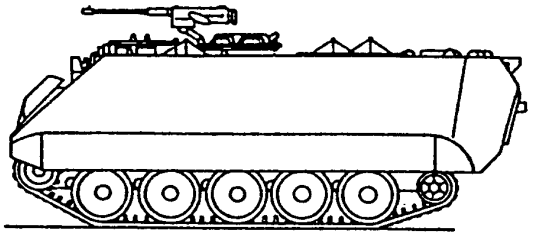

Armoured Personnel Carrier

(b) *Typical Suspended Off-Road Vehicles.*

Figure 1.2 Examples of wheeled and tracked off-road vehicles.
(courtesy of DND and SAE)

of far higher speeds [3].

The problems associated with ride dynamic behaviour of off-road vehicles are essentially similar to those for road vehicles. The objectives for ensuring ride comfort and safety are the same, namely, (a) to provide an acceptable ride environment for the vehicle operator and crew members, (b) to enable the operator to retain suitable control of the vehicle and its ancillary devices, and (c) to ensure the welfare of vehicle components and cargo. The mobility performance of off-road vehicles is often limited by the ability of the driver to withstand transmitted acceleration levels and maintain control. Over the years, a number of methods for quantifying ride vibration levels and their effects on vehicle operators have been established based on subjective and objective human response [4]. A detailed review of these methods is provided later in this chapter.

Non-Suspended Off-Road Vehicles

The majority of ride dynamic studies for non-suspended vehicles have considered wheeled vehicles only, especially agricultural tractors. The ride dynamic behaviour of non-suspended tracked vehicles have received little attention since they are relatively small in number, and because they operate at very low speeds [3]. Non-suspended wheeled vehicles, such as agricultural tractors are equipped with large and significantly soft tires which offer very low damping, thus the ride vibration of such vehicles is characterized by lightly damped resonant behaviour. The ride vibration environment of these vehicles is of low frequency and large magnitude in nature, where the vehicle vibrations, mainly transmitted from irregular terrains, are directly transmitted to the driver's seat through unsprung chassis and the cab [5]. Terrain-induced ride vibration

of wheeled off-road vehicles predominate in the frequency range 0.5 - 5.0 Hz , and r.m.s. acceleration levels are typically upto 0.2 g in the vertical and 0.15 g in the lateral and longitudinal directions with peaks of upto 2 g [3].

Over the years, various studies have established the adverse effects of low frequency and high amplitude ride vibration. Prolonged exposure to excessive low frequency vibration have been found to cause the operator bodily discomfort, physiological damage, and inefficient performance [6]. Two forms of degenerative health effects have been associated with prolonged exposure: stomach sickness and spinal disorders [7]. The inefficient performance of the vehicle operator has been attributed to several factors such as slow reaction time, impaired tracking ability, difficulty in maintaining constant foot pressure, and deterioration of visual acuity [5].

In view of poor ride quality, ride dynamics of non-suspended wheeled off-road vehicles has gained considerable attention. Various approaches to improve ride quality have been investigated, namely: suitable tires, primary suspensions, and secondary (cab and seat) suspensions [8]. The pneumatic tires for these vehicles are primarily selected to provide maximum traction, and ride improvement based on tires alone is considered infeasible due to the need for considerably soft, thus larger tires. The option of primary suspension, however, requires complex alterations in the vehicle design. Subsequently, suitable seat suspension and cab mounts for non-suspended wheeled off-road vehicles have been considered as the most favourable options [5]. Although, the seat suspension is the simplest option, the requirement for softer seat suspension leads to excessive relative motion between the driver and vehicle controls.

Alternatively, cab suspensions or mounts are considered as effective ride vibration isolators for non-suspended wheeled vehicles [9].

Suspended Off-Road Vehicles

Vehicles in this category are designed for relatively higher operational speeds (upto 50 km/h) across rough terrains [10]. Therefore, these vehicles are equipped with primary suspension systems in order to meet demands of ride comfort and safety, and vehicle control. Similar to non-suspended vehicles, these vehicles fall into two general categories depending on whether ground contact is with wheels or tracks. Wheeled vehicles are usually for general purpose cross-country or military applications, whereas tracked vehicles are almost exclusively for military applications. Like non-suspended vehicles, ride vibration levels experienced by the operators of suspended vehicles, whether wheeled or tracked, have been long recognized as unacceptably high [10].

The suspension system development for off-road wheeled vehicles has primarily followed the knowledge and experience gained on road vehicles [3]. Literature specifically dealing with suspension dynamics of off-road wheeled vehicles is scarce. The recent trend is towards the use of advanced suspension concepts such as active and semi-active suspension systems [11,12]. An exhaustive amount of literature dealing with active and semi-active suspension systems mainly for road vehicles is available [13,14]. For off-road operations, the basic suspension design considerations are low natural frequency and long wheel travel so as to achieve vibration isolation and to maintain good wheel-ground contact. Semi-active and active suspension designs were shown to offer technical advantages for off-road applications but the associated cost penalty has so far limited their adoption. Conventional suspension systems for these

vehicles are of greater variety and more complicated than those for tracked vehicles.

High mobility tracked vehicles, such as armoured personnel carriers, military battle tanks, are designed for mobility over a wide range of terrains. The performance requirements for military tracked vehicles have been increasing faster than the capabilities in the associated technology [15]. Upgrading power-to-weight ratio and mobility of advanced military vehicles have lead to considerable increase in the magnitude of ride vibrations [16]. In view of rough off-road terrains, a continual demand for increased power-to-weight ratio and higher speeds, research and development efforts have been mounted to develop an effective running gear for such vehicles. Tracked vehicles are generally fitted with passive suspension systems utilizing torsion bars and shock absorbers to attenuate the terrain-induced shocks and vibrations. Torsion bars idealize coil spring systems, and have the advantage that they can be mounted externally to the vehicle body (hull) but their bulk limits spring size and hence available travel [17]. In view of improving suspension performance of tracked vehicles, feasibility analysis involving fluidically-controlled suspension systems offering variable damping and springing characteristics have been long conducted by the U.S. Army [18,19]. The present trend is towards the use of hydrogas suspensions since these tend to be lighter and more compact. They can be mounted externally to the hull, incorporating integral damping arrangements and often easier implementation of static height correction or active control [20]. A study conducted by the British Army revealed that a tracked vehicle fitted with hydrogas suspension units exhibited higher limiting speeds with acceptable vibration levels [21].

Many of the requirements and suspension features of tracked vehicles are similar to those for wheeled vehicles. In fact, the mathematical model of tracked vehicle ride dynamics is developed similar to wheeled vehicles, however, considering certain modifications unique to the track. The enveloping characteristics of the track, wheel catching effects of the track on rebound movement, etc. contribute considerably to the ride dynamic behaviour of the tracked vehicle.

1.2.2 Review of Previous Studies

Ride dynamic simulation of off-road vehicles in the presence of highly irregular terrain surface is a time-consuming and difficult procedure due to the need for high resolution vehicle-terrain dynamical models [22]. In general, a *good* ride simulation model for an off-road vehicle must consider large deflections, nonlinearities due to suspension kinematics, spring and damping effects, wheel/tire enveloping characteristics, an appropriate model for wheel-track connectivity and track-terrain interaction. These considerations in the analytical modeling lead to complex formulations and high computing costs. However, these models are most effective for predicting ride dynamics when implemented with the above considerations using efficient computational algorithms. Previous studies have primarily employed time-domain mathematical models of varying complexities to study the ride dynamic behaviour of off-road vehicles. Various mathematical formulations have been proposed to model dynamic wheel-track-terrain interactions for off-road vehicles. A brief literature survey of previous investigations is presented in chronological order.

Eppinger *et al.* [23] developed and analyzed an in-plane model of a

six-wheeled tracked vehicle to demonstrate the influence of dynamic track loads on the ride response. The vehicle was modeled as a two-degrees-of-freedom (bounce and pitch motions of hull) dynamic system incorporating nonlinear suspension characteristics and wheel lift-off. The track was modeled as a massless elastic band capable of transmitting only tensile forces considered linearly proportional to change in the total track length. The terrain was assumed to be a non-deformable continuous profile, and was described through horizontal and vertical coordinates of successive points, where intermediate points were determined based on linear interpolation. The analytical model was validated against the laboratory measured response of a one-tenth scale model of a tank traversing a trapezoidal-shaped bump with and without the track. The experimental and analytical studies revealed that the addition of track alters and increases the hull dynamic response considerably.

In 1972, Lessem and Murphy [24] conducted an experimental investigation to study the influence of track on the ride dynamic response of high speed tracked vehicles. For this purpose, four military tracked vehicles, namely, M29, M113, M114, and M4 vehicles, were towed with and without the track over an assortment of half-round rigid obstacles and ditches, and ride acceleration data was gathered. Based on this study, it was concluded that dynamic effects of track are strongly influenced by the vehicle speed (i.e. inclusion of track improves the ride quality at low speed, however deteriorates it at higher speeds), and the ride simulation model must incorporate track contribution. Consequently, an in-plane ride model was developed for M60A1 tank traversing non-deformable terrain profile at constant speed. The ride model included the degrees-of-freedom associated with bounce and pitch

motions of hull, and bounce motion of each road wheel and axle assembly. The torsion bar suspension configuration was modeled as a parallel combination of vertical spring and damper. The road wheels were modeled as radially segmented discrete springs, where each segmented spring is assumed to deflect independently of its neighbour as it enters the wheel-terrain contact zone. Thus, the total contact force was given as sum of segment forces. Dynamic track tensioning effects were modeled as *local* tensioning effects, while neglecting the overall track tension. Track tension was modeled by hypothetical linear springs interconnecting road wheels, which effectively generate a vertical force whenever there is a relative displacement between wheels. The terrain profile was modeled similar to ref. [23]. This ride model configuration was adopted by Murphy *et al.* [25], and further extended in the development of a Vehicle Ride Dynamic Module (VEHDYN) for general use in support of the Army Mobility Code (AMC-74). This was developed based on an Army Mobility Model (AMM) and used for comprehensive evaluation of cross-country vehicle mobility [26]. VEHDYN's primary purpose was to predict the ride- and shock-limiting vehicle speeds for typical high speed wheeled or tracked off-road vehicles. The ride simulation model used in VEHDYN was formulated considering four basic suspension configurations: rigid or unsprung, independent, walking beam, and bogie suspensions, such that wide range of off-road vehicles can be conveniently modeled.

Wheeler [27] developed a computer code for an in-plane ride dynamic simulation of XM1 tank subjected to non-deformable terrains. The ride model considered pitch and bounce degrees-of-freedom associated with vehicle sprung mass and an additional degree-of-freedom for each road wheel. Overall track tension was considered to account for track dynamic

effects, and the input at the wheel-terrain interface was restricted to be only vertical. The terrain profile was modeled similar to previous studies. The forces acting on a road wheel were assumed to be vertical only, and included road arm force, contact force due to wheel deflection, and force due to the track restricting the downward motion of the wheel. The horizontal forces incorporated in the model were only due to track tension in the inclined front and rear track segments, but were assumed to be algebraically balanced. Computer program employed MIMIC simulation language for solving differential equations of motion, which allowed for variations in the vehicle parameters. The predicted response time histories were compared against field measurements with some apparent success. Although program was developed for tank dynamics, it has been applied to a 3/4-ton truck and the combat tracked vehicle signature duplicator, CTVSD.

Smith [28] studied the ride dynamics of a farm tractor via a three-dimensional thirteen-degrees-of-freedom mathematical model having five-degrees-of-freedom (lateral, bounce, and three rotational) for the tractor chassis; roll-degree-of-freedom for front axle assembly; six-degrees-of-freedom (three translational and three rotational) for the cab; and a pitch-degree-of-freedom for the driver's seat. The tire-terrain interaction was modeled based on the radially segmented discrete springs as proposed by Lessem and Murphy [24] and tire vertical viscous damping. Lateral tire forces were modeled by parallel combination of a linear spring and damper. Cab mount forces and seat suspension forces were modeled based on the experimentally measured force-deflection and force-velocity relations. The ride model was extensively used to study the effect of a wide variety of design changes on the ride.

Hoogterp [29] developed a ride simulation model incorporating vertical and pitch motions of the sprung mass as well as the vertical motion of each road wheel. The vehicle suspension and road wheels were modeled as linear vertical springs and dampers. The ride model also allowed for a pair of wheels to be joined in tandem arrangement, and the inclusion of a fifth wheel type trailer hitch with full pitch freedom. Although the proposed ride model was suitable to simulate wheeled vehicles only, it was employed to simulate tracked vehicles while ignoring track dynamics altogether. Computer simulations of two military tracked vehicles crossing over various rough terrain were validated against field tests in terms of driver's comfort limiting velocity as a function of terrain roughness. Results indicated the obvious that comfort limiting velocity decreases for rougher terrains.

Captain *et al.* [30] presented a comparative study with an aim to demonstrate the influence of analytical tire model on the ride predictions of a wheeled vehicle subjected to rough, rigid terrain undulations. Four basic tire models suitable for ride dynamic simulation were adopted and formulated, namely, *point contact*, *rigid tread band*, *fixed foot-print* and *adaptive foot-print*. The tire models were compared through a ride simulation of a 5 ton, 6x6 cargo truck, which is a three-axle military truck having an independent suspension in the front and bogie suspension in the rear. The truck was modeled as a six-degrees-of-freedom dynamical system having pitch and bounce motions associated with vehicle sprung body, bounce motion of front wheel and axle assembly, and bounce (for wheel pair) and pitch motions for rear bogie assembly configuration. This study concluded that the point contact and rigid tread band model consistently over-estimate the transmitted vertical tire

forces, particularly in the frequency range 1-100 Hz, while the fixed foot-print under-estimates them. Adaptive foot-print tire model showed a relatively closer agreement with the field-measured tire force spectra.

Garnich and Grimm [31] proposed an in-plane ride simulation model for a M-60 battle tank crossing discrete half-round obstacle of specified radius at constant forward speed. The vehicle was modeled as an eight-degrees-of-freedom dynamical system, incorporating the vertical and pitch motions of hull, and rotational motion for all six road arm and wheel assemblies. The torsion bar suspension configuration was modeled as a constant rate torsional spring, while the inclined shock absorber mounted at the first and the last road wheels were replaced by equivalent viscous torsional dampers in parallel with torsional spring. The road wheels were represented by discrete radial springs and dampers and overloading springs were used to model bump stops. Track dynamics was represented by four different track tension effects : (i) *Global Track Tension* - an uniform overall track tension caused by stretching of the track belt, (ii) *Drive Sprocket Induced Tension* - estimated from an average applied torque as the vehicle passes over a half-round obstacle, (iii) *Track Bridging Effect* - caused by the track creating a flexible bridge spanning terrain discontinuities, and (iv) *Tension due to Track Compensating Linkage* - induced by a compensating link between idler and adjacent road wheel, so that as road wheel moves up, idler moves forward to take up slack in the track. The global track tension was found to cause substantial changes in vehicle dynamic response to large discrete obstacles which created high track tension magnitude and significant road wheel-terrain separation.

Crolla *et al.* [32] investigated the ride dynamics of three different

non-suspended wheeled vehicles employed for agricultural use, namely, tractor and plough, tractor and trailer, and farm transport truck. The purpose of these investigations was two-fold: (i) to study the effect of cultivation implements and trailers on the ride dynamics of agricultural tractor, and (ii) to study whether an industrial dump truck adopted for agricultural transport would offer any advantages over a typical tractor-trailer vehicle in terms of ride comfort. Authors developed three in-plane ride models: four-degrees-of-freedom model for the tractor and 3 furrow plough, six-degrees-of-freedom model for the tractor and trailer considering compliant hitch, and three-degrees-of-freedom model for the truck. Results indicated that tractors are grossly affected by the addition of implements and trailers. Unlike the trailer, the addition of plough was shown to dampen the tractor pitching significantly, thus reducing vertical ride vibration. The farm transport truck was shown to provide comfortable ride in comparison with a tractor and trailer, especially for laden configurations. The results were partially verified based on field measurements. This study demonstrated that simple ride models in conjunction with an appropriate tire-terrain representation can be very useful in understanding the ride behaviour of non-suspended wheeled off-road vehicles.

Craighead and Brown [33] proposed ride dynamic models for a 25 ton articulated dump truck, and a Vickers Mk 3b/3 battle tank. The dump truck was modeled as a six-degrees-of-freedom dynamical system (bounce and pitch motions associated truck sprung body, bounce motions of front and rear axle assemblies, and roll motions of tractor and trailer units). Vehicle suspension units were modeled considering nonlinearities associated with spring and damping effects, whereas tire units were

modeled as parallel combination of vertical springs and dampers. Articulation between tractor and trailer units was considered as a constant torque coupling rolling motions of both units. The military tank was initially modeled considering fifteen-degrees-of-freedom (bounce, pitch and roll motions of hull, vertical motions of twelve independent trailing arm-road wheel assemblies). However, it was found that roll contributes significantly less to ride discomfort. Thus, the ride model was reduced to an in-plane representation removing roll and six road wheels degrees-of-freedom, and the computing time was considerably reduced. Track contribution was realized as a phenomenon restricting the downward motion of road wheels, and nonlinearities associated with torsion-bar suspension system were incorporated in the ride model. Simulation runs were made to predict ride dynamic response for the vehicles traversing discrete triangular bumps and an arbitrary terrain profile at constant speeds.

McCullough and Haug [34] extended the concept of super-element representation of recurring subsystems in mechanical systems to model a typical high mobility tracked vehicle. The running gear subsystems, including the track, drive sprocket, idler, road wheels and road arms, were defined as super-elements. The model incorporated the track tension, track-wheel-ground forces, track connectivity and bridging, and primary suspension forces. In particular, the track tension was obtained based on the catenary equation approximating the relationship between track tension and the length of track hanging between drive sprocket and idler. The track belt stretching was also accounted for in conjunction with a simple relaxation of ideal catenary equation. The super-element modeling strategies were used in conjunction with the multi-body computer code

DADS for the purpose of simulation and shown to be much faster than the conventional multi-body approach. Based on an in-plane ride simulation of a military armoured personnel carrier crossing an 8-in semicircular obstacle, it was shown that the inclusion of track bridging in the track model contributes to an improved ride quality.

Krupka [35] formulated a comprehensive three-dimensional mathematical model of a military battle tank. The tank was treated as three distinct bodies, each having six-degrees-of-freedom: the hull, the turret, and the main gun. The equations of motion were derived using Lagrangian formulation. All three rigid bodies were connected by a set of kinematic constraints, which provide the physical interface of the system. The main emphasis of proposed model was to study the dynamics associated with gun such as gun bending effects, etc. This study, however, did not report any simulation results.

Bennett *et al.* [36] proposed an in-plane tracked vehicle ride model having three-degrees-of-freedom (pitch, bounce and longitudinal) for the hull, and bounce degree-of-freedom for each road wheel. The suspension compliances were modeled as main spring element (torsion bar), bump and rebound stops, and road wheel stiffness. Friction damping and damping due to shock absorbers (if applicable) were introduced at all road wheel stations. The mass of the track portion resting on drive sprocket and idler was added to the sprung mass. The track was considered as a light string with an exponential elastic characteristics measured from an initial fitted track tension. The predicted response time histories of a battle military tank crossing discrete obstacles were validated against the measured results obtained from field testing of an actual vehicle, and one-eighth scale model.

Craighead *et al.* [37] conducted field tests for the purpose of validating the ride simulation models for a DJB D25 dump truck and a Vickers Main Battle Tank. Details of the mathematical models are reported in ref. [33]. Both vehicles were driven over an assortment of triangular rigid obstacles, and vehicle speed and ride acceleration data was gathered. For specified test conditions, simulations were performed based on the point-contact representation of the wheel/track-terrain interaction. But, it was found necessary to use more sophisticated wheel/track models to achieve closer correlation between computer predictions and field measurements. Consequently adaptive foot-print model [24] was employed to represent the wheel/track-terrain interaction, and corresponding simulation results showed a relatively better agreement with field measurements. Ride comfort of both vehicles was assessed in terms of a vibration dose value (VDV) computed from both predicted and measured bounce ride acceleration traces. The predicted vibration dose values were found to be within 25% of the measured value.

In 1986, Creighton [38] reported an improved version of the AMC-74 Vehicle Ride Dynamic Module, VEHDYN [25]. The revised ride prediction module, referred to as VEHDYN II, is currently used for general use in support of the NATO Reference Mobility Model (NRMM), where NRMM was, in fact, a new name given to the Army Mobility Model (AMM) in 1978 following its acceptance as a standard reference by a NATO working group composed of representatives from the United States, Canada, France, Germany, the United Kingdom, and the Netherland [38]. NRMM is a comprehensive computer code mainly used for evaluating the cross-country mobility performance of military vehicles [39,40]. Like VEHDYN, VEHDYN II predicts the gross motions of a tracked or wheeled vehicle traversing an arbitrary non-

deformable terrain at a constant forward speed, and computes an average absorbed power (ride performance criterion) and peak vertical acceleration value at the driver's location or any other specified location in the vehicle (shock performance criterion). Basic vehicle-terrain simulation model is the same as in VEHDYN, however, the analytical models for sub-systems, such as suspension spring and damping characteristics, and dynamic wheel-track-terrain interaction were modified in view of model improvement. In particular, the dynamic wheel/track-terrain interaction characterizing the net foot-print at the wheel-terrain interface was modeled using the concept of a continuous ring of radial spring instead of discrete radially segmented group of springs. The dynamic track tensioning effects were further enhanced by incorporating track feeler-terrain interaction, which employed a hypothetical linear spring placed perpendicular to the feeler at the location of maximum displacement due to interaction with terrain profile. In addition, the height of the vehicle and horizontal force effects were incorporated.

Afonso [41] investigated the ride dynamics of a typical high mobility tracked vehicle subjected to deterministic and random terrain excitations. Two in-plane ride models of a five-wheeled tracked vehicle were developed in view of primary suspension modeling strategies: first model with idealized parallel combination of springs and dampers while ignoring the kinematics associated with conventional torsion bar/trailing arm suspension; and second model with kinematic considerations. Both models were represented as seven-degrees-of-freedom dynamical system (bounce and pitch motions of vehicle sprung mass, and bounce motion of each road wheel). The nonlinearities due to damping characteristics of the shock absorbers, Coulomb friction and bump stops were considered. The

road wheel was assumed to have point contact with ground, whose equivalent vertical stiffness was computed based on in-series wheel and track pad springs. The contribution of track dynamics to the vehicle ride response was modeled using linear vertical springs as proposed by Lessem and Murphy [24]. Main highlight of this study was the development of a linearized frequency-domain ride model in addition to a non-linear time-domain model. An energy-based linearization technique [42] was employed in the frequency-domain analysis. This study revealed that the inclusion of track, and the trailing arm suspension model with kinematic considerations contribute to an improved ride quality.

A time-domain simulation model for predicting ride quality of wheeled and tracked off-road vehicles was recently proposed by Galway [43]. A ride model was formulated assuming rigid deterministic terrain profile and constant vehicle speed. The vehicle was modeled as a three-degrees-of-freedom dynamical system (bounce, pitch, and roll motions of vehicle sprung body) equipped with nonlinear models of independent and trailing arm/torsion bar suspension configurations. The trajectories of road wheel centres were computed prior to the simulation, where filtering effects of road wheel traversing deterministic terrain profile were considered. Track tensioning effects were modeled based on the assumption of an inelastic track belt, while ignoring track belt extensibility. A pseudo-catenary approximation of the track segment hanging between drive sprocket and idler was used in the computation of track tension. The ride model was validated against field measurements of an armoured personnel carrier traversing a concrete sinusoidal course at 8 km/h, and also compared with results predicted by VEHDYN II [38]. Ride quality predictions showed relatively close agreement with field-measured ride

data (less than 27% difference), while VEHDYN II results overpredicted ride severity by as much as 112%.

As observed from previous studies, the terrain surfaces are usually considered rigid or non-deformable for ride dynamic study of off-road vehicles since deformable surfaces tend to reduce the ride severity. The mobility performance of an off-road vehicle over a rigid terrain is primarily dictated by the driver's ability to withstand the transmitted vibration and shock. However, terramechanics involving wheel/track-terrain interactions such as sinkage and ground compaction has also drawn considerable attention in the past. Most studies focussed only on the mobility/tractive performance of high-speed tracked vehicles. Vodyanik [44] developed a set of force equations describing the soil-track interactions. Kogure [45] focussed on the external motion resistance of a tracked vehicle due to sinkage/compaction of underlying soil. More recently, Wong [46] proposed a computer model for predicting the ground pressure distribution and tractive performance of tracked vehicles over snow and sand.

1.2.3 Ride Assessment Criteria

Ride quality is concerned with the driver's sensation or feel in the dominant terrain-induced vibration environment of a vehicle, and is generally difficult to determine. Considerable research has, however, been conducted by a number of investigators to establish ride assessment criteria for the preservation of driver's comfort, health and safety, and performance. These criteria take into account four parameters, namely, intensity of vibration, frequency of vibration, exposure time, and axis of application to the body. These criteria have been proposed for exposure to whole body vibration through subjective ride assessment,

shake table tests, ride simulator experiments and ride measurements in vehicles [47]. In general, these methods attempt to correlate the response of test objects in qualitative terms, such as *uncomfortable* and *extremely uncomfortable* in terms of vibrational parameters such as displacement, velocity, acceleration, and jerk over the frequency range of interest. The assessment of human response to vibration is complex in that the results are influenced by the variations in individual sensitivity, and the diversity of test methods and sensation levels used by different investigators [48]. Over the years, numerous ride comfort criteria have been proposed, however, a generally acceptable criterion is yet to be established. Some of the proposed ride criteria are summarized as follows.

Earlier investigations on human body response to vibration were primarily carried out using subject-shake table experiments with vertical sinusoidal vibrations [49]. In 1947, Dieckmann [50] proposed a constant "K" related to comfort zones and fatigue time limits for passenger car vibrations. The Dieckmann's constant, K, is based on levels of constant acceleration upto 5 Hz, constant velocity from 5-50 Hz, and constant displacement above this frequency. The Dieckmann's criterion is summarized by the following formulae:

$$K = \begin{cases} df^2 & ; \ 0 \le f \le 5 \text{ Hz} \\ 5df & ; \ 5 \le f \le 50 \text{ Hz} \\ 200d & ; \ 50 \le f \le 200 \text{ Hz} \end{cases} \qquad (1.1)$$

where d is the peak displacement amplitude in millimeters, and f is the frequency in Hz. The comfort zones are defined as:

$$K = \begin{cases} 0.1\text{-}1 & : \text{imperceptible to slightly uncomfortable} \\ 1\text{-}10 & : \text{slightly disagreeable to disagreeable with a fatigue time of 1 hour} \\ 10\text{-}100 & : \text{very disagreeable to exceedingly disagreeable with a fatigue time of 1 minute} \end{cases}$$

Goldmann [51] averaged vibration data from seven sources in 1948, and established three comfort levels for automotive passenger: *perceptible*, *unpleasant*, and *intolerable*, as a function of frequency and peak acceleration response in the vertical mode. The vibration data used by Goldmann were obtained from a variety of experiments where the subjective and physical environments varied greatly.

In 1948, Janeway [52] recommended exposure limits to passenger car vertical vibration, which are expressed as:

$$J = \begin{cases} 1/6\ df^3 & ;\ \text{for } f = 1\text{-}6 \text{ Hz} \\ df^2 & ;\ \text{for } f = 6\text{-}20 \text{ Hz} \\ 20\ df & ;\ \text{for } f = 20\text{-}60 \text{ Hz} \end{cases} \qquad (1.2)$$

where d is the peak displacement amplitude in inches. This criterion differs from Dieckmann's in that the range 1-6 Hz is constant jerk; from 6-20 Hz is constant acceleration; and from 20-60 Hz is constant velocity.

A comparison of the Dieckmann, Goldmann, and Janeway ride criteria revealed that the human is most sensitive to vertical vibration below 20 Hz [49]. Although reasonable similarity in the proposed comfort criteria has been shown with respect to input frequency, the subjective response data provides an insufficient and inconsistent criteria in view of vibration intensity. The validity of these subjective tests is questioned due to a multitude of inconsistencies, namely semantic problems, age and moods of subjects at the time of experiments, etc.

Since these criteria have been established based on sinusoidal vibrations at a constant frequency, their application to assess the vehicle's random ride vibrations is questionable. However, Butkunas [53] attempted to apply the proposed comfort criteria to random vibration enviroments of vehicles.

The German *k*-factor, as a measure of vibration intensity and a function of frequency and rms acceleration, velocity or displacement, was proposed based on subjective assessment [54]. The *k*-factor is evaluated according to the following formulae:

$$k = \alpha \frac{\alpha_1}{\sqrt{1 + (f/f_o)^2}} \tag{1.3}$$

$$k = \nu \frac{\alpha_2 f}{\sqrt{1 + (f/f_o)^2}} \tag{1.4}$$

$$k = \sigma \frac{\alpha_3 f^2}{\sqrt{1 + (f/f_o)^2}} \tag{1.5}$$

where α is the rms acceleration (m/s^2), ν is the rms velocity (mm/s) and σ is the rms displacement (mm), and constants are: f_o= 10 Hz, α_1= 18 ($k/m/s^2$), α_2= 0.112 ($k/mm/s^2$) and α_3= 0.71 ($k/mm/s^2$). The *k*-factor criterion has been actively applied in Germany for approval or rejection of agricultural tractor seats, and must have a value of 25 or less to be acceptable.

In 1965, based on a purely mechanical approach (ride simulator tests) while excluding subjective evaluation, Lee and Pradko [55] proposed a scalar quantity called *absorbed power* for subjective assessment of ride severity. The absorbed power is a measure of the average rate at which

energy is dissipated by the human body as a result of the complex damped elastic properties of the anatomy. Average absorbed power is determined from the intensity and frequency of the input sinusoidal vibration as [56]:

$$P = \sum_{i=1}^{n} \mathcal{K}_i a_i^2 \tag{1.6}$$

where P is the average absorbed power (watts), a_i is the rms acceleration at frequency i (ft/s^2), and n is the number of discrete harmonic frequencies. $\mathcal{K}_i$, the absorbed power constant of the body at frequency i, is expressed through an empirical relation for vibration along each of three translational axes as:

$$\mathcal{K}_i = 1.356\ k_0 \left[\frac{F_1 F_4 - F_2 F_3}{F_3^2 + \omega_i^2 F_4^2} \right] \tag{1.7}$$

where ω_i ($= 2\pi f_i$) is the frequency in rad/s, and remaining quantities are derived from the experimental data. For instance, they are given for vertical vibration as follows [56]:

$k_0 = 4.35373$

$F_1 = -0.10245296 \times 10^{-9}\omega_i^6 + 0.17583343 \times 10^{-5}\omega_i^4 - 0.44600722 \times 10^{-2}\omega_i^2 + 1.0$

$F_2 = 0.12881887 \times 10^{-7}\omega_i^4 - 0.93394367 \times 10^{-4}\omega_i^2 + 0.10543059$

$F_3 = -0.45416156 \times 10^{-9}\omega_i^6 + 0.37667129 \times 10^{-5}\omega_i^4 - 0.56104406 \times 10^{-2}\omega_i^2 + 1.0$

$F_4 = -0.21179193 \times 10^{-11}\omega_i^6 + 0.5172811 \times 10^{-7}\omega_i^4 - 0.17946748 \times 10^{-3}\omega_i^2 + 0.10543059$

For exposure to multi-axes vibrations, ride severity is assessed by the scalar sum of absorbed power associated with each of three translational axes.

The concept of absorbed power is appealing due to its simplicity that it provides a single number rating of the ride environment, which is function of the vibratory modes, intensities, frequency contents, and body orientation, posture, etc. This criterion is also supported by the Janeway recommended safe limits [52] in the low frequency range i.e. the 2.7 W power curve coincides very closely with the Janeway limit up to about 5 Hz [57]. Average absorbed power in the range 6-10 W is considered acceptable for off-road vehicles, and has been extensively used to assess military vehicle ride.

The International Organization for Standardization has set forth three vibration exposure criteria (ISO-2631) as a function of exposure time in the frequency range 1-80 Hz, under vertical (*bounce*) and horizontal (*longitudinal & lateral*) vibrations [58]. The proposed exposure limits are: (i) *Health and Safety Limits* for occupational exposure, (ii) *Fatigue Decreased Proficiency Limits* associated with preservation of working efficiency, and (iii) *Reduced Comfort Limits* for ride comfort. Figure 1.3 shows the *fatigue decreased proficiency* rms acceleration limits in 1/3 octave frequency bands up to 80 Hz for various exposure times to vertical and horizontal vibration. As shown, minimum tolerance is in the 4 to 8 Hz range for vertical vibration and is below 2 Hz for horizontal vibrations, and human tolerance of vibration decreases with increasing exposure time.

Smith [59] proposed a procedure to convert the ISO guide to a form usable for direct comparison with ride vibration data presented in power spectral density (PSD) form. The ISO boundaries as shown in Figure 1.3, are straight line segments on log-log plots of the form,

$$\log \bar{a}(\bar{f}) = m_1 \log \bar{f} + b_1 \qquad (1.8)$$

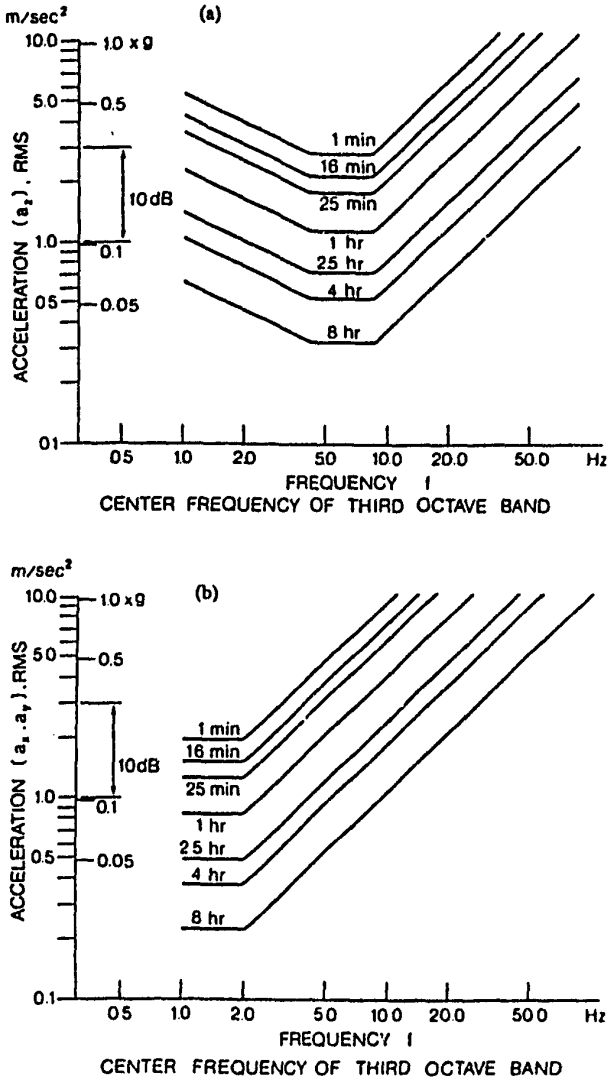

Figure 1.3 ISO specified limits of whole-body vibration for fatigue decreased proficiency in (a) vertical direction, and (b) transverse direction [2].

where $\bar{a}(\bar{f})$ is the rms acceleration value at centre frequency, $\bar{f}$, and m_i and b_i are the slope and intercept respectively, for the i^{th} segment. By definition, the average PSD is expressed as,

$$\bar{S}(\bar{f}) = \frac{\bar{a}^2(\bar{f})}{0.23\ \bar{f}} \tag{1.9}$$

Taking the logarithim of Eqn. (1.9) and substituting Eqn. (1.8) yields the ISO boundaries in terms of PSD's also consisting of straight line segments [59],

$$\log \bar{S}(\bar{f}) = (2m_i - 1)\ \log \bar{f} + (2b_i - \log 0.23) \tag{1.10}$$

The ISO-2631 ride assessment criteria is most widely accepted, and is applicable to whole-body vibration. However, the standard fails to quantify ride criteria under rotational modes of vibration. ISO has also proposed weighting factors in the frequency range 1-80 Hz in order to quantify the ride quality by a single number. In this method, the measured ride vibration is frequency weighted using the filters to compute an overall root mean square (rms) acceleration value. This method of assessing the ride has been gaining popularity due to its simplicity. However, there has been a growing controversy associated with the measurement procedure, and vibration limits proposed in ISO-2631. For instance, a study by Boileau *et al.* [60] demonstrated the limitations of ISO-2631 for assessment of off-road vehicle vibrations with high crest factors (≥ 6). The concept of "vibration dose value (VDV)" based on fourh power criteria has been introduced by Griffin [61] for assessing ride comfort of off-road vehicle vibration with high crest factors. It provides a single-number rating which represents the cummulative effect of the vibration over time, and is defined as [61],

$$VDV = \left[\int_0^T a^4(t)\, dt \right]^{1/4} \quad (ms^{-1.75}) \qquad (1.11)$$

where $a(t)$ is the frequency-weighted instantaneous acceleration (m/s^2), and T is the integration or exposure time in seconds. The "fourth power" criteria has been recently accepted for inclusion in the new draft of ISO-2631 guide.

1.3 SCOPE OF THE PRESENT STUDY

A review of existing literature reveals that a number of simulation models have been developed to study the ride dynamics of various tracked and wheeled off-road vehicles largely employed for high-speed military operations. In particular, subsystems of the basic vehicle-terrain dynamical model, such as wheel and track models, have been developed employing analytical techniques of varying complexities. A few of the proposed ride simulation models have been validated against field measurements with some apparent success. These studies have shown that a worthwhile ride dynamic simulation of off-road vehicles traversing rough, rigid terrain undulations generally demands good analytical models for vehicle suspension systems and dynamic wheel-track-terrain interactions. It was pointed out earlier in this chapter that vehicle-terrain analytical modeling and ride simulation using general-purpose software (DADS, ADAMS, etc.) is, however, tedious and expensive. Consequently, development and employment of specialized analytical models with efficient computational algorithms is the most effective approach to study the ride dynamics of a specific type or class of off-road vehicle(s).

Majority of existing simulation models were primarily developed to

study the ride dynamic behaviour of a specific type of off-road vehicle (either tracked or wheeled) with the exception of ride model employed in VEHDYN II code [38]. But, almost all ride models have certain limitations in view of subsystem modeling, e.g. certain tracked vehicle ride models incorporated a comprehensive analytical representation of the wheel-terrain interaction but under-estimated the dynamic track loads; or the vehicle suspension system was idealized; or the ride model was specifically formulated for only certain types of terrain profile. The best of proposed wheel and track models for ride simulation purposes, especially the adaptive foot-print wheel model [30,38], and the track model by McCullough and Haug [34] can be still further improved in view of quick and accurate ride predictions. The reviewed literature did not indicate any study comparing various wheel and track models in view of analytical comlexity (cost) and simulation realism (in reference with field measurements), so that the relative performance of ride simulation models of off-road vehicles (especially tracked) can be assessed. Field validation of only a few of previous ride models have been performed. In general, field validation of previous ride models is considered not comprehensive due to such reasons as the use of a reduced-scale prototype of the vehicle rather than the actual vehicle, or only discrete obstacles as the test courses, etc.

Consequently, the scope of current research program is built based on the above-mentioned considerations, and the objectives are outlined as follows.

1.3.1 Objectives

The overall objective of this study is to contribute to the improvement of ride, thus mobility performances of wheeled/tracked off-road

vehicles primarily employed for high-speed operations. This is sought via the development of a comprehensive time-domain ride dynamic simulation model, model validation using field test data, and refinement of the ride simulation model. The ride model, thus evolved, would be an effective, accurate and inexpensive design tool to study and improve the ride dynamic behaviour of an off-road vehicle.

Proposed ride simulation model (RIDSIM) is to be formulated considering the following:

- A variety of suspension configurations such as *unsprung*, *independent*, *walking beam* and *bogie* suspension systems will be included. In addition, a detailed analytical model for the *torsion bar/trailing arm* suspension system largely employed for high mobility tracked vehicles is to be incorporated. The ride model, thus developed, could be conveniently employed to simulate ride and suspension dynamics of a wide variety of off-road vehicles.
- An effective wheel model to characterize the wheel/track-terrain interaction will be considered. The wheel model is to be formulated based on an improved adaptive foot-print concept.
- An effective track model to characterize the dynamic track loads will be included. The track model is to be formulated considering track pre-tension, track sag and stretching, track bridging, wheel-track-terrain separation and an appropriate definition of wheel-track connectivity.
- An effective algorithm to establish *zero-force and static equilibrium* configurations of the vehicle prior to the simulation will be developed.

The sequence of steps adopted to meet the objectives of this study

are as follows:

1. Selection of a candidate off-road vehicle and courses for the purpose of field testing.
2. Development of a preliminary ride model of the candidate vehicle (MODEL I). This model would: (a) assist in devising an appropriate test plan such as a range of safe vehicle speeds for specified test courses, and (b) serve as a reference for the development of the proposed ride simulation model (RIDSIM).
3. Lay-out of a test plan for field testing of the candidate vehicle, indicating appropriate instrumentation/equipment and their locations and mounting methods, and a detailed outline of test runs in view of vehicle configurations, test courses, and vehicle speeds.
4. Field testing of the candidate vehicle as dictated by the test plan, and conditioning and reduction of the acquired field measurements.
5. Field validation of MODEL I, and identification of potential modeling improvements in the preliminary ride model.
6. Refinement of the ride model in view of its subsystem modeling strategies primarily associated with wheel and track (MODEL II). Field validation and assessment of MODEL II.
7. Formulation of wheel and track models employed in previous studies [30,34,38] to carry out ride performance evaluation of the candidate vehicle with MODEL II. Comparison of different wheel and track models based on the field validation of ride predictions.
8. Development of a refined ride model for the candidate vehicle in view of the detailed kinematics of vehicle suspension system (MODEL III).
9. Assessment of MODEL III with respect to field measurements and MODEL II. Carry out a *parametric sensitivity* analyses to study the

influence of vehicle suspension and wheel parameters on the ride dynamics of the candidate vehicle.

10. Development of a multi-purpose ride simulation model, RIDSIM, based on the modeling strategies adopted for the candidate vehicle.

The present research project has been conducted over the past three years and has resulted in several publications as listed in Ref. [62-67].

1.3.2 Organization of the Thesis

In Chapter 2, configuration of a candidate off-road vehicle adopted for this study, is described. A preliminary ride dynamic model of the candidate vehicle (MODEL I) is developed employing simplified yet credible mathematical formulations of subsystems of the basic vehicle-terrain dynamical systems. Details and assumptions associated with the modeling of vehicle suspension system, wheel, and track are provided. The mathematical procedure to compute vehicle's *zero-force* and *static equilibrium* configuration is derived. The structure of computational procedure adopted to perform the simulation is described. MODEL I developed in this Chapter, is intended to assist in devising an appropriate test plan for field testing, and serve as a reference model for the development of the multi-purpose ride simulation model (RIDSIM).

In Chapter 3, details regarding field testing, such as description of test vehicle and courses, instrumentation/equipment, their locations and mounting methods, and sequence of test runs in view of test vehicle configurations, test courses and vehicle speeds, are provided. The computational procedure adopted for the conditioning and reduction of field measurements is presented. An overview of the field-measured ride response is provided. For specified test conditions, computer simulations are performed with MODEL I, and ride predictions are directly compared

with the field measurements. Limitations of MODEL I assessed based on the field validation results, are discussed.

In Chapter 4, MODEL I is refined in view of its subsystem modeling strategies primarily associated with wheel and track. The refined ride model, termed as MODEL II, is described along with details of improved wheel and track models. Field validation of MODEL II is carried out. Various wheel and track models considered in previous studies [30,34,38] are integrated into MODEL II, and the ride performance of the candidate vehicle is evaluated and compared with field-measured ride data in order to assess the relative performance of different wheel and track models.

The ride prediction models, MODEL I *and* MODEL II, are formulated assuming an *idealized* independent configuration of vehicle primary suspension system. In Chapter 5, the suspension linkage kinematics is developed along with refined wheel and track models. The new ride model, termed as MODEL III, is assessed based on the field validation results. MODEL III is, then, employed to carry out a parametric sensitivity analyses to demonstrate the influence of vehicle suspension and wheel parameters on the ride dynamic behaviour of the candidate vehicle. In addition, simulations are performed with hydrogas suspension in order to assess its ride performance potentials.

In Chapter 6, a multi-purpose ride simulation model, RIDSIM, is developed primarily based on the modeling strategies employed for the candidate vehicle. The sub-model for vehicle suspension is formulated considering various suspension configurations which are commonly employed for off-road vehicles. Applications of RIDSIM are demonstrated with examples involving two different off-road vehicles. Finally, Chapter 7 presents general conclusions and some recommendations for future work.

Chapter 2

DEVELOPMENT OF A RIDE DYNAMIC MODEL FOR WHEELED/TRACKED OFF-ROAD VEHICLES

2.1 INTRODUCTION

In general, two methods are available for simulating ground vehicles for ride performance, namely, *frequency-domain* and *time-domain*. In comparison, the frequency-domain technique is a convenient and economical option, however, only suited for simulating vehicle ride models described through *linearized* equations of motion. Consequently, one has to make a number of simplifying assumptions in the formulation of ride model. The frequency-domain technique has been widely used to study the ride dynamic behaviour of road vehicles. However, the ride dynamic simulation of off-road vehicles in the presence of highly irregular terrain surface is only worthwhile, if the model is formulated considering the non-linear dynamic wheel-track-terrain interactions. These considerations in the analytical modeling lead to complex formulations which are characterized through a set of highly nonlinear coupled differential equations, and can only be solved in the time-domain using a direct integration technique.

In view of analytical modeling, a tracked off-road vehicle represents a more complex dynamical system, and requires special modeling considerations. In fact, the ride model of a tracked vehicle is developed similar to a wheeled vehicle, however, considering certain special requirements caused by the track. For the purpose of this study, a typical *tracked* off-road vehicle designed for high-speed operations, is selected. In this chapter, the selected vehicle configuration, termed as *candidate vehicle*, is discussed in view of its running gear and general characteristics. A building-block approach employing simplified yet credible formulations of vehicle suspension system, wheel, and track is

used to develop a ride dynamic model of the candidate vehicle, MODEL I. The systematic development of the ride model is presented along with underlying assumptions. The procedure used for performing digital computer simulation of the ride dynamic model is also outlined.

2.2 SELECTION OF A CANDIDATE OFF-ROAD VEHICLE

High mobility tracked vehicles such as battle tanks and armoured personnel carriers (Figure 1.2), designed for mobility over a wide range of terrain surfaces, impose severe ride environment due to dynamic wheel-track-terrain interactions. These vehicles, although varying widely in size, shape, and general physical appearance, share many common characteristics in the track and suspension assembly. Accordingly, for example, the physical description of an armoured personnel carrier can provide general information about other high mobility tracked vehicles. For the purpose of this study, a conventional armoured personnel carrier, M113 APC, is chosen as the *reference candidate vehicle* for model development and field testing.

Figure 2.1 shows various cross-sections of a typical M113 APC. The vehicle is supported by five road wheels on each track, where each road wheel is linked to the hull chassis via a torsion bar/trailing arm suspension, and each track is extended around the road wheels by the sprocket and idler located on either side of the hull. In view of general physical description, an M113 APC can be divided into track and suspension components, and hull components. The former group includes the track, road wheel and suspension assemblies and hull wheels (sprocket and idler), whereas the hull represents collectively all remaining components of the vehicle.

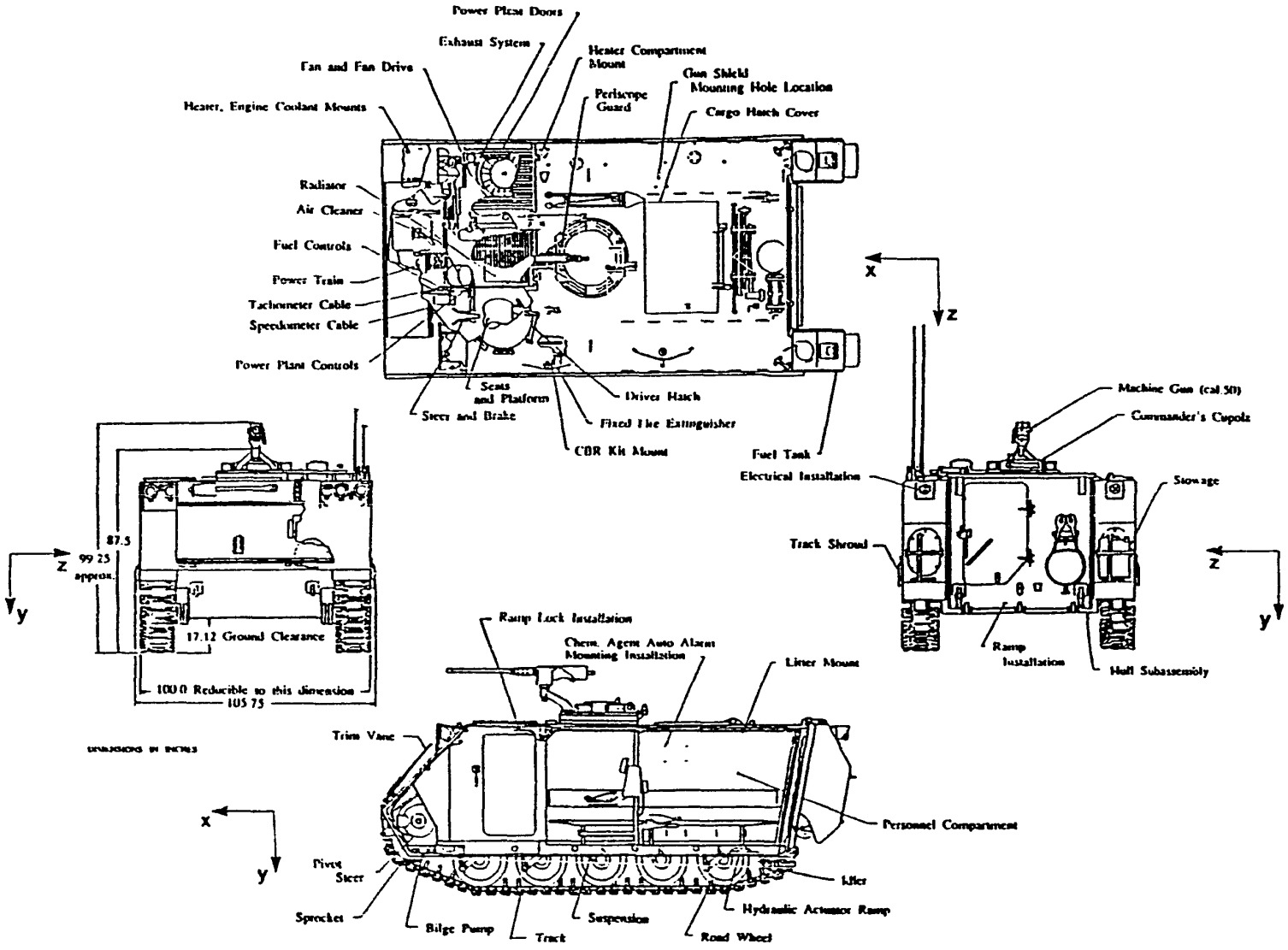

Figure 2.1 Cross-sections of a typical M113 APC [41].

Track

The M113 APC track consists of interconnected steel track shoes with synthetic rubber pads on their inner and outer surfaces. The right track on an M113 APC consists of 64 shoes, whereas the left track consists of 63 shoes. The track rubber pads help reduce the noise and vibration. The inner pads prevent metal-to-metal contact during the shoe-wheel interaction, while the outerpads soften the shoe-ground interaction, and protect paved roads from premature wear during vehicle operations over such surfaces. To prevent track disengagement, the track consists of track guides which mesh into the circumferences of road and hull wheels.

Two types of track, the single-pin and double-pin track, are widely used in high mobility tracked vehicles. The single-pin track consists of partially overlapping track shoes like door hinges, which are connected by a single pin as shown in Figure 2.2a. In the double-pin track, adjacent shoes are joined by a set of connectors and two pins (Figure 2.2b). Most M113 APC's are equipped with the German-made double-pin Diehl 213G track.

Road Wheel and Suspension Assembly

The road wheels have an all-metal body (hub, web, and tread) with a rubber tire vulcanized to the metal tread for vibration isolation, as shown in Figure 2.3a. Each road wheel is independently mounted to the hull by means of a road arm or trailing arm, and a torsion bar. As shown in Figure 2.3b, each road wheel is mounted on a road arm splined to a torsion bar, where the torsion bars extend over the width of the chassis. The shock absorbers are mounted between the hull chassis and the selected road arms at an inclined position (Figure 2.3a). At the upper and lower bounds of road arm travel, rubber bumpers are mounted to prevent the road

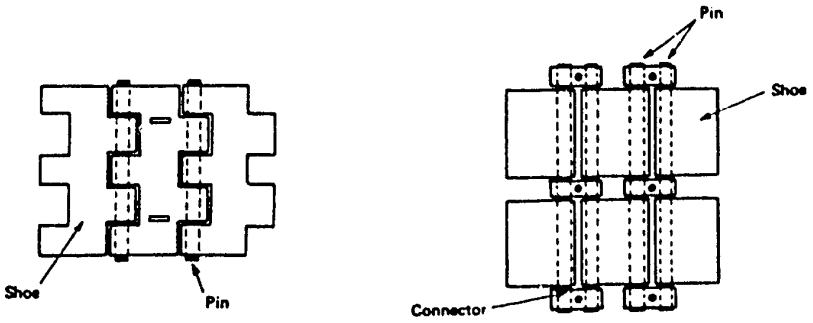

(a) Single-pin track. (b) Double-pin track.

Figure 2.2 Track classification [68].

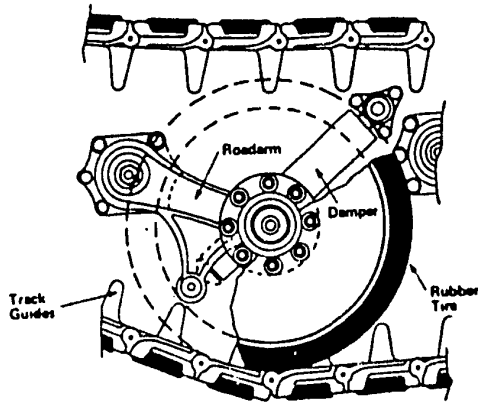

(a) Front road wheel and suspension assembly [68].

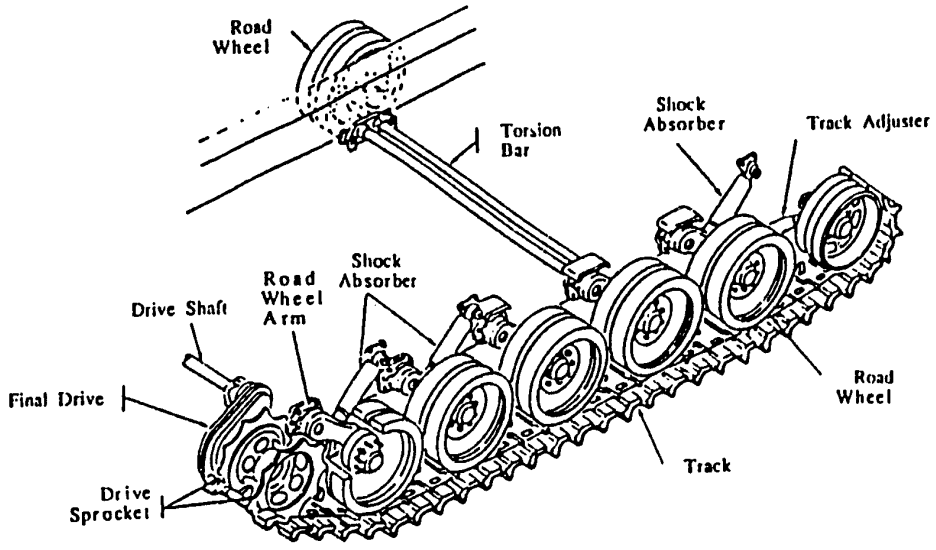

(b) An overview [courtesy of DND].

Figure 2.3 Schematic of road wheel and suspension assembly for M113 APC.

wheel from hitting the hull chassis and driving the track into the ground.

The M113 APC, in general, employs three primary suspension configurations, referred to as A1, A2, and A1$\frac{1}{2}$. All three suspension configurations employ trailing arm/torsion bar suspension at each road wheel. However, the A1, A2, and A1$\frac{1}{2}$ suspension designs differ in number and location of shock absorbers, torque-deflection characteristics of torsion bar, and force-velocity characteristics of shock absorbers. The A1 suspension configuration employs two shock absorbers at the first and last road wheel stations on each track of the vehicle. The A2 suspension utilizes three shock absorbers, located at first, second, and last road wheel stations, on each track of the vehicle. The torsion bars employed in A2 suspension are relatively softer than those employed in A1 suspension, while the shock absorbers used in A2 suspension offers higher damping forces than those used in A1 suspension. The A1$\frac{1}{2}$ suspension is a combination of A1 torsion bars and A2 shock absorbers i.e it employs three shock absorbers on each track, similar to the A2 suspension, and A1 torsion bars at all road wheels. Apart from the differences in suspension characteristics, the M113 A1, M113 A2, and M113 A1$\frac{1}{2}$ APCs exhibit certain variations in the vehicle geometry, and mass/inertia.

Hull Wheels - Drive Sprocket and Idler

The drive sprocket, which is connected to the vehicle engine through a drive train, develops the track tension necessary to set the vehicle in motion. It is hard-mounted to the hull, and normally located near the engine, which is near the front of M113 APC. The idler stabilizes the motion of the upper track strand and maintains the track segment past the last road wheel at a desirable slope. The idler is hard-mounted to the

hull near the back of the M113 APC. However, its position can be statically adjusted by means of a hydraulic actuator to increase or reduce the track pre-tension.

Hull

The hull is the primary superstructure of the vehicle which contains the engine room, driver's chamber, and the personnel compartment. The engine room, located by the side of the driver's chamber, contains vehicle power plant and power train. The power plant consists of 210 hp V6 Diesel engine and the transmission, which drives the sprocket, provides one reverse and three forward speeds. Steering manoeuvres are achieved via a differential mechanism while the braking is performed by pivot disc brakes. The fuel tanks may be mounted either externally or internally. The driver's chamber contains the steering, braking, and fuel controls. The personnel compartment of the hull has a capacity for twelve persons not including the driver. The compartment also allows for storage for ammunition and other cargo necessary for combat. On top of the hull, a machine gun and turret is mounted near the commander's cupola.

2.3 DEVELOPMENT OF NONLINEAR RIDE MODEL FOR CANDIDATE VEHICLE: MODEL I

In general, an off-road vehicle should be analytically represented through three-dimensional mathematical model incorporating six degrees-of-freedom for vehicle body mass center, appropriate number of degrees-of-freedom for each of the road wheel assemblies, and an additional degrees-of-freedom for driver and seat dynamical system and/or any other vehicle component considered as separate bodies. However, previous studies have demonstrated that an in-plane model provides sufficient information for detailed analysis of suspension dynamics and associated

shock and vibration environment of the vehicle.

For the purpose of this study, an in-plane ride dynamic simulation model of a high mobility tracked vehicle traversing an arbitrary but specified non-deformable terrain at a constant forward speed, is developed, and described in the following sub-sections.

2.3.1 Description of Vehicle Ride Model

The ride dynamic model is formulated as a "3+N" degrees-of-freedom dynamical system, where N is the specified number of road wheels on one side of the vehicle, and is equal to 5 for M113 APC. As shown in Figure 2.4, the ride model is two-dimensional with symmetry assumed about a plane defined by a vertical axis and the vehicle's longitudinal axis, incorporating two degrees-of-freedom (pitch and bounce) associated with vehicle sprung body (hull) and an optional vertical degree-of-freedom for the driver and seat. Each road wheel and axle assembly is represented by a lumped unsprung mass with a vertical degree-of-freedom. The vehicle suspension units are modeled using *idealized* independent suspension configuration, which is a parallel combination of vertical spring and damper, whose characteristics can be either linear or nonlinear, and are described through look-up tables. Each road wheel resting on the track pad is represented by a continuous radial spring, and an equivalent damper model. The sprocket and idler are also treated similarly, when they come in contact with the terrain. The track is modeled as a continuous elastic belt capable of transmitting only tensile forces.

2.3.2 Description of Terrain Profile

The representation of the terrain is an integral part of the

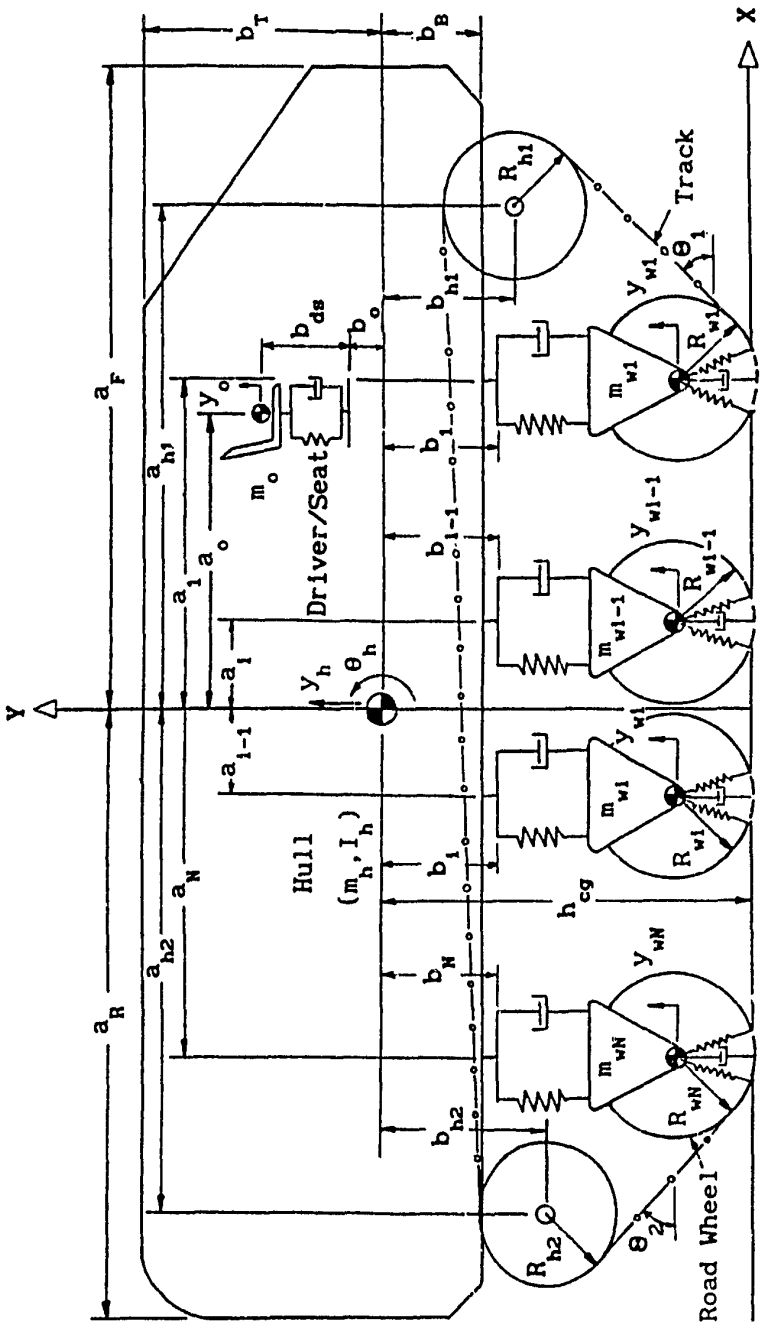

Figure 2.4 In-plane model representation of a typical high mobility tracked vehicle employing idealized independent suspension configuration.

formulation of dynamic wheel-track-terrain interaction. For this study, the terrain profile is assumed to be non-deformable and is described by linear segments adjoining the horizontal and vertical coordinates of successive points on the profile. Consequently, the terrain profile is described through a look-up table containing horizontal and vertical coordinates of successive points, which are either equally or unequally spaced. The intermediate profile points are determined based on linear interpolation assuming a continuous profile.

The vehicle is positioned on a flat ground prior to the rough section, as illustrated in Figure 2.5. Therefore, the entire horizontal range of the profile section left to the first profile point is made flat by adding an extra point which has a large negative value of horizontal coordinate (e.g. X = -1000 m) and same elevation as the first point. Similarly, the entire horizontal range right to the last profile point is made flat by adding another profile point at X = 1000 m, which has the same elevation as the last profile point.

2.3.3 Equations of Motion

The dynamic equations governing the bounce (y_h) and pitch (θ_h) motions of the hull, the bounce motion of the i^{th} road wheel assembly (y_{wi}, i=1,2,..,N), and bounce motion of the driver/seat (y_o) are written based on Newton's second law of motion, and are expressed from the vehicle's zero-force position. The zero-force reference is chosen over the static equilibrium reference so that the influence of gravity term can be incorporated for an effective simulation of the vehicle-terrain contact loss. Consequently, equations of motion are given as (refer to Figures 2.4 and 2.6):

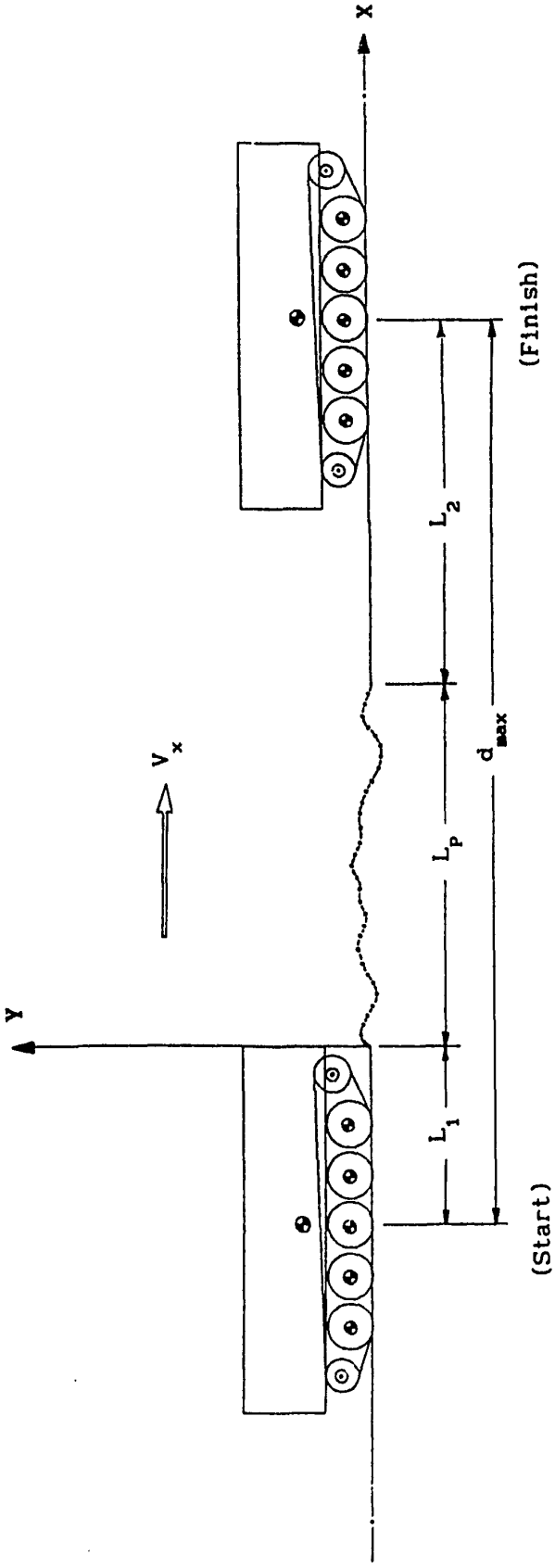

Figure 2.5 Terrain profile description and vehicle positioning.

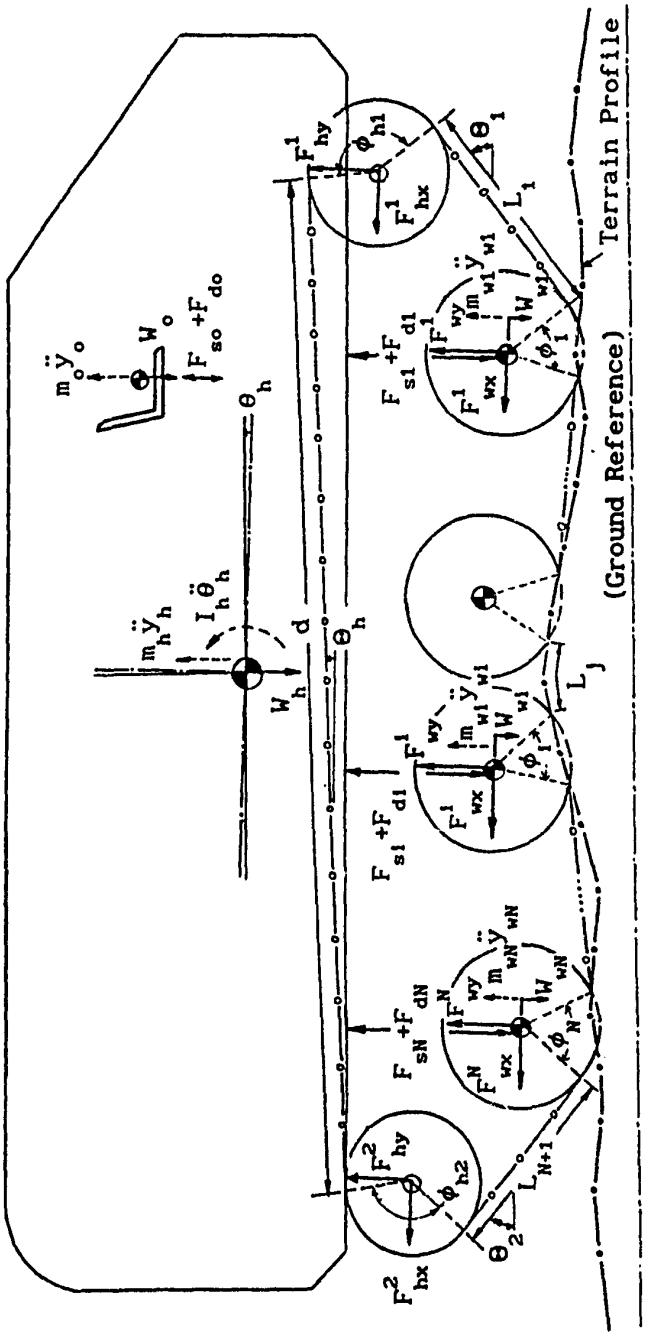

Figure 2.6 Forces resulting from dynamical vehicle-terrain interaction.

Bounce Motion of Hull:

$$\ddot{y}_h = \frac{1}{m_h}\left[\sum_{i=1}^{N}(F_{si}+F_{di}) - (F_{so}+F_{do}) + \sum_{k=1}^{2}F_{hy}^{k}\right] - g \qquad (2.1)$$

Pitch Motion of Hull:

$$\ddot{\theta}_h = \frac{1}{I_h}\left[\sum_{i=1}^{N}\{(F_{si}+F_{di})(a_iC_\theta - b_iS_\theta) + b_{wi}F_{wx}^{i}\} - (F_{so}+F_{do})(a_oC_\theta - b_oS_\theta)\right.$$

$$\left. + \sum_{k=1}^{2}a_{hk}[F_{hx}^{k}S_\theta + F_{hy}^{k}C_\theta] + b_{hk}[F_{hx}^{k}C_\theta - F_{hy}^{k}S_\theta]\right] \qquad (2.2)$$

Bounce Motion of Road Wheel Assembly:

$$\ddot{y}_{wi} = \frac{1}{m_{wi}}\left[F_{wy}^{i} - (F_{si}+F_{di})\right] - g \qquad (2.3)$$

Bounce Motion of Driver and Seat:

$$\ddot{y}_o = \frac{1}{m_o}\left[(F_{so}+F_{do})\right] - g \qquad (2.4)$$

For rigidly connected driver's seat, the bounce response is obtained by kinematic constraint equation, given as:

$$\ddot{y}_o = \ddot{y}_h + a_o[\ddot{\theta}_hC_\theta - \dot{\theta}_h^{2}S_\theta] \qquad (2.5)$$

where $C_\theta = \cos\theta_h$ and $S_\theta = \sin\theta_h$. m_h and I_h are the mass and pitch mass moment of inertia corresponding to half of the hull. m_{wi} and m_o correspond to unsprung mass of the i^{th} road wheel assembly (on one side of the vehicle), and equivalent suspended mass of the driver and seat. b_{wi} indicates the instantaneous elevation of i^{th} road wheel center with respect to c.g. of the vehicle, given as:

$$b_{wi} = Y_{wi} - Y_{cg} \qquad (2.6)$$

where Y_{cg} and Y_{wi} correspond to the vertical coordinate of the vehicle c.g. and the i^{th} road wheel center, respectively, at a given instant.

F_{si} and F_{di} are the spring and damping forces, respectively, due to the i^{th} primary suspension unit, and are evaluated based on the linear interpolation of corresponding look-up tables for instantaneous relative displacement and velocity across the respective suspension unit, which are given as

$$r_i = y_{wi} - y_h - a_i S_\theta \tag{2.7}$$

$$\dot{r}_i = \dot{y}_{wi} - \dot{y}_h - a_i \dot{\theta}_h C_\theta \tag{2.8}$$

Similarly, F_{so} and F_{do} are the spring and damping forces, respectively, due to the secondary (seat) suspension, and are computed based on:

$$r_o = y_h + a_o S_\theta - y_o \tag{2.9}$$

$$\dot{r}_o = \dot{y}_h + a_o \dot{\theta}_h C_\theta - \dot{y}_o \tag{2.10}$$

F^i_{wx} and F^i_{wy} are the net horizontal and vertical forces acting at the i^{th} ($i = 1,..,N$) road wheel center due to dynamic wheel-track-terrain interaction, given as (refer to Figure 2.7a):

$$F^i_{wx} = \mathbb{F}^i_{wx} - T^i_{wx} \tag{2.11}$$

$$F^i_{wy} = \mathbb{F}^i_{wy} + T^i_{wy} \tag{2.12}$$

where,

$$\mathbb{F}^i_{wx} = F^i_{wn} \sin \gamma_i \quad ; \quad \mathbb{F}^i_{wy} = F^i_{wn} \cos \gamma_i \tag{2.13}$$

$$T^i_{wx} = \sum_{j=i}^{i+1} T_{tr} \cos \varepsilon^j \quad ; \quad T^i_{wy} = \sum_{j=i}^{i+1} T_{tr} \sin \varepsilon^j \tag{2.14}$$

where, $$j = \begin{cases} 1 \text{ for } j = i \\ 2 \text{ for } j = i+1 \end{cases}$$

where, $\mathbb{F}^i_{wx}$ and $\mathbb{F}^i_{wy}$ are the horizontal and vertical components of the net foot-print force, F^i_{wn}, which characterizes the road wheel/track-terrain interaction and acts at an angle γ_i with respect to the vertical axis. T^i_{wx} and T^i_{wy} are the horizontal and vertical components of the net dynamic track load acting at the i^{th} road wheel center, where T_{tr} is the overall track tension considered to account for dynamic track load, and ε^j_1 and ε^j_2 correspond to the horizontal inclinations of j^{th} track segment at its both ends. The mathematical models for net footprint force and dynamic track load are described in detail in the next section.

Similarly, F^i_{hx} and F^i_{hy} are the net horizontal and vertical forces acting at the k^{th} (k = 1,2) hull wheel center due to dynamic wheel-track-terrain interaction, given as (refer to Figure 2.7b and 2.7c):

$$F^k_{hx} = \mathbb{F}^k_{hx} - T^k_{hx} \tag{2.15}$$

$$F^k_{hy} = \mathbb{F}^k_{hy} + T^k_{hy} \tag{2.16}$$

where,

$$\mathbb{F}^k_{hx} = F^k_{hn} \sin \gamma_{hk} \quad ; \quad \mathbb{F}^k_{hy} = F^k_{hn} \cos \gamma_{hk} \tag{2.17}$$

$$T^k_{hx} = T_{tr}(\cos \varepsilon^j_j + \cos \Theta) \quad ; \quad T^k_{hy} = T_{tr}(\sin \varepsilon^j_j + \sin \Theta) \tag{2.18}$$

where, $$j = \begin{cases} 1 \\ N+1 \end{cases}, \; j = \begin{cases} 2 \\ 1 \end{cases} \text{ and } \Theta = \begin{cases} \Theta_B \text{ ; for } k = 1 \\ \Theta_A \text{ ; for } k = 2 \end{cases}$$

where Θ_B and Θ_A are the horizontal inclinations of the track segment at the top of the drive sprocket and the idler, respectively, and are computed based on the instantaneous inclination, Θ_h, of the tangent adjoining the top points of both hull wheels as:

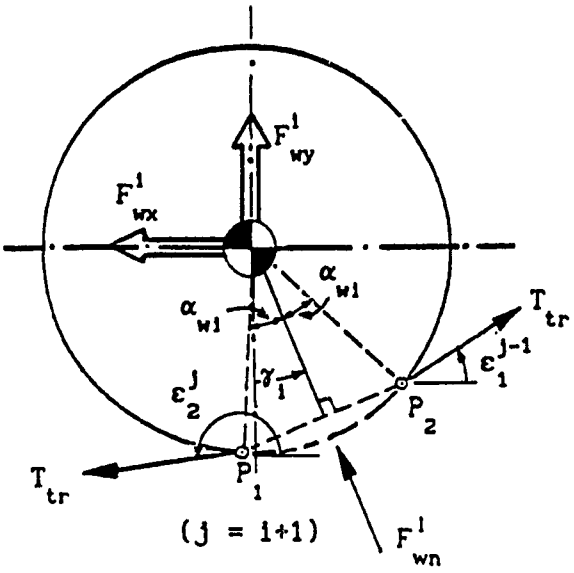

(a) i^{th} Road Wheel

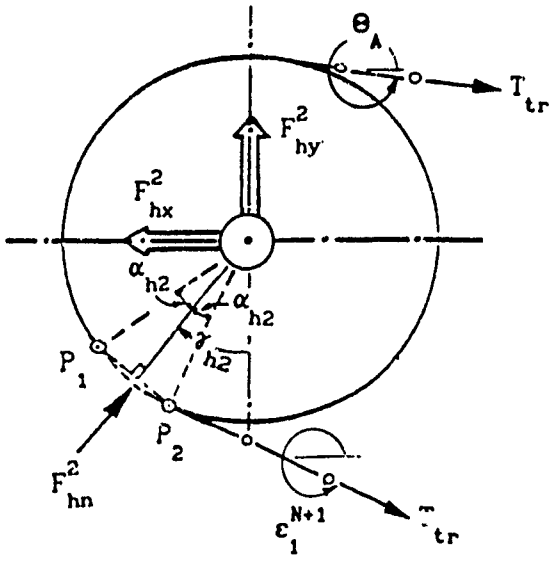

(b) Rear Hull Wheel

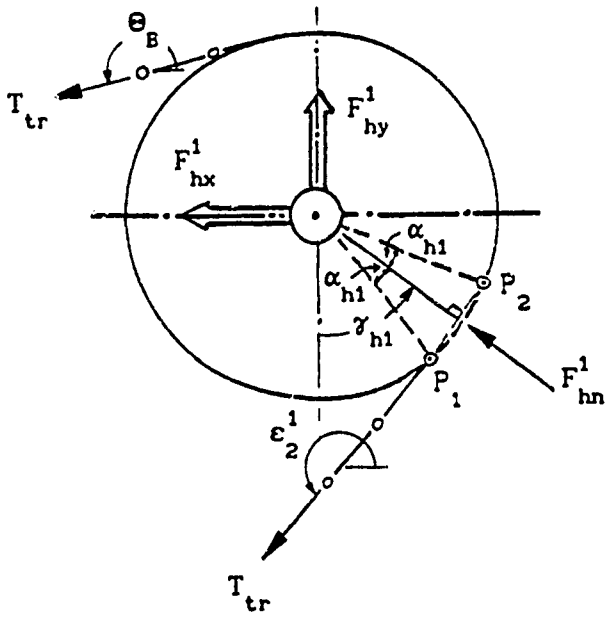

(c) Front Hull Wheel

Figure 2.7 Resultant horizontal and vertical forces acting at wheel centre.

$$\Theta_A = \Theta_h + 2\pi \quad ; \quad \Theta_B = \Theta_h + \pi \tag{2.19}$$

The interaction between k^{th} hull wheel and terrain is modeled similar to the road wheel/track-terrain interaction. The continuous radial spring and an equivalent damper based on the stiffness and damping characteristics of the track pad are used to compute the net footprint force, F^k_{hn}.

2.4 DYNAMIC WHEEL-TRACK-TERRAIN INTERACTION

The dynamic wheel-track-terrain interaction is realized as: (i) the wheel/track-terrain interaction to account for the ground normal force (i.e. *net foot-print force*) which is transferred to the wheel through the underlying track pad, and (ii) the dynamic track tensioning effects to account for the *dynamic track load* which is transferred to the wheel stations based on the geometric considerations of track wraps around wheels and terrain profile. Details regarding the modeling aspects of net foot-print force and dynamic track load are presented in the following sub-sections.

2.4.1 Net Foot-Print Force

The road wheel/track-terrain interaction is modeled based on the concept of continuous radial spring representation [38], and is expanded to include the damping effects. Following assumptions are made in the formalism:

- Road wheel (with rubberized rim) and track shoe (with rubber pad) are combined to form an equivalent vertical suspension unit. This assumption implies that the static footprint is within the contact patch area of a single track shoe, and the wheel and track forces due

to compression vary in the same manner.

- Wheel/track sinkage is considered negligible due to the assumption of non-yielding ground.
- Shear stresses in the footprint are negligible, since braking, acceleration, and turning operations are not included in the simulation model.

As illustrated in Figure 2.8, the road wheel/track-terrain interaction is represented by a radially distributed continuous spring and a damping element taking into account an equivalent stiffness, and dissipative characteristics of the road wheel and the track pad. The expression for net footprint force is obtained by considering a differential element of the wheel-terrain contact patch as shown in Figure 2.9, which represents a radial force, dF_w applied at an angle α corresponding to the radial deflection, δ, due to interaction with the non-deformable terrain. The radial force is, then, expressed as:

$$dF_w = (K_{rw}\, d\alpha)\, \delta \tag{2.20}$$

where K_{rw} is the radial spring constant (N/m/rad), and $(K_{rw}\, d\alpha)$ represents an equivalent spring constant for the differential element. Assuming an idealized wheel deflection characterized by a straight line joining the first and last wheel-terrain contact points on the lower wheel circumference ($\overline{P_1 P_2}$), the radial deflection, δ, can, then, be conveniently expressed as:

$$\delta = R_w - \frac{\hat{R}_w}{\cos \alpha} \tag{2.21}$$

where $\hat{R}_w$ is the deflected road wheel radius. The normal and tangential components of the radial force are given as:

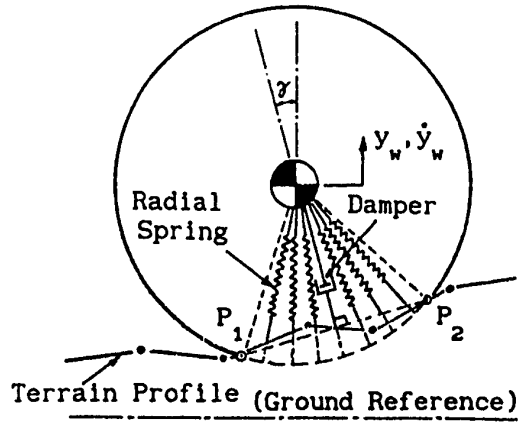

Figure 2.8 Analytical model for wheel/track-terrain interaction.

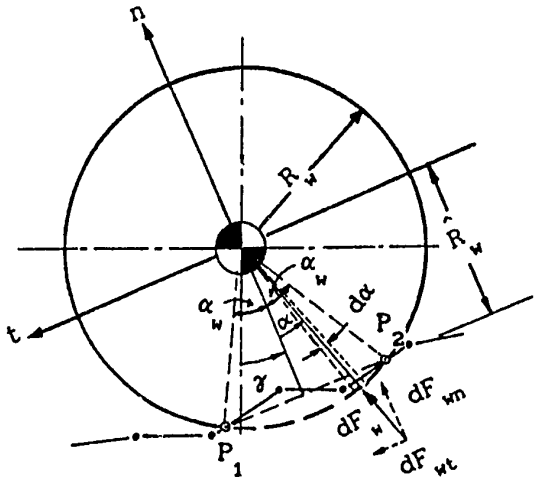

Figure 2.9 Determination of net foot-print force.

$$dF_{wn} = dF_w \cos \alpha \tag{2.22}$$

$$dF_{wt} = dF_w \sin \alpha \tag{2.23}$$

Substituting equations (2.20) and (2.21) into equation (2.22), and integrating over the entire contact patch area, the net normal force is obtained as:

$$F_{wn} = 2 K_{rw} R_w [\sin \alpha_w - \alpha_w \cos \alpha_w] \tag{2.24}$$

where, α_w is the one-half of the wheel-terrain contact patch angle, given as:

$$\alpha_w = \cos^{-1}\left[\frac{\hat{R}_w}{R_w}\right] \tag{2.25}$$

The radial spring constant, K_{rw}, is established by measuring the static deflection of wheel center, Δ_w, on a flat surface under a vertical load, P. Using equation (2.24):

$$K_{rw} = \frac{P}{2 R_w [\sin \alpha_{ws} - \alpha_{ws} \cos \alpha_{ws}]} \tag{2.26}$$

where α_{ws} is given as:

$$\alpha_{ws} = \cos^{-1}\left[\frac{R_w - \Delta_w}{R_w}\right] \tag{2.27}$$

The damping force can be conveniently incorporated in the net normal force, F_{wn}, by computing the terrain-imposed vertical velocity input at the mid-point of wheel-terrain contact patch, given as:

$$\dot{y} = V_x \tan \gamma \tag{2.28}$$

where V_x is the forward velocity of the vehicle, and the term (tan γ)

accounts for the slope of terrain profile at the mid-point of contact patch. The wheel damping force is expressed as $F_{dw} = C_{rw}\dot{r}_w$, where C_{rw} is the viscous damping coefficient and $\dot{r}_w$ is the relative velocity given as:

$$\dot{r}_w = (\dot{y}-\dot{y}_w)\cos\gamma = V_x \sin\gamma - \dot{y}_w \cos\gamma \qquad (2.29)$$

Therefore, the net normal force, F_{wn}, can be rewritten as follows:

$$F_{wn} = 2\,K_{rw}\,R_w\,[\sin\alpha_w - \alpha_w \cos\alpha_w] + F_{dw} \qquad (2.30)$$

It should be noted that the damping force, F_{dw}, can also account for the soil damping effects in addition to the dissipative characteristics of road wheel and track pad.

The net tangential component, F_{wt}, is, however, equal to zero due to the equilateral construction of contact patch triangle, as shown in Figure 2.9.

Wheel-Terrain Contact Patch

In order to compute the net footprint force (equation 2.30), the wheel-terrain contact patch is to be first established based on the contact patch angle, β_1, and the horizontal inclination of the line, $\overline{P_1P_2}$ (or the vertical inclination of net footprint force), γ_1. As shown in Figure 2.10, the contact patch angle is obtained as:

$$\beta_1 = \beta_{2i} - \beta_{1i} \qquad (2.31)$$

where, $\beta_{1i} = \text{ATAN3}((Y_1^i - Y_{wi}),(X_1^i - X_{wi}))$

and, $\beta_{2i} = \text{ATAN3}((Y_2^i - Y_{wi}),(X_2^i - X_{wi}))$

where, (X_{wi},Y_{wi}) indicates instantaneous location of the i^{th} road wheel centre, while (X_1^i,Y_1^i) and (X_2^i,Y_2^i) represent the first and last wheel-

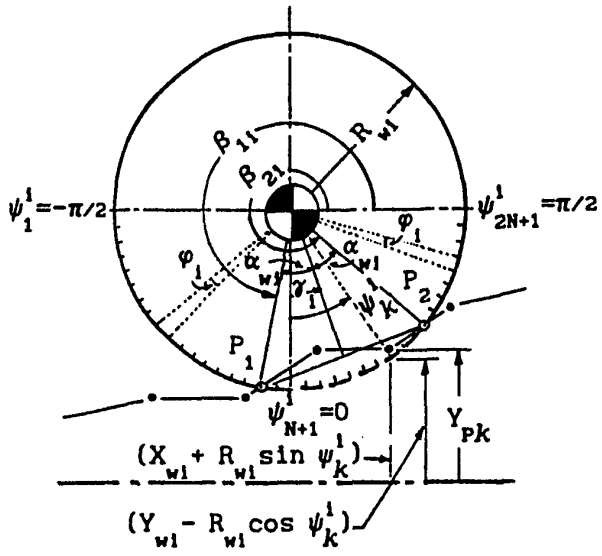

Figure 2.10 Wheel-terrain contact patch.

terrain contact points (P_1 and P_2), respectively. The function ATAN3 yields the angle value such that it is always measured in a counter-clockwise sense, as illustrated in Figure 2.10. The angle γ_1 is computed as:

$$\gamma_1 = \beta_{11} + \alpha_{w1} - 1.5\pi \tag{2.32}$$

where, $$\alpha_{w1} = \beta_1/2$$

It is apparent that determination of wheel-terrain contact points, P_1 and P_2, along the lower circumference of the road wheel, is essential in order to compute the net foot-print force. Also, P_1 and P_2 are vital to the proper definition of the track wrap around the road wheel as it would be seen later in this chapter. One basic approach to locate P_1 and P_2 is illustrated in Figure 2.10, where the lower circumference of i^{th} road wheel is divided into a sufficient number of segments ($k = 1,..,2N+1$; $N = \pi/2\varphi_1$; where φ_1 = specified segmentation angle). Consequently, P_1 and P_2 are established by checking the elevation of each segmented point ($Y_{w1} - R_{w1}\cos\psi_k^1$) with respect to the terrain profile elevation (Y_{Pk}) at the respective horizontal location ($X_{w1} + R_{w1}\sin\psi_k^1$), where ψ_k^1 is the corresponding vertical inclination (positive if counterclockwise), and Y_{Pk} is computed based on the linear interpolation of the look-up table containing cartesian coordinates of the specified terrain profile. This method, however, does not offer an efficient and economical solution due to the need for sufficiently high number of segments, which requires high computational time. Alternatively, a more effective algorithm is developed for fast and accurate computation of the wheel-terrain contact patch. The new method is based on a simple *circle-line intersection*, and is found to be more accurate and 5-6 times faster than the previous

approach.

Basis of the new computational procedure for establishing wheel-terrain contact patch, can be described by considering a circle intersected by a line as illustrated in Figure 2.11, where circle and line represent a wheel of specified radius (R) and centre coordinates (X_C, Y_C), and a linear segment of the terrain profile with specified end points $(X_{L1}, Y_{L2};\ X_{L2}, Y_{L2})$. The circle equation can be written as:

$$Y_c = Y_C \pm \sqrt{R^2 - (X_c - X_C)^2} \tag{2.33}$$

where, equation (2.33) yields two values of Y_c, which correspond to elevations of arbitrary points located on upper-half and lower-half of the circle circumference at the longitudinal location, X_c. Since, the wheel-terrain contact occurs along the lower-half circumference only, the circle equation can be rewritten as:

$$Y_c = Y_C - \sqrt{R^2 - (X_c - X_C)^2} \tag{2.34}$$

The equation describing a line is given as:

$$Y_1 = Y_{L1} + m\ (X_1 - X_{L1}) \tag{2.35}$$

where, $$\text{slope, } m = \frac{Y_{L2} - Y_{L1}}{X_{L2} - X_{L1}}$$

where, any arbitrary point along the line is indicated by (X_1, Y_1).

At the circle-line intersection points, the following condition is satisfied,

$$X_c = X_1 = X \text{ and } Y_c = Y_1 = Y \tag{2.36}$$

Therefore, following quadratic equation is derived from equations

(2.34) and (2.35) in conjunction with above-mentioned condition,

$$a\,X^2 + b\,X + c = 0 \tag{2.37}$$

where, $a = 1 + m^2$; $b = 2\,(A\,m - X_C)$; $c = A^2 - R^2 + X_C^2$

and $A = Y_{L1} - Y_C - m\,X_{L1}$

The solution of equation (2.37) is given as:

$$X_{1,2} = -\frac{b}{2a} \pm \sqrt{\left(\frac{b}{2a}\right)^2 - \left(\frac{c}{a}\right)} \tag{2.38}$$

Subsequently, elevations of intersection points (Y_1, Y_2) can, then, be obtained by substituting the respective horizontal coordinate (X_1, X_2) into either equation (2.34) or (2.35). However, the true intersection point for left-hand-side ($\ell.h.s.$) line is indicated by $P_1(X_1, Y_1)$, whereas $P_2(X_2, Y_2)$ represents the true intersection point for right-hand-side ($r.h.s.$) line, as illustrated in Figure 2.11.

Figure 2.11 illustrates a geometrical situation where one end of the line is inside the circle, which ensures the circle-line intersection. For a geometrical situation as illustrated in Figure 2.12, where both ends of the line are outside the circle, it becomes essential to confirm the possibility of circle-line intersection prior to computing the intersection points. For such a situation, the intersection is possible, if and only if,

$$h < R \quad \text{and} \quad X_{L1} < (X_C + \Delta_X) < X_{L2} \tag{2.39}$$

where, $h = \Delta_Y \cos \Phi$; $\Delta_X = h \sin \Phi$; $\Delta_Y = Y_C - (Y_{L1} + m(X_C - X_{L1}))$

and $\Phi = \tan^{-1}(m)$

Consequently, a computational procedure is devised in order to

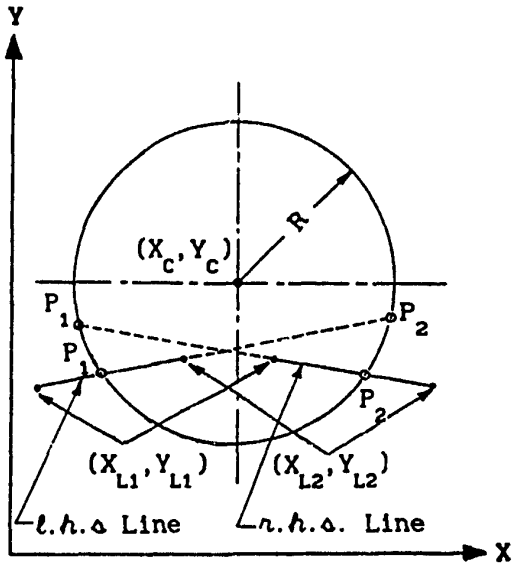

Figure 2.11 Circle-line intersection - one end of the line inside the circle.

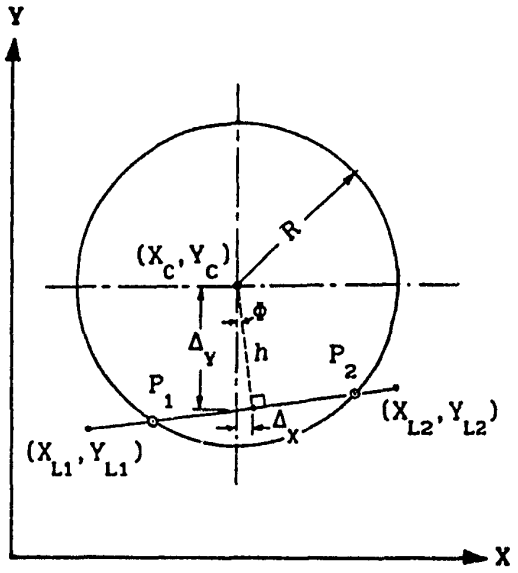

Figure 2.12 Circle-line intersection - both ends of the line outside the circle.

establish the first and last points (P_1,P_2) of the wheel-terrain contact patch, which involves the following steps:

(a) Terrain profile points, which lie within the *shadow* of a given wheel are established as: X_{sn},Y_{sn}, $n = 1,..,N_s$, where the *shadow* is defined by the horizontal range between $X_{w1} - R_{w1}$ and $X_{w1} + R_{w1}$, as shown in Figure 2.13.

(b) There are two possible geometrical situations as a result of the number of terrain profile points found within the wheel shadow (N_s), which are treated as follows:

- $N_s = 0$: corresponds to the geometrical situation where end points of the line lie outside the circle as illustrated in Figure 2.12. Consequently, the possibility of wheel-terrain contact due to the profile segment defined by its end points located on either side of the wheel, is confirmed prior to computing the intersection points, as explained above (equation 2.39), **or**
- $N_s > 0$: terrain profile points which lie inside the wheel are, then, identified based on the following criteria,

$$\left\{Y_{w1} - \sqrt{R_{w1}^2 - (X_{sn} - X_{w1})^2}\right\} - Y_{sn} < 0 \quad ; n = 1,..,N_s \tag{2.40}$$

and are indicated by N_I, where $N_I \leq N_s$.

Step (C) is followed only if $N_s > 0$.

(c) There are two possible geometrical situations based on the number of profile points found inside the wheel, which are treated as follows:

- $N_I = 0$: corresponds to similar geometrical situation as illustrated in Figure 2.12, where the possibility of wheel-terrain contact due to each profile segment (fully or partially) within the wheel shadow is confirmed (equation 2.39) prior to computing the

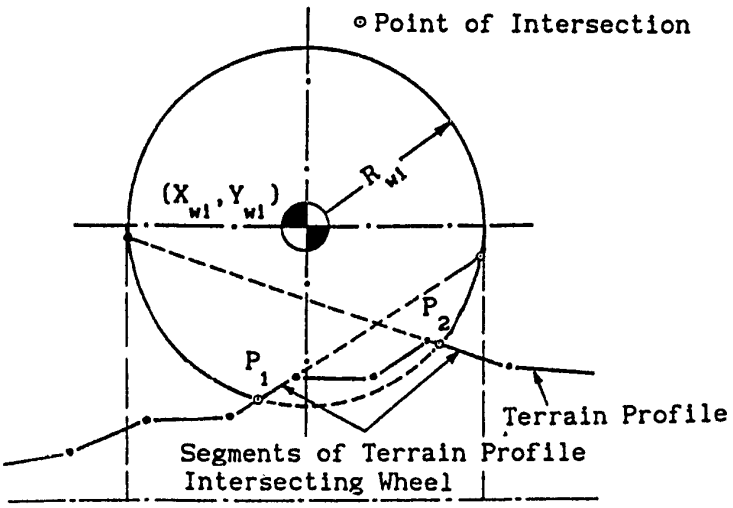

Figure 2.13 Determination of wheel-terrain contact patch based on circle-line intersection.

corresponding intersection points. Consequently, the first wheel-terrain contact point (P_1) is computed as the first intersection point of the very first profile segment confirmed to intersect the wheel; whereas the last wheel-terrain contact point (P_2) is computed as the last intersection point of the very last profile segment confirmed to intersect the wheel, or

- $N_I > 0$: corresponds to the general situation as illustrated in Figure 2.11, where the first and last profile points which lie inside the wheel, are identified in order to establish the $\ell.h.s.$ and $r.h.s.$ profile segments intersecting the wheel (Figure 2.13), and to compute the corresponding appropriate intersection points as explained above.

2.4.2 Dynamic Track Load

An accurate prediction of dynamic track loads would generally require a comprehensive model incorporating dynamics of each track shoe. Such a track model was proposed by Galaitsis [68], where equation of motion for the track loop were developed by considering the inertia of shoes, stiffness and damping characteristics of the rubber bushings, and shoe-wheel interactions. However, such a track model in conjunction with rest of the vehicle would yield a significantly large degrees-of-freedom dynamical system, which would be very ineffective for ride simulation purposes. Moreover, the kinematic constraining effects of the track on the vehicle suspension system have more pronounced influence in ride dynamic studies than track dynamic effects.

For the purpose of this study, the track is modeled based on kinematic considerations only while ignoring track loop vibrations. For MODEL I, track pre-tension and track belt extensibility are considered to

account for dynamic track load imposed at each wheel station. Consequently, the overall track tension is given as a sum of track pre-tension and tension caused by the stretching of the track belt:

$$T_{tr} = \begin{cases} K_{tr}(L_{tr} - L_{tr}^{0}) + T_{tr}^{0} & ; \quad L_{tr} > L_{tr}^{0} \\ T_{tr}^{0} & ; \quad L_{tr} \leq L_{tr}^{0} \end{cases} \tag{2.41}$$

where T_{tr} and L_{tr} represents the overall track tension, and total track length at any instant, and their initial values at time, t = 0 are T_{tr}^{0} and L_{tr}^{0}. K_{tr} is the longitudinal stiffness coefficient characterizing the track extensibility. The total track length, which varies with the terrain and overall geometry of the vehicle, is computed at each integration step by summing up the various segments which constitutes the entire circumferential length of the track. The total track length is expressed as (refer to Figure 2.6):

$$L_{tr} = \sum_{i=1}^{N} \phi_i \, R_{wi} + \sum_{k=1}^{2} \phi_{hk} \, R_{hk} + L_h + \sum_{j=1}^{N+1} L_j \tag{2.42}$$

Track Wrap Around i^{th} Road Wheel

The track wrap angle, ϕ_i, around i^{th} road wheel is assumed to be either equal to:

(a) β_i, the contact patch angle (equation 2.31), for the road wheel in contact with the terrain, as illustrated in Figure 2.14 (a), **or**

(b) η_i, the angle defined by the track-wheel tangency points (P_1^T and P_2^T), for the road wheel lost contact with the terrain, as shown in Figure 2.14 (b), is given as:

$$\eta_i = \text{ATAN3}((Y_{T2}^{i} - Y_{wi}), (X_{T2}^{i} - X_{wi})) - \text{ATAN3}((Y_{T1}^{i} - Y_{wi}), (X_{T1}^{i} - X_{wi})) \tag{2.43}$$

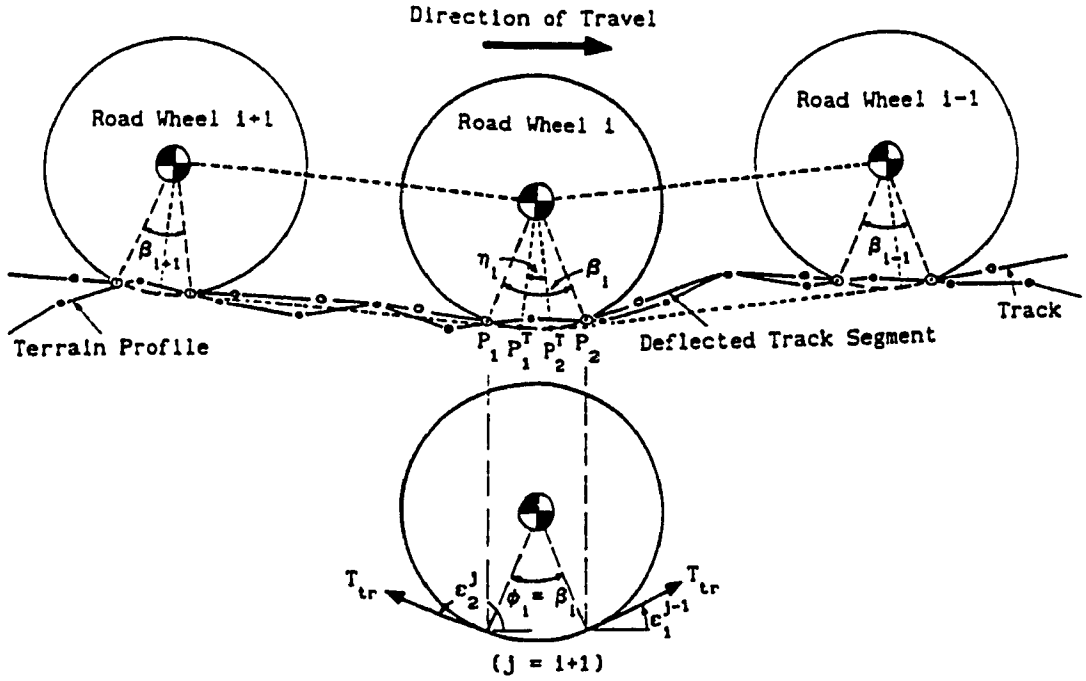

(a) Road wheel in contact with terrain.

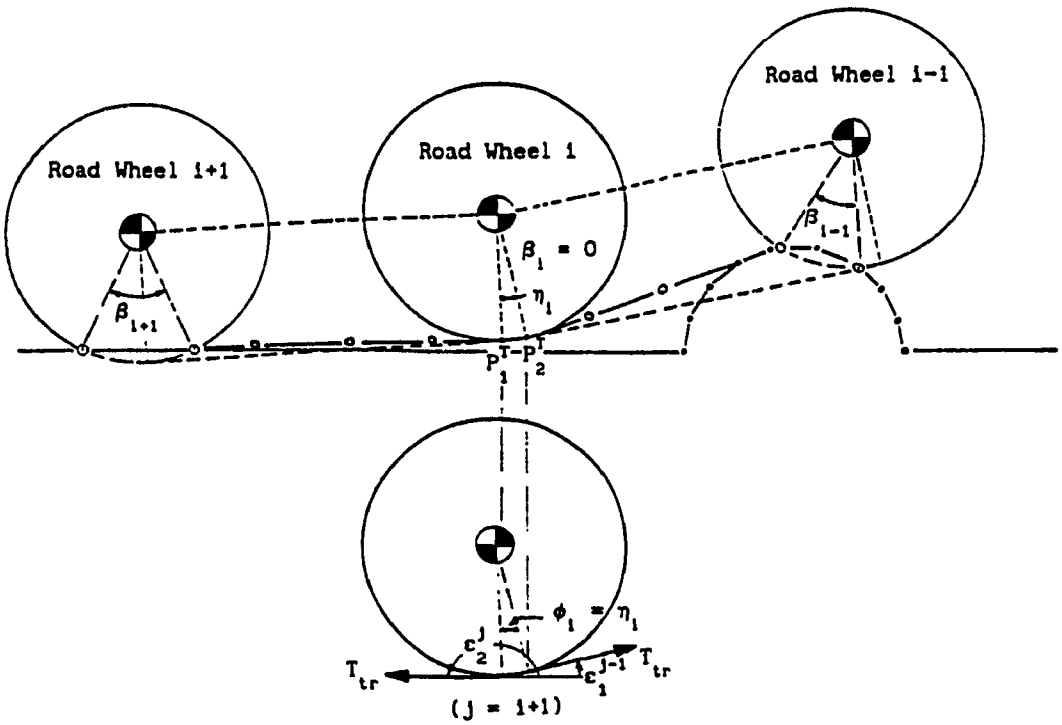

(b) Road wheel lost contact with terrain.

Figure 2.14 Determination of track wrap around the road wheel.

where, the first and the last track-wheel tangency points are indicated by $P_1^T(X_{T1}^i, Y_{T1}^i)$ and $P_2^T(X_{T2}^i, Y_{T2}^i)$, respectively. The track-wheel tangency points are computed as the contact points for a line tangent to two given circles whose center coordinates and radii are known. As illustrated in Figure 2.15 two basic configurations, termed as: (a) Front track feeler, and (ii) Rear track feeler, are used as a basis for computing $P_2^T(X_{T2}^i, Y_{T2}^i)$ and $P_1^T(X_{T1}^i, Y_{T1}^i)$, respectively, in addition to establishing the respective track feeler orientation. In accordance with Figure 2.15, the cartesian coordinates of track-wheel tangency points are given as:

$$\begin{aligned} X_1^T &= R_1 \cos(\Psi) + X_1 \; ; \; Y_1^T = R_1 \sin(\Psi) + Y_1 \\ X_2^T &= R_2 \cos(\Psi) + X_2 \; ; \; Y_2^T = R_2 \sin(\Psi) + Y_2 \end{aligned} \tag{2.44}$$

where, $\Psi = \begin{cases} \vartheta + \pi/2 \; ; \; \textit{if Front feeler} \\ \vartheta - \pi/2 \; ; \; \textit{if Rear feeler} \end{cases}$ and $\vartheta = \text{ATAN3}(Y_2 - Y_1, X_2 - X_1)$

and, the track feeler horizontal inclination is computed as:

$$\Theta = \text{ATAN3}(Y_2^T - Y_1^T, X_2^T - X_1^T) \tag{2.45}$$

Consequently, the first and last track-wheel tangency points (P_1^T, P_2^T) for the i^{th} road wheel are obtained using (X_2^T, Y_2^T) as given in equation (2.44), where, $(X_2 = X_{wi}, Y_2 = Y_{wi}, R_2 = R_{wi})$. The first track-wheel tangency point, P_1^T, is computed based on $(X_1 = X_{wi+1}, Y_1 = Y_{wi+1}, R_1 = R_{wi+1}$ for $i = 1,..,N-1$; $X_1 = X_{h2}, Y_1 = Y_{h2}, R_1 = R_{h2}$ for $i = N)$, whereas $(X_1 = X_{h1}, Y_1 = Y_{h1}$, $R_1 = R_{h1}$ for $i = 1$; $X_1 = X_{wi-1}, Y_1 = Y_{wi-1}, R_1 = R_{wi-1}$ for $i = 2,..,N)$ is used to compute P_2^T.

For front and rear road wheels in contact with terrain, a special *check* is made to assure a correct representation of respective track wrap angle, and track feeler. For this, the horizontal coordinates of wheel-

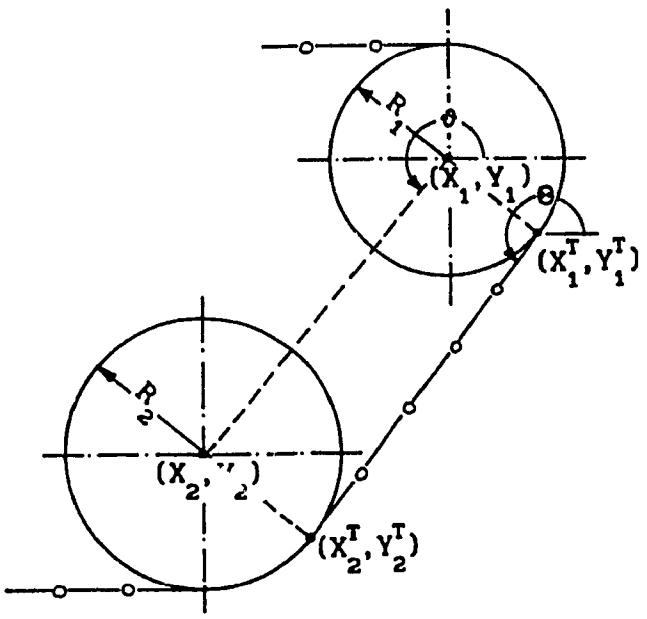

(a) Front track feeler.

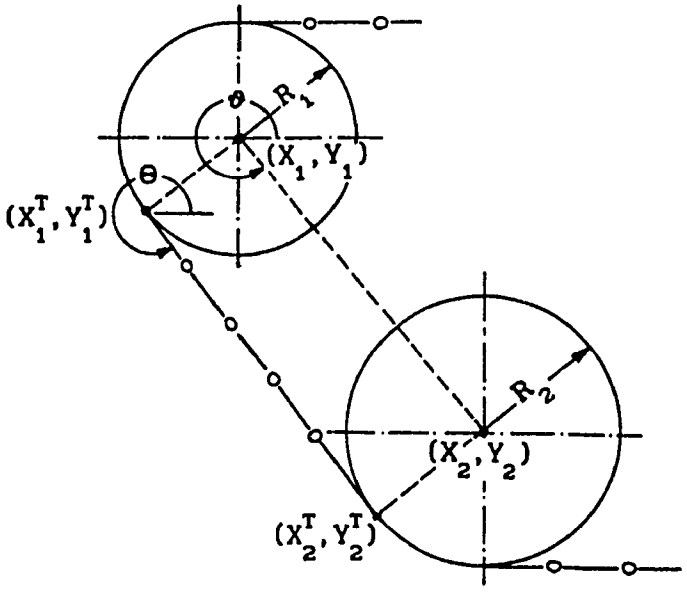

(b) Rear track feeler.

Figure 2.15 Determination of track-wheel tangency points.

terrain contact point (X_2^1, if i=1; X_1^1, if i=N), and corresponding track-wheel tangency point (X_{T2}^1, if i=1; X_{T1}^1, if i=N) are compared to compute the correct track wrap angle, and/or to re-establish the correct point from which the track feeler is tangent onto the hull wheel. For instance, Figure 2.16 illustrates two such geometrical situations, where the track wrap angle, and track feeler inclination are accounted for correction. As shown in Figure 2.16 (a), the track wrap angle around front road wheel (ϕ_1) is equal to the wheel-terrain contact patch angle (β_1), however, the front track feeler horizontal inclination is re-established based on the tangent computed from $P_2(X_2^1, Y_2^1)$ onto the hull wheel. Figure 2.16 (b) shows a geometrical situation, where the horizontal inclination of rear track feeler is unchanged, however, the track wrap angle is recomputed as

$$\phi_N = \beta_{2N} - \text{ATAN3}(Y_{T1}^N - Y_{wN},\ X_{T1}^N - X_{wN}) \tag{2.46}$$

where, β_{2N} is computed as given in equation (2.31) for i=N.

In order to correct the track feeler inclination, θ (equation 2.45), the hull wheel tangency point due to a tangent originated from a specified point (e.g. P_2 as shown in Figure 2.16 (a)), needs to be computed. As illustrated in Figure 2.17, two basic geometric configurations are employed to compute the (hull) wheel tangency point, whose coordinate are then given as:

$$X = \begin{cases} X_P + b\cos(\theta-\Delta\theta) \\ X_P - b\cos(\theta+\Delta\theta) \end{cases};\quad Y = \begin{cases} Y_P + b\sin(\theta-\Delta\theta) & ;\ \textit{if Front Feeler} \\ Y_P - b\sin(\theta+\Delta\theta) & ;\ \textit{if Rear Feeler} \end{cases} \tag{2.47}$$

where, $b = \sqrt{r^2 - R^2}$, $\theta = \tan^{-1}\left(\dfrac{Y_C - Y_P}{X_C - X_P}\right)$, $\Delta\theta = \tan^{-1}\left(\dfrac{R}{b}\right)$

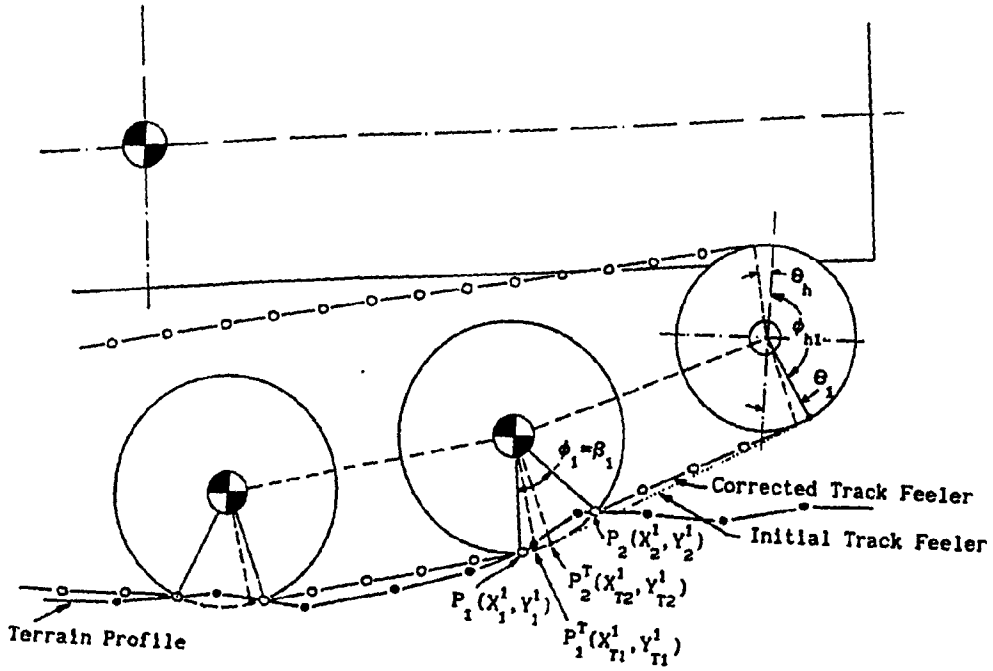

(a) Corrected track feeler.

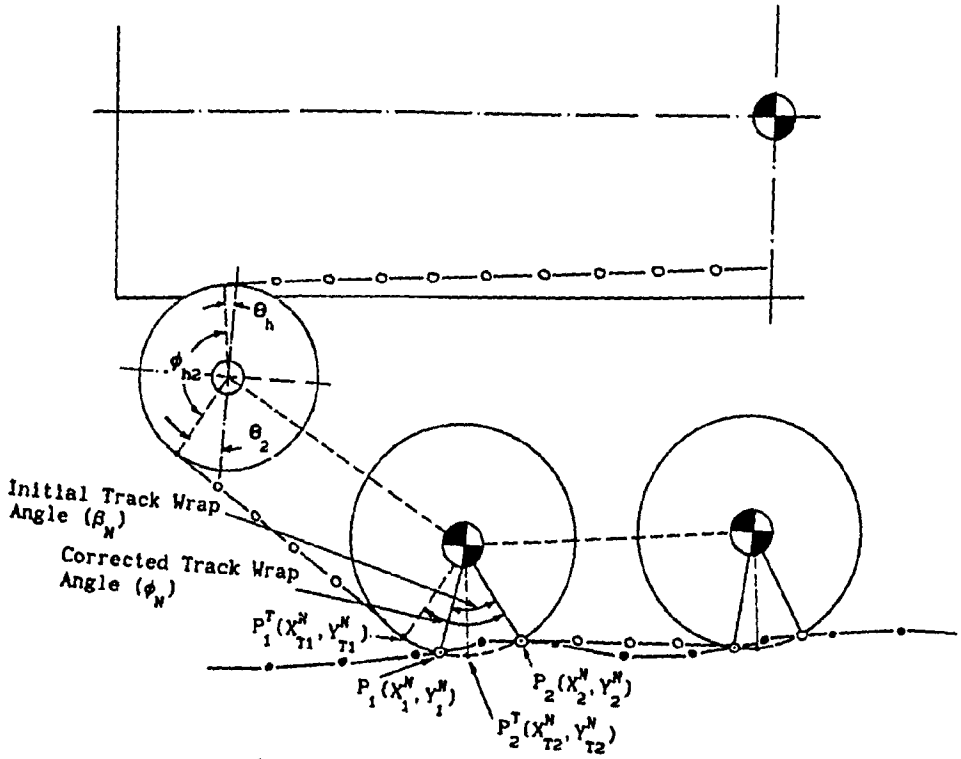

(b) Corrected track wrap angle.

Figure 2.16 Track-wheel connectivity for front and rear road wheels.

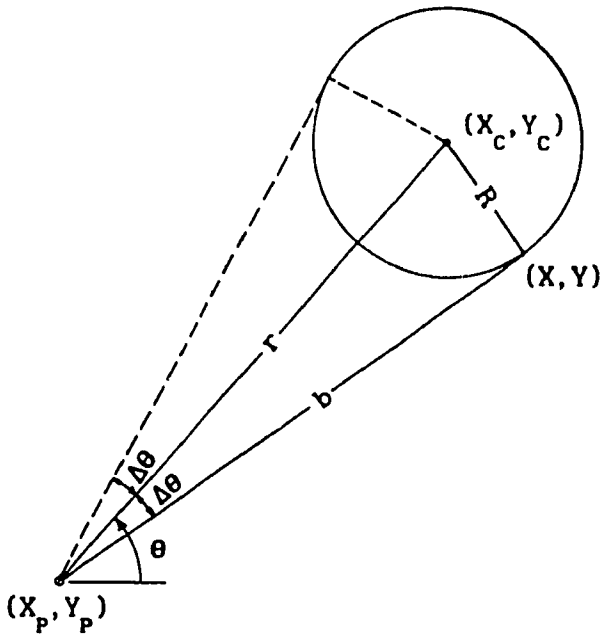

(a) Front track feeler

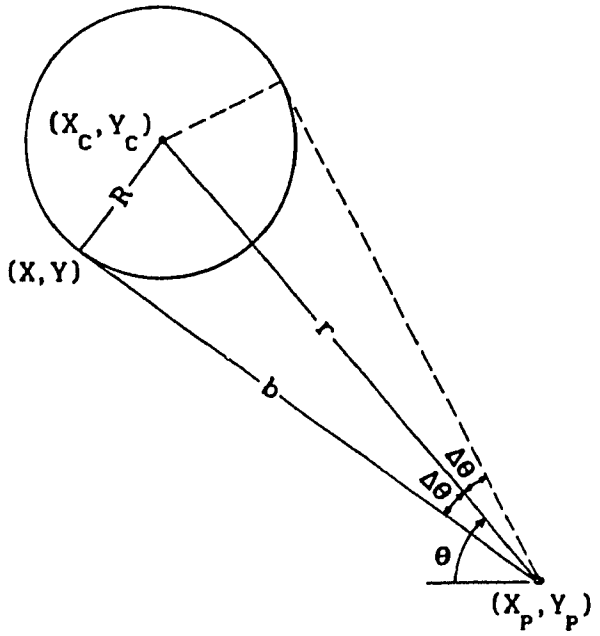

(b) Rear track feeler

Figure 2.17 Determination of a wheel tangency point.

and $$r = \sqrt{(X_C - X_P)^2 + (Y_C - Y_P)^2}$$

Track Wrap Around k^{th} Hull Wheel

The track wrap angle, ϕ_{hk}, around k^{th} hull wheel is computed as:

$$\phi_{hk} = \begin{cases} \pi - \Theta_k + \Theta_h \; ; \; \Theta_k = \Theta - \pi \text{ for } k = 1 \\ \pi - \Theta_k - \Theta_h \; ; \; \Theta_k = 2\pi - \Theta \text{ for } k = 2 \end{cases} \qquad (2.48)$$

where, Θ_k and Θ_h are the inclinations of track feeler tangent onto k^{th} hull wheel, computed based on the horizontal inclination, Θ (equation 2.45) in conjunction with the *check* as explained above, and upper track segment supported on hull wheels, respectively, as illustrated in Figure 2.6.

Track Segmental Lengths

L_h is the length of the track segment supported on drive sprocket and idler, and is assumed to be equal to the magnitude of tangent, d, adjoining the top points of drive sprocket and idler. The tangent is specified as:

$$d = \sqrt{(X_B - X_A)^2 + (Y_B - Y_A)^2} \quad ; \quad \Theta_h = \tan^{-1}\left[\frac{Y_B - Y_A}{X_B - X_A}\right] \qquad (2.49)$$

where, $$X_A = X_{h2} - R_{h2}\sin\Theta_h' \quad ; \quad Y_A = Y_{h2} + R_{h2}\cos\Theta_h'$$

$$X_B = X_{h1} - R_{h1}\sin\Theta_h' \quad ; \quad Y_B = Y_{h1} + R_{h1}\cos\Theta_h'$$

$$\Theta_h' = \tan^{-1}\left[\frac{Y_{h1} - Y_{h2}}{X_{h1} - X_{h2}}\right]$$

and (X_{h1}, Y_{h1}) and (X_{h2}, Y_{h2}) are the instantaneous centre coordinates of sprocket and idler, respectively, and R_{h1} and R_{h2} are the corresponding

radii.

The track-terrain contact patch represents the deflection of a track segment between adjacent wheels due to interaction with the non-deformable terrain profile, as illustrated in Figure 2.18, where L_j is the resulting length of the j^{th} track segment as it conforms or *adapts* to the local shape of the terrain profile. Consequently, each track segment (front track feeler: j=1, between road wheels: j=2,..,N, and rear track feeler: j=N+1) is checked for deflection resulting from interaction with terrain profile. A computational procedure is devised, which involves following steps in order to establish the deflected or stretched track segment:

(a) As shown in Figure 2.19, the j^{th} undeflected track segment spanning between $P_2(X_2^{i+1},Y_2^{i+1})$ and $P_1(X_1^i,Y_1^i)$ is segmented as:

$$\bar{X}_{jl} = X_{Pl} \quad \text{and} \quad Y_{jl} = Y_2^{i+1} + m_j(\bar{X}_{jl} - X_2^{i+1}) \quad ; \quad l = 1,..,M+1 \qquad (2.50)$$

where, $$m_j = \frac{Y_1^i - Y_2^{i+1}}{X_1^i - X_2^{i+1}}$$

and M is the number of terrain profile segments, fully or partially, within the *shadow* of the j^{th} track segment, which is defined by the horizontal range between X_2^{i+1} and X_1^i, and the corresponding cartesian coordinates of profile points including the end points are defined as

$$X_{Pl} = \begin{cases} X_2^{i+1} \\ X_{Si} \\ X_1^i \end{cases} \quad \text{and} \quad Y_{Pl} = \begin{cases} Y_2^{i+1} & ; \; l = 1 \\ Y_{Si} & ; \; l = 2,..,M \;\; (i = l-1) \\ X_1^i & ; \; l = M+1 \end{cases} \qquad (2.51)$$

where $(X_{Si},Y_{Si},\ i = 1,..,M-1)$ correspond to the profile points found within the end points.

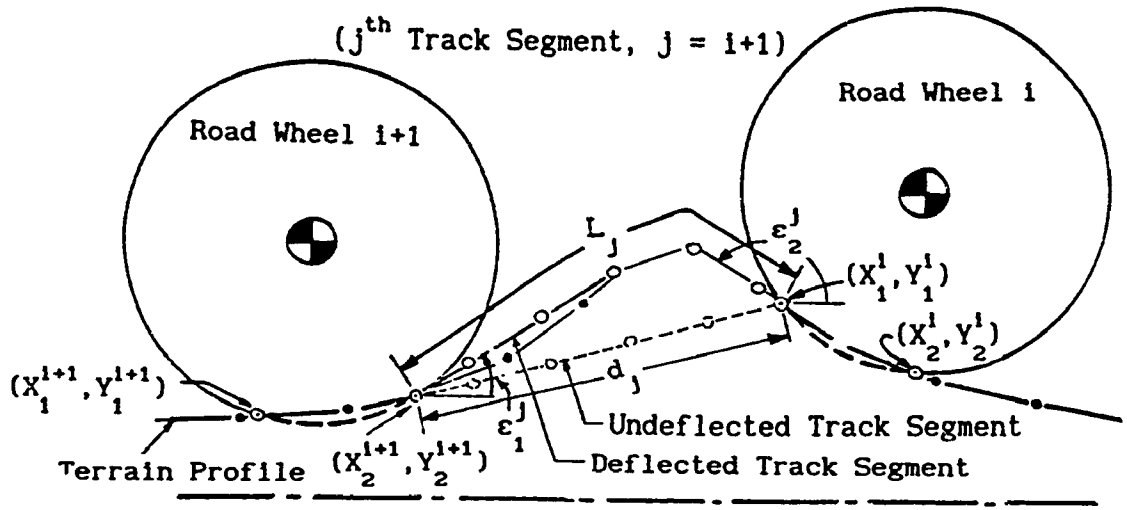

Figure 2.18 Track-terrain contact patch.

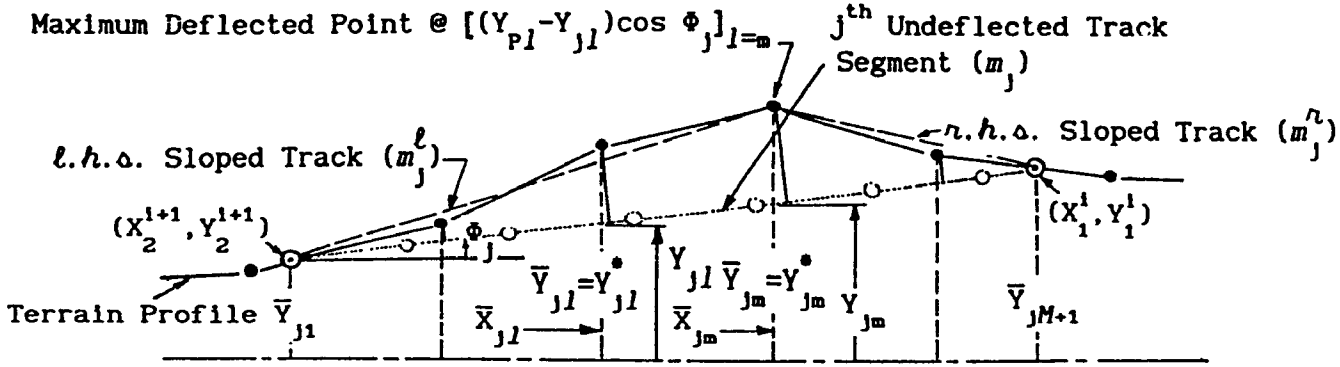

Figure 2.19 Determination of deflected/stretched track segment.

(b) The elevation of each segmented point (Y_{jl}, l = 2,..,M) is checked with respect to the elevation of the terrain pofile (Y_{Pl}) at the respective horizontal location ($\bar{X}_{jl}$), such that the undeflected track is deflected in accordance with the local shape of the terrain profile. The deflected track segment is, then, defined as:

$$Y^{*}_{jl} = \begin{cases} Y_{Pl} \ ; \text{ if } (Y_{Pl}-Y_{jl}) > 0 \\ Y_{jl} \ ; \text{ otherwise} \end{cases} \quad ; \ l = 2,..,M \tag{2.52}$$

and, $Y^{*}_{jl} = Y_{jl}$ for l = 1 or M+1.

However, further check is made in order to assure a correct representation of the stretched track segment, which involves following steps:

(c) The maximum deflected point ($\bar{X}_{jm}$,Y^{*}_{jm}; l=m) on the track segment is, first, determined based on the criterion (refer to Figure 2.19):

$$h_{max} = [(Y_{Pl}-Y_{jl}) \cos(\Phi_j)]_{max} \tag{2.53}$$

where, $$\Phi_j = \tan^{-1}(m_j)$$

Following slopes with respect to ($\bar{X}_{jm}$,Y^{*}_{jm}) are, then, computed as:

$$m^{\ell}_{j} = \frac{Y^{*}_{jm} - Y^{l+1}_{2}}{\bar{X}_{jm} - X^{l+1}_{2}} \quad ; \quad m^{r}_{j} = \frac{Y^{l}_{1} - Y^{*}_{jm}}{X^{l}_{1} - \bar{X}_{jm}} \tag{2.54}$$

where, m^{ℓ}_{j} and m^{r}_{j} correspond to the track slope on the left-hand-side ($\ell.h.s.$) and right-hand-side ($r.h.s.$) of the maximum deflected point ($\bar{X}_{jm}$,Y^{*}_{jm}), respectively.

(d) Final step is to shift the vertical coordinates of the deflected track segment (Y^{*}_{jl} in equation 2.52) such that a more accurate shape of the stretched track segment is obtained. It is carried out by

computing the vertical coordinate of the sloped track (on each side of the maximum deflected point) at every specified horizontal location ($\bar{X}_{jl}$), and comparing it with corresponding terrain profile elevation. Consequently, the stretched track segment is defined as:

$$\bar{Y}_{jl} = \begin{cases} \begin{cases} Y^{*}_{jl} \ ; \text{ if } (Y_{Pl}-(Y_2^{i+1}+m_j^{\ell}(\bar{X}_{jl}-X_2^{i+1})) > 0 \\ Y_2^{i+1} + m_j^{\ell}(\bar{X}_{jl} - X_2^{i+1}) \ ; \text{ otherwise} \end{cases} & ; \ 2 \le l < (m-1) \\ Y^{*}_{jm} & ; \ l = m \\ \begin{cases} Y^{*}_{jl} \ ; \text{ if } (Y_{Pl}-(Y^{*}_{jm}+m_j^{n}(\bar{X}_{jl}-\bar{X}_{jm})) > 0 \\ Y^{*}_{jm} + m_j^{n}(\bar{X}_{jl} - \bar{X}_{jm}) \ ; \text{ otherwise} \end{cases} & ; \ m+1 \le l \le M \end{cases} \tag{2.55}$$

and, $\bar{Y}_{jl} = Y^{*}_{jl}$ for $l = 1$ or $M+1$.

The total length of the stretched track segment is, then, obtained as

$$L_j = \sum_{l=1}^{M} \left[(\bar{X}_{jl+1} - \bar{X}_{jl})^2 + (\bar{Y}_{jl+1} - \bar{Y}_{jl})^2 \right]^{1/2} \tag{2.56}$$

and horizontal inclinations of the deflected track segment at its both ends (ε_1^j, ε_2^j) are computed as:

$$\begin{aligned} \varepsilon_1^j &= \text{ATAN3}(\bar{Y}_{j2} - Y_{j1}, \ \bar{X}_{j2} - \bar{X}_{j1}) \\ \varepsilon_2^j &= \text{ATAN3}(\bar{Y}_{jM} - \bar{Y}_{jM+1}, \ \bar{X}_{jM} - \bar{X}_{jM+1}) \end{aligned} \tag{2.57}$$

2.5 VEHICLE'S ZERO-FORCE CONFIGURATION

Static loads under all road wheels corresponding to the static equilibrium of the vehicle are required to compute the static deflections associated with the vehicle response variables, and to establish the zero-force configuration. Static loads are either to be measured on the

real vehicle settled on a flat surface, or to be obtained analytically. Analytical approach is certainly an obvious choice due to its apparent advantages. Due to *statically indeterminate* nature of the problem (since number of road wheels on either side of the vehicle are usually more than two), a method is devised to approximate the static loads under all road wheels without sacrificing the equilibrium of the vehicle. However, prior to application of the proposed method to the multi-wheeled tracked vehicle, its basis can be best explained by considering an uniform rigid beam of weight, W, and length, L. As shown in Figure 2.20(a), the beam is subjected to an applied momemnt (M_a), and is supported by " N " number of supports, whose longitudinal locations (a_i's) with respect to the c.g. are known.

The procedure starts by assuming identical supprot loads. This assumption does satisfies the force balance equation, i.e.

$$\sum_{i=1}^{N} F_{wi}^{o} = W \; ; \; \text{where } F_{wi}^{o} = \frac{W}{N} \tag{2.58}$$

However, the moment balance equation is not necessarily satisfied,

$$\sum_{i=1}^{N} F_{wi}^{o} a_i + M_a = \mu \tag{2.59}$$

In order to satisfy both balance equations simultaneously, identical support loads are perturbed based on the amount of residual moment unbalance, μ, and on their relative locations with respect to the c.g. The perturbed support loads are, then, expressed as:

$$F_{wi} = F_{wi}^{o} + \Delta f_i \; ; \; i = 1,..,N \tag{2.60}$$

satisfying the static equilibrium of the beam such that,

$$\sum_{i=1}^{N} \Delta f_i = 0 \quad \text{and} \quad \sum_{i=1}^{N} \Delta f_i a_i = -\mu \tag{2.61}$$

The corrective force factors (Δf_i's) are obtained using equation (2.61) with an assumption of a linear distribution of correction factors associated with intermediate support loads between two end supprots, as illustrated in Figure 2.20(b). Equation (2.61) can be rewritten in the form as follows:

$$\sum_{j=1}^{N_r} \Delta f_j^r + \sum_{k=1}^{N_\ell} \Delta f_k^\ell = 0 \quad \text{and} \quad \sum_{j=1}^{N_r} \Delta f_j^r \, a_j^r + \sum_{k=1}^{N_\ell} \Delta f_k^\ell \, a_k^\ell = -\mu \tag{2.62}$$

where, N_r and N_r correspond to total number of supports on the right-hand-side ($r.h.s.$) and left-hand-side ($\ell.h.s.$) of the c.g., respectively, and $N = N_r + N_\ell$. Δf_j^r and Δf_k^ℓ are the corrective force factors associated with j^{th} $r.h.s.$ support load, and k^{th} $\ell.h.s.$ support load, respectively, and a_j^r (>0) and a_k^ℓ (<0) are the corresponding longitudinal locations. The corrective force factors for intermediate supports are expressed as:

$$\Delta f_j^r = \Delta f_{N_r}^r \left(\frac{a_j^r}{a_{N_r}^r} \right) \quad ; \quad j = 1,2,..N_r-1 \tag{2.63}$$

$$\Delta f_k^\ell = \Delta f_{N_\ell}^\ell \left(\frac{a_k^\ell}{a_{N_\ell}^\ell} \right) \quad ; \quad k = 1,2,..N_\ell-1 \tag{2.64}$$

Substituting equations (2.63) and (2.64) into equation (2.62) yields two equations with two unknowns. Thus, the corrective force factors associated with the end supports are obtained as:

$$\Delta f_1 = \Delta f_{N_r}^r = \frac{-\mu}{v_1 - \rho \, v_2} \tag{2.65}$$

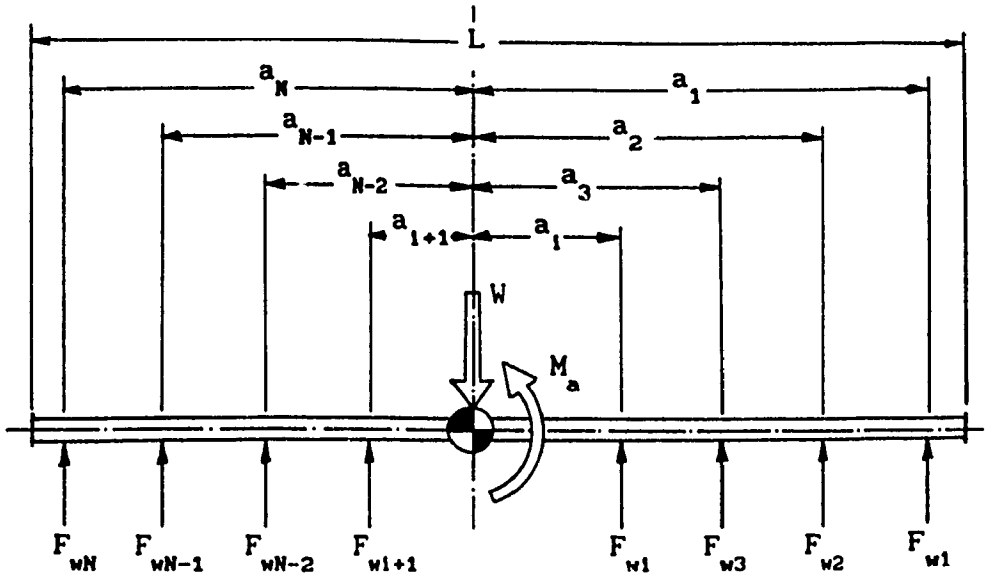

(a) An uniform rigid beam configuration.

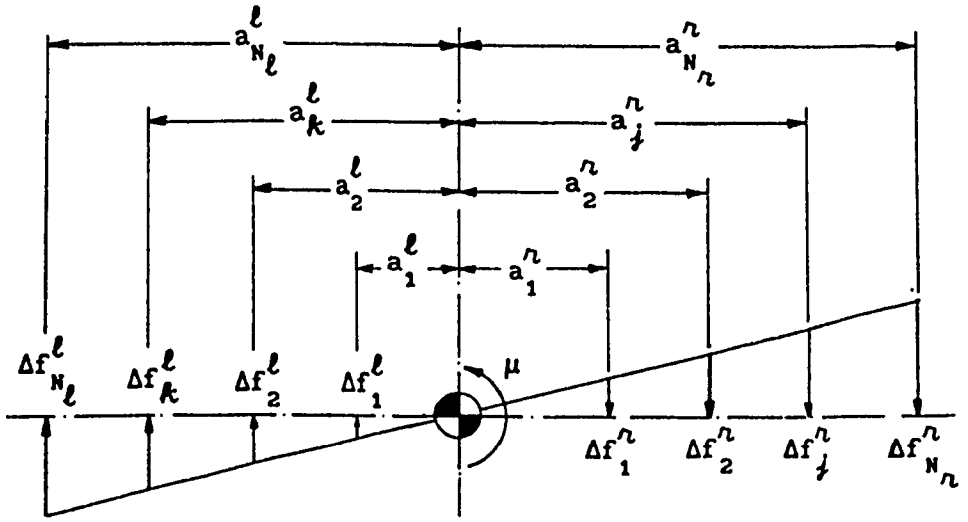

(b) Residual moment unbalance and corrective force factors.

Figure 2.20 Approximated static equilibrium of a statically indeterminate structure.

where, $$\upsilon_1 = \frac{1}{a_1}\sum_{j=1}^{N_r}(a_j^r)^2 \quad ; \quad \upsilon_2 = \frac{1}{a_N}\sum_{k=1}^{N_\ell}(a_k^\ell)^2$$

and $$\rho = \left(\frac{a_N}{a_1}\right)\left(\sum_{j=1}^{N_r} a_j^r \Big/ \sum_{k=1}^{N_\ell} a_k^\ell\right)$$

$$\Delta f_N = \Delta f_{N_\ell}^{\ell} = -\rho\, \Delta f_1 \tag{2.66}$$

The corrective force factors for intermediate supports are, then, obtained using equations (2.63) and (2.64).

The proposed method, as described above, is employed to approximate the static loads under the road wheels of the "N-wheeled" tracked vehicle as shown in Figure 2.4. The identical road wheel loads are computed as:

$$F_{wi}^{o} = \frac{W_h + \sum_{i=1}^{N} W_{wi}}{N} \; ; \; i = 1,..,N \tag{2.67}$$

where W_h and W_{wi} correspond to half of the hull weight, and the weight of i^{th} road wheel assembly on one side of the vehicle.

As per proposed method, the identical road wheel loads are perturbed in order to satisfy the static equilibrium of the vehicle system. Following steps are, then, followed in order to compute the settled position of each road wheel center, and to establish the zero-force configuration of the vehicle based on the initial generalized static deflections:

(a) The settled height of each road wheel center on a *horizontal flat surface* is evaluated by computing its deflection under the respective static load, which are updated to include the static track load due to the track pre-tension (T_{tr}^{o}), especially for front and rear road wheels, and are given as:

$$F_{wi} = F^{o}_{wi} + \Delta f_i - T^{i}_{wy} \; ; \text{ where } T^{i}_{wy} = \begin{cases} T^{0}_{tr}\sin\Theta_1 & ; \text{ if } i = 1 \\ T^{0}_{tr}\sin\Theta_2 & ; \text{ if } i = N \\ 0 & ; \text{ otherwise} \end{cases} \tag{2.68}$$

where Θ_1 and Θ_2 are the specified inclinations of the front and rear track feelers, as shown in Figure 2.4.

The deflection of each road wheel centre is obtained using equation (2.24), which is non-linear. Therefore, a *piece-wise linear* approach is employed to compute the deflection. For this, a look-up table containing net footprint force for gradually increasing wheel-terrain contact patch angle (α_{wi}), is constructed. The table is, then, linearly interpolated for the respective static load in order to obtain the corresponding contact patch angle, (α_{wi}). The height of the settled road wheel centre is, then, given as:

$$h_{wi} = R_{wi}\cos\alpha_{wi} \; ; \; i = 1,..,N \tag{2.69}$$

(b) The static loads are, then, carried over to the suspensions, given as

$$F^{o}_{si} = F_{wi} - W_{wi} + T^{i}_{wy} \; ; \; i = 1,..,N \tag{2.70}$$

The static suspension loads (F^{o}_{si}, i=1,..,N) are the initial values, which satisfy the static force balance, given as:

$$\sum_{i=1}^{N} F^{o}_{si} = W_h + \sum_{k=1}^{2} T^{k}_{hy} \tag{2.71}$$

The static suspension loads are, however, corrected to satisfy the moment balance about hull c.g. taking into account the net applied moment due to the static track loads. The applied moment is given as:

$$M_a = \sum_{k=1}^{2} a_{hk} T^{k}_{hy} + b_{hk} T^{k}_{hx} + \sum_{i=1}^{N} b_{wi} T^{i}_{wx} \tag{2.72}$$

where, $$T^k_{hx} = \begin{cases} -T^0_{tr}\cos\theta_1 \\ T^0_{tr}\cos\theta_2 \end{cases}; \quad T^k_{hy} = \begin{cases} -T^0_{tr}\sin\theta_1 & ; \text{ if } k = 1 \\ -T^0_{tr}\sin\theta_2 & ; \text{ if } k = 2 \end{cases};$$

$$T^i_{wx} = \begin{cases} -T^0_{tr}\cos\theta_1 & ; \text{ if } i = 1 \\ T^0_{tr}\sin\theta_2 & ; \text{ if } i = N \\ 0 & ; \text{ otherwise} \end{cases} \quad ; \text{ and } b_{wi} = h_{wi} - h_{cg}$$

(c) The static deflection of each suspension spring due to the corresponding suspension load, then, are computed based on the linear-interpolation of the specified force-deflection look-up table. The initial static displacements corresponding to hull bounce and pitch are computed based on the linear-interpolation of frontmost and rearmost suspension deflections, since the hull is assumed to be rigid. The initial vertical displacement for each road wheel center is obtained such that its vertical distance with respect to the hull c.g. (b_{wi}) is maintained. The initial vertical displacement for the suspended seat simply corresponds to the suspended weight of the driver and seat (W_o). Thus, the initial generalized displacements in order to establish the zero-force configuration of the vehicle are given as:

$$\delta^0_h = \Delta^0_N + a_N \left[\frac{\Delta^0_1 - \Delta^0_N}{a_1 - a_N}\right] \tag{2.73}$$

$$\theta^0_h = \tan^{-1}\left[\frac{\Delta^0_1 - \Delta^0_N}{a_1 - a_N}\right] \tag{2.74}$$

$$\delta^0_{wi} = \delta^0_h - \Delta^0_i \quad ; \quad i = 1,2,..,N \tag{2.75}$$

where δ^0_h, θ^0_h, δ^0_{wi}, and Δ^0_i correspond to vertical displacement of hull

c.g, pitch displacement of hull, vertical displacement of i^{th} road wheel center, and the deflection of i^{th} suspension unit under corresponding static load.

(d) Finally, the vehicle settled under its own weight is shifted vertically upwards using initial displacements such that the suspension springs do not feel any force. As illustrated in Figure 2.21, this is carried out by shifting upward the hull by its c.g. initial vertical displacement and keeping the hull frame horizontal. Similarly, the road wheel centers are placed in a vertical sense according to their respective initial displacements, and suspended seat is shifted vertically upwards by δ_o^0, which is the seat spring deflection due to W_o. The vertical coordinates of hull c.g., road wheel centres, and suspended driver's seat associated with vehicle's zero-force configuration are, then, specified as:

$$Y_{cg}^0 = h_{cg} + \delta_{cg}^0 \tag{2.76}$$

$$Y_{wi}^0 = h_{wi} + \delta_{wi}^0 \; ; \; (i=1,..,N) \tag{2.77}$$

$$Y_{ds}^0 = Y_{cg}^0 + b_o + b_{ds} + \delta_o^0 \tag{2.78}$$

2.6 VEHICLE SETTLEMENT - STATIC EQUILIBRIUM

The determination of static equilibrium of a tracked vehicle settled on a horizontally flat profile, is a statically indeterminate problem. The nonlinear force-displacement characteristics of the suspension springs introduce additional complexities in evaluating the static equilibrium. However, an approximation solution to the problem is sought without sacrificing the static equilibrium of the vehicle system. As explained in section 2.5, the proposed method approximates the static

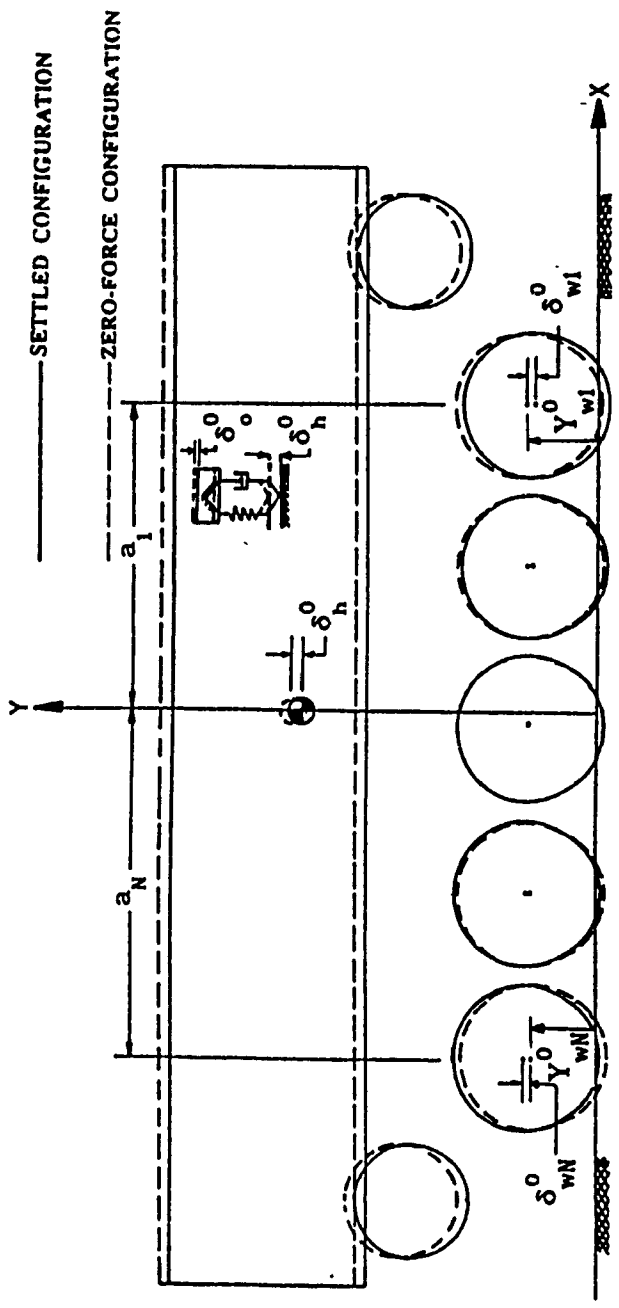

Figure 2.21 Vehicle's zero-force configuration.

loads under all road wheels and corresponding suspension loads, which are required to compute the initial generalized displacements associated with static equilibrium of the vehicle model and to establish its zero-force configuration. Due to approximations associated with the computation of initial generalized displacements, initial transients in the vehicle response were observed for the vehicle moving on a horizontally flat profile, and were, however, characterized to decay exponentially. Therefore, the vehicle was allowed to travel on the flat profile for a sufficient time so that the initial transients were fully ceased prior to the actual vehicle-terrain negotiation. However, this approach led to an unnecessary increase in the computational time. Consequently, it became apparent to take further steps in order to assure static equilibrium of the vehicle model.

Prior to the dynamical vehicle-terrain interaction, the static equilibrium of the tracked vehicle positioned on a horizontally flat profile with front hull wheel just aft of the specified profile (Figure 2.5), is assured using an iterative process. During this part of the computational process, the vehicle is allowed to settle under its own weight from the zero-force reference, and subsequently the initial generalized displacement vector characterizing static equilibrium of the vehicle, is obtained.

An *iterative stiffness method* based on the linear spring theory, is adopted for the vehicle settlement phase. In this method, the initial generalized displacements corresponding to the vehicle's zero-force configuration, are used as the starting values. As explained in section 2.4.3, the initial generalized displacements are indicated by δ_h^0, θ_h^0, δ_{wi}^0 ($i = 1,..,N$), and δ_o^0. The relative displacements across all suspension

and road wheel are, then, computed and used to obtain appropriate spring constants from the input spring curves and wheel model. The stiffness method is, then, applied to obtain new values for the displacements. The process is repeated until these displacements converge.

The governing equation for the iterative stiffness method is given as

$$\{ u_i \} = [K_{i-1}]^{-1} \{ F_a \} \tag{2.79}$$

where, the stiffness matrix as being a function of generalized displacements obtained in the previous step (i-1), is given as:

$$[K_{i-1}] = \begin{bmatrix} -(K_o + \sum_{i=1}^{N} K_i) & -(K_o a_o + \sum_{i=1}^{N} K_i a_i) & K_1 \ldots\ldots K_N & K_o \\ & -(K_o a_o^2 + \sum_{i=1}^{N} K_i a_i^2) & K_1 a_1 \ldots K_N a_N & K_o a_o \\ & & -(K_1 + K_{w1}) \ldots 0 & 0 \\ & \text{- SYMMETRIC -} & \ddots \quad \vdots & \vdots \\ & & -(K_N + K_{wN}) & 0 \\ & & & -K_o \end{bmatrix} \tag{2.80}$$

where, K_o is the spring constant for seat suspension obtained from the corresponding force-deflection look-up table as:

$$K_o = \text{Spring Force at } \Delta_o/\Delta_o \text{ ; where } \Delta_o = \{ \delta_h + a_o\theta_h - \delta_o \}_{i-1} \tag{2.81}$$

Similarly, K_i is the spring constant for i^{th} suspension unit obtained as:

$$K_i = \text{Spring Force at } \Delta_i/\Delta_i \text{ ; where } \Delta_i = \{ \delta_{wi} - \delta_h - a_i\theta_h \}_{i-1} \tag{2.82}$$

K_{wi} is the spring constant for i^{th} road wheel obtained from the plane footprint as:

$$K_{wi} = 2\, K'_{rw}\, R_{wi} \left(\sin \alpha_{wi} - \alpha_{wi} \cos \alpha_{wi} \right) / \Delta_{wi} \tag{2.83}$$

where $\alpha_{wi} = \cos^{-1}(R_{wi} - \Delta_{wi} / R_{wi})$ and $\Delta_{wi} = R_{wi} - (Y^0_{wi} + \delta_{wi})_{i-1}$

$\{ u_i \}$ is the up-dated initial generalized displacement vector given as:

$$\{ u_i \} = \{ \delta_h, \theta_h, \delta_{w1}, \ldots\ldots, \delta_{wN}, \delta_o \}'_i \tag{2.84}$$

$\{ F_a \}$ is the applied force vector, given as:

$$\{ F_a \} = \begin{Bmatrix} W_h - \sum_{k=1}^{2} F^k_{hy} \\ - M_a \\ W_{w1} + \kappa_{w1} (Y^0_{w1} - R_{w1}) - T^1_{wy} \\ \vdots \\ W_{wN} + \kappa_{wN} (Y^0_{wN} - R_{wN}) - T^N_{wy} \\ W_o \end{Bmatrix} \tag{2.85}$$

where W_h, W_{wi}, and W_o correspond to the weight of hull, the weight of i^{th} road wheel, and the weight of driver/seat, respectively. Y^0_{wi} is the vertical coordinate of i^{th} road wheel center as given in equation (2.77). M_a is the applied moment given by equation (2.72), where T^1_{wx} and T^1_{wy}, and T^k_{hx} and T^k_{hy} are computed based on equations (2.14) and (2.18) instead.

Natural Frequencies and Associated Mode Shapes

In addition to establishing the static equilibrium, the iterative stiffness method facilitates the estimation of undamped natural frequencies and associated mode shapes of the nonlinear tracked vehicle ride model. The stiffness matrix corresponding to the converged static displacement vector (static equilibrium), is used for the eigenvalue analysis.

For the free vibration, the general matrix form of equations of motion characterizing the dynamics of a linear vehicle model, is given as

$$[\ M\ ]\{\ \ddot{\alpha}\ \} + [\ K\ ]\{\ \alpha\ \} = \{\ 0\ \} \tag{2.86}$$

where, the mass/inertia matrix is given as:

$$[\ M\ ] = \begin{bmatrix} m_h & & & & \\ & I_h & & - 0 - & \\ & & m_{w1} & & \\ & & & \cdot & \\ & - 0 - & & & m_{wN} \\ & & & & & m_o \end{bmatrix} \tag{2.87}$$

The stiffness matrix corresponds to the converged stiffness matrix obtained during the iterative stiffness procedure, given as:

$$[\ K\ ] = -\ [\ K\ ]_{CONVERGED} \tag{2.88}$$

and $\{\ \alpha\ \}$ corresponds to the generalized displacement coordinates, given as:

$$\{\ \alpha\ \} = \{\ y_h,\ \theta_h,\ y_{w1}, \ldots\ldots,\ y_{wN},\ y_o\ \}' \tag{2.89}$$

The eigenvalue analysis of equation (2.86) yields natural frequencies (*eigenvalues*), and associated mode shapes (*eigenvectors*), which are vital to the study of vehicle's dynamic behaviour. In addition, the estimation of vehicle's highest natural frequency is used in the selection of an appropriate integration time step for the simulation.

2.7 COMPUTATIONAL PROCEDURE

The key elements of the computational procedure employed for performing simulation, are briefly discussed as follows:

Input

An input file containing simulation control parameters, terrain

profile description, and appropriate vehicle parameters is compiled. The control parameters correspond to the vehicle speed, the maximum vehicle horizontal travel distance (d_{max}) or maximum simulation time (t_{max}), and the incremental time steps for integration (Δ_t) and output files. The maximum travel distance, d_{max}, is usually specified based on the given vehicle's length, and the total stretch of specified terrain profile. As illustrated in Figure 2.5, the maximum horizontal travel distance is computed as:

$$d_{max} = L_1 + L_P + L_2 \tag{2.90}$$

where, L_1 indicates the initial horizontal positioning of the vehicle c.g. with respect to the begining of terrain profile's bumpy section, such that $X^0_{cg} = - L_1$, and is normally taken as equal to the longitudinal distance of hull's front end (a_F, as shown in Figure 2.4). L_P is the total stretch of the specified terrain profile, as illustrated in Figure 2.5. L_2 indicates the horizontal location of the vehicle c.g. with respect to the end of terrain profile's bumpy section, and should be specified so as to allow sufficient time for vehicle's dynamic response to cease. Consequently, L_2 is strongly dependent on the severity of the terrain profile and the vehicle speed, however, it is normally taken as total length of the hull frame. The maximum simulation time is, then, computed based on constant vehicle speed, V_x, as:

$$t_{max} = d_{max}/V_x \tag{2.91}$$

The incremental time step for integration, Δ_t, is generally selected based on the *rule of thumb* as " $1/(50.f_{max})$ ", where f_{max} is the highest natural frequency of the vehicle ride model. The incremental time steps for various output files are usually taken as an integer multiple of Δ_t.

As mentioned earlier (section 2.3.2), the desired terrain profile is input through a look-up table containing horizontal and vertical coordinates of successive points on the profile. The vehicle parameters, as indicated in Figure 2.4, constitute the input, where the suspension characteristics are described through force-deflection (spring) and force-velocity (damper) look-up tables. It should be noted that there is no need to input the elevation of each road wheel center, and the static load under each road wheel, since they are automatically computed in the initialization phase.

Initialization

The initialization phase sets up all appropriate parameters so that terrain negotiation phase can begin. This phase primarily assures static equilibrium of the vehicle positioned on a horizontally flat profile with front hull wheel just aft of the desired profile (Figure 2.5). As discussed in section 2.5, the vehicle's zero-force configuration is first established, which includes: (i) estimation of static loads under all road wheels and corresponding static deflections associated with the generalized coordinates, and (ii) vertical upward shift of the vehicle using estimated initial deflections. Next, the vehicle is allowed to settle under its own weight from the zero-force datum so as to compute the initial generalized displacment vector characterizing static equilibrium of the vehicle. As discussed in section 2.6, an iterative stiffness method is employed for vehicle settlement phase. In addition, the vehicle's natural frequencies and associated mode shapes are estimated based on the generalized static (equilibrium) deflections, and the vehicle's highest natural frequency is used in the selection of an appropriate integration time step for the simulation.

The initial values for the generalized displacements are, then, set equal to the values computed during the vehicle settlement phase with corresponding velocities and accelerations initialized to zero. At this point, the simulation begins by incrementing time with the vehicle horizontally moving forward with specified speed.

Solution of Equations of Motion

As a result of dynamical vehicle-terrain interaction, the net horizontal and vertical forces at all road wheel centers (F^{i}_{wx},F^{i}_{wy}, i = 1,..,N) as given in equations (2.11) and (2.12), and hull wheel centers (F^{k}_{hx},F^{k}_{hy}, k = 1,2) as given in equation (2.15) and (2.16), are computed. Primary suspension forces (F_{si},F_{di}, i = 1,2,..,N), and seat suspension forces (F_{so},F_{do}) are computed based on corresponding relative displacements and velocities as given by equations (2.7) to (2.10), where values of generalized displacements and velocities correspond to the previous time step. Equations of motions are, then, integrated to obtain velocity and displacement for each degree-of-freedom. A numerical integration technique based on Hammings Modified Predictor-Corrector method (a *variable time-step* approach), is used.

All key coordinates on the vehicle are updated using the corresponding displacements as they undergo two types of motion: (i) as a result of the solution of the equations of motion obtained at the end of the previous time step, and (ii) the horizontal translation of the c.g. The key coordinates are given as:

Hull Frame:

$$X_{cg} = X^{o}_{cg} + V_x.t \quad ; \quad Y_{cg} = Y^{o}_{cg} + y_h \tag{2.92}$$

where, t is the time incremented by Δ_t. The location of any point rigidly

connected to the hull frame, such as seat base (X_b, Y_b), hull wheel centers $(X_{hk}, Y_{hk}, k=1,2)$, and hull frame's front top corner (X_{hf}, Y_{hf}) and rear bottom corner (X_{hr}, Y_{hr}), is computed as:

$$\begin{Bmatrix} X \\ Y \end{Bmatrix} = \begin{bmatrix} C_\theta & -S_\theta \\ S_\theta & C_\theta \end{bmatrix} \begin{Bmatrix} a \\ b \end{Bmatrix} + \begin{Bmatrix} X_{cg} \\ Y_{cg} \end{Bmatrix} \tag{2.93}$$

i^{th} *Road Wheel Centre* (i=1,..,N):

$$X_{wi} = X_{cg} + a_i.C_\theta - b_i.S_\theta \quad ; \quad Y_{wi} = Y^0_{wi} + y_{wi} \tag{2.94}$$

Suspended Seat:

$$X_{ds} = X_{cg} + a_o.C_\theta - b_o.S_\theta \quad ; \quad Y_{ds} = Y^0_{ds} + y_o \tag{2.95}$$

This process continues until $t = t_{max}$.

Output

The output data is obtained as a table of time histories of response variables of interest. The output data serves as an input to the post-processor for data reduction and conditioning, such as signal filtering and FFT operation to produce information in the frequency domain for the purpose of ride quality assessment using ISO 2631, and absorbed power, and for a graphical display of response variables. In addition, an animation program is developed as a part of the post-processor, and is used to visualize the dynamic behaviour of the vehicle traversing the off-road terrain. A file containing the record of horizontal and vertical coordinates of the key locations serves as input to the animation program.

2.8 SUMMARY

In this chapter, an off-road high mobility tracked vehicle configuration, is selected as a candidate vehicle for model development and field testing purposes, and described in view of its running gear. A ride dynamic model, MODEL I, for the candidate vehicle is developed employing simplified yet credible formulations for vehicle suspension system, and dynamic wheel-track-terrain interactions. The procedure used for performing digital computer simulation of MODEL I, is discussed.

Nonlinear in-plane ride model, MODEL I, is formulated assuming constant forward vehicle speed and non-deformable arbitrary terrain profile. It is represented as a "3+N" degrees-of-freedom dynamic system comprising of generalized coordinates: bounce and pitch motions of hull, bounce motion of each of N road wheels, and bounce motion of driver/seat, where the magnitude of vehicle motion along the generalized coordinates is assumed to be large, and specified with respect to the vehicle's zero-force configuration. The highlights of MODEL I are summarized as follows:

- The wheel/track-terrain interaction (*net foot-print force*) is modeled using an equivalent damper and continous radial spring model, where the wheel-terrain contact patch is *idealized* by a straight line while ignoring small terrain irregularities within the foot-print. An effective computational procedure is devised for establishing the contact patch.
- Dynamic track load, imposed at each wheel station, is formulated based on an overall track tension, which is computed based on track pre-tension and track belt extensibility. An effective algorithm is developed for establishing the track-wheel connectivity and track-terrain contact patch.

- A mathematical procedure is developed for establishing vehicle's zero-force configuration, which involves estimating initial static road wheel and suspension loads, and associated generalized static deflection; and vertical upward shift of vehicle based on estimated deflections.
- A procedure based on an iterative stiffness approach is developed to compute the initial generalized displacement vector characterizing the vehicle's static equilibrium configuration and the associated undamped natural frequencies and mode shapes.

Chapter 3

FIELD TESTING AND VALIDATION OF RIDE MODEL I

3.1 INTRODUCTION

A computer simulation model (MODEL I) for analyzing the ride dynamic behaviour of high mobility tracked vehicles, is developed and presented in Chapter 2. Computer simulations can, however, only be beneficial if the analytical model reflects accurately the behaviour of the vehicle. Consequently, field testing of a representative vehicle becomes absolutely essential in order to assess the limitations of the computer model, and to validate the predictions of the vehicle ride performance.

During the summer-fall period of 1990, field testing of an in-service M113 APC was carried out by Land Engineering Test Establishment (LETE) at their facility for various vehicle configurations, vehicle speeds, and field courses. Prior to field testing of the M113 APC, a test plan indicating appropriate instrumentation/equipment, their locations and mounting methods, and a detailed outline of test runs in view of vehicle configurations, terrain profiles, and speeds, was prepared by CONCAVE in collaboration with LETE. The test plan was devised such that the field testing could be conducted in a systematic manner so as to ensure reliable measurements with minimum number of field tests. A large amount of measurement data was gathered during field testing, which was, then, conditioned and reduced for the purpose of ride quality assessment and validation of the computer ride model.

In this chapter, the details of the experimental phase of this study are presented in view of the test vehicle and field courses, instrumentation, test runs, and field-measured ride data to be collected. For

specified test conditions, simulations are performed using MODEL I, and the ride predictions are directly compared with the field measurements. Based on field validation, the limitations of MODEL I are assessed in view of further modeling improvements.

3.2 TEST VEHICLE AND COURSES

The first, and most important step in the field testing, is to select a representative vehicle, and appropriate field courses. For the purpose of this study, the M113 APC in its A1 version (CFR No. 65-35026 - a LETE reference vehicle) was selected to represent the present fleet of in-service M113 family of vehicles. In Chapter 2 (section 2.2), a typical M113 APC is described in view of its running gear and three primary suspension configurations: A1, A2, and A1$\frac{1}{2}$. The M113A1 APC was tested under two configurations - loaded (*laden*) and unloaded (*unladen*). The loaded condition was intended to simulate the combat-loaded state of the APC. The laden configuration was achieved by employing a load consisted of filled sandbags constrained within a plywood ballast box placed on the floor of the crew compartment. The total load was approximately 1850 kg.

Field testing of the unladen configuration was conducted with three different levels of track pre-tension (T_{tr}^{0}): nominal; 75% of nominal; and 125% of nominal. For M113 family of vehicles, the track pre-tension is generally selected according to a certain specified gap between the bottom of the track segment hanging between drive sprocket and idler, and the top of the second road wheel, as illustrated in Figure 3.1. The nominal track pre-tension for a typical M113 APC is 10 kN, and the corresponding gap is approximately 20 mm. The static track tension measurements for the Diehl 213G track on M113A1 APC, were made by LETE

for gradually incremented gap so as to establish a functional relationship. Figure 3.2 shows the schematic of the test set-up, and the functional relationship between track pre-tension and the gap obtained by fitting an exponential regression curve through the measured data. As shown, the track tension increases almost linearly for the specified range of the gap above the second road wheel.

A considerable number of dimensional measurements were made by LETE in order to gather physical data describing the test vehicle. The data was gathered through direct and photographic measurements. This data is essential to generate an accurate input data for the computer ride models.

The field courses selected for field testing of the M113A1 APC include a sinusoidal course, a random course, Belgian Pavé, and discrete half round obstacles of various radii. These courses represent a wide spectrum of inputs from a single-frequency vibratory input to shock inputs with wide frequency contents. Table 3.1 and Figure 3.3 exhibits the general description and characteristics of all four types of terrain profiles.

3.3 INSTRUMENTATION

The instrumentation requirements for the field testing of the M113A1 APC were established on the basis of the number and type of the required output signals. In addition to continously monitoring the vehicle speed, the primary instrumentation requirements were to measure acceleration levels corresponding to: (i) bounce, pitch, and roll motions of the hull; (ii) longitudinal, lateral, and bounce motions of the driver's seat; and (iii) angular motion of each road wheel assembly about

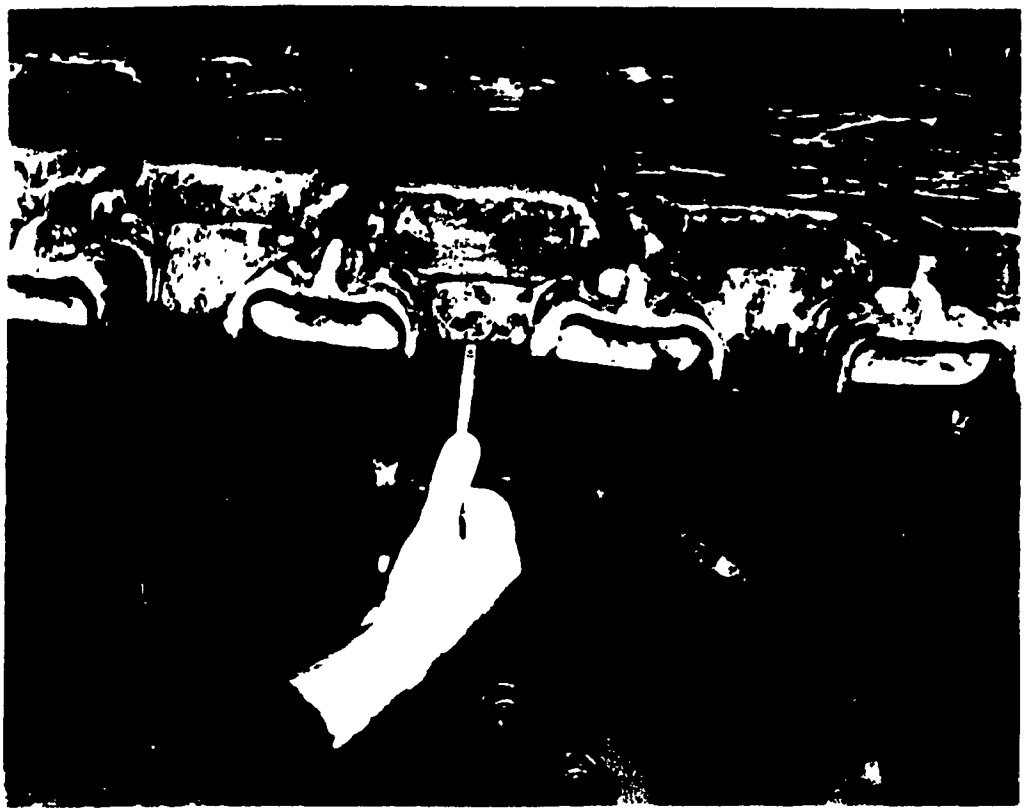

Figure 3.1 Track pre-tension setting - measurement of track gap at second road wheel [69].

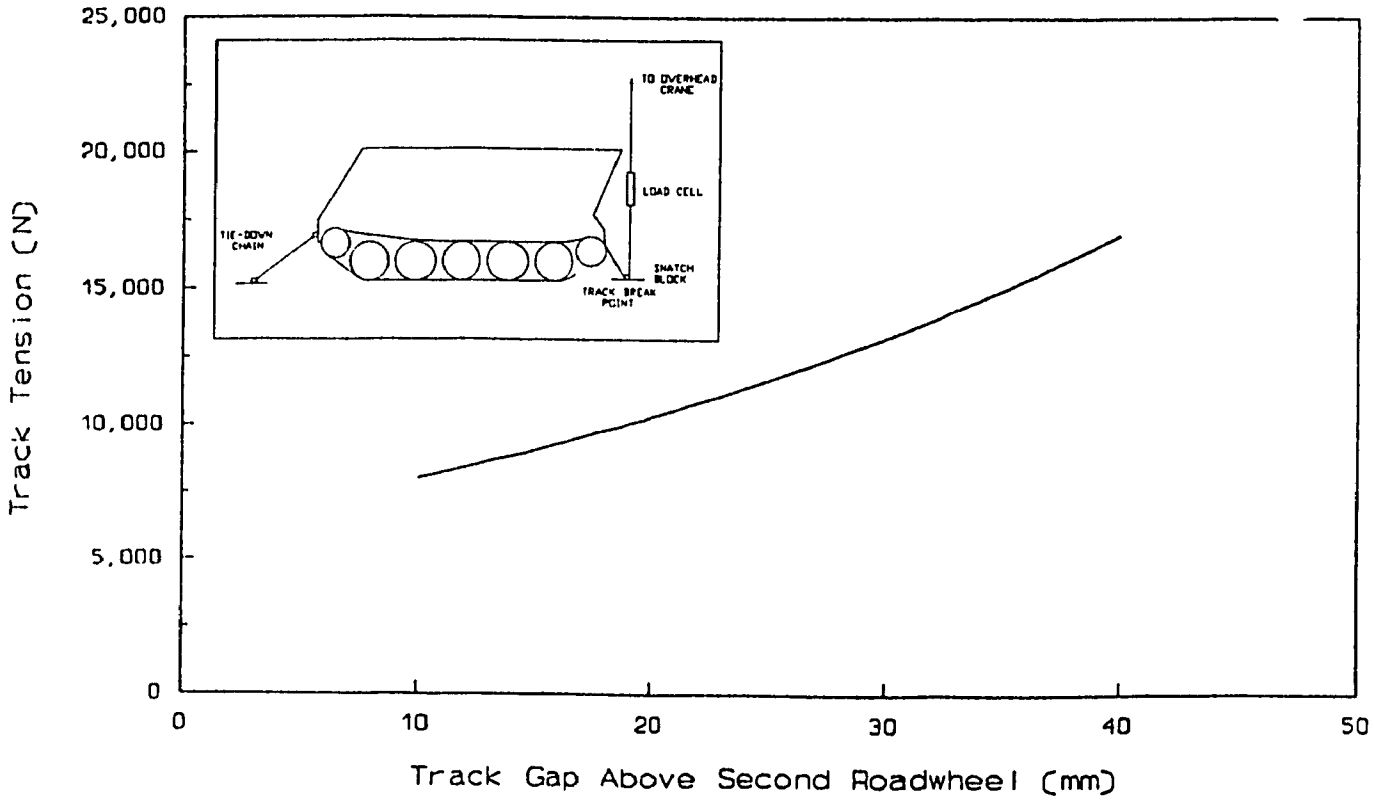

Figure 3.2 Track tension versus track gap - experimental set-up for static track tension measurement [69].

Table 3.1 Selected LETE field courses for testing.

Course	*Description*	*Length* m (in)	rms *Roughness* m (in)
6" Half-Round Obstacle	An obstacle of a 6-in. radius section of steel pipe, cut in half along its longitudinal axis, and filled with Concrete	0.3048 (12)	0.124 (4.90)
8" Half-Round Obstacle	Same as 6" obstacle, except with obstacle radius of 8 in.	0.4064 (16)	0.166 (6.53)
Sine Course	Eastern Half of a Concrete Course with sinusoidal profile. The course wavelength is 0.76 m (30 in), and the Peak-to-Peak amplitude is approximately 0.14 m (5.4 in)	121.5 (4783.5)	0.048 (1.91)
Random Course # 48	Natural Course running East-West created by removing top soil, vegetation, etc. from underlying granite out-cropping	70 (2755.9)	0.059 (2.31)
Belgian Pavé	Cobblestone Course constructed with bricks	243 (9567)	0.012 (0.46)

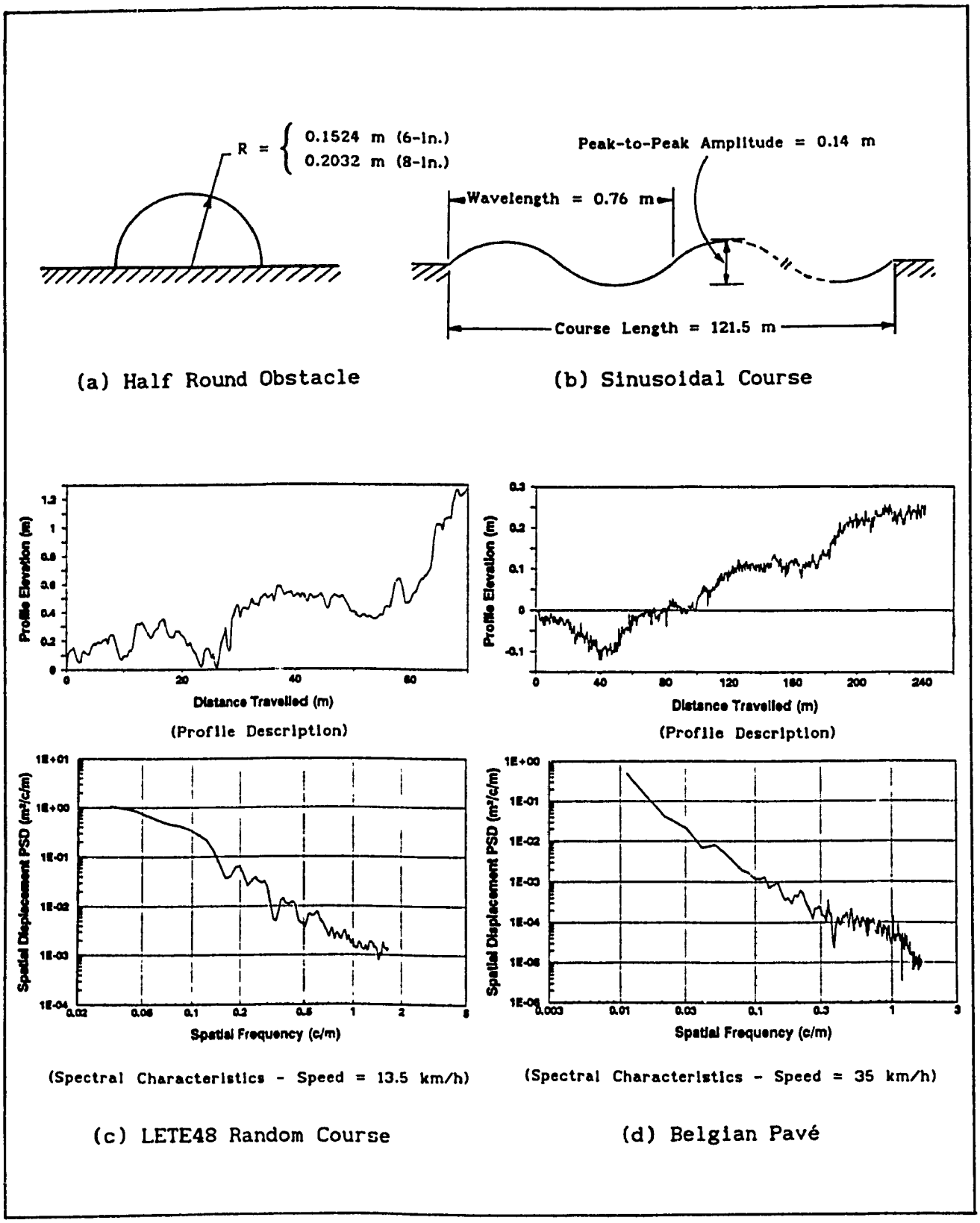

Figure 3.3 Description/characteristics of test courses.

its torsion bar centre, atleast for one side of the vehicle. Consequently, several instruments were installed on the vehicle, which included a sprocket-mounted optical encoder to record vehicle speed, and 16 accelerometers placed at various points of interest on the vehicle. A data acquisition system digitized and stored on magnetic tape cartridge all measured signals from the transducers (encoder and accelerometers). A schematic of the setup is shown in Figure 3.4, where each transducer input is referred to as a channel, indicated by $\mathbb{C}_i$, i=1,..,17.

The data acquisition system used was a portable unit, MegaDAC Model 2210C, from Optim Electronics Corporation. This unit was placed behind the driver at one side of the cargo compartment on shock mounts, and was configured to sample each of the 17 data channels 150 times per second. The unit was remotely controlled using a LETE customized smart switch, which was mounted at the commander's hatch.

The vehicle speed was recorded indirectly by means of a shaft-mounted optical encoder fixed to the left drive-sprocket, as shown in Figure 3.5. The encoder generates 300 pulses per revolution, which is satisfactory for measurement of even low vehicle speed. The output from the encoder was sent to a pulse counter which was polled 150 times per second by the MegaDAC. The digitized vehicle forward speed (V_x, m/s), at i^{th} time instant (t_i, s) is computed as:

$$V_x(t_i) = \frac{2\,\pi\,R_{h1}}{300}\left[\frac{\mathbb{C}_1(i) - \mathbb{C}_1(i-I+1)}{\Delta T\ (I-1)}\right] \qquad (3.1)$$

where, $t_i = (i-1)\,\Delta T \;\;;\;\; \Delta T = \frac{1}{150}\ (s) \;\;;\;\; i = 1,2,\ldots,(T_r/\Delta T)+1$

T_r is the total duration (seconds) of the recorded time history, $\mathbb{C}_1(i)$ is the output from the optical encoder digitized at i^{th} time instant of the

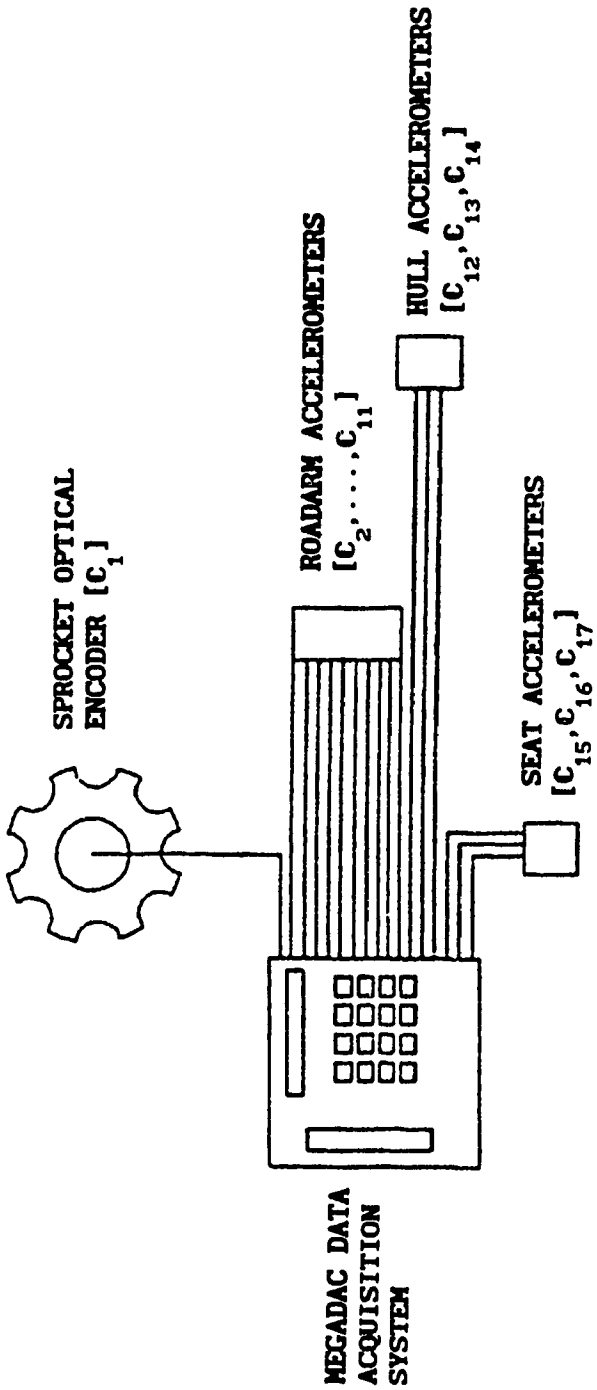

Figure 3.4 Schematic of installed instrumentation [69].

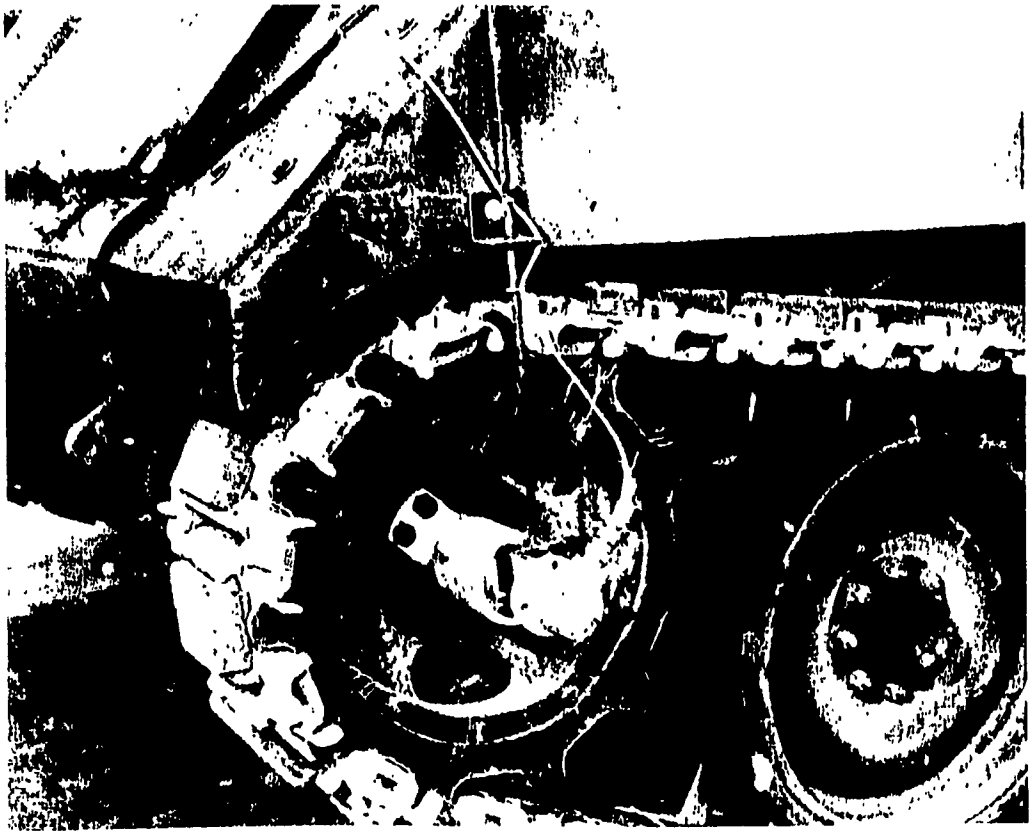

Figure 3.5 Rotary optical encoder installed on the left drive sprocket [69].

recorded time history, R_{h1} is the radius of drive sprocket, and I is an arbitrary integer (≥ 1), intended to yield an average vehicle speed over a relatively longer duration than the sampling increment, ΔT. For instance, the vehicle speed for I=20, is computed based on every 20th digitized output with time increment of 0.127 s.

The equation (3.1) can, then, be rewritten as:

$$V_x(t_i) = 3.6\ \pi\ R_{h1} \left[\frac{C_1(i) - C_1(i-I+1)}{(I-1)} \right] ;\ (km/h) \qquad (3.2)$$

To measure angular acceleration of the road wheel assembly about torsion bar centre, each roadarm on the left side of the vehicle was instrumented with two accelerometers mounted along and perpendicular to the roadarm centreline. As illustrated in Figure 3.6, this arrangement permits direct calculation of the angular acceleration of the road wheel assembly about its torsion bar centre. The tangential acceleration or acceleration perpendicular to the roadarm centreline of the i^{th} road wheel assembly at two specified locations can be expressed as:

$$a^i_{t1} = a^i_t + r^i_1\ \ddot{\theta}_{wi} \qquad (3.3)$$

$$a^i_{t2} = a^i_t + r^i_2\ \ddot{\theta}_{wi} \qquad (3.4)$$

where, a^i_t is the tangential acceleration at i^{th} torsion bar centre due to the hull spatial motion, and is unknown; and r^i_1 and r^i_2 are the known radial locations of the tangential acceleration measurement points along i^{th} roadarm centreline.

The angular acceleration of i^{th} road wheel assembly about its torsion bar centre, is conveniently obtained by subtracting equation (3.4) from equation (3.3), which eliminates the unknown acceleration, a^i_t.

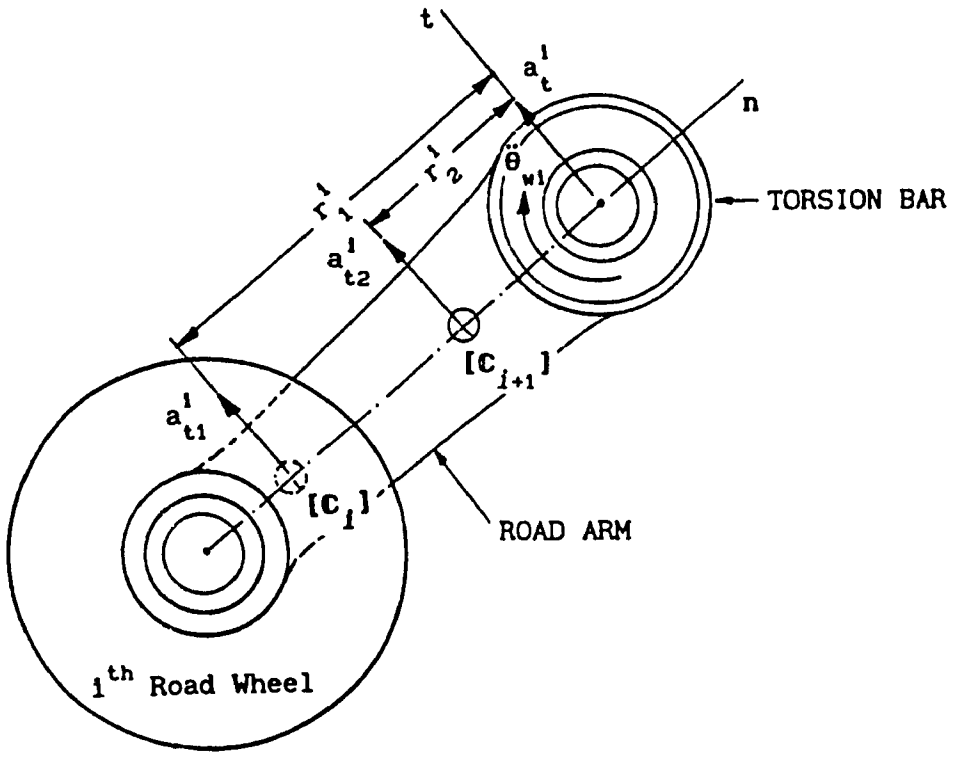

Figure 3.6 Schematic representation of i^{th} road wheel assembly showing two accelerometers mounted at specified radial locations to measure angular acceleration.

Consequently, the angular acceleration of i^{th} road wheel assembly at i^{th} time instant is given as:

$$\ddot{\theta}_{wi}(t_i) = \frac{a^i_{t1} - a^i_{t2}}{r^i_1 - r^i_2} = \frac{\mathbb{C}_i(i) - \mathbb{C}_{i+1}(i)}{r^i_1 - r^i_2} \qquad (3.5)$$

$$(i = 5,4,3,2,1 \quad \& \quad i = 2,4,6,8,10)$$

where, $\mathbb{C}_i(i)$ is the output from i^{th} accelerometer digitized at i^{th} time instant of the recorded time history. The channel assignments for each pair of accelerometers attached at an individual roadarm, as given in equation (3.5), are indicated by 2 and 3 for fifth (last) road wheel assembly, 4 and 5 for fourth road wheel assembly, and so on.

The accelerometers were stud-mounted on small steel blocks welded to the roadarms. The mounting locations for the accelerometers were chosen as close as possible to the roadarm centreline so as to measure accurately the tangential acceleration with respect to the torsion bar centre. On roadarms 2, 3, and 4, these blocks were placed on the inner side of the roadarm (i.e. facing the vehicle's belly). However, because of the inclined shock absorbers on roadarms 1, and 5, accelerometers were placed on the outer side of the roadarms. The measured radial locations of each pair of accelerometers with respect to the torsion bar centre are:

$$r^i_1 = \begin{cases} 0.120 \text{ m} \\ 0.127 \text{ m} \end{cases} ; \quad r^i_2 = \begin{cases} 0.246 \text{ m ; for i = 1,5} \\ 0.317 \text{ m ; for i = 2,3,4} \end{cases}$$

All ten accelerometers were from Brüel & Kjaer (B&K) piezoelectric type 4371. The accelerometer signals were fed into a bank of B&K charge amplifiers (type 2651) powered by B&K type 2805 power supply, and then

recorded directly in the MegaDAC as digital data.

The acceleration levels associated with hull bounce, pitch, and roll motions were calculated from the measured vertical acceleration signals at three corner locations on top of the APC. As illustrated in Figure 3.7, the vertical displacements at the three measurement locations can be expressed in terms of hull c.g. vertical and angular displacements through the following kinematic constraint equations:

$$y_1 = y_h + \ell_1 \sin \theta_h + w_1^* \sin \phi_h \tag{3.6}$$

$$y_2 = y_h - \ell_2 \sin \theta_h + w_1 \sin \phi_h \tag{3.7}$$

$$y_3 = y_h - \ell_2 \sin \theta_h - w_2 \sin \phi_h \tag{3.8}$$

where, y_h, θ_h, and ϕ_h correspond to hull bounce, pitch, and roll displacements Double differentiation of above set of equations with respect to time yields the following set of acceleration equations:

$$\ddot{y}_1 = \ddot{y}_h + \ell_1 \dot{\Omega}_P + w_1^* \dot{\Omega}_R \tag{3.9}$$

$$\ddot{y}_2 = \ddot{y}_h - \ell_2 \dot{\Omega}_P + w_1 \dot{\Omega}_R \tag{3.10}$$

$$\ddot{y}_3 = \ddot{y}_h - \ell_2 \dot{\Omega}_P - w_2 \dot{\Omega}_R \tag{3.11}$$

where, $\dot{\Omega}_P$ and $\dot{\Omega}_R$ correspond to hull pitch and roll accelerations, respectively, expressed as:

$$\dot{\Omega}_P = \ddot{\theta}_h \cos \theta_h - \dot{\theta}_h^2 \sin \theta_h \tag{3.12}$$

$$\dot{\Omega}_R = \ddot{\phi}_h \cos \phi_h - \dot{\phi}_h^2 \sin \phi_h \tag{3.13}$$

Assuming small angular displacements (i.e. $\sin \theta_h \cong \theta_h$; $\sin \phi_h \cong \phi_h$) yield, $\dot{\Omega}_P = \ddot{\theta}_h$, and $\dot{\Omega}_R = \ddot{\phi}_h$. Rewriting equations (3.10) and (3.11), the

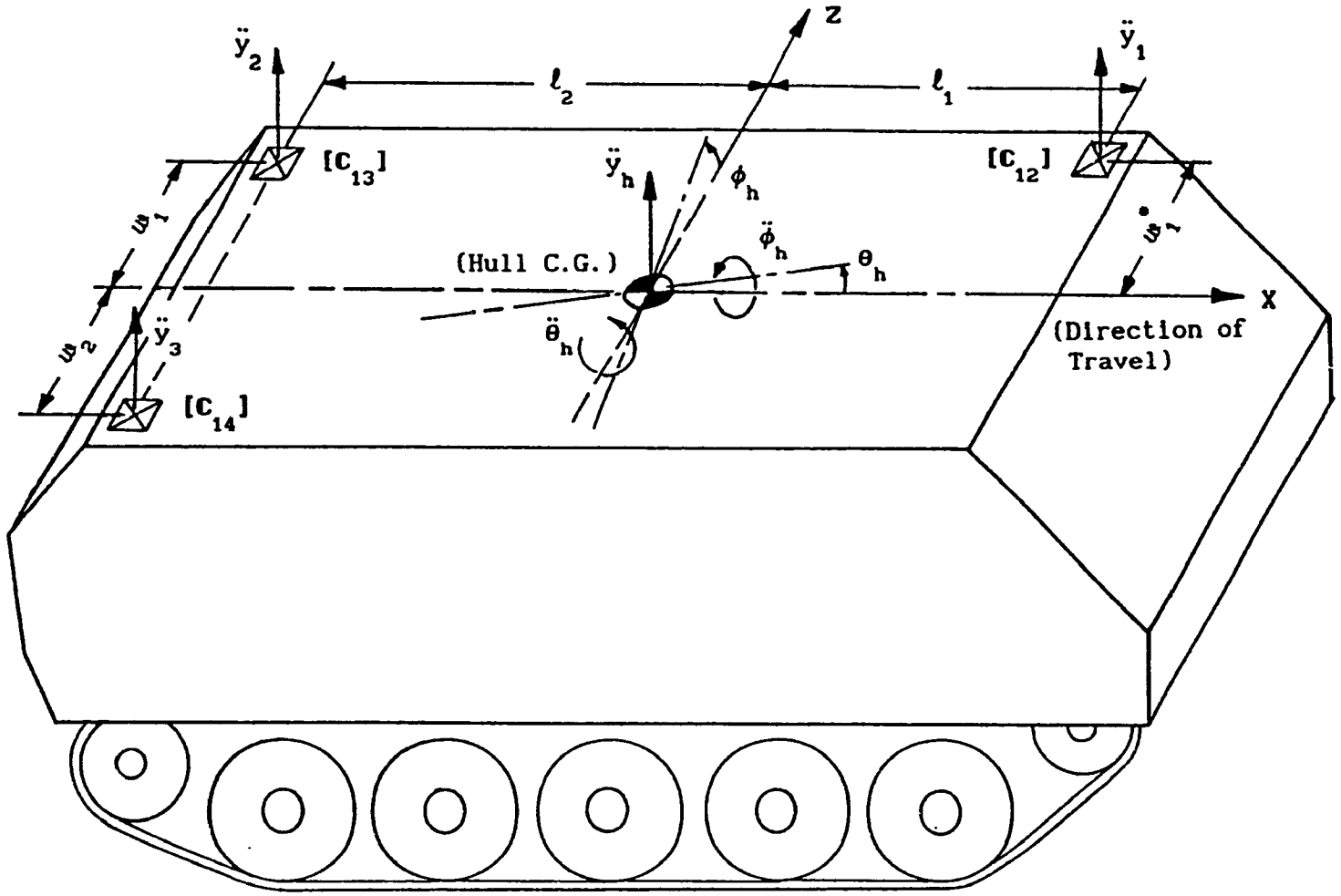

Figure 3.7 Schematic representation of test vehicle showing three accelerometers mounted at specified corner locations to measure hull bounce, pitch, and roll accelerations.

hull roll acceleration can be expressed as:

$$\dot{\Omega}_R(t_i) = \frac{\ddot{y}_2 - \ddot{y}_3}{w_1 + w_2} = \frac{C_{13}(i) - C_{14}(i)}{w_1 + w_2} \qquad (3.14)$$

The hull pitch acceleration is, then, obtained by subtracting equation (3.10) from equation (3.9), and substituting for $\dot{\Omega}_R$, and is given by:

$$\dot{\Omega}_P(t_i) = \frac{\ddot{y}_1 - \ddot{y}_2 - (w_1^* - w_1)\dot{\Omega}_R}{\ell_1 + \ell_2} = \frac{C_{12}(i) - C_{13}(i) - (w_1^* - w_1)\dot{\Omega}_R(t_i)}{\ell_1 + \ell_2} \qquad (3.15)$$

Finally, the hull bounce acceleration is obtained once hull pitch and roll accelerations, are known. The hull bounce acceleration can be conveniently obtained using equation (3.9), given as:

$$\ddot{y}_h(t_i) = \ddot{y}_1 - \ell_1 \dot{\Omega}_P - w_1^* \dot{\Omega}_R = C_{12}(i) - \ell_1 \dot{\Omega}_P(t_i) - w_1^* \dot{\Omega}_R(t_i) \qquad (3.16)$$

The hull roll, pitch, and bounce accelerations, as expressed through equations (3.14), (3.15), and (3.16), respectively, are obtained as digitized time histories using measured signals recorded in channels: C_{12}, C_{13}, and C_{14}. The accelerometers were Endevco piezoresistive type 2262C-25, and epoxied to the bare metal. The signal were relayed to three Endevco signal conditioners (type 4423) powered by an Endevco type 4225 power supply, and then recorded in the MegaDAC as digital data.

The acceleration levels along the three principle axes (X-,Y-, and Z-axes) at the driver-seat interface were measured using a B&K type 4322 triaxial seat accelerometers taped to the driver's seat, as shown in Figure 3.8. The seat accelerometers are of piezoelectric type with unity gain, which were initially connected to three Honeywell-CEC charge amplifiers (type 1-303-0001). However, two of these charge amplifiers had

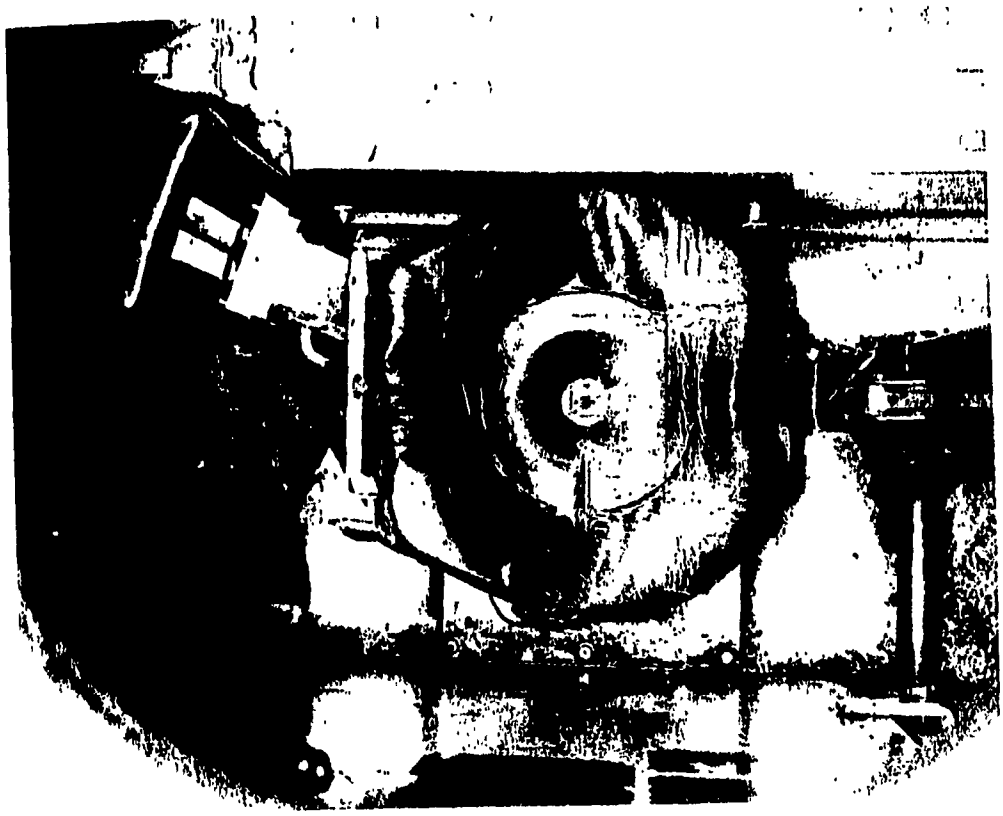

Figure 3.8 B & K seat cushion as seen from above [69].

to be replaced by B&K charge amplifiers (types 2651 and 2634), due to their unsatisfactory low frequency characteristics. Due to the lack of availability of an additional charge amplifier for the third seat axis, the Z-axis (lateral) signal was not measured. The bounce acceleration at the seat base was measured by employing an Endevco 2262C-25 accelerometer epoxied to the floor beneath the driver's seat. The channels in the MegaDAC for acceleration measurements associated with driver's seat, were assigned as: C_{15} for bounce acceleration at the seat base; C_{16} for fore-aft acceleration at driver-seat interface; and C_{17} for bounce acceleration at driver-seat interface.

3.4 FIELD TESTING AT LETE

A detailed test procedure outlining the test runs in view of vehicle configurations, terrain profiles, and vehicle speeds was prepared in collaboration with LETE. The test procedure was conceived based on: (i) maximizing the number of measurements with minimum number of field tests, and (ii) recommending a range of vehicle speeds for each test course, so as to ensure safeguard of personnel and instrumentation. Table 3.2 lists the range of vehicle speeds, which were recommended for each test course. The maximum vehicle speeds for the specified test course approximate the *ride-* and/or *shock-limiting speeds*. The *ride-limiting speed* corresponds to the speed at which the 6-watt average absorbed power level occurs at the driver/crew location for test courses with rms surface roughness of 0.5 - 3.5 in. The *shock-limiting speed* corresponds to the speed which a 2.5 g peak acceleration occurs over a group of discrete obstacle that cover an acceptable range of obstacle height (half round obstacles· 6 - 16 in.) [38]. The limiting vehicle

Table 3.2 Recommended vehicle speeds for field testing.

(i) Vehicle Speeds for 6" Half Round Obstacle: V_{6-1} = 16.0 km/h V_{6-2} = 24.0 km/h V_{6-3} = 32.0 km/h
(ii) Vehicle Speeds for 8" Half Round Obstacle: V_{8-1} = 8.0 km/h V_{8-2} = 16.0 km/h V_{8-3} = 24.0 km/h
(iii) Vehicle Speeds for Sine Wave: V_{S1} = 3.2 km/h V_{S2} = 4.8 km/h V_{S3} = 6.4 km/h V_{S4} = 8.0 km/h
(iv) Vehicle Speeds for Random Course # 48: V_{R1} = 6.5 km/h V_{R2} = 10.0 km/h V_{R3} = 13.0 km/h V_{R4} = 16.0 km/h V_{R5} = 19.0 km/h
(v) Vehicle Speeds for Belgian Pavé: V_{B1} = 16.0 km/h V_{B2} = 24.0 km/h V_{B3} = 32.0 km/h V_{B4} = 40.0 km/h

speeds for each test course were established from the experimental studies conducted on M113 APC's [70], and simulation runs made using MODEL I.

A calibration check of all instruments was performed prior to installation. All instruments, as discussed previously, were installed at the appropriate locations in the vehicle using the specified methods. Prior to the actual field testing, few dry runs (*instrumentation shake-down*) were made in order to insure proper operation of instruments, and to judge the quality of recorded field data . However, regular checks of the instrumentation were also made during the actual field testing.

The M113A1 APC was driven over the selected test courses (Table 3.1 and Figure 3.3) at the corresponding recommended vehicle speeds (Table 3.2). The acceleration signals were digitized, and recorded employing the MegaDAC data acquisition system. Similarly, the output from the drive sprocket-mounted optical encoder was digitized and recorded for the purpose of computing the vehicle speed trace (equation 3.2).

Field testing of the M113A1 APC was conducted using four vehicle configurations, which corresponds to vehicle's loading condition, and specified initial track tension. The four basic vehicle configurations are outlined as below:

- Configuration A: *Laden Vehicle with Nominal Track Pre-Tension*

  The vehicle was driven over sine course, Belgian Pavé, and LETE48 random course for specified speeds.

- Configuration B: *Unladen Vehicle with Nominal Track Pre-Tension*

  The vehicle was driven over sine course, Belgian Pavé, LETE48 random course, and 6" and 8" half round obstacles for specified speeds.

- Configuration C: *Unladen Vehicle with 75% of Nominal Track Pre-*

Tension

The vehicle was driven over LETE48 random course, and 6" half round obstacle for specified speeds.

- Configuration D: *Unladen Vehicle with* 125% *of Nominal Track Pre-Tension*

  Same as configuration C.

3.5 AN OVERVIEW OF FIELD MEASUREMENTS

A large amount of measurement data was gathered during field testing. The measured data was conditioned and reduced for the purpose of ride quality assessment, and validation of the computer ride model. A computer program was developed for the analysis of the field-measured data, employing algorithms for the signal windowing and filtering, computation of record peak and rms values, and FFT analysis to produce information in the frequency-domain. The computer program performes the following functions in a specified order:

(a) Reads the binary data file containing raw vibration data,

(b) Creates corresponding ASCII files for vehicle speed trace using equation (3.2); angular acceleration traces for all five road wheel assemblies based on equation (3.5); hull roll, pitch, and bounce acceleration traces using equations (3.14) to (3.16); fore-aft acceleration trace for driver's seat; and bounce acceleration traces associated with seat base and driver-seat interface,

(c) Particular acceleration trace of interest is selected, and windowed based on a specified initial time (t_i) indicating the time instant just before the vehicle came into contact with the terrain, and final time (t_f) indicating the end of vehicle-terrain negotiation. The

windowed acceleration trace is, then, filtered beyond a specified frequency (usually 25 Hz) using an algorithm for a digital low pass filter, and

(d) Calculates peak magnitude, rms value, power spectral density (PSD) and rms acceleration frequency spectra.

Field measured data in its entirety was analyzed using the computer program. A final list of data files containing the good field measurements was prepared and grouped for each type of test course. For instance, Table 3.3 lists test data files, and corresponding test conditions, for 6" half round obstacle. The data file number is specified in a format so as to indicate the month, the day, the test set number, and the number of test run. The segment of the test file used for analysis was windowed by t_i and t_f, as discussed above. The desired vehicle speed is the recommended speed as listed in Table 3.2, and the actual vehicle speed is the rms value of the measured vehicle speed trace.

The response plots indicating the vehicle's shock and ride performance in terms of absolute peak acceleration and average absorbed power at the driver's seat for the bounce mode, are presented and discussed. As mentioned in section 3.4, the peak value (g's) found in the vertical acceleration trace at the driver-seat interface indicates the shock-performance of the vehicle traversing discrete half round obstacles. Figure 3.9 shows the vertical peak acceleration found in the field-measured acceleration data at the driver's seat of the test vehicle configuration B crossing discrete half round obstacles of radii 6" and 8" at various speeds. As it is clearly shown, the shock-performance due to 6" obstacle is significantly superior, and the shock-limiting speed is

Table 3.3 Test run index for 6" half round obstacle.

Test Data File No.	*Loading Condition*	*Track Pre-Tension (Gap,mm)*	*File Segment:* $t_i - t_f$, s *(Total Time)*	*Vehicle Speed: Desired/Actual,* km/h
S-25-2-1	Unladen	Low (12)	19.4 - 21.9 (2.5)	16.0/14.9
S-25-2-2	Unladen	Low (12)	16.9 - 18.9 (2.0)	24.0/22.3
S-25-2-3	Unladen	Low (12)	21.4 - 23.0 (1.6)	32.0/28.2
S-19-1-3	Unladen	Nominal (20)	42.4 - 45.4 (3.0)	16.0/14.3
S-19-1-4	Unladen	Nominal (20)	22.15 - 24.65 (2.5)	24.0/20.1
S-19-1-5	Unladen	Nominal (20)	22.15 - 23.95 (1.8)	32.0/29.4
S-25-3-1	Unladen	High (26)	21.8 - 24.3 (2.5)	16.0/15.4
S-25-3-2	Unladen	High (26)	23.0 - 25.0 (2.0)	24.0/22.3
S-25-3-3	Unladen	High (26)	21.0 - 22.6 (1.6)	32.0/28.5

unlimited. The shock-limiting speed for 8" obstacle is, however, approximated at 14 km/h. Figure 3.10 illustrates the influence of track pre-tension on the shock performance of the unladen M113A1 APC (vehicle configurations: B, C, and D) crossing 6" obstacle at various speeds. The data does not exhibits any significant changes in the vehicle's shock performance due to variation in the track pre-tension.

The ride dynamic behaviour of M113A1 APC traversing sine course at various speeds in its configurations A and B, is exhibited in terms of rms acceleration at the driver's seat versus excitation frequency (Hz), as shown in Figure 3.11. The excitation frequency is computed as:

$$f = \frac{V_x}{\lambda} \; ; \; (\text{Hz}) \qquad (3.17)$$

where, V_x (m/s) is the actual vehicle speed, and λ (m) is the wavelength of the sine course (Figure 3.3). For laden and unladen configurations of M113A1 APC, the peak values of rms acceleration occur at 1.7 Hz (4.7 km/h) and 1.9 Hz (5.4 km/h), respectively, as shown by the data exhibited in Figure 3.11.

Figure 3.12 illustrates the ride performance of M113A1 APC traversing the LETE48 random course in its configurations A and B. The ride performance of laden M113A1 APC is slightly superior at lower vehicle speed (< 8 km/h). However, the ride-limiting speed of laden M113A1 APC is approximated at 14 km/h in comparison with 17.5 km/h for unladen configuration. In other words, the mobility performance of M113A1 APC in view of its ride quality is deteriorated as a result of the loading condition. Figure 3.13 exhibits the average absorbed power versus vehicle speed for the unladen M113A1 APC traversing the LETE48 random course with three different settings of track pre-tension (vehicle configurations: B,

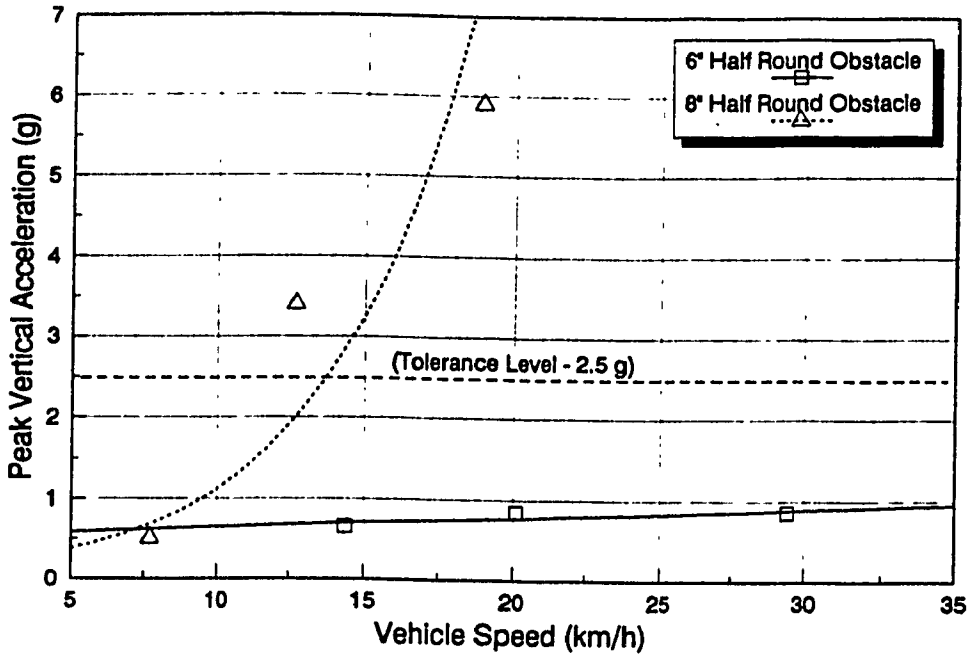

Figure 3.9 Shock performance of test vehicle traversing 6" and 8" obstacles at various speeds - vehicle configuration B.

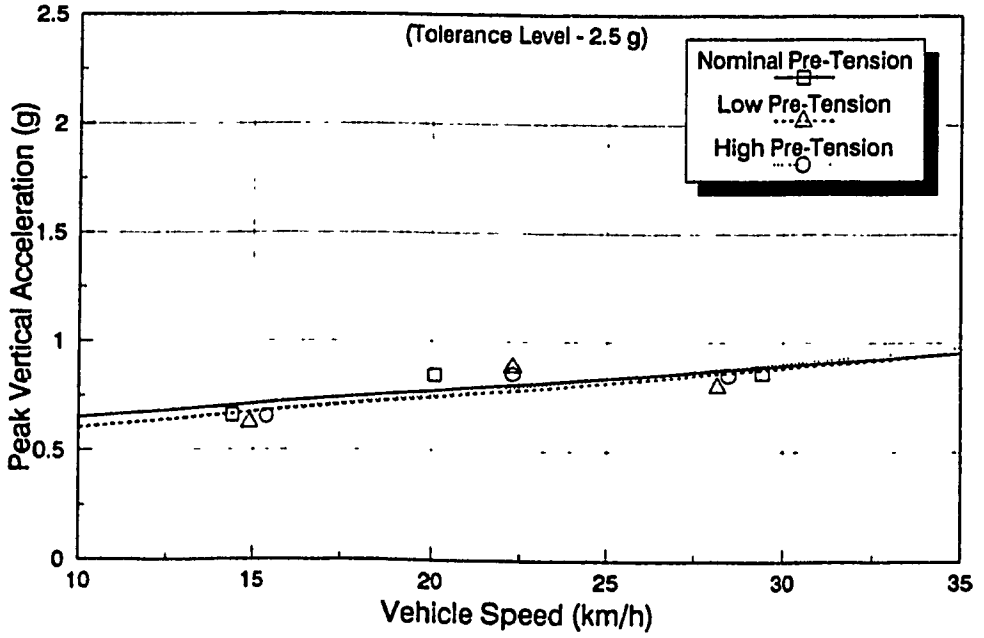

Figure 3.10 Shock performance of test vehicle traversing 6" obstacle at various speeds - vehicle configurations B, C, and D.

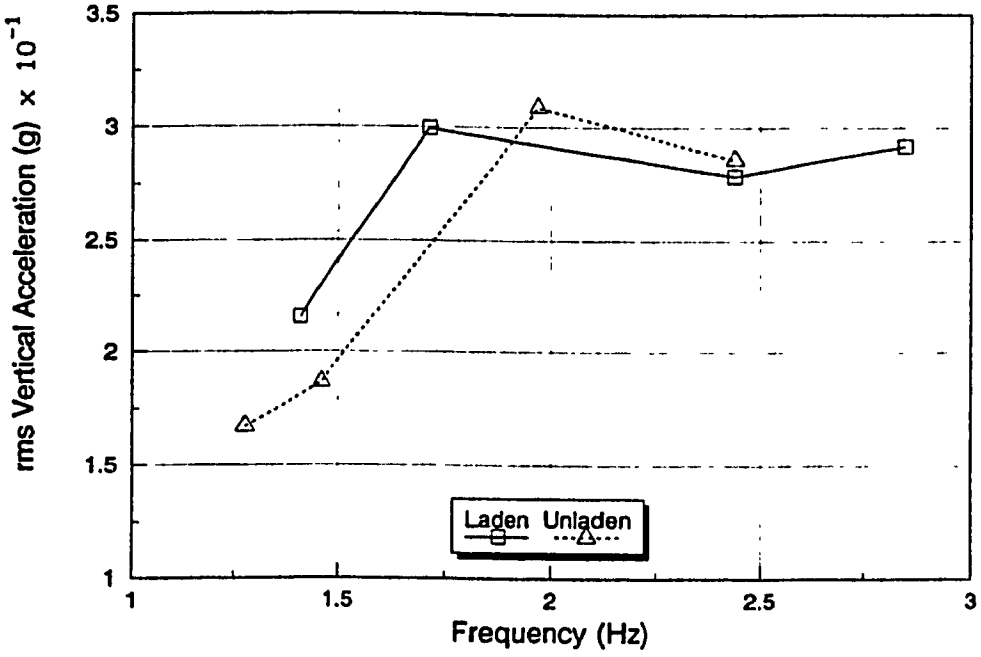

Figure 3.11 rms vertical acceleration at driver-seat interface for test vehicle subjected to sine course at various excitation frequencies - vehicle configurations A and B.

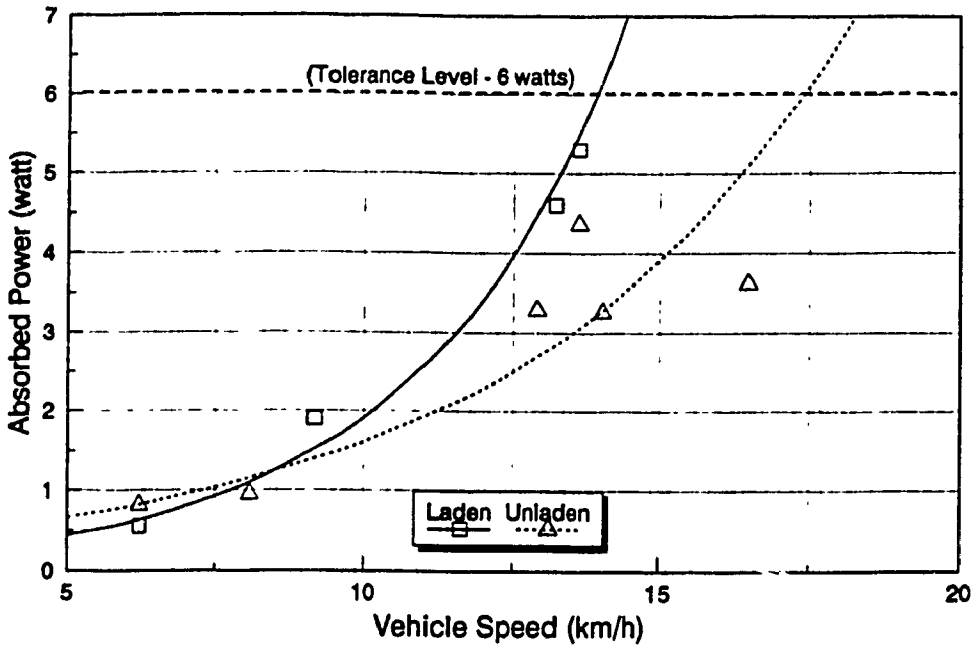

Figure 3.12 Ride performance of test vehicle traversing LETE48 random course at various speeds - vehicle configurations A and B.

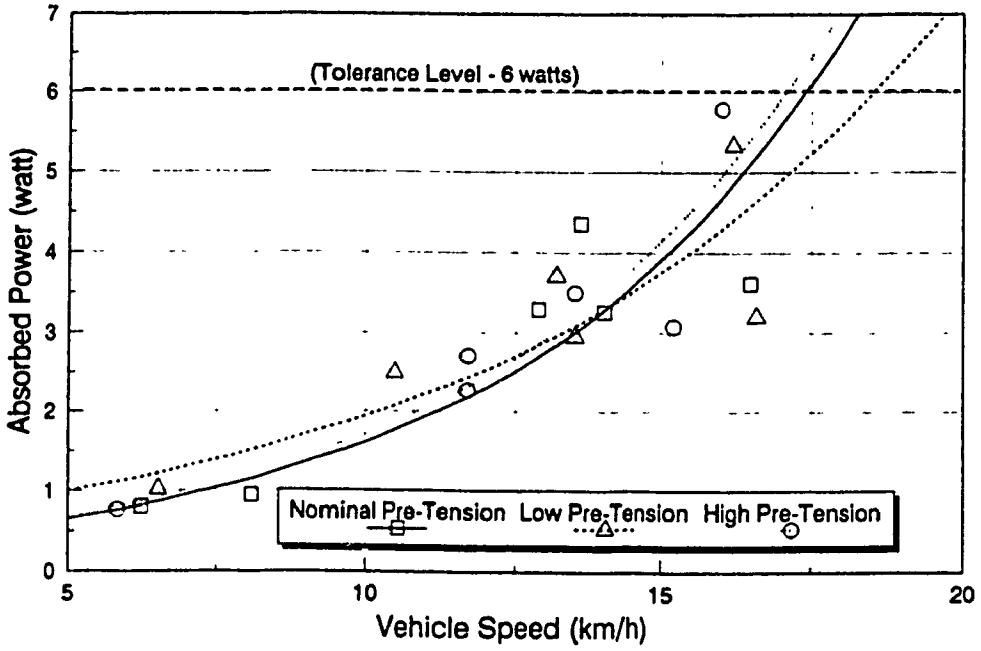

Figure 3.13 Ride performance of test vehicle traversing LETE48 random course at various speeds - vehicle configurations B, C, and D.

C, and D). As shown, the average absorbed power is below the limiting value of 6 watts for all test conditions. The ride performance of M113A1 APC with low track pre-tension is slightly deteriorated at lower vehicle speed. However, the ride-limiting speed as a result of low track pre-tension is relatively increased.

The ride performance of M113A1 APC traversing the Belgian Pavé in its configurations A and B, is illustarted in Figure 3.14. The average absorbed power for specified vehicle configurations and speeds, is below the tolerance level of 6 watts. It can also be seen that the vehicle's ride performance improves at higher speeds, and unladen M113A1 APC yields poor ride in comparison with the laden configuration.

3.6 FIELD VALIDATION OF MODEL I

In this section, MODEL I is assessed using the field measurements. The computer simulations of the field-tested vehicle for representative test conditions, are performed using MODEL I, and the results have been superimposed on the field-measured ride data. Details regarding the input data, and field validation results are presented as below.

3.6.1 Input Data for Simulation

Table 3.4 lists the physical data describing the field-tested vehicle, where mass/inertia and dimensional parameters for laden vehicle are estimated based on the unladen vehicle, and the plywood ballast box filled with sand bags. The radial spring constants, K^{i}_{rw} ($i = 1,..,5$) and K^{k}_{hw} ($k = 1,2$) are computed based on an input deflection of wheel centre (Δ_w) and corresponding vertical load, P, of a representative point from the measured force-deflection curve, as described in section 2.4.1 (equation 2.26).

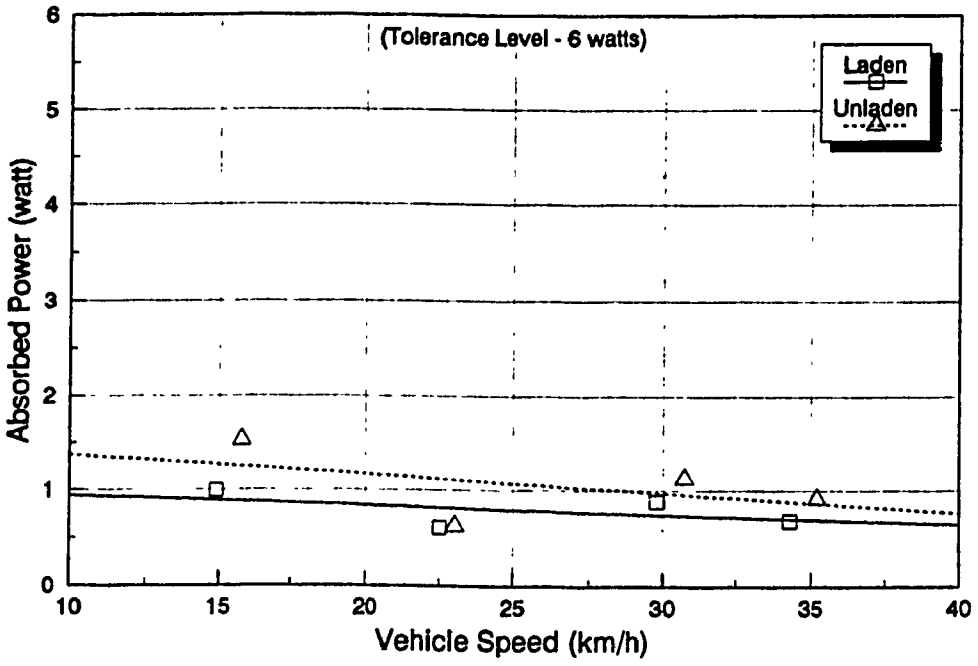

Figure 3.14 Ride performance of test vehicle traversing Belgian pavé at various speeds - vehicle configurations A and B.

Table 3.4 Parameters of field-tested M113A1 APC [38,69].

Description	*Symbol*	*Vehicle Configuration*	
		Laden	*Unladen*
Mass/Inertia:			
Hull mass, kg	m_h	4 585	3 660
Hull pitch moment of inertia, $kg.m^2$	I_h	6 964	6 445
Road wheel mass, kg	m_{wi} $i=1..5$	113.5	113.5
Horizontal Dimension:			
Horizontal distance from c.g. to:			
Drive sprocket, m	a_{h1}	2.059	1.981
Idler, m	a_{h2}	-1.927	-2.005
Suspension # 1, m	a_1	1.405	1.327
Suspension # 2, m	a_2	0.732	0.654
Suspension # 3, m	a_3	0.082	0.004
Suspension # 4, m	a_4	-0.601	-0.679
Suspension # 5, m	a_5	-1.269	-1.347
Driver's seat, m	a_o	1.076	0.998
Hull's front end	a_F	2.415	2.337
Hull's rear end	a_R	-2.449	-2.527
Vertical Dimension:			
Hull c.g. height, m	h_{cg}	0.896	0.928
Vertical distance from c g. to:			
Drive sprocket, m	b_{h1}	-0.374	-0.406
Idler, m	b_{h2}	-0.498	-0.531
Suspension # i, m (i = 1,..,5)	b_i	-0.279	-0.311
Driver's Seat, m	b_o	0.243	0.211
Hull's top end, m	b_T	0.835	0.803
Hull's bottom end, m	b_B	-0.279	-0.311

NOTE: m_h and I_h correspond to half of the hull mass and pitch inertia, and m_{wi} is the unsprung mass of i^{th} road wheel assembly on one side of the APC.

(Table 3.4 - continued)

Table 3.4 Parameters of field-tested M113A1 APC [38,69].

Description	*Symbol*	*Vehicle Configuration*	
		Laden	*Unladen*
Radius:			
Road wheel, m	R_{wi} $i=1..5$	0.3048	0.3048
Drive sprocket, m	R_{h1}	0.2438	0.2438
Idler, m	R_{h2}	0.2222	0.2222
Track Inclination with Ground:			
Front track feeler, deg	Θ_1	21.5	21.5
Rear track feeler, deg	Θ_2	15.0	15.0
Radial Spring Constants:			
Road wheel/track, N/m/rad	K^i_{rw} $i=1..5$	1 121 256	1 121 256
Drive sprocket/track N/m/rad	K^1_{hw}	1 634 508	1 634 508
Idler/track, N/m/rad	K^2_{hw}	1 559 657	1 559 657
Longitudinal Stiffness of Track Belt, N/m	K_{tr}	304 147	304 147
Damping Constants:			
Road wheel/track, N.s/m	C^i_{rw} $i=1..5$	0.0	0.0
Drive sprocket/track N.s/m	C^1_{hw}	0.0	0.0
Idler/track, N.s/m	C^2_{hw}	0.0	0.0

Appropriate look-up tables are developed to describe the nonlinear characteristics of the vehicle suspension system. In general, the force-deflection characteristics of suspension spring exhibits a hysteresis loop bounded by the loading and unloading curves, which represents the energy dissipated/cycle due to the Coulomb friction in the suspension. Consequently, the suspension is normally represented as a directly coupled friction damping system, where a spring and a friction damper act in parallel. Figure 3.15 shows the force-deflection curve for an equivalent vertical spring for the A1 torsion bar employed at all five road wheel stations. As indicated, the total road wheel travel is approximated at 0.216 m, and the upper bump stop is relatively softer in comparison with the lower one. The upper bump stop is mounted to prevent the road wheel from hitting the hull chassis, whereas the lower bump stop is mounted to prevent the road wheel from driving the track into the ground. A friction damper, as characterized through a force-velocity curve in Figure 3.16, is incorporated in parallel with the A1 spring to account for the suspension hysteresis. The force-velocity characteristics of a typical shock absorber employed for M113A1 APC are shown in Figure 3.17, where the solid line represents an inclined shock absorber, and the dotted line represents an equivalent vertical shock absorber. The equivalent force-velocity curve data representing vertical shock absorbers mounted at the first and last road wheels of M113A1 APC, are selected for simulation.

The terrain profile, as mentioned in section 2.3.2, is input as a look-up table containing horizontal and vertical coordinates of successive points on the proile, which are either equally or unequally spaced. All test courses (Figure 3.3) except discrete half round

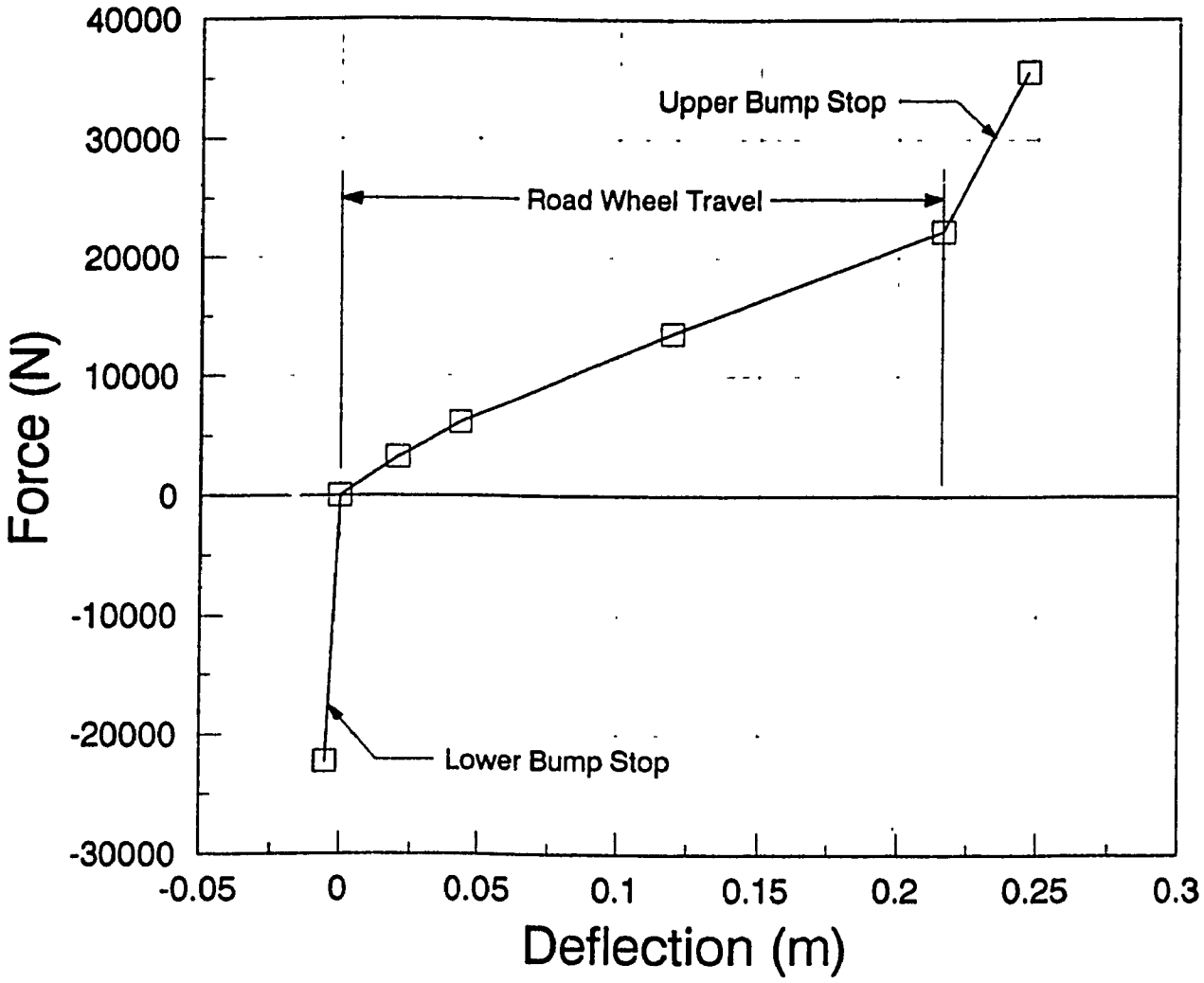

Figure 3.15 Force-deflection characteristics for an equivalent vertical spring for A1 torsion bar suspension system [courtesy of DND].

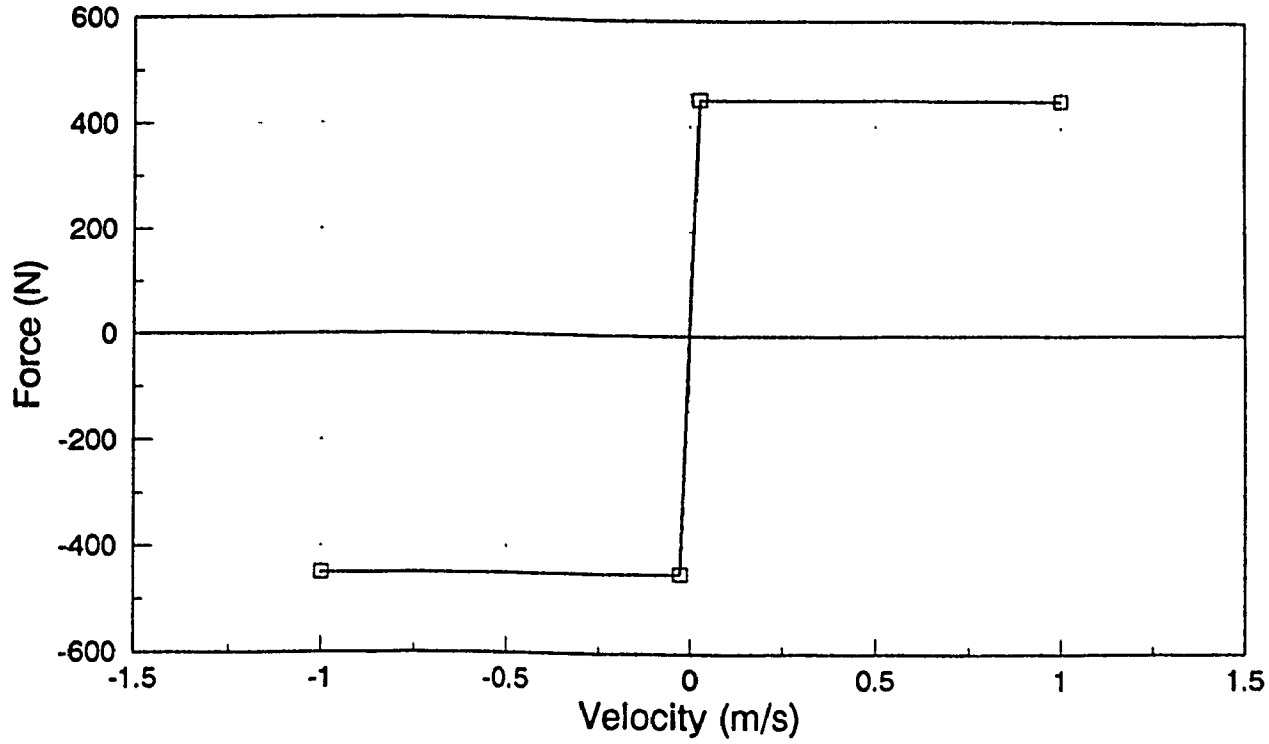

Figure 3.16 Coulomb friction damping characteristics.

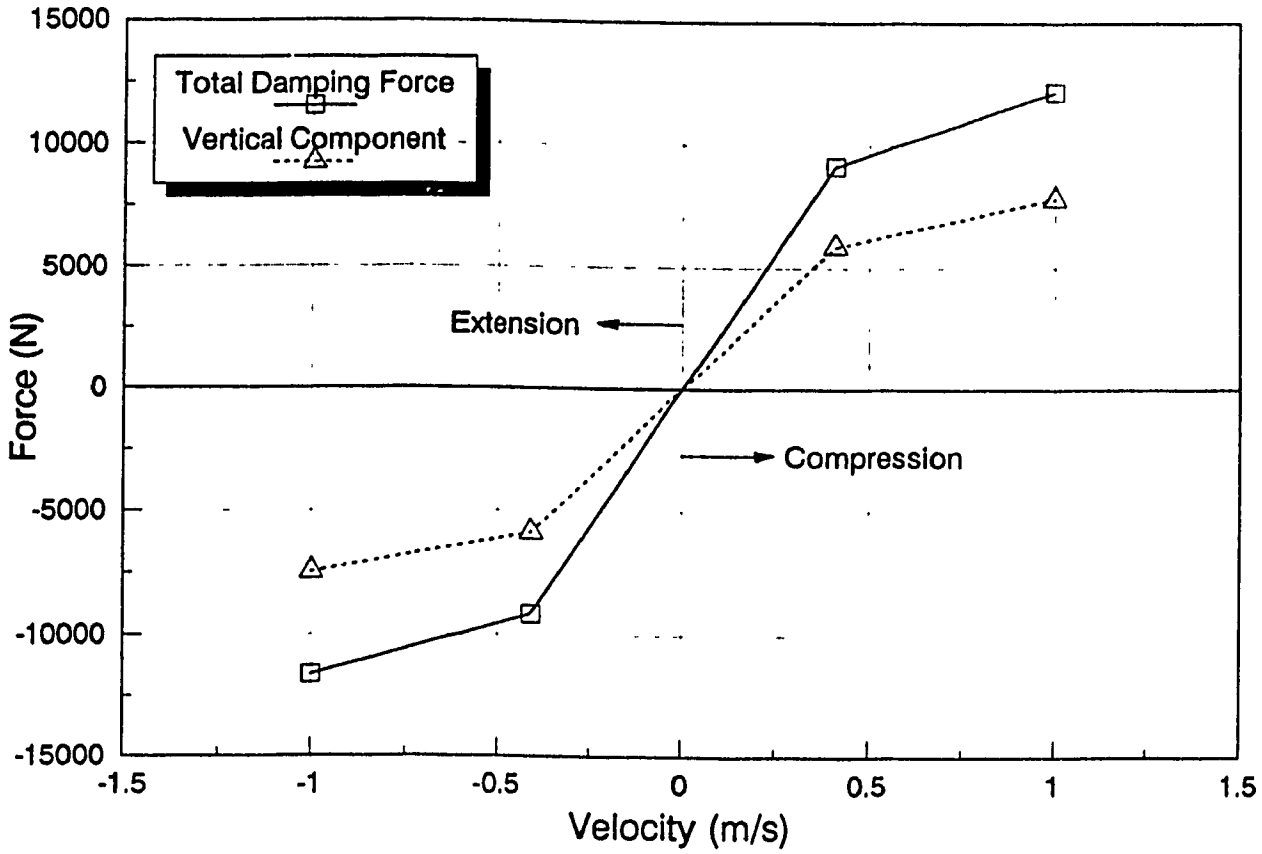

Figure 3.17 Force-velocity characteristics for A1 shock absorber [courtesy of DND].

obstacles are described through vertical coordinates of equally spaced successive points on the profile. The spacing is equal to 0.3048 m (12") for LETE random course and Belgian pavé, and 0.0635 m (2.5") for sine course. The look-up tables for LETE48 random course and Belgian pavé were supplied by LETE.

3.6.2 Validation Results and Discussion

Discussions on the validation results are presented in view of the ride resonant frequencies, and the ride vibration levels.

Resonant Frequencies

For the test vehicle, the undamped natural frequencies and associated dominant deflection modes are predicted based on the iterative stiffness method as discussed in section 2.6, and are listed in Table 3.5 for specified vehicle configuration. The natural frequencies corresponding to the bounce and pitch modes of the laden vehicle are slightly lower than the corresponding unladen configuration, while the natural frequencies of all road wheels bounce are slightly higher. The influence of varying the track pre-tension is demonstrated in the last three columns of the table. As shown, an increase in the track pre- tension slightly decreases the natural frequencies associated with hull bounce and pitch motions, and bounce motion of first and last road wheels, whereas the natural frequencies associated with bounce motion of intermediate road wheels are slightly increased.

The predicted ride resonant frequencies (hull bounce and pitch) are compared with the ones estimated from the sine course testing of M113A1 APC. The measured ride resonant frequencies are estimated based on equation (3.17), and are the ones at which the rms value of measured

acceleration trace is maximum (Figure 3.11). As shown in Table 3.6, the comparison shows a good aggreement between measured and predicted values.

Ride Vibration Levels

The ride simulation model, MODEL I, is validated for representative test conditions. Since vehicle speed during actual terrain negotiation was very difficult to be maintained at a specified constant level, the vehicle speed for simulation purposes, is considered as the rms value of the recorded vehicle speed trace. For instance, Figure 3.18 illustrates the actual speed traces during 6" obstacle negotiation for various values of track pre-tension, and Tables 3.3 lists the rms values of vehicle speed traces. The integration time step (Δ_t) for simulation, is considered equal to "$1/(50.f_{max})$", where f_{max}, the highest natural frequency for the test vehicle ride model, is approximated at 12 Hz (Table 3.5). Consequently, Δ_t is $1/4^{th}$ of the sampling time interval ($\Delta T = 1/150$ s) used for digitizing the measured acceleration signals. The incremental time step for output is, however, taken equal to ΔT.

Discussions on the validation results are presented in view of a specific type of terrain profile. For half round discrete obstacles and sinusoidal course, the simulation model is validated through direct comparison of simulated and field measured acceleration traces associated with driver's seat bounce and hull pitch motions. However, for random course and Belgian Pavé, the validation is carried out based on the comparison of corresponding acceleration spectra, and the absorbed power associated with driver's seat bounce.

Discrete Half Round Obstacles

Figures 3.19 and 3.20 show the measured and predicted acceleration

Table 3.5 Natural frequencies and associated deflection modes (MODEL I).

Undamped Natural Frequencies (Hz)				Dominant Deflection Mode
Test Vehicle Configuration				
A	B	C	D	
1.654	1.856	1.866	1.848	y_h
1.239	1.316	1.325	1.307	θ_h
11.39	11.32	11.47	11.17	y_{w1}
12.20	12.08	12.03	12.13	y_{w2}
12.26	12.05	12.00	12.09	y_{w3}
12.34	12.01	11.98	12.05	y_{w4}
11.97	11.41	11.53	11.29	y_{w5}

Table 3.6 Predicted and measured ride resonant frequencies.

Test Vehicle Configuration	Natural Frequency (Hz) [Measured/Predicted]	
	Hull Bounce	Hull Pitch
Laden (A)	1.71/1.65	1.41/1.24
Unladen (B)	1.97/1.86	1.28/1.32

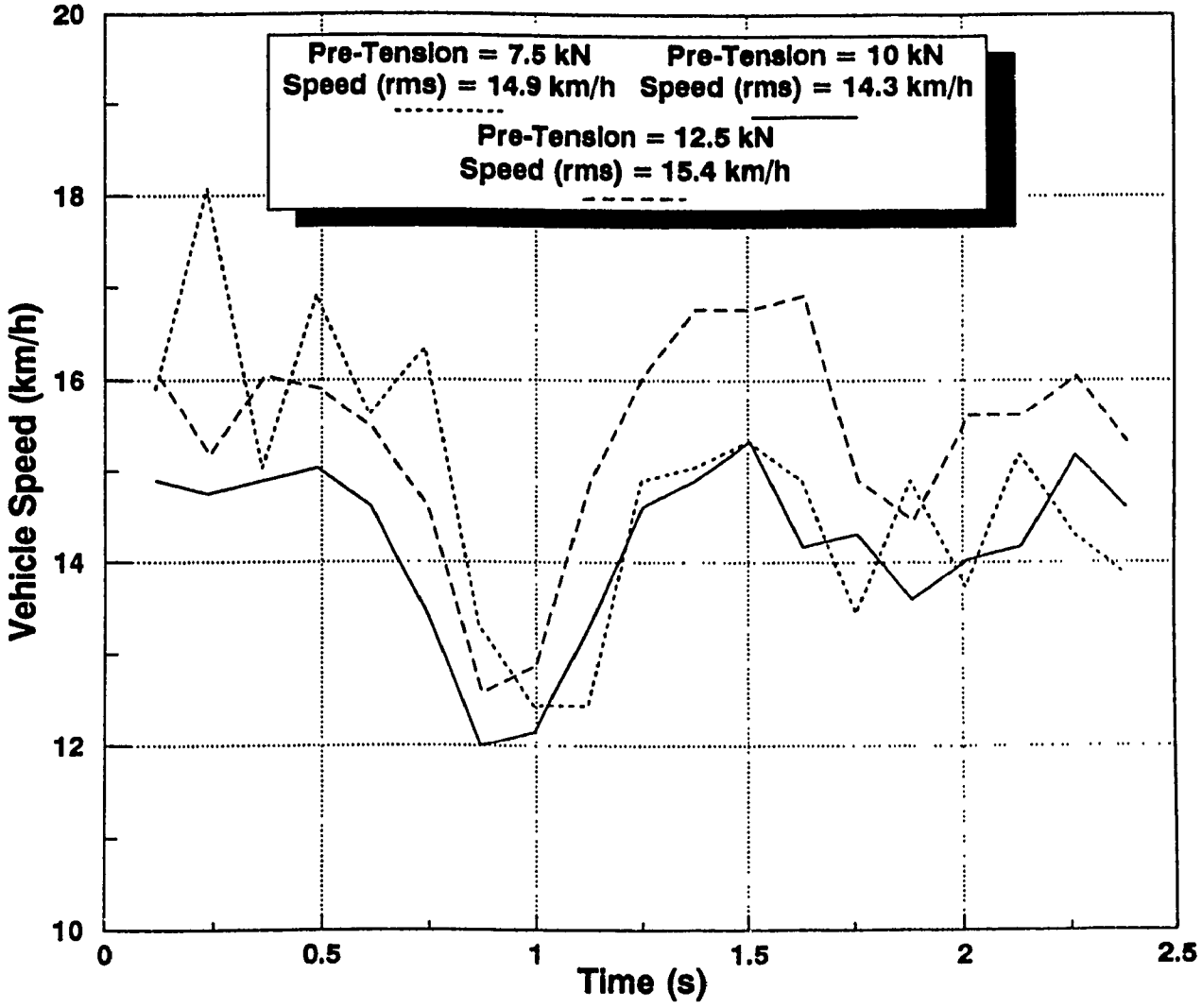

Figure 3.18 Measured speed trace during 6" obstacle crossing.

traces corresponding to the driver's seat vertical and hull pitch motions for the test vehicle crossing over a 6" half round obstacle with three different values of track pre-tension (vehicle configurations: B, C, and D). The computed and measured results show generally good agreement, although it is noted that there are phase shifts between the measured and simulated peak responses. This discrepancy can be attributed to the fact that the simulations were carried out at constant speeds (rms values of the measured speed traces). From the measured and predicted results in Figures 3.19 and 3.20, it can be seen that varying the initial track tension by ±25% for the vehicle traversing a 6" obstacle at approximately constant speed, does not have significant influence on the overall ride response.

Figures 3.21 and 3.22 demonstrate the comparison of measured and predicted acceleration traces for test vehicle cofiguration B traversing 8" half round obstacle at approximately 7.8 km/h and 12.8 km/h. As it can be seen, the vehicle response is significantly deteriorated at higher speed. The measured and predicted hull pitch acceleration exhibit a distinct downward peak as shown in Figure 3.22, for vehicle speed of 7.8 km/h. This happens due to impact of idler with the obstacle as the vehicle trailing-end is crossing over the obstacle. The measured vehicle responses for vehicle speed of 12.8 km/h, as illustrated in Figures 3.21 and 3.22, show distinct upward peak. This is caused by the drive sprocket-ground interaction just after the vehicle has crossed over the obstacle. The corresponding simulated response, however, does not exhibit similar behaviour.

Sinusoidal Course

The ride dynamic behaviour of the vehicle due to a sinusoidal

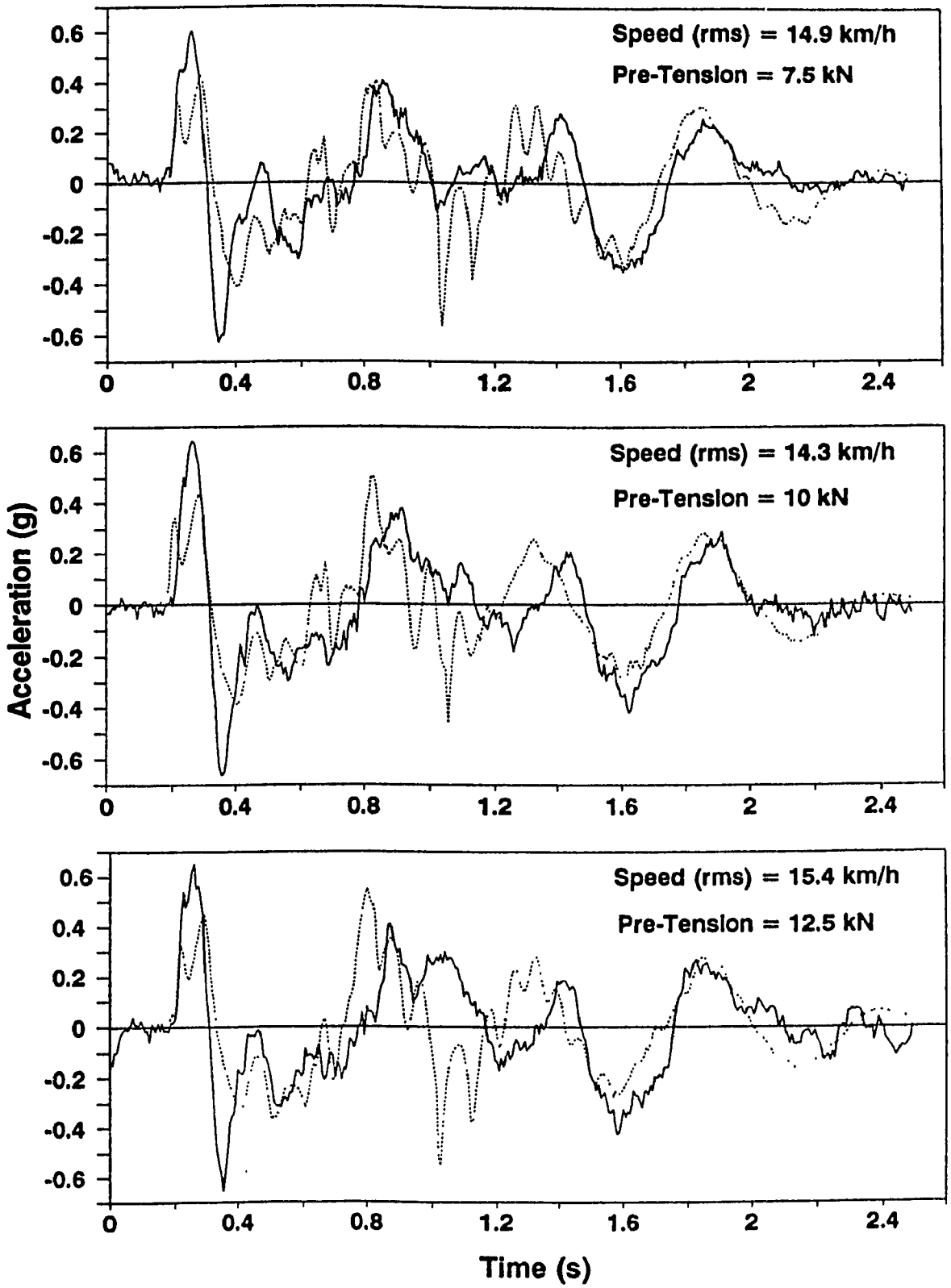

Figure 3.19 Seat vertical acceleration traces - field validation of MODEL I's predictions for vehicle configurations B, C, and D traversing 6" obstacle (———— Field Test, ... Simulation).

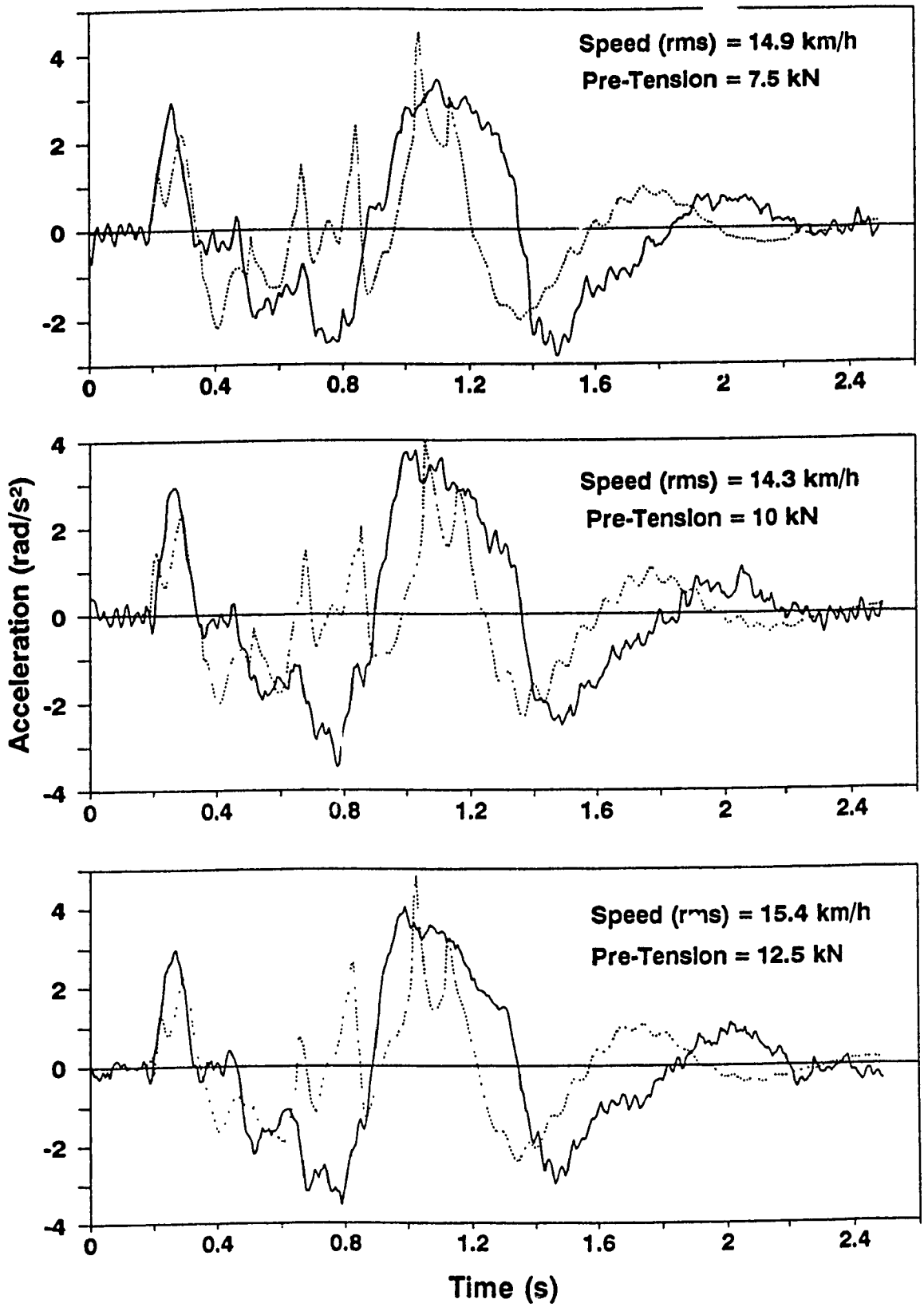

Figure 3.20 Hull pitch acceleration traces - field validation of MODEL I's predictions for vehicle configurations B, C, and D traversing 6" obstacle (——— Field Test, ... Simulation).

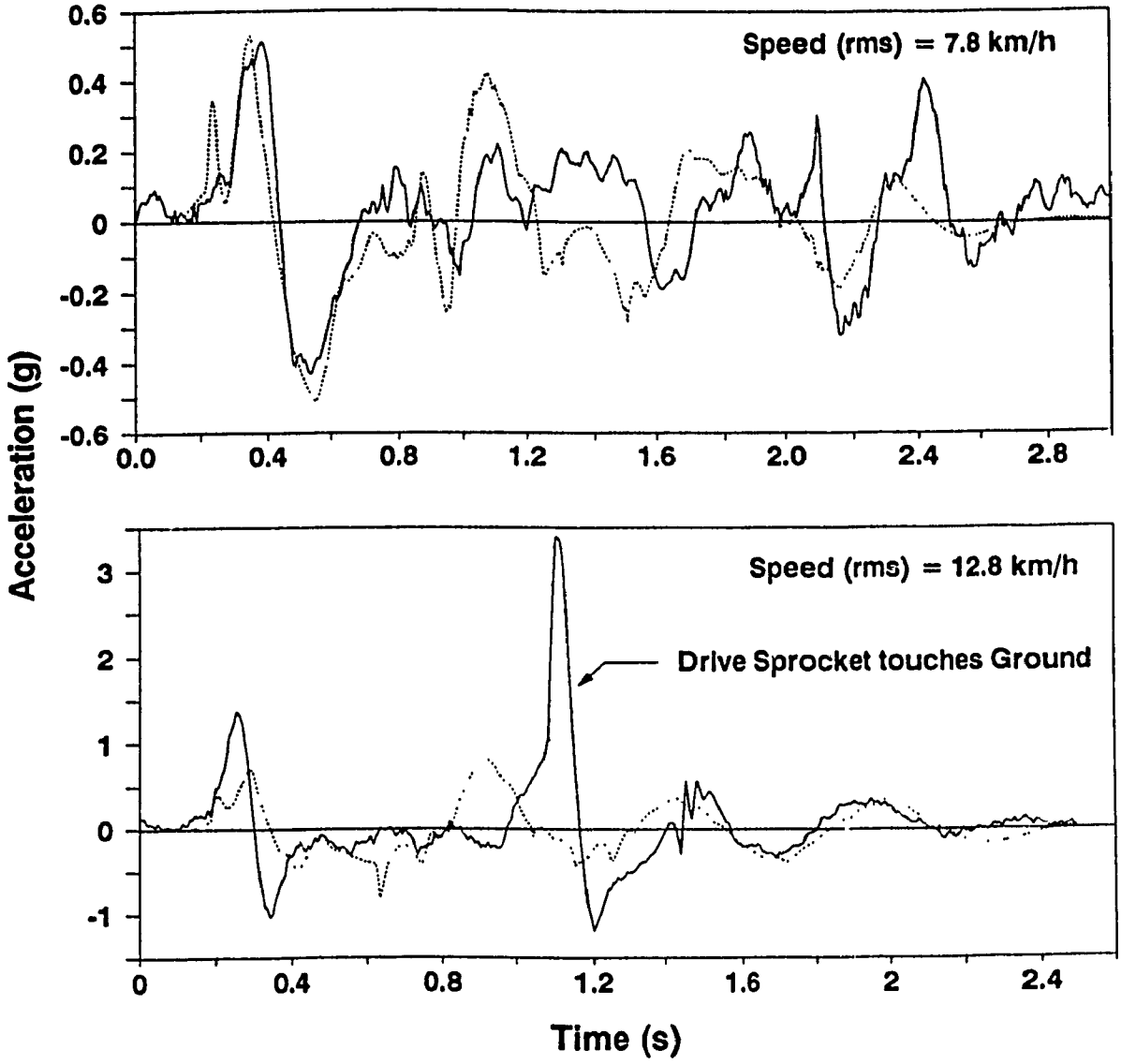

Figure 3.21 Seat vertical acceleration traces - field validation of MODEL I's predictions for vehicle configuration B traversing 8" obstacle (———— Field Test, ... Simulation).

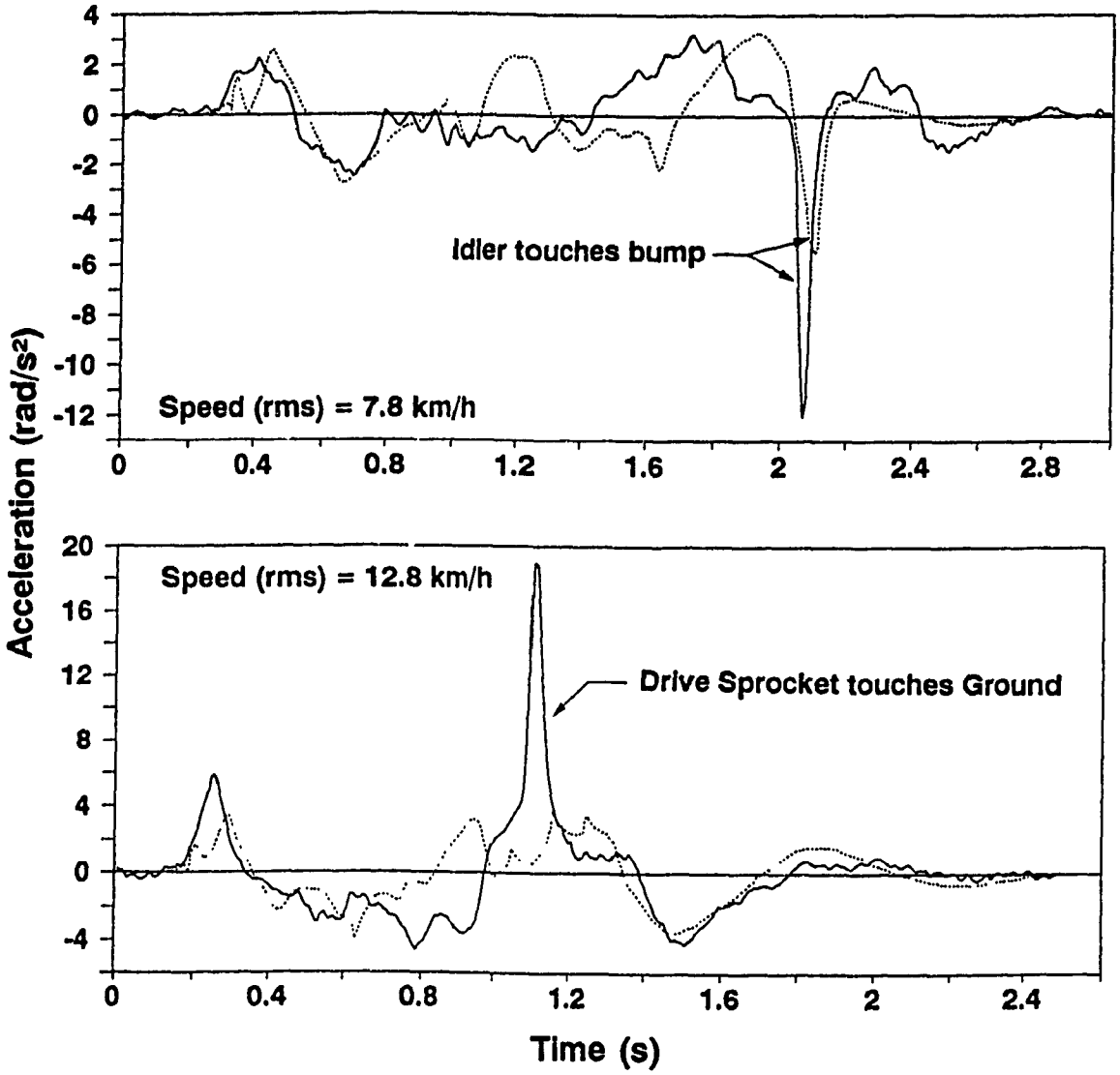

Figure 3.22 Hull pitch acceleration traces - field validation of MODEL I's predictions for vehicle configuration B traversing 8" obstacle (——— Field Test, ... Simulation).

excitation is investigated. The excitation frequency based on the vehicle speed (V_x = 6.7 km/h) and the wavelength (λ = 0.76 m) is computed as approximately 2.4 Hz. Figures 3.23 and 3.24 show samples of measured and simulated acceleration time histories corresponding to the driver's seat vertical and hull pitch motions, respectively, for vehicle configurations A and B. The overall ride response is not significantly influenced as a result of vehicle's loading condition, as clearly demonstrated by both measured and predicted results. However, in comparison with the pitch responses (Figure 3.24), the seat vertical acceleration response (Figure 3.23) has better validation. As discussed in the case of half round obstacles, the phase shifts between measured and predicted responses can be attributed to the fluctuations in vehicle speed during the field testing. Further, the relatively higher discrepancies observed between the measured and predicted pitch responses (Figure 3.24) can be attributed to the fact that the hull pitch acceleration is approximated based on the kinematic relationships of the three measured acceleration signals on top surface of the hull as explained in section 3.3.

LETE48 *Random Course*

The acceleration power spectral density (PSD) responses corresponding to the driver's seat vertical and the hull pitch motions are computed through an FFT analysis of measured and simulated acceleration traces. The seat bounce acceleration PSD response is assessed with respect to the ISO *fatigue decreased proficiency* (FDP) limits [58,59]. In addition, the seat bounce response is evaluated in terms of average absorbed power [56]

Figures 3.25 and 3.26 demonstrate the comparison of measured and predicted ride acceleration spectra for test vehicle configurations A and B traversing LETE48 random course at approximately 13.5 km/h,

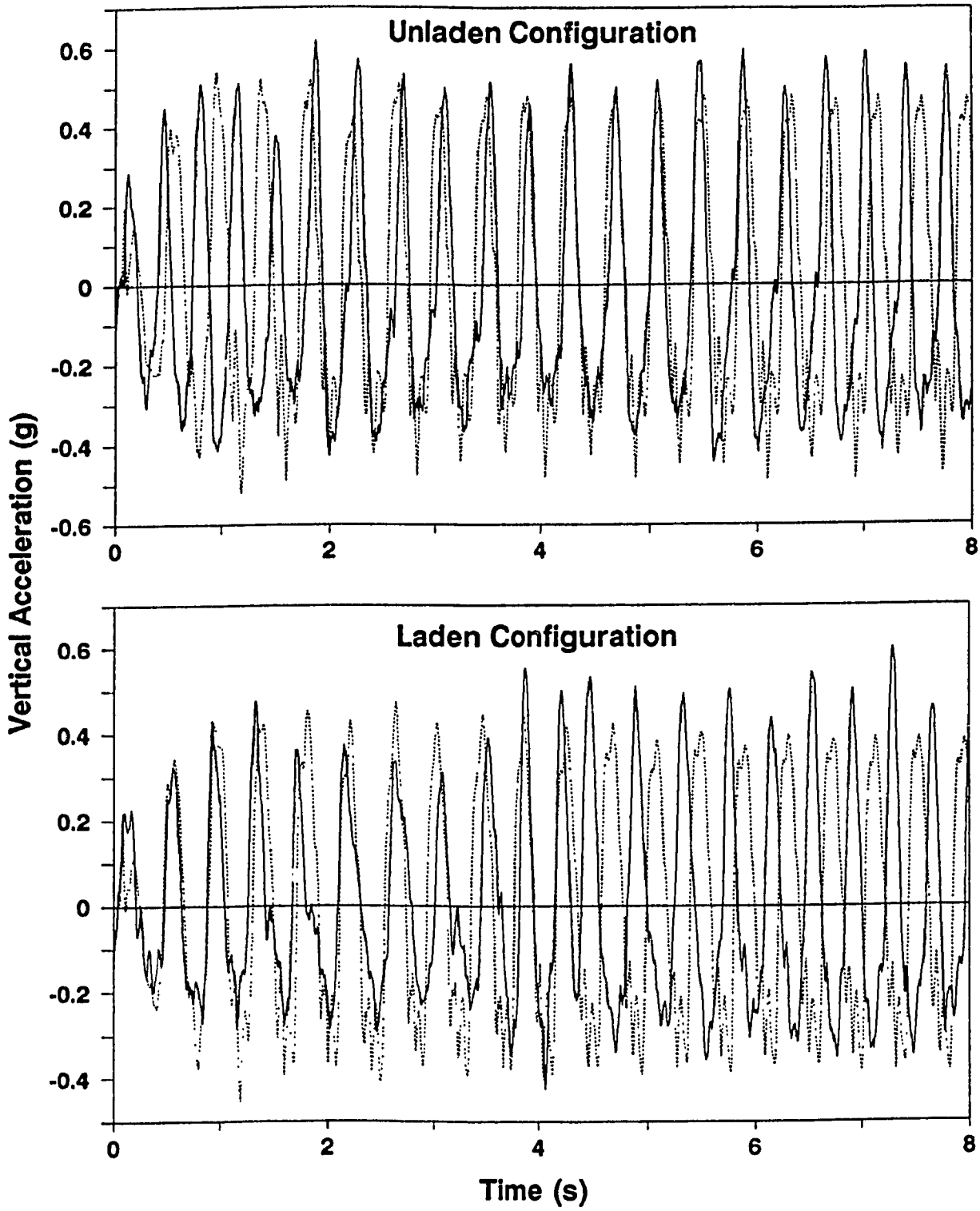

Figure 3.23 Seat vertical acceleration traces - field validation of MODEL I's predictions for vehicle configurations A and B traversing sine course at 6.7 km/h (——— Field Test, ... Simulation).

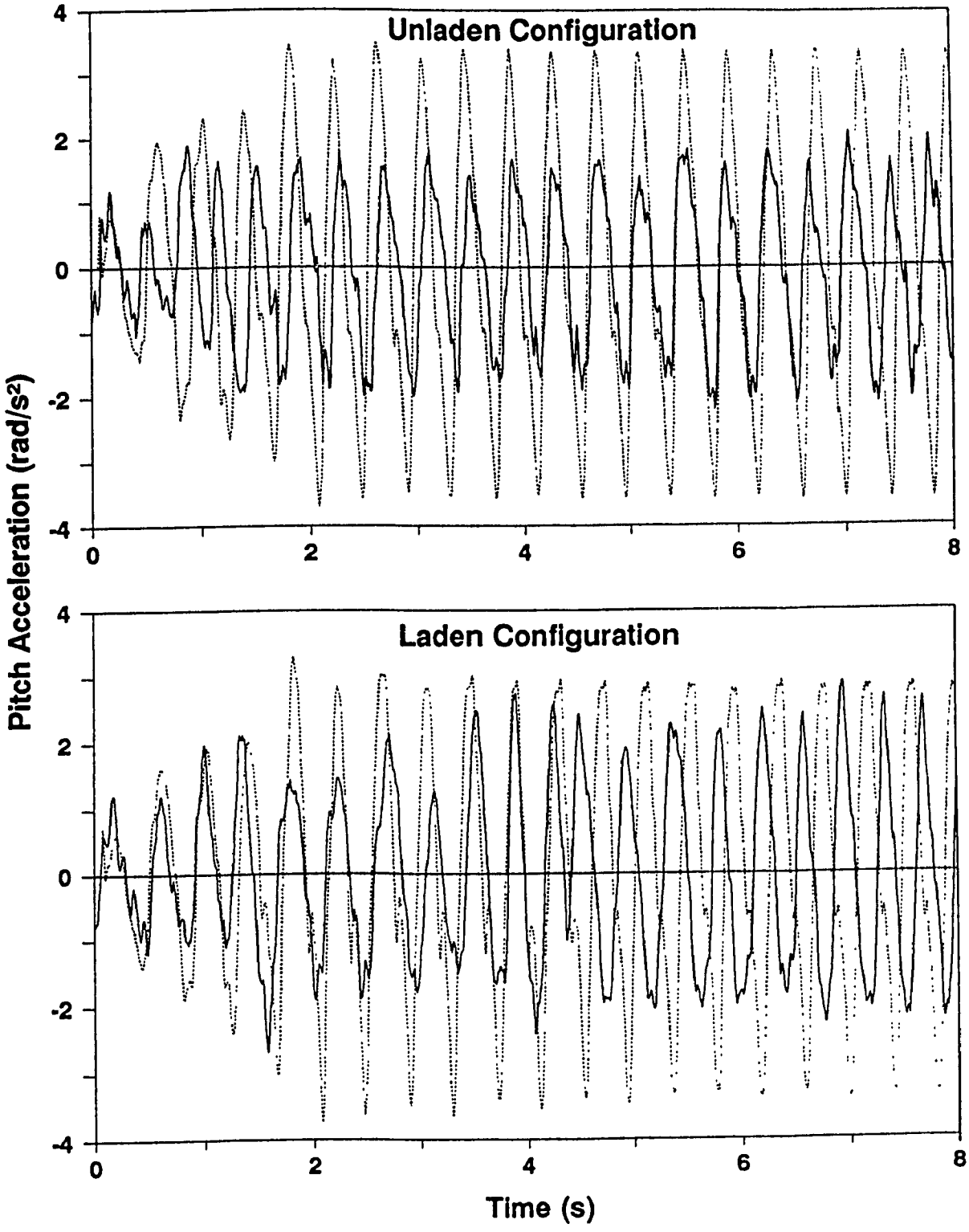

Figure 3.24 Hull pitch acceleration traces - field validation of MODEL I's predictions for vehicle configurations A and B traversing sine course at 6.7 km/h (——— Field Test, ... Simulation).

respectively. The comparison shows generally good agreement in terms of overall response characteristics such as dominant peaks and corresponding frequencies. As shown, the ride vibration levels at the driver's seat in the bounce mode are observed to be within 1 h exposure FDP limit.

Table 3.7 presents the comparison between field-measured and predicted average absorbed power associated with the driver's seat bounce motion and rms value of the hull pitch acceleration for all four test vehicle configurations. As it can be seen, the average absorbed power associated with all vehicle configurations is below the limiting value of 6 watts. In comparison with field-measured hull pitch accleration, the predicted rms values are higher.

Belgian Pavé

Figure 3.27 demonstrate the comparison of measured and predicted acceleration spectra of the test vehicle configuration A traversing Belgian Pavé at approximately 35 km/h. Table 3.8 summarizes the comparison between measured and predicted ride performance. The comparison shows a good agreement. In reference to the limiting value of 6 watts, the vehicle speed of 35 km/h is safe.

3.7 IDENTIFICATION OF POTENTIAL MODELING IMPROVEMENTS

In the previous section, the ride acceleration responses obtained using MODEL I, are compared with the field-measured data in order to validate the predictions of vehicle ride performance, and to assess the limitations of MODEL I. The comparison between measured and predicted ride data is generally good. However, there are certain discrepancies, which can be attributed to:

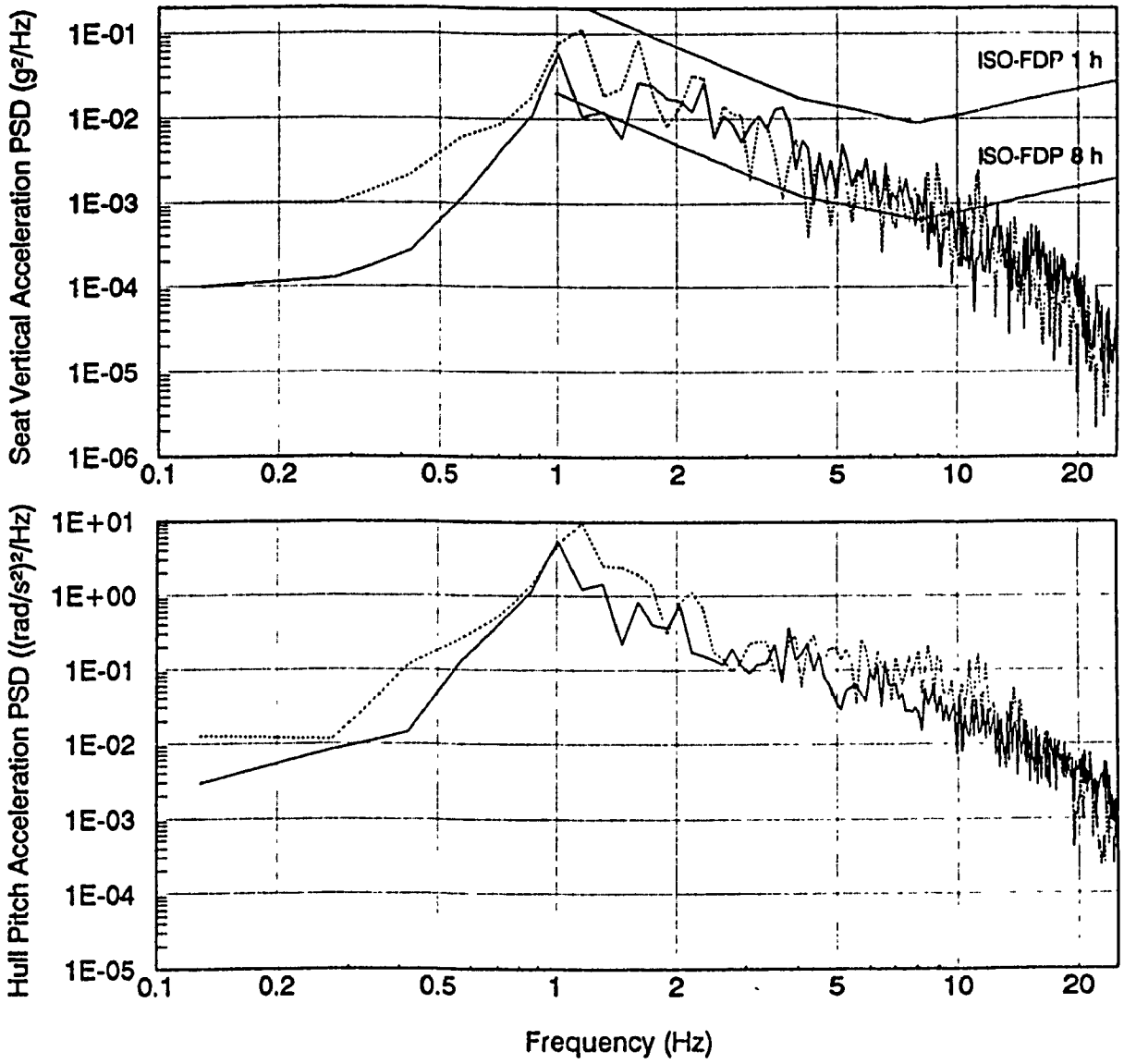

Figure 3.25 Ride acceleration spectra - field validation of MODEL I's predictions for vehicle configuration A traversing LETE48 random course at 13.5 km/h (——— Field Test, ····· Simulation).

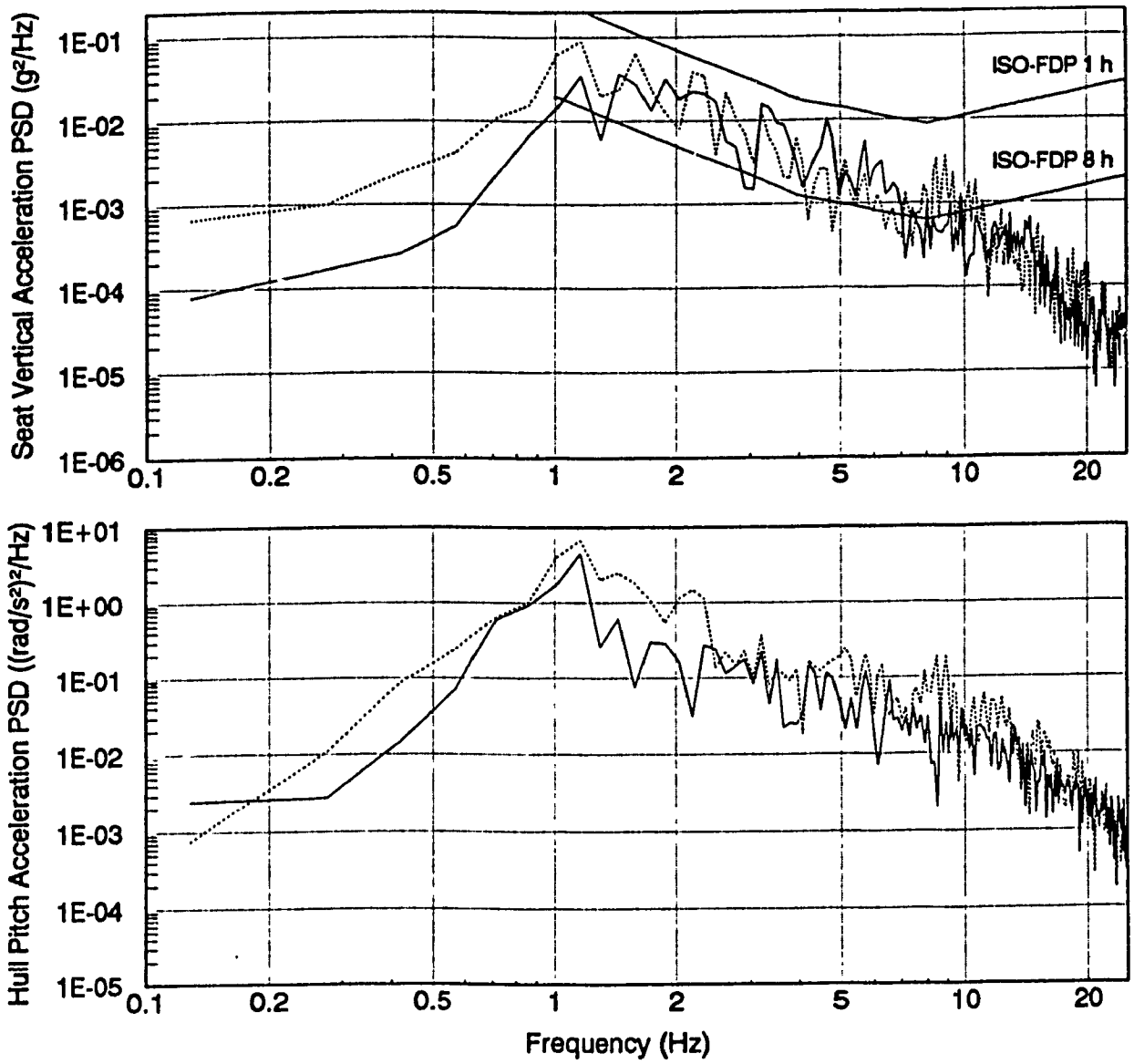

Figure 3.26 Ride acceleration spectra - field validation of MODEL I's predictions for vehicle configuration B traversing LETE48 random course at 13.5 km/h (——— Field Test, ... Simulation).

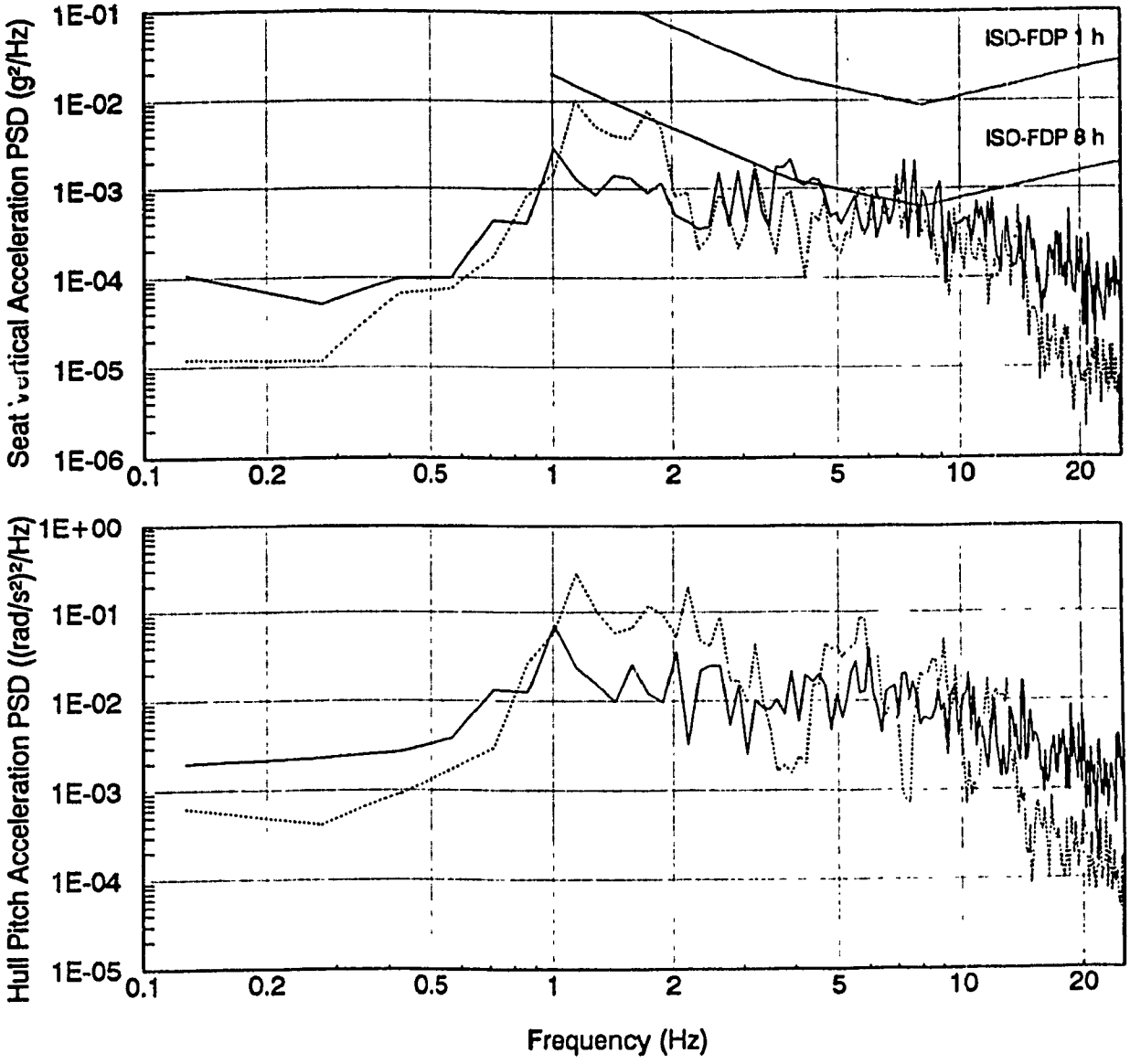

Figure 3.27 Ride acceleration spectra - field validation of MODEL I's predictions for vehicle configuration A traversing Belgian pavé at 35 km/h (———— Field Test, ... Simulation).

Table 3.7 Field validation of MODEL I (LETE48 course; speed=13.5 km/h).

Vehicle Configuration	Absorbed power (watts)/rms acceleration (rad/s^2)	
	Field Test	Simulation
A	4.5/1.61	4.0/2.50
B	4.4/1.65	3.9/2.31
C	3.7/1.30	3.3/2.22
D	3.5/1.29	4.1/2.51

Table 3.8 Field validation of MODEL I (Belgian pavé; speed = 35 km/h).

Vehicle Configuration	Absorbed power (watts)/rms acceleration (rad/s^2)	
	Field Test	Simulation
A	0.940/0.492	0.646/0.613
B	0.921/0.526	0.922/0.723

- assumptions made in the ride model formulism, such as *idealization* of net foot-print force, dynamic track load and trailing arm suspension dynamics;
- use of estimated vehicle parameters in the simulation;
- vehicle speed variation during the field testing; and
- measurement errors during field testing.

Evidentally, it is worthwhile to refine the ride model in order to achieve an even closer correlation between measured and predicted ride responses.

The analytical wheel-track-terrain interaction, modeled through net foot-print force and dynamic track load, is of primary consideration for accurately representing the ride dynamic behaviour of high mobility tracked vehicles. In MODEL I, the net foot-print force is computed based on an *idealized* deflection characterized by a straight line adjoining first and last wheel-terrain contact points (Figure 2.9), while ignoring the terrain irregularities within the foot-print. This formulation yields an accurate net foot-print force, if the local terrain profile within the foot-print is flat. Otherwise, this assumption could over- or under-estimate the net force based on the shape of local terrain profile. For instance, the first peak in the simulated ride accleration traces shown in Figure 3.19 indicates the interaction of front road wheel with 6" obstacle, where the net foot-print force (F^1_{wn}) is under-estimated due to the *straight line idealization* of the rounded terrain profile within the foot-print. Consequently, the net foot-print force should be computed considering an *adaptive* deflection, which conforms to the shape of the local terrain profile.

In MODEL I, the analytical model for predicting dynamic track load is

only based on track stretching or extensibility, where an increase in the track tension above its initial level (T^0_{tr}), is linearly proportional to net increase in the overall track length. Although track extensibility is of primary consideration in modeling the dynamic track tensioning effects, track inextensibility considering the sag of upper track strand hanging beween two hull wheels, is essential for simulating a drop in the track tension from its initial level, and accurate track inclinations at both hull wheels. Consequently, the track model should be improved to account for track inextensibility as well. In addition, wheel-track connectivity algorithms employed in MODEL I, can be further enhanced for an appropriate definition of track wrap around road wheels, wheel-track-terrain separation, and track bridging.

The equations of motion for MODEL I (section 2.3.3) were derived assuming *strictly vertical* suspension units. An independent suspension unit is, in fact, rigidly fixed to the vehicle frame, and thus should remain perpendicular to the frame. Consequently, the equations of motion should be re-derived in view of realistic independent suspension configuration.

3.8 SUMMARY

This chapter presents a detailed overview of the field testing of an in-service M113A1 APC, which was carried out at LETE (Ottawa). The general characteristics of test vehicle configurations, and test courses (discrete half round obstacles, sine course, LETE48 random course, and Belgian pavé) are presented. The instrumentation and equipments employed for the field testing are discussed in view of their types, location and mounting methods. Mathematical procedure adopted to manipulate the

measured signals for the computation of vehicle speed trace and acceleration traces associated with the vehicle's principle degrees of freedom, is discussed. A test procedure containing a detailed outline of test runs for specified test conditions (vehicle configurations, terrain profiles and vehicle speeds) is presented. The procedure for conditioning and reduction of field test data is presented. An overview of field measurements exhibiting vehicle's ride and shock performance is presented.

In this chapter, the ride dynamic model, MODEL I, is validated using field-measured ride data. An input data for test vehicle ride model and test courses is compiled for simulation purposes. The computer simulations of the field-tested vehicle for representative test conditions, are performed using MODEL I, and the results have been superimposed on the field-measured ride data. Based on the field validation results, MODEL I is assessed, and considered for further refinement in an attempt to achieve even a closer correlation between simulated and measured ride responses. The ride model refinement is discussed in view of modeling strategies adopted for vehicle suspension system and dynamic wheel-track-terrain interactions.

Chapter 4

REFINEMENT OF RIDE MODEL I AND ITS ASSESSMENT

4.1 INTRODUCTION

In chapter 3, the ride dynamic model, MODEL I, is validated and assessed using field-measured ride data, which was gathered during an extensive field testing of an in-service M113A1 APC. Details about field testing and measurement data are provided in Chapter 3. Computer simulations of M113A1 APC for representative test conditions (i.e. vehicle configurations, test courses, and vehicle speeds), are performed using MODEL I, and the results are directly compared with field-measured ride data. The ride predictions exhibited a generally good agreement with field measurements. The discrepancies are attributed to: (i) assumptions made in the ride model formulism, such as *idealization* of net foot-print force, dynamic track load and trailing arm suspension dynamics, (ii) use of estimated vehicle parameters in the simulation, (iii) vehicle speed variation during the field testing, etc. Consequently, refinement of MODEL I in view of modeling strategies adopted for suspension system and dynamic wheel-track-terrain interactions, is considered in order to further improve the correlation between measured and predicted ride responses.

In this chapter, the ride dynamic model is re-derived based on the refinement of MODEL I. The re-derived ride model, referred to as MODEL II, is described along with details of improved wheel and track models. Field validation of MODEL II is carried out, and the results are presented. Various wheel and track models considered in previous studies [30,34,38] are formulated and employed for performing ride simulations of the field-tested vehicle in conjunction with MODEL II, and corresponding

ride predictions are compared with field-measured ride data. Primary objectives of this exercise are to demonstrate the influence of different wheel and track models on ride predictions, and to assess the relative performance of these proposed models.

4.2 RIDE DYNAMIC MODEL: MODEL II

In this section, the dynamic wheel-track-terrain interaction is refined, where (i) net foot-print force is established based on the analytical model as illustrated in Figure 2.8, but considering an *adaptive* deflection of the wheel/track due to interaction with the non-deformable terrain profile, and (ii) dynamic track load is computed based on an improved analytical model, which, in addition to the track extensibility (equation 2.41), also includes the track inextensibility (sag of the hanging track segment between drive sprocket and idler), and refined wheel-track connectivity algorithms to yield appropriate definitions of track wrap around road wheels, road wheel-track-terrain separation and track bridging. Also, the equations of motions are rewritten considering the realistic representation of an independent suspension configuration. The refined computer ride model is referred to as MODEL II.

4.2.1 An Adaptive Model for Wheel/Track-Terrain Interactions

Assuming an *idealized* wheel/track deflection characterized by a straight line adjoining the first and last wheel-terrain contact points on the lower wheel circumference ($\overline{P_1P_2}$, as shown in Figure 2.9), the net foot-print force acting at the i^{th} road wheel center is given by equation (2.30) as:

$$F^i_{wn} = 2\, K^i_{rw}\, R_{wi}\, [\sin \alpha_{wi} - \alpha_{wi} \cos \alpha_{wi}] + F^i_{dw} \qquad (4.1)$$

The above formulation for net foot-print force, however, lacks the ability to envelop small terrain irregularities within the footprint. The analytical model is, thus, further enhanced using an adaptive footprint configuration, which envelopes small terrain irregularities through local deformations within the footprint. It primarily involves fine-tuning the idealized wheel deflection such that the contact patch *adapts* to the shape of non-deformable terrain profile. As shown in Figure 4.1, the lower circumference of road wheel is discretized into a number of pie-shaped elements, where φ_i is the angular dimension and $(K^i_{rw}.\varphi_i)$ is an equivalent spring constant of each discrete element. The net footprint force acting at the i^{th} road wheel center is, then, obtained as:

$$F^i_{wn} = K^i_{rw} \left\{ 2\, R_{wi} [\sin \alpha_{wi} - \alpha_{wi} \cos \alpha_{wi}] + \varphi_i \sum_{k=1}^{N_e} \Delta^i_k \cos \alpha^i_k \right\} + F^i_{dw} \qquad (4.2)$$

where, N_e represents the number of discrete elements found within the footprint. Δ^i_k is the required change in the radial deflection of the k^{th} element of the i^{th} road wheel, given as:

$$\Delta^i_k = \delta^i_{k_A} - \delta^i_{k_I} \qquad (4.3)$$

where, the actual radial deflection is given as:

$$\delta^i_{k_A} = y^i_k \left\{ \frac{\sin \sigma_2}{\sin \sigma_1} \right\} \; ; \; (\; y^i_k > 0 \text{ and } \delta^i_{k_A} = y^i_k \text{ for } \psi^i_k = 0) \qquad (4.4)$$

and, the idealized radial deflection is given as:

$$\delta^i_{k_I} = \frac{R_{wi}(\cos \alpha^i_k - \cos \alpha_{wi})}{\cos \alpha^i_k} \qquad (4.5)$$

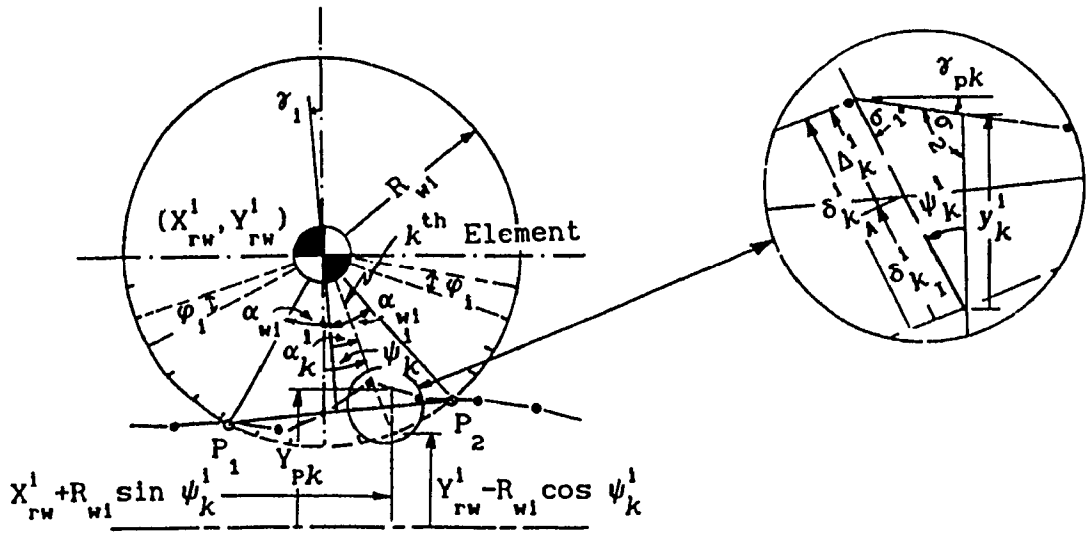

Figure 4.1 An adaptive wheel/track-terrain interaction.

where, $\sigma_1 = \begin{cases} \pi/2 + \gamma_{pk} - \psi_k^i \\ \pi/2 - \gamma_{pk} + \psi_k^i \end{cases}$; $\sigma_2 = \begin{cases} \pi/2 - \gamma_{pk} \; ; \; \psi_k^i > 0 \\ \pi/2 + \gamma_{pk} \; ; \; \psi_k^i < 0 \end{cases}$

and $\alpha_k^i = \psi_k^i - \gamma_1$

where y_k^i is the vertical deflection of k^{th} element, ψ_k^i is the corresponding vertical inclination, and γ_{pk} corresponds to the *local* slope of terrain profile. All angles measured in counter-clockwise sense are considered positive. It should be noted that a positive value of Δ_k^i indicates that actual radial deflection is greater than the idealized value; thus represents the amount of deflection by which the corresponding elemental spring should be further compressed. Consequently, the net footprint force is increased by an appropriate amount. Similarly, a negative value of Δ_k^i indicates the amount of deflection by which the corresponding elemental spring should be stretched, thus reducing the over-estimated net footprint force.

During simulation, the net footprint force is, however, computed either using an *idealized* wheel/track-terrain interaction (equation 4.1) or an *adaptive* wheel/track-terrain interaction (equation 4.2). The choice is determined by the nature of wheel-terrain contact patch. As explained in section 2.4.1, special cases, such as (i) $N_S = 0$ ($\therefore N_I = 0$), and (ii) $N_S > 0$ and $N_I = 0$ (provided only one profile segment is confirmed to intersect) represents the only geometrical situations, where the circle is simply intersected by a straight line; therefore, net footprint force is accurately computed using equation (4.1). This approach reduces the computing time significantly.

4.2.2 An Adaptive Model for Predicting Dynamic Track Loads

In MODEL I, the dynamic track load at each wheel station was computed based on track pre-tension plus tension due to track belt stretching (equation 2.41), where track inextensibility in view of the sag of upper track strand was ignored. Also, the wheel-track connectivity algorithm employed for computing the overall track length and the track inclinations around each wheel, only partially accounted for the track wrap around road wheels, the road wheel-track-separation, and the track bridging. In this section, the analytical model for predicting dynamic track loads is refined in view of these considerations.

4.2.2.1 Track Sag

For tracked vehicles, the track sag corresponds to a certain amount of slack which is observed in the hanging track between two hull wheels, where the amount of slack determines the track pre-tension (T^{0}_{tr}). As mentioned earlier (section 3.2), the nominal track pre-tension for the M113A1 APC, is 10 kN, and is set according to a gap of approximately 20 mm between the bottom of the hanging upper track strand and the top of the second road wheel. As shown in Figure 3.2, the tension in the upper track strand increases as the gap increases or the hanging track length decreases. Consequently, a functional relationship between track tension and the length of upper track strand will dictate how track tension depends upon the kinematic state of the tracked vehicle with respect to terrain profile.

A track hanging between any two hull wheels can be treated as a cable hanging under its own weight between two fixed supports A and B as shown in Figure 4.2. Although this may not be realistic for pin-linked track, it is a reasonable approximation if there are sufficient number of track

links between hull wheels. Classical approach to obtain the tension at any point along the hanging cable is formulated based on the following assumptions [71]:

(a) *Parabolic Cable*: cable carries a load uniformly distributed along the horizontal, or

(b) *Catenary*: cable carries a load uniformly distributed along its length.

A cable hanging under its own weight is generally not loaded uniformly along the horizontal, and does not form a parabola. Consequently, the hanging cable shown in Figure 4.2, is best approximated by a catenary equations, given as [71]:

$$T = w\, c \cosh \frac{x}{c} \quad ; \quad \ell = c \sinh \frac{x}{c} \quad ; \text{ and } \quad \tan \theta = \ell / c \qquad (4.6)$$

where,

$$c = \frac{T_o}{w}$$

and T is the tension at a specified point D(x,y) along the cable, ℓ is the cable length from lowermost point (C-origin) on the hanging cable to the specified point, T_o is the minimum (horizontal) tension at C, w is the cable's weight per unit length, and x is horizontal distance of D with respect to C.

It should be noted that the catenary relations can not be solved explicitly, and one usually employs an iterative numerical technique for its solution. In addition, the location of end supports A and B must be known with respect to the lowermost point, C, in order to compute the tension vectors at the supports. Consequently, catenary approximation of hanging track segment is not a suitable option for simulation purposes. An alternate approach based on quadratic polynomial approximation is developed and discussed as below.

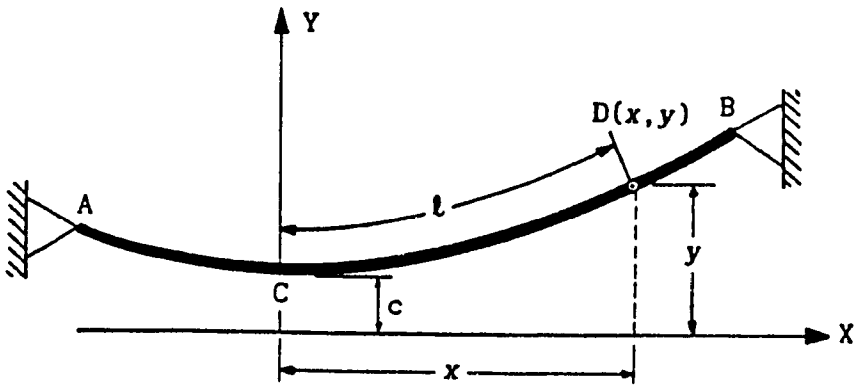

(a) Geometric considerations

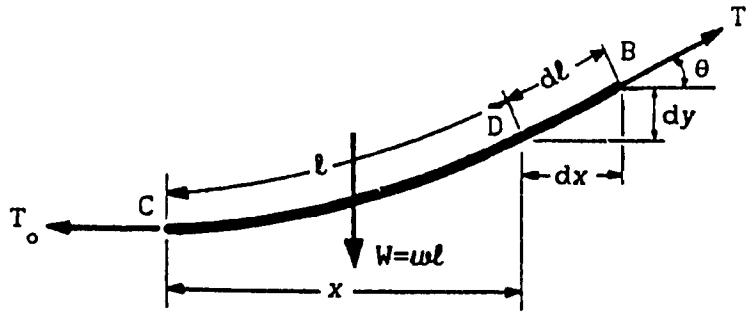

(b) Force considerations

Figure 4.2 Catenary approximation of hanging cable [71].

Consider a track hanging between two hull wheels (Figure 4.3), where the centre coordinates of both hull wheels are known. The curve assumed by the hanging track can be approximated via a quadratic polynomial, given as:

$$y(x) = a_o + a_1 x + a_2 x^2 \tag{4.7}$$

where, the polynomial constants a_o, a_1, and a_2 can only be obtained if and only if three points on the curve (hanging track) are known. Therefore, the end points (X_A,Y_A and X_B,Y_B) of the supported track are selected as two of the three required points (equation 2.49). As illustrated in Figure 4.3 (a), the third point is selected to coincide with point D on the track, whose coordinates are computed as:

$$X_D = X_A + \frac{d}{2}\cos\Theta_h + S_T \sin\Theta_h \; ; \; Y_D = Y_A + \frac{d}{2}\sin\Theta_h - S_T\cos\Theta_h \tag{4.8}$$

where, S_T, the track sag, represents the height of the perpendicular drawn from the mid-point of the line $\overline{AB}$ to point D on the hanging track. d and Θ_h, as given in equation (2.49), defines the tangent adjoining the top points of the hull wheels.

The polynomial constants are obtained using equation (4.7) in conjunction with the known coordinates of three points A, B, and D on the hanging track, and given as:

$$\begin{aligned} a_o &= Y_B - a_1 X_B - a_2 X_B^2 \\ a_1 &= \tan\Theta_{h/2} - a_2(X_B + X_D) \\ a_2 &= \frac{\tan\Theta_h - \tan\Theta_{h/2}}{X_A - X_D} \end{aligned} \tag{4.9}$$

where,

$$\tan\Theta_{h/2} = \left[\frac{Y_B - Y_D}{X_B - X_D}\right]$$

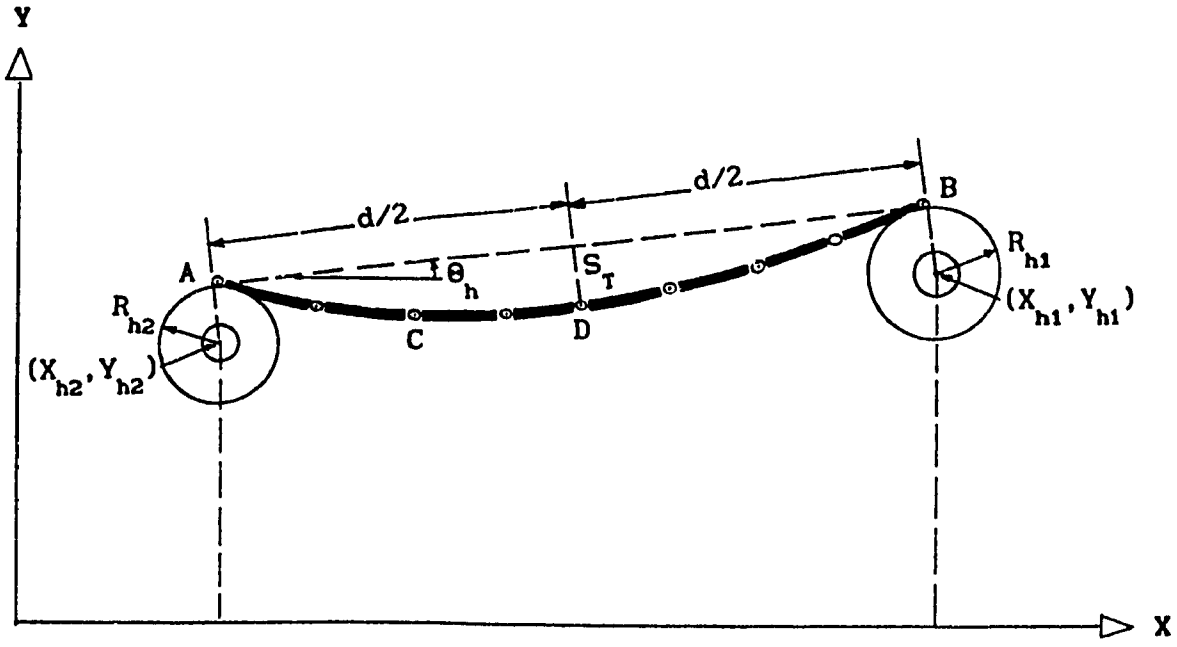

(a) Geometric considerations

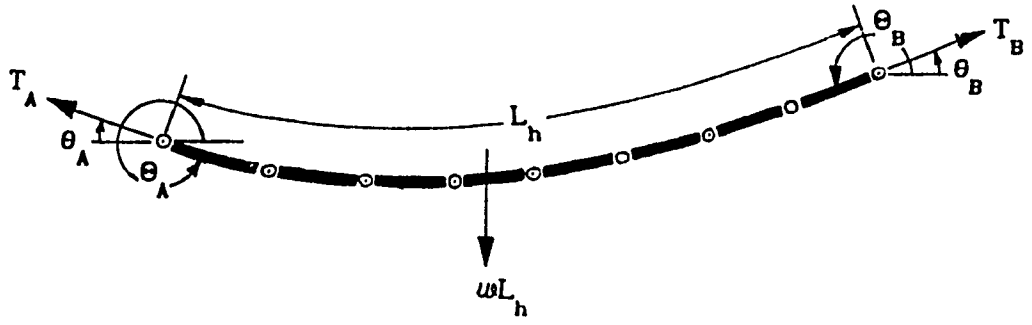

(b) Force considerations

Figure 4.3 Quadratic polynomial approximation of hanging track.

The quadratic polynomial approximating the curve assumed by the hanging track, is thus established. The hanging track length, L_h, is computed as:

$$L_h = \int_{X_A}^{X_B} \sqrt{1 + (dy/dx)^2}\, dx \tag{4.10}$$

The track length can also be evaluated based on the discretization of the analytical track profile (equation 4.7), expressed as:

$$L_h = \sum_{n=1}^{N} \left[(X_{n+1} - X_n)^2 + (Y_{n+1} - Y_n)^2 \right]^{1/2} \tag{4.11}$$

where,

$$X_n = \begin{cases} X_B \\ X_B - (n-1)(X_B - X_A)/N \\ X_A \end{cases} ; \quad Y_n = \begin{cases} Y_B & ; \text{ for } n = 1 \\ a_o + a_1 X_n + a_2 X_n^2 & ; \text{ for } n = 2,..,N \\ Y_A & ; \text{ for } n = N+1 \end{cases} \tag{4.12}$$

where N corresponds to number of track profile segments. and can be considered as a number of track shoes in the hanging track.

Track inclinations at both ends (θ_A, θ_B) are given by the slope, dy/dx, as:

$$\tan \theta_A = a_1 + 2\, a_2 X_A \quad ; \quad \tan \theta_B = a_1 + 2\, a_2 X_B \tag{4.13}$$

The horizontal inclinations of hanging track segment at both ends, as illustrated in Figure 4.3 (b), are then specified as:

$$\begin{aligned} \Theta_A &= \theta_A + 2\pi \quad (\theta_A < 0) \\ \Theta_B &= \theta_B + \pi \quad (\theta_B > 0) \end{aligned} \tag{4.14}$$

It is evident that dy/dx = 0 at the lowermost point C, thus, its

coordinates can be obtained as:

$$X_C = -\frac{a_1}{2\,a_2} \quad ; \quad Y_C = a_o + a_1 X_C + a_2 X_C^2 \tag{4.15}$$

Consequently, the magnitudes of track tension vectors at the supports (Figure 4.3 (b)) are conveniently obtained based on the static force balance equations in the X- and Y-direction, and given as:

$$T_A = \frac{T_o}{\cos\,\theta_A} \quad \text{and} \quad T_B = \frac{T_o}{\cos\,\theta_B} \tag{4.16}$$

where, T_A and T_B are the track tension at the top of idler and drive sprocket, respectively. The minimum or horizontal track tension is given as:

$$T_o = \frac{w\,L_h}{\tan\,\theta_B - \tan\,\theta_A} \tag{4.17}$$

where, w is track's weight/unit length (= 670 N/m for Diehl 213G track).

For Diehl 213G track supported on sprocket and idler of the field-tested vehicle, the proposed method is employed to evaluate track hanging length (L_h), track inclinations (θ_A,θ_B), and tension magnitudes (T_A,T_B, T_o) as a function of track sag. Figure 4.4 exhibits the relationships, which are obtained by gradually incrementing the track sag, S_T, at a small interval of 0.0254 m. It should be noted that the track tension at idler (T_A) is slightly less in comparison with the track tension at the drive sprocket (T_B), especially for higher values of track sag, since the elevation of point B is relatively higher. The procedure adopted to obtain the relationships exhibited in Figure 4.4, is also used to obtain initial desired track setting for specified track pre-tension, T_{tr}^o. For this, the procedure is continued until T_{avg} (= $(T_A + T_B)/2$) approaches

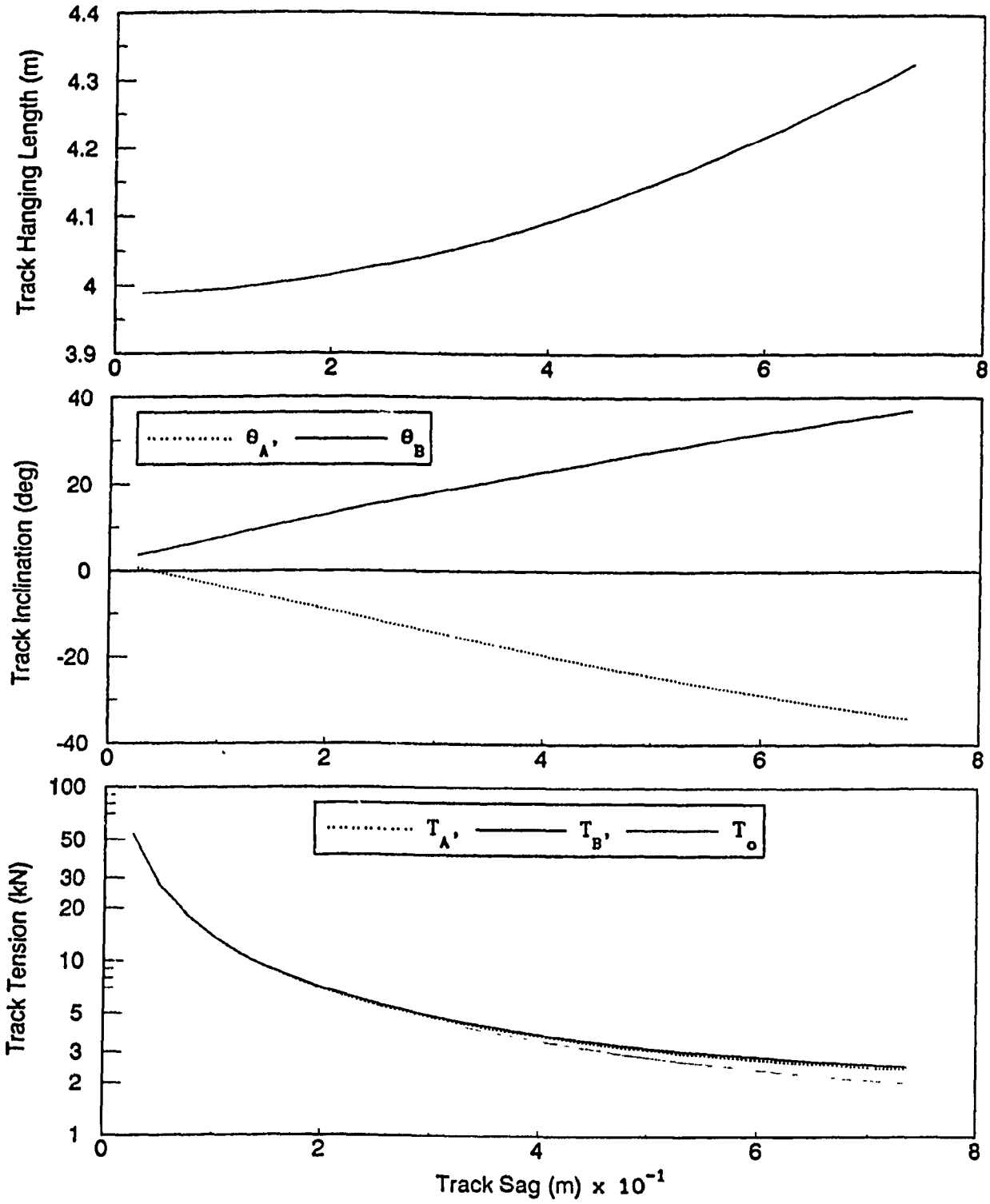

Figure 4.4 Hanging track characteristics based on quadratic polynomial.

T^0_{tr}, and corresponding track sag and length are then indicated by S^0_T and L^0_h, respectively. Consequently, S^0_T, L^0_h and T^0_{tr} collectively represent the desired initial track setting.

Quadratic polynomial approximation of the hanging upper track profile, is validated against measured static track profiles on the field-tested vehicle for three different settings of track pre-tension, T^0_{tr}. As illustrated in Figure 4.5, the comparison between measured and analytical hanging track profiles shows generally good agreement. The measured track profile exhibits a relatively less track sag especially for lower track pre-tension settings. It is primarily due to the fact that the part of the hanging track rests on top of the third and fourth road wheels. The analytical approximation, however, does not consider the interaction between the hanging track and the road wheels.

In the course of simulation, the track sag , S_T, must be known at every instant in order to apply the proposed method. For specified track and hull wheel parameters, a functional relationship between the track sag and the track hanging length is established prior to the simulation, given as:

$$S_T = b_o + b_1 L_h + b_2 L_h^2 \tag{4.18}$$

where constants b_o, b_1, and b_2 are computed considering three known values of L_h and corresponding S_T. The selection and computation of three data set is crucial in order to establish a correct representation of equation (4.18).

It is apparent that the assumption of track inextensibility or track sag becomes unreasonable as "L_h approaches d" (as shown in Figure 4.3(a)). Thus, track stretching is accounted for in establishing the

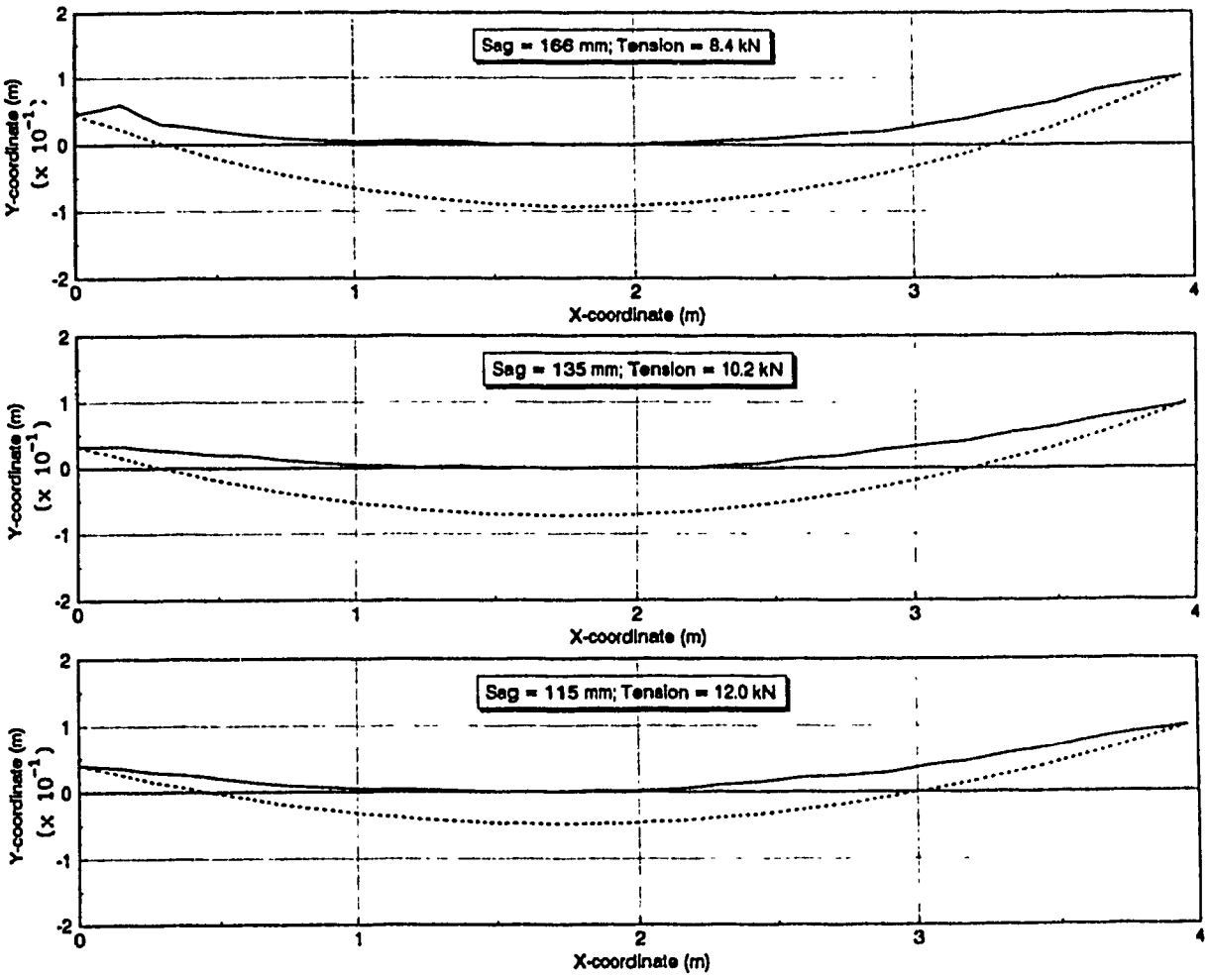

Figure 4.5 Measured and analytical profiles of hanging track strand for three track pre-tension settings (——— Measured, ... Analytical).

functional relationship (equation 4.18). The track sag is considered to be the dominant tension determining phenomenon up to the point where the slope "dT/dL" equals the track longitudinal stiffness, K_{tr}, and beyond this point, the track tension is computed based on track extensibility [34]. Thus, this point of track stretching or extensibility is considered as the first among the three required data set. In order to determine this point, "dT/dL" is computed as the absolute slope based on two consecutive values of T_{avg} and L_h (which are obtained for gradually incremented track sag as discussed previously), and compared against K_{tr}. Figure 4.6 shows the slope, dT/dL, as a function of track sag, length, and tension, where the point of track stretching at $dT/dL = K_{tr}$ is characterized by $(S_T^1,\ L_h^1,\ T_{tr}^1)$. Second and third data points are chosen at $2\ S_T^1$ and $3\ S_T^1$, and characterized by $(S_T^2,\ L_h^2,\ T_{tr}^2)$ and $(S_T^3,\ L_h^3,\ T_{tr}^3)$, respectively. Alternatively, second and third points can also be selected at S_T^0 and $2\ S_T^0$ if initial desired track tension, T_{tr}^0, is significantly lower compare to T_{tr}^1 (e.g. relative difference $\geq$ 25%). Three data points indicating track sag and associated track length are thus obtained, and used to compute the constants b_o, b_1, and b_2 based on equations (4.9), where $(X_A = L_h^1,\ Y_A = S_T^1)$, $(X_B = L_h^3,\ Y_B = S_T^3)$ and $(X_D = L_h^2,\ Y_D = S_T^2)$.

The synthesized functional relationship between track sag and track hanging length (equation 4.18) is verified by comparing it with the actual relationship. The actual relationship is obtained by gradually incrementing the track sag and computing the corresponding track hanging length and track tension. Figure 4.7 shows track sag and average track tension as a function of track hanging length between drive sprocket and idler of the field-tested vehicle. As shown, solid curve indicates the actual relationships. Dotted curve indicates the relationships obtained

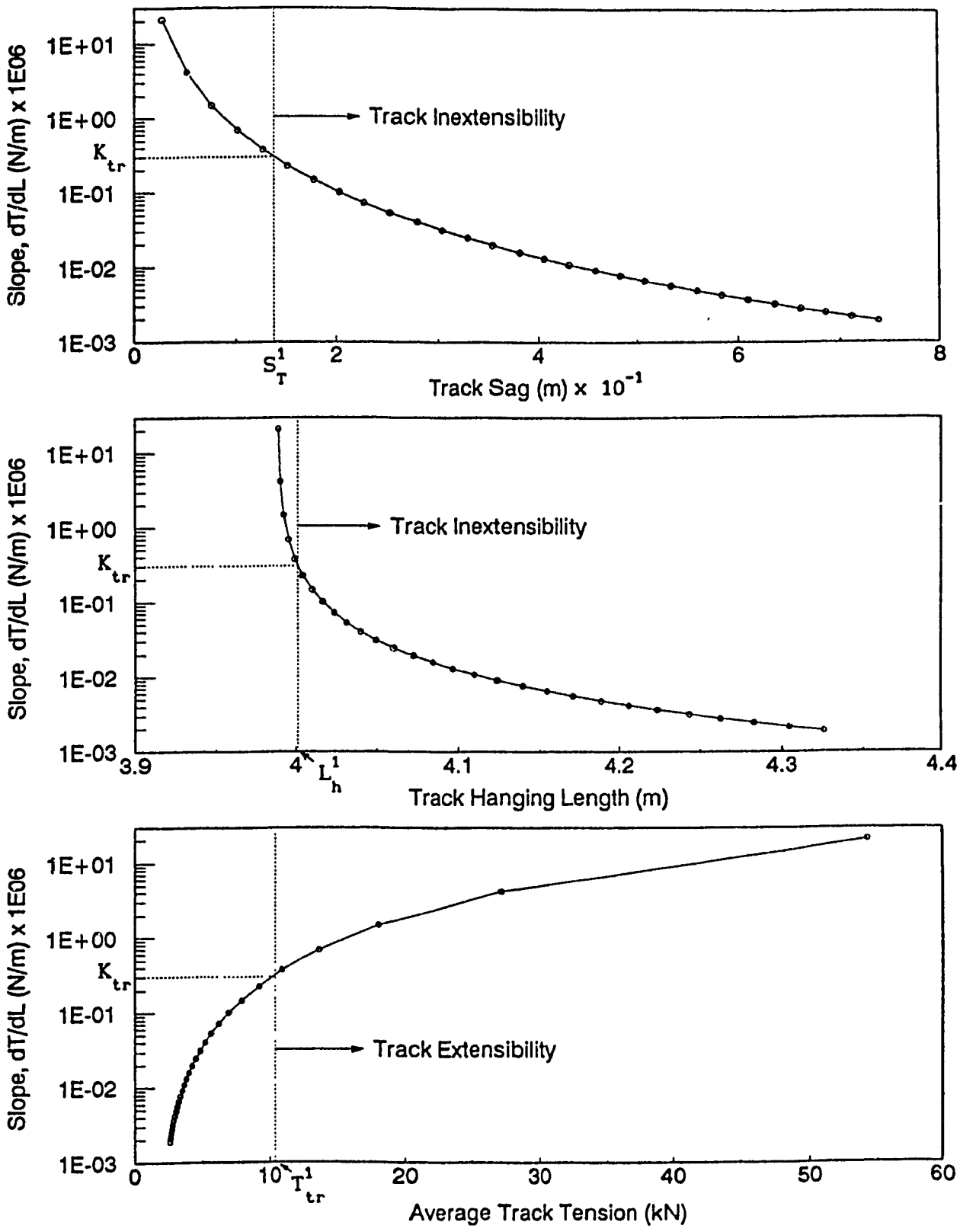

Figure 4.6 Determination of the point of track extensibility.

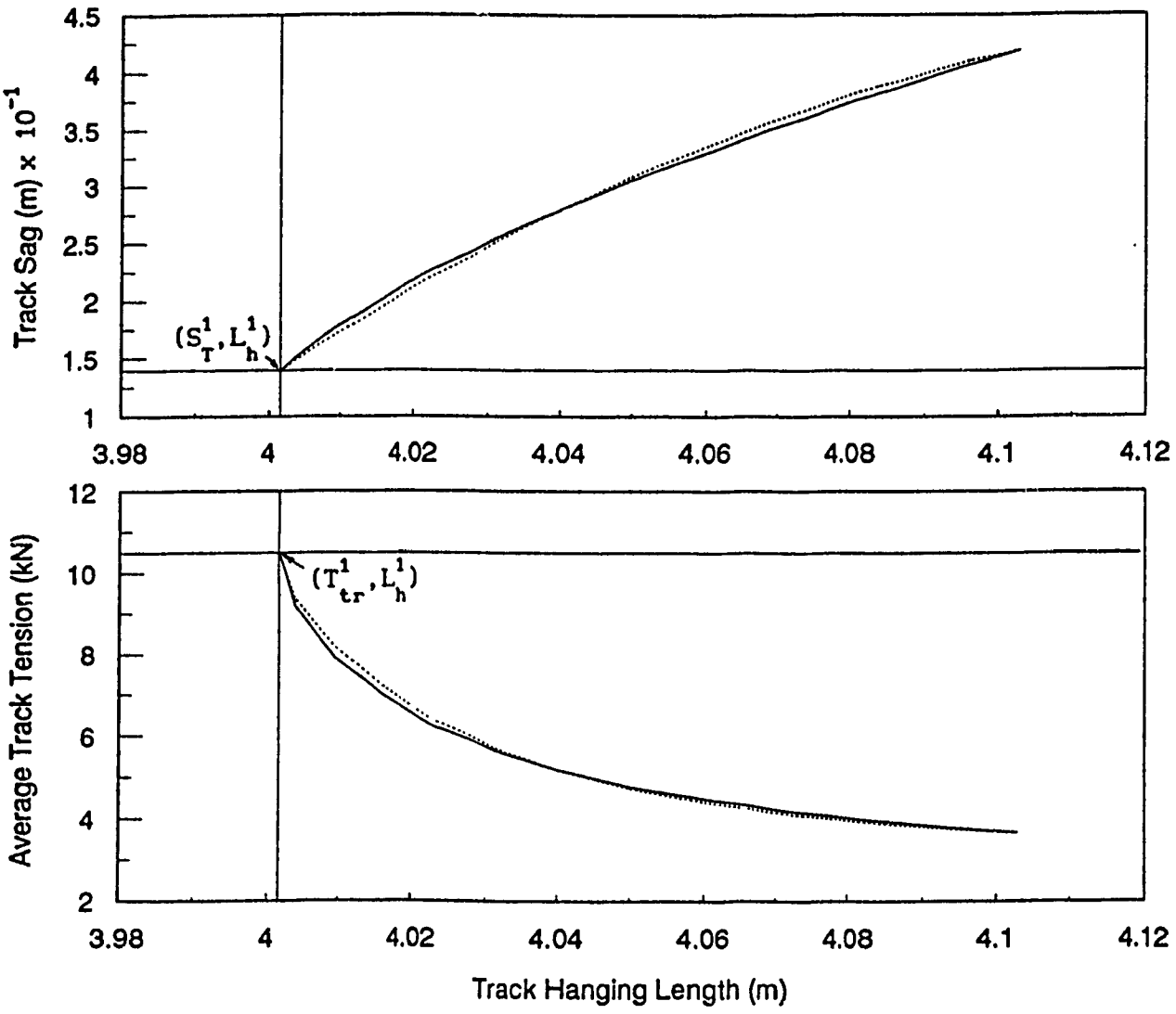

Figure 4.7 Hanging track characteristics based on track inextensibility (——— Actual, ····· Synthesized).

based on equation (4.18), where values of track hanging length obtained for solid curve were used to generate the data.

4.2.2.2 Wheel-Track Connectivity

In view of computation, and reflection of the track dynamic load at each wheel station, an appropriate track connectivity is necessary to define how the track wraps around wheels and terrain profile. The track connectivity is continuously dependent on generalized coordinates associated with road wheels and hull, and the terrain profile. The connectivity algorithm must include three basic geometrical states, which are:

(a) the coincident road wheel-track-terrain contact,

(b) the road wheel-track contact without the track-terrain contact, and

(c) no contact between road wheel and track, where track is either in or out of contact with terrain.

The wheel-track connectivity algorithm employed in MODEL I, is refined to yield an appropriate definition of the track wrap angles around road wheels. In MODEL I, the track wrap angle around i^{th} road wheel, ϕ_i, is either computed as wheel-ground contact patch angle, β_i (geometrical state: a), or wheel-track tangency angle, η_i, (geometrical state: b). The track wrap angle is correctly computed for state (b), but not for (a). For example, Figure 4.8 illustrates a geometrical situation where ϕ_i is a linear combination of β_i and η_i, and thus must be computed correctly. For this, the horizontal coordinates of road wheel-ground contact points and track tangency points are compared to establish the first and last points of the track wrap around the road wheel, which are specified as $\mathbb{P}_1$ (= P_1 or P_1^T) and $\mathbb{P}_2$ (= P_2 or P_2^T), respectively. The track wrap angle is then computed as:

$$\phi_i = \text{ATAN3}(Y^i_2 - Y_{wi},\ X^i_2 - X_{wi}) - \text{ATAN3}(Y^i_1 - Y_{wi},\ X^i_1 - X_{wi}) \qquad (4.19)$$

In addition, the geometrical state (c) which suggests the road wheel-track-terrain separation, is also incorporated to further enhance the track connectivity algorithm. For intermediate road wheels (i = 2,.., N-1), which are neither in contact with track ($\eta_i < 0$) nor with terrain ($\beta_i = 0$), corresponding first and last track points are computed as (refer to Figure 4.9):

$$X^i_1 = X^i_2 = X_{wi} \quad ; \quad Y^i_1 = Y^i_2 = \begin{cases} Y_T & ; \text{ if } Y_T > Y_P \\ Y_P & ; \text{ otherwise} \end{cases} \qquad (4.20)$$

where,
$$Y_T = Y^{i\ell}_2 + \left(\frac{Y^{ir}_1 - Y^{i\ell}_2}{X^{ir}_1 - X^{i\ell}_2} \right) (X_{wi} - X^{i\ell}_2)$$

and Y_P is the elevation of terrain profile at X_{wi}. $(X^{i\ell}_2, Y^{i\ell}_2)$ indicates the last track point for the road wheel on left-hand-side (including last road wheel), which is in geometrical state (a) or (b). Similarly, (X^{ir}_1, Y^{ir}_1) indicates the first track point for the road wheel on right-hand-side (including first road wheel), which is in geometrical state (a) or (b). First and last track points, as given by equation (4.20), are then used to define the end points of adjacent track segments, which are subsequently checked for deflection as described in section 2.4.2 (Figure 2.18).

4.2.2.3 Track Bridging:

By definition, track bridging effect is a support transmitted to i^{th} road wheel in the form of an upward vertical component of the net dynamic track load, T^i_{wy}. It is evident from equation (2.14) that the computation

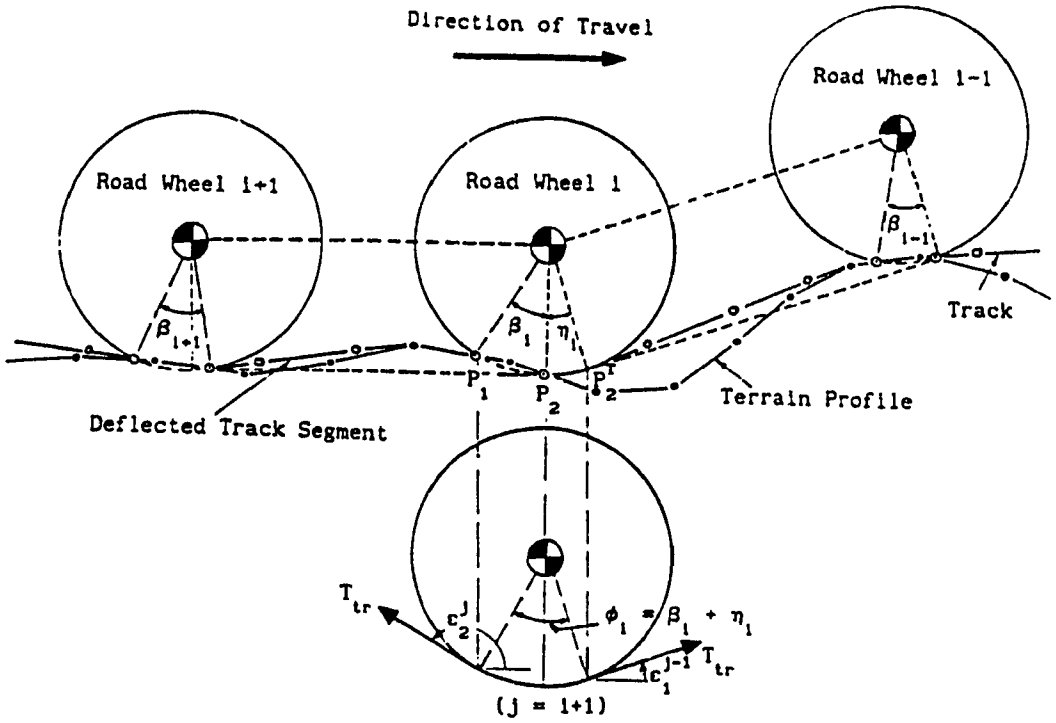

Figure 4.8 Determination of track wrap angle around i^{th} road wheel.

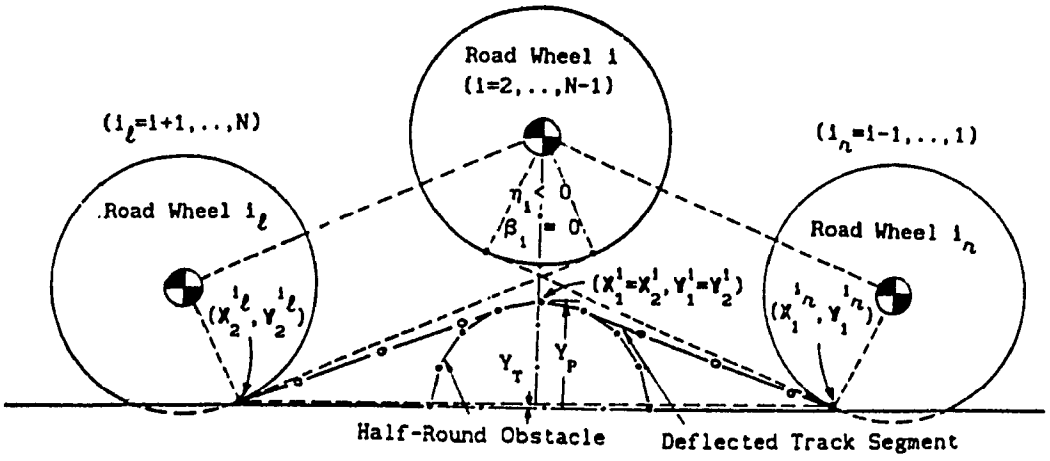

Figure 4.9 Road wheel-track separation (geometrical state C).

of T^{i}_{wy} is dependent upon the horizontal inclinations of track segments on left (ε_2^{i+1}) and right (ε_1^{i}) sides of the road wheel. Thus, calculation of the angles at which the track wraps around the wheels is a way to model bridging effects.

In MODEL I, the track bridging effects are correctly modeled only when: (a) track segment is deflected due to interaction with terrain profile, or (b) track segment is tangent to the wheel. For instance, Figure 4.8 illustrates the geometrical state where track segment on left side of the road wheel is deflected and track segment on right side is tangent, thus, track bridging is accurately modeled. Now, consider a tracked vehicle moving over a flat profile. As shown in Figure 4.10 (a), there is no support from the intermediate track segment (between road wheels), since they are neither deflected nor tangent to road wheels. On a flat profile, high mobility tracked, however, do get little support from intermediate track segment. An estimate of actual phenomenon can be achieved by defining midpoints of the intermediate track segments and computing the wheel tangency points of adjacent wheels from these points [34]. The wheel tangency points of i^{th} road wheel are determined using geometric schemes shown in Figure 2.17. As shown in Figure 4.10 (b), the horizontal inclinations of tangents can then be used to compute vertical and horizontal components of net dynamic track load imposed at each wheel station. Consequently, this approach is adopted to improve track bridging effects, as demonstrated in Figure 4.11.

4.2.2.4 Net Dynamic Track Load

The net dynamic track load is computed as:

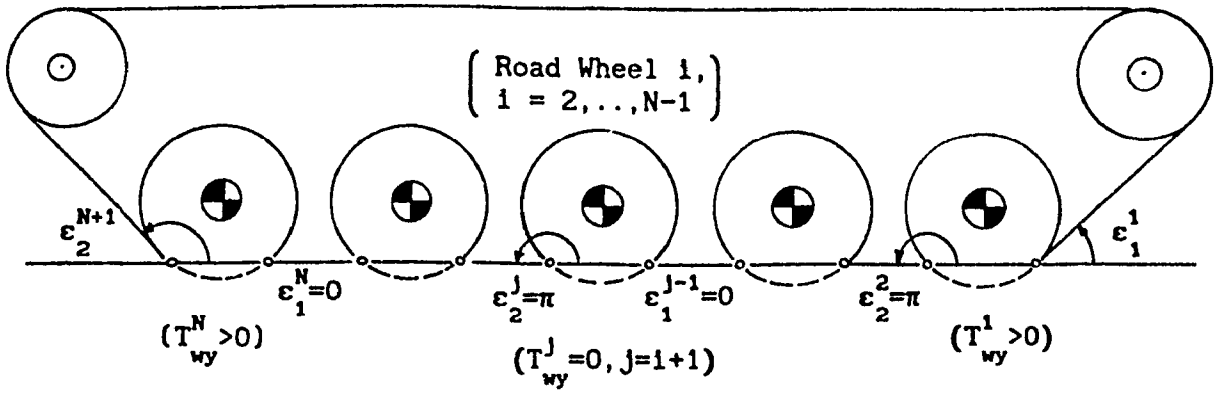

(a) Without bridging

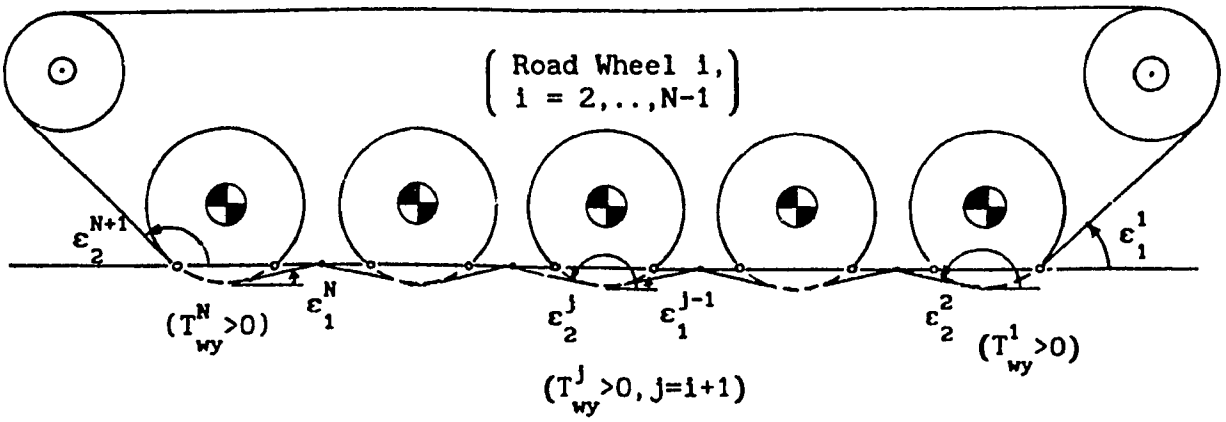

(b) With bridging

Figure 4.10 Definition of track bridging.

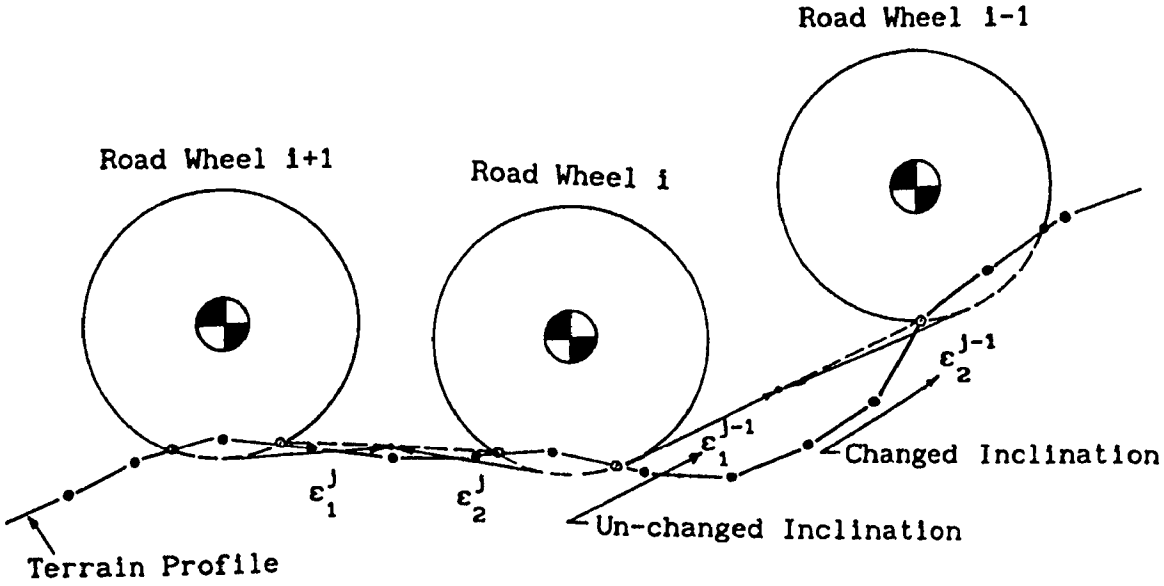

Figure 4.11 An improved track bridging.

$$T_{tr} = \begin{cases} (T_A + T_B)/2 & ; L_h > L_h^1 \text{ (Track Inextensibility)} \\ K_{tr}(L_{tr} - L_{tr}^0) + T_0 & ; L_h \leq L_h^1 \text{ (Track Extensibility)} \end{cases} \quad (4.21)$$

where T_A and T_B are the track tension at idler and drive sprocket, respectively, computed based on equation (4.16). T_0 is the reference tension for determining T_{tr} based on track extensibility, given as:

$$T_0 = \begin{cases} T_{tr}^0 & ; \quad L_h^0 \leq L_h^1 \text{ (Track is pre-stretched)} \\ T_{tr}^1 & ; \quad \text{Otherwise} \end{cases} \quad (4.22)$$

L_{tr}, the instantaneous length of track required to wrap from top of the front hull wheel (point B), around the road wheels, and up to top of the rear hull wheel (point A), is expressed based on equation (2.42) as:

$$L_{tr} = \sum_{i=1}^{N} \phi_i R_{wi} + \sum_{k=1}^{2} \phi_{hk} R_{hk} + \sum_{j=1}^{N+1} L_j \quad (4.23)$$

and its initial value at time, t = 0, is L_{tr}^0. L_h is the instantaneous length of track hanging between drive sprocket and idler, given as:

$$L_h = L_{tr}^0 - L_{tr} \quad (4.24)$$

where, the initial overall track length is given as:

$$L_{tr}^0 = L_{tr}^0 + L_h^0 \quad (4.25)$$

and L_h^0 is the initial value which corresponds to the desired track pre-tension, T_{tr}^0. The total track length, L_{tr}, is expressed as:

$$L_{tr} = \begin{cases} L_{tr}^0 & ; L_h > L_h^1 \\ L_{tr}^0 + (L_{tr} - L_{tr}^0) & ; L_h \leq L_h^1 \end{cases} \quad (4.26)$$

Equation (4.26) indicates that L_{tr} is either equal to or greater than

its initial value, L^0_{tr}. However, L_{tr} could also become less than L^0_{tr} at certain instances during simulation. It only happens for the case when track is pre-stretched ($L^0_h < L^1_h$) and $L^0_h < L_h \leq L^1_h$ (a point between the point of track initial setting and the point of track stretching). Consequently, the term $(L_{tr} - L^0_{tr})$ in equation (4.26), which is also equal to $(L^0_h - L_h)$, becomes negative. It represents a peculiar situation, where the overall track tension, T_{tr} (equation 4.21) is evaluated based on track extensibility ($L_h \leq L^1_h$), but indicates a drop from its initial value, T^0_{tr}.

The horizontal and vertical components of the overall track tension, T_{tr}, acting at the i^{th} road wheel are computed using equation (2.14), where track inclination angles ε^j_j (j=1,2) are, however, computed in view of improved track bridging effects. The mathematical expressions for horizontal and vertical components of dynamic track load acting at k^{th} hull wheel are, however, different from equation (2.18), and are given as

$$T^k_{hx} = T_{tr}\cos\,\varepsilon^j_j + T\cos\Theta \quad ; \quad T^k_{hy} = T_{tr}\sin\,\varepsilon^j_j + T\sin\Theta \qquad (4.27)$$

where $j = \begin{cases} 1 \\ N+1 \end{cases}$, $j = \begin{cases} 2 \\ 1 \end{cases}$, $T = \begin{cases} T_B \\ T_A \end{cases}$ and $\Theta = \begin{cases} \Theta_B & ; \text{ for } k = 1 \\ \Theta_A & ; \text{ for } k = 2 \end{cases}$

As evident from equation (4.27), T and Θ constitute track tension vectors acting at the top of drive sprocket and idler. These vectors are defined by equations (4.14) and (4.16) for the case of track inextensibility ($L_h > L^1_h$). However, they become equal and opposite for the case of track extensibility ($L_h \leq L^1_h$), where their magnitude, $T = K_{tr}(L_{tr} - L^0_{tr}) + T_0$, and horizontal inclination, Θ, is given by equation (2.19).

The computational procedure for obtaining overall track tension, T_{tr},

can be summarized in the following two steps:

(a) *Prior to simulation*, the functional relationship between track sag and track hanging length (equation 4.18) is computed based on specified vehicle and track parameters. Control parameters for determining overall track tension, T_{tr}, such as track lengths: L_h^0, L_h^1, L_{tr}^0 and L_{tr}^0 and track tensions: T_{tr}^0, T_{tr}^1 and T_0 are established for the tracked vehicle positioned on a flat ground.

(b) *During simulation*, track length, L_{tr} (equation 4.23) is computed at each integration step, where L_{tr} is based on instantaneous kinematic state of tracked vehicle with respect to terrain profile. Track hanging length, L_h, is, then, obtained using equation (4.24). Finally, overall track tension, T_{tr} (equation 4.21) is computed based on:

- if $L_h > L_h^1$: instantaneous track sag, S_T, is obtained using equation (4.18), and coordinates of point D (X_D, Y_D) are evaluated from equation (4.8), where end coordinates of hanging track (X_A,Y_A, and X_B,Y_B) are updated based on instantaneous centre coordinates of sprocket and idler (equation 2.49). Consequently, instantaneous hanging track profile is approximated by quadratic polynomial (equation 4.9), and corresponding track tension vectors (T_A, Θ_A) and (T_B, Θ_B) are computed using equations (4.14) and (4.16), **or**
- If $L_h \leq L_h^1$: net dynamic track load is computed based on track extensibility, and corresponding tension vectors T_A and T_B are equal and opposite.

4.2.3 Equations of Motion

In MODEL I, the equations of motion were derived assuming a *strictly vertical* suspension configurations. However, an independent suspension is

rigidly fixed to the vehicle frame, and thus remains perpendicular to the frame. Consequently, the equations of motion are re-written as:

Bounce Motion of Hull:

$$\ddot{y}_h = \frac{1}{m_h}\left[\sum_{i=1}^{N}(F_{si}+F_{di})C_\theta - (F_{so}+F_{do})C_\theta + \sum_{k=1}^{2}F_{hy}^{k}\right] - g \qquad (4.28)$$

Pitch Motion of Hull:

$$\ddot{\theta}_h = \frac{1}{I_h}\left[\sum_{i=1}^{N}\{(F_{si}+F_{di})a_i + b_{wi}[F_{wx}^{i}C_\theta - (F_{wy}^{i}-W_{wi})S_\theta]\} - (F_{so}+F_{do})a_o \right.$$
$$\left. + \sum_{k=1}^{2}a_{hk}[F_{hx}^{k}S_\theta + F_{hy}^{k}C_\theta] + b_{hk}[F_{hx}^{k}C_\theta - F_{hy}^{k}S_\theta]\right] \qquad (4.29)$$

Bounce Motion of Road Wheel Assembly:

$$\ddot{y}_{wi} = \frac{1}{m_{wi}}\left[F_{wy}^{i} - (F_{si}+F_{di})C_\theta\right] - g \qquad (4.30)$$

Bounce Motion of Driver and Seat:

$$\ddot{y}_o = \frac{1}{m_o}\left[(F_{so}+F_{do})C_\theta\right] - g \qquad (4.31)$$

where, b_{wi} indicates the instantaneous elevation of i^{th} road wheel center with respect to c.g. of the vehicle, and is measured along the line which is perpendicular to the vehicle frame and passess through the road wheel center,

$$b_{wi} = \frac{Y_{wi} - Y_{cg} - a_i S_\theta}{C_\theta} \qquad (4.32)$$

The horizontal coordinate of i^{th} road wheel centre is then given by:

$$X_{wi} = X_{cg} + a_i.C_\theta - b_{wi}.S_\theta \qquad (4.33)$$

The relative displacement and velocity across the primary and secondary suspension units, are given as:

$$r_i = [y_{wi} - y_h - a_i S_\theta]C_\theta - b_i S_\theta^2 \qquad (4.34a)$$

$$\dot{r}_i = [\dot{y}_{wi} - \dot{y}_h]C_\theta - [y_{wi} - y_h]\dot{\theta}_h S_\theta - a_i\dot{\theta}_h[C_\theta^2 - S_\theta^2] - 2\, b_i\dot{\theta}_h S_\theta C_\theta \qquad (4.34b)$$

$$r_o = [y_h + a_o S_\theta - y_o]C_\theta + b_o S_\theta^2 \qquad (4.35a)$$

$$\dot{r}_o = [\dot{y}_h - \dot{y}_o]C_\theta - [y_h - y_o]\dot{\theta}_h S_\theta + a_o\dot{\theta}_h[C_\theta^2 - S_\theta^2] + 2\, b_o\dot{\theta}_h S_\theta C_\theta \qquad (4.35b)$$

The net horizontal and vertical forces acting at road wheels (F^i_{wx}, F^i_{wy}, $i=1,..,N$) and hull wheels ($F^k_{hx}, F^k_{hy}, k=1,2$) are computed based on the refined wheel and track models.

The zero-force configuration of MODEL II is established in similar manner as for MODEL I (section 2.5). However, the net dynamic track loads acting at road wheels ($T^i_{wx}, T^i_{wy}, i=1,..,N$) and hull wheels ($T^k_{hx}, T^k_{hy}$, $k=1,2$) are computed based on the refined track models. Similarly, the vehicle static equilibrium is established based on the iterative stiffness approach (section 2.6).

4.3 FIELD VALIDATION OF MODEL II

In this section, the ride response predictions for the field-tested vehicle are evaluated using the refined ride model, MODEL II, and validated against field-measured ride data. Discussions on the validation results are presented in view of specific type of terrain profile.

Discrete Half Round Obstacles

The ride acceleration traces for the unladen test vehicle crossing

over 6" and 8" half-round obstacles at various speeds, are evaluated and superimposed over measured ones. For 6" obstacle-crossing, the test vehicle configurations: B, C, and D, are considered, while configuration B is considered for 8" obstacle-crossing.

6" Obstacle

Figure 4.12 illustrates the direct comparison between predicted and measured acceleration traces for the test vehicle configuration B crossing the obstacle at 14.3 km/h. In comparison with ride predictions obtained using MODEL I (Figures 3.19 and 3.20), the ride predictions in Figure 4.12 exhibit an improved correlation with the field measurements (especially pitch acceleration). The acceleration levels predicted using MODEL II are relatively high primarily due to the adaptive foot-print formulation of the wheel/track-terrain interaction (section 4.2.1), which yields relatively higher foot-print forces during obstacle-crossing. It should be noted that the energy dissipation due to the i^{th} road wheel/track-terrain interaction, modeled through the damping coefficient C^{i}_{rw}, has been excluded in the evaluation of ride predictions presented so far (i.e. results in Figure 4.12 as well as the ride predictions evaluated using MODEL I). In fact, there is dissipation of transmitted ground/soil energy at the wheel/track-terrain interface. Thus, it is essential to consider damping in order to realistically predict the ride response especially in the high-speed terrain negotiations. A base value of 5 kN.s/m is selected for C^{i}_{rw} such that the predicted angular acceleration traces of intermediate road arm-wheel assemblies (ones without the shock absorbers) exhibit a reasonably good correlation with the field measurements. This is discussed in detail in Chapter 5 (section 5.3). Figure 4.13 shows the field-validation of ride predictions, which are re-

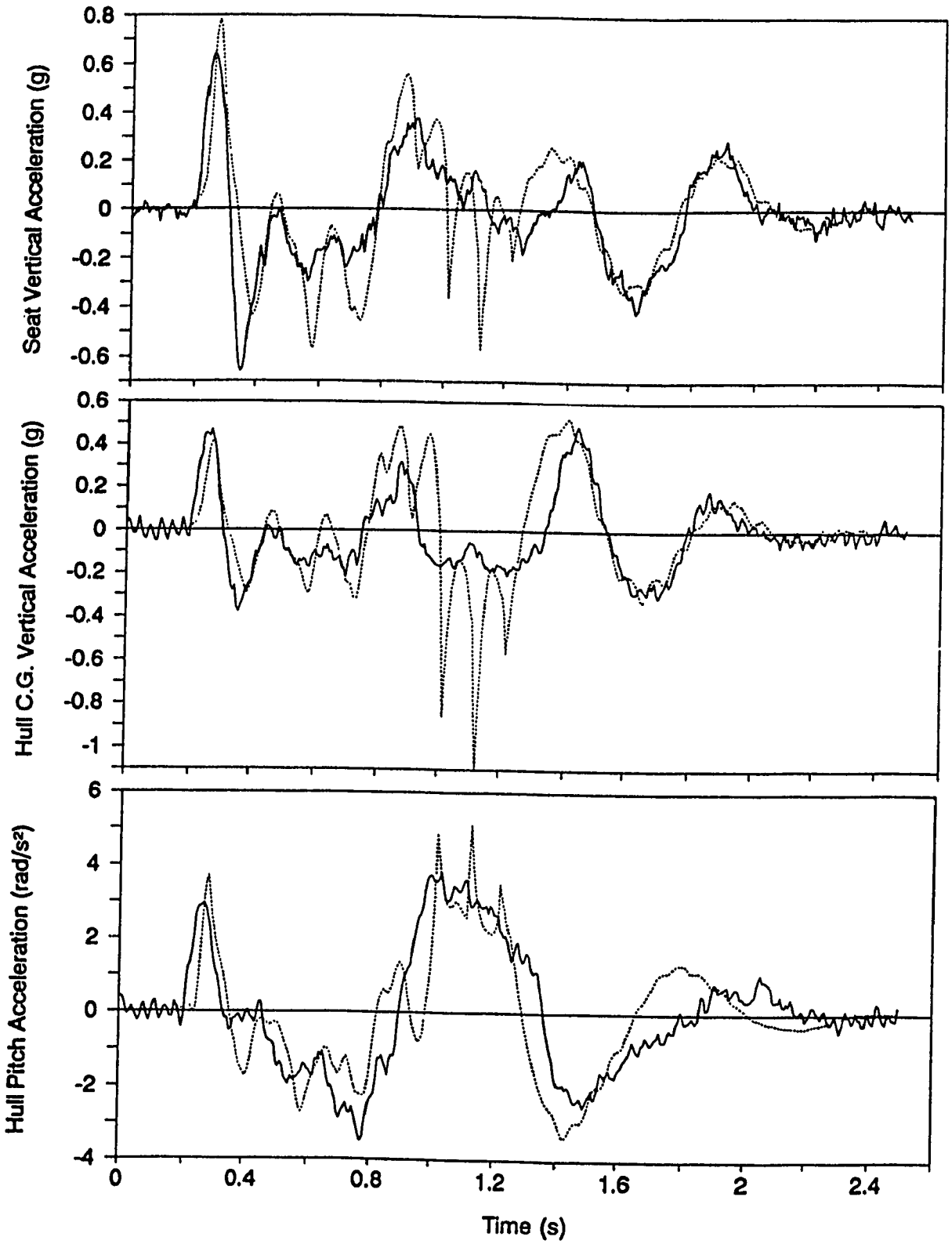

Figure 4.12 Ride acceleration traces - field validation of MODEL II's predictions for test vehicle configuration B traversing 6" obstacle at 14.3 km/h - C^{i}_{rw} = 0.0 N.s/m (i = 1,..,5)
(——— Field Test, ... Simulation).

evaluated using C'_{rw} = 5 kN.s/m. The introduction of damping have smoothened the ride, and predicted traces exhibit even a closer correlation with field-measured data.

As shown in Figure 4.13, first five peaks in the simulated seat and hull c.g. vertical acceleration traces are observed when each road wheel hits the obstacle, while remaining peaks are due to the vehicle impact and settlement on the flat ground after crossing the obstacle. Similarly, first two peaks in the pitch acceleration traces are the indications of wheel-obstacle interaction (net foot-print force) for first two road wheels, whereas peaks 3 and 4 are primarily due to the overall track tension (dynamic track load), which is dictated by the instantaneous vehicle suspension geometry after first three road wheels have crossed the obstacle. The peak 5 is due to a second ground impact of the vehicle prior to its settlement, and may be more important than the first peak in the discrete obstacle-crossing ride analysis of tracked vehicles.

Figures 4.14 and 4.15 show the measured and predicted acceleration time histories of driver's seat vertical and hull pitch motions for the test vehicle configuration B traversing the obstacle at 20 km/h and 29 km/h. As shown, MODEL II's predictions exhibit good correlation with the measured ride data.

The ride acceleration traces are evaluated for the test vehicle crossing over 6" obstacle with low and high track pre-tension settings. Figures 4.16 and 4.17 show the measured and predicted acceleration traces of driver's seat vertical and hull pitch motions for the test vehicle configuration C crossing the obstacle at 14.9 km/h and 22.2 km/h. Similarly, Figures 4.18 and 4.19 exhibit the comparison between predicted and measured ride acceleration traces for the test vehicle configuration

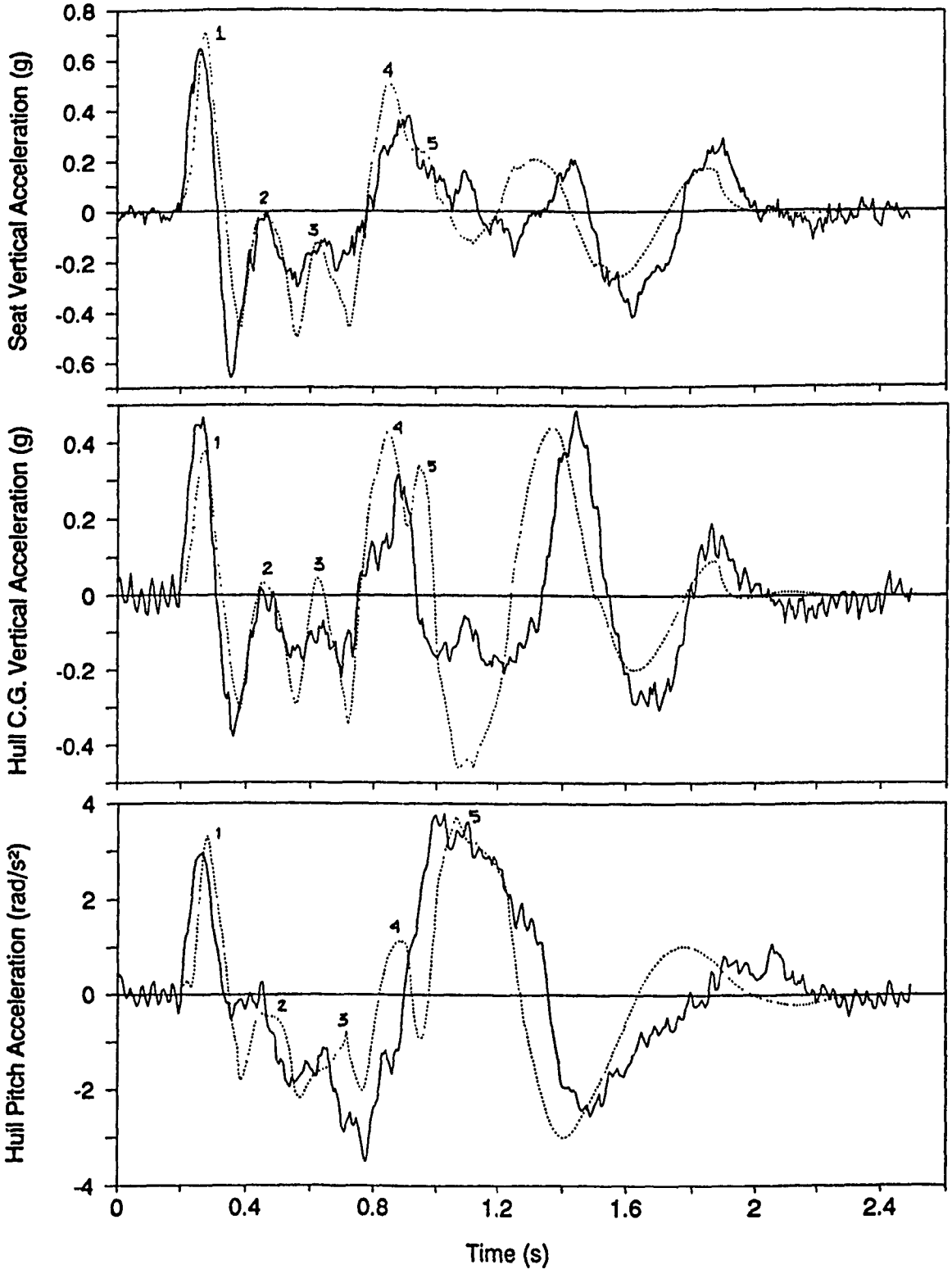

Figure 4.13 Ride acceleration traces - field validation of MODEL II's predictions for test vehicle configuration B traversing 6" obstacle at 14.3 km/h - C^{i}_{rw} = 5.0 kN.s/m (i = 1,..,5)
(——— Field Test, ... Simulation).

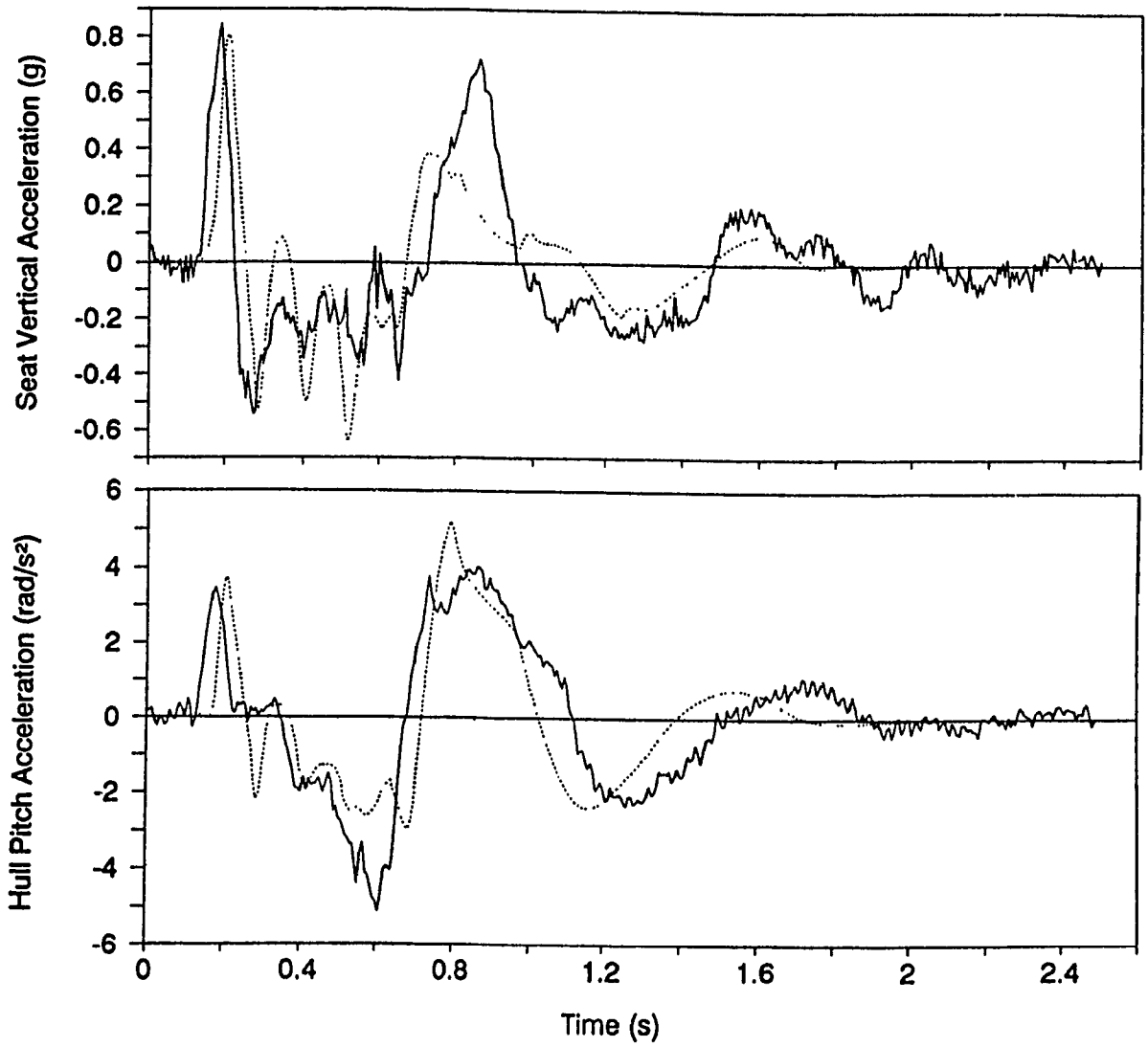

Figure 4.14 Ride acceleration traces - field validation of MODEL II's predictions for test vehicle configuration B traversing 6" obstacle at 20 km/h (——— Field Test, ... Simulation).

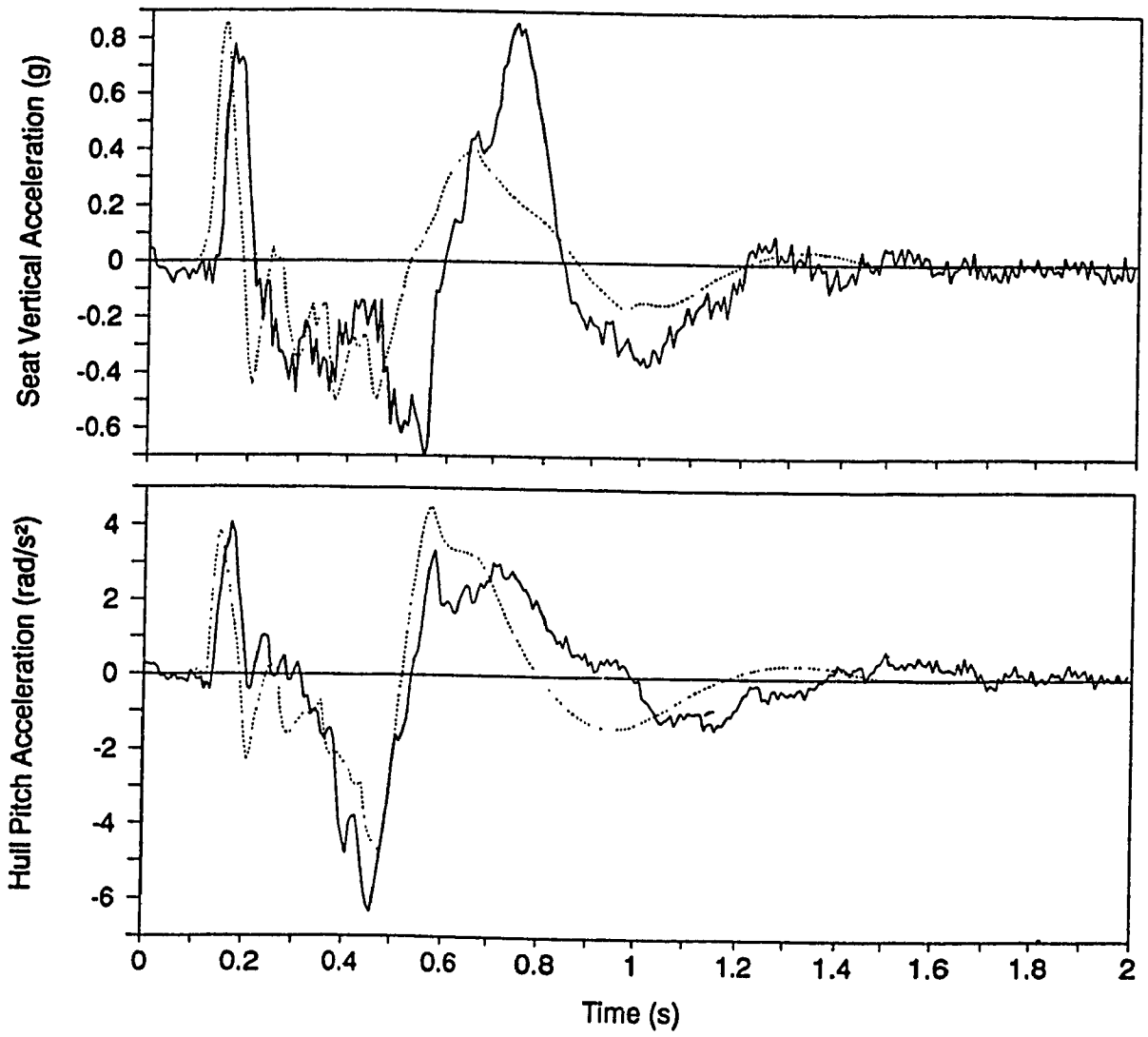

Figure 4.15 Ride acceleration traces - field validation of MODEL II's predictions for test vehicle configuration B traversing 6" obstacle at 29 km/h (——— Field Test, ····· Simulation).

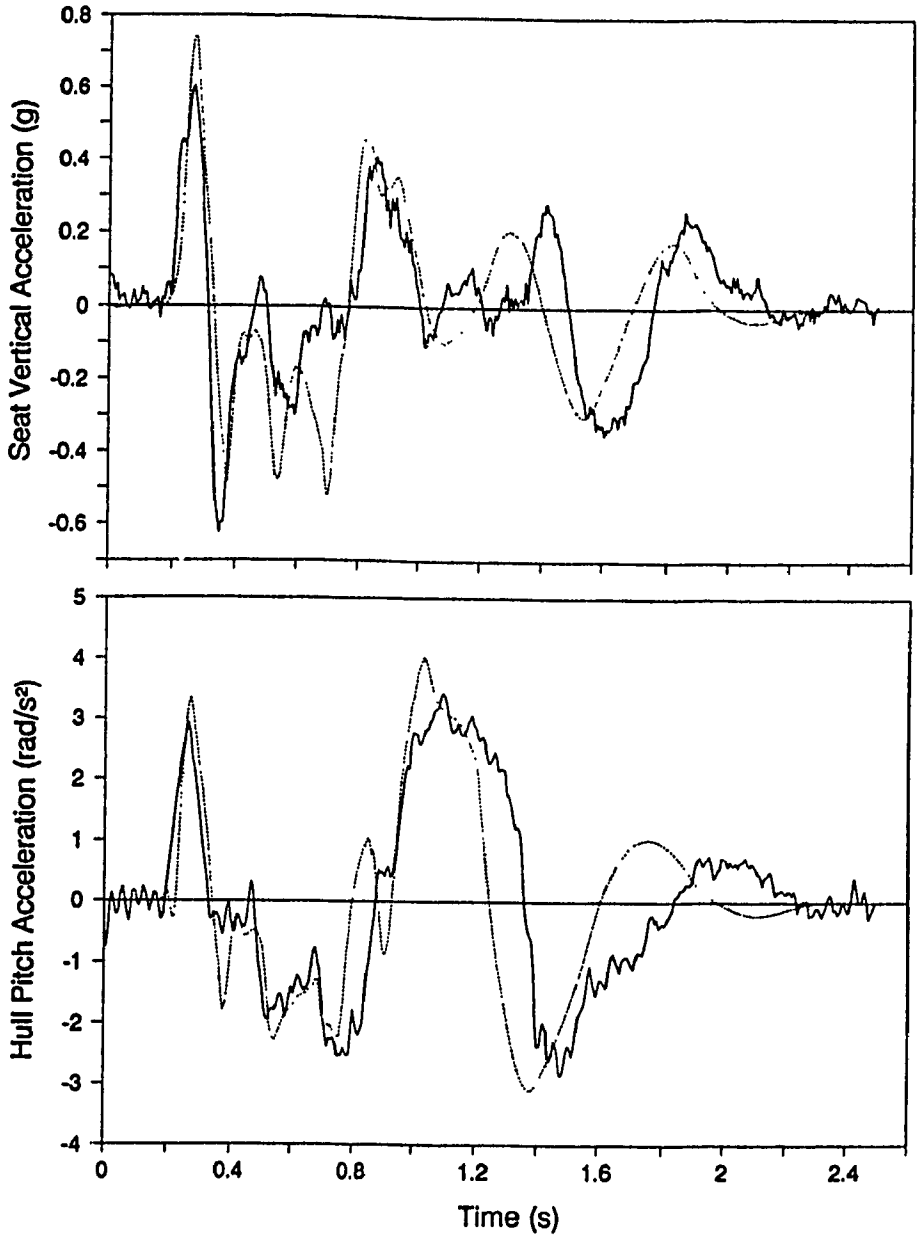

Figure 4.16 Ride acceleration traces - field validation of MODEL II's predictions for test vehicle configuration C traversing 6" obstacle at 14.9 km/h (——— Field Test, ... Simulation).

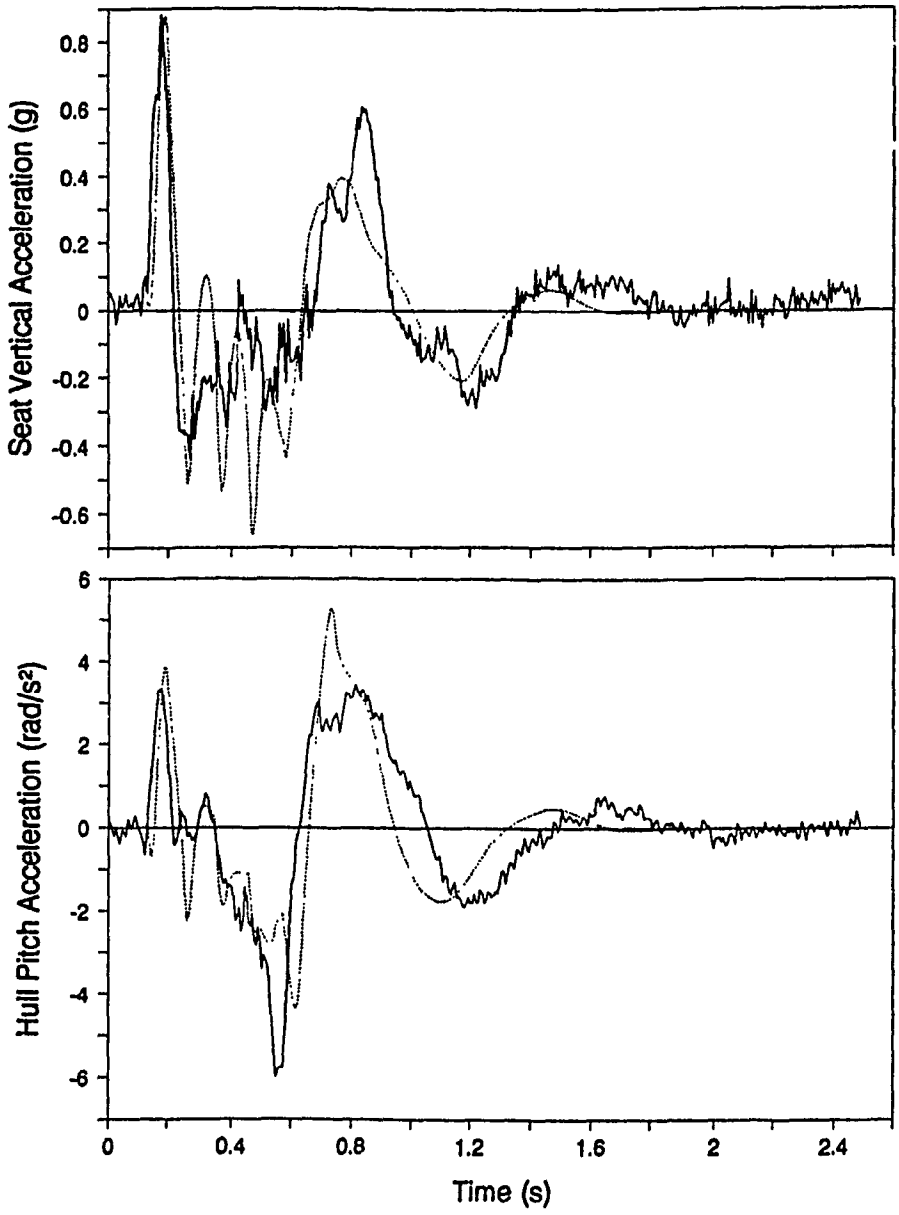

Figure 4.17 Ride acceleration traces - field validation of MODEL II's predictions for test vehicle configuration C traversing 6" obstacle at 22.2 km/h (——— Field Test, ... Simulation).

D traversing the obstacle at 15.4 km/h and 22.5 km/h. As shown, ride acceleration traces obtained using both track pre-tension settings are very similar, and exhibit a generally good agreement with the field measurement. It is demonstrated by both predicted and measured results that the specified variations in the track pre-tension setting does not have any significant influence on the ride and shock performance of the test vehicle.

Comparison of the animated pictures with the numerical/graphical output at various time steps is very useful in understanding and analyzing the ride responses of the vehicle. Figure 4.20 represents a few selected snapshots of the test vehicle traversing 6" obstacle with a low and a high track pre-tension settings. These snapshots are obtained from the animation program (post-processing). Indeed, the response results presented so far are well explained by the related animation pictures in Figure 4.20.

8" Obstacle:

Figure 4.21 illustrates the comparison of MODEL II's ride predictions with field measurements for the test vehicle configuration B crossing the obstacle at 7.8 km/h. The measured and predicted hull pitch acceleration traces exhibit a distinct downward peak, which occured as a consequence of the idler-obstacle interaction. Figures 4.22 and 4.23 show predicted and measured ride acceleration traces for the test vehicle configuration B negotiating the obstacle at 12.8 km/h and 18.9 km/h. In comparison, the predicted accleration traces exhibit superior ride and shock performance. As shown, there are two dominant upward peaks in the measured traces: first peak was due to the first road wheel-obstacle interaction, and the second dominant peak was due to the sprocket-ground interaction just

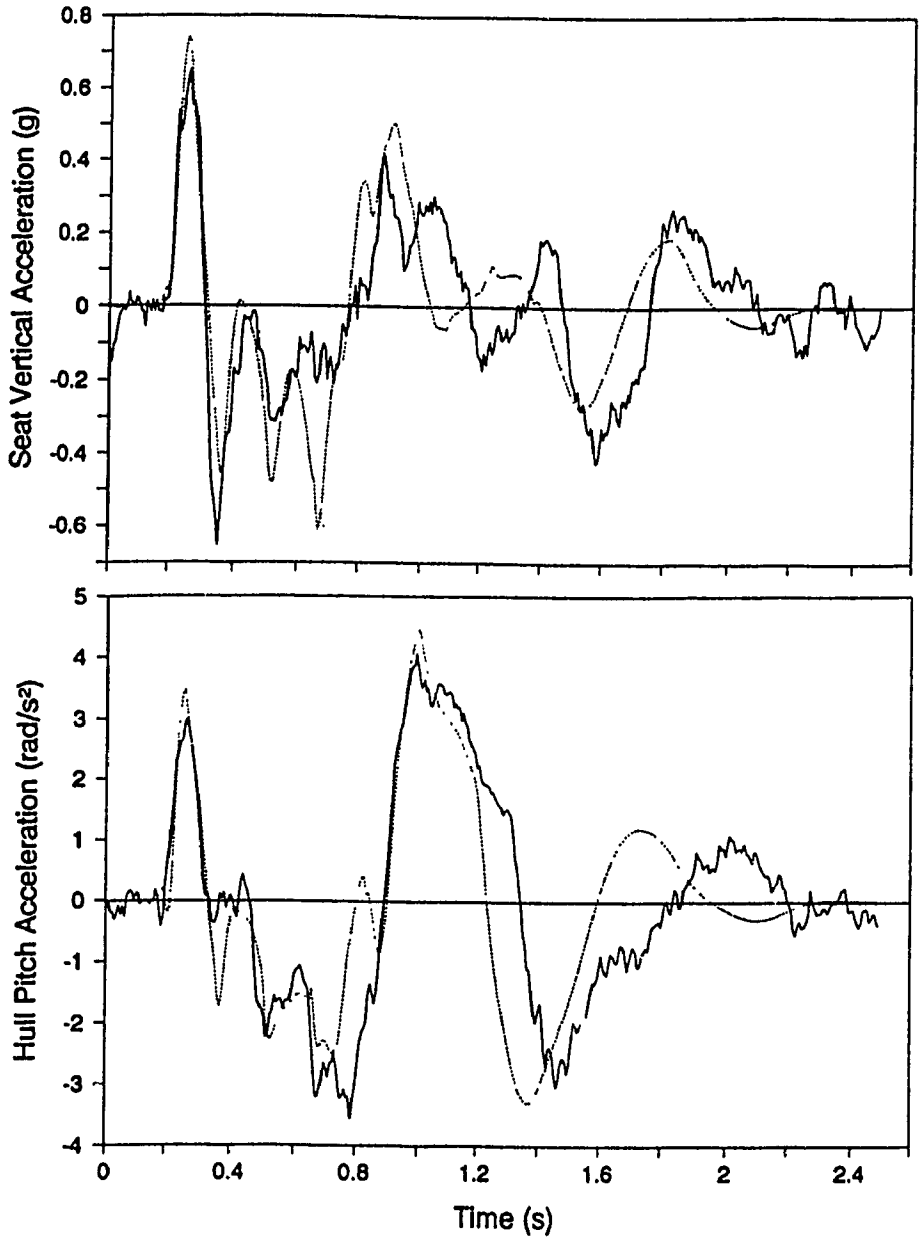

Figure 4.18 Ride acceleration traces - field validation of MODEL II's predictions for test vehicle configuration D traversing 6" obstacle at 15.4 km/h (——— Field Test, ... Simulation).

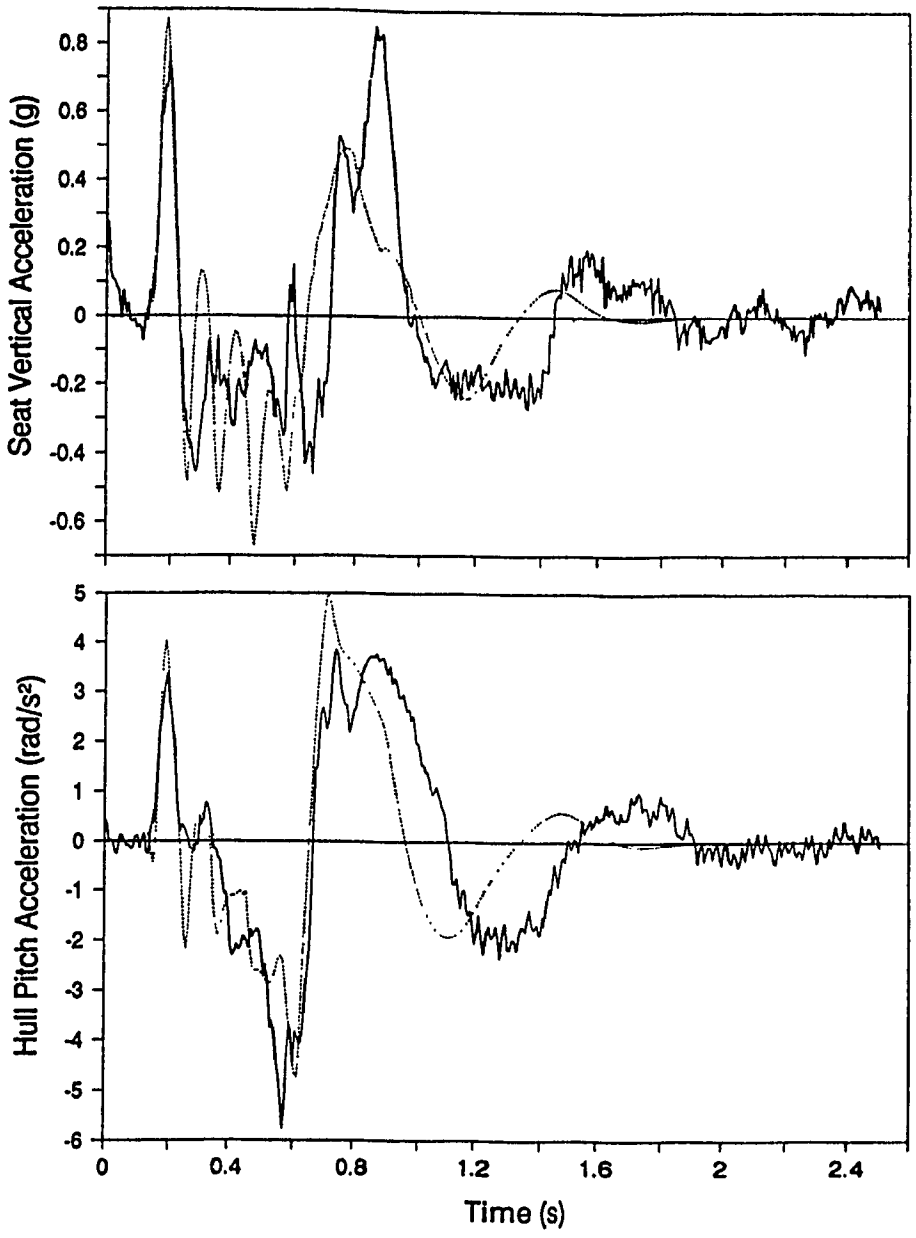

Figure 4.19 Ride acceleration traces - field validation of MODEL II's predictions for test vehicle configuration D traversing 6" obstacle at 22.5 km/h (——— Field Test, ... Simulation).

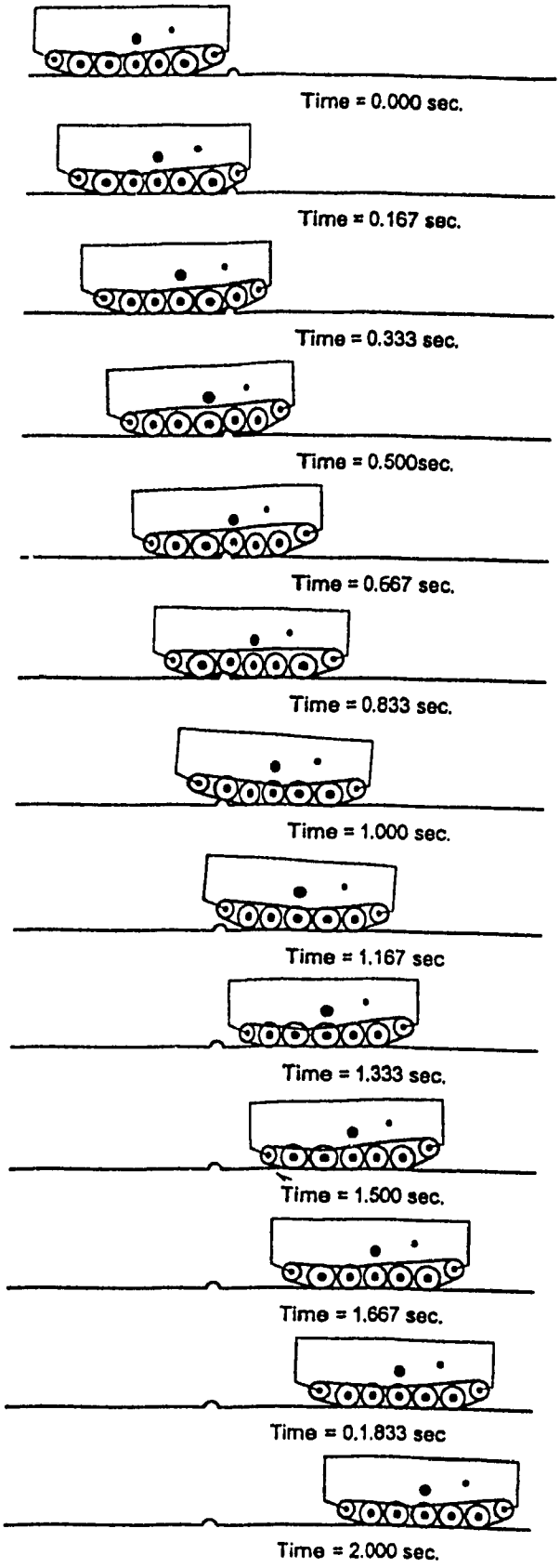

(a) Configuration C; V_x = 14.9 km/h

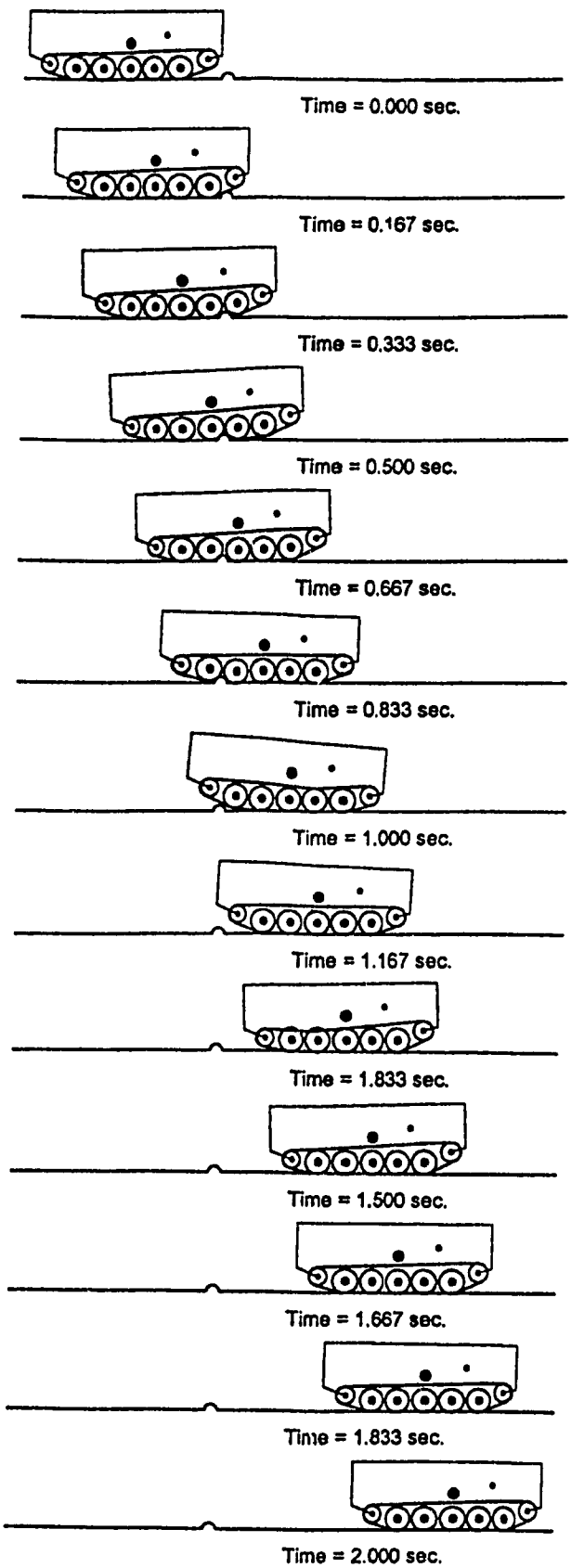

(b) Configuration D; V_x = 15.4 km/h

Figure 4.20 Animation of M113A1 APC traversing 6" half round obstacle.

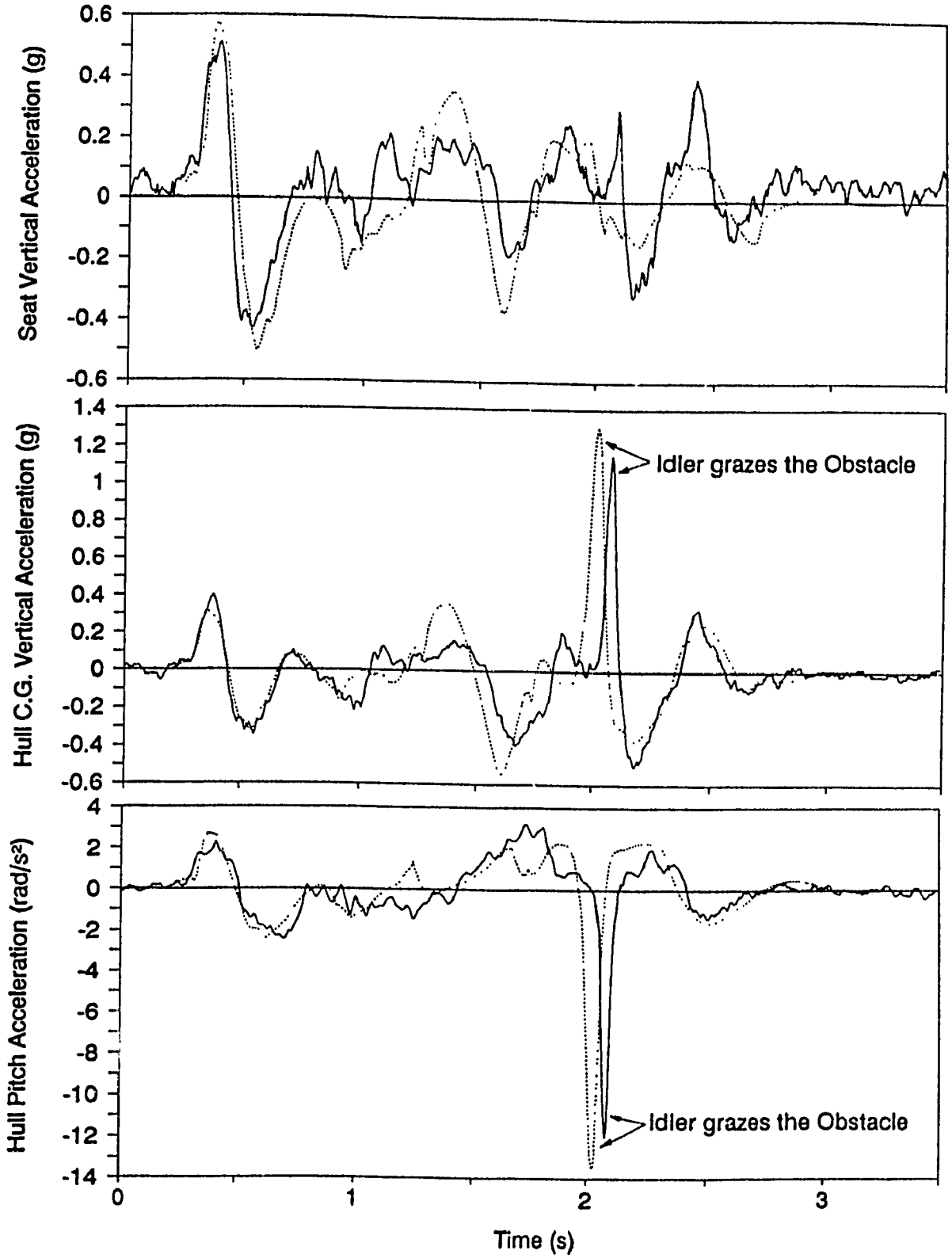

Figure 4.21 Ride acceleration traces - field validation of MODEL II's predictions for test vehicle configuration B traversing 8" obstacle at 7.8 km/h (——— Field Test, ... Simulation).

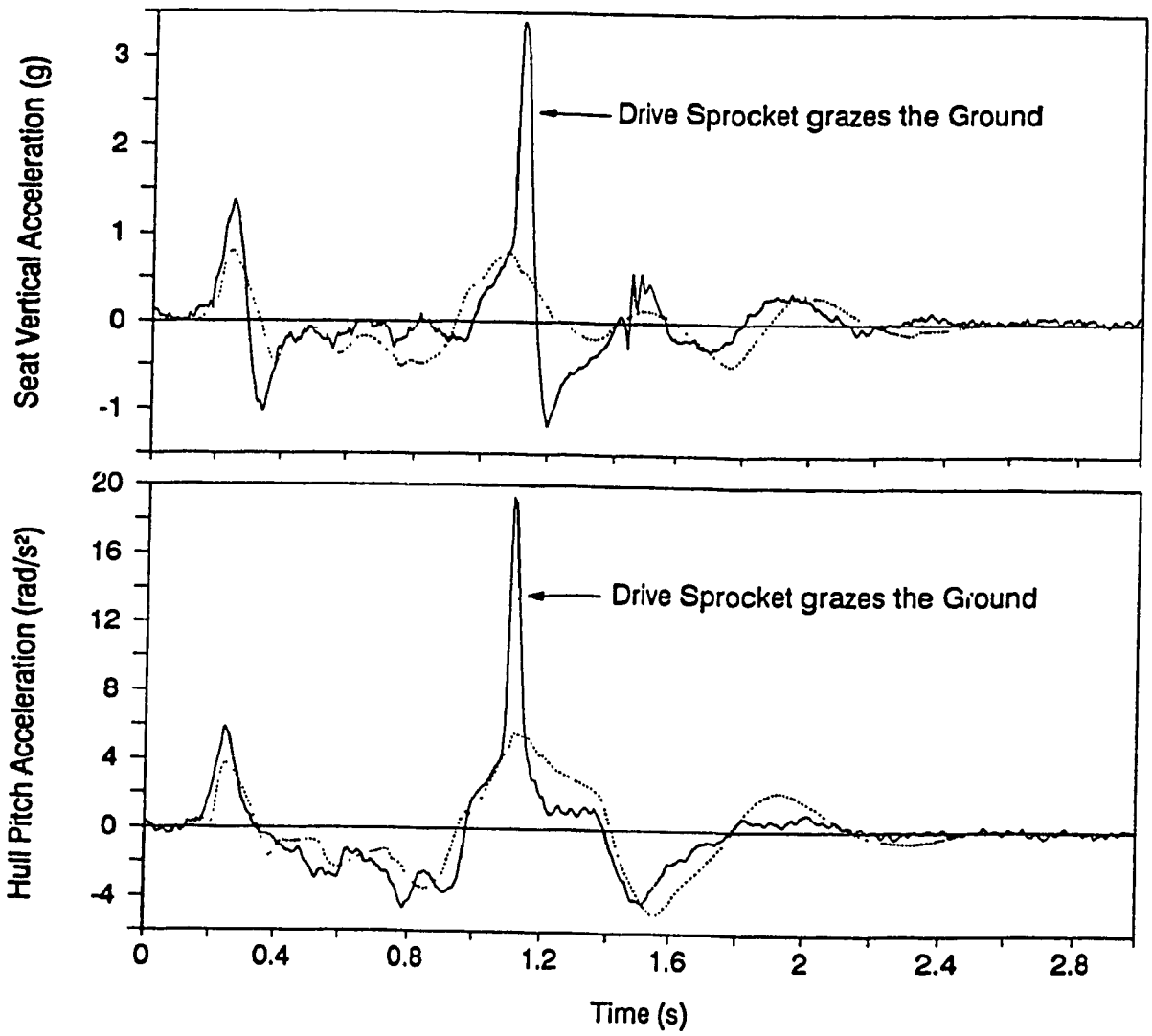

Figure 4.22 Ride acceleration traces - field validation of MODEL II's predictions for test vehicle configuration B traversing 8" obstacle at 12.8 km/h (——— Field Test, ... Simulation).

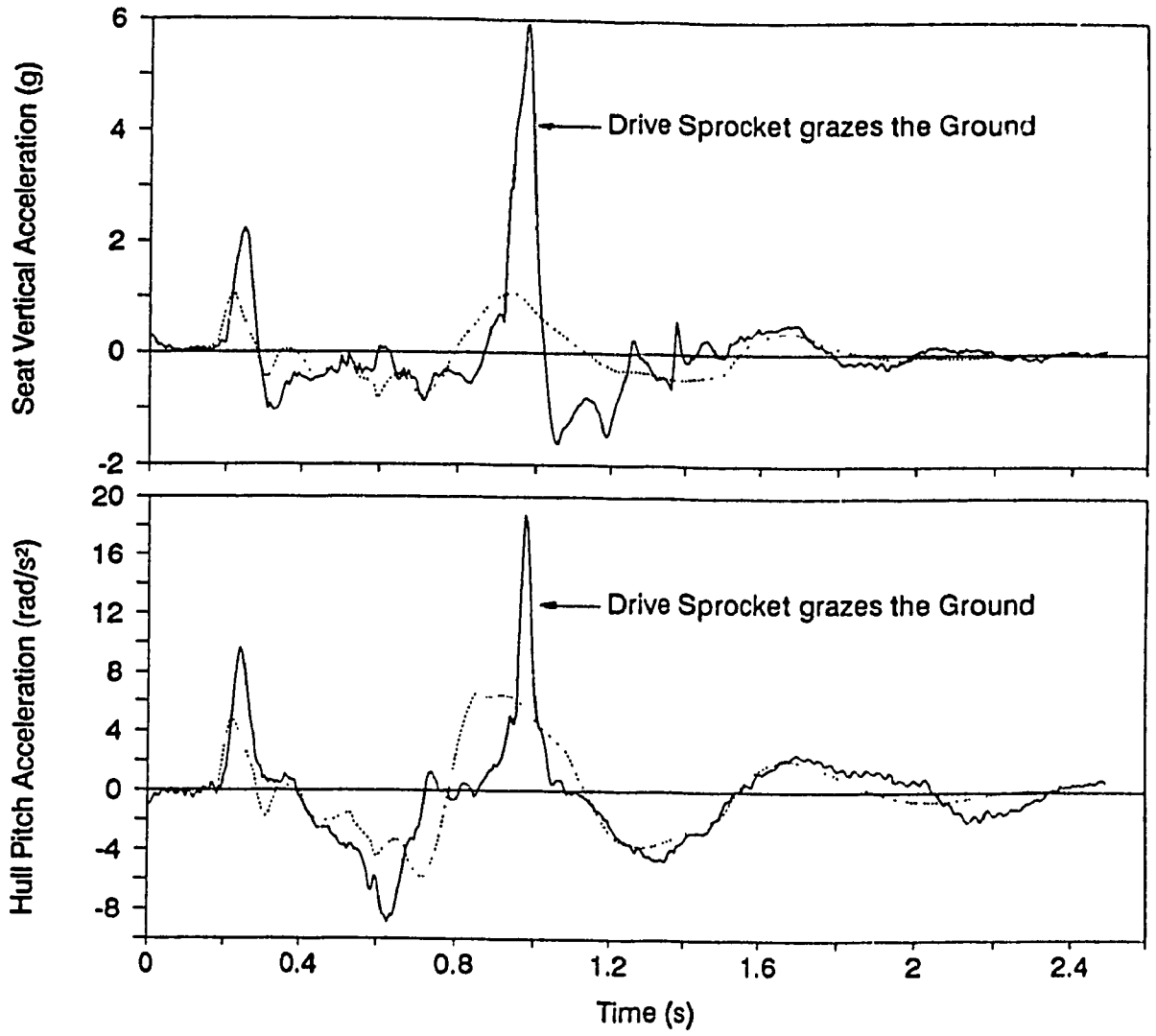

Figure 4.23 Ride acceleration traces - field validation of MODEL II's predictions for test vehicle configuration B traversing 8" obstacle at 18.9 km/h (——— Field Test, ... Simulation).

after the vehicle has crossed the obstacle. First peak in the simulated trace is relatively lower, because the severity of front road wheel-obstacle interaction was reduced due to the front track feeler-obstacle interaction, which simply caused an increase in the net vertical dynamic track load (T^1_{wy}), and lifted and carried the road wheel over the obstacle. The second predicted peak is due to the vehicle impact on the ground prior to its settlement, and does not indicate sprocket-ground contact.

Sinusoidal Course

In this section, the ride dynamic response of the test vehicle configurations A and B subjected to a sinusoidal excitation, is evaluated and compared against field measurements. The excitation frequency based on the selected vehicle speed (V_x = 6.7 km/h) and the wavelength (λ = 0.76 m) is approximately 2.4 Hz. Figures 4.24 and 4.25 show samples of measured and simulated acceleration traces for vehicle configurations A and B, respectively. The comparison between measured and predicted acceleration traces obtained using vehicle configuration B (unladen) is relatively better, since the mass/inertia and dimensional parameters for vehicle configuration A (laden) were only roughly estimated, as explained in section 3.6.1.

LETE48 *Random Course*

The ride acceleration spectra for all four test vehicle configurations (A, B, C, and D) traversing the LETE48 random course at 13.5 km/h, are evaluated and superimposed on the corresponding measured spectra. As shown in Figures 4.26 to 4.29, the predicted response spectra exhibit good correlation with the field measured spectra in terms of

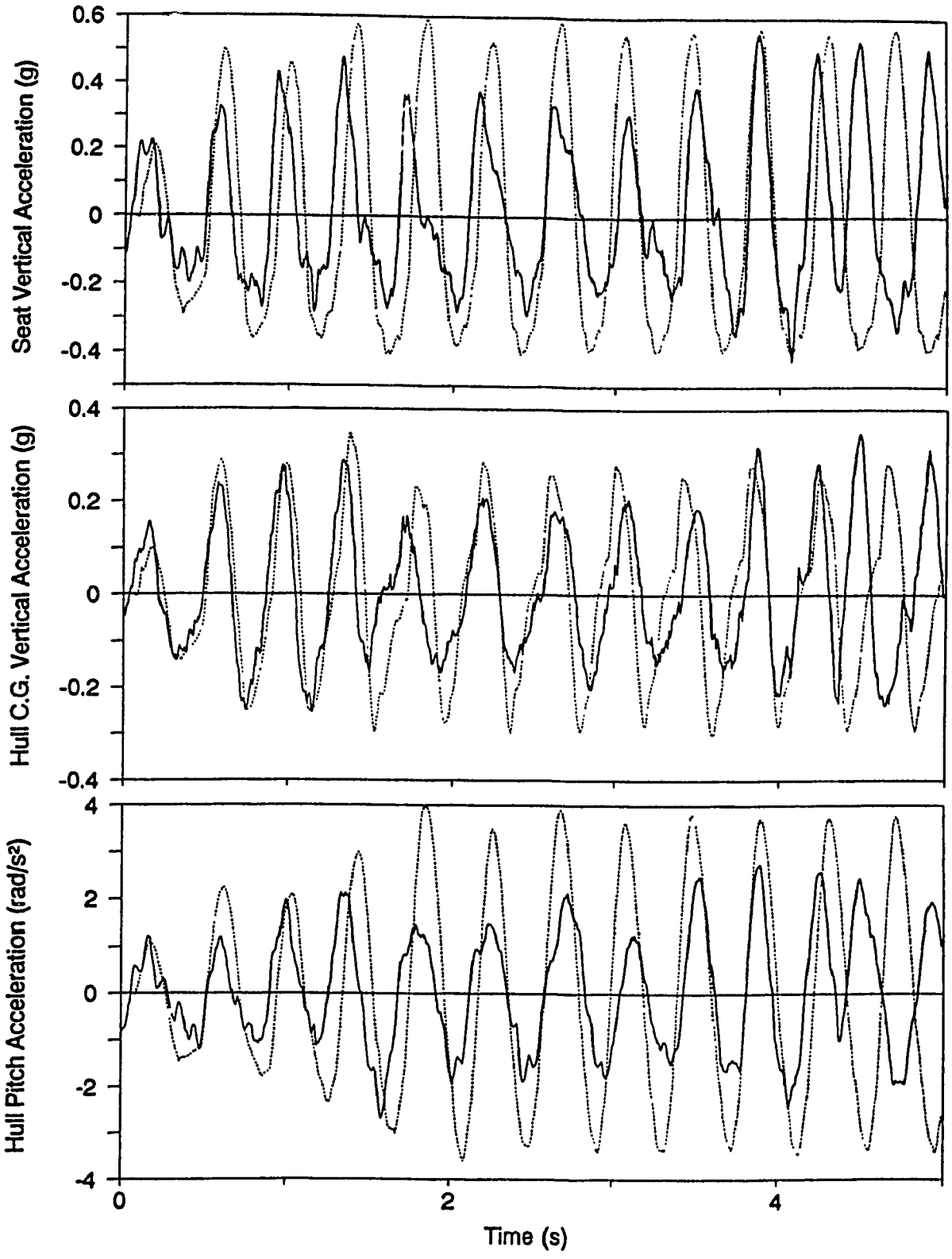

Figure 4.24 Ride acceleration traces - field validation of MODEL II's predictions for test vehicle configuration A traversing sine course at 6.7 km/h (——— Field Test, ... Simulation).

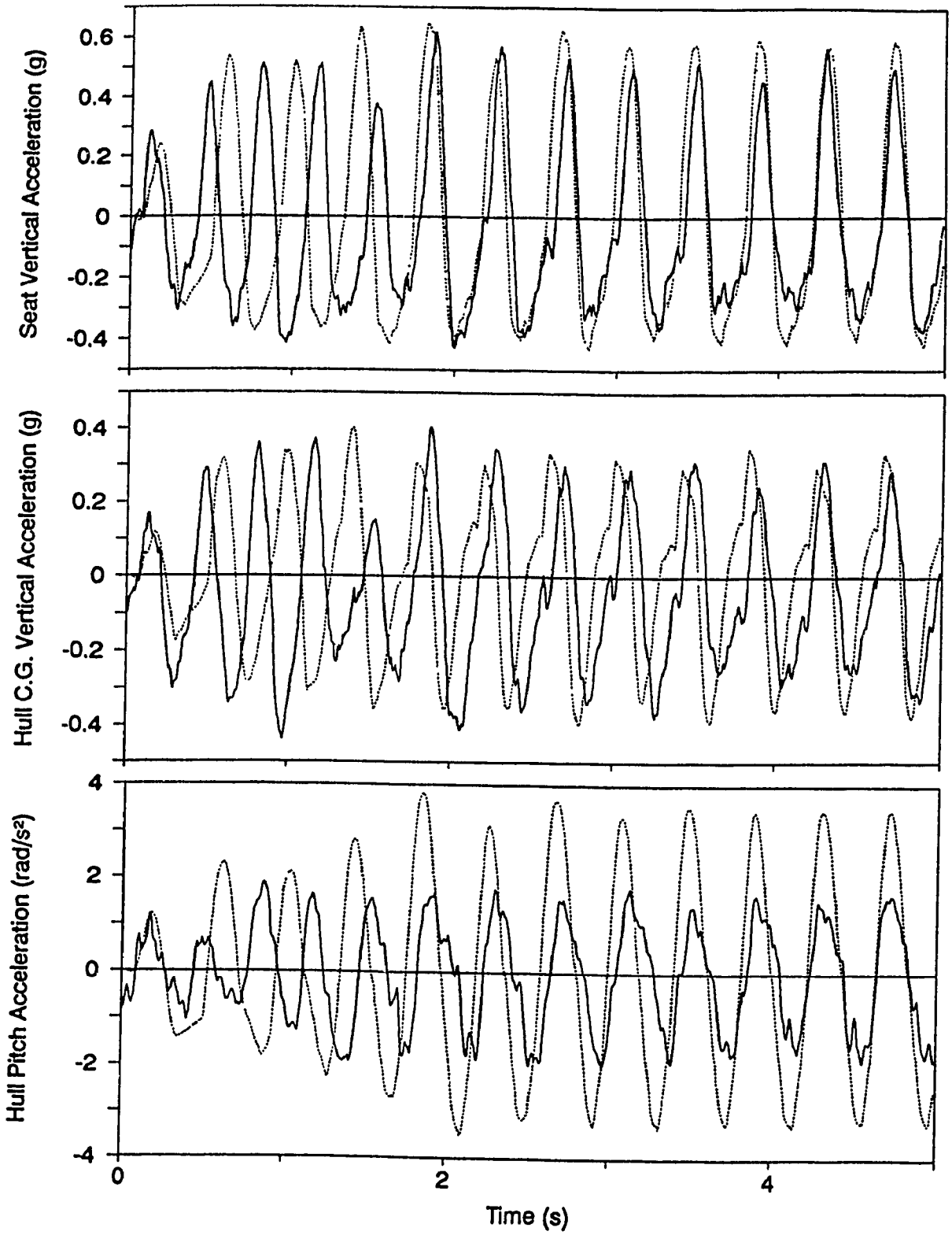

Figure 4.25 Ride acceleration traces - field validation of MODEL II's predictions for test vehicle configuration B traversing sine course at 6.7 km/h (——— Field Test, ... Simulation).

overall response characteristics such as dominant peaks and corresponding frequencies. For all cases, the measured and predicted bounce ride vibration levels at the driver-seat interface are observed to be within the ISO specified 1 h exposure FDP limit. Table 4.1 lists the measured and predicted values of average absorbed power, and rms pitch acceleration.

Belgian Pavé

Figures 4.30 and 4.31 presents the comparison of measured and predicted ride acceleration spectra of the test vehicle configurations A and B traversing Belgian pavé at 35 km/h, respectively. Table 4.2 lists the measured and predicted values of average absorbed power and rms pitch acceleration.

4.4 ASSESSMENT OF WHEEL AND TRACK MODELS

In this study, the wheel-track-terrain interactions are represented based on the two wheel and track models of varying complexities (MODEL I and MODEL II). In previous ride dynamic studies reported in the literature, wheel and track have been modeled using various other modeling strategies. However, no study has attempted to compare these models such that the relative performance of wheeled/tracked vehicle ride models can be assessed in view of analytical complexity (cost) and simulation realism (in reference with field-measured ride data). In this section, different wheel and track models available in the literature are used in conjunction with MODEL II to carry out ride simulation of the field-tested vehicle, and corresponding ride predictions are validated against field measurements. Primary objectives of this exercise are twofold:

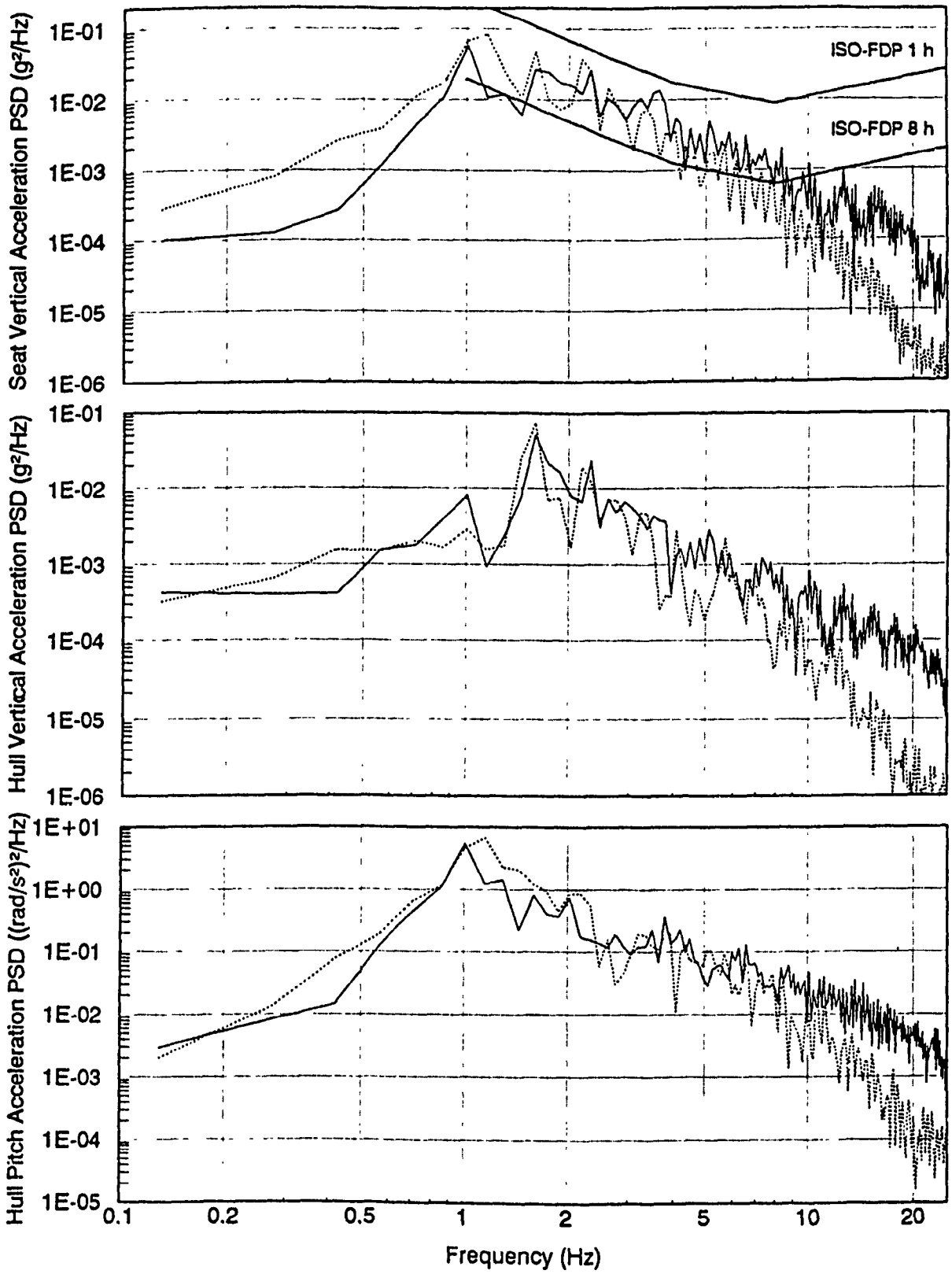

Figure 4.26 Ride acceleration spectra - field validation of MODEL II's predictions for test vehicle configuration A traversing LETE48 random course at 13.5 km/h(——— Field Test, ····· Simulation).

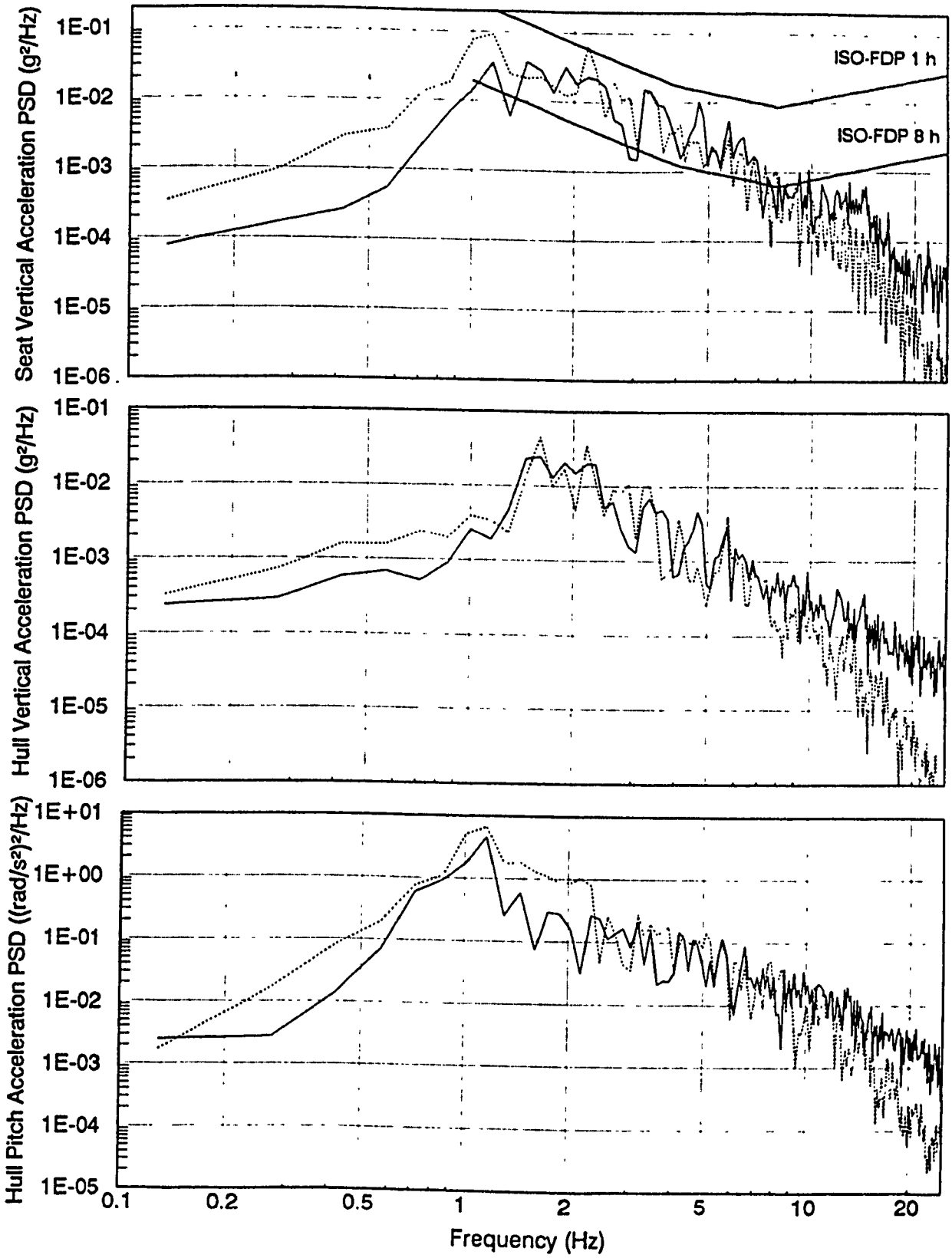

Figure 4.27 Ride acceleration spectra - field validation of MODEL II's predictions for test vehicle configuration B traversing LETE48 random course at 13.5 km/h(——— Field Test, ... Simulation).

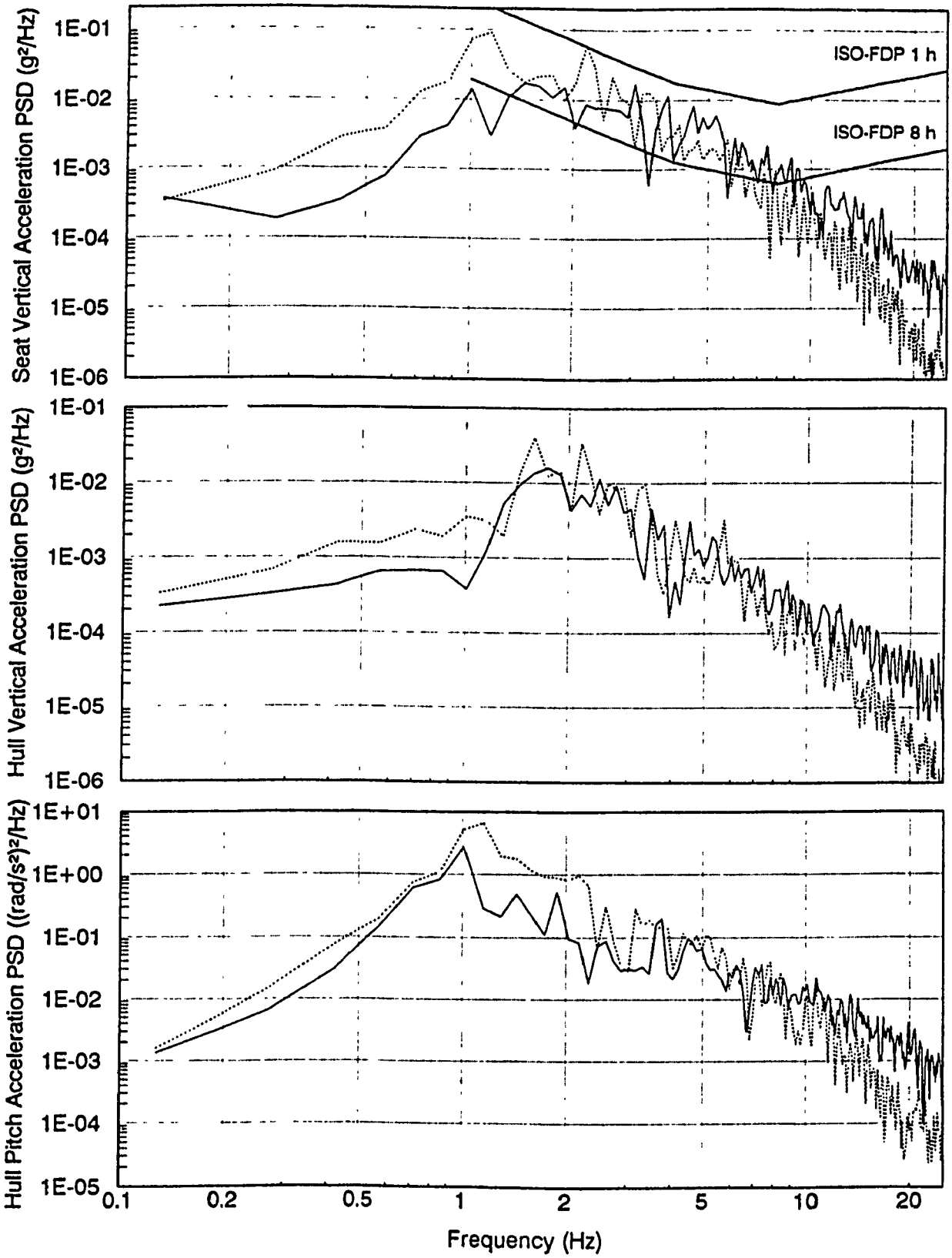

Figure 4.28 Ride acceleration spectra - field validation of MODEL II's predictions for test vehicle configuration C traversing LETE48 random course at 13.5 km/h(——— Field Test, ... Simulation).

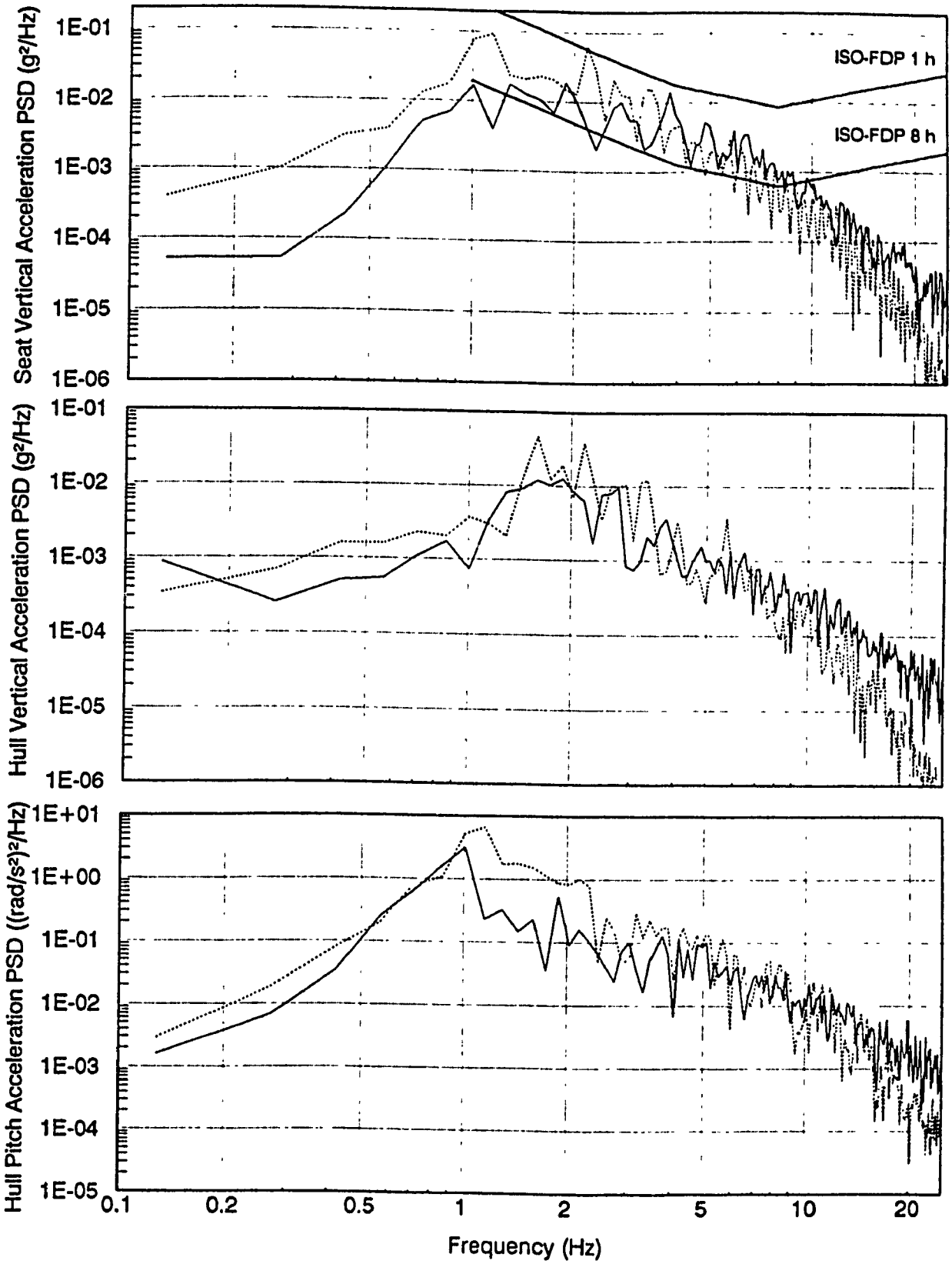

Figure 4.29 Ride acceleration spectra - field validation of MODEL II's predictions for test vehicle configuration D traversing LETE48 random course at 13.5 km/h(——— Field Test, ... Simulation).

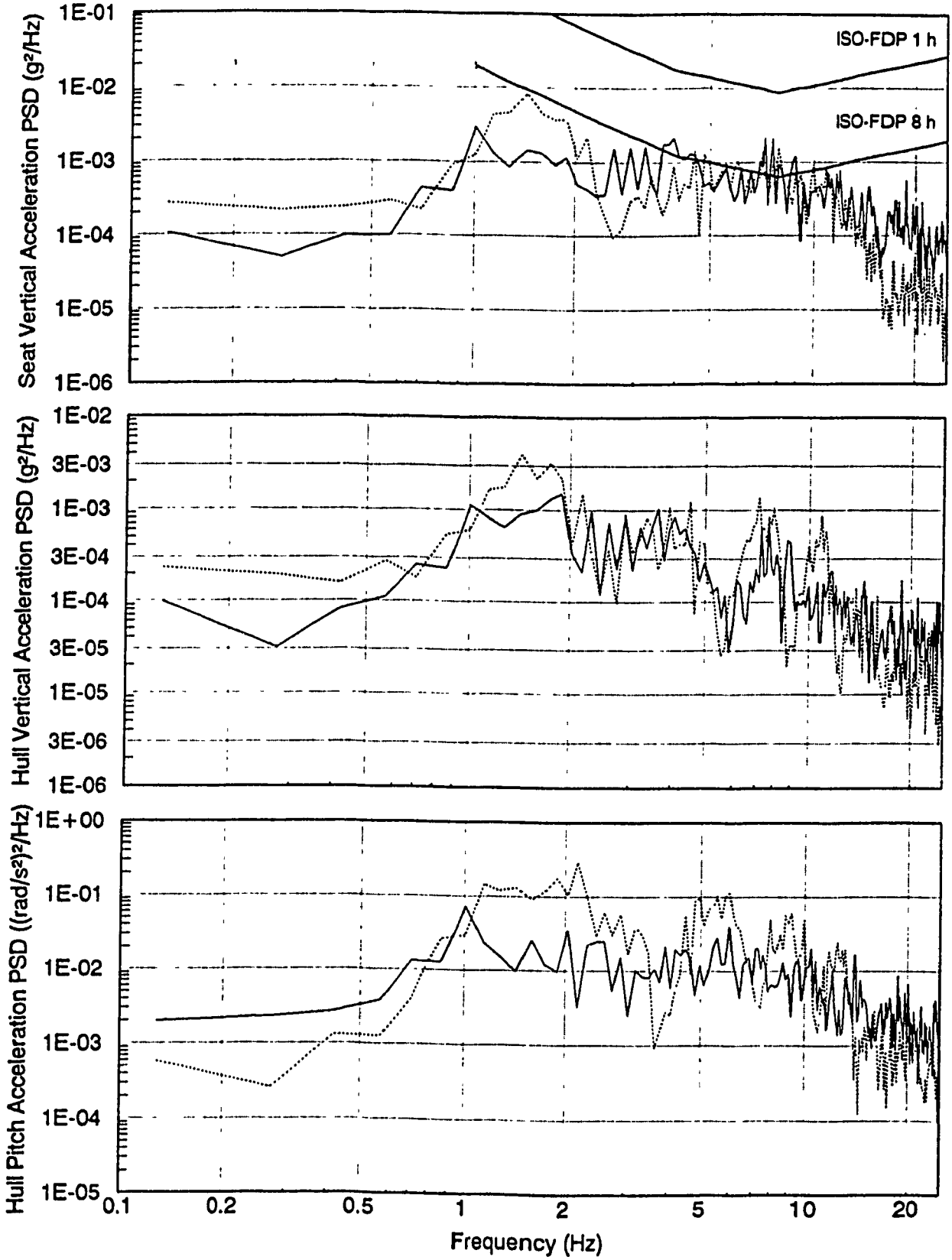

Figure 4.30 Ride acceleration spectra - field validation of MODEL II's predictions for test vehicle configuration A traversing Belgian pavé at 35 km/h (——— Field Test, ····· Simulation).

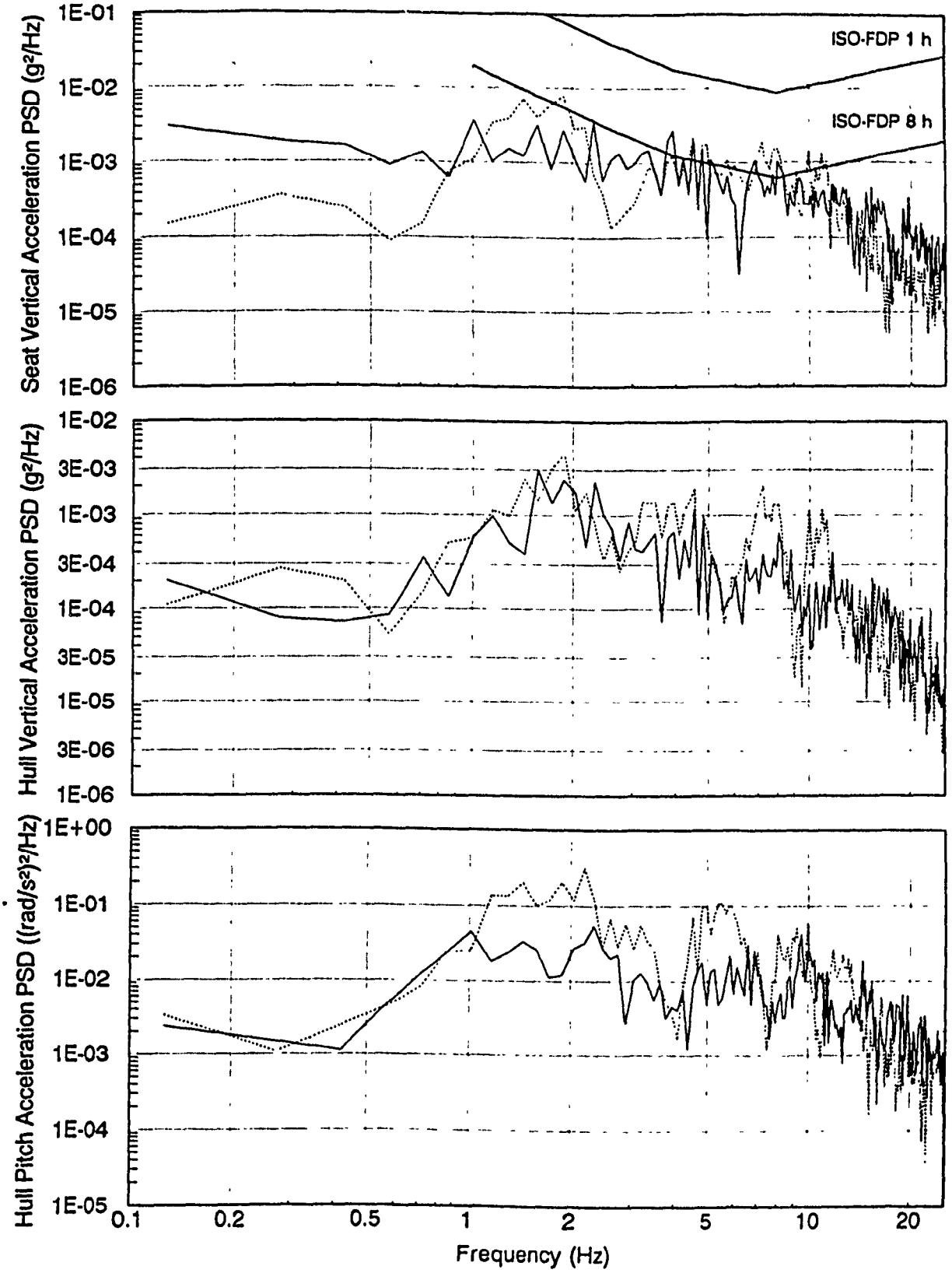

Figure 4.31 Ride acceleration spectra - field validation of MODEL II's predictions for test vehicle configuration B traversing Belgian pavé at 35 km/h (——— Field Test, ... Simulation).

Table 4.1 Field validation of MODEL II (LETE48 course; speed=13.5 km/h).

Vehicle Configuration	Absorbed power (watts)/rms acceleration (rad/s^2)	
	Field Test	Simulation
A	4.5/1.61	3.1/2.16
B	4.4/1.65	4.3/2.19
C	3.7/1.30	3.9/2.16
D	3.5/1.29	4.4/2.22

Table 4.2 Field validation of MODEL II (Belgian pavé; speed = 35 km/h).

Vehicle Configuration	Absorbed power (watts)/rms acceleration (rad/s^2)	
	Field Test	Simulation
A	0.940/0.492	0.763/0.729
B	0.921/0.526	1.070/0.770

(a) to assess the relative performance of proposed wheel and track models, and

(b) to demonstrate the influence of individual wheel and track models on the ride predictions.

4.4.1 Comparison of Wheel Models

In the current research program, the wheel/track-terrain interaction has been modeled using two analytical representations:

- *idealized continuous spring model* (employed in MODEL I), and
- *adaptive continuous spring model* (employed in MODEL II).

Both wheel models are conceived based on the concept of a continuous ring of springs radially distributed over the wheel-terrain foot-print, and an equivalent damper. The *idealized* wheel model assumes the wheel deflection averaged by a straight line adjoining the first and last wheel-terrain contact points, while ignoring the terrain irregularities or slope-changes within the foot-print. The *adaptive* wheel model is an enhanced version of the *idealized* representation, where terrain irregularities, *if found within the foot-print*, are accounted for through the deformations.

In previous studies, the wheel for dynamic simulation purposes has been modeled using four basic analytical models:

- *point contact*,
- *rigid tread band*,
- *fixed foot-print*, and
- *adaptive foot-print*.

Captain *et al.* [30] compared these wheel models based on the ride dynamic study of an off-road wheeled vehicle (cargo truck) traversing rough, rigid terrain undulations. All four wheel models are formulated and employed for performing ride simulation of the field-tested tracked

vehicle in conjunction with MODEL II, and corresponding ride predictions are compared with field measurements. The wheel models are described in detail in Appendix I.1. The spring and damping parameters for all wheel models (including proposed ones) are listed in Table 4.3. As discussed earlier (section 3.6.1 and appendix I.1), the spring constants are computed based on the wheel-terrain contact patch formed on a flat surface for specified static vertical load (P) and corresponding deflection of wheel centre (Δ_w). The static load, P, for Δ_w = 0.0254 m is taken as 15568 N for road wheels, and 25400 N for hull wheels [38]. The segmentation angle, φ (only for rigid tread band, fixed foot-print, adaptive foot-print, and adaptive continuous spring models) is taken as 2 degrees. The contact patch length, L (only for fixed foot-print model) is considered equal to the wheel radius. Discussions on the results are presented as follows.

The undamped natural frequencies and associated dominant deflection modes for the test vehicle configuration B, predicted based on the converged stiffness matrix (section 2.6) in conjunction with specified wheel models, are listed in Table 4.4. The natural frequencies obtained in conjunction with point contact, rigid tread band, and fixed foot-print models are slightly higher, whereas adaptive foot-print and continuous spring models yield the similar values.

The ride acceleration traces for the vehicle configuration B traversing 6" obstacle at 14.3 km/h, are evaluated in conjunction with the specified wheel models. Figure 4.32 shows the direct comparison between predicted and measured traces. The ride response evaluated using point contact model, is found to be significantly higher than those of the other models, and shows poor correlation with the measured ride data.

Table 4.3 Spring and damping constants for wheel models.

Wheel Model Type	Road Wheel/Track (i = 1,..,5)	Sprocket/Track	Idler/Track
Point Contact and Rigid Tread Band	K^1_{rw} = 612 913 N/m C^1_{rw} = 5000 N.s/m	K^1_{hw} = 1 x 10^6 N/m C^1_{hw} = 5000 N.s/m	K^2_{hw} = 1 x 10^6 N/m C^2_{hw} = 5000 N.s/m
Fixed Foot-Print	k^1_{rw} = 46 673 N/m c^1_{rw} = 161 N.s/m	k^1_{hw} = 59 860 N/m c^1_{hw} = 161 N.s/m	k^2_{hw} = 55 644 N/m k^2_{hw} = 161 N.s/m
Adaptive Foot-Print	k^1_{rw} = 38 469 N/m c^1_{rw} = 223 N.s/m	k^1_{hw} = 55 834 N/m c^1_{hw} = 192 N.s/m	k^2_{hw} = 53 167 N/m c^2_{hw} = 192 N.s/m
Continuous Spring (Idealized and Adaptive)	K^1_{rw} = 1 121 256 N/m/rad C^1_{rw} = 5000 N.s/m	K^1_{hw} = 1 634 508 N/m/rad C^1_{hw} = 5000 N.s/m	K^2_{hw} = 1 559 657 N/m/rad C^2_{hw} = 5000 N.s/m

Table 4.4 Predicted natural frequencies for test vehicle configuration B in view of wheel models.

Dominant Deflection Mode	Undamped Natural Frequency [Hz]			
	Point Contact & Rigid Tread Band	Fixed Foot-Print	Adaptive Foot-Print	Continuous Spring
y_h	1.885	1.866	1.842	1.843
θ_h	1.343	1.324	1.307	1.307
y_{w1}	12.82	11.89	11.32	11.34
y_{w2}	12.87	12.59	11.95	11.97
y_{w3}	12.85	12.54	11.91	11.93
y_{w4}	12.84	12.50	11.88	11.89
y_{w5}	12.83	11.94	11.37	11.39

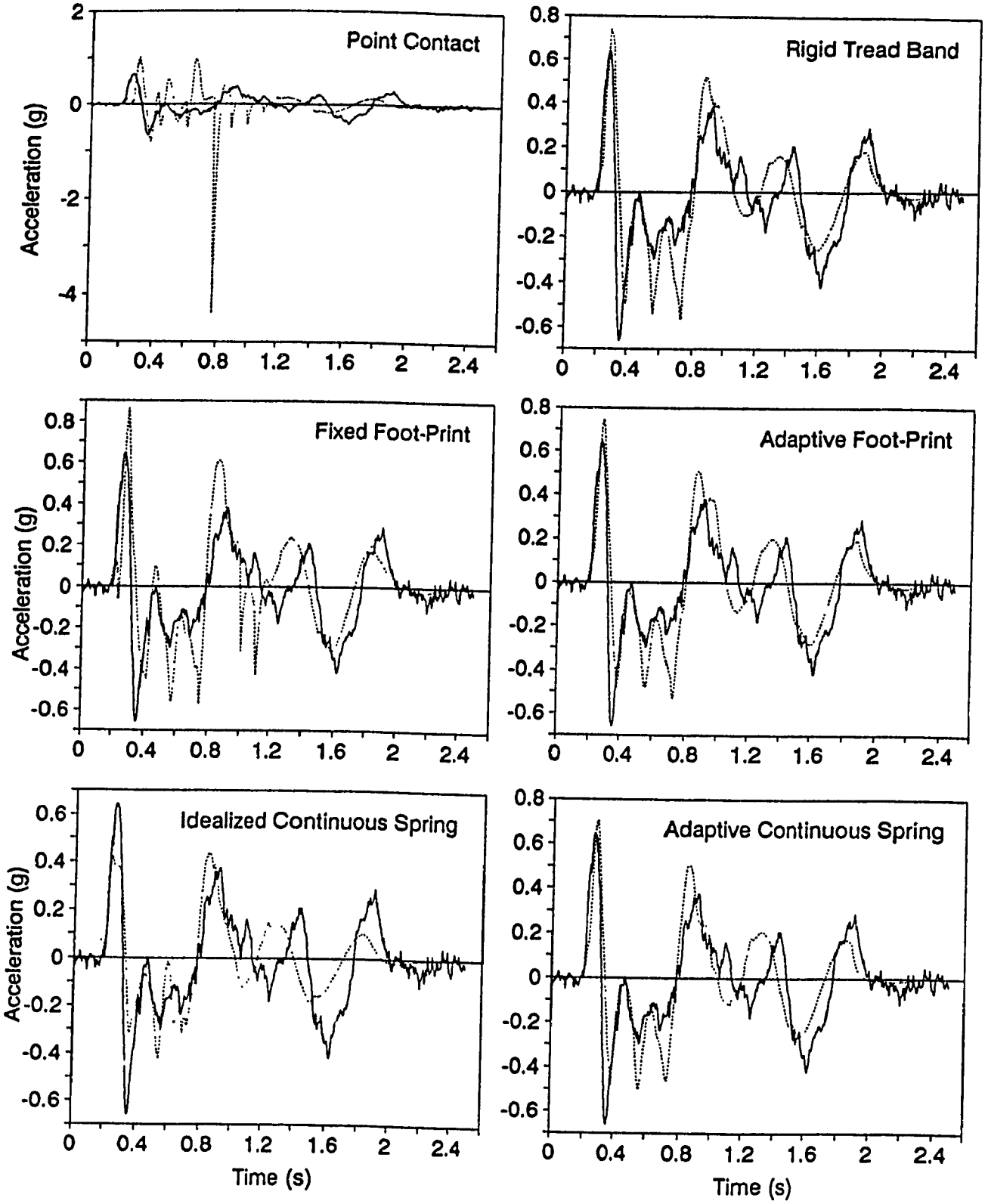

Figure 4.32 Comparison of wheel models - ride acceleration traces for test vehicle configuration B crossing 6" obstacle at 14.3 km/h (——— Field Test, ... Simulation).

On the other hand, the response obtained in conjunction with idealized continuous spring model shows softer ride due to the under-estimation of obstacle profile (as explained in section 3.7). The ride acceleration traces obtained using rigid tread band, adaptive foot-print, and adaptive continuous spring models, are very similar, whereas fixed foot-print model yields slightly higher ride acceleration levels. The comparison between measured and predicted vertical acceleration levels in terms of absolute peak value found in the acceleration time history, and its rms value, is summarized in Table 4.5, along with the respective percentage errors, and seconds of computer run time consumed with different wheel models for total simulation time of 2.5 s. In comparison, the adaptive continuous spring model predictions show the best correlation with the measured values. In terms of run time, the proposed model is almost as fast as a point contact model for the discrete obstacle-crossing analysis.

The performances of wheel models are evaluated based on the comparison of traces associated with wheel centre coordinate, net foot-print force, and overall track tension. The trace of the centre coordinate of the first road wheel in reference with the obstacle profile, is shown in Figure 4.33. Unlike point contact model, the traces of remaining wheel models exhibit similar trend, where the profile filtering effects are pronounced. It should be noted that the filter characteristics in the simulation of tracked vehicles not only depend on the wheel model, but is also dictated by the track effects. The traces shown in Figure 4.33, indicate the track influence, where the front road wheel, once crosses over the obstacle (after the first peak), is primarily supported by the adjacent inclined track feeler (track bridging

Table 4.5 Assessment of wheel models (6" obstacle, V_x=14.3 km/h, t_{max}=2.5 s).

	peak value (g)/rms value (g)	% error	run time† (s)
Field Test	0.660/0.197	—	—
Point Contact	4.39/0.374	565/89.8	281
Rigid Tread Band	0.740/0.219	12.1/11.2	470
Fixed Foot-Print	0.864/0.227	30.9/15.2	470
Adaptive Foot-Print	0.746/0.217	13.0/10.1	541
Idealized Continuous Spring	0.439/0.157	33.5/20.3	273
Adaptive Continuous Spring	0.704/0.201	6.7/2.0	293

(† computer run time on a MicroVAX)

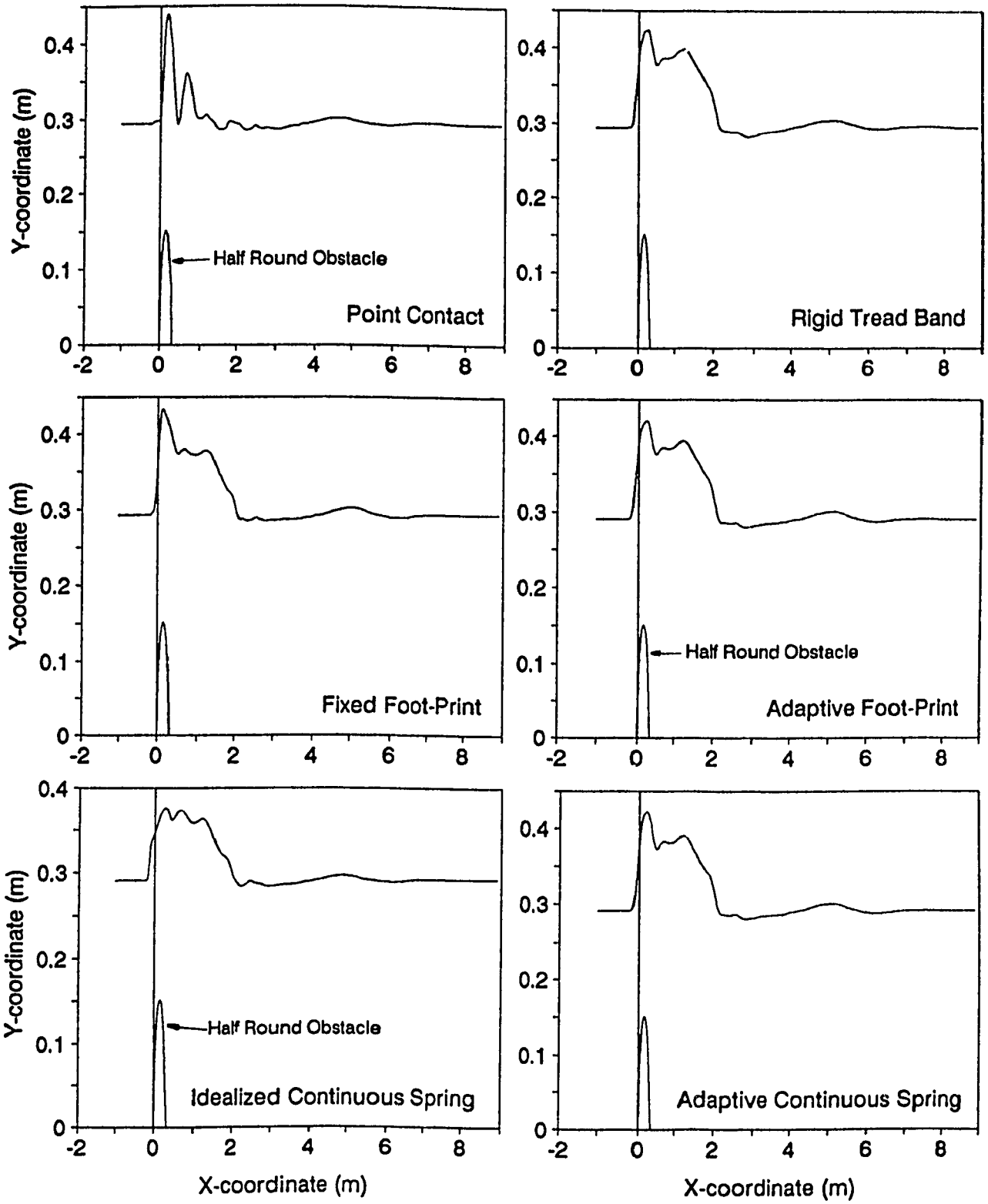

Figure 4.33 Comparison of wheel models - traces of first road wheel centre for vehicle configuration B crossing 6" obstacle at 14.3 km/h.

or catching effects). Figure 4.34 shows the traces of the second road wheel centre determined with different wheel models. In comparison with front road wheel, the second road wheel has lesser track support as it is evident from the comparison of respective traces. Figures 4.35 and 4.36 show the time histories of horizontal and vertical components of net foot-print force for first and second road wheels, respectively. As expected, the response of the point contact wheel is found to be significantly higher than that of the other models. The magnitude of the horizontal component is significantly high for point contact and fixed foot-print models. The force trace obtained in conjunction with the rigid tread band exhibits high frequency fluctuations, caused by the failure to satisfy the slope condition within the specified tolerance (equation I.4). Figure 4.37 compares the overall track tension traces (equation 4.21), where the peak magnitudes are significantly higher when evaluated using the point contact model.

The wheel models are further used to carry out ride simulations for the test vehicle configuration B subjected to other test courses. Figure 4.38 shows the traces of measured and predicted vertical ride acceleration for the vehicle traversing the sine course at 6.7 km/h. Table 4.6 summarizes the comparison in terms of the rms value of acceleration traces, and the computer run time. The performance of the idealized continuous spring model in terms of the ride prediction accuracy and the run time, is better in comparison with the other models.

Figure 4.39 and Table 4.7 compares the wheel models based on the ride performance of the test vehicle configuration B traversing LETE48 random course at 13.5 km/h. The predicted vertical ride acceleration spectra, as shown in Figure 4.39, are almost identical. Based on the corresponding

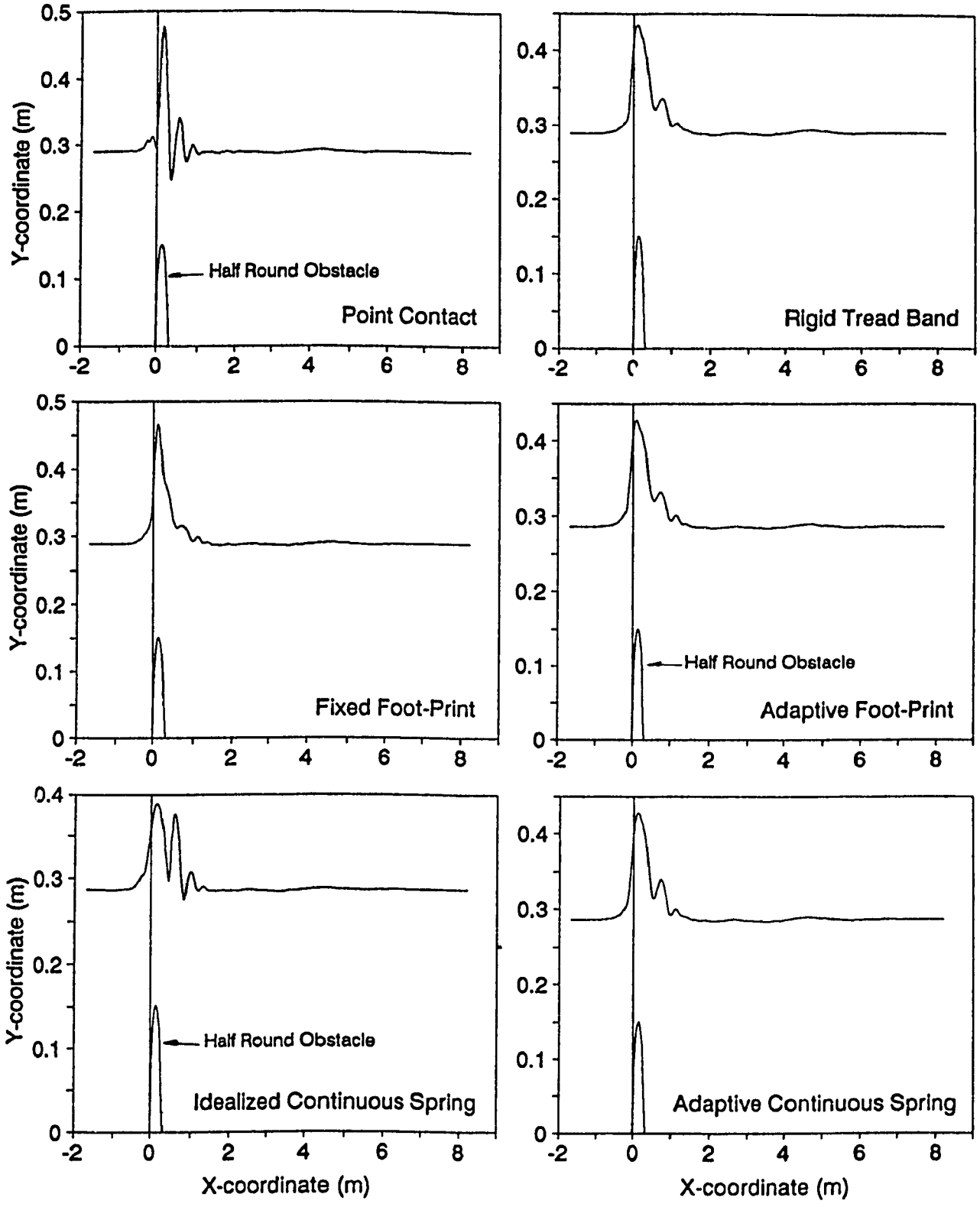

Figure 4.34 Comparison of wheel models - traces of second road wheel centre for vehicle configuration B crossing 6" obstacle at 14.3 km/h.

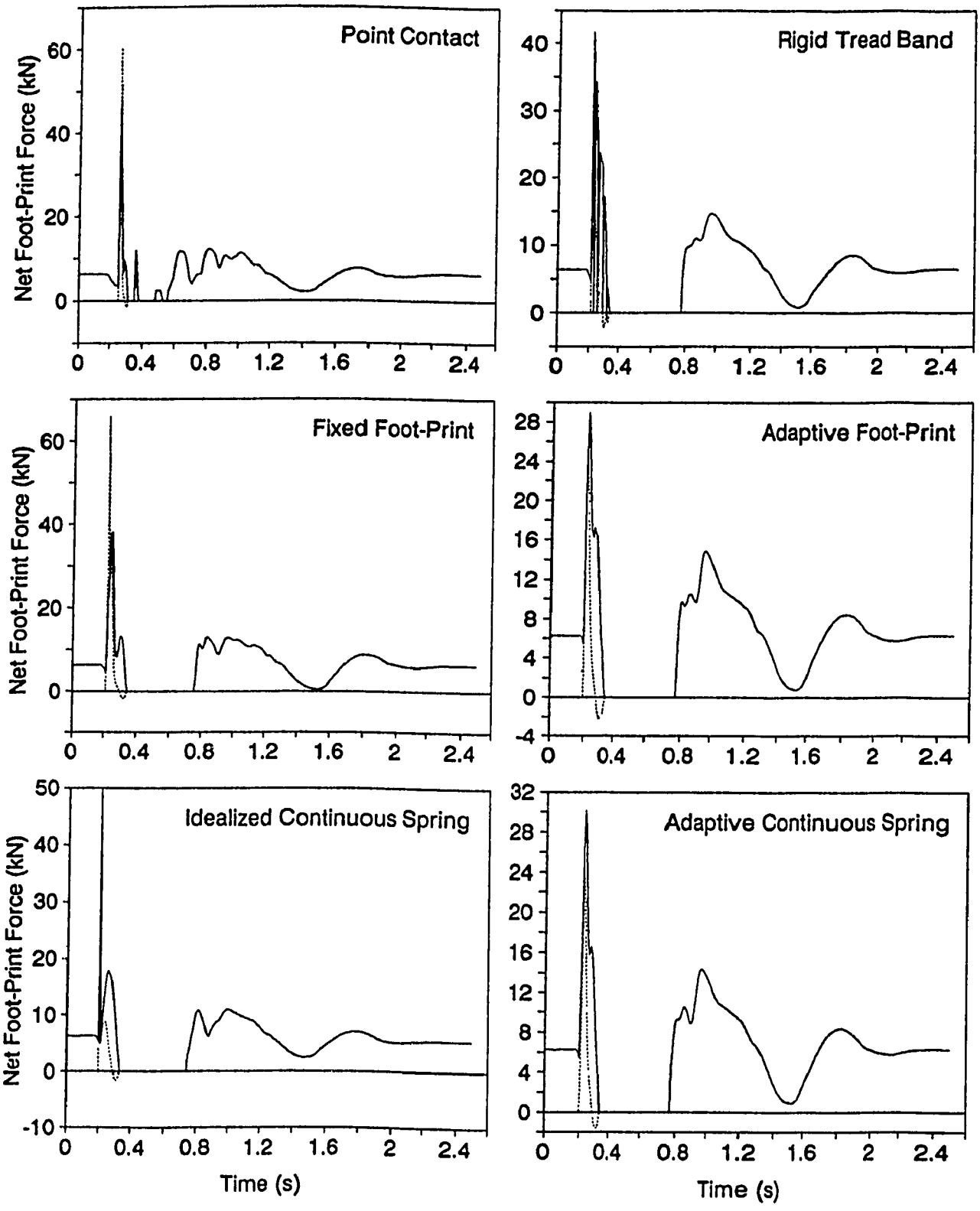

Figure 4.35 Comparison of wheel models - traces of net foot-print force for first road wheel for vehicle configuration B crossing 6" obstacle at 14.3 km/h (——— X-component, ——— Y-component).

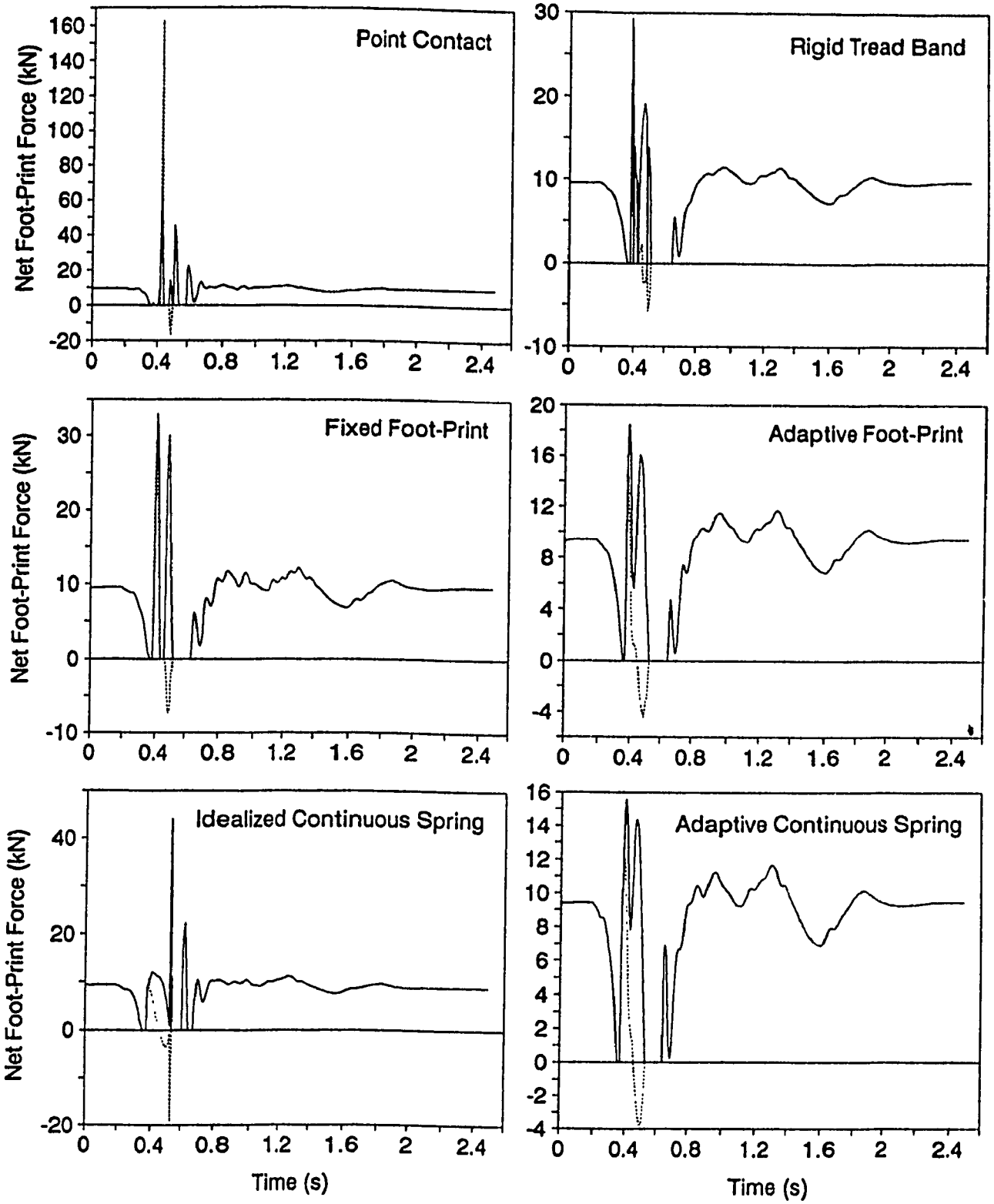

Figure 4.36 Comparison of wheel models - traces of net foot-print force for second road wheel for vehicle configuration B crossing 6" obstacle at 14.3 km/h (——— X-component, ——— Y-component).

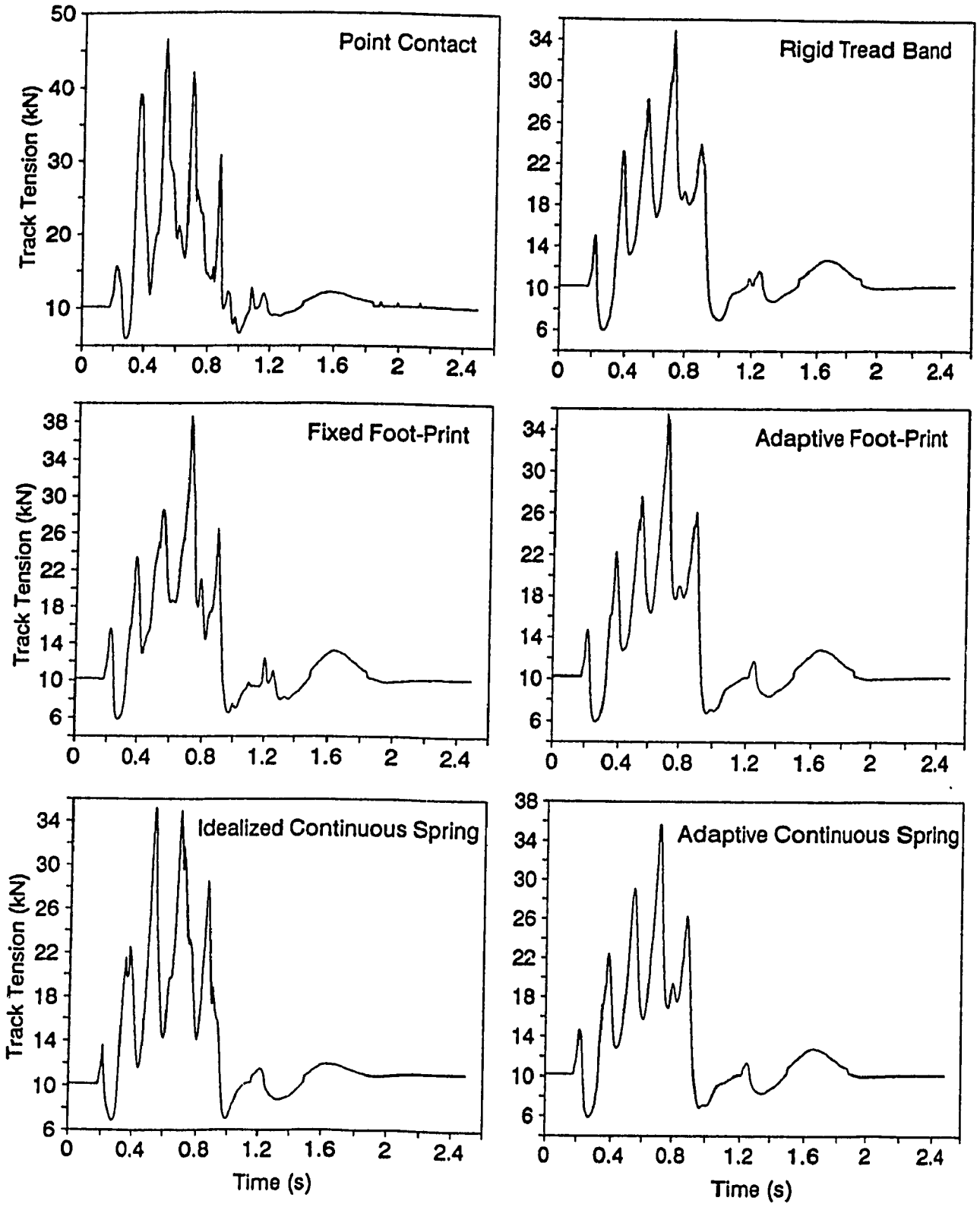

Figure 4.37 Comparison of wheel models - traces of overall track tension for vehicle configuration B crossing 6" obstacle at 14.3 km/h.

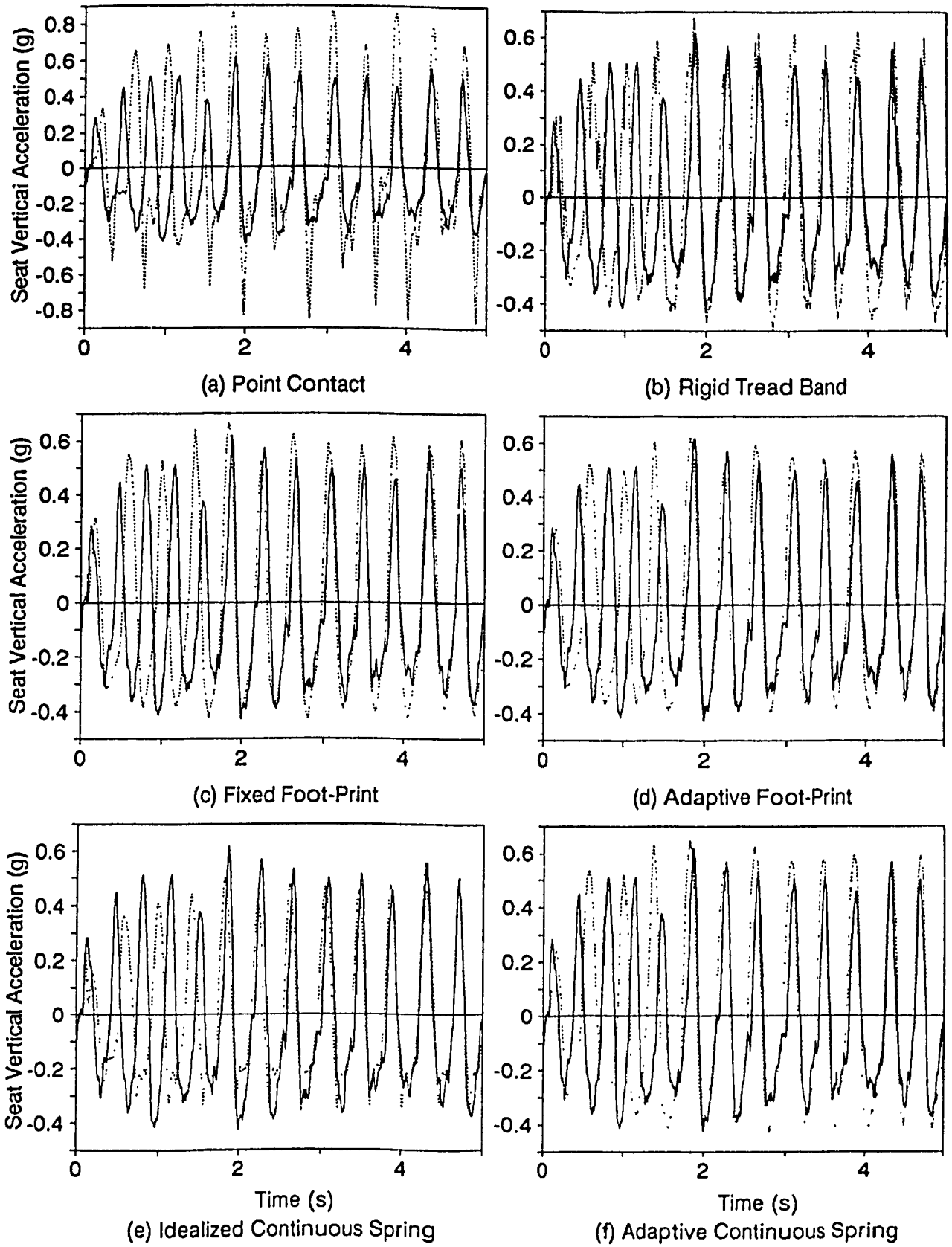

Figure 4.38 Comparison of wheel models - ride acceleration traces for test vehicle configuration B traversing sine course at 6.7 km/h (——— Field Test, ····· Simulation).

Table 4.6 Assessment of wheel models (Sine Course, V_x=6.7 km/h, t_{max}=5 s).

	rms value (g)	% error	run time (s)
Field Test	0.278	—	—
Point Contact	0.408	46.7	725
Rigid Tread Band	0.330	18.7	1126
Fixed Foot-Print	0.336	20.9	1125
Adaptive Foot-Print	0.321	15.5	1256
Idealized Continuous Spring	0.245	11.8	709
Adaptive Continuous Spring	0.325	16.9	1260

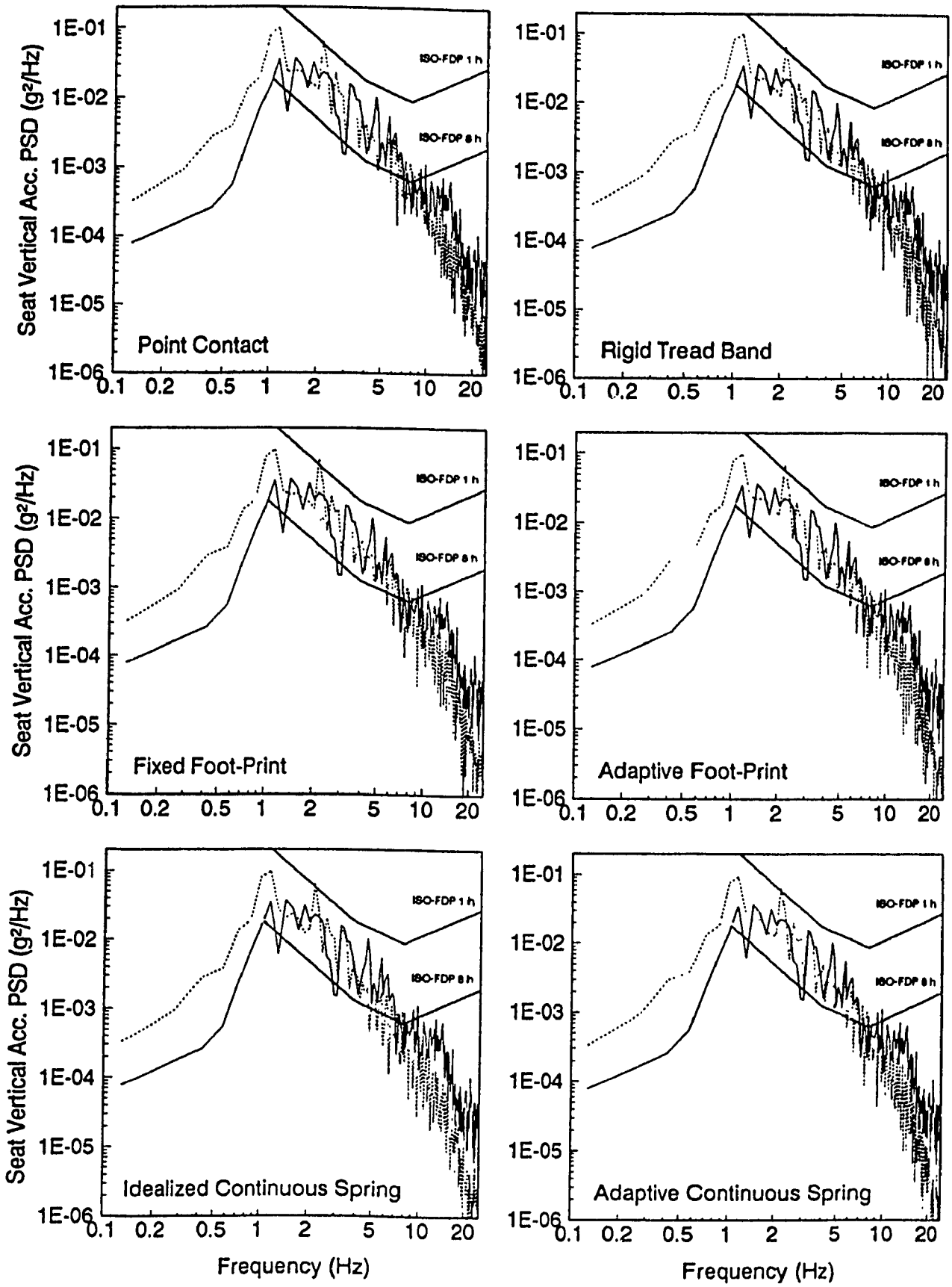

Figure 4.39 Comparison of wheel models - ride acceleration spectra for test vehicle configuration B traversing LETE48 course at 13.5 km/h (——— Field Test, ... Simulation).

Table 4.7 Assessment of wheel models (LETE48 Course, V_x=13.5 km/h, t_{max}=20 s)

	Abs. Power (W)	% error	run time (s)
Field Test	4.36	—	—
Point Contact	4.38	0.46	2806
Rigid Tread Band	4.38	0.46	6784
Fixed Foot-Print	4.60	5.50	6892
Adaptive Foot-Print	4.39	0.69	7689
Idealized Continuous Spring	3.90	10.5	2617
Adaptive Continuous Spring	4.33	0.69	6188

absorbed power values (watts) listed in Table 4.7, the idealized continuous spring model exhibits relatively less agreement, but, requires the least run time seconds. The point contact model's predictions are as good as those of the other high resolution models, because the specified random course is a gradually varying course (i.e. the spacing between successive profile points is equal to the road wheel radius), and thus the profile filtering effects are negligible unlike those for discrete half round obstacles, and sine course. The ride response predictions evaluated based on the simulation of the test vehicle traversing Belgian pavé at 35 km/h, showed similar trend.

Based on this comparative study, following observations are made:

(a) The proposed *idealized continuous spring* representation of wheel/ track-terrain interaction requires the least computational time in comparison with the other models, and yields ride predictions which exhibit a generally good agreement with the field test data.

(b) The ride predictions evaluated in conjunction with the proposed *adaptive continuous spring model* show an excellent correlation with the field test data. Overall, this model performs very well in comparison with the other wheel models. For instance, for the discrete obstacle-crossing simulation, this proposed model is almost as fast as its simplified version (i.e. the idealized continuous spring model), yet predicts very accurately in comparison with the other models.

(c) The ride response of the test vehicle traversing over discrete obstacle and sine course, is significantly high when evaluated using the point contact wheel model. However, for LETE48 random course and Belgian pavé, where the changes in the profile elevation are gradual,

the point contact model predicts as well as other high resolution wheel models.

(d) The adaptive foot-print model, which is of the highest resolution among the previous models, yields ride predictions similar to those of the proposed adaptive model, but requires excess computational time.

(e) The performance of the rigid tread band model is comparable to that of the adaptive foot-print model, whereas the fixed foot-print model yields slightly higher ride acceleration levels.

4.4.2 Comparison of Track Models

In this study, the dynamic track tensioning effects have been modeled using two track models of varying complexities:

- track model # 1 (employed in MODEL I), and
- track model # 2 (employed in MODEL II).

In track model # 1, dynamic track load imposed at each wheel station is evaluated considering track pre-tension plus tension due to track extensibility, while ignoring the track inextensibility in view of the track sag between sprocket and idler. Track model # 2 is an improved version of the track model # 1, where the track sag is modeled using the quadartic polynomial approximation; the wheel-track connectivity is improved to yield an appropriate definition of track wrap around road wheels and road wheel-track-terrain separation; and the track bridging is enhanced to define appropriate track inclination angles around road wheels. For comparative study presented in this section. track model # 1 is, however, considered to incorporate the improved wheel-track connectivity as discussed for track model # 2.

In previous studies, a number of track models of varying complexities

have been employed for simulation purposes. In particular, a high resolution track model by McCullough *et al.* [34], and a simplified track model employed in VEHDYN II code [38] represent two totally different approaches to account for track effects. McCullough *et al.* [34] employed a catenary-based approach to account for track inextensibility, and proposed an ideal non-dimensional catenary solution for computing track tension in the track segment hanging between sprocket and idler. The track extensibility was accounted for in conjunction with a simple relaxation of the ideal catenary equation. For this study, an additional track model, referred to as track model # 3, is developed based on the proposed track model # 2, but considering the ideal catenary approach for track inextensibility [34], and is described in detail in Appendix I.2. The track model employed in VEHDYN II code [38] is conceived based on hypothetical linear springs interconnecting adjacent wheel pairs, which generate local tensioning effects. This track representation is considered for this study, and referred to as track model # 4 (discussed in Appendix I.2). The values of the track spring constants (only for track model # 4) corresponding to the nominal initial track setting for the field-tested vehicle, are listed in Table 4.8. Table 4.9 lists the undamped natural frequencies and associated modes for the test vehicle configuration B estimated based on the converged stiffness matrix obtained from the iterative stiffness procedure (section 2.6), where the applied force vector given in equation (2.85) is evaluated in conjunction with specified track models. Discussions on the ride predictions and their correlation with field test data, are presented in the following paragraphs.

The ride acceleration traces for the test vehicle configuration B

Table 4.8 Track spring constants for track model # 4 [38].

Track Segment	Spring Constant (N/m)
Front Feeler (k_t^1)	105 071
Between Road Wheels ($k_t^2,..,k_t^5$)	65 670
Rear Feeler (k_t^6)	105 071

Table 4.9 Predicted natural frequencies for test vehicle configuration B in view of track models.

Dominant Deflection Mode	Undamped Natural Frequency [Hz]			
	Track Model # 1	Track Model # 2	Track Model # 3	Track Model # 4
y_h	1.856	1.843	1.841	1.820
θ_h	1.316	1.307	1.306	1.345
y_{w1}	11.34	11.34	11.37	11.97
y_{w2}	12.08	11.97	11.99	11.94
y_{w3}	12.05	11.93	11.95	11.93
y_{w4}	12.01	11.89	11.92	11.95
y_{w5}	11.40	11.39	11.43	11.92

crossing over 6" obstacle at 14.3 km/h, are evaluated using specified track models. As shown in Figure 4.40, the ride acceleration traces obtained in conjunction with first three track models are very similar, and show good correlation with the measured trace. On the other hand, the ride response evaluated using track model # 4 is found to be in poor agreement with the test data. Table 4.10 summarizes the comparison in terms of absolute peak and rms values associated with vertical ride acceleration traces, and computer run time required for simulation. As listed, the predicted values obtained using the proposed track model # 2 show the closest agreement with the measured ones. In terms of computer run time, track model # 4 is the fastest.

Track model # 2 yields a better representation of the track effects, and allows one to visualize the track sag in a direct relation with track tension For instance, Figure 4.41 illustrates the time histories of track sag for the test vehicle traversing 6" obstacle with three different track pre-tension settings, where the vehicle speed is nearly the same (also refer to Figure 4.20). The track sag for high pre-tension setting (T^0_{tr} = 12 kN) is initially set equal to zero, since the track is considered pre-stretched ($T^0_{tr} > T^1_{tr}$). As shown, there are three common dominant peaks, where the first peak is observed when the first road wheel is right on top of the obstacle, and indicates the maximum drop in the track pre-tension; whereas remaining two peaks are observed after the last road wheel hits the obstacle and before the vehicle settlement on the ground. The track sag values for the time duration between first and second peaks are primarily zero, and corresponds to the instances during which the intermediate road wheels and track segments are negotiating the obstacle, where the overall track tension is computed based on the track

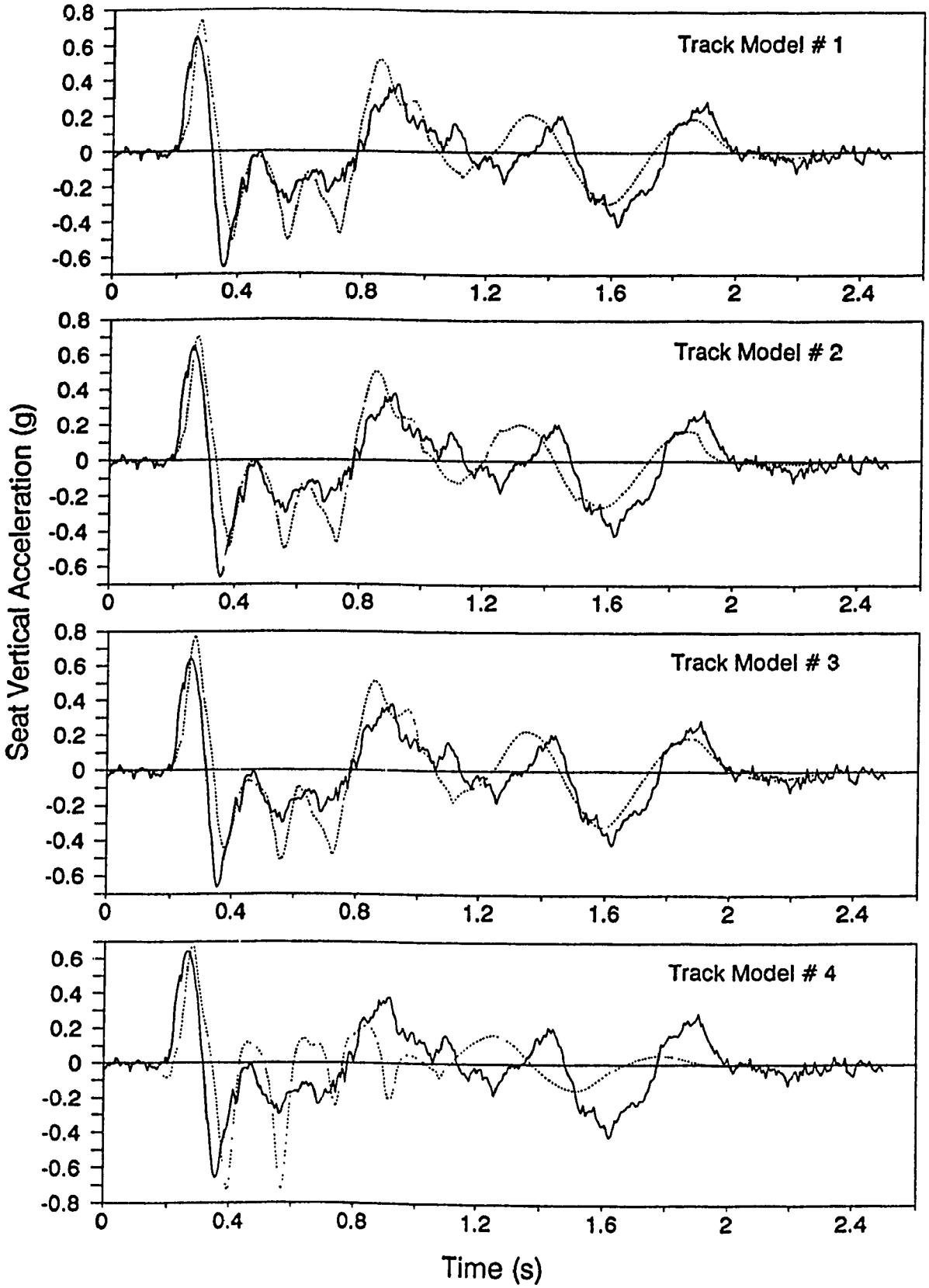

Figure 4.40 Comparison of track models - ride acceleration traces for test vehicle configuration B crossing 6" obstacle at 14.3 km/h (——— Field Test, ... Simulation).

Table 4.10 Assessment of track models (6" obstacle, V_x=14.3 km/h, T_{max}=2.5 s)

	peak value (g)/rms value (g)	% error	run time† (s)
Field Test	0.660/0.197	—	—
Track Model # 1	0.748/0.208	13.3/5.6	271
Track Model # 2	0.704/0.201	6.7/2.0	293
Track Model # 3	0.778/0.210	17.9/6.6	300
Track Model # 4	0.726/0.168	10.0/14.7	224

(† computer run time on a MicroVAX)

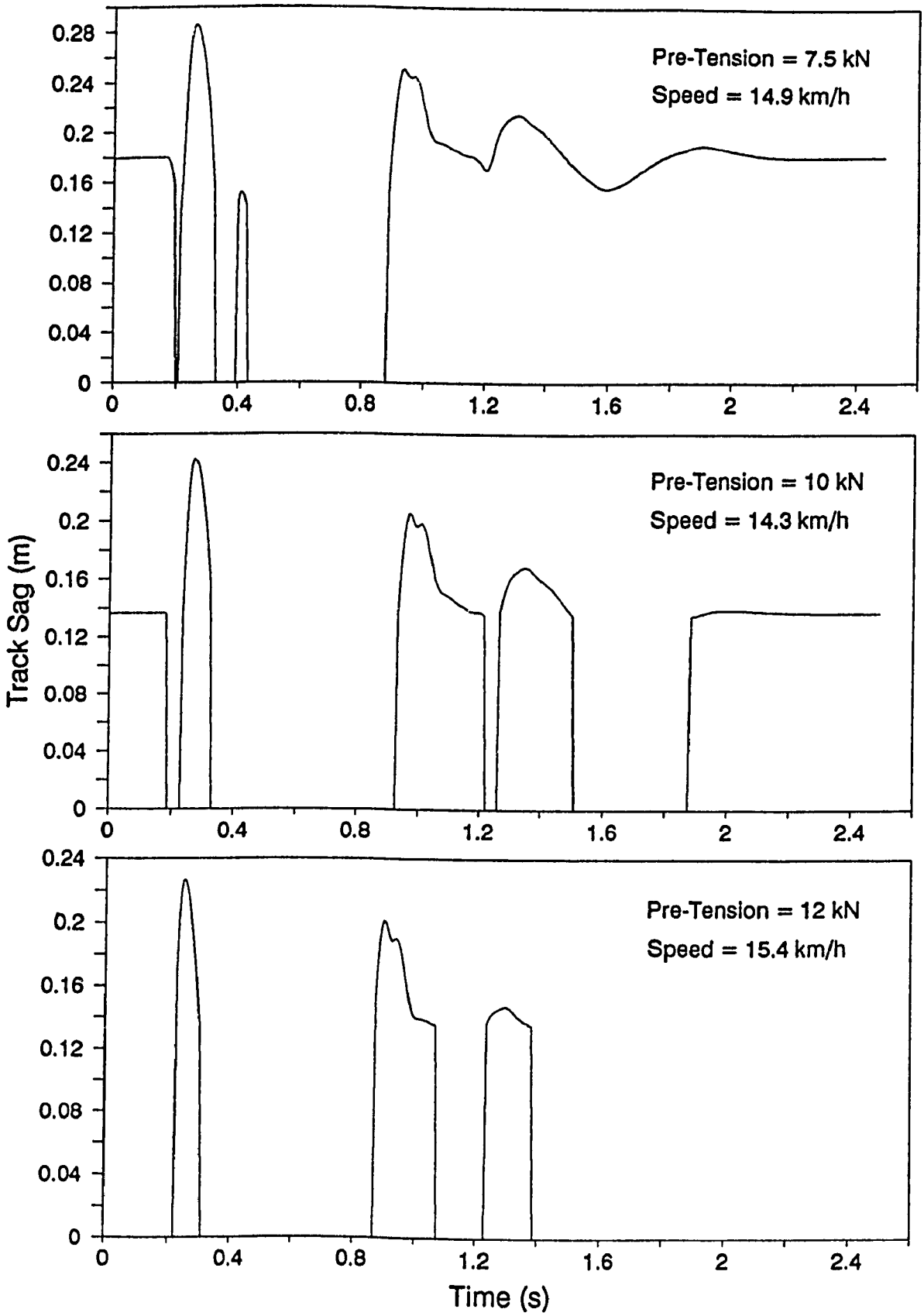

Figure 4.41 Time histories of track sag for test vehicle configuration B traversing 6" obstacle.

belt extensibility. For low and nominal track pre-tension settings, the track sag briefly disappears prior to first road wheel-obstacle interaction. It is due to the front track feeler deflection as it comes in contact with obstacle profile.

Track model # 2 is considered as a reference to assess the performance of other track models. Figure 4.42 shows the traces associated with track parameters such as overall track tension (T_{tr}), total track length (L_{tr}), and net vertical track forces acting at first and second road wheels (T^1_{wy} and T^2_{wy}) for the test vehicle configuration B traversing 6" obstacle at 14.3 km/h. As shown in Figure 4.42 (a), the un-stretched track length computed using track model # 2 remains constant at its initial level, and is relatively higher due to higher value of L^0_h (whereas L^0_h = d for track model # 1), and corresponds to the instances where the overall track tension is computed based on track inextensibility. However, the track length computed using track model # 1 can decrease from its initial level, for which the overall track tension is assumed to be constant at its initial level. As demonstrated by both track models, an increase in total track length from its initial level indicates a stretch of track belt, and an associated increase in the tension computed based on track extensibility. As shown, first five peaks in the tension traces are primarily due to the interactions of intermediate track segments (including front track feeler) with the obstacle; whereas the corresponding valleys are observed when each road wheel is on top of the obstacle.

Figure 4.42 (b) exhibits the predictions of track model # 3 in reference with those of track model # 2. As shown, the primary peaks in the tension trace obtained using the track model # 3 are relatively

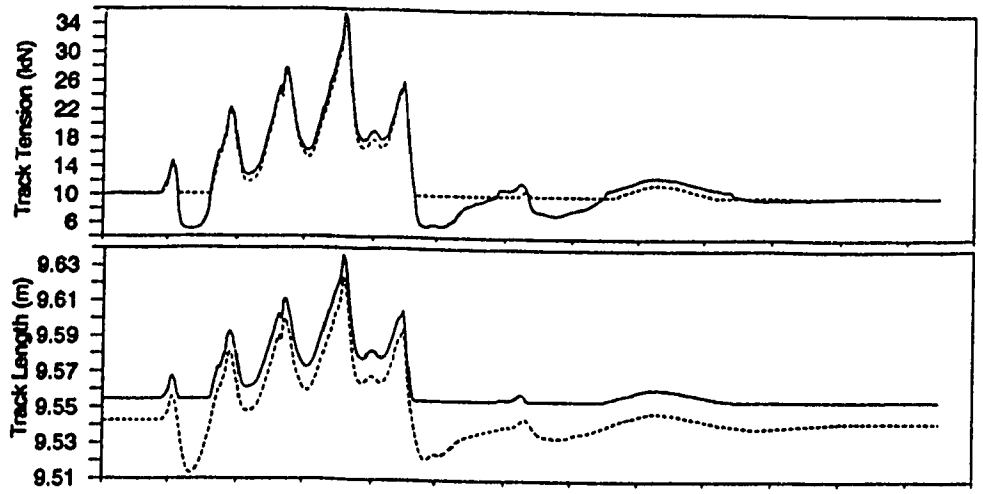

(a) ..... Track Model # 1, ——— Track Model # 2

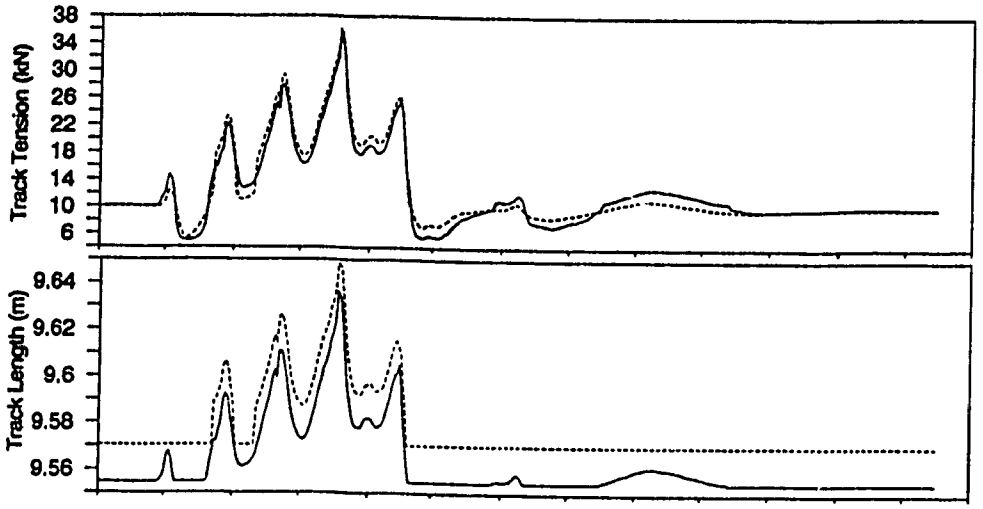

(b) ..... Track Model # 3, ——— Track Model # 2

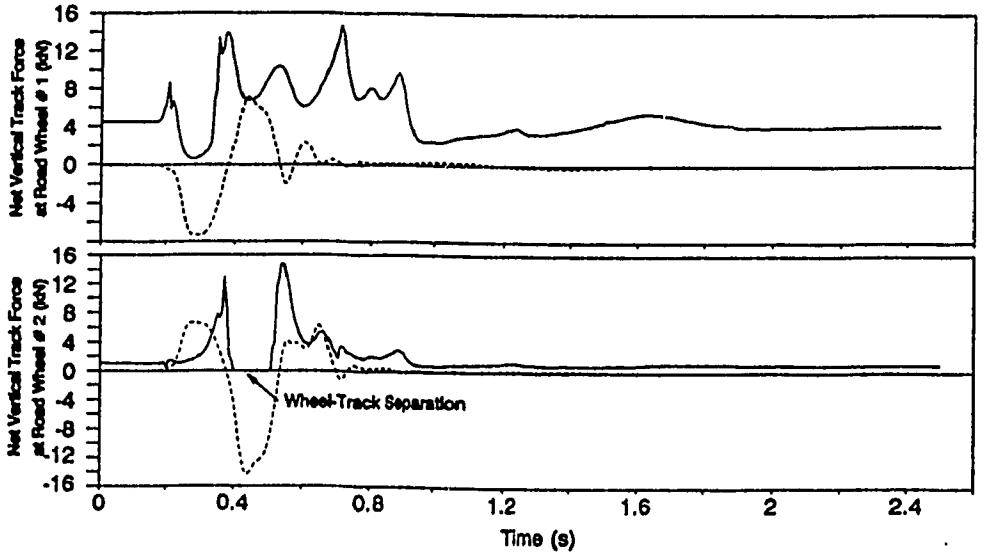

(c) ..... Track Model # 4, ——— Track Model # 2

Figure 4.42 Comparison of track models - traces of track parameters for test vehicle configuration B crossing 6" obstacle at 14.3 km/h.

higher, because the reference tension, T_o, is estimated at 12.5 kN, whereas T_o= 10.5 kN for the track model # 2 (refer Figure I.6). The initial or un-stretched track length computed using track model # 3 is relatively higher. Figure 4.42 (c) shows the predictions of track model # 4 in terms of the time histories of vertical component of dynamic track load acting at first and second road wheel centres. Unlike track model # 2, model # 4 ignores the track support for the road wheel when the vehicle is traversing on a flat ground profile. Track model # 2 (also model #'s 1 and 3) yields vertical track force, which is always acting upward (> 0), since the negative value indicates road wheel-track separation, as shown for the second road wheel. Due to the modeling strategies employed in track model # 4 (i.e. bi-directional track springs) the net vertical track force occasionally becomes negative, which tends to pull the road wheel downward into the terrain profile, which results in higher net foot-print forces. Consequently, fluctuations of higher magnitude are observed in the ride acceleration traces (Figure 4.40).

The track models are further compared based on the simulations of test vehicle configuration B traversing various other test courses. Figure 4.43 shows the traces of measured and predicted vertical ride acceleration for the vehicle crossing over 8" obstacle at 7.7 km/h. As before, the ride predictions based on first three track models are very similar, and in good agreement with test data. The trace evaluated using track model # 4 indicates significantly high magnitudes of acceleration levels. Based on the comparison presented in Table 4.11, the track model # 2 yields the best ride predictions. The time histories of track parameters are presented in Figure 4.44. In comparsion with the traces

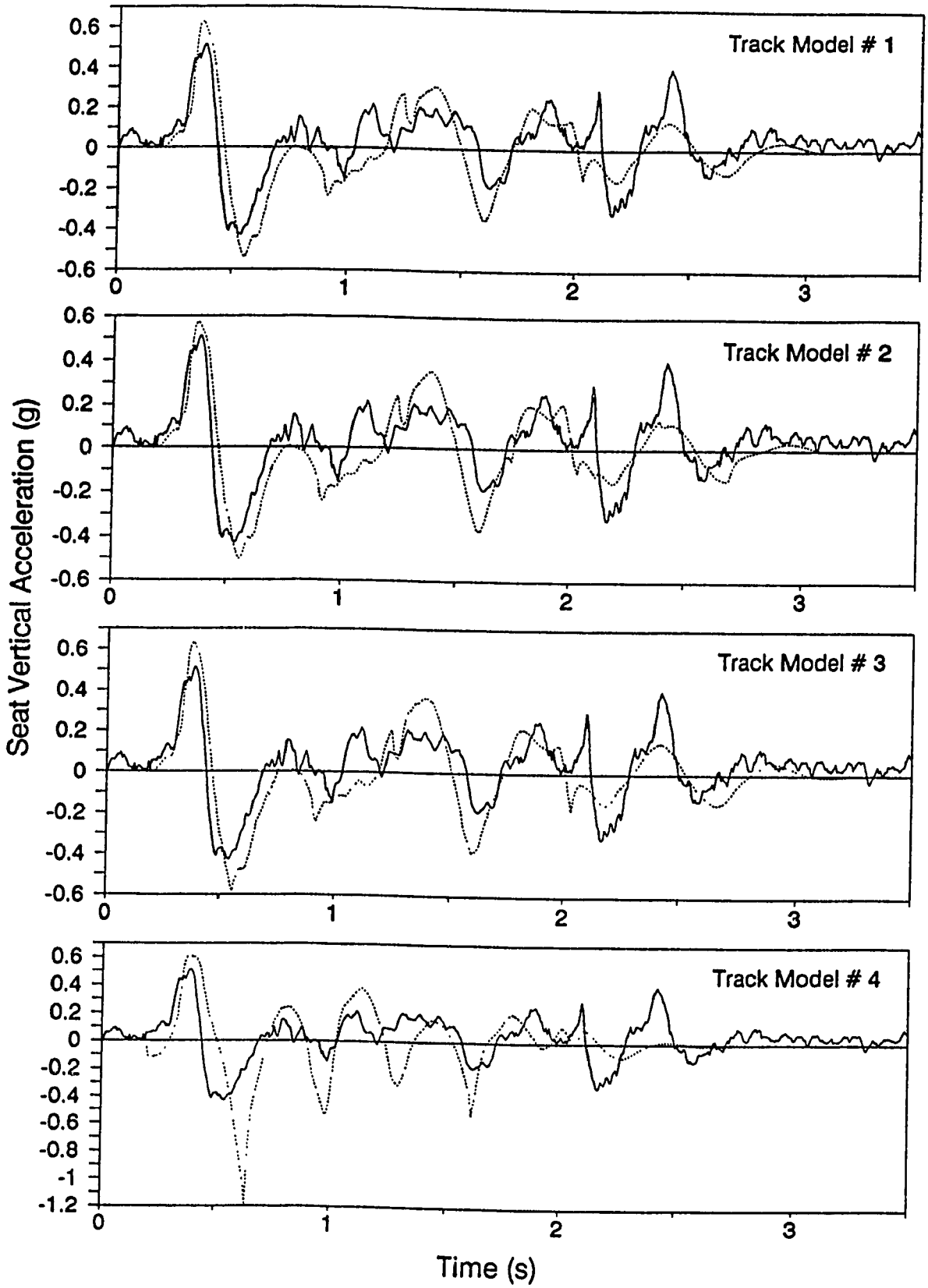

Figure 4.43 Comparison of track models - ride acceleration traces for test vehicle configuration B crossing 8" obstacle at 7.7 km/h (——— Field Test, ... Simulation).

Table 4.11 Assessment of track models (8" obstacle, V_x=7.7 km/h, T_{max}=3.5 s).

	peak value (g)/rms value (g)	% error	run time (s)
Field Test	0.510/0.165	—	—
Track Model # 1	0.627/0.179	22.9/8.5	401
Track Model # 2	0.583/0.177	14.3/7.3	439
Track Model # 3	0.632/0.185	23.9/12.1	446
Track Model # 4	1.192/0.217	133.7/31.5	331

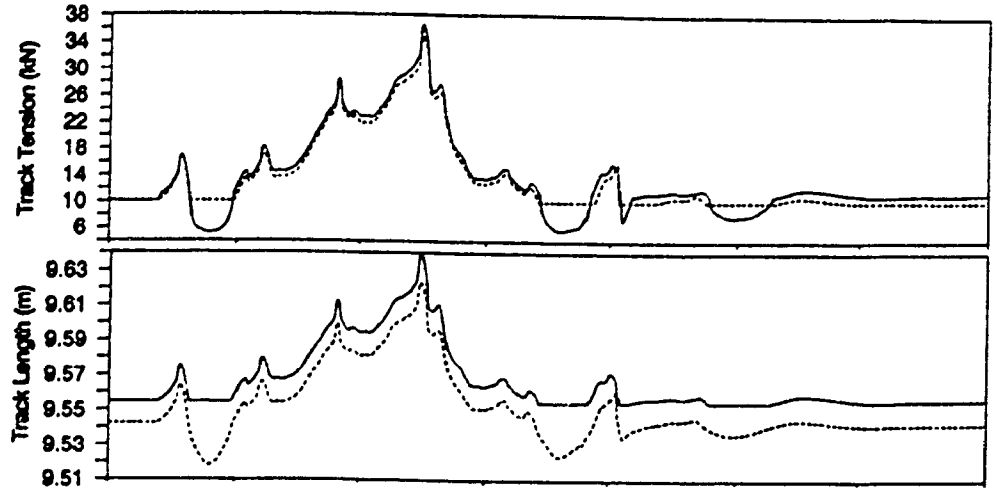

(a) ..... Track Model # 1, ——— Track Model # 2

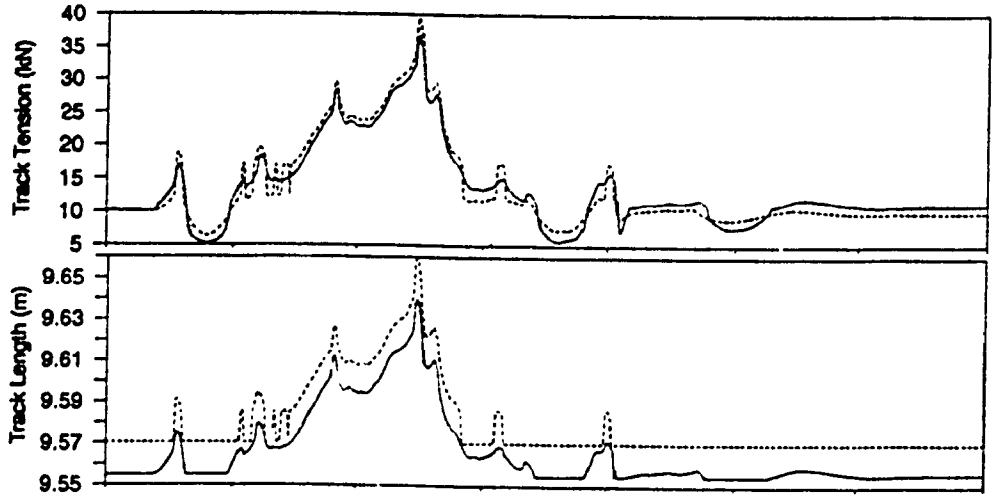

(b) ..... Track Model # 3, ——— Track Model # 2

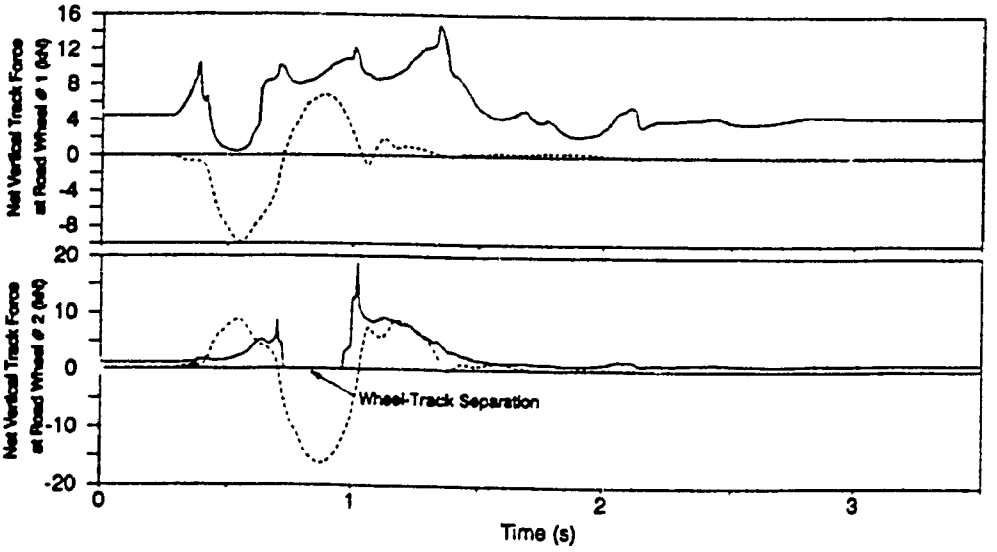

(c) ..... Track Model # 4, ——— Track Model # 2

Figure 4.44 Comparison of track models - traces of track parameters for test vehicle configuration B crossing 8" obstacle at 7.7 km/h.

obtained for 6" obstacle (Figure 4.42), the traces in Figure 4.44 are significantly different.

Figure 4.45 and Table 4.12 compare the performance of track models based on the ride simulation of test vehicle traversing sinusoidal course at 6.7 km/h. Similar observations are made as for the case of half round obstacles. Based on the rms values listed in Table 4.12, the track model # 3 predicts closest to the field test data. Figure 4.46 illustrates the traces associated with track parameters, where the respective differences can be explained in a similar manner as for half round discrete obstacles.

Table 4.13 compares track models based on the ride quality predictions for the test vehicle negotiating LETE48 course at 13.5 km/h. As shown, the average absorbed power values computed in conjunction with first three track models are almost the same, and exhibit an excellent agreement with measured value. The average absorbed power value evaluated using track model # 4 under-estimates the ride harshness considerably.

Based on the comparative study presented in this section, following observations are made:

(a) The performance of a relatively simpler track model # 1 is comparable to that of a more detailed track model # 2.

(b) The quadratic polynomial approach employed to model track inextensibility in track model # 2 yields similar results as an ideal catenary-based approach used in track model # 3. However, track model # 2 permits direct visualization of the track sag in relation with track tension.

(c) The ride predictions obtained in conjunction with track model # 2 generally shows a superior agreement with field test data.

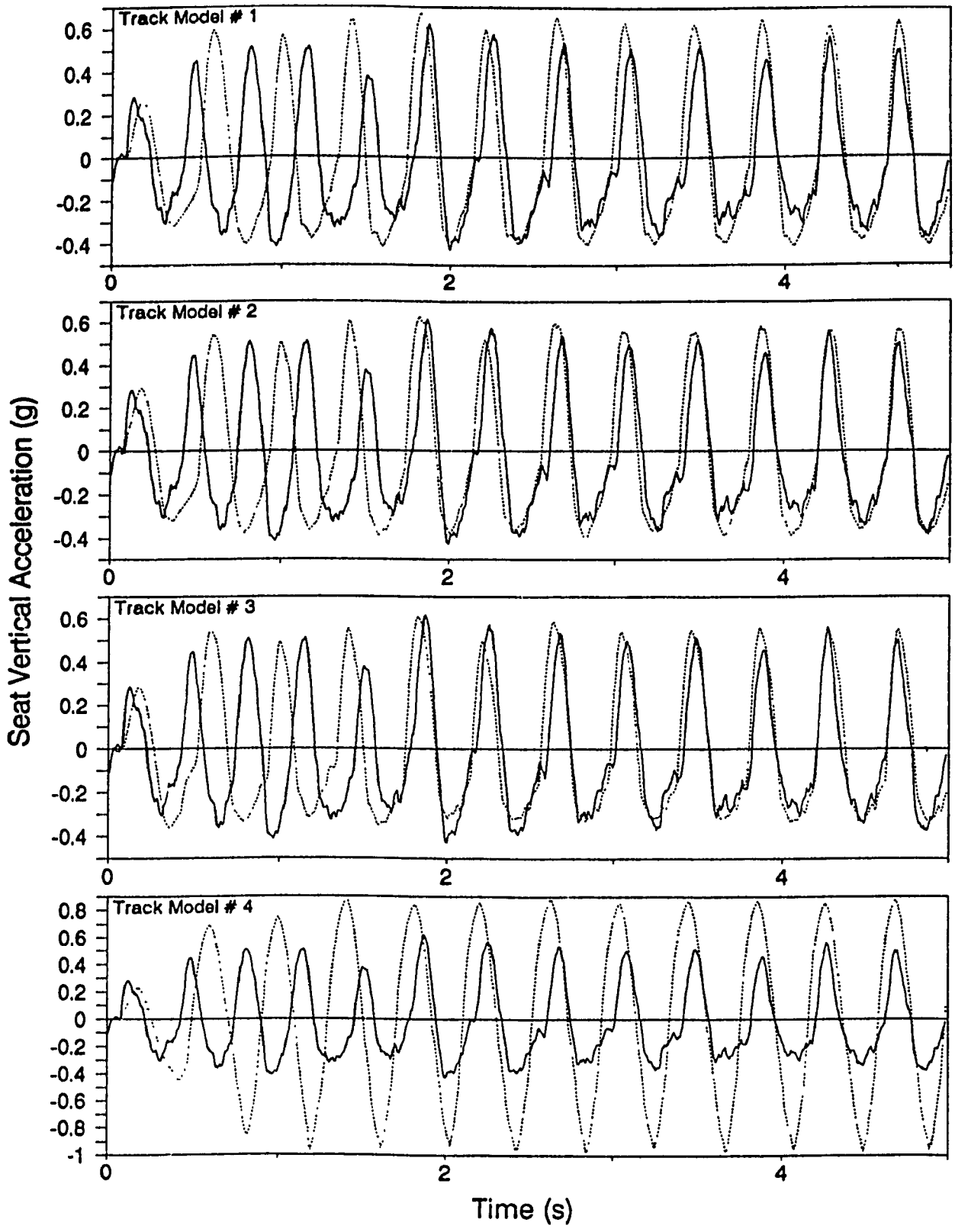

Figure 4.45 Comparison of track models - ride acceleration traces for test vehicle traversing sinusoidal course at 6.7 km/h (——— Field Test, ... Simulation).

Table 4.12 Assessment of track models (Sine Course, V_x=6.7 km/h, T_{max}=5 s).

	rms value (g)	% error	run time (s)
Field Test	0.278	—	—
Track Model # 1	0.347	24.8	1159
Track Model # 2	0.325	16.9	1260
Track Model # 3	0.310	11.5	1285
Track Model # 4	0.584	110.0	945

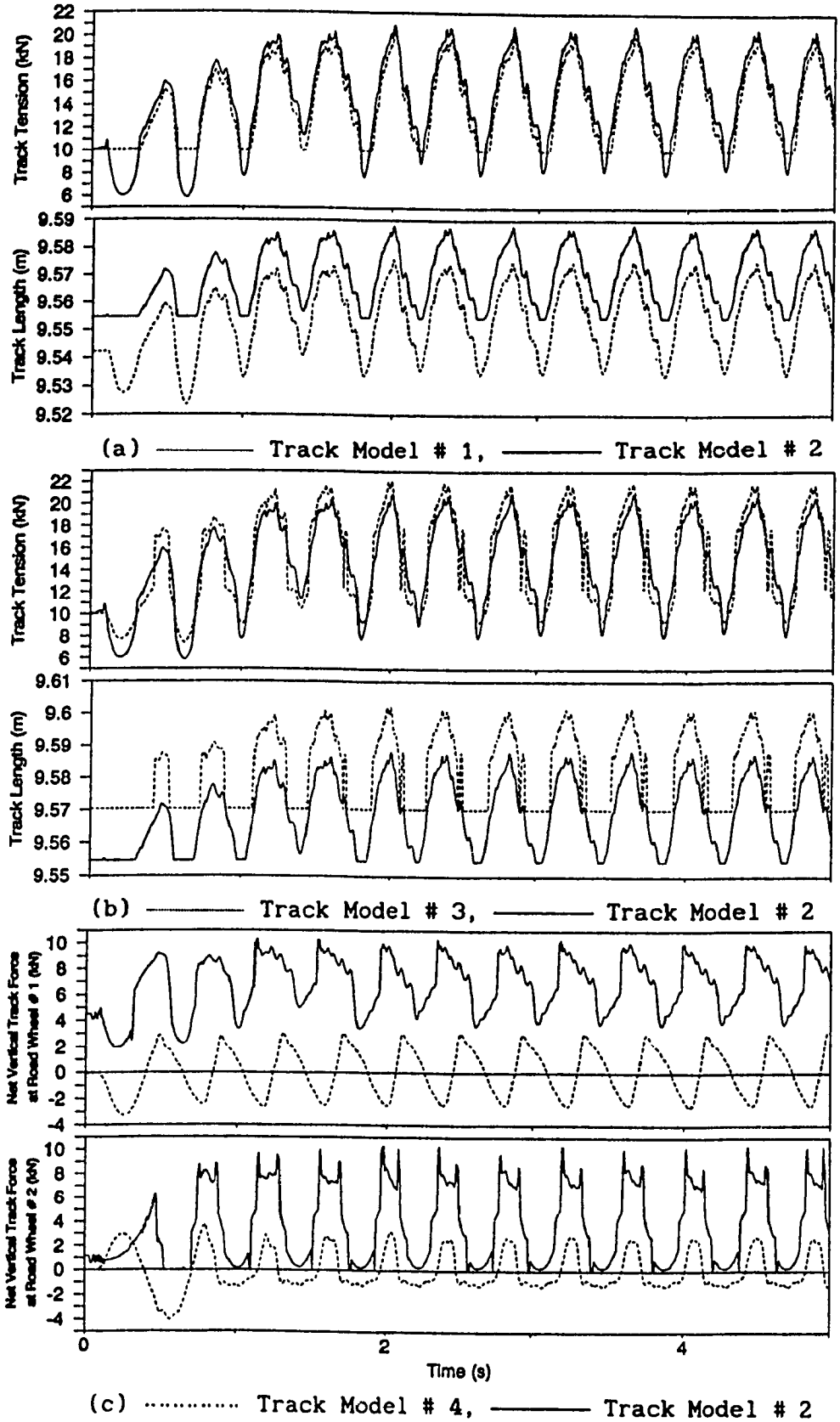

Figure 4.46 Comparison of track models - traces of track parameters for test vehicle configuration B sinusoidal course at 6.7 km/h.

Table 4.13 Assessment of track models (LETE48 course, V_x=6.7 km/h,T_{max}=20 s).

	Abs. Power (W)	% error	run time (s)
Field Test	4.36	—	—
Track Model # 1	4.31	1.15	5877
Track Model # 2	4.33	0.69	6188
Track Model # 3	4.40	0.92	6375
Track Model # 4	2.0	54.1	4703

(d) The ride predictions based on track model # 4 exhibit the least agreement with field test data. Although track model # 4 requires relatively less computer run time, the accuracy of ride predictions obtained with track model # 2 outweighs the increase in computer run time.

4.5 SUMMARY

In this chapter, the ride dynamic model, MODEL I, is refined in view of the sub-system modeling strategies associated with the dynamic wheel-track-terrain interactions and vehicle suspension system. The refinements are:

- The net foot-print force is evaluated based on an adaptive formulation of the idealized continuous spring model, where, the terrain irregularities, if found within the contact patch, are accounted for through the local deformations.
- Dynamic track load imposed at each wheel station is evaluated based on an improved track model, which in addition to track extensibility, also incorporates track inextensibility, which is modeled based on quadratic polynomial approximation of the track segment hanging between sprocket and idler. In addition, the wheel-track connectivity is improved to properly define the track wrap angle around road wheels, and the road wheel-track-terrain separation, and to include enhanced modeling of the track bridging effects.
- The equations of motion are re-written based on a realistic suspension configuration, where the independent suspension unit is considered to remain perpendicular to the vehicle frame.

The re-derived model, MODEL II, is then assessed using field test data.

The ride responses evaluated for various test conditions have shown an improved correlation with the field test data.

In order to assess the performance of proposed wheel and track models, various other wheel and track modeling strategies used by other researchers are formulated and employed for performing ride simulations of the field-tested vehicle in conjunction with MODEL II. Corresponding ride predictions are validated against field test data. This comparative study has provided a detailed assessment of individual wheel and track models in view of the accuracy of ride predictions, and associated computational time. In comparison, the ride predictions evaluated in conjunction with proposed wheel and track models have shown a superior agreement with the field test data.

Chapter 5

RIDE DYNAMIC STUDY OF THE CANDIDATE VEHICLE WITH TRAILING ARM SUSPENSION CONFIGURATION

5.1 INTRODUCTION

The ride prediction models, MODEL I and MODEL II, are formulated assuming an *idealized* representation of the torsion bar/trailing arm suspension system employed in the candidate vehicle. The torsion bar stiffness and the inclined shock absorber are idealized by an equivalent independent suspension configuration (a parallel combination of rectilinear spring and damping elements), while ignoring the kinematics of the trailing arm (or road arm) and shock absorber linkages. As shown in Figure 2.3, each road wheel is mounted on a road arm splined to a torsion bar, and experiences swing like motion as the vehicle negotiates rough terrain undulations. Thus, the road wheel not only displaces in a vertical direction (as assumed for MODELs I and II), but experiences horizontal motion as well. Evidentally, the alternate choice of the rotational degree-of-freedom associated with rotation of the road arm-road wheel assembly about the torsion bar centre, is vital in view of an accurate representation of the vehicle ride dynamics. The ride model formulation considering rotational degrees-of-freedom for road arm-road wheel assemblies in conjunction with kinematic considerations for road arm and inclined shock absorber likages, would thus correctly represent the suspension components, and serve as a design-oriented tool for analyzing the expected field performances of the suspension components.

In this chapter, the ride dynamic model for the candidate vehicle is re-derived in view of the above-mentioned considerations, and incorpo-

rates the refined wheel and track sub-models employed in MODEL II. This new ride model is referred to as MODEL III. The relative performance of MODEL III is assessed based on the field validation results. MODEL III is then employed to carry out parameteric sensitivity analyses to demonstrate the influence of the variations in vehicle suspension parameters on the ride dynamic behaviour of the candidate vehicle. In addition, simulations are performed with advanced suspension system, such as a typical hydrogas or hydropneumatic suspension configuration developed for high mobility tracked vehicles, in order to investigate its potential in improving the ride performance of the candidate vehicle.

5.2 DEVELOPMENT OF RIDE DYNAMIC MODEL IN VIEW OF TORSION BAR/TRAILING ARM SUSPENSION CONFIGURATION: MODEL III

The trailing arm/torsion bar suspension system comprises of four major components: torsion bar, road arm (with or without overhang), shock absorber, and lower and upper bump stops. The schematics of suspension components are presented in Figure 5.1. As discussed earlier (Figure 2.3), each road wheel is independently attached to the hull through a road arm splined to a transverse torsion bar, which extends over the width of the chassis and is clamped on the other end. The shock absorbers are mounted between the road arm (with overhang) and the hull chassis at an inclined position. For the field-tested vehicle, the shock absorbers are only mounted at the first and the fifth road wheel stations. At the upper and lower bounds of road arm travel, rubber bumpers are mounted to prevent the road wheel from hitting the hull chassis and driving the track into the ground.

The ride dynamic model (MODEL III) is developed incorporating the

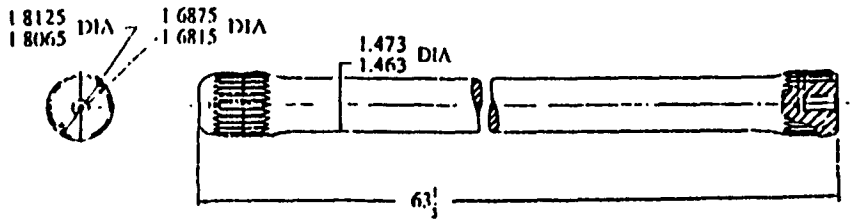

(a) Torsion bar

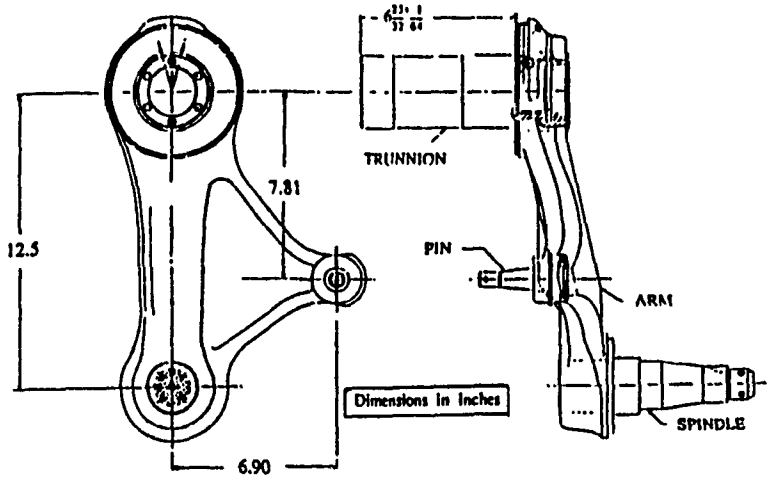

(b) Road arm with overhang

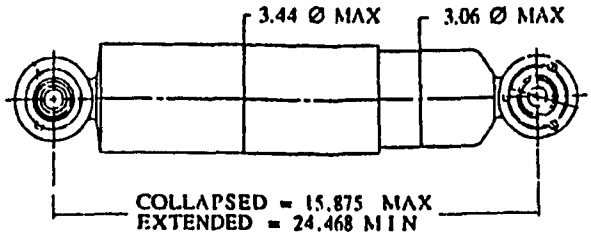

(c) Shock absorber

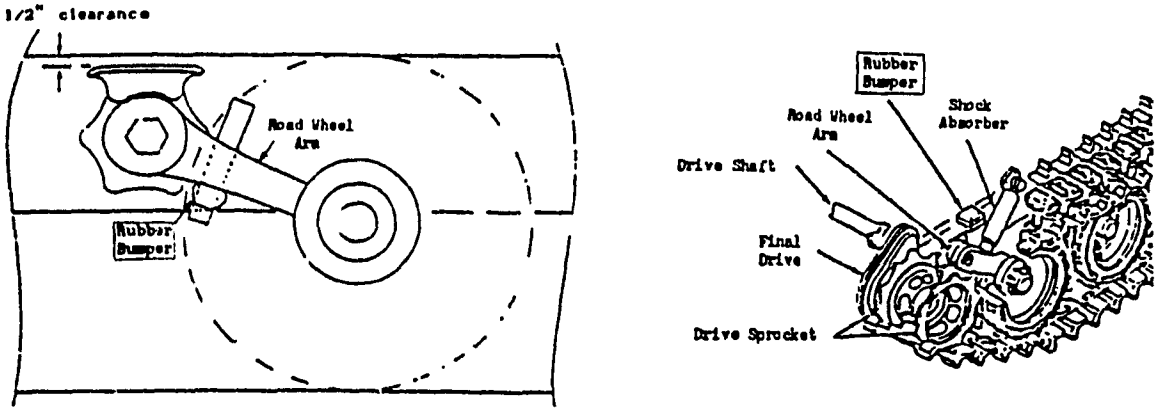

(d) Location of upper and lower bump stops

Figure 5.1 Schematics of primary suspension components.

kinematic relations to account for the linkage assembly comprising of the torsion bars, road arms, and inclined shock absorbers. As illustrated in Figure 5.2, the in-plane ride model is characterized by a heavy central body (hull) supported by a system of relatively light-weight road arm-road wheel assemblies. The road arms are coplanar mechanical systems directly connected to the hull body. MODEL III is also described by a set of "3+N" differential equations: bounce and pitch motion of central (hull) body, bounce motion (optional) of driver/seat, and rotational motions of "N" road arm and wheel assemblies about their respective torsion bar centres. Non-linear differential equations of motion are derived using Lagrange's energy method.

5.2.1 Langrangian Formulation

The dynamic equations governing the vehicle motion along the generalized coordinates can be conveniently derived using the Langrangian formulation in its classical form, given as:

$$\frac{d}{dt}\left(\frac{\partial T}{\partial \dot{q}_i}\right) - \frac{\partial T}{\partial q_i} + \frac{\partial U}{\partial q_i} = Q_i \qquad (5.1)$$

where,
$$\frac{d}{dt}\left(\frac{\partial T}{\partial \dot{q}_i}\right) = \sum_{j=1}^{N+3}\left(\frac{\partial^2 T}{\partial \dot{q}_i \partial \dot{q}_j}\,\ddot{q}_j + \frac{\partial^2 T}{\partial \dot{q}_i \partial q_j}\,\dot{q}_j\right)$$

and, T is the kinetic energy, U is the potential energy, q_i is the i^{th} generalized coordinate and Q_i is the corresponding generalized force due to internal force elements, track, and ground. The kinematics of the vehicle ride model is described by "3+N" degrees-of-freedom or generalized coordinates. The first and second generalized coordinates describe bounce and pitch motions of the hull body (y_h,θ_h), respectively.

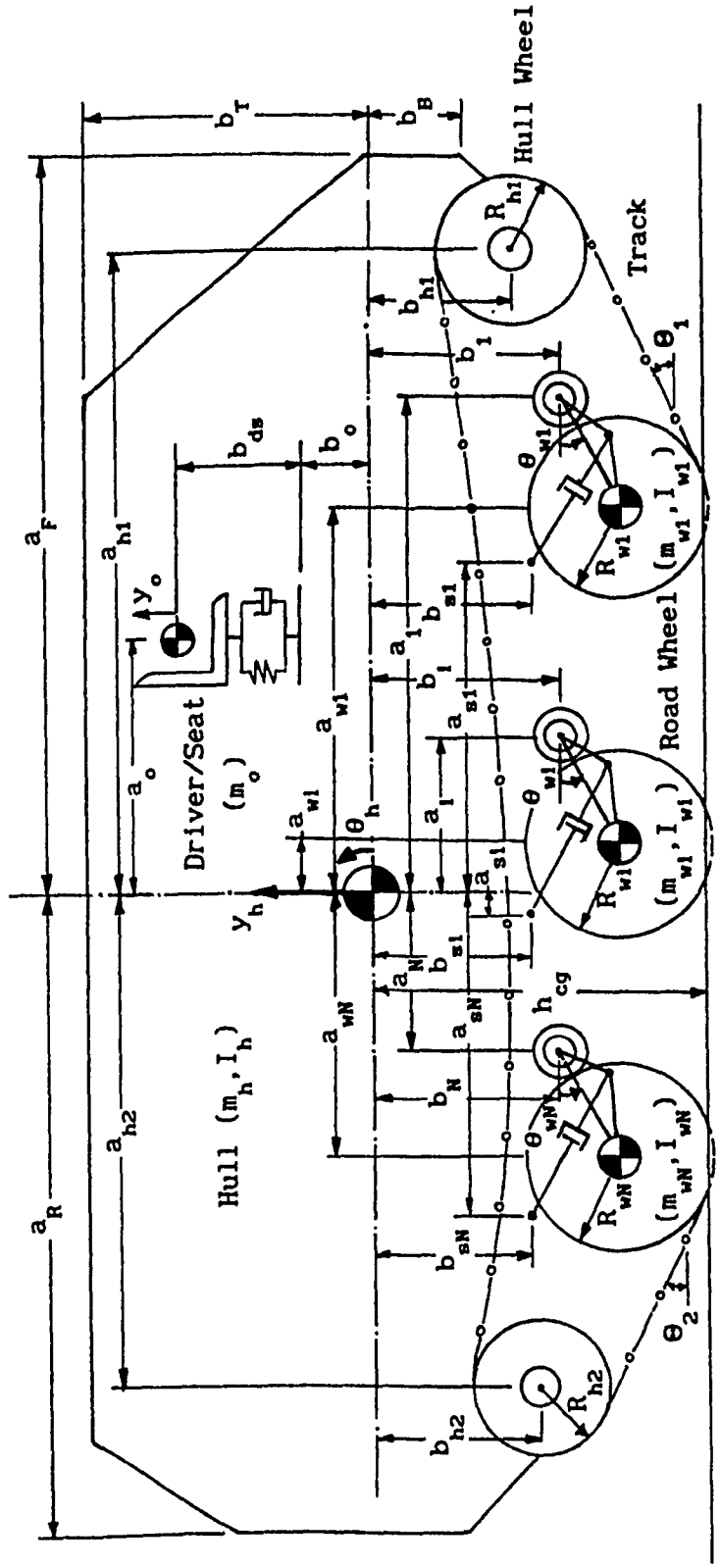

Figure 5.2 In-plane model representation of a typical high mobility tracked vehicle employing torsion bar/trailing arm suspension configuration.

The other N generalized coordinates are the angles between road arms and hull chassis (θ_{wi}, i = 1,..,N). The last generalized coordinate (optional) is the bounce displacement of the suspended driver/seat (y_o).

Before deriving the energy expressions, it is essential to select reference frames to describe the motion of the vehicle and its suspension components. As illustrated in Figure 5.3, three reference frames are chosen: (1) the fixed/global reference frame (**X**,**Y**), (2) the centroidal body-fixed reference frame ($\bar{X}_{CG}$,$\bar{Y}_{CG}$), and (3) the reference frame attached to the i^{th} torsion bar centre describing the rotation of the road arm with respect to the hull chassis ($\bar{X}_c$,$\bar{Y}_c$). The position of the centroidal body (hull c.g) with respect to the fixed reference frame is given as:

$$P_{CG} = \begin{Bmatrix} X_{cg} \\ Y_{cg} \end{Bmatrix} = \begin{Bmatrix} X^0_{cg} + V_x.t \\ Y^0_{cg} + y_h \end{Bmatrix} \tag{5.2}$$

Similarly, the position of the i^{th} road wheel centre is described by the following transformation:

$$P_{wi} = \mathbb{T}_{CG}\,{}^{CG}\mathbb{T}_c\,{}^{c}P_{wi} \tag{5.3}$$

where, the transformation matrix describing the frame ($\bar{X}_{CG}$,$\bar{Y}_{CG}$) with respect to the global frame (**X**,**Y**) is given as:

$$\mathbb{T}_{CG} = \begin{bmatrix} C_\theta & -S_\theta & X_{cg} \\ S_\theta & C_\theta & Y_{cg} \\ 0 & 0 & 1 \end{bmatrix} \tag{5.4}$$

The transformation matrix describing the frame ($\bar{X}_c$,$\bar{Y}_c$) in reference to the body-fixed frame ($\bar{X}_{CG}$,$\bar{Y}_{CG}$) is given as:

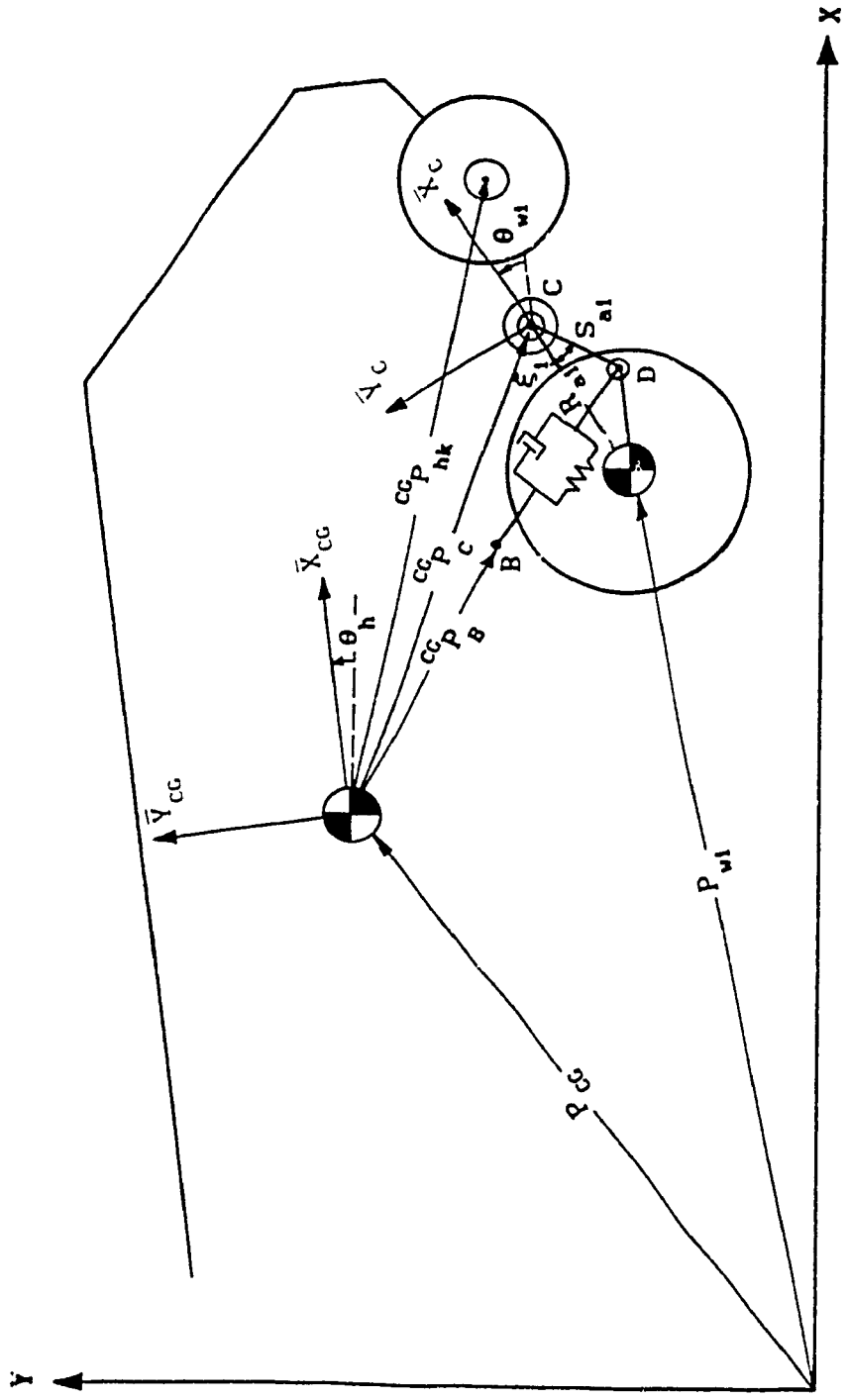

Figure 5.3 Three reference frames.

$$ {}^{CG}\mathbb{T}_C = \begin{bmatrix} C_\theta^i & -S_\theta^i & a_i \\ S_\theta^i & C_\theta^i & b_i \\ 0 & 0 & 1 \end{bmatrix} \tag{5.5} $$

where $C_\theta^i = \cos(\theta_{wi})$ and $S_\theta^i = \sin(\theta_{wi})$.

The vector indicating the position of road wheel centre with respect to the frame $(\bar{X}_C, \bar{Y}_C)$ is given as:

$$ {}^{C}P_{wi} = \begin{Bmatrix} -R_{ai} \\ 0 \\ 1 \end{Bmatrix} \tag{5.6} $$

where, R_{ai} is the length of the road arm. Subsequently, the vector P_{wi} is obtained as:

$$ P_{wi} = \begin{Bmatrix} X_{wi} \\ Y_{wi} \end{Bmatrix} = \begin{Bmatrix} d_{xi} + a_i C_\theta - b_i S_\theta + X_{cg} \\ d_{yi} + a_i S_\theta + b_i C_\theta + Y_{cg} \end{Bmatrix} \tag{5.7} $$

where, $d_{xi} = -R_{ai}\cos(\theta_h + \theta_{wi})$ and $d_{yi} = -R_{ai}\sin(\theta_h + \theta_{wi})$

Similarly, the position of the k^{th} hull wheel centre (rigidly attached to the central body) with respect to the global reference frame is described by the following transformation:

$$ P_{hk} = \mathbb{T}_{CG}\, {}^{CG}P_{hk} \tag{5.8} $$

where, the vector indicating the position of the hull wheel centre with respect to the body-fixed frame is given as:

$$ {}^{CG}P_{hk} = \begin{Bmatrix} a_{hk} \\ b_{hk} \\ 1 \end{Bmatrix} \tag{5.9} $$

Thus, P_{hk} is obtained as:

$$P_{hk} = \begin{Bmatrix} X_{hk} \\ Y_{hk} \end{Bmatrix} = \begin{Bmatrix} a_{hk}C_\theta - b_{hk}S_\theta + X_{cg} \\ a_{hk}S_\theta + b_{hk}C_\theta + Y_{cg} \end{Bmatrix} \tag{5.10}$$

The kinetic and potential energies of the whole vehicle (excluding the suspended driver/seat) are given by the following expressions:

$$T = \frac{1}{2} m_h \dot{P}^2_{cg} + \frac{1}{2} I_h \dot{\theta}^2_h + \frac{1}{2} \sum_{i=1}^{N} m_{wi} \dot{P}^2_{wi} + I_{wi}(\dot{\theta}_h + \dot{\theta}_{wi})^2 \tag{5.11}$$

$$U = g \left[m_h Y_{cg} + \sum_{i=1}^{N} m_{wi} Y_{wi} \right] \tag{5.12}$$

Upon appropriate substitutions from equations (5.2) and (5.7), the energy expressions are re-written in the expanded form as:

$$T = \frac{1}{2} m_h \dot{y}^2_h + \frac{1}{2} I_h \dot{\theta}^2_h + \frac{1}{2} \sum_{i=1}^{N} m_{wi}[(-a_i S_\theta - b_i C_\theta - d_{yi})\,\dot{\theta}_h - d_{yi}\,\dot{\theta}_{wi}]^2$$

$$+ \frac{1}{2} \sum_{i=1}^{N} m_{wi}[\dot{y}_h + (a_i C_\theta - b_i S_\theta + d_{xi})\,\dot{\theta}_h + d_{xi}\,\dot{\theta}_{wi}]^2$$

$$+ \frac{1}{2} \sum_{i=1}^{N} I_{wi}(\dot{\theta}_h + \dot{\theta}_{wi})^2 \tag{5.13}$$

$$U = g \left[m_h(Y^0_{cg} + y_h) + \sum_{i=1}^{N} m_{wi}(d_{yi} + a_i S_\theta + b_i C_\theta + Y^0_{cg} + y_h) \right] \tag{5.14}$$

The inertial properties of the i^{th} road arm-road wheel assembly are described by m_{wi} and I_{wi}, where m_{wi} is the combined mass, and I_{wi} is the mass moment of inertia relative to its mass centre, generally expressed as:

$$m_{wi} = m^i_{ra} + m^i_{rw} \tag{5.15}$$

$$I_{wi} = I^i_{ra} + m^i_{ra}|{}^cP_{wi} - {}^cP^i_{ra}|^2 + I^i_{rw} + m^i_{rw}|{}^cP_{wi} - {}^cP^i_{rw}|^2 \qquad (5.16)$$

where, m^i_{ra} and m^i_{rw} correspond to mass of the i^{th} road arm and road wheel, respectively. I^i_{ra} and I^i_{rw} are mass moment of inertias of the i^{th} road arm and road wheel about their respective mass centres. ${}^cP_{wi}$, ${}^cP^i_{ra}$, and ${}^cP^i_{rw}$ are position vectors with respect to the torsion bar centre ($\bar{X}_c$,$\bar{Y}_c$-frame) indicating the mass centre of the i^{th} road arm-road wheel assembly, road arm alone, and road wheel alone, respectively. Since, the mass centre of the road arm-road wheel assembly is assumed to coincide with the mass or geometric centre of the road wheel alone (i.e ${}^cP_{wi}={}^cP^i_{rw}$), equation (5.16) is re-written as:

$$I_{wi} = I^i_{ra} + m^i_{ra}|{}^cP_{wi} - {}^cP^i_{ra}|^2 + I^i_{rw} \qquad (5.17)$$

The generalized force Q_i in equation (5.1) is derived using the virtual work principle, obtained as:

$$Q_i = \sum_{j=1}^{N+2} \left[\bar{F}_j \frac{\partial \bar{r}_j}{\partial q_i} + \bar{M}_j \frac{\partial \bar{\theta}_j}{\partial q_i} \right] \qquad (5.18)$$

where $\bar{F}_j$ and $\bar{M}_j$ are internal and external forces and moments in the system, respectively, and $\bar{r}_j$ and $\bar{\theta}_j$ are the corresponding translational and rotational coordinates. Subsequently, the generalized force can be expressed as:

$$Q_i = Q^E_i + Q^I_i \qquad (5.19)$$

where, Q^E_i is the external generalized force due to the dynamic wheel-track-terrain interactions (i.e. foot-print forces and dynamic track load), and Q^I_i is the internal generalized force created by the suspension

components. The derivation of these forces is provided as follows.

External Generalized Forces

The external generalized force is expressed as:

$$Q_i^E = \sum_{i=1}^{N} \left[-F_{wx}^i \frac{\partial X_{wi}}{\partial q_i} + F_{wy}^i \frac{\partial Y_{wi}}{\partial q_i} \right] + \sum_{k=1}^{2} \left[-F_{hx}^k \frac{\partial X_{hk}}{\partial q_i} + F_{hy}^k \frac{\partial Y_{hk}}{\partial q_i} \right] \qquad (5.20)$$

where, the centre coordinate of i^{th} road wheel (X_{wi}, Y_{wi}) and k^{th} hull wheel (X_{hk}, Y_{hk}) are given by equations (5.7) and (5.10), respectively. The net horizontal and vertical forces acting at the centre of i^{th} road wheel (F_{wx}^i, F_{wy}^i) and the k^{th} hull wheel (F_{hx}^k, F_{hy}^k) are obtained based on the refined wheel and track sub-models employed for MODEL II (discussed in section 4.2).

Consequently, the external generalized forces for the specified degrees-of-freedom are derived using equation (5.20), given as:

$i = 1$:
$$Q_1^E = \sum_{i=1}^{N} F_{wy}^i + \sum_{k=1}^{2} F_{hy}^k \qquad (5.21a)$$

$i = 2$:
$$Q_2^E = \sum_{i=1}^{N} F_{wx}^i (a_i S_\theta + b_i C_\theta + d_{yi}) + F_{wy}^i (a_i C_\theta - b_i S_\theta + d_{xi}) + \sum_{k=1}^{2} F_{hx}^k (a_{hk} S_\theta + b_{hk} C_\theta) + F_{hy}^k (a_{hk} C_\theta - b_{hk} S_\theta) \qquad (5.21b)$$

$i = i+2$:
$$Q_i^E = F_{wx}^i \, d_{yi} + F_{wy}^i \, d_{xi} \quad ; \quad i = 1,..,N \qquad (5.21c)$$

Internal Generalized Forces

The internal generalized force for the tracked vehicle system can be expressed as:

$$Q_i^I = \sum_{i=1}^{N} F_S^i \frac{\partial r_i}{\partial q_i} + M_T^i \frac{\partial \theta_{wi}}{\partial q_i} \tag{5.22}$$

where, F_S^i and M_T^i represent the force due to the rectilinear suspension unit mounted between the hull chassis and the road arm with overhang (e.g. inclined shock absorber), and the moment due to the torsion bar, respectively.

The rectilinear suspension unit can be modeled using some analytical functions or interpolated from look-up tables of empirically determined force-displacement and force-velocity data. In general, the suspension force is expressed as:

$$F_S^i = f(r_i, \dot{r}_i) \tag{5.23}$$

where, r_i and $\dot{r}_i$ indicate the relative displacement and velocity across the suspension unit, respectively. For the tracked vehicle model, r_i and $\dot{r}_i$ are evaluated based on the generalized coordinate θ_{wi} only, since it is measured with respect to the centroidal-body fixed reference system.

The relative displacement or the displacement due to the extension of the suspension unit (as implied by the specified direction of θ_{wi}) is obtained as:

$$r_i = |{}^D P_B^0| - |{}^D P_B| \tag{5.24}$$

where, ${}^D P_B$ is the vector indicating point B (the hull-suspension connection point) with respect to the point D (road arm-suspension connection point), and ${}^D P_B^0$ is the vector corresponding to the vehicle's zero-force configuration (discussed in the following section). The vector ${}^D P_B$ is expressed as (refer to Figure 5.3):

$$ {}^{D}P_{B} = {}^{CG}P_{B} - {}^{CG}P_{D} \tag{5.25} $$

where, the vector indicating point B in the central-body system is given as:

$$ {}^{CG}P_{B} = \begin{Bmatrix} a_{si} \\ b_{si} \\ 1 \end{Bmatrix} \tag{5.26} $$

and the vector indicating point D in the central-body system is given as:

$$ {}^{CG}P_{D} = {}^{CG}\mathbb{T}_{C}\,{}^{C}P_{D} \tag{5.27} $$

where, the transformation matrix ${}^{CG}\mathbb{T}_{C}$ is given by equation (5.5), and the vector indicating point D in the reference frame attached to the torsion bar centre, is given as:

$$ {}^{C}P_{D} = \begin{Bmatrix} -S_{ai}\cos\xi_{i} \\ -S_{ai}\sin\xi_{i} \\ 1 \end{Bmatrix} \tag{5.28} $$

where, S_{ai} and ξ_{i} are the length and the angle of the overhang as indicated in Figure 5.3. Subsequently, the vector ${}^{D}P_{B}$ is obtained as:

$$ {}^{D}P_{B} = \begin{Bmatrix} \Delta_{ai} + S_{ai}\cos(\theta_{wi}+\xi_{i}) \\ \Delta_{bi} + S_{ai}\sin(\theta_{wi}+\xi_{i}) \end{Bmatrix} \tag{5.29} $$

where, $\Delta_{ai} = a_{si} - a_{i}$ and $\Delta_{bi} = b_{si} - b_{i}$

and the vector ${}^{D}P_{B}^{O}$ is then expressed as:

$$ {}^{D}P_{B}^{O} = \left\{ \begin{array}{l} \Delta_{ai} + S_{ai}\cos(\theta_{wi}^{O}+\xi_{i}) \\ \Delta_{bi} + S_{ai}\sin(\theta_{wi}^{O}+\xi_{i}) \end{array} \right\} \qquad (5.30) $$

where, θ_{wi}^{O} indicates the angular orientation of the i^{th} road arm for which the torque due to the torsion bar (M_{T}^{i}) is zero (i.e. zero-force configuration).

The expression for the relative or extension velocity is then obtained based on the time derivative of equation (5.24), given as:

$$ \dot{r}_{i} = -\left|{}^{D}\dot{P}_{B}\right| = - S_{ai}\,\dot{\theta}_{wi} \qquad (5.31) $$

The moment due to the torsion bar, M_{T}^{i}, is modeled based on piece-wise linear spring characteristics. As shown in Figure 5.4, K_{Ti} is the torsional spring rate corresponding to the normal wheel travel range, which is defined by angles θ_{wi}^{U} and θ_{wi}^{L} indicating locations of upper and lower bump stops. The bump stops are modeled as equivalent torsional springs, whose stiffness values (K_{Ti}^{U},K_{Ti}^{L}) are estimated based on the linear stiffness of the bump stop material (K_{b}^{U},K_{b}^{L}) and their radial distance with respect to the torsion bar centre (r_{bU},r_{bL}), as demonstrated in Figure 5.4. The moment, M_{T}^{i}, is then obtained as:

$$ M_{T}^{i} = - \left\{ \begin{array}{ll} K_{Ti}(\theta_{wi}^{U} - \theta_{wi}^{O}) + K_{Ti}^{U}(\theta_{wi} - \theta_{wi}^{U}) & ; \quad \theta_{wi} > \theta_{wi}^{U} \\ K_{Ti}(\theta_{wi} - \theta_{wi}^{O}) & ; \quad \theta_{wi}^{L} \leq \theta_{wi} \leq \theta_{wi}^{U} \\ K_{Ti}(\theta_{wi}^{L} - \theta_{wi}^{O}) + K_{Ti}^{L}(\theta_{wi} - \theta_{wi}^{L}) & ; \quad \theta_{wi} < \theta_{wi}^{L} \end{array} \right. \qquad (5.32) $$

A torsional damper, which may have highly non-linear characteristics such as Coulomb friction damping can be easily incorporated in M_{T}^{i}, where the damping torque is simply expressed as a function of $\dot{\theta}_{wi}$.

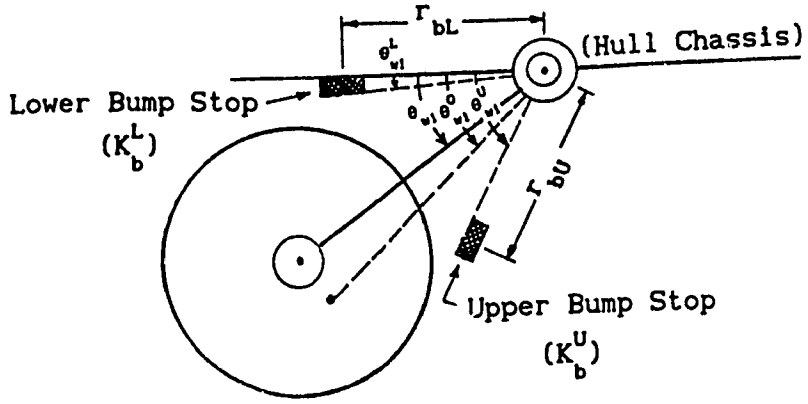

(a) Angular orientation of road arm and location of bump stops

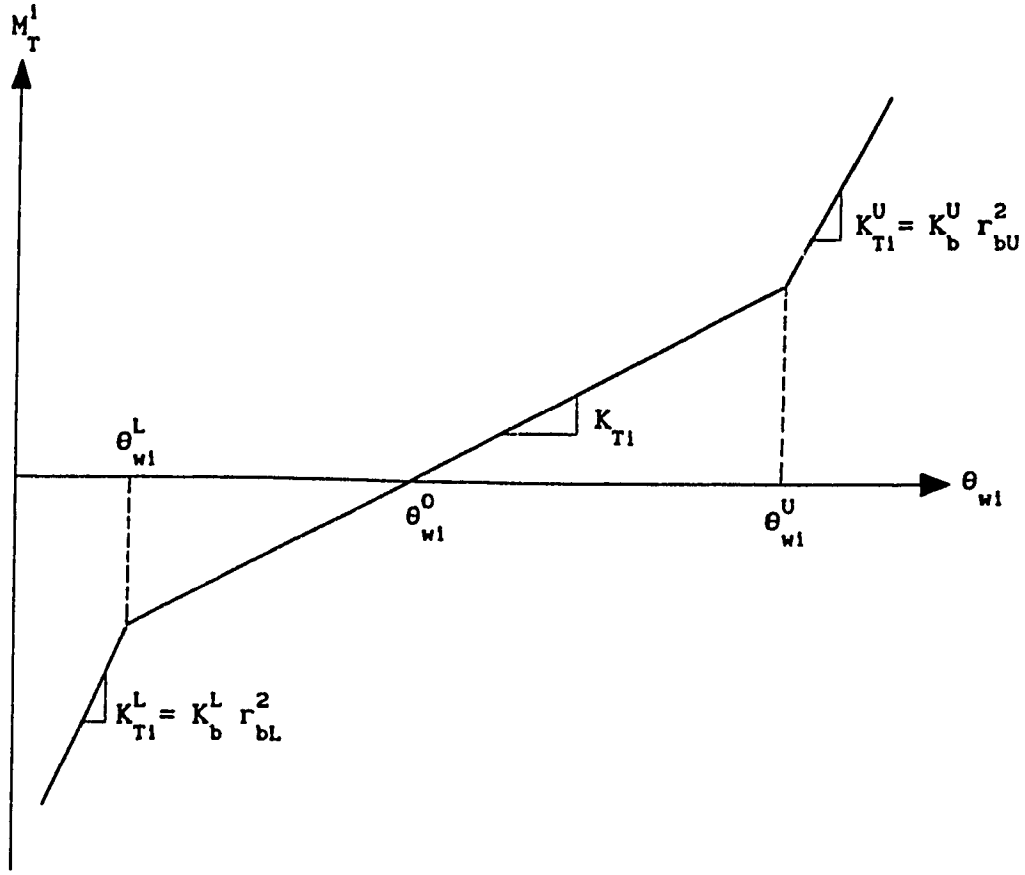

(b) Torsional spring characteristics

Figure 5.4 Torsion bar/trailing arm description.

Having modeled the forces due to the suspension components, the internal generalized forces for the specified degrees-of-freedom are thus obtained from equation (5.22) as:

$$Q_i^I = \begin{cases} 0 & ; i = 1,2 \\ F_S^1 \, d_1 + M_T^1 & ; i = i+2, \; i=1,\ldots,N \end{cases} \tag{5.33}$$

where,

$$d_1 = - \frac{S_{a1}(\Delta_{a1}\sin(\theta_{w1}+\xi_1) - \Delta_{b1}\cos(\theta_{w1}+\xi_1))}{|{}^D P_B|} \tag{5.34}$$

5.2.2 Equations of Motion

The equations of motion as derived based on equation (5.1) can be re-written in the form:

$$[\, \mathbf{M} \,]\{\, \ddot{\mathbf{q}} \,\} = \{\, \mathbf{F} \,\} \tag{5.35}$$

where, the elements of the mass matrix, **M**, can be directly obtained as:

$$m_{ij} = \frac{\partial^2 T}{\partial \dot{q}_i \partial \dot{q}_j} \tag{5.36}$$

Subsequently, the mass matrix is given as:

$$
[\,M\,]=\begin{bmatrix}
m_h+\sum_{i=1}^{N} m_{wi} & \sum_{i=1}^{N} m_{wi}[a_i C_\theta - b_i S_\theta + d_{xi}] & m_{w1}d_{x1} & \cdots & m_{wN}d_{xN} & 0 \\
 & I_h+\sum_{i=1}^{N} I_{wi}+m_{wi}[a_i^2+b_i^2+R_{ai}(R_{ai}-2c_i)] & I_{w1}+m_{w1}[R_{a1}(R_{a1}-c_1)] & \cdots & I_{wN}+m_{wN}[R_{aN}(R_{aN}-c_N)] & 0 \\
 & & I_{w1}+m_{w1}R_{a1}^2 & \cdots & 0 & 0 \\
 & \text{- SYMMETRIC -} & & \ddots & \vdots & \vdots \\
 & & & & I_{wN}+m_{wN}R_{aN}^2 & 0 \\
 & & & & & m_o
\end{bmatrix} \quad (5.37)
$$

(N+3 x N+3)

where, $c_i = a_i C_\theta^i + b_i S_\theta^i$

The vector of generalized coordinates q_i is given as:

$$\{ q \} = \{y_h,\ \theta_h,\ \theta_{w1},\ \ldots\ ,\theta_{wN}, y_o\}' \qquad (5.38)$$

where " ' " indicates the transpose.

The elements of the right-hand-side force vector **F** are given as:

$$F_i = Q_i - \sum_{j=1}^{N+2} \frac{\partial^2 T}{\partial \dot{q}_i \partial q_j}\dot{q}_j + \frac{\partial T}{\partial q_i} - \frac{\partial U}{\partial q_i} \qquad (5.39)$$

Thus, the vector **F** is written in its expanded form as:

$$\{F\}=\begin{Bmatrix} \sum_{i=1}^{N}(F^i_{wy}-W_{wi})+\sum_{k=1}^{2}F^k_{hy}-W_h+\sum_{i=1}^{N}m_{wi}[(a_iS_\theta+b_iC_\theta)\dot\theta_h^2+d_{yi}(\dot\theta_h+\dot\theta_{wi})^2] \\ \sum_{i=1}^{N}F^i_{wx}(a_iS_\theta+b_iC_\theta+d_{yi})+[F^i_{wy}-W_{wi}](a_iC_\theta-b_iS_\theta+d_{xi})+\sum_{k=1}^{2}F^k_{hx}(a_{hk}S_\theta+b_{hk}C_\theta) \\ \quad +F^k_{hy}(a_{hk}C_\theta-b_{hk}S_\theta)-\sum_{i=1}^{N}m_{wi}R_{ai}(a_iS^i_\theta-b_iC^i_\theta)(2\dot\theta_h+\dot\theta_{wi})\dot\theta_{wi} \\ F^1_{wx}d_{y1}+(F^1_{wy}-W_{w1})d_{x1}+F^1_S d_1+M^1_T+m_{w1}R_{a1}(a_1S^1_\theta-b_1C^1_\theta)\dot\theta_h^2 \\ \vdots \\ F^N_{wx}d_{yN}+(F^N_{wy}-W_{wN})d_{xN}+F^N_S d_N+M^N_T+m_{wN}R_{aN}(a_NS^N_\theta-b_NC^N_\theta)\dot\theta_h^2 \\ F_{so}+F_{do}-W_o \end{Bmatrix}_{(N+3\ x\ 1)} \tag{5.40}$$

5.2.3 Initialization

As discussed in section 2.7, the initialization phase sets up the zero-force reference, and computes initial generalized deflection vector using the iterative stiffness approach.

Vehicle's Zero-Force Configuration

The procedure for establishing zero-force reference for MODEL III is similar to the one devised for MODEL II (section 4.2.3), however, with slight modifications to account for trailing arm/torsion bar suspension system. The initial static value of the road arm angle is first computed as:

$$\theta^s_{wi} = \tan^{-1}\left[\frac{b_i - b_{wi}}{a_i - a_{wi}}\right] \tag{5.41}$$

where, the dimensional parameters a_i, b_i, and a_{wi} are the input, and b_{wi} is computed based on the settled height of the road wheel centre, h_{wi},

(equation 2.69), given as:

$$b_{wi} = \frac{h_{wi} - h_{cg} - a_i S_\theta}{C_\theta} \tag{5.42}$$

where $S_\theta = \sin(\theta_h^s)$, $C_\theta = \cos(\theta_h^s)$, and θ_h^s is the specified initial static angle of the hull chassis. The road arm angle corresponding to vehicle's zero-force configuration is then obtained as:

$$\theta_{wi}^o = \theta_{wi}^s - \delta_{\theta i} \tag{5.43}$$

where, the change in the road arm angle is expressed as:

$$\delta_{\theta i} = \frac{F_{si}^o \, d_{xi} + T_{wx}^i \, d_{yi}}{K_{Ti}} \tag{5.44}$$

where, $d_{xi} = -R_{ai}\cos(\theta_h^s + \theta_{wi}^s)$, $d_{yi} = -R_{ai}\sin(\theta_h^s + \theta_{wi}^s)$

and F_{si}^o is given in equation (2.70). The equivalent linear deflection, Δ_i^o, for computing the hull bounce displacement, y_h^o (equation 2.73), and pitch angle, θ_h^o (equation 2.74), and thus establishing the vehicle's zero-force configuration, is obtained as:

$$\Delta_i^o = d_{xi} \, \delta_{\theta i} \tag{5.45}$$

Vehicle Settlement - Static Equilibrium

As before, an iterative stiffness approach (section 2.6) is employed for establishing vehicle's static equilibrium, and to compute the corresponding initial generalized defelection vector. Consequently, the procedure is the same, however, the governing equation (2.79) is modified in view of the stiffness matrix and applied static force vector.

The stiffness matrix as being a function of generalized displacements

obtained in the $(i\text{-}1)^{th}$ step of the iterative procedure is given as:

$$[K_{i-1}]=\begin{bmatrix} -(K_o+\sum_{i=1}^{N}K_{wi}) & -(K_o a_o+\sum_{i=1}^{N}K_{wi}a_{wi}) & -K_{w1}V_1 \;\; \ldots . -K_{wN}V_N & K_o \\ -(K_o a_o+\sum_{i=1}^{N}K_{wi}a_{wi}) & -(K_o a_o^2+\sum_{i=1}^{N}K_{wi}a_{wi}^2) & -K_{w1}V_1 a_{w1} \ldots . -K_{wN}V_N a_{wN} & K_o a_o \\ -K_{w1}d_{x1} & -K_{w1}d_{x1}a_{w1} & K_{w1}V_1 d_{x1} - \ldots . \; 0 & 0 \\ & & K_{T1}-K_1 S_{a1} d_1 & \\ \vdots & \vdots & \vdots \quad\quad \vdots & \vdots \\ -K_{wN}d_{xN} & -K_{wN}d_{xN}a_{wN} & 0 \quad\quad K_{wN}V_N d_{xN} - & 0 \\ & & K_{TN}-K_N S_{aN} d_N & \\ K_o & K_o a_o & 0 \quad\quad 0 & -K_o \end{bmatrix} \tag{5.46}$$

where, $a_{wi} = a_i + d_{xi}$, $V_i = d_{yi} / \theta_{wi}$

and $d_{xi} \cong -R_{ai}C^i_\theta$, $d_{yi} \cong -R_{ai}S^i_\theta$ (since $\theta_h \ll \theta_{wi}$)

K_o is the spring constant for seat suspension obtained from equation (2.81), and K_{wi} is the spring constant for the i^{th} road wheel/track pad evaluated using equation (2.83). K_i is the spring constant for the inclined suspension unit associated with the i^{th} road wheel-road arm assembly, obtained as:

$$K_i = \text{Spring Force @ } \Delta_i \;/\; \Delta_i \;\; ; \;\; \text{where } \Delta_i = S_{ai}(\theta^0_{wi} - \theta_{wi}) \tag{5.47}$$

Simialrly, K_{Ti} is the spring constant for i^{th} torsion bar obtained as:

$$K_{Ti} = M^i_T \;/\; (\theta_{wi} - \theta^0_{wi}) \tag{5.48}$$

The applied force vector F_a is given as:

$$\{ F_a \} = \begin{Bmatrix} W_h - \sum_{k=1}^{2} F_{hy}^{k} - \sum_{i=1}^{N} W_{wi} - T_{wy}^{1} + \kappa_{w1}(Y_{cg}^{0} + b_1 - R_{w1}) \\ -M_a + \sum_{i=1}^{N} [W_{wi} - T_{wy}^{1} + \kappa_{w1}(Y_{cg}^{0} + b_i - R_{w1})]d_{x1} - T_{wx}^{1} d_{y1} \\ -T_{wx}^{1} d_{y1} + [W_{w1} - T_{wy}^{1} + \kappa_{w1}(Y_{cg}^{0} + b_1 - R_{w1})]d_{x1} - \kappa_{T1}\theta_{w1}^{0} - \kappa_1 S_{a1} d_1 \theta_{w1}^{0} \\ \vdots \\ -T_{wx}^{N} d_{yN} + [W_{wN} - T_{wy}^{N} + \kappa_{wN}(Y_{cg}^{0} + b_N - R_{wN})]d_{xN} - \kappa_{TN}\theta_{wN}^{0} - \kappa_N S_{aN} d_N \theta_{wN}^{0} \\ W_o \end{Bmatrix} \quad (5.49)$$

5.3 FIELD VALIDATION OF MODEL III

In this section, ride response predictions for the field-tested vehicle are evaluated using MODEL III, and validated against field measurements. Details regarding the input data required for simulation, and field validation results are presented as below.

The physical data describing the field-tested vehicle is listed in Table 3.4, where the specified parameters are in accordance with the description of MODEL I and II. However, additional input information is required to describe MODEL III in light of the parameters associated with the description of torsion bar/trailing arm suspension system. Table 5.1 lists the dimensional parameters, where the horizontal distances for road wheel centres (a_{wi}'s) are same as the distances specified for the hull-suspension attachement points (a_i's) in Table 3.4. The mass of the road arm-road wheel assembly (m_{wi}) is given in Table 3.4, whereas I_{wi} is taken as 5 kg.m^2. The torsion bar characteristics are provided in Table 5.2. In parallel with torsional spring, torsional damping is introduced as a frictional damping torque of magnitude of 150 (N.m.s/rad). The force-velocity characteristics of the inclined shock absorber mounted at the

Table 5.1 Additional dimensional parameters required for MODEL III [69].

Description	*Symbol*	*Vehicle Configuration*	
		Laden	*Unladen*
Horizontal distance from c.g. to:			
Road wheel # 1, m	a_{w1}	1.407	1.327
Road wheel # 2, m	a_{w2}	0.734	0.654
Road wheel # 3, m	a_{w3}	0.084	0.004
Road wheel # 4, m	a_{w4}	-0.599	-0.679
Road wheel # 5, m	a_{w5}	-1.267	-1.347
Torsion bar # 1, m	a_1	1.699	1.619
Torsion bar # 2, m	a_2	1.026	0.946
Torsion bar # 3, m	a_3	0.376	0.296
Torsion bar # 4, m	a_4	-0.307	-0.387
Torsion bar # 5, m	a_5	-0.975	-1.055
Shock absorber # 1,m	a_{s1}	1.167	1.087
Shock absorber # 2,m	a_{s2}	0.494	0.414
Shock absorber # 3,m	a_{s3}	-0.156	-0.236
Shock absorber # 4,m	a_{s4}	-0.839	-0.919
Shock absorber # 5,m	a_{s5}	-1.545	-1.625
Vertical distance from c.g. to:			
Torsion bars, m	$b_{i\ i=1..5}$	-0.482	-0.514
Shock absorbers, m	b_{si}	-0.382	-0.414
Road arm length, m	R_{al}	0.317	0.317
Arm overhang length, m	S_{al}	0.284	0.284
Overhang angle, deg	ξ_{al}	39.0	39.0

NOTE: The field-tested vehicle has shock absorbers mounted at first and last road wheel stations only, and intermediate shock absorbers are only considered for parameteric study presented in the following sections.

first and fifth road wheel station are shown by the solid curve in Figure 3.17.

The overall structure of the computational procedure adopted for MODEL III is similar to the one described in section 2.5. The undamped natural frequencies and associated deflection modes, predicted based on converged stiffness matrix, are listed in Table 5.3 for specified test vehicle configurations. The natural frequencies corresponding to the bounce and pitch modes are slightly lower in comparison with the ones listed in Table 3.5 (MODEL I). The rotational modes associated with road arm-road wheel assemblies are active between 9-10 Hz.

The computer simulation of the field-tested vehicle are performed for all test conditions. The performance of MODEL III is thus assessed based on the direct comparison of measured and predicted acceleration traces associated with the seat bounce, hull bounce and pitch, and rotation of road arm-road wheel assemblies, and corresponding spectra, rms values and average absorbed power. As before, discussions on the field validation results are provided in view of specific type of test course.

Discrete Half Round Obstacles

Figure 5.5 and 5.6 illustrate direct comparsion between measured and simulated acceleration traces for the test vehicle configuration B traversing 6" obstacle at 14.3 km/h. It should be noted that the damping coefficient characterizing energy dissipation due to road wheel/track-terrain interaction (C^{i}_{rw} i=1,..,N) was considered equal to zero for the simulation run. As evident from the simulated traces, there are fluctuations of high magnitudes associated with the angular motion of the road arm-road wheel assemblies (Figure 5.6), especially the intermediate

Table 5.2 Torsion bar characteristics [69].

Description	*Symbol*	*Value*
Torsion bar spring rate, N.m/rad	K_{Ti} (i=1..5)	9884
Equivalent torsional spring rate for bump stops, N.m/rad	K^{U}_{Ti}, K^{L}_{Ti}	133520
Radial clearance for upper bump stop, deg	θ^{U}_{wi}	46.0
Radial clearance for lower bump stop, deg	θ^{L}_{wi}	0.0

Table 5.3 Natural frequencies and associated deflection modes (MODEL III).

Undamped Natural Frequencies (Hz)				Dominant Deflection Mode
Test Vehicle Configuration				
A	B	C	D	
1.539	1.699	1.702	1.694	y_h
1.163	1.196	1.199	1.189	θ_h
9.253	8.971	9.071	8.778	θ_{w1}
9.606	9.401	9.387	9.346	θ_{w2}
9.522	9.313	9.303	9.254	θ_{w3}
9.460	9.249	9.244	9.184	θ_{w4}
9.110	8.834	8.929	8.648	θ_{w5}

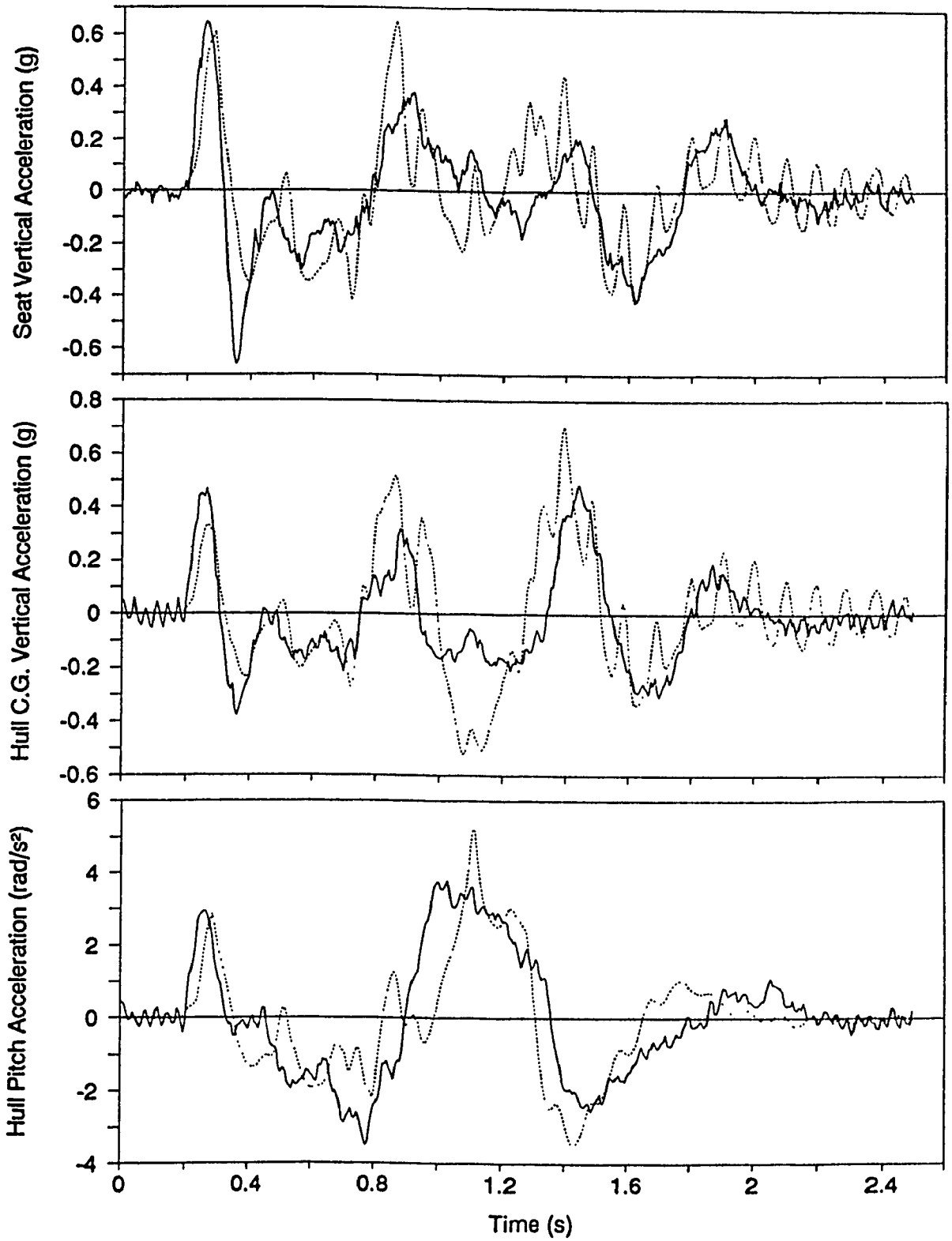

Figure 5.5 Ride acceleration traces - field validation of MODEL III's predictions for test vehicle configuration B traversing 6" obstacle at 14.3 km/h - C^{i}_{rw} = 0.0 N.s/m (i = 1,..,5)

(——— Field Test, ... Simulation).

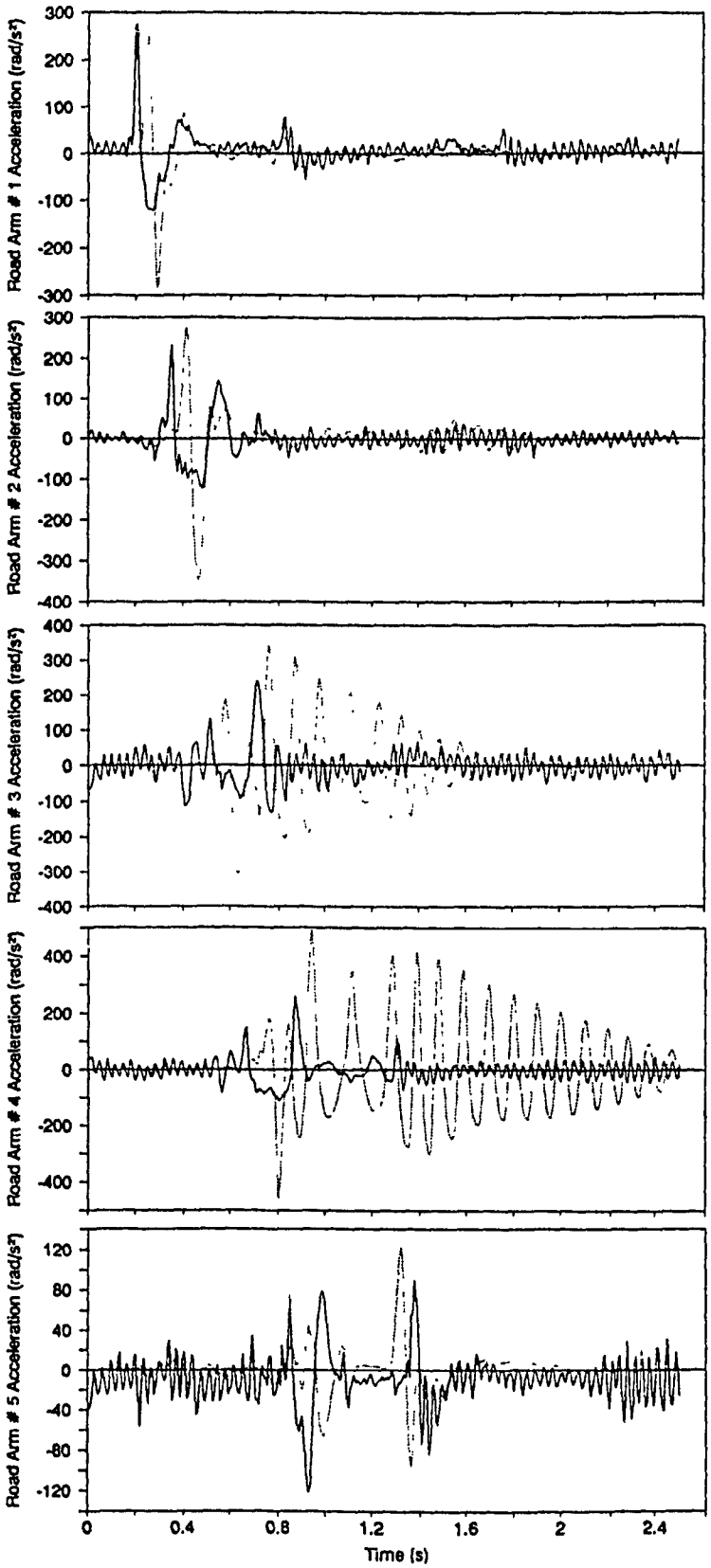

Figure 5.6 Road arm acceleration traces - field validation of MODEL III's predictions for test vehicle configuration B traversing 6" obstacle at 14.3 km/h - C'_{rw} = 0.0 N.s/m (i = 1,..,5)

(——— Field Test, ····· Simulation).

ones due to absence of shock absorbers. These may be attributed to the lack of energy dissipation at the road wheel/track-terrain interface. Consequently, a number of simulation runs were made with gradually incremented values of C^{i}_{rw} so that the predicted angular acceleration traces of intermediate road arm-road wheel assemblies exhibit reasonably good correlation with the test data. Subsequently, a base value of 5 kN.s/m was selected and used for forth-coming simulations. Figure 5.7 and 5.8 exhibit the field validation of re-evaluated acceleration traces. As expected, the introduction of damping has smoothened the ride acceleration traces, and road arm acceleration traces exhibit better correlation with the test data. In comparison with the ride acceleration traces evaluated using MODEL II (Figure 4.13), the traces in Figure 5.7 exhibit relatively smoother ride as a consequence of the modeling of the trailing arm suspension system. The trailing arm suspension model allows the road wheel to swing back upon impact with the obstacle, thus reducing the severity of the impact considerably. Figure 5.9 presents animated snapshots of the test vehicle negotiating the obstacle, which, indeed, provide a clear picture of the swing movements of the road arm-road wheel assemblies.

Figure 5.10 and 5.11 demonstrate direct comparison between measured and predicted acceleration traces for the test vehicle configuration B traversing 6" obstacle at 20 km/h, whereas Figure 5.12 shows ride acceleration traces for a speed of 29 km/h. The MODEL III's ride predictions for a higher speed, as shown in Figure 5.12, exhibit relatively higher levels of acceleration in comparison with the ones evaluated using MODEL II (Figure 4.15), and closer correlation with test data.

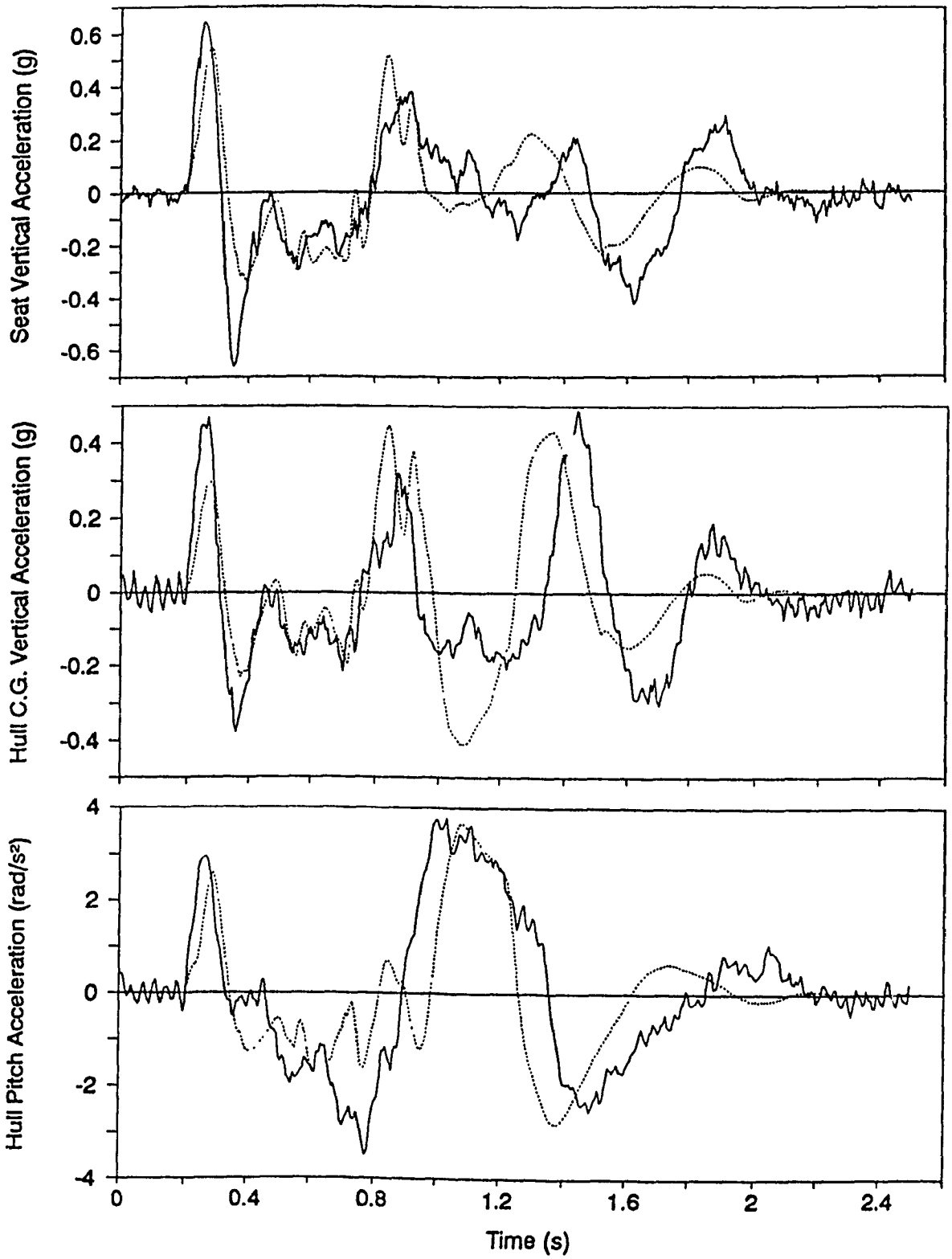

Figure 5.7 Ride acceleration traces - field validation of MODEL III's predictions for test vehicle configuration B traversing 6" obstacle at 14.3 km/h - C^{i}_{rw} = 5.0 kN.s/m (i = 1,..,5)

(——— Field Test, ····· Simulation).

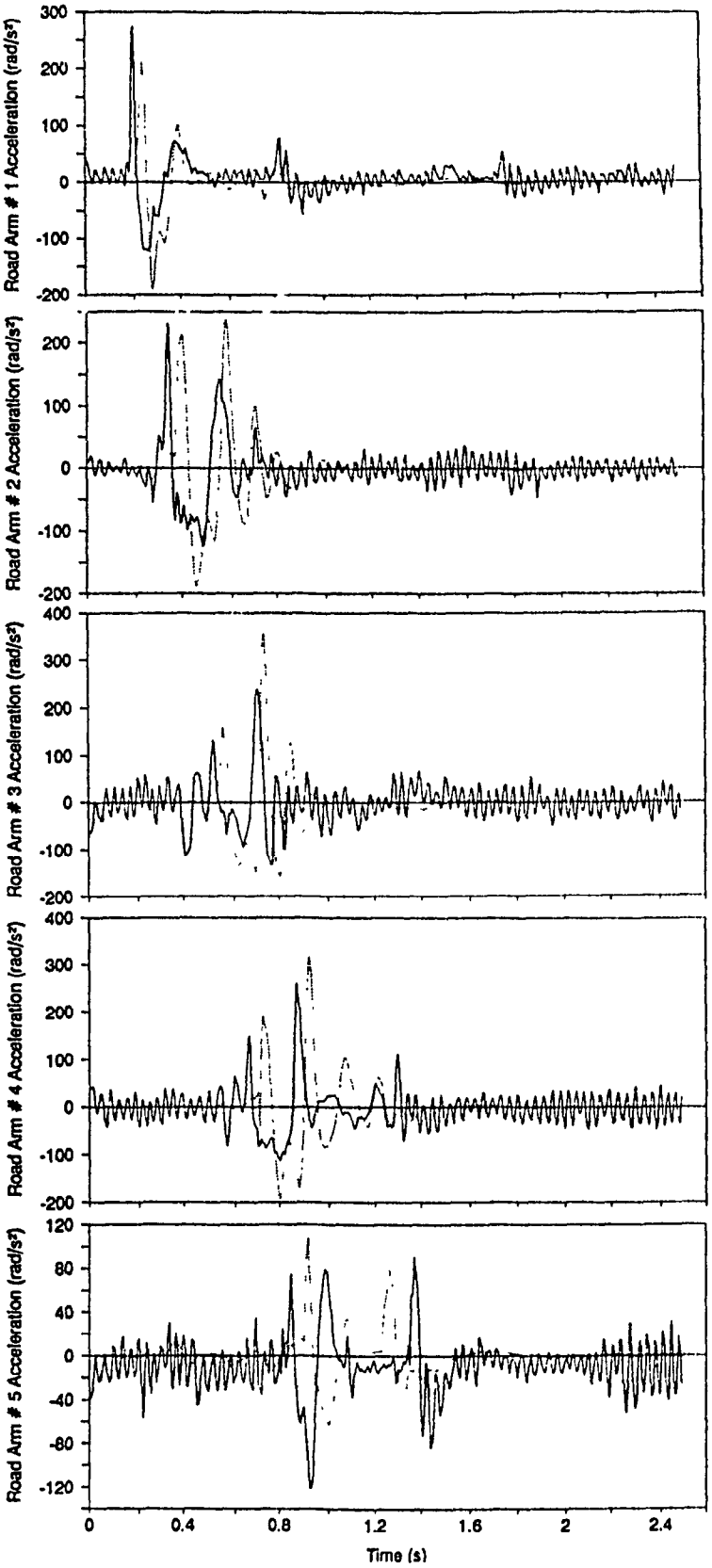

Figure 5.8 Road arm acceleration traces - field validation of MODEL III's predictions for test vehicle configuration B traversing 6" obstacle at 14.3 km/h - C^{i}_{rw} = 5.0 N.s/m (i = 1,..,5)

(——— Field Test, ... Simulation).

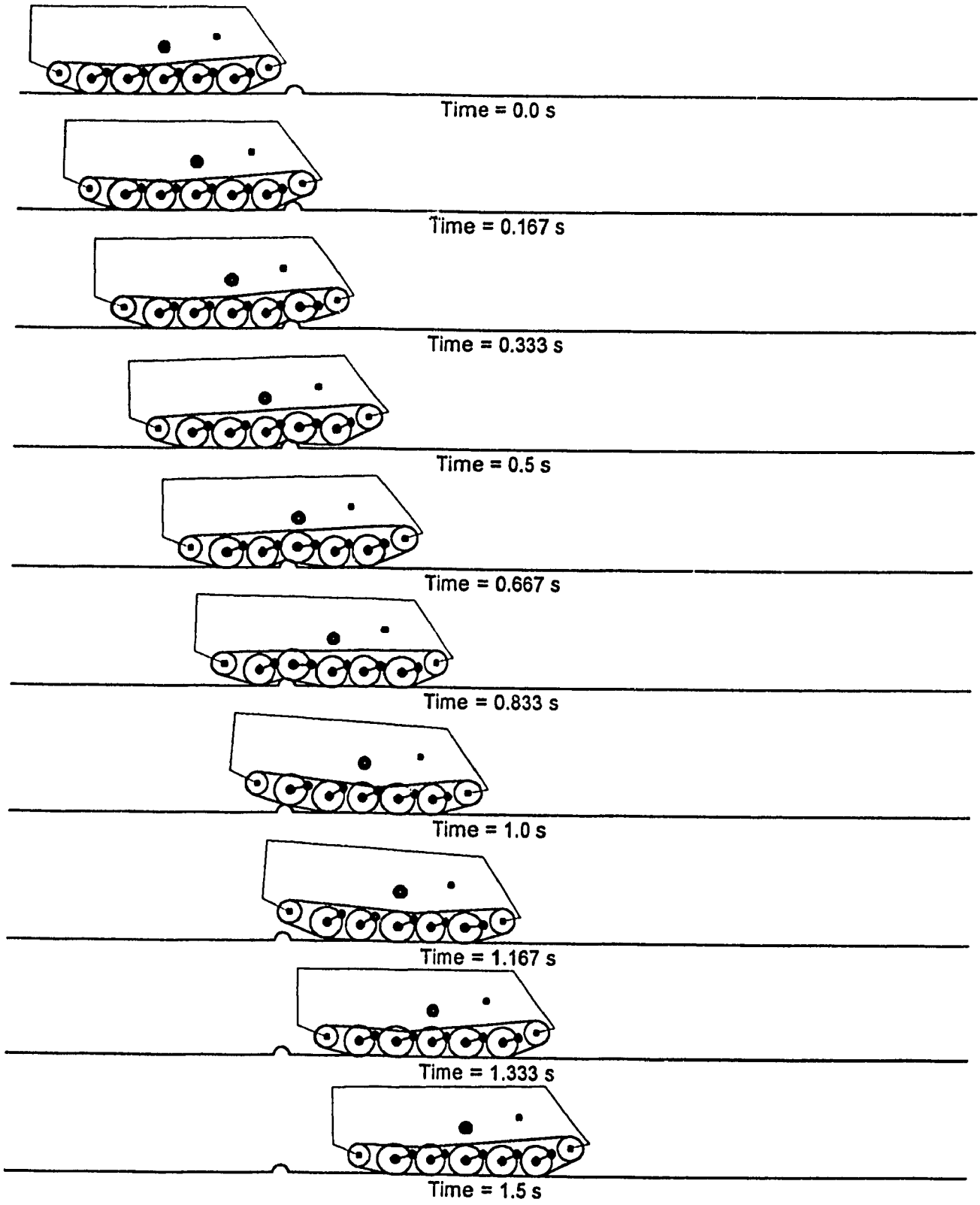

Figure 5.9 Animated snapshots of test vehicle configuration B traversing 6" half round obstacle at 14.3 km/h

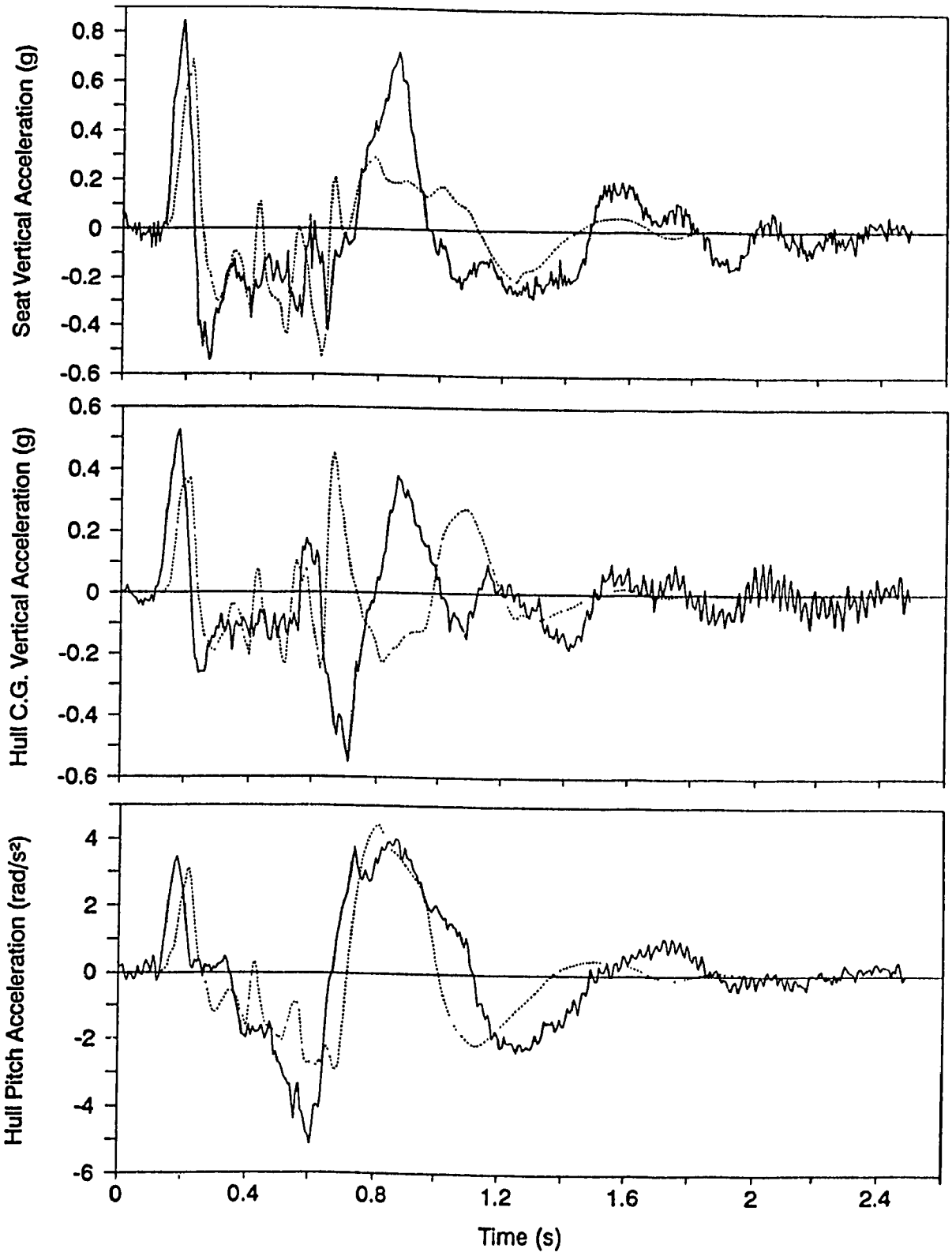

Figure 5.10 Ride acceleration traces - field validation of MODEL III's predictions for test vehicle configuration B traversing 6" obstacle at 20 km/h (——— Field Test, ... Simulation).

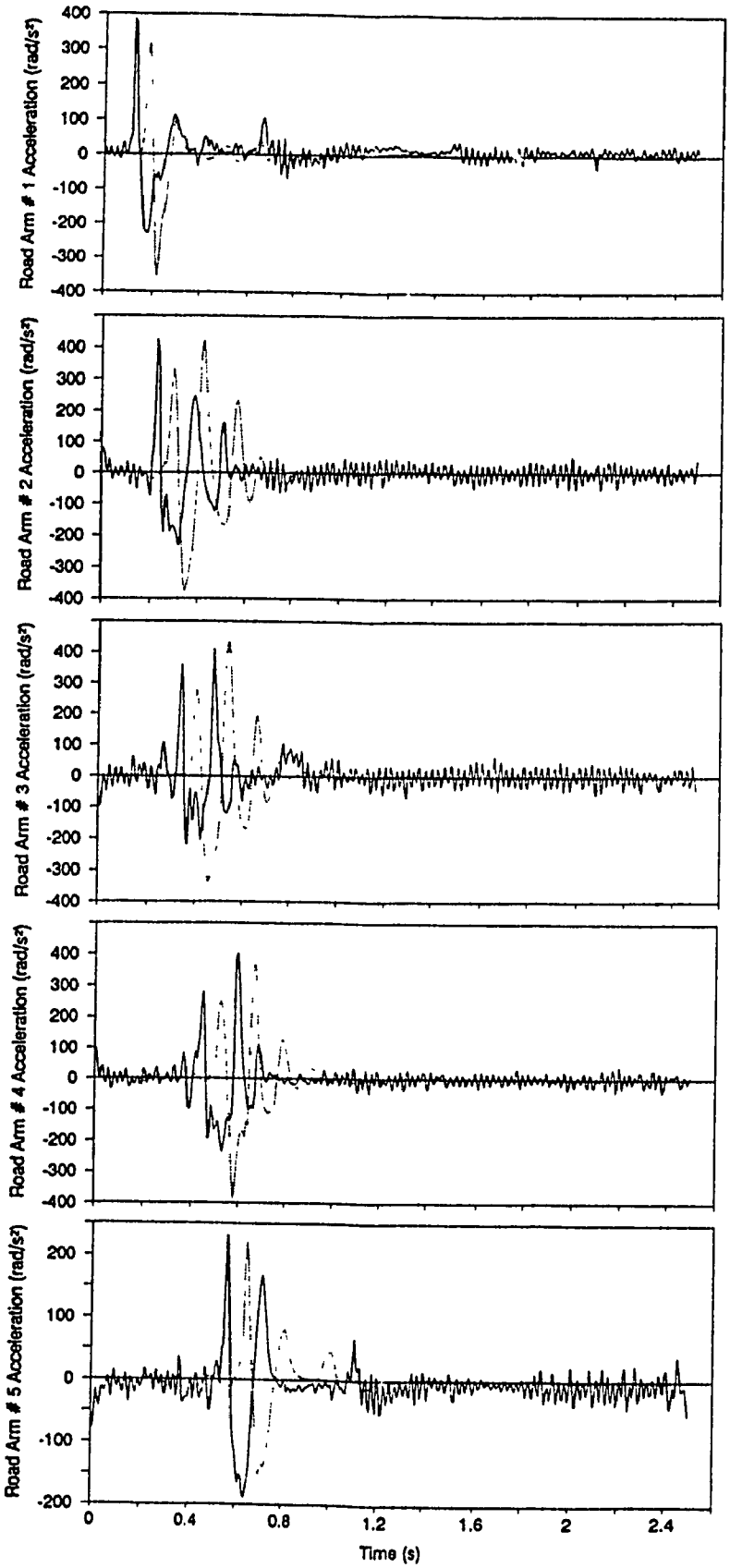

Figure 5.11 Road arm acceleration traces - field validation of MODEL III's predictions for test vehicle configuration B traversing 6" obstacle at 20 km/h (——— Field Test, ... Simulation).

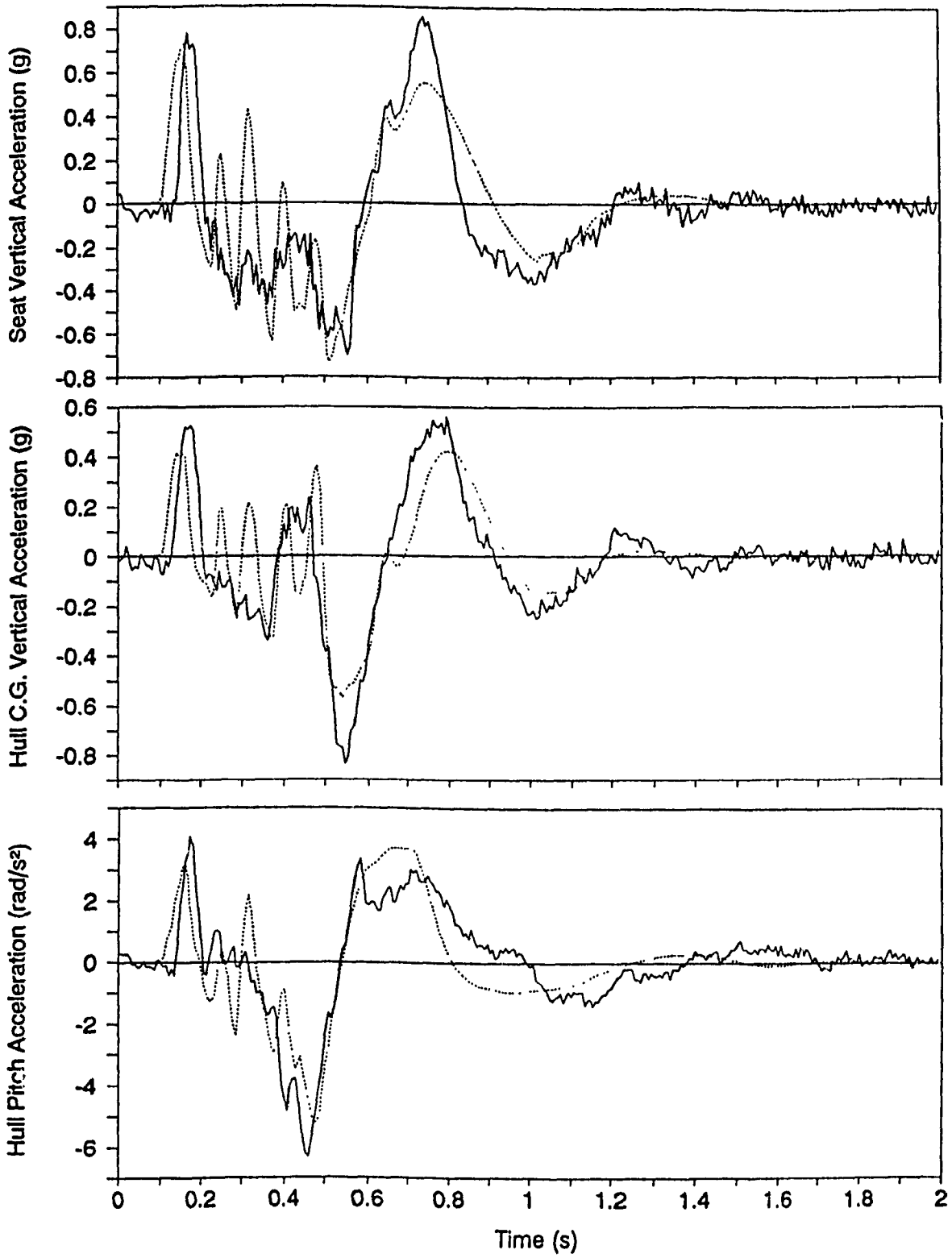

Figure 5.12 Ride acceleration traces - field validation of MODEL III's predictions for test vehicle configuration B traversing 6" obstacle at 29 km/h (——— Field Test, ····· Simulation).

The ride responses are evaluated for the test vehicle crossing 6" obstacle with low and high track pre-tension settings, and superimposed on the measured ones. Figures 5.13 to 5.15 demonstrate field validation of MODEL III's ride predictions for test vehicle configuration C crossing the obstacle at 14.9 km/h, 22.2 km/h, and 28.2 km/h. In comparison with MODEL II's predictions as shown in Figures 4.16 and 4.17, the simulated traces in Figures 5.13 and 5.14 exhibit relatively closer correlation. Figures 5.16 to 5.18 illustrate the direct comparison of MODEL III's ride predictions with measured data for test vehicle configuration D traversing 6" obstacle at 15.4 km/h, 22.5 km/h, and 28.5 km/h. As shown, the MODEL III's ride predictions show good agreement with the test data. It is demonstrated by both measured and predicted results that the specified variations in the track pre-tension settings do not have significant influence on the ride acceleration levels.

The acceleration traces for test vehicle configuration B crossing 8" obstacle at 7.7 km/h, 12.7 km/h, and 18.9 km/h are evaluated using MODEL III, and superimposed on the measured ones as shown in Figures 5.19 to 5.21. A closer examination of these results with the ones evaluated using MODEL II (shown in Figures 4.21 to 4.23) reveal that MODEL III predicts relatively closer, which is undoubtedly achieved as a consequence of the detailed representation of the vehicle suspension system. Figure 5.22 exhibit comparison between measured and simulated acceleration traces associated with angular motion of road arm-road wheel assemblies for a speed of 18.9 km/h.

The field validation of MODEL III's ride predictions for discrete half round obstacles (6" and 8") is summarized in Tables 5.4 and 5.5, where measured and predicted values associated with the absolute peak

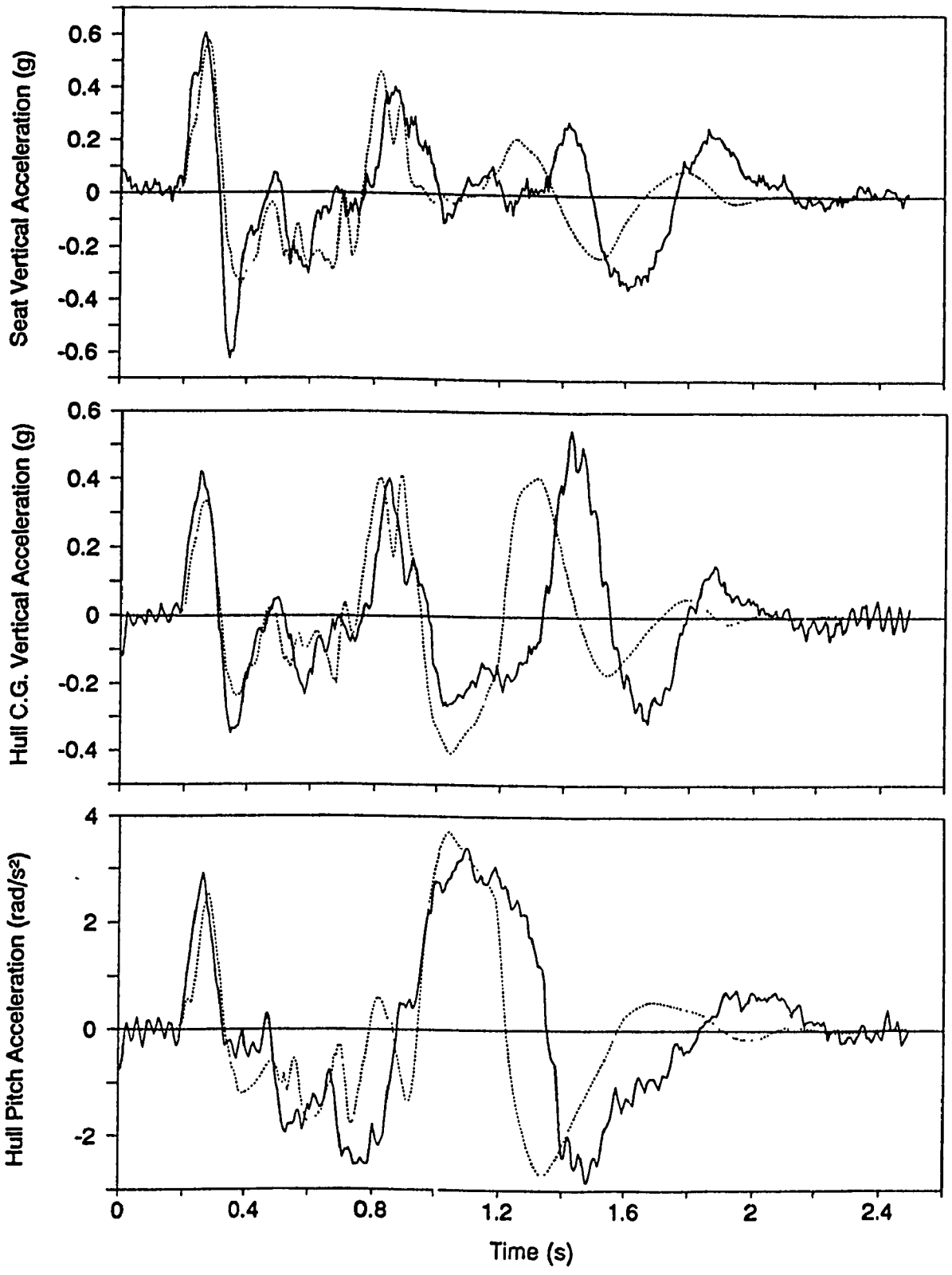

Figure 5.13 Ride acceleration traces - field validation of MODEL III's predictions for test vehicle configuration C traversing 6" obstacle at 14.9 km/h (——— Field Test, ····· Simulation).

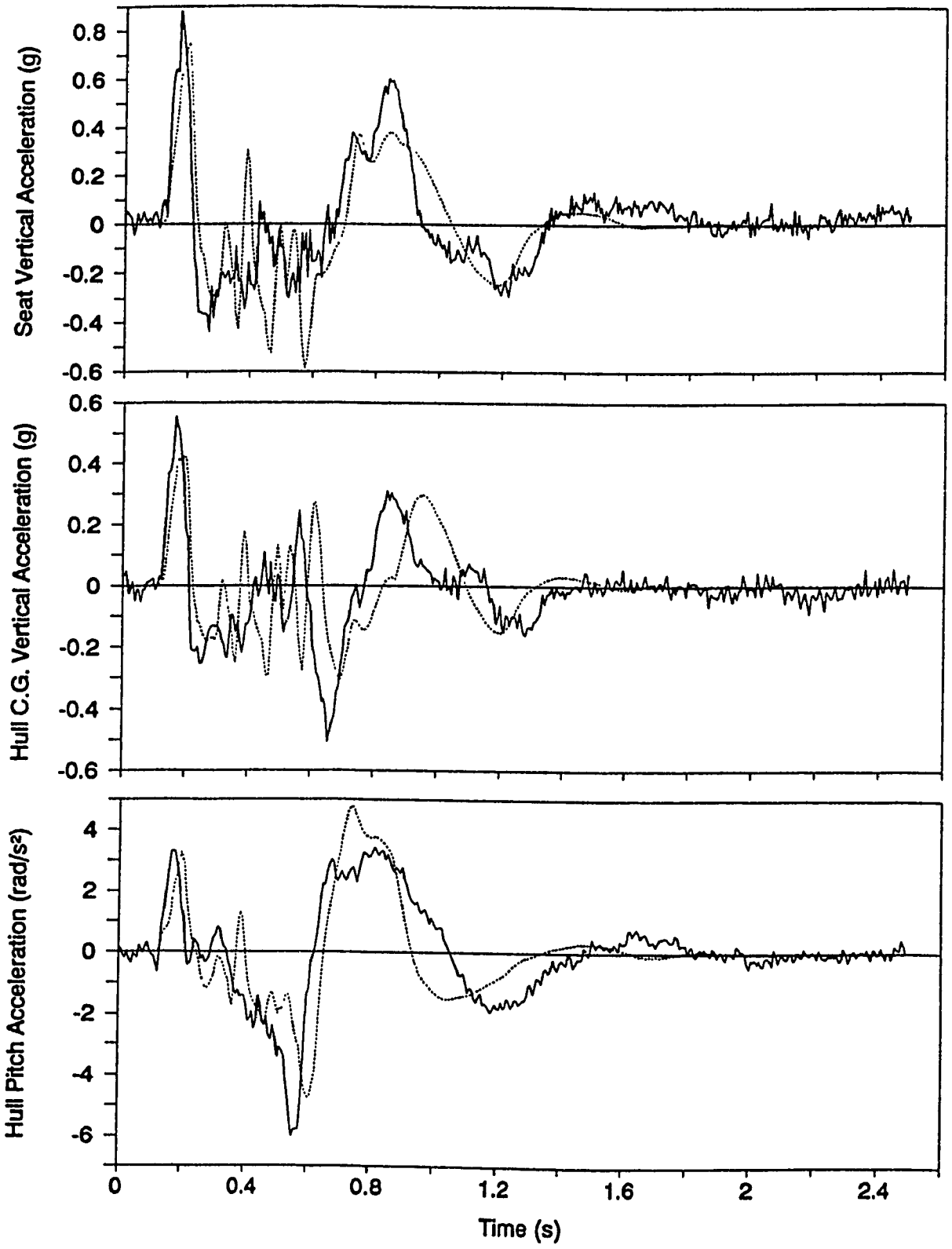

Figure 5.14 Ride acceleration traces - field validation of MODEL III's predictions for test vehicle configuration C traversing 6" obstacle at 22.2 km/h (——— Field Test, ... Simulation).

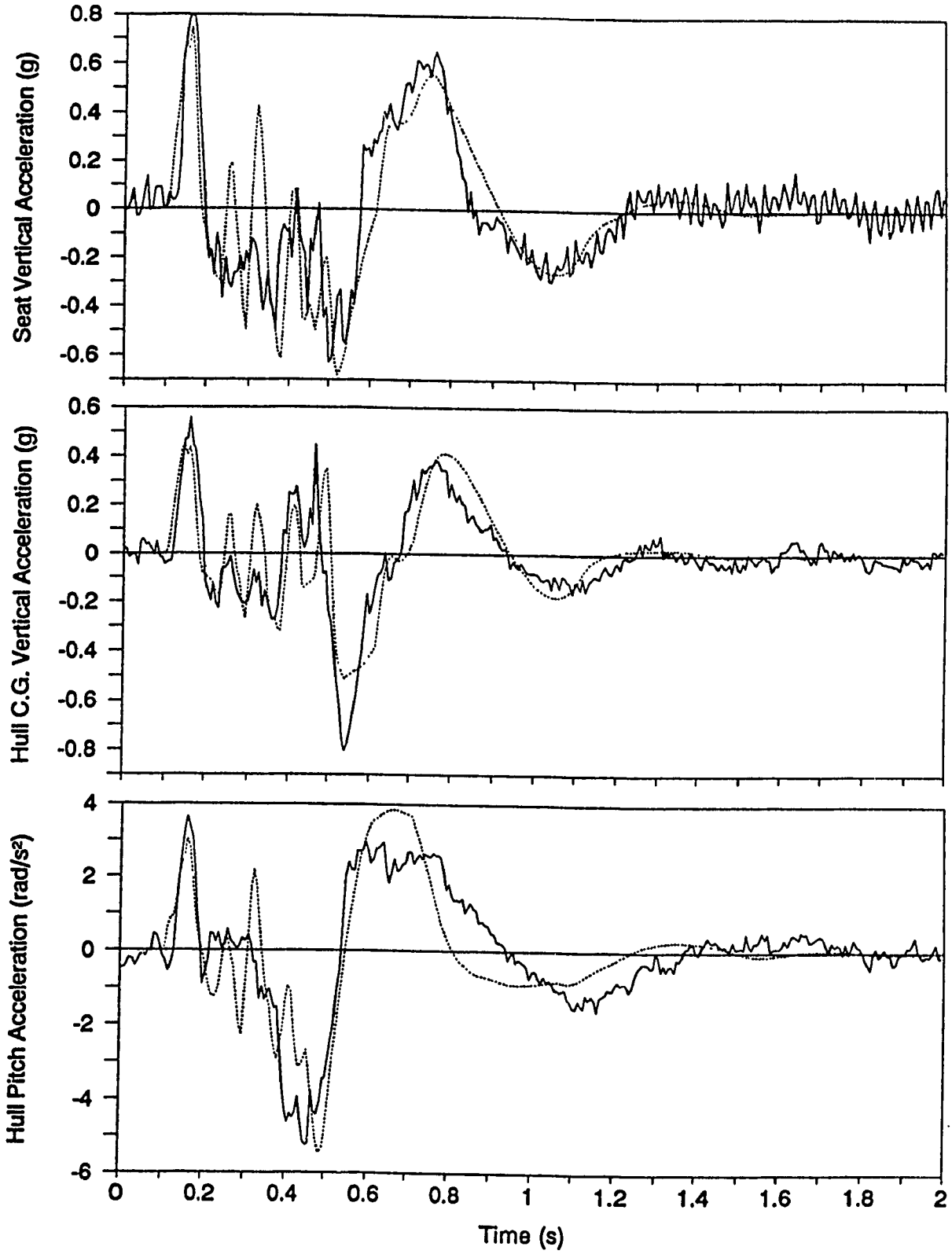

Figure 5.15 Ride acceleration traces - field validation of MODEL III's predictions for test vehicle configuration C traversing 6" obstacle at 28.2 km/h (——— Field Test, ... Simulation).

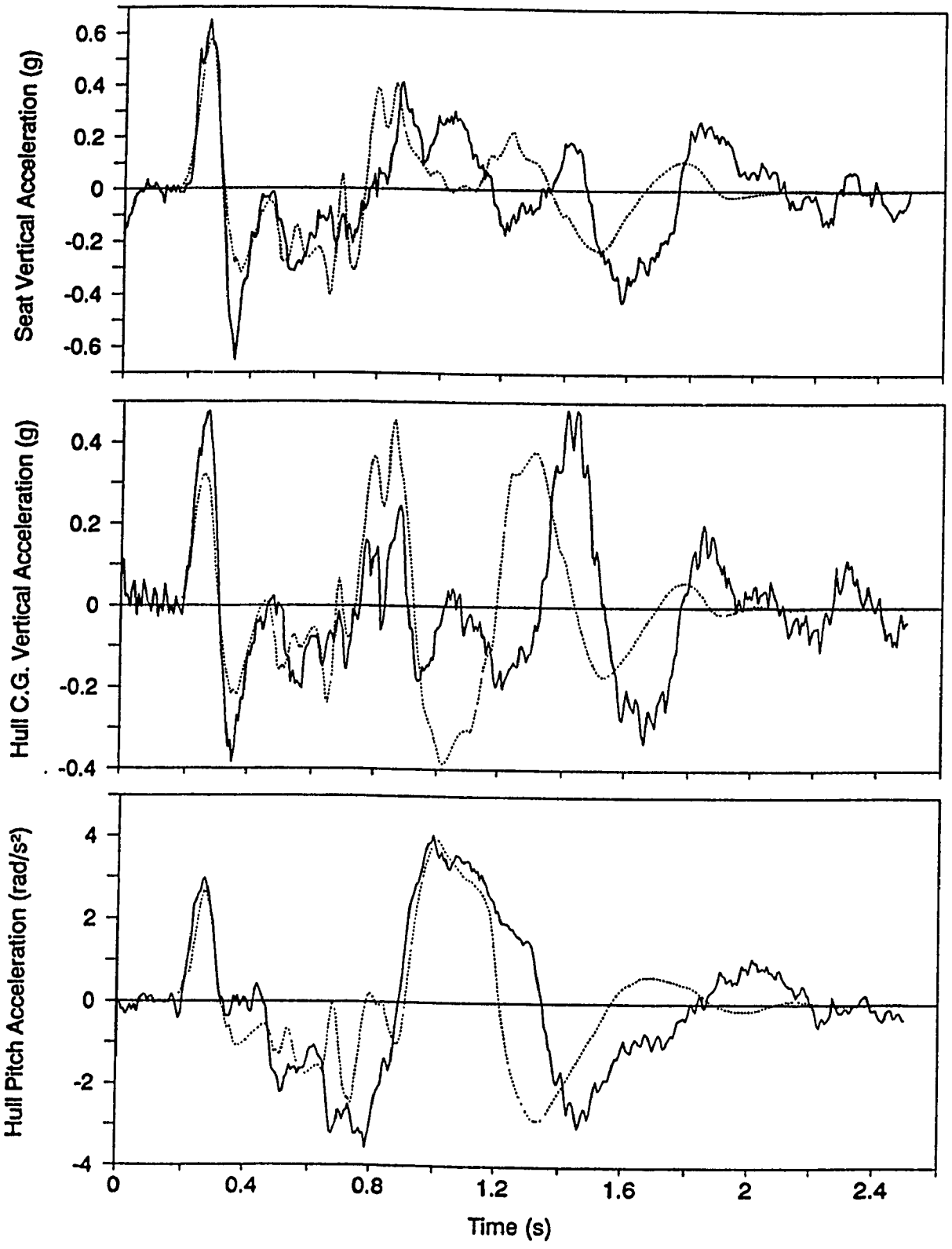

Figure 5.16 Ride acceleration traces - field validation of MODEL III's predictions for test vehicle configuration D traversing 6" obstacle at 15.4 km/h (——— Field Test, ... Simulation).

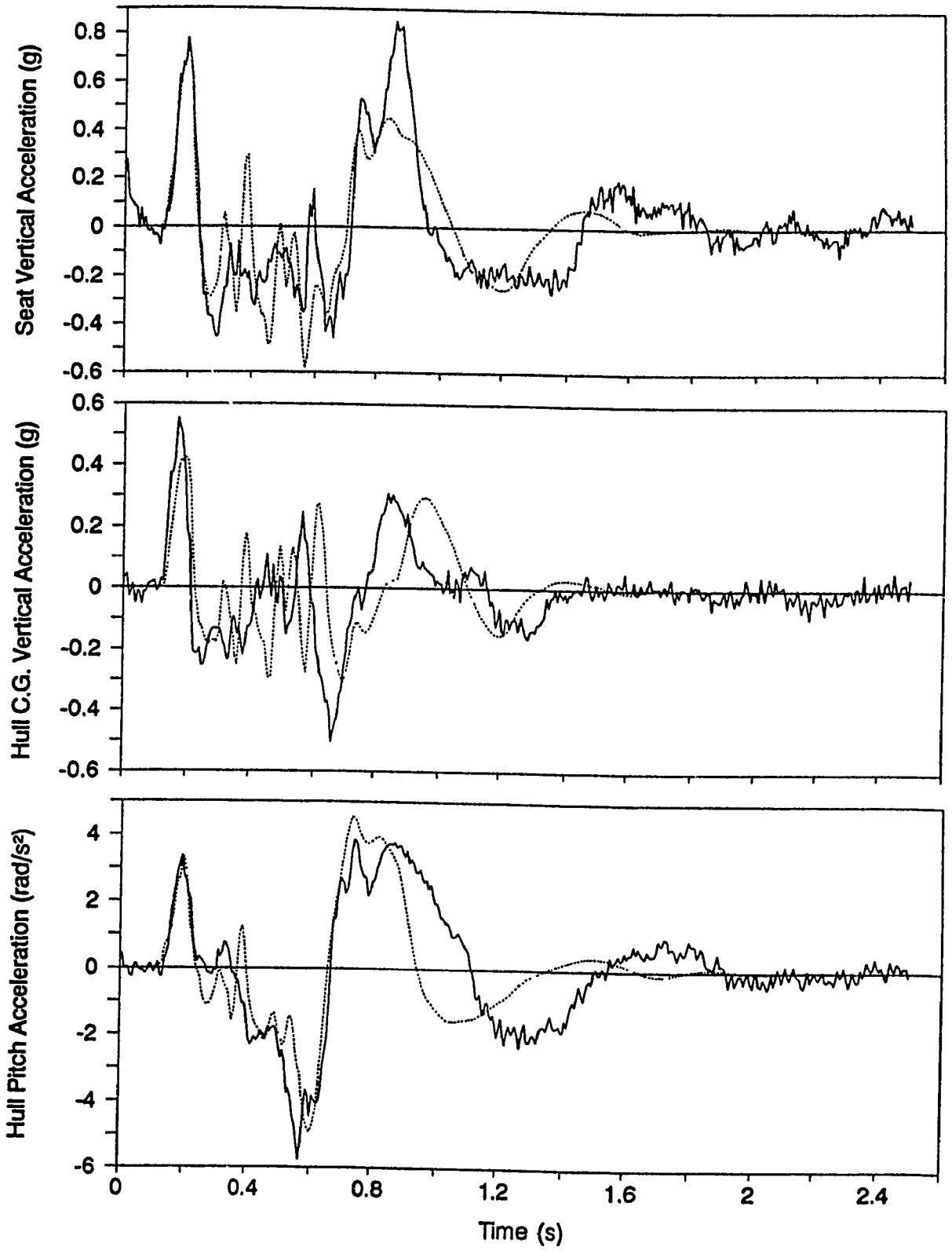

Figure 5.17 Ride acceleration traces - field validation of MODEL III's predictions for test vehicle configuration D traversing 6" obstacle at 22.5 km/h (——— Field Test, ... Simulation).

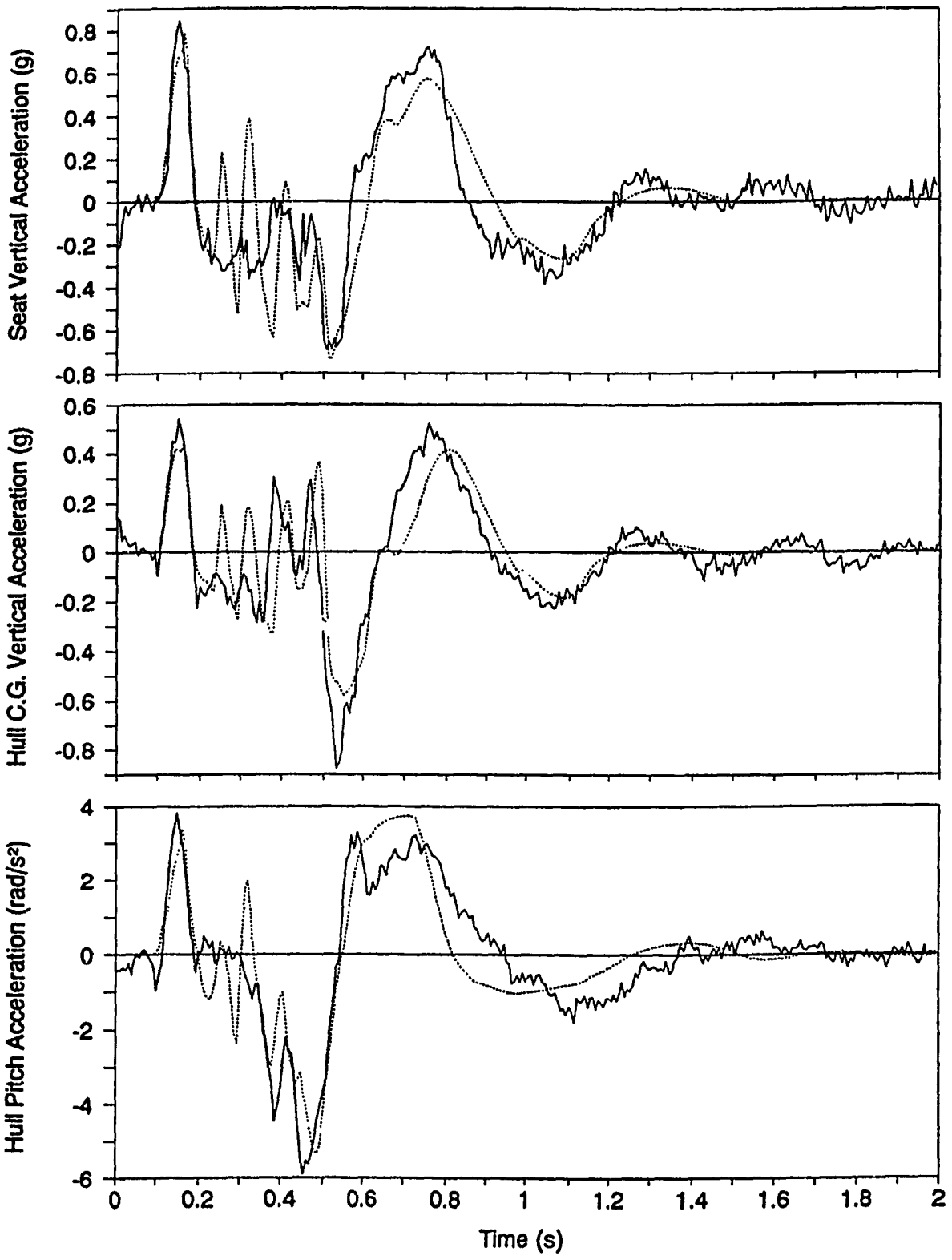

Figure 5.18 Ride acceleration traces - field validation of MODEL III's predictions for test vehicle configuration D traversing 6" obstacle at 28.5 km/h (——— Field Test, ... Simulation).

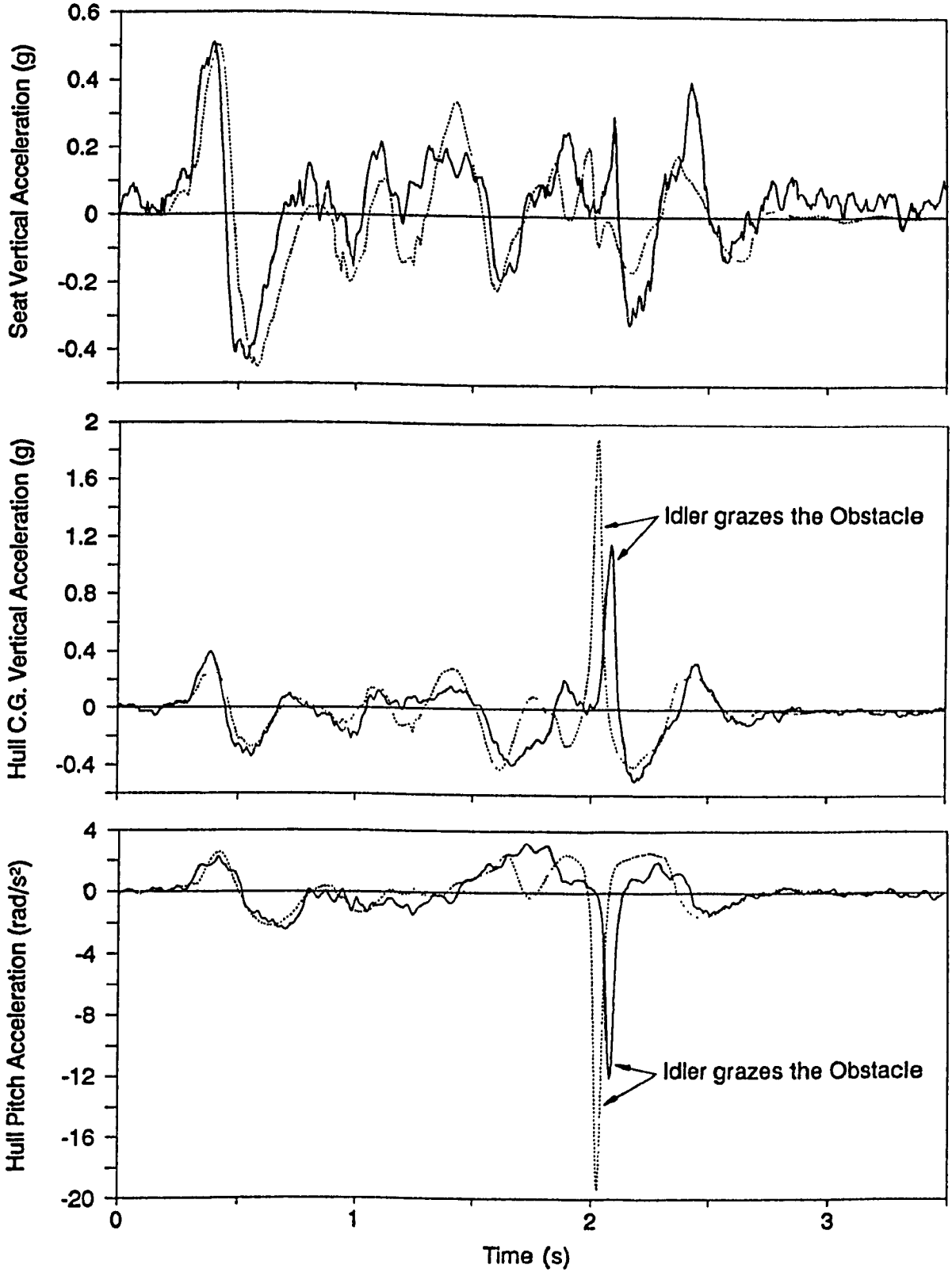

Figure 5.19 Ride acceleration traces - field validation of MODEL III's predictions for test vehicle configuration B traversing 8" obstacle at 7.8 km/h (——— Field Test, ... Simulation).

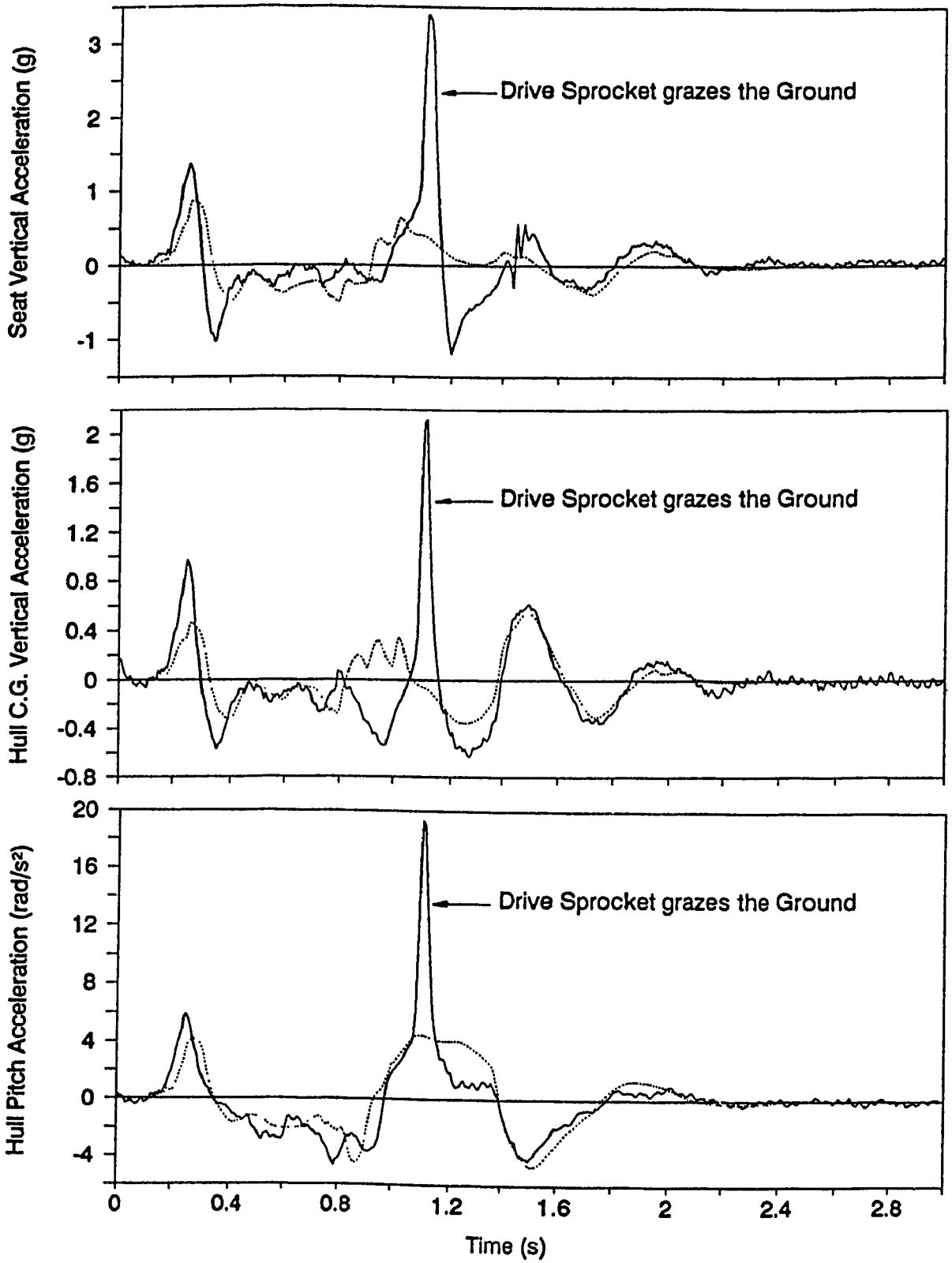

Figure 5.20 Ride acceleration traces - field validation of MODEL III's predictions for test vehicle configuration B traversing 8" obstacle at 12.8 km/h (——— Field Test, ... Simulation).

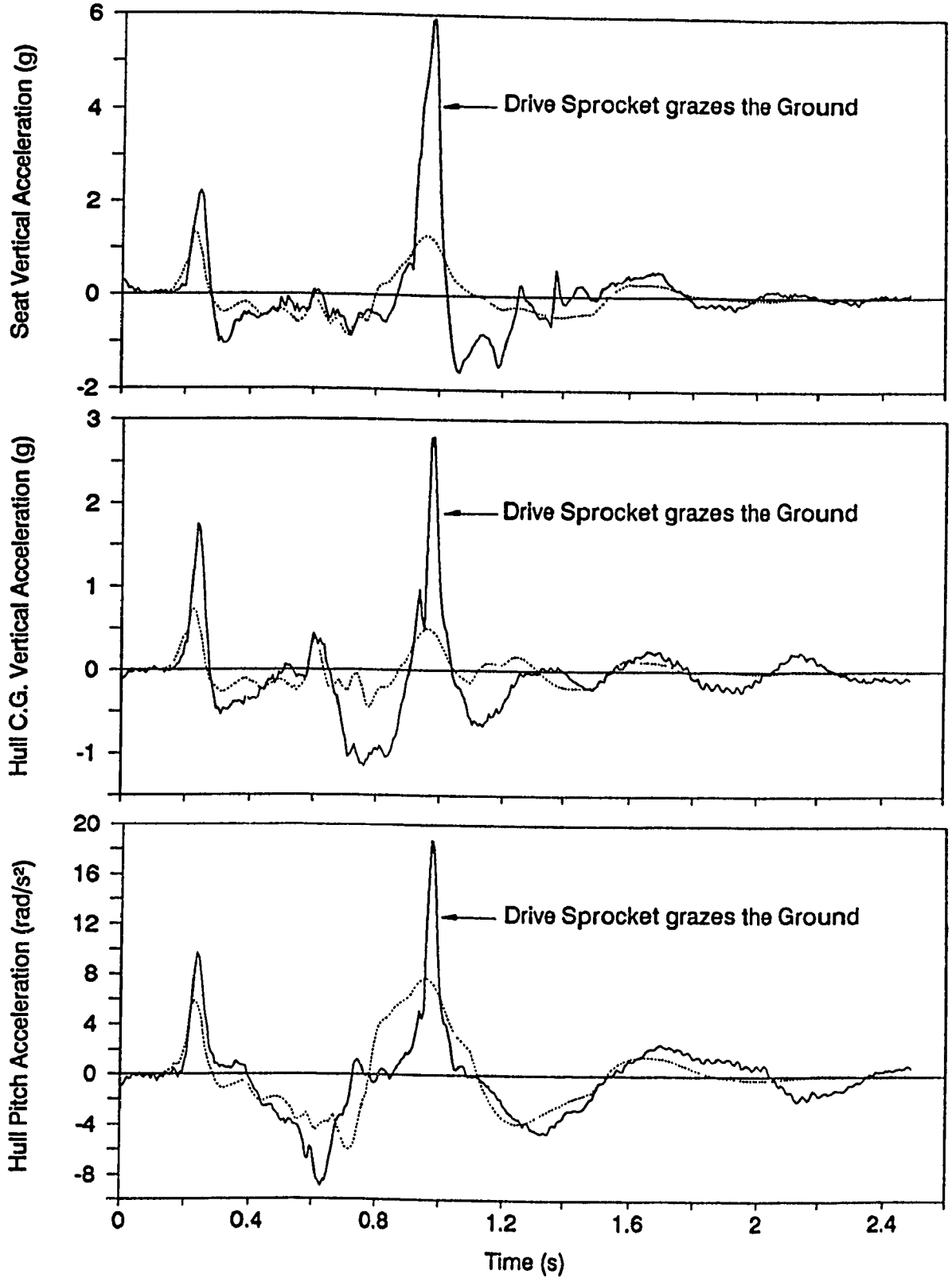

Figure 5.21 Ride acceleration traces - field validation of MODEL III's predictions for test vehicle configuration B traversing 8" obstacle at 18.9 km/h (——— Field Test, ... Simulation).

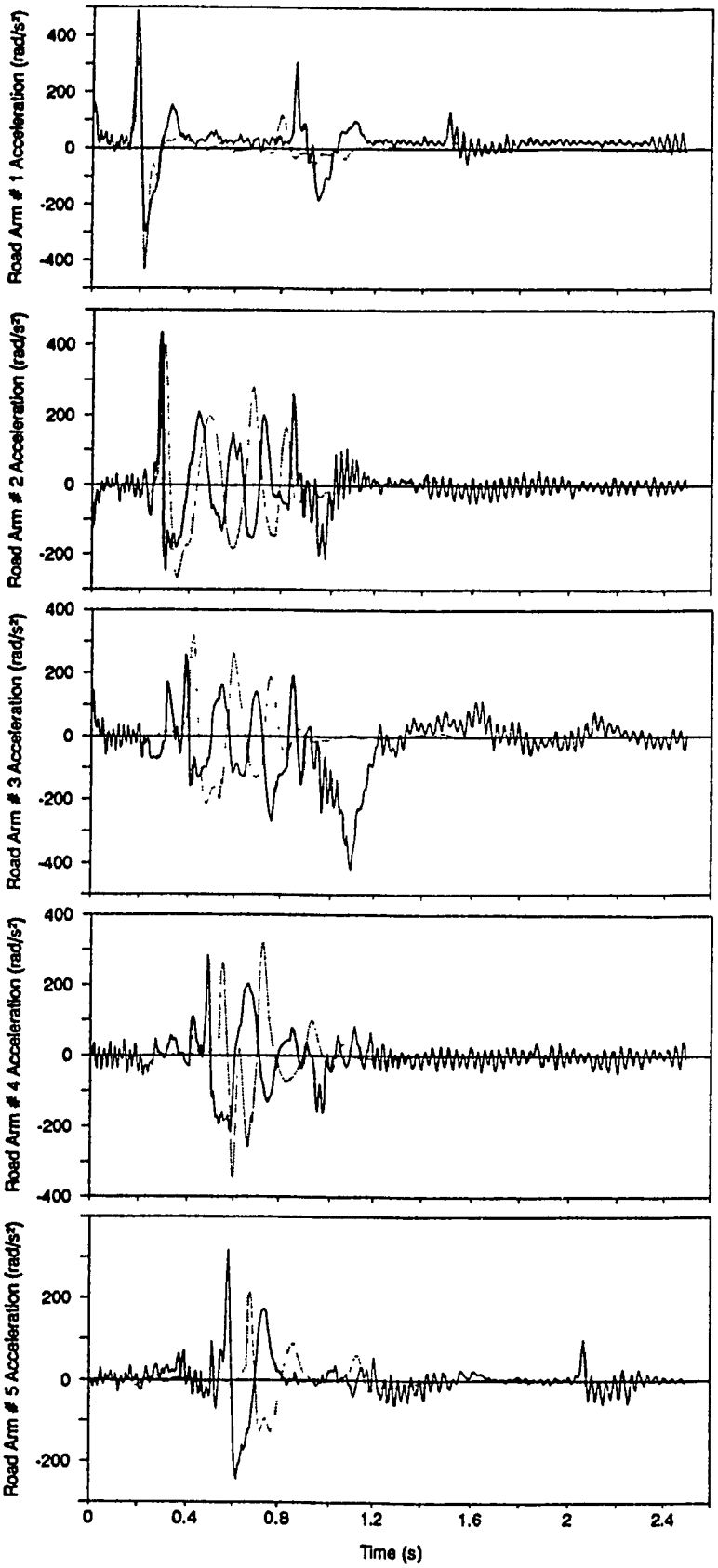

Figure 5.22 Road arm acceleration traces - field validation of MODEL III's predictions for test vehicle configuration B traversing 8" obstacle at 18.9 km/h (——— Field Test, ····· Simulation).

Table 5.4 Field validation of MODEL III (6" half round obstacle).

Test Condition		Peak (g)*/rms (g)*/rms (rad/s^2)**		Error (%) = $\left\lvert\frac{PV - MV}{MV}\right\rvert$ x100
Vehicle Configuration	Speed (km/h)	Measured Values (MV)	Predicted Values (PV)	
B	14.3	0.660/0.197/1.60	0.583/0.175/1.45	11.7/11.2/9.4
	20.0	0.847/0.230/1.75	0.705/0.180/1.50	16.8/21.7/14.3
	29.0	0.859/0.280/1.59	0.735/0.254/1.55	14.4/9.3/2.5
C	14.9	0.624/0.188/1.48	0.584/0.164/1.32	6.4/12.8/10.8
	22.2	0.884/0.198/1.55	0.752/0.192/1.49	14.9/3.0/3.9
	28.2	0.797/0.249/1.58	0.745/0.247/1.54	6.5/0.8/2.5
D	15.4	0.654/0.201/1.70	0.582/0.162/1.41	11.0/19.4/17.0
	22.5	0.852/0.239/1.73	0.764/0.201/1.54	10.3/15.9/11.0
	28.5	0.848/0.275/1.63	0.789/0.263/1.57	6.9/4.4/3.7

(* Seat vertical acceleration, ** Hull pitch acceleration)

Table 5.5 Field validation of MODEL III (8" half round obstacle).

Test Condition		Peak (g)*/rms (g)*/rms (rad/s^2)**		Error (%) = $\left\lvert\frac{PV - MV}{MV}\right\rvert$ x100
Vehicle Configuration	Speed (km/h)	Measured Values (MV)	Predicted Values (PV)	
B	7.7	0.510/0.161/1.55	0.505/0.155/2.10	1.0/3.7/35.5
	12.8	3.39†/0.506/2.69	0.874/0.240/2.07	74.2/52.5/23.0
	18.9	5.94†/0.930/3.25	1.32/0.393/2.72	77.8/57.7/16.3

(† Drive sprocket hit the ground)

value (g) found in the seat vertical acceleration trace, its rms value (g), and the rms value of the hull pitch acceleration trace (rad/s^2), and respective percentage errors are listed.

Sinusoidal Course:

In this section, MODEL III's ride predictions for field-tested vehicle subjected to sinusoidal course at various speeds or excitation frequencies ($f = V_x/\lambda$) are validated against measured data. Figures 5.23 and 5.24 demonstrate samples of measured and predicted ride acceleration traces for test vehicle configurations A and B traversing the course at 6.7 km/h (f = 2.44 Hz). In comparison with MODEL II's predictions (Figures 4.24 and 4.25), the simulated traces in Figures 5.23 and 5.24 exhibit relatively lower acceleration levels, and closer correlation with the measured ones. Table 5.6 summarizes the comparison between measured and predicted rms values associated with seat vertical and pitch acceleration traces for all test conditions. As demonstrated by both field testing and simulation, the maximum rms values of seat vertical acceleration for vehicle configurations A and B occurs at 1.71 Hz (4.7 Km/h) and 1.9 Hz (5.4 km/h), respectively. The predicted rms levels of pitch acceleration are consistently higher in comparison with the measured ones.

LETE48 *Random Course*:

For LETE48 random course, a large number of field tests were conducted using all four test vehicle configurations (A,B,C, and D), and atleast four speeds for each vehicle configuration (Chapter 3). Subsequently, the test vehicle is simulated for all these test conditions using MODEL III. For example, Figure 5.25 presents measured and predicted ride

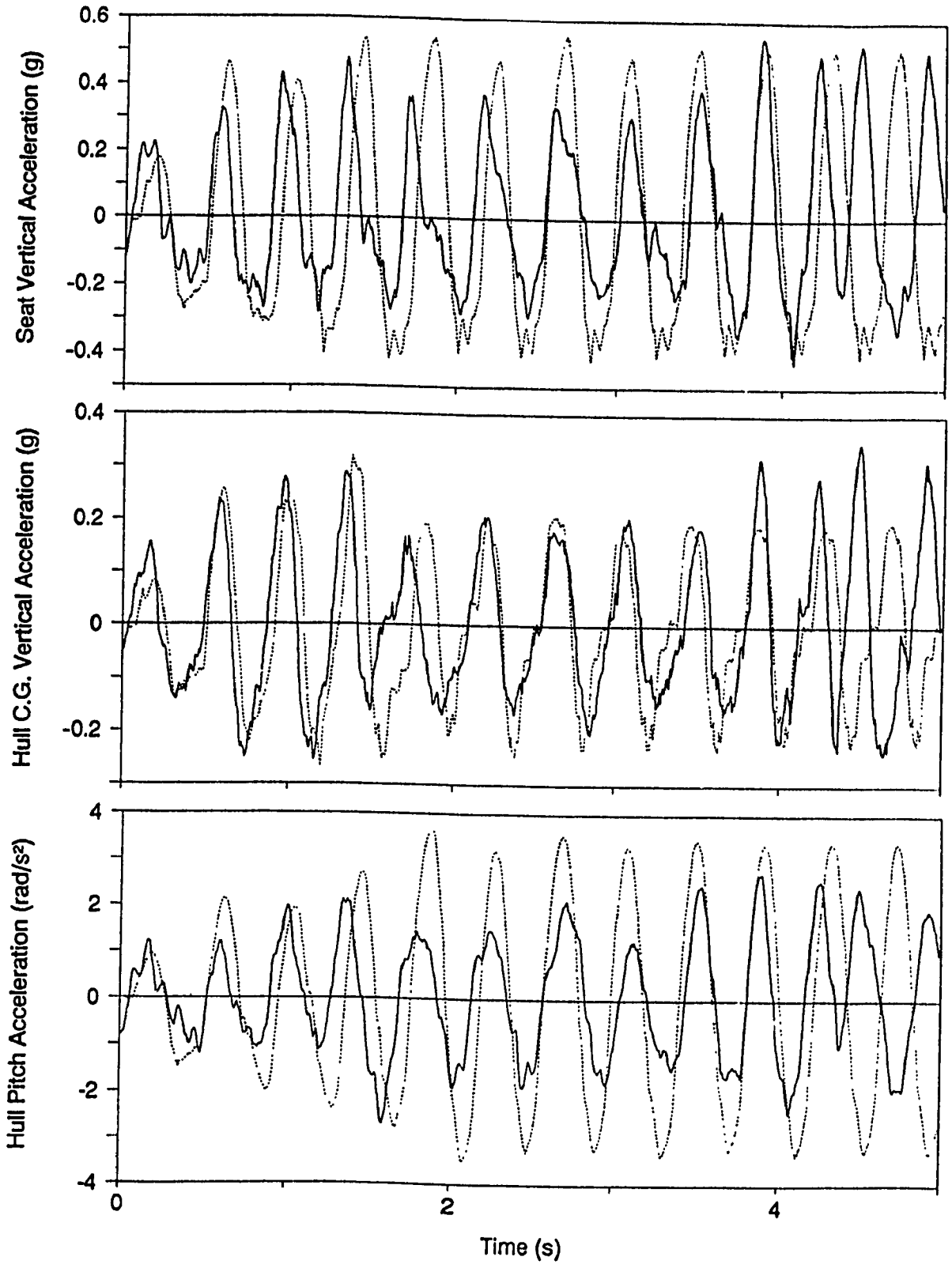

Figure 5.23 Ride acceleration traces - field validation of MODEL III's predictions for test vehicle configuration A traversing sine course at 6.7 km/h (——— Field Test, ... Simulation).

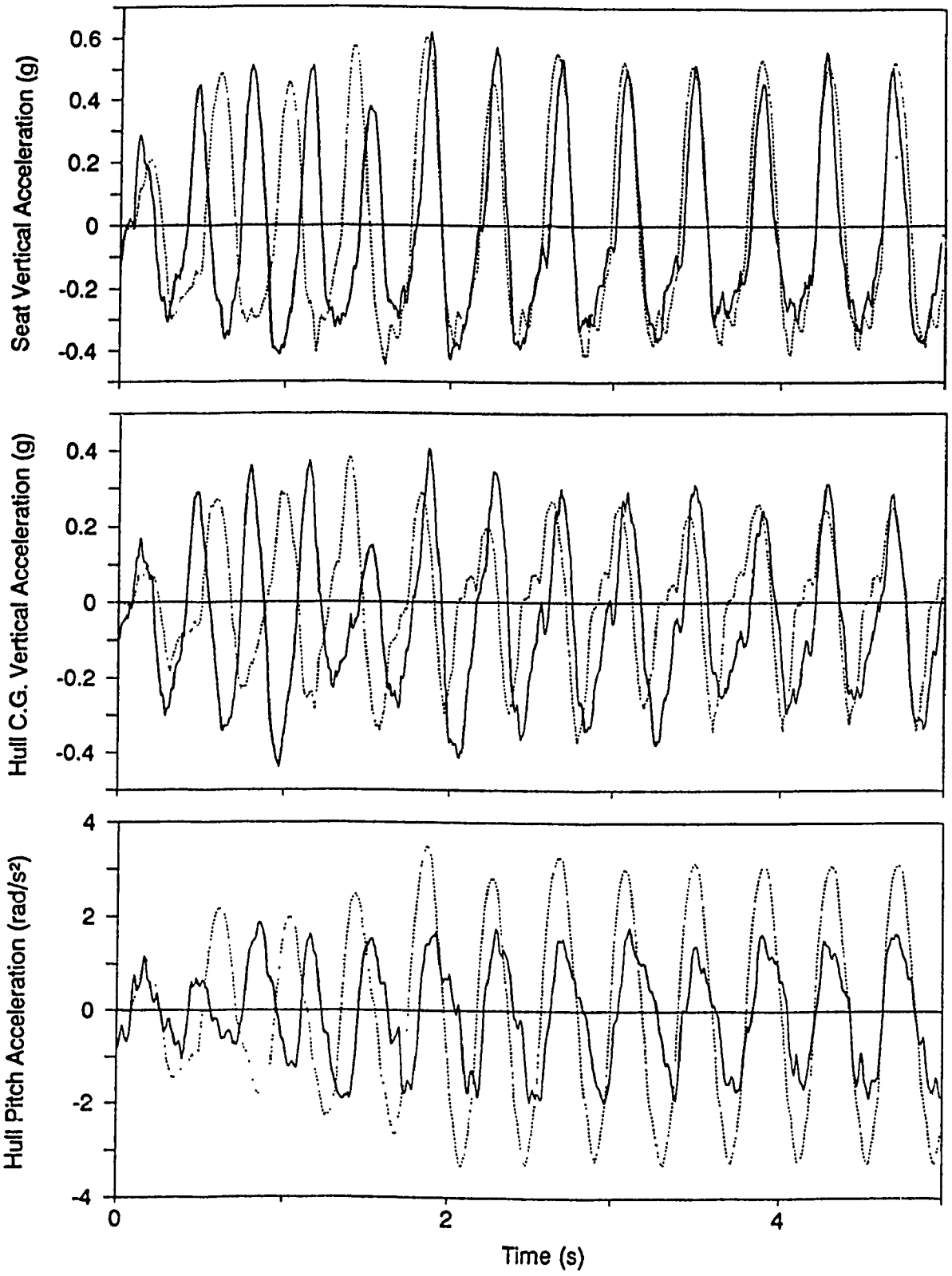

Figure 5.24 Ride acceleration traces - field validation of MODEL III's predictions for test vehicle configuration B traversing sine course at 6.7 km/h (——— Field Test, ... Simulation).

Table 5.6 Field validation of MODEL III (Sinusoidal course).

Test Condition		rms (g)* / rms (rad/s^2)**		Error (%) = $\left\|\frac{PV - MV}{MV}\right\| \times 100$
Vehicle Configuration	Speed (km/h) (f, Hz)	Measured Values (MV)	Predicted Values (PV)	
A	3.9 (1.41)	0.215/1.73	0.301/2.32	40.0/34.0
	4.7 (1.71)	0.299/1.55	0.352/2.33	17.7/50.3
	6.7 (2.44)	0.279/1.52	0.312/2.13	11.8/40.1
	7.9 (2.84)	0.292/1.83	0.284/2.00	2.7/9.3
B	3.5 (1.28)	0.167/1.80	0.168/2.80	0.6/55.5
	4.0 (1.46)	0.186/1.77	0.249/2.71	33.9/53.1
	5.4 (1.97)	0.309/1.33	0.333/2.09	7.8/57.1
	6.7 (2.44)	0.286/1.15	0.309/2.02	8.0/75.6

(* Seat vertical acceleration, ** Hull pitch acceleration)

acceleration spectra for vehicle configuration A traversing the random course at 13.5 km/h. In comparison with the MODEL II's predictions (Figure 4.26), the predicted spectra in Figure 5.25 exhibits slightly lower acceleration levels, especially around the dominant peaks, and closer agreement with the measured ones. Figure 5.26 presents direct comparison between measured and predicted spectra associated with the angular motions of all five road arm-road wheel assemblies. As shown, there is a generally good agreement between measured and predicted spectra for frequencies upto approximately 10 Hz. Figures 5.27 to 5.29 provide further field validation of the MODEL III's ride predictions for test vehicle configuration B, C, and D subjected to the random course at 13.5 km/h. Again, the predicted ride spectra exhibit relatively better agreement with the test data when compared with the spectra evaluated using MODEL II (Figures 4.27 to 4.29).

The comparison between the MODEL III's ride predictions for all test conditions, and corresponding measured data has been summarized in Table 5.7, where the average absorbed power (watts) and the rms value (g) for the seat bounce acceleration, and the rms value (rad/s^2) of the hull pitch acceleration are listed along with the respective percentage errors. Overall, the predicted rms values of seat bounce acceleration trace are in a good agreement with the measured ones, whereas the predicted rms values of pitch acceleration are consistently higher.

Belgian Pavé:

The ride simulations are performed using MODEL III for all test conditions employed for field testing on the Belgian pavé. Figures 5.30 and 5.31 demonstrate the samples of the field validation of predicted

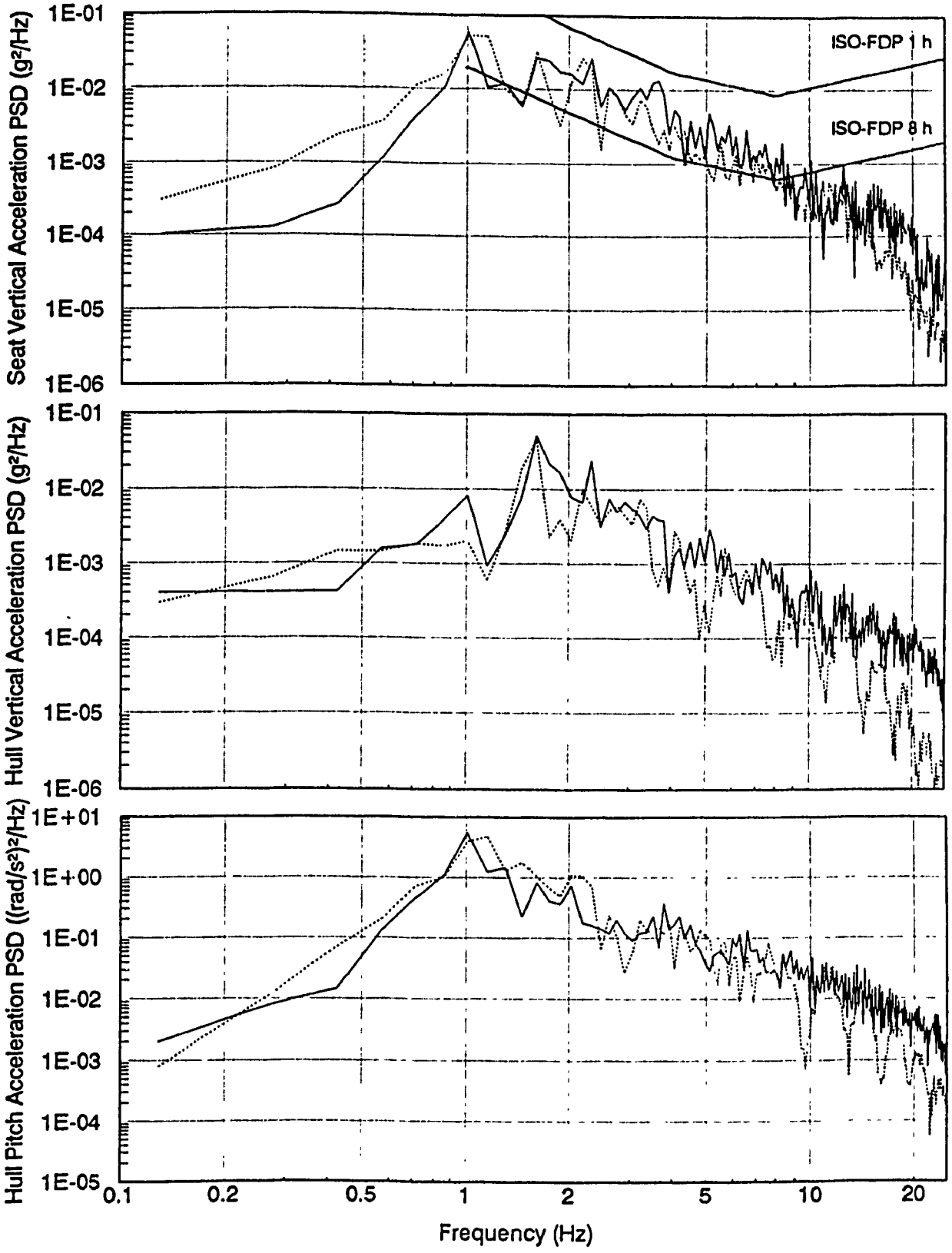

Figure 5.25 Ride acceleration spectra - field validation of MODEL III's predictions for test vehicle configuration A traversing LETE48 random course at 13.5 km/h(——— Field Test, ····· Simulation).

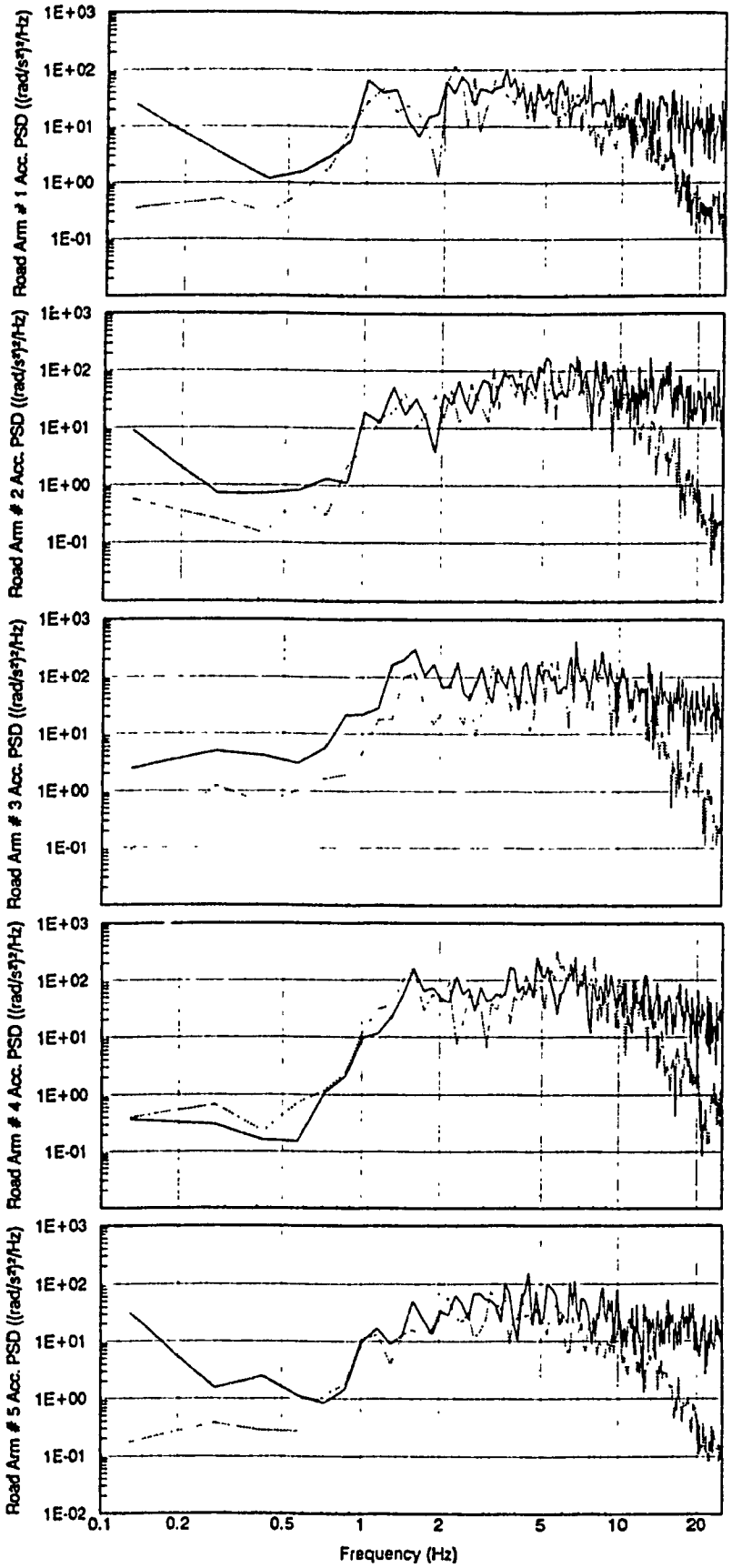

Figure 5.26 Road arm acceleration spectra - field validation of MODEL III's predictions for test vehicle configuration A traversing LETE48 random course at 13.5 km/h(——— Field Test, ... Simulation).

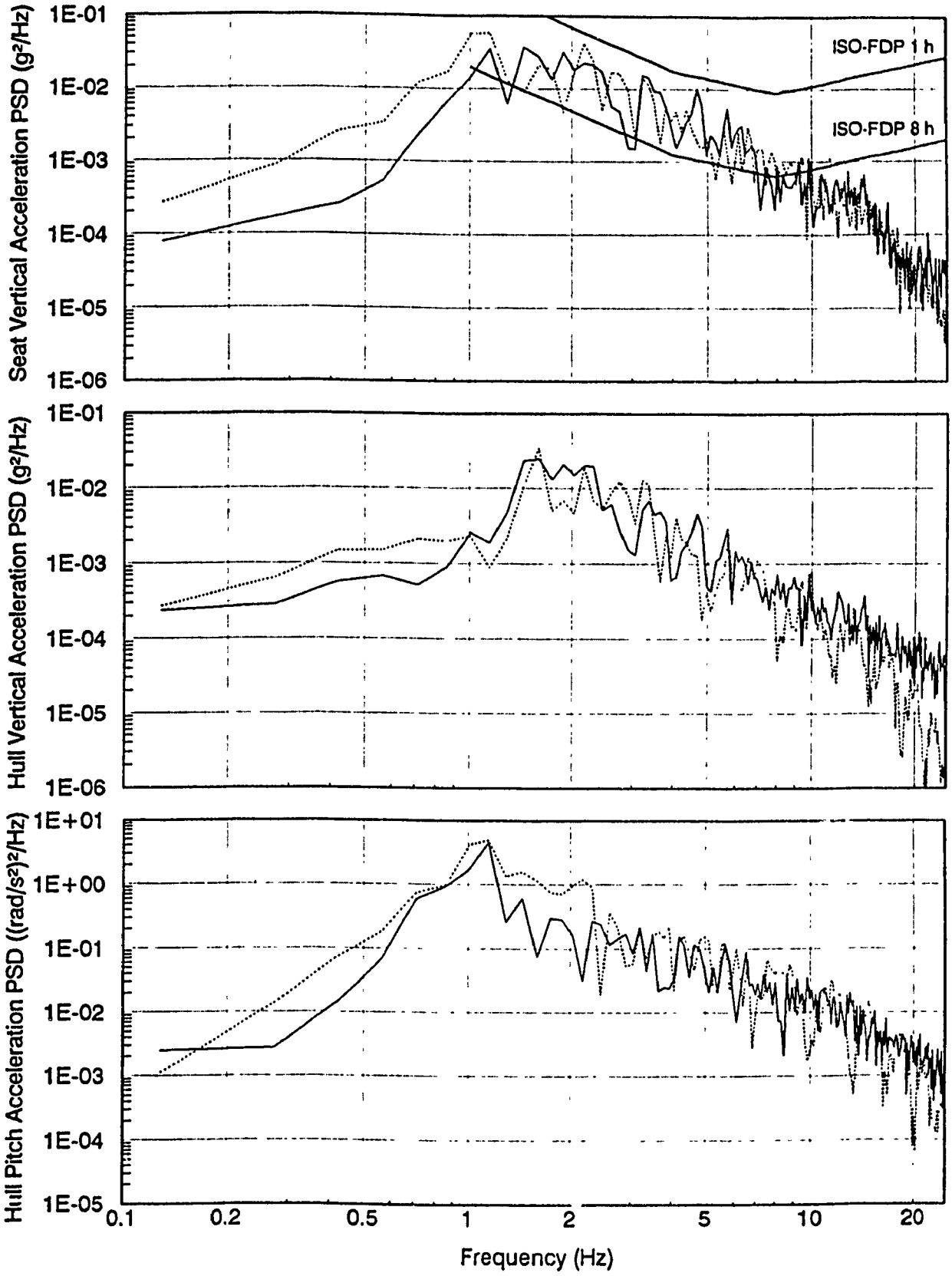

Figure 5.27 Ride acceleration spectra - field validation of MODEL III's predictions for test vehicle configuration B traversing LETE48 random course at 13.5 km/h(——— Field Test, ... Simulation).

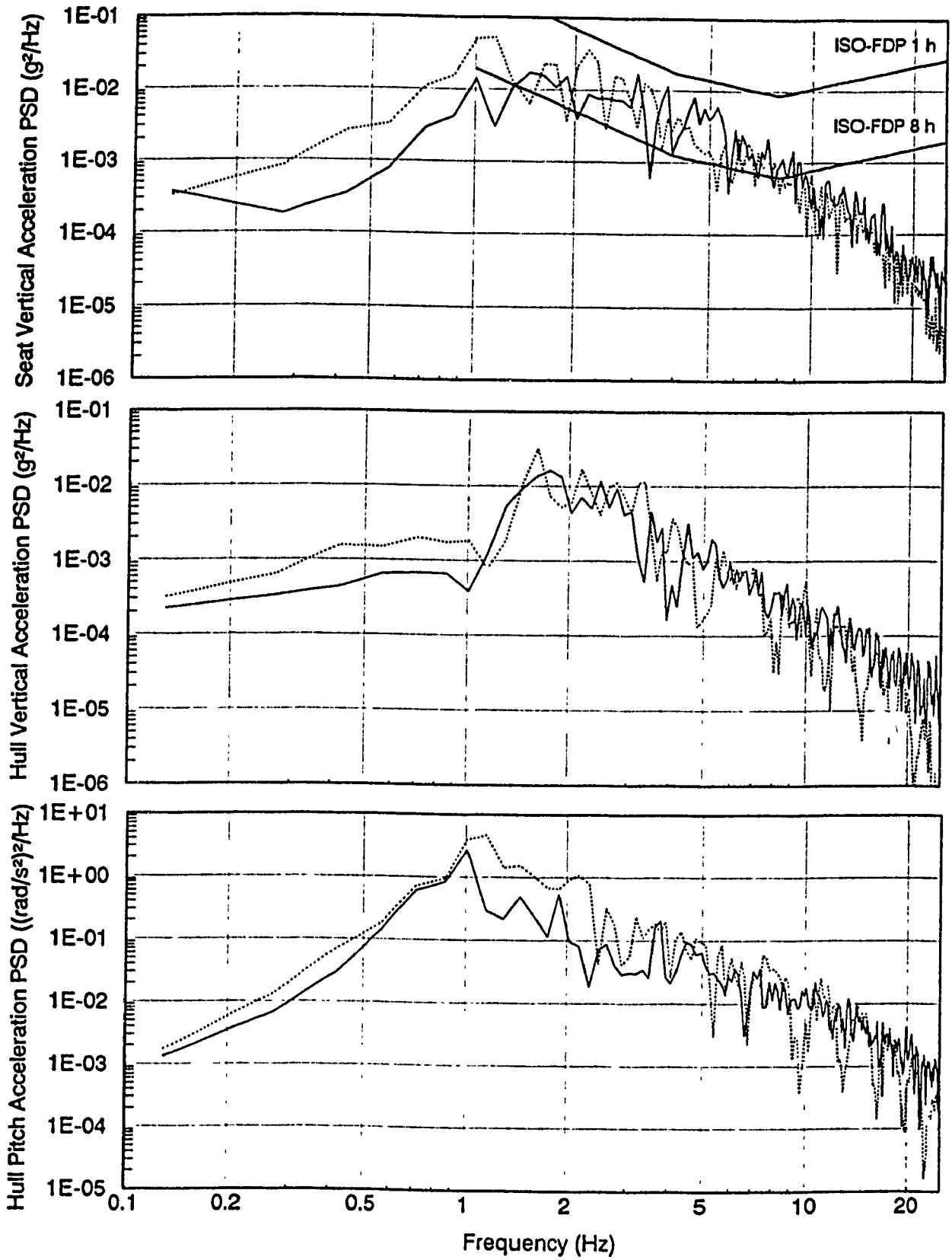

Figure 5.28 Ride acceleration spectra - field validation of MODEL III's predictions for test vehicle configuration C traversing LETE48 random course at 13.5 km/h(——— Field Test, ... Simulation).

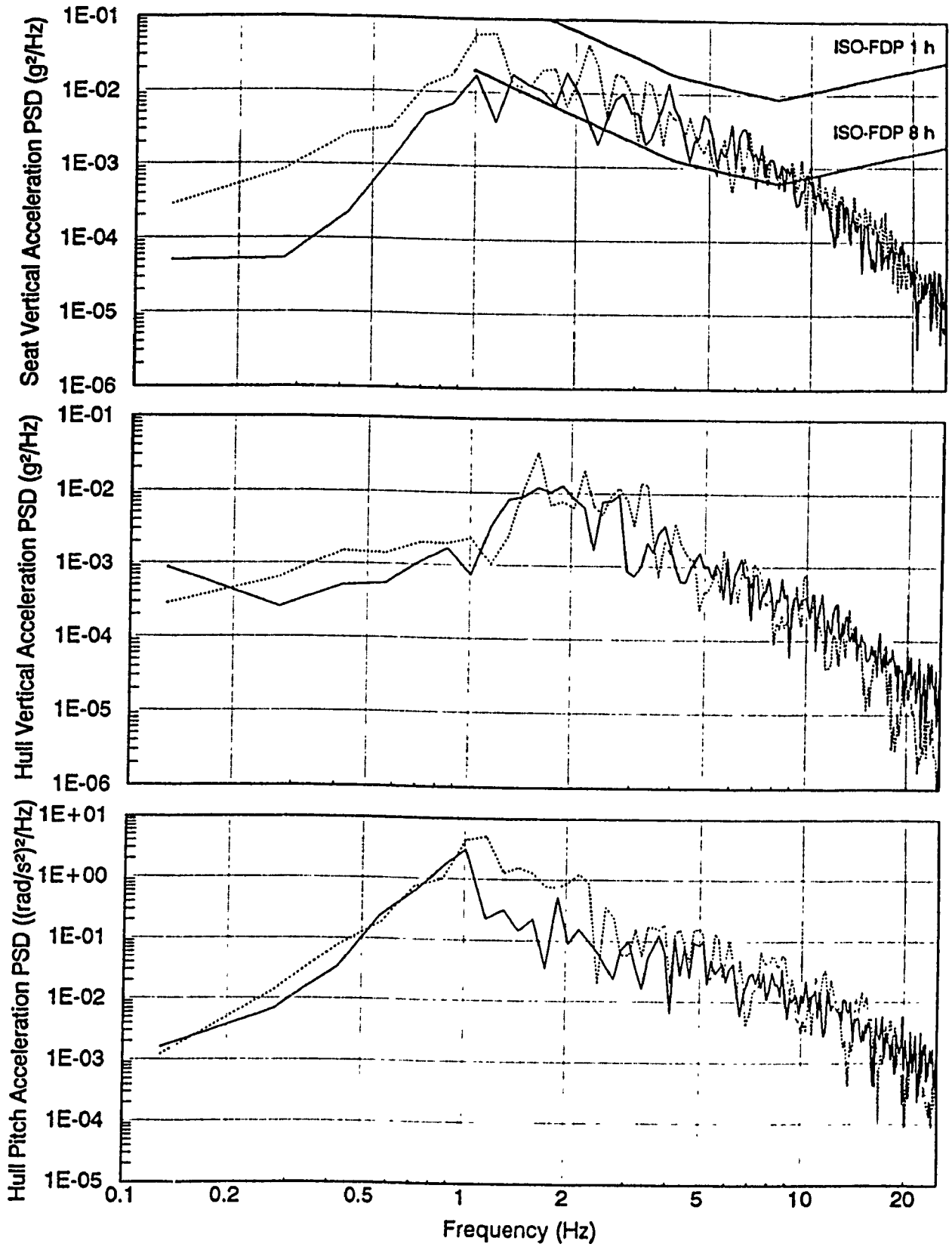

Figure 5.29 Ride acceleration spectra - field validation of MODEL III's predictions for test vehicle configuration D traversing LETE48 random course at 13.5 km/h(——— Field Test, ... Simulation).

Table 5.7 Field validation of MODEL III (LETE48 course).

Test Condition		Abs. Power(W)*/rms(g)*/rms(rad/s^2)†		Error (%) = $\left\|\frac{PV - MV}{MV}\right\| x100$
Vehicle Configuration	Speed (km/h)	Measured Values (MV)	Predicted Values (PV)	
A	6.2	0.55/0.099/0.509	0.40/0.094/0.790	27.3/5.0/55.2
	9.2	1.80/0.149/0.902	1.00/0.136/1.20	44.4/8.7/33.0
	13.5	4.50/0.260/1.61	2.90/0.251/2.02	35.5/3.5/25.5
	14.0	5.20/0.291/1.74	3.00/0.257/2.07	42.3/11.7/18.9
B	6.2	0.80/0.109/0.601	0.45/0.102/0.690	43.7/6.4/14.8
	8.1	0.94/0.131/0.720	0.60/0.136/0.935	36.2/3.8/29.9
	12.9	3.20/0.244/1.26	2.60/0.245/1.84	18.7/0.4/46.0
	13.5	4.40/0.287/1.65	4.00/0.284/2.07	9.1/1.0/25.4
	14.0	3.30/0.277/1.34	3.85/0.304/2.18	16.7/9.7/62.7
	16.5	4.60/0.344/1.93	7.60/0.460/2.82	65.2/33.7/46.1
C	6.5	1.00/0.120/0.583	0.50/0.110/0.725	50.0/8.3/24.3
	10.5	2.45/0.165/0.861	1.80/0.179/1.24	26.5/8.5/44.0
	13.5	3.70/0.235/1.29	3.40/0.271/1.99	8.1/15.3/54.3
	16.5	5.33/0.321/1.70	7.50/0.448/2.79	40.7/39.6/64.1
D	5.8	0.77/0.108/0.542	0.40/0.099/0.676	48.0/8.3/24.7
	11.7	2.27/0.166/0.908	2.00/0.207/1.53	11.9/24.7/68.5
	13.5	3.50/0.222/1.29	3.60/0.282/2.05	2.8/27.0/58.9
	15.2	3.10/0.259/1.39	5.50/0.382/2.52	77.4/47.5/81.3
	16.0	5.80/0.354/1.72	7.60/0.445/2.77	31.0/25.7/61.0

(* Seat vertical acceleration, † Hull pitch acceleration)

ride spectra obtained for test vehicle configurations A and B traversing Belgian pavé at 35 km/h. As before, the predicted ride levels are relatively lower when compared with the MODEL II's predictions (Figure 4.30 and 4.31), and exhibit better agreement with the test data. Table 5.8 summarizes the comparison between the field measurements and the MODEL III's predictions for all test conditions.

Based on the field validation results presented in this section, it is concluded that the relative performance of MODEL III is, indeed, superior when assessed in reference with MODEL II. The ride predictions evaluated in conjunction with MODEL III generally exhibit smoother ride due to the detailed modeling strategies adopted to describe the vehicle suspension kinematics. As mentioned earlier, the trailing arm suspension model allows the road wheel to swing back upon impact with a rougher section of the terrain profile, thus reducing the severity of the shock considerably.

In addition to carrying out the conventional ride analyses as presented so far, MODEL III is also used for detailed design and analyses of the vehicle suspension system. In the forth-coming sections, MODEL III is employed to study the influence of primary suspension parameters on the ride dynamic behaviour of the test vehicle, and to assess the performance of an advanced suspension system (such as a typical hydrogas suspension system) if it were to replace the conventional suspension system of the test vehicle.

5.4 PARAMETRIC SENSITIVITY ANALYSES

In general, the ride dynamic behaviour of a vehicle is influenced by a number of factors, such as terrain profile, vehicle speed, and vehicle

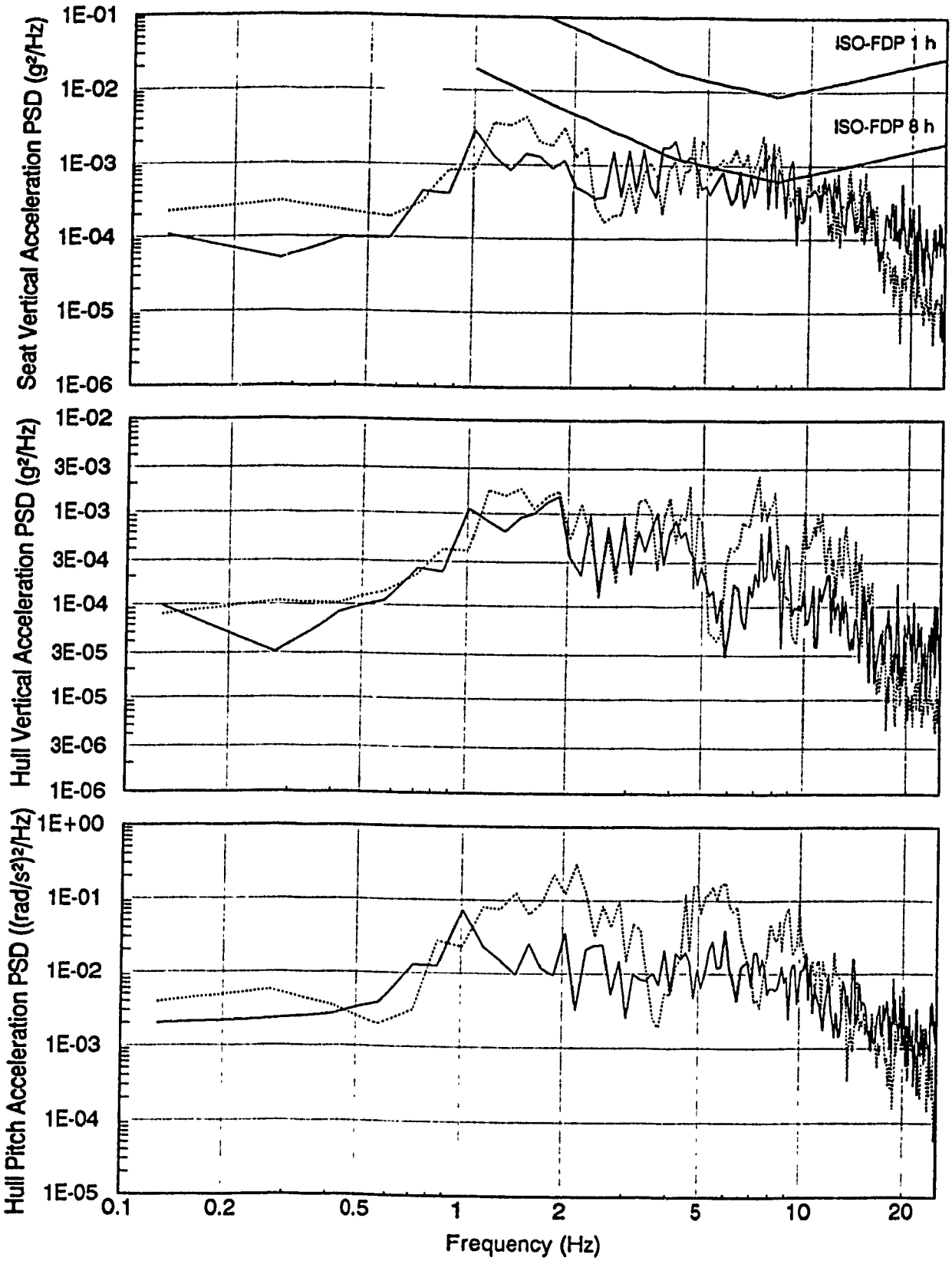

Figure 5.30 Ride acceleration spectra - field validation of MODEL III's predictions for test vehicle configuration A traversing Belgian pavé at 35 km/h (——— Field Test, ... Simulation).

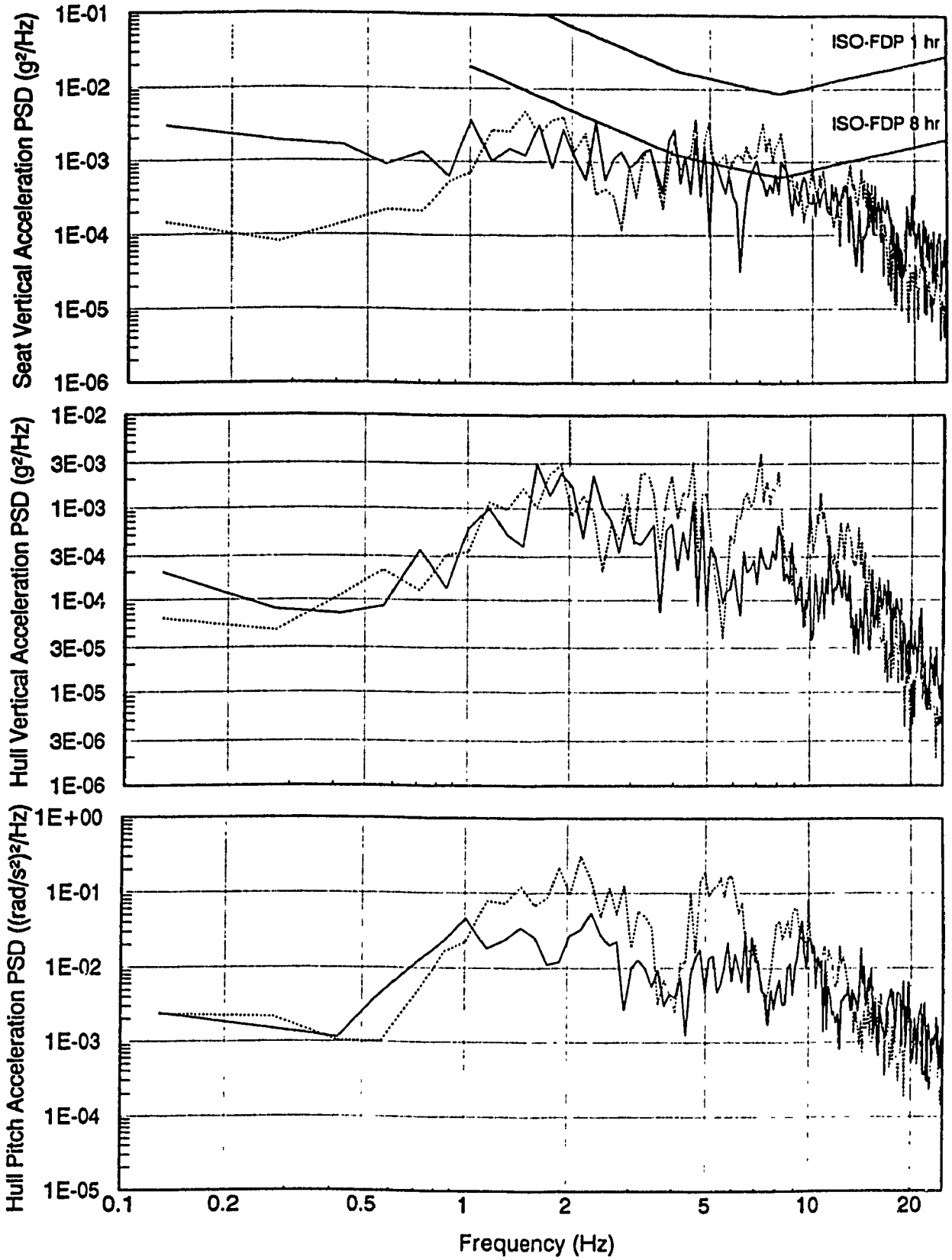

Figure 5.31 Ride acceleration spectra - field validation of MODEL III's predictions for test vehicle configuration B traversing Belgian pavé at 35 km/h (——— Field Test, ... Simulation).

Table 5.8 Field validation of MODEL III (Belgian pavé).

Test Condition		Abs. Power(W)*/rms(g)*/rms(rad/s^2)†		Error (%) = $\left\|\frac{PV - MV}{MV}\right\| \times 100$
Vehicle Configuration	Speed (km/h)	Measured Values (MV)	Predicted Values (PV)	
A	14.9	0.99/0.119/0.441	0.50/0.089/0.562	49.5/25.2/27.4
	22.5	0.61/0.110/0.491	0.77/0.097/0.697	26.2/11.8/41.9
	29.8	0.88/0.124/0.523	0.67/0.113/0.777	23.9/8.9/48.6
	35.0	0.94/0.116/0.492	1.10/0.117/0.810	17.0/0.9/64.6
B	15.8	1.53/0.115/0.422	0.97/0.094/0.601	36.6/18.3/42.4
	23.0	0.62/0.102/0.471	0.99/0.110/0.726	59.7/7.8/54.1
	30.7	1.13/0.115/0.484	0.84/0.127/0.790	25.7/10.4/63.2
	35.0	0.92/0.134/0.526	1.50/0.132/0.850	63.0/1.5/61.6

(* Seat vertical acceleration, † Hull pitch acceleration)

system parameters associated with loading conditions, geometry, suspension systems, etc. A better understanding of these factors is achieved through a parameteric study of the vehicle ride model. The parametric study results indicate a trend on the effect of various parameters on the response and provides a basis for selecting the parameters that yield optimal ride.

For test vehicle, factors such as terrain profile, vehicle speeds, loading conditions, and track pre-tension, have been already studied in detail through field tests and simulations. It was shown that the vehicle ride deteriorates with rougher terrain profile and higher speeds, whereas the loading condition (laden and unladen) and track pre-tension setting exhibit less influence on the ride dynamic behaviour. The objective of the parameteric study presented in this section is to demonstrate the influence of variations in the primary suspension parameters (design parameters) on the ride dynamic behaviour of the field-tested vehicle. The parameters considered for variations are: equivalent stiffness of road wheel and track pad, torsion bar spring rate, and damping characteristics and location/number of inclined shock absorbers. For this parameteric study, the test vehicle configuration B is considered to traverse over 6" obstacle at 14.3 km/h, and LETE48 random course at 13.5 km/h.

5.4.1 Influence of Road Wheel/Track Pad Stiffness

The stiffnesses of the rubber rim (vulcanized to the all-metal body of the road wheel), and the underlying rubber track pad are combined as a single unit to characterize the equivalent vertical stiffness, K'_{rw}, or continuous radial stiffness, K'_{rw} (section 2.4). Therefore, the equivalent

spring rate can be varied by replacing either or both of the existing road wheel rim or the track pad with a softer or harder rubber material. The nominal value of K^i_{rw} (i = 1,..5), and corresponding K^i_{rw} are 613 KN/m and 1121256 N/m/rad, respectively, which are obtained from the wheel-terrain contact patch formed on a flat ground under a vertical static load, P = 15568 N and corresponding deflection of the wheel centre, Δ_w = 0.0254 m [38]. The parametric sensitivity analyses is carried out by considering low and high values of the equivalent vertical stiffness in the vicinity of the nominal value, which are K^i_{rw} = 500 kN/m (P = 12700 N, Δ_w = 0.0254 m), and K^i_{rw} = 750 kN/m (P = 19050 N, Δ_w = 0.0254 m).

The influence of the specified variations in K^i_{rw} is demonstrated in Figure 5.32, which shows the ride acceleration traces for test vehicle crossing the obstacle. As shown, there is insignificant influence as the resulting acceleration traces are almost similar. However, a closer examination of the traces reveals that an increase in the value of K^i_{rw} yields slightly higher acceleration levels especially around the dominant peaks. Figure 5.33 shows the influence of K^i_{rw} on the ride acceleration spectra for the test vehicle traversing the random course. Again, the influence is generally negligible, except around the pitch resonant frequency (1.2 Hz), where there is a slight increase in the seat bounce spectra due to the decrease in the nominal value of K^i_{rw}.

5.4.2 Influence of Torsion Bar Stiffness

The torsional stiffness of a uniform rod is, in general, dependent on the cross-section diameter, the length, and the shear modulus of the rod. Thus, the torsion bar spring rate can be varied by appropriately selecting the torsion bars of different diameters. The nominal value of

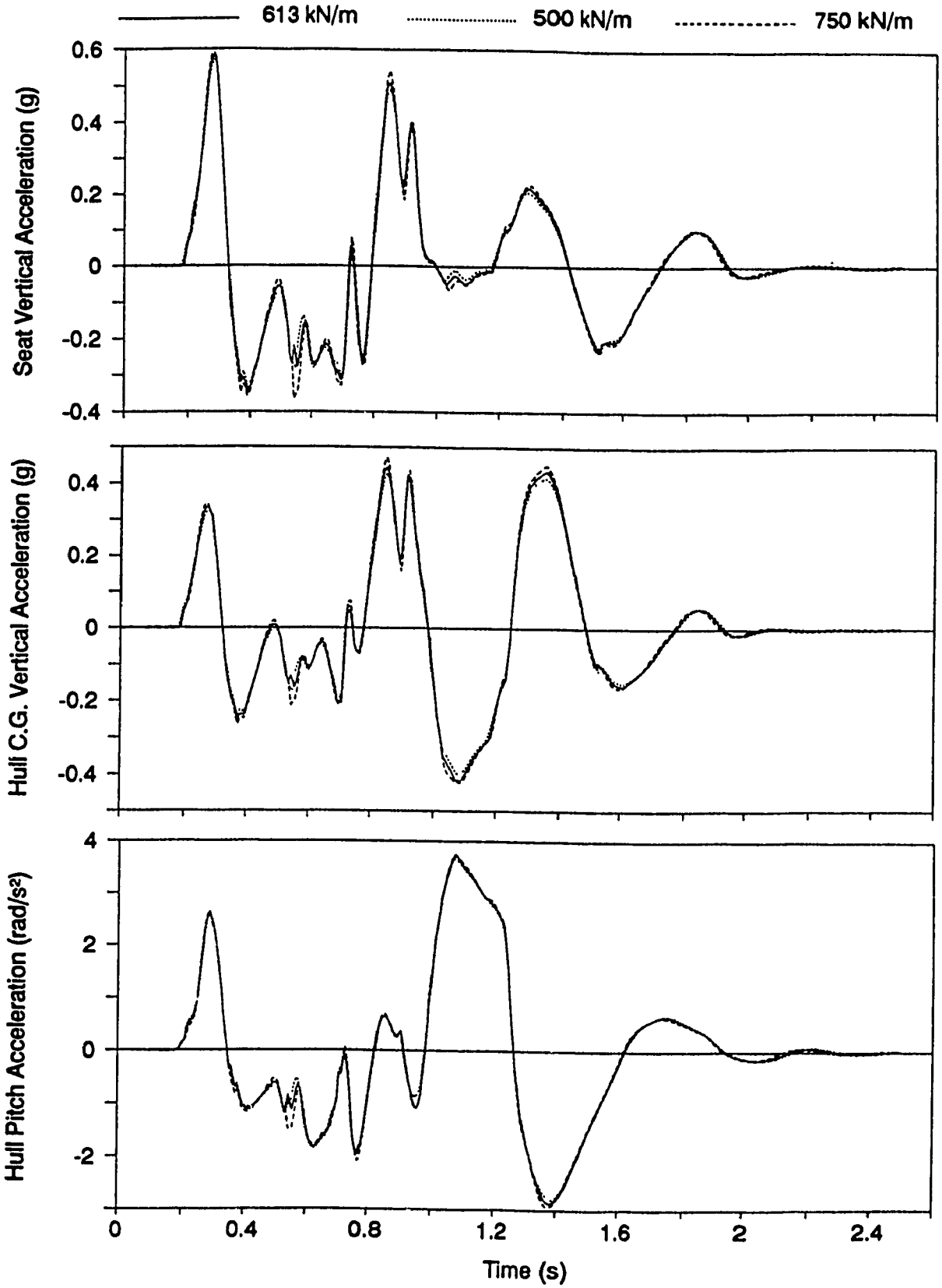

Figure 5.32 Influence of road wheel/track pad stiffness - ride acceleration traces for test vehicle configuration B traversing 6" obstacle at 14.3 km/h.

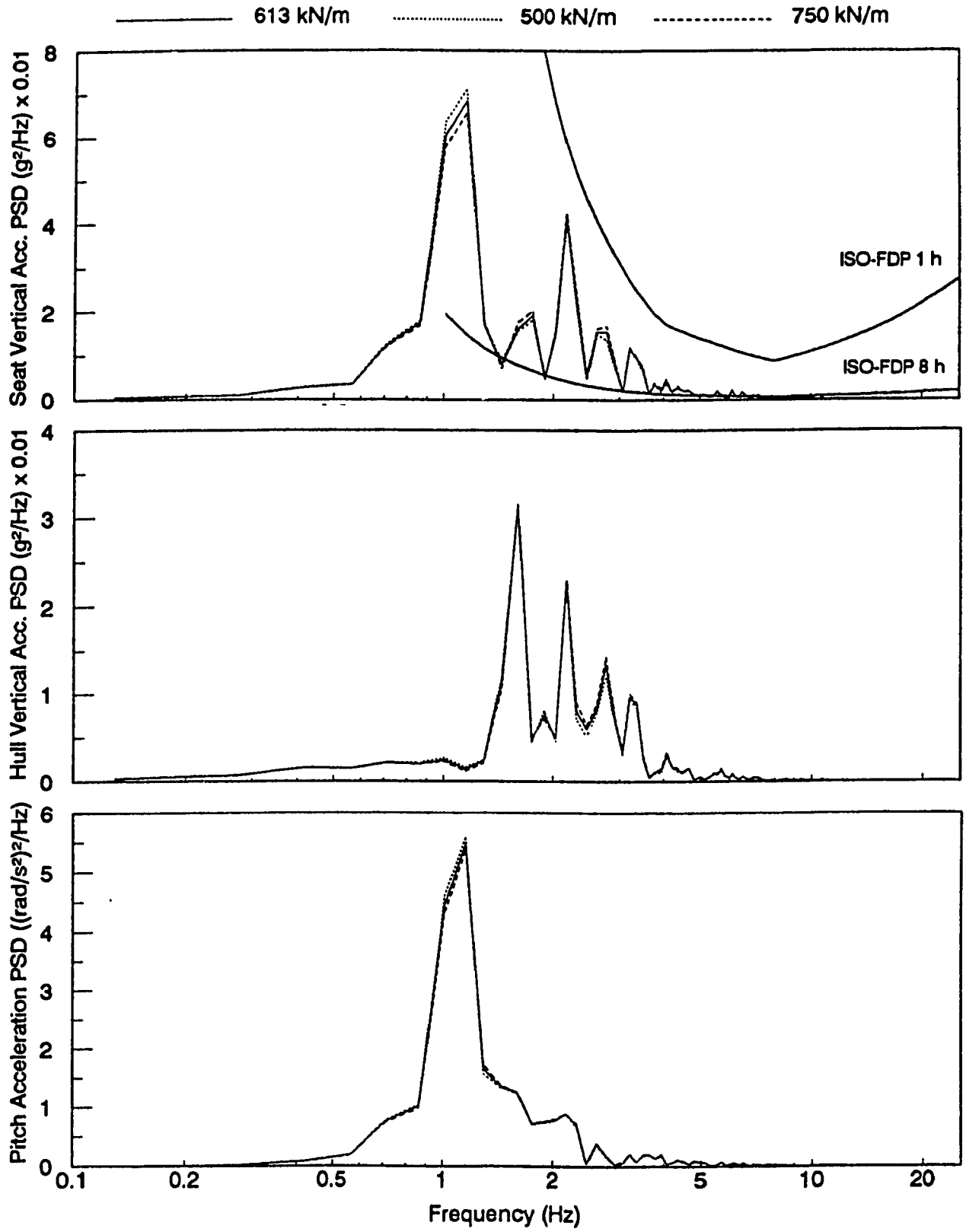

Figure 5.33 Influence of road wheel/track pad stiffness - ride acceleration spectra for test vehicle configuration B traversing LETE48 random course at 13.5 km/h.

torsional stiffness, K_{Ti} (i = 1,..,5) is 9884 N.m/rad (Table 5.3). The influence of torsional stiffness on the ride dynamic behaviour of the test vehicle is investigated by selecting low and high values of K_{Ti} in the vicinity of nominal value, which are 7500 N.m/rad and 12000 N.m/rad.

Figure 5.34 demonstrates ride acceleration traces for test vehicle crossing the obstacle, evaluated with three different values of the torsional stiffness. As shown, the stiffer torsion bar or suspension yields relatively higher acceleration levels since more energy is transmitted to the sprung mass or central body. The influence of suspension stiffness is further demonstrated based on the ride acceleration sepctra evaluated for test vehicle traversing the random course. As shown in Figure 5.35, the softer torsion bar yields a relatively comfortable ride. Specified variations in the torsion bar spring rate are found to change the average absorbed power by almost 1 watt. Softer suspension yields an uniform reduction in the pitch spectra, however, the hull bounce spectra exhibit a significant increase in the primary peak occuring at bounce resonant frequency (1.7 Hz).

5.4.3 Influence of Inclined Shock Absorber

The typical force-velocity characteristics of the shock absorber mounted at the first and last road wheel stations of the test vehicle, are indicated in Figure 3.17 by the solid curve. As shown, the force-velocity curve indicates high damping coefficient (slope) corresponding to the low relative velocity and the damping coefficient decreases significantly as the relative velocity exceeds certain break velocity (0.4064 m/s). The influence of shock absorber or suspension damping is studied by dual parameteric variations:

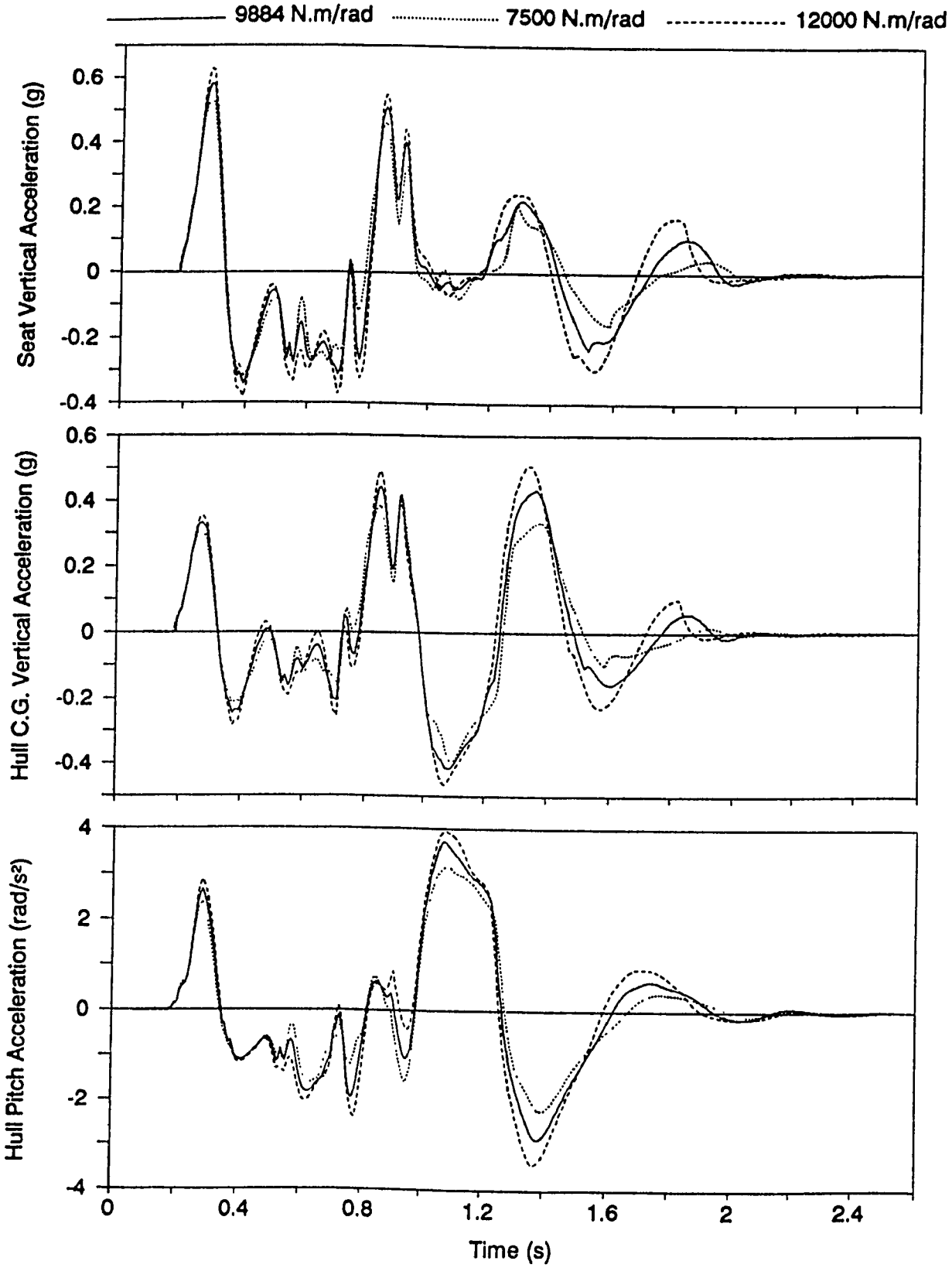

Figure 5.34 Influence of torsion bar stiffness - ride acceleration traces for test vehicle configuration B traversing 6" obstacle at 14.3 km/h.

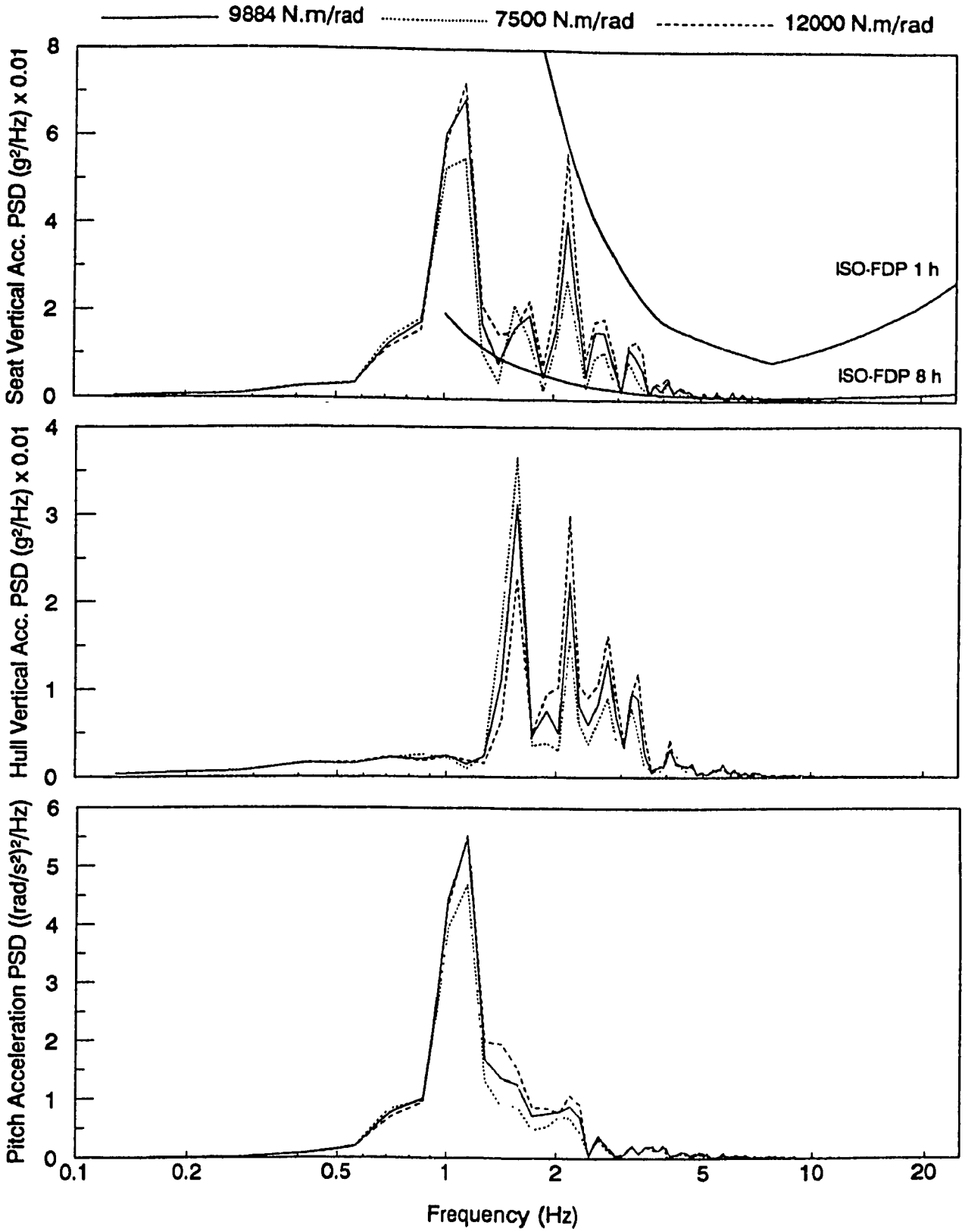

Figure 5.35 Influence of torsion bar stiffness - ride acceleration spectra for test vehicle configuration B traversing LETE48 random course at 13.5 km/h.

(a) The force-velocity characteristics are modified to yield low and high resistive damping force. This is achieved by reducing or increasing the damping force values in the look-up table by 25%. For instance, the dotted curve in Figure 3.17 represents the lowered damping characteristics.

(b) The number of shock absorbers are varied by locating them at intermediate road wheel stations. Two vehicle configurations are considered: (i) the shock absorbers are mounted at the first, second, and last wheel stations, and (ii) shock absorbers are mounted at all wheel stations.

The influence of the variations in the suspension damping is demonstrated in Figures 5.36 and 5.37. The ride acceleration traces in Figure 5.36 reveal that a reduction in suspension damping yields a better obstacle-crossing performance of the test vehicle. However, the ride acceleration spectra presented in Figure 5.37 demonstrate a significant improvement in the bounce ride levels due to high damping, especially in the vicinity of the pitch resonant frequency. The specified reduction in the suspension damping is found to increase the average absorbed power by 1 watt. The hull bounce spectra does not indicate any significant changes, whereas the pitch levels are considerably reduced as a consequence of high damping.

Figures 5.38 and 5.39 presents the outcome of installing the shock absorber at intermediate road wheel stations of the test vehicle. As indicated by the acceleration traces in Figure 5.38, the obstacle-crossing performance of the test vehicle is improved by introducing the shock absorbers at intermediate wheel stations. First peak (frontal impact) is reduced as well as the vehicle settling time (after it has

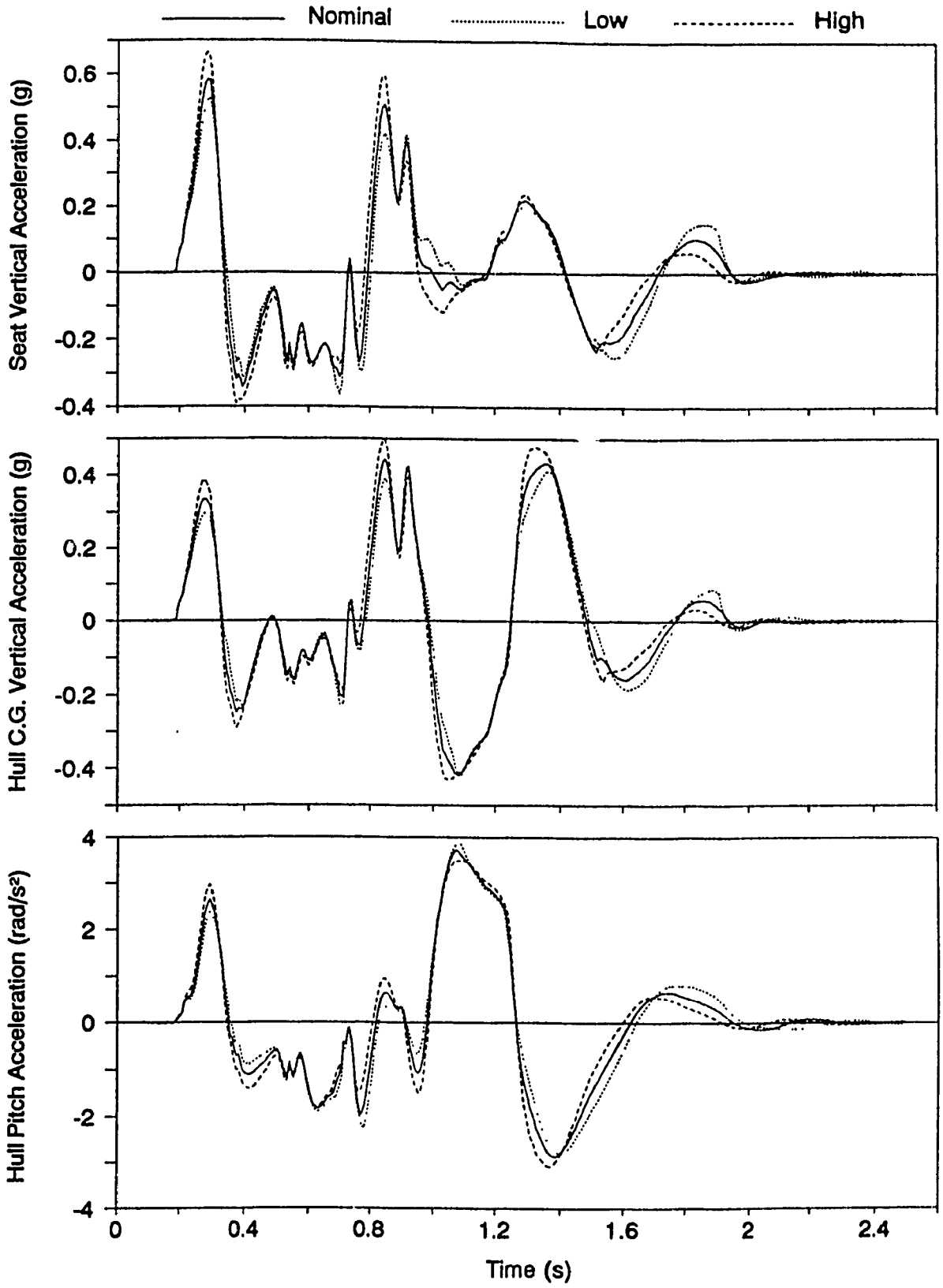

Figure 5.36 Influence of suspension damping - ride acceleration traces for test vehicle configuration B traversing 6" obstacle at 14.3 km/h.

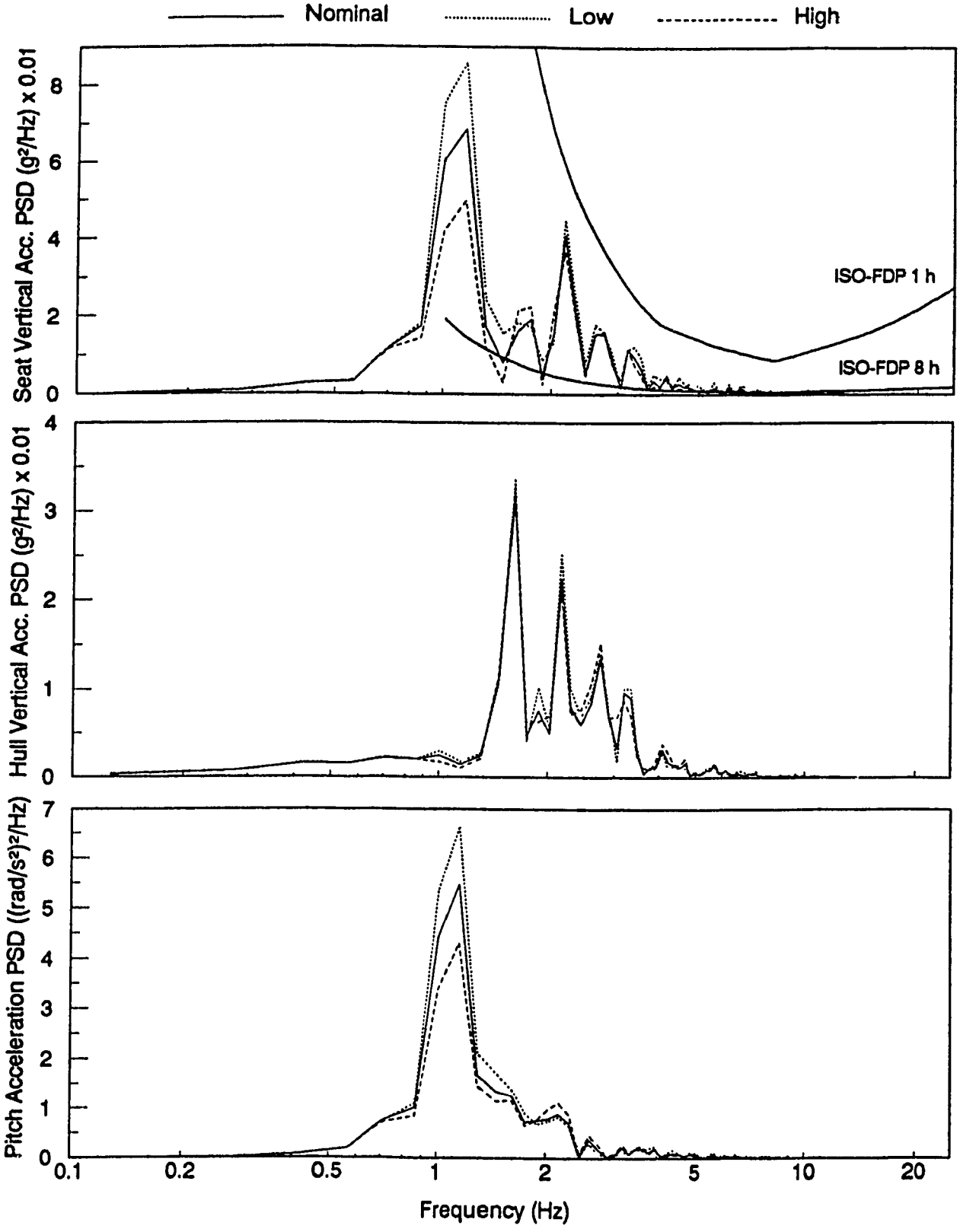

Figure 5.37 Influence of suspension damping - ride acceleration spectra for test vehicle configuration B traversing LETE48 random course at 13.5 km/h.

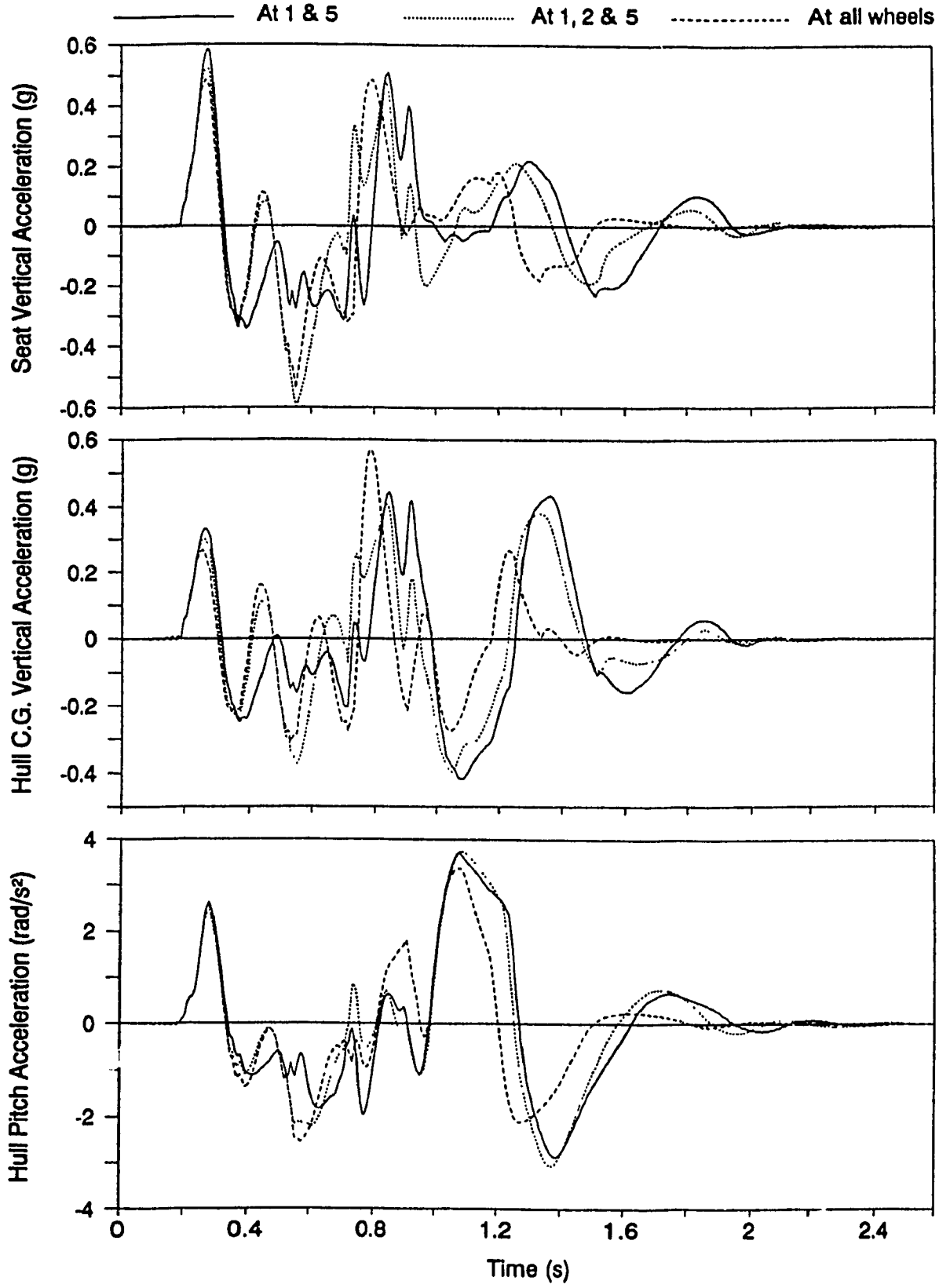

Figure 5.38 Influence of location/number of inclined shock absorbers - ride acceleration traces for test vehicle configuration B traversing 6" obstacle at 14.3 km/h.

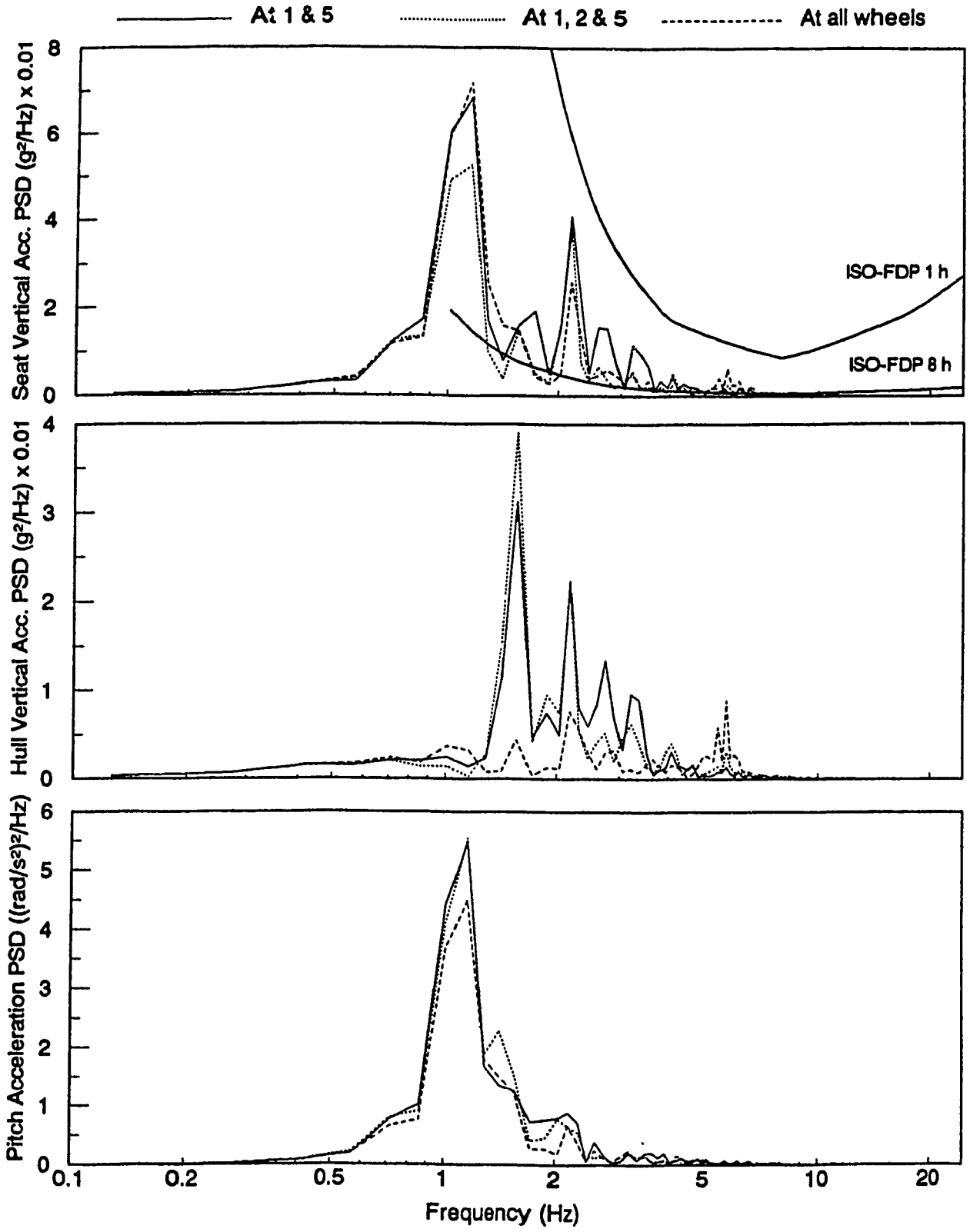

Figure 5.39 Influence of location/number of inclined shock absorbers - ride acceleration spectra for test vehicle configuration B traversing LETE48 random course at 13.5 km/h.

crossed the obstacle) is significantly reduced. Similarly, the acceleration spectra in Figure 5.39 indicate an improved trend, where the average absorbed power is reduced by atleast 1 watt. The hull bounce levels are significantly suppressed as a consequence of introducing shock absorbers at all intermediate wheel stations. The implementation of shock absorber at the second wheel station alone leads to a considerable increase in the hull bounce spectra at the bounce resonant frequency (1.7 Hz), and the pitch levels are not reduced. However, the seat bounce spectra indicate a reduction at the pitch resonant frequency (1.2 Hz).

5.5 VEHICLE RIDE IMPROVEMENT VIA ADVANCED SUSPENSION

Although, the conventional torsion bar/trailing arm suspension system offer the advantages of simplicity and low costs, the inherent limitations of these suspensions are well known. The primary limitations include excessive weight, requirements for considerable mounting space, and lack of load-leveling capabilities due to fixed torsion bar spring rate. With a continual demand for increased power-to-weight ratio and higher speeds, present trend is towards the use of advanced suspension systems such as hydrogas suspensions since these tend to be lighter and more compact, can be mounted external to the hull, incorporate integral damping arrangements, and offer load-leveling capabilities due to their nonlinear progressively stiffening spring characteristics [21].

Hydrogas suspension designs have been developed by various manufacturers to improve ride and handling performance of high mobility tracked vehicles. Although these suspension systems exhibit several design variations, they consist of an energy storage element (spring), and a dissipative element (damper), contained in a single unit, as

illustrated in Figure 5.40. The suspension system contains both hydraulic fluid and compressed gas, usually nitrogen, separated by either a floating piston or a flexible diaphragm. The suspension forces are generated by fluid pressure acting on the main piston. Damping forces are generated by the flow of hydraulic fluid through constrictions provided by a either a damper plate or a valve housing, while the restoring forces are generated by the compression/extension of the gas charge. The compression/extension of the nitrogen gas follows a *polytropic process* leading to a nonlinear, progressively stiffening spring characteristics. For nitrogen gas, the value of *polytropic constant* lies between 1.0 and 1.4, depending upon the assumed nature of compression/extension process. For instance, for a slow compression/extension process, where the change in temperature is insignificant, the value of polytropic constant is taken as 1.0 (*isothermal process*). These suspension systems are also equipped with travel limiting bump stops, which are hard rubber stops mounted at the limits of the piston's compression and extension travel.

In this section, the ride performance potentials of a hydrogas suspension system especially developed for applications with M113 APC's are investigated via computer simulation of the candidate vehicle. The hydrogas suspension system, similar to one illustrated in Figure 5.40, replaces both the torsion bar and inclined shock absorber of the test vehicle. The mounting points for hydrogas suspension coincide directly with those of the conventional suspension, i.e. axle arm pivot point of hydrogas suspension system (Figure 5.40) coincides with the torsion bar centre; the distance between pivot point and road wheel centre is equal to the length of the road arm (R_{ai}), the distance between pivot point and the attachement point for connecting rod of the hydrogas suspension unit

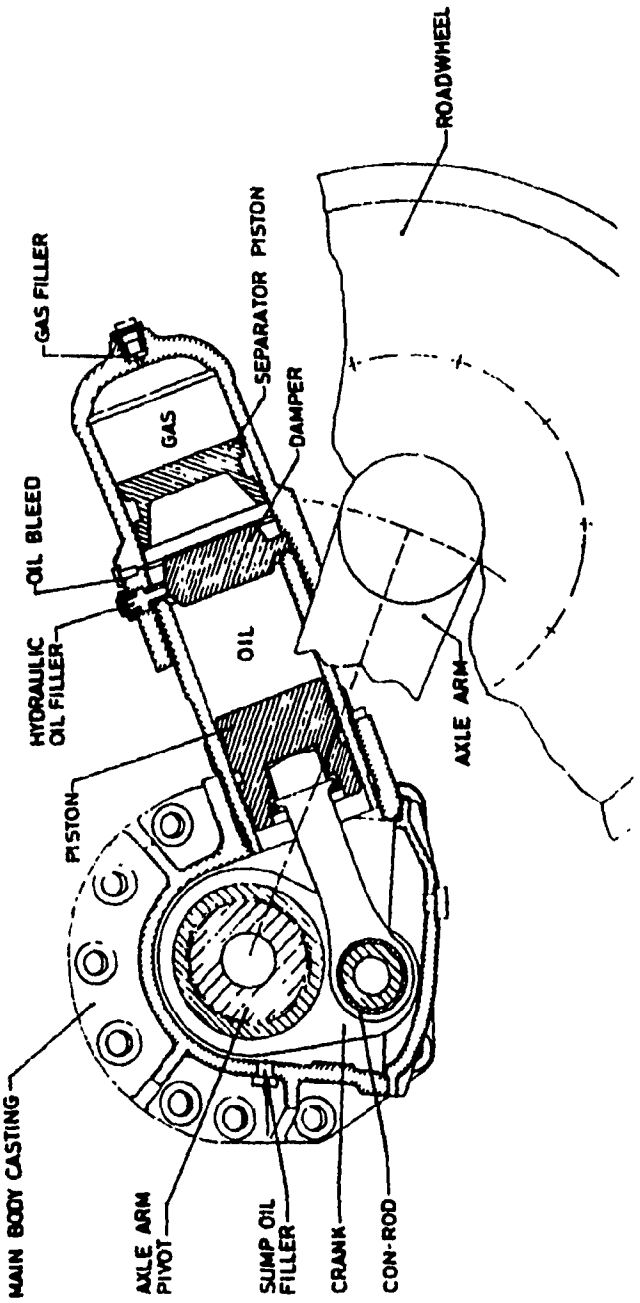

Figure 5.40 Schematic of Challenger battle tank hydrogas suspension system [21].

is equal to the length of the road arm overhang (S_{ai}); and the hydrogas suspension unit itself is oriented in a inclined manner identical to the conventional shock absorber. The nonlinear force-displacement and force-velocity characteristics of the inclined hydrogas suspension unit under study are illustrated in Figures 5.41 and 5.42, respectively. The spring characteristics (Figure 5.41) follow the *isothermal process*, and reveals that under compression the spring force increases rapidly as the bump stop is approached. The exhibited force-displacement data yield the gas spring characteristics corresponding to the permissible travel limits of the piston, and are described with resect to the static equilibrium reference. As shown, the zero deflection and corresponding spring force indicate the static values. In order to perform simulation using MODEL III, the specified force-displacement data needs to be re-described with respect to the zero-force reference. It is achieved by shifting the curve such that the zero deflection point coincides with specified/ desired values of the initial static deflection, δ^i_{HS}, and force, F^i_{HS}, due to the hydrogas suspension unit mounted at the i^{th} road wheel station. The procedure to obtain δ^i_{HS} and F^i_{HS} is described as below.

Under static condition, a couple is produced on the trailing arm due to the static weight being supported. This static couple is given according to equation (5.44) as:

$$\text{Static Couple} = F^o_{si}\, d_{xi} + T^i_{wx}\, d_{yi} \qquad (5.50)$$

This couple must be balanced by a reaction torque supplied by the inclined hydrogas suspenion unit, given as:

$$\text{Reaction Torque} = F^i_{HS}\, d_i \qquad (5.51)$$

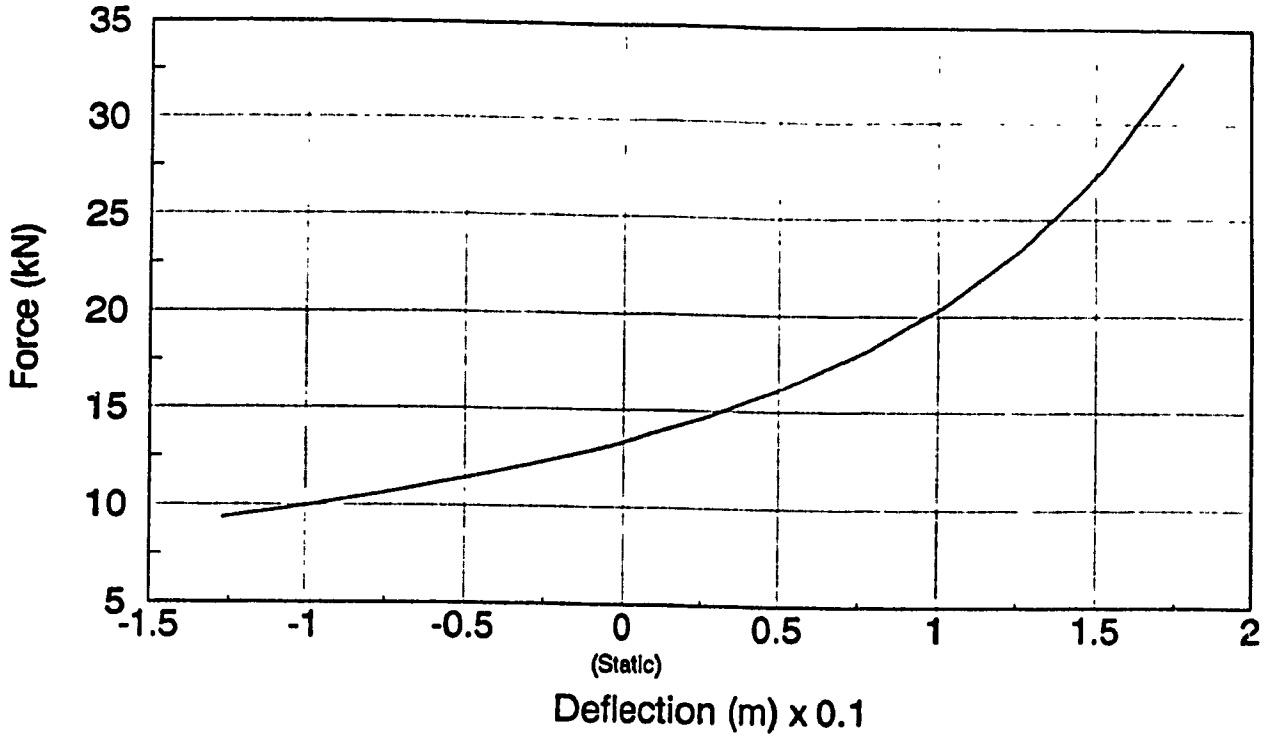

Figure 5.41 Typical force-displacement characteristics of hydrogas suspension system developed for M113 APC's.

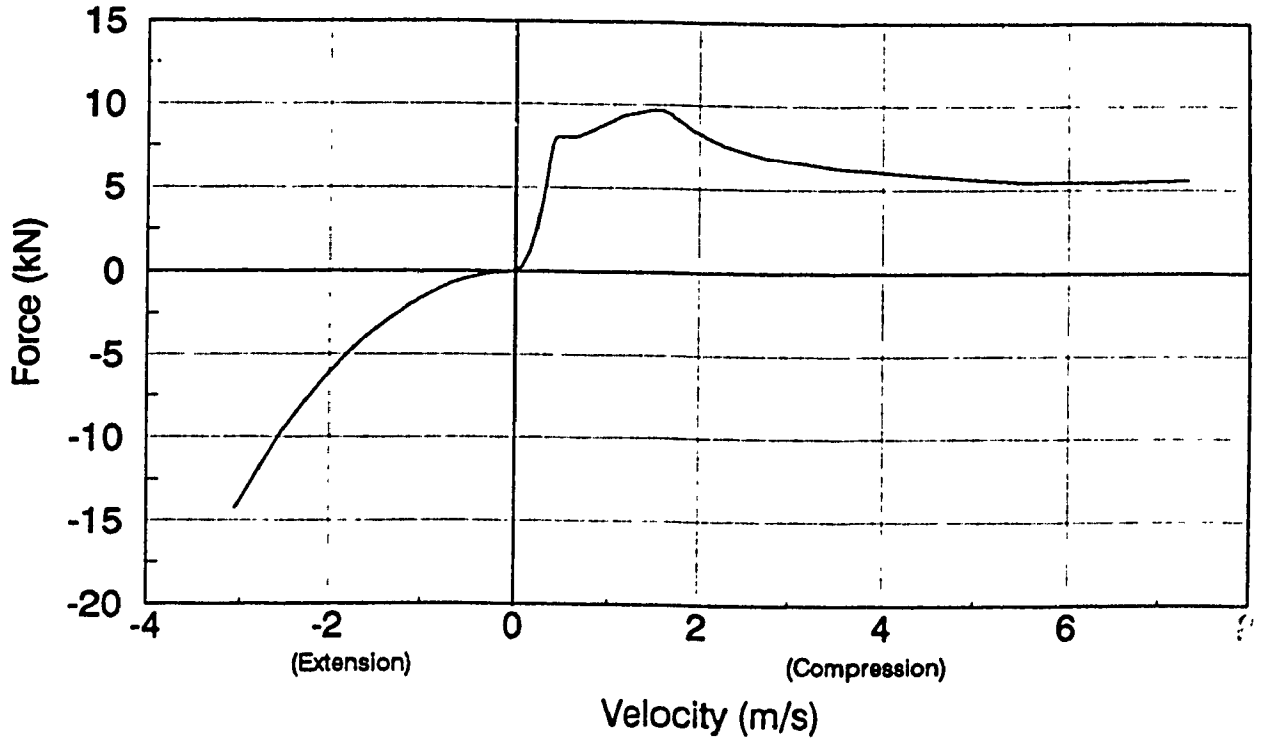

Figure 5.42 Typical force-velocity characteristics of hydrogas suspension system developed for M113 APC's.

where, the perpendicular distance from the trailing arm pivot to the hydrogas suspension mounting point, d_1, is computed using equation (5.34) in conjunction with the initial static value of the road arm angle, θ^s_{w1}, given by equation (5.41). Therefore, equating equations (5.50) and (5.51), the initial static force is given as:

$$F^1_{HS} = \frac{F^o_{s1}\ d_{x1} + T^1_{wx}\ d_{y1}}{d_1} \tag{5.52}$$

The initial static deflection or compression, δ^1_{HS}, is determined based on an equivalent torque developed by the conventional torsion bar spring, given as:

$$\delta^1_{HS} = - S_{a1}\ \delta_{\theta 1} \tag{5.53}$$

where, $\delta_{\theta 1}$ is given by equation (5.44). The force-displacement curve (Figure 5.41) is thus shifted according to δ^1_{HS} and F^1_{HS} in order to establish the desired curve (look-up table) for the hydrogas suspension unit mounted at the i^{th} road wheel station. In addition, stiff bump stop characteristics are incorporated.

The relative performance of hydrogas suspension system is assessed based on simulation of the test vehicle configuration B traversing over 6" obstacle at 14.3 km/h, and LETE48 random course at 13.5 km/h. First, the performance of the test vehicle equipped with hydrogas suspension units at all five wheel stations is compared with the conventional vehicle configuration. Secondly, the influence of installing hydrogas suspension units at only few selected wheel stations, such as 1st and 5th, and at 1st, 2nd and 5th, is studied.

Figure 5.43 shows the direct comparison of ride acceleration traces

for test vehicle crossing the obstacle in its conventional configuration and equipped with hydrogas suspension units at all wheel stations. The traces (especially vertical acceleration) evaluated in conjunction with hydrogas suspension system exhibit small initial transients, which are attributed to the assumption made in the evaluation of the vehicle's static equilibrium - the magnitude of relative displacement (Δ_i) across hydrogas suspension is computed assuming small angular displacement of the road arm (equation 5.47) during the iterative stiffness procedure, whereas it is accurately evaluated using equation (5.24) during simulation. The hydrogas suspension has reduced the acceleration levels (first peak and rms value), as shown in Figure 5.43, however, at the expense of high displacement magnitudes and long vehicle settling time (Figure 5.44). Figure 5.45 illustrates the angular acceleration traces of all five road arm - road wheel assemblies. The traces for intermediate wheel stations exhibit significant improvement, whereas first and last wheels experience considerably high acceleration levels with hydrogas suspension. The ride performance potentials of the hydrogas suspension are further assessed based on the computer simulation of the test vehicle traversing the random course. Figure 5.46 compares the ride acceleration spectra evaluated in conjunction with conventional and hydrogas suspension configurations of the vehicle. With hydrogas suspension, the ride bounce/pitch resonant frequency has been slightly lowered with a considerable increase in the associated primary peak level, and a significant reduction in the acceleration levels at higher frequencies. In terms of ride quality, the average absorbed power has been almost reduced by 2 watts. Figure 5.47 shows the angular acceleration spectra for the road arm - road wheel assemblies. As before, there is a consider-

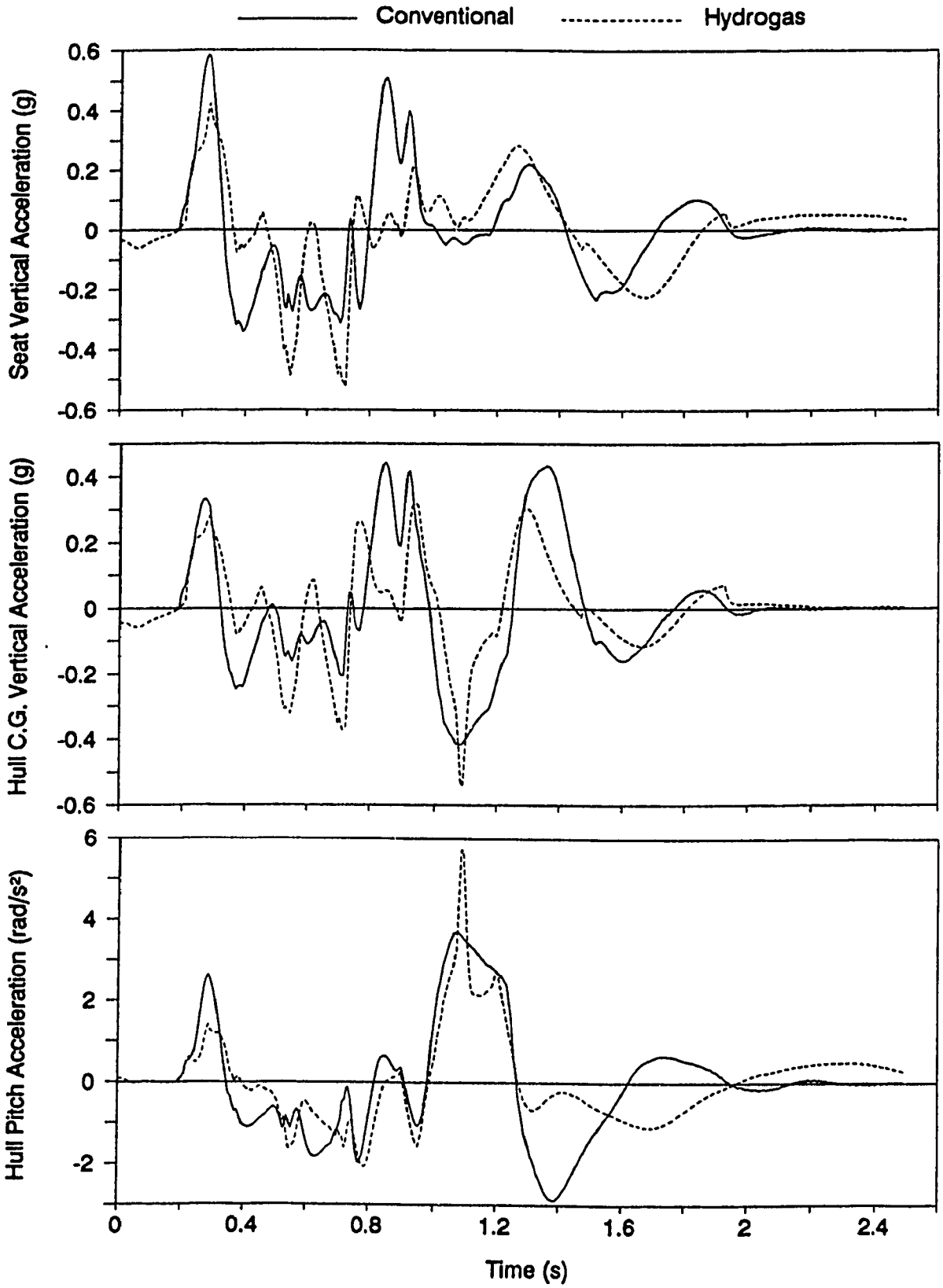

Figure 5.43 Comparison of conventional and hydrogas suspension systems - ride acceleration traces for test vehicle configuration B crossing 6" obstacle at 14.3 km/h.

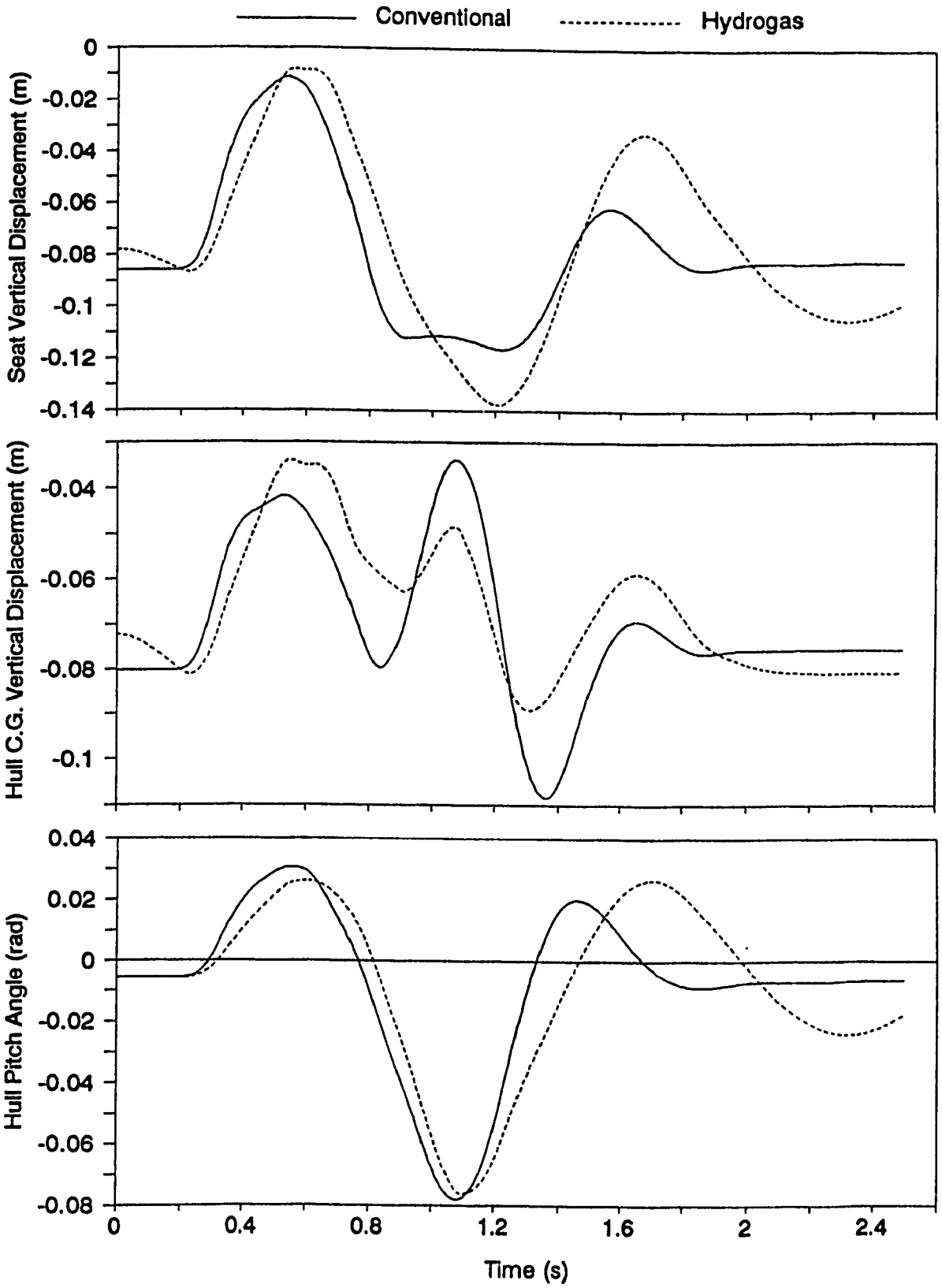

Figure 5.44 Comparison of conventional and hydrogas suspension systems - ride displacement traces for test vehicle configuration B crossing 6" obstacle at 14.3 km/h.

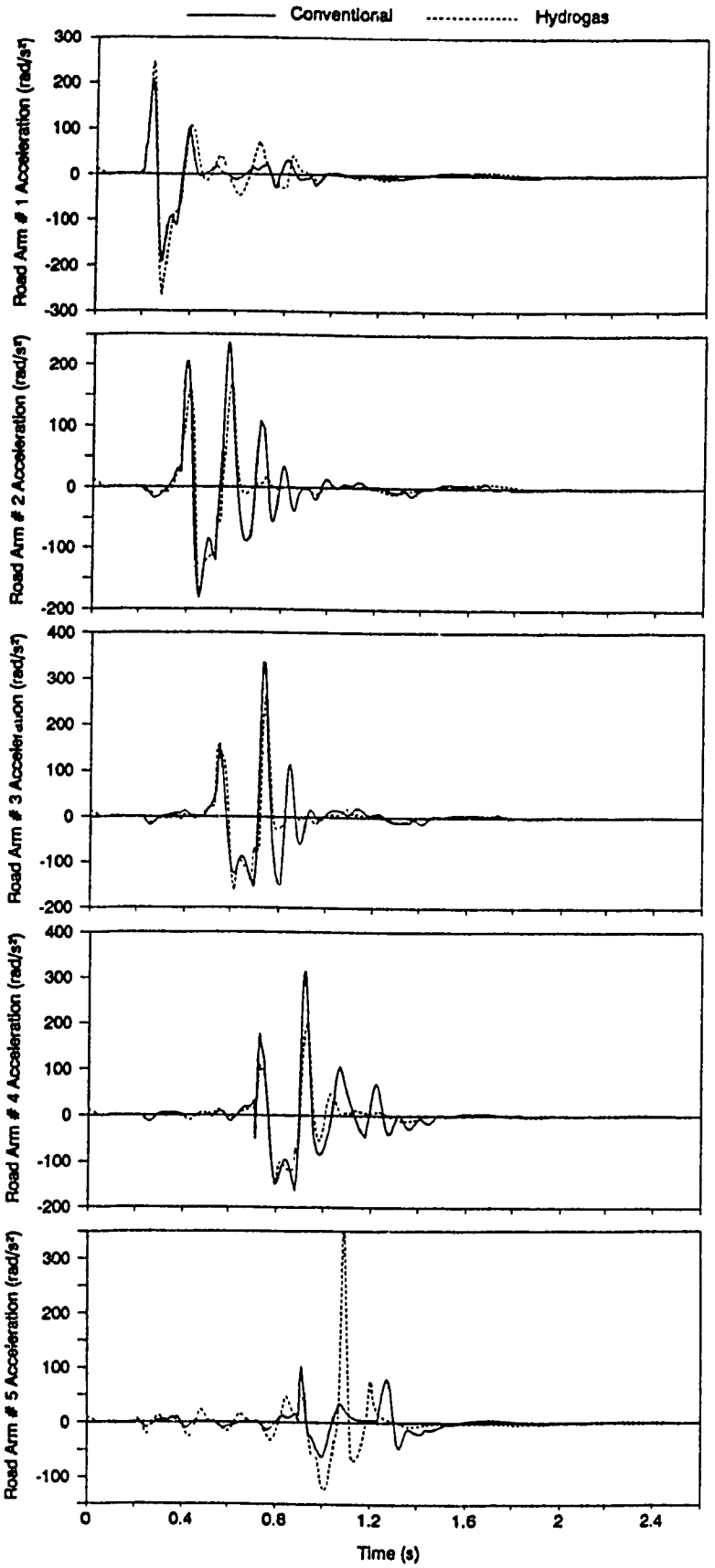

Figure 5.45 Comparison of conventional and hydrogas suspension systems - road arm acceleration traces for test vehicle configuration B crossing 6" obstacle at 14.3 km/h.

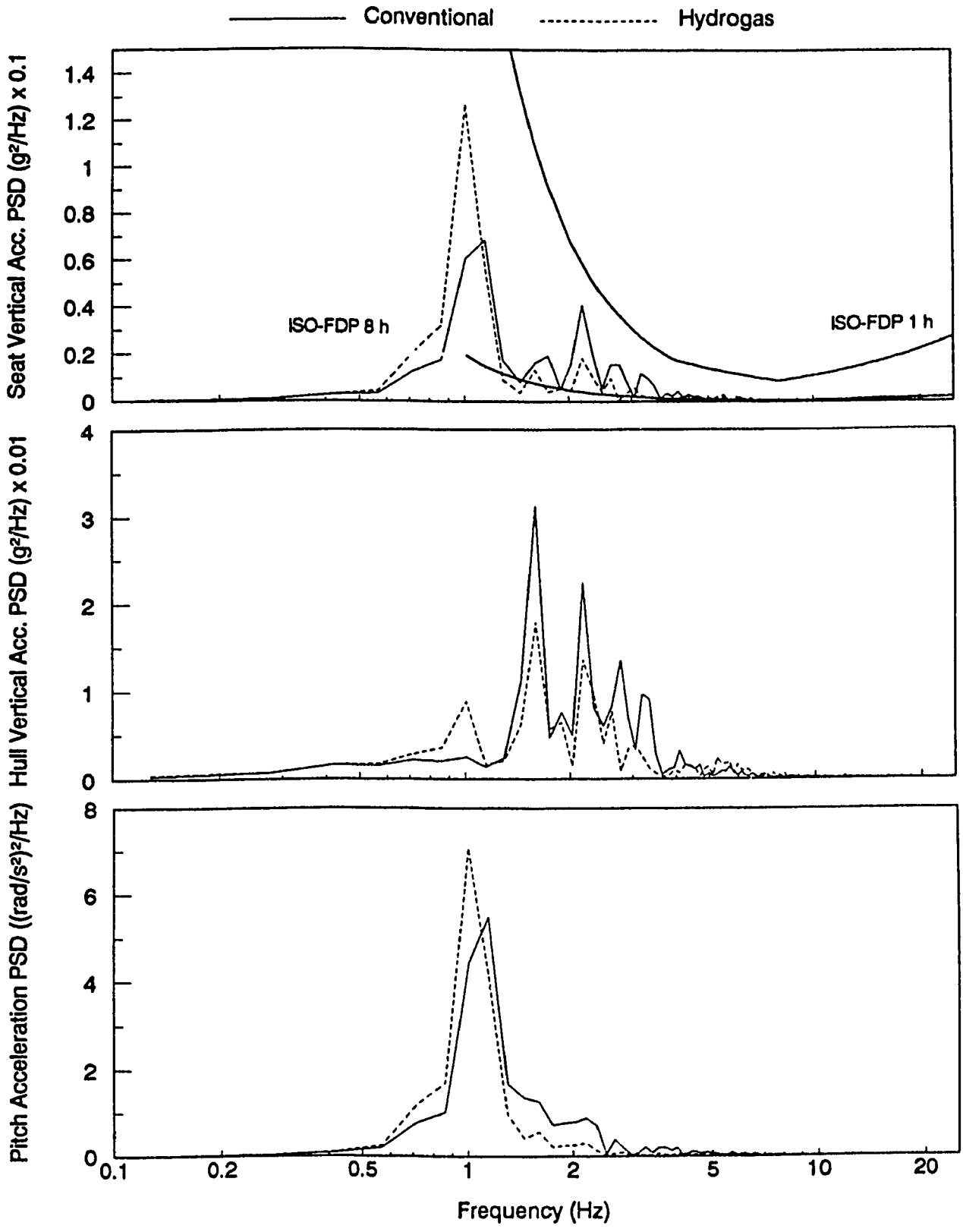

Figure 5.46 Comparison of conventional and hydrogas suspension systems - ride acceleration spectra for test vehicle configuration B traversing LETE48 random course at 13.5 km/h.

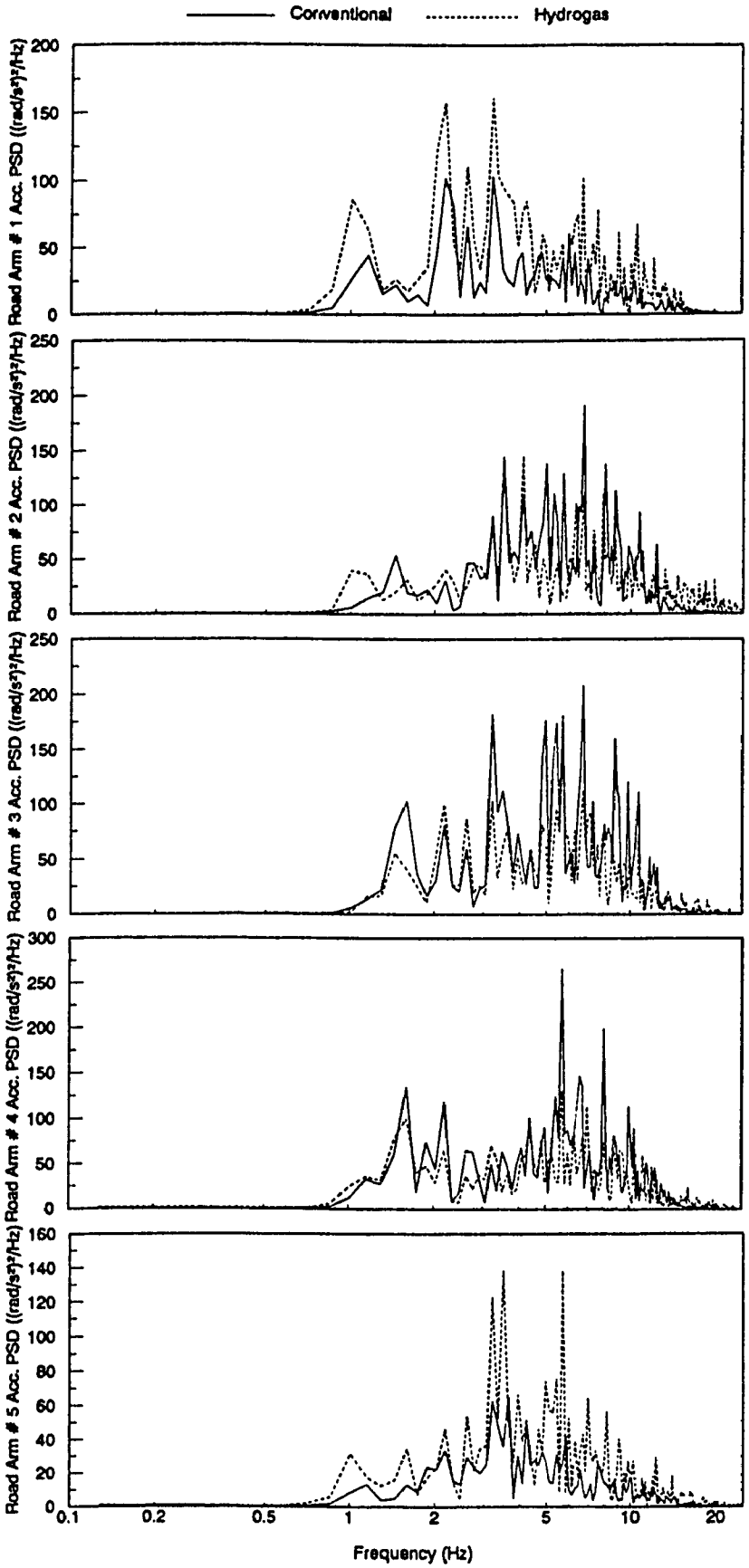

Figure 5.47 Comparison of conventional and hydrogas suspension systems - road arm acceleration spectra for test vehicle configuration B traversing LETE48 random course at 13.5 km/h.

able reduction in the acceleration levels for intermediate wheel stations, and further deterioration in the performance of first and last wheel stations, which are thus prone to endure high stress levels and early fatigue failure.

It would be quite expensive to install hydrogas suspension units at all wheel stations of the test vehicle. Subsequently, it is prudent to further investigate the possibilities of installing hydrogas suspension units at few selected wheel stations only. As indicated by the acceleration traces in Figure 5.48, there is a consistent deterioration (i.e. higher rms levels) as the number of hydrogas suspension units are gradually reduced. Based on the acceleration spectra in Figure 5.49, the seat bounce and pitch acceleration levels for the test vehicle equipped with hydrogas suspension units at the 1st, 2nd and 5th wheel stations only, are found to be only sligthly higher in comparison with those for "at all wheels", and respective average absorbed power values are almost similar. However, the hull bounce spectra exhibit a considerably high resonant peak for hydrogas suspension units mounted at the 1st, 2nd, and 5th wheel stations (similar observation in Figure 5.39). This study also revealed that installing hydrogas suspension units at the first and last wheel stations alone, does not offer any potential improvements over the conventional torsion bar suspension configuration.

5.6 SUMMARY

In this chapter, a ride dynamic model for the candidate vehicle is re-derived in view of the detailed kinematics of the torsion bar/ trailing arm suspension configuration, and is referred to as MODEL III. The Langrange's energy approach is employed to formulate the ride model,

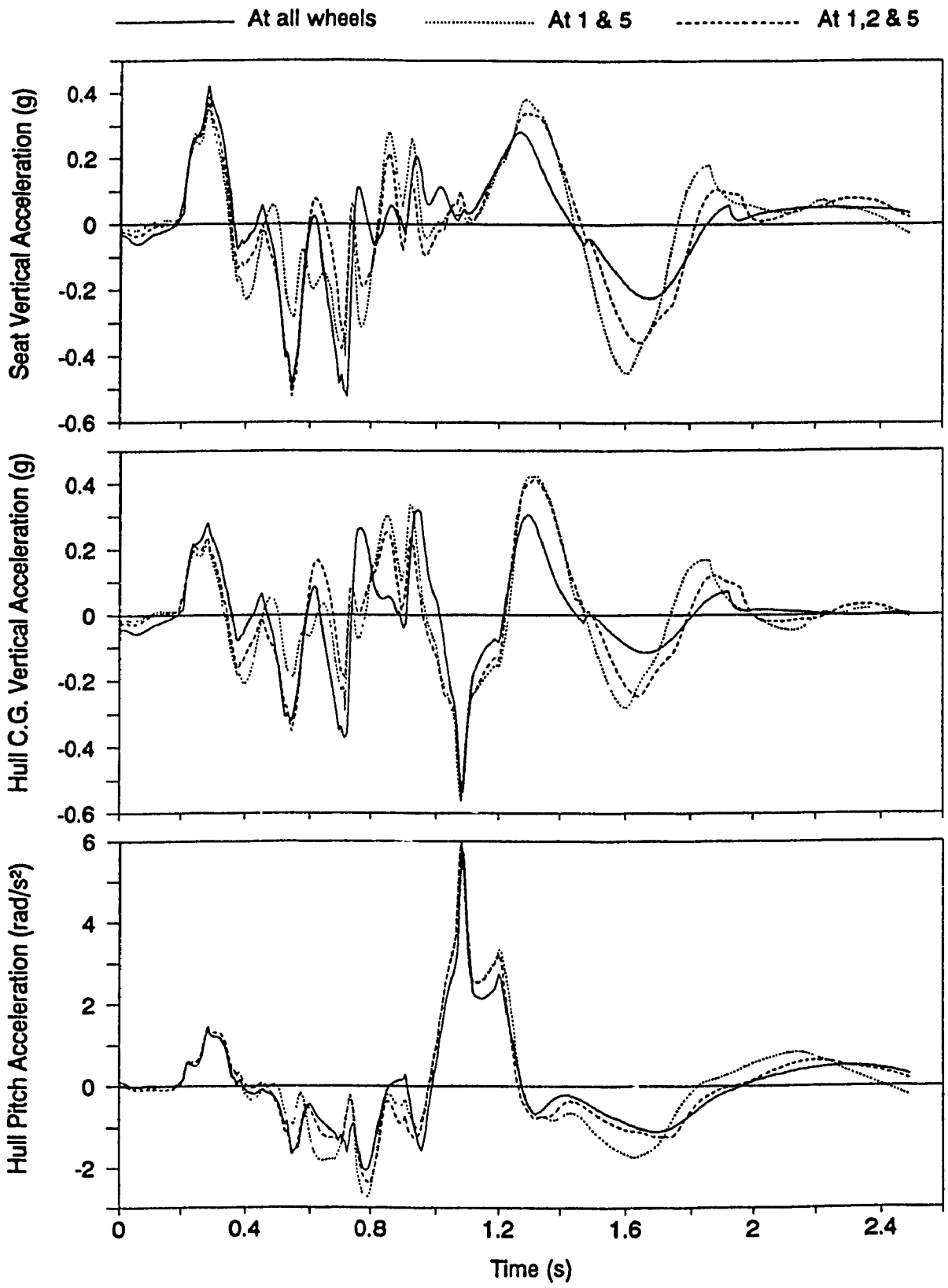

Figure 5.48 Influence of number/location of hydrogas suspension units - ride acceleration traces for test vehicle configuration B crossing 6" obstacle at 14.3 km/h.

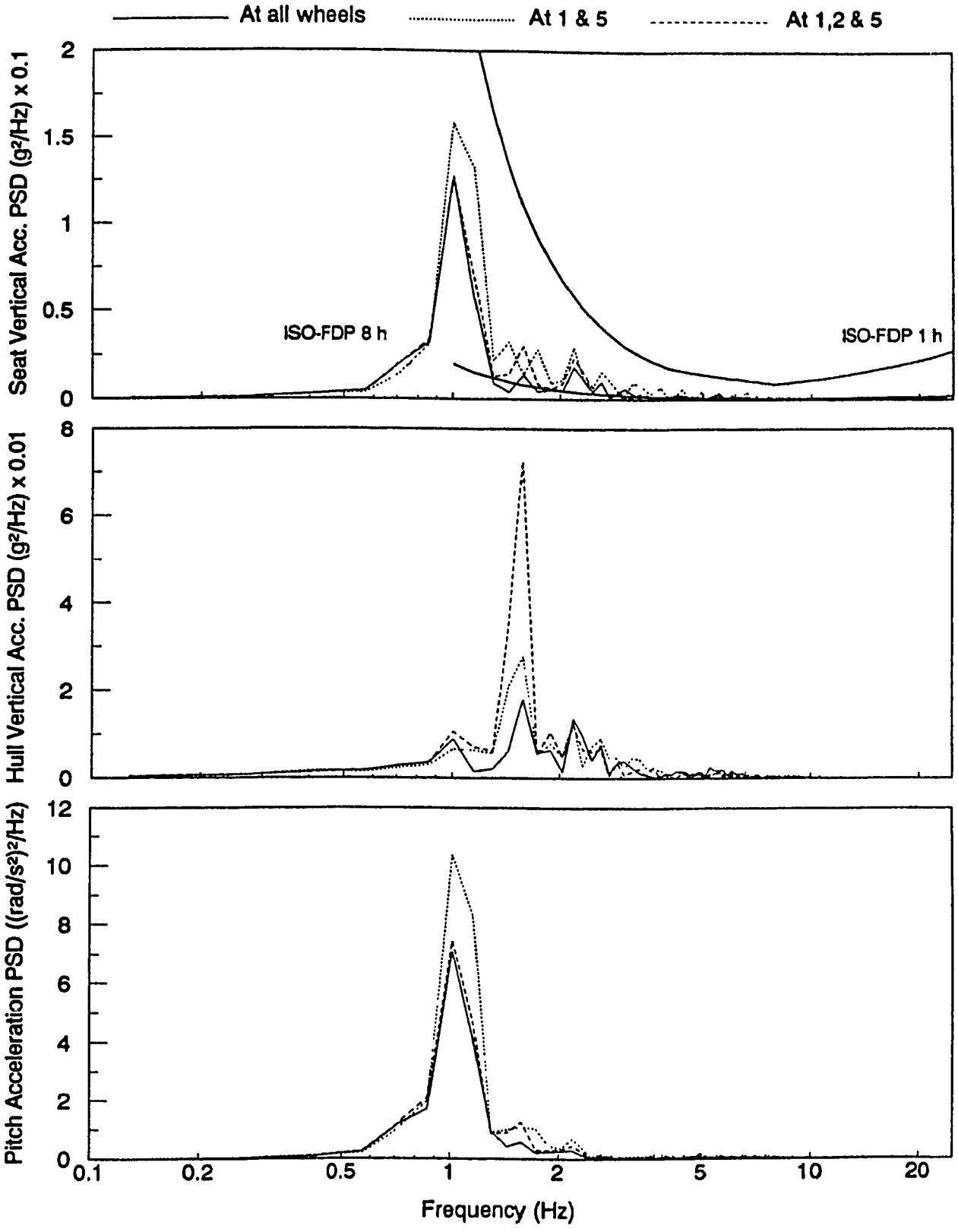

Figure 5.49 Influence of number/location of hydrogas suspension units - ride acceleration spectra for test vehicle configuration B traversing LETE48 random course at 13.5 km/h.

which is also described through "3+N" generalized coordinates: hull bounce and pitch coordinates (y_h,θ_h), road arm angle with respect to hull frame (θ_{wi},i=1,..,N), and an optional bounce coordinate for suspended seat/driver (y_o). The generalized forces include internal forces due to torsion bar stiffness, bump stops and rectilinear (inclined) spring and damper, and external track and ground forces which are evaluated using the refined track and wheel sub-models employed for MODEL II. In addition to carrying out routine and repeated ride simulations, MODEL III is also oriented for detailed design and analyses of conventional suspension components as well as advanced suspension system such as hydrogas suspensions developed for high mobility tracked vehicles.

The relative performance of MODEL III is assessed based on an extensive field validation of its ride predictions. In comparison with MODEL II's ride predictions, the MODEL III's predictions exhibit generally smoother ride and relatively closer agreement with the measured ride data. In terms of computer run time, MODEL III is found to be almost as fast as MODEL II.

A parameteric sensitivity analyses is carried out using the field-validated MODEL III in order to study the influence of test vehicle's primary suspension parameters: equivalent stiffness of road wheel/track pad, torsion bar stiffness, and suspension damping due to the inclined shock absorber. Based on the parametric study, it is shown that:

- The equivalent stiffness of road wheel/track pad has very little influence, whereas lowering the torsion bar stiffness improves the ride performance.
- A reduction in the suspension damping improves the vehicle transient response to a half round obstacle, however, the vehicle's ride

performance over a random course is deteriorated.

- The ride dynamic behaviour of the test vehicle is considerably improved by mounting the shock absorbers at all wheel stations.

In addition, the ride performance potentials of a hydrogas suspension system especially developed for application with M113 APC's are investigated. The results indicated that replacing the conventional suspension system with hydrogas suspension units at all wheel stations reduces the ride acceleration levels, however at the expense of higher magnitudes of displacement and angular accelerations of first and last wheel stations. The ride responses evaluated in conjunction with hydrogas suspension units mounted at few selected wheel stations indicated:

- The overall ride performance with hydrogas suspension units mounted at 1st, 2nd and 5th wheel stations is comparable to that of the vehicle equipped with hydrogas suspension units at all wheel stations.
- The hydrogas suspension units at the first and last wheel stations alone do not offer significant improvement over the conventional torsion bar suspension configuration.

Chapter 6

RIDSIM: COMPUTER SIMULATION MODEL FOR RIDE ANALYSIS OF WHEELED/TRACKED OFF-ROAD VEHICLES

6.1 INTRODUCTION

The usage of general-purpose mutli-body software for off-road vehicle ride analysis has been limited due to the complications associated with the system modeling, tedious input requirements, and high computer run time/costs [1]. The computer simulation models developed in this study represent a simplified yet effective approach to study the ride dynamics of a specific type or class of off-road vehicles. The ride dynamic study of the candidate vehicle has, however, demonstrated that a worthwhile simulation in the presence of highly irregular terrain surface generally demands for high resolution sub-models for vehicle suspension system and dynamic wheel-track-terrain interactions. The sub-systems modeling strategies and computational algorithms proposed in this study have been established to yield fairly accurate ride predictions while consuming least computer run time.

The primary objective of the current research program has been to develop a comprehensive computer simulation model which would be an economical and convenient tool to investigate the ride/suspension dynamics of a wide variety of both wheeled as well as tracked vehicles. The proposed computer model, referred to as RIDSIM (Ride Dynamic Simulation), is developed primarily based on the modeling strategies adopted for the candidate vehicle. In the formulation of RIDSIM, the sub-model for vehicle suspension system is incorporated considering various suspension types in addition to wheel and track sub-models, which have been proposed in this study as well as previous studies (Section 4.4).

Thus, RIDSIM permits a convenient vehicle model construction based on the user-specified sub-system models. The purpose of this Chapter is to present the mathematical development of RIDSIM, and demonstrate its usage.

6.2 DEVELOPMENT OF MULTI-PURPOSE RIDE DYNAMIC SIMULATION MODEL: RIDSIM

The mathematical development of RIDSIM is based on the basic assumptions made in the modeling process for the candidate vehicle: two-dimensional ride dynamics, constant forward vehicle speed, and non-deformable arbitrary terrain profile. Figure 6.1 shows the schematic representation for typical wheeled and tracked off-road vehicle configurations. From modeling point of view, the wheeled vehicle is concieved in a manner similar to the tracked vehicle, while ignoring track and hull wheels (sprocket, idler, and roller supports). The basic model description is same as for the ride dynamic models developed for the candidate vehicle (Figures 2.4 and 5.2) - vertical and pitch degrees-of-freedom associated with the vehicle sprung mass, an optional vertical degree-of-freedom for the suspended driver/seat system, and "N-number" of road wheel and axle assemblies represented by the unsprung mass lumped at the wheel centre. However, the track geometric description has been extended to account for "M-number" of hull wheels, where M is greater than or equal to 1 (e.g. M=2 for the candidate vehicle), and special vehicle configurations where not all the road wheels are *confined* by the track. Subsequently, in addition to a conventional tracked vehicle configuration as shown in Figure 6.1(b), various miscellaneous configurations as illustrated in Figure 6.2 can be conveniently modeled using RIDSIM. It should be noted that a hull wheel located between the

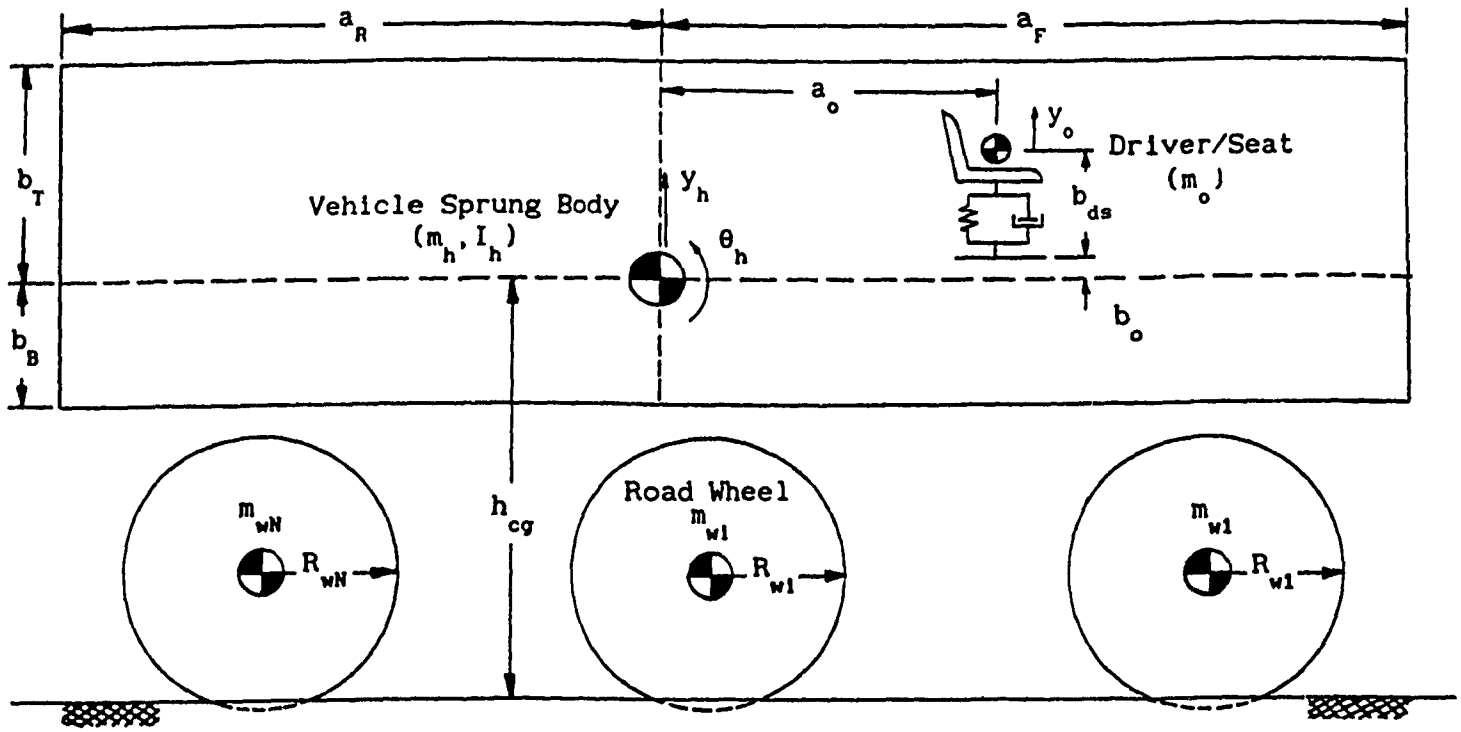

(a) A Typical Wheeled Vehicle

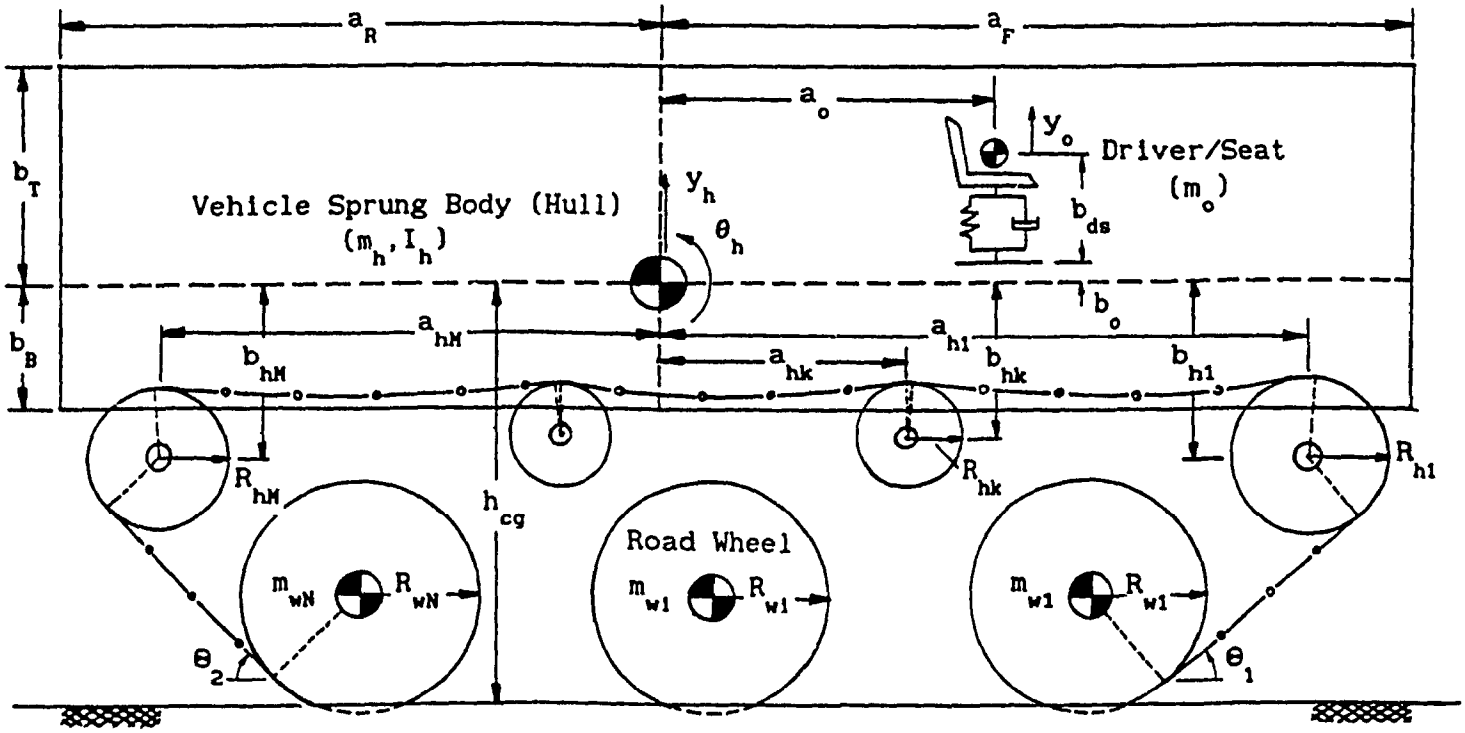

(b) A Typical Tracked Vehicle

Figure 6.1 In-plane model representation of a typical off-road vehicle.

frontmost and rearmost road wheels, is automatically excluded from the computational wheel-terrain dynamic interaction, since it would be impossible for it to make contact in any way with the terrain profile. For instance, intermediate hull wheels (roller supports) in Figure 6.1(b), second hull wheel in Figure 6.2(b), and both hull wheels in Figures 6.2(c) are excluded. Similarly, the road wheels not confined by the track (Figure 6.2c) are free of dynamic track load.

The dynamic wheel-track-terrain interaction is formulated considering the proposed wheel and track sub-models (idealized and adaptive continuous spring wheel models, and track model #'s 1 and 2), and ones proposed in the previous studies (Appendix I). The user specifies the sub-models of choice. The vehicle ride model can thus be conceived based on a varying degree of complexity, which could assist the user in choosing *optimum* wheel and track sub-models for specified simulation conditions (terrain profile roughness and vehicle speed).

The sub-model for vehicle suspension system is formulated considering various suspension configurations commonly employed for off-road vehicles. There are undoubtedly a greater variety of conventional passive suspension systems for these vehicle, and recent trend is towards the use of active and semi-active suspension controls. Whether passive or active, the most commonly employed suspension configurations can be modeled using the five basic models:

- Unsprung/rigid suspension
- Independent suspension
- Torsion bar/trailing arm suspension
- Walking beam suspension
- Bogie suspension

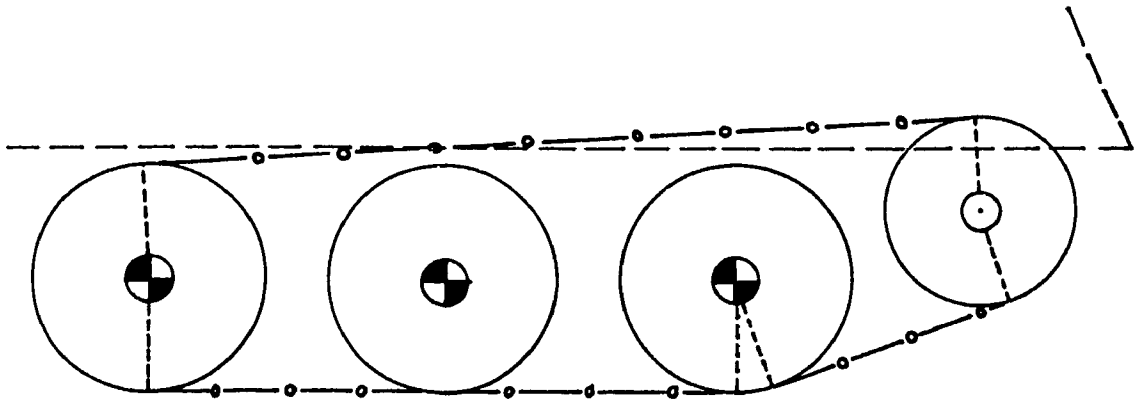

(a)

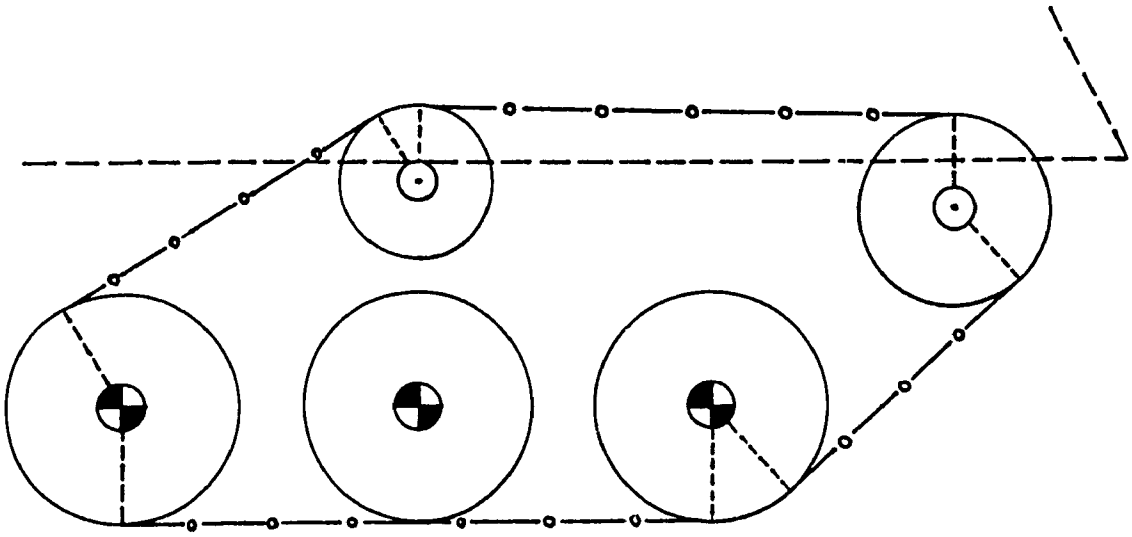

(b)

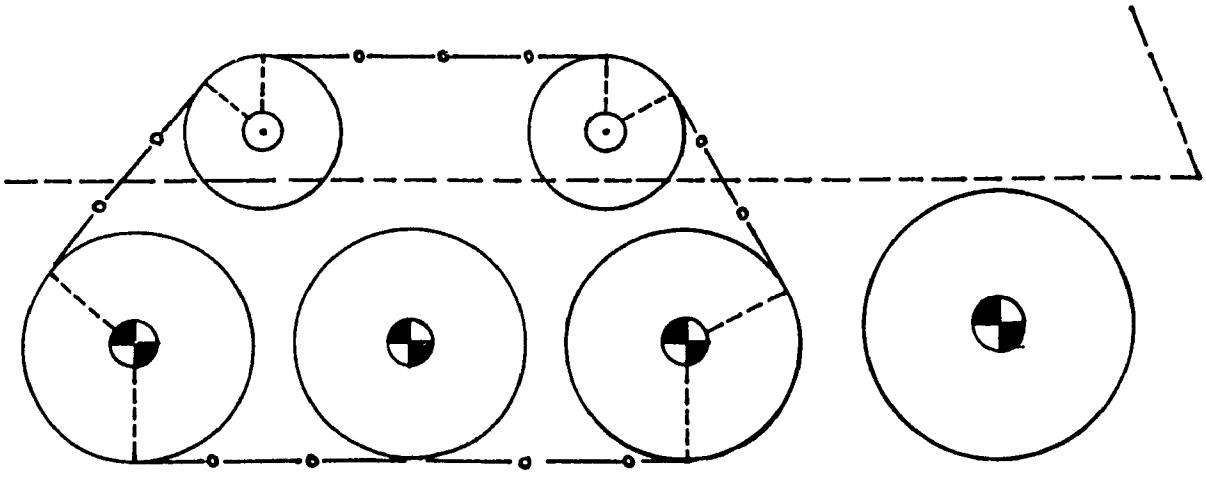

(c)

Figure 6.2 Miscellaneous tracked vehicle configurations.

For instance, the ride model of a farm tractor is formulated using unsprung or rigid suspension, since the large, soft wheels are rigidly connected to the chassis. The independent suspension model is a realistic representation of a commonly employed pillar suspension (with collinear telescopic damper and coil spring), or even an *idealized* representation of more complex suspension systems such as torsion bar/trailing arm suspension (MODEL II). As discussed in Chapter 2, the high-speed tracked military vehicles, such as the candidate vehicle, are generally fitted with torsion bar/trailing arm suspension system to attenuate terrain-induced shock and vibration. This suspension type has been modeled in detail in Chapter 5 (MODEL III). The new generation of high-speed wheeled military vehicles (LAV's - light armoured vehicles) incorporate both pillar as well as torsion bar/trailing arm suspension systems. The walking beam and bogie suspension models are commonly employed to represent the suspension systems fitted to the rearmost wheel set of heavy wheeled vehicles such as cargo and dump trucks. Both suspension systems primarily incorporate a set of wheel pair linked by a rigid beam, and require more than one generalized coordinate to describe the kinematic state. The kinematics of walking beam suspension is described through vertical and rotational coordinates, whereas the bogie suspension involves three degrees-of-freedom (two vertical and one rotational coordinate). These suspension models are discussed in detail in Appendix II.

RIDSIM is formulated based on a *modular* or *building-block approach*, where the dynamic equation(s) governing the motion of each of above-mentioned suspension types are derived in parallel with the associated equations describing bounce and pitch motions of vehicle sprung body. All

equations are provided in Appendix II. Subsequently, the ride dynamics of a wheeled/tracked vehicle with any mixture of suspension types can be simulated using RIDSIM. It should be noted that the capabilities of RIDSIM can be easily extended by incorporating newer specialized suspension models.

6.3 COMPUTATIONAL PROCEDURE

The ride simulation model (RIDSIM) is programmed entirely in FORTRAN, and currently operated on a MicroVAX computer. The key elements of the computational procedure are essentially the same as the ones discussed in Section 2.7:

- *Input*,
- *Initialization*,
- *Solution of equations of motion*, and
- *Output*.

The input data, as discussed in section 2.7, includes simulation control parameters, terrain profile description, and appropriate vehicle parameters. The vehicle input information required for RIDSIM, however, depends on user-specified suspension, wheel, and track sub-models. RIDSIM lets the user create vehicle and terrain profile data files with stacked multiple data sets, where each set begins with an identifier name. The desired vehicle and profile data sets are then selected based on the *matching* of the user-specified search names with the identifier names.

The vehicle ride model is automatically formulated in conjunction with the user-specified sub-models for suspension, wheel, and track, where, the equations of motion are compiled based on equation (II.2). The static analysis is carried out in the initialization phase, where the

vehicle's zero-force and static equilibrium configurations are established. The dynamic simulation then begins by incrementing time with the vehicle horizontally moving forward with specified speed. The dynamic wheel, track, and suspension forces are computed based on the specified sub-models, and the right-hand-side generalized force vector is compiled. The equations of motion are integrated based on Hammings Modified Predictor-Corrector method (a variable time-step approach). All key coordinates on the vehicle are then updated using the corresponding displacements. This process continues until the pre-assigned maximum simulation time is reached. The results are obtained as traces of response variables of interest, which serves as an input to the post-processor for a graphical display (animation), and FFT signal-processing.

6.4 APPLICATIONS OF VEHICLE RIDE ANALYSIS

In this section, applications of RIDSIM are demonstrated with examples involving two different wheeled off-road vehicles - surrogate fast attack vehicle (SFAV), and 5 ton cargo truck (M923). The ride simulations are carried out using the proposed *adaptive continuous spring model* for the dynamic wheel- terrain interaction.

6.4.1 Surrogate Fast Attack Vehicle (SFAV)

This vehicle is a cross-country utility vehicle (Figure 1.2b) employed for military applications. The vehicle is supported on two wheels on each side, where the rear wheel is slightly larger than the front wheel. The suspension units fitted at front and rear wheel stations are simple pillar suspension systems. The driver's seat is considered to be rigidly connected to the vehicle body. Subsequently, SFAV is represented as 4 degrees-of-freedom ride dynamic model incorporating the

independent suspension sub-model, where the generalized coordinate vector (equation II.3) is compiled as:

$$\{ q \} = \{ y_h, \theta_h, y_{w1}, y_{w2} \}' \qquad (6.1)$$

where, y_{w1} and y_{w2} represent the vertical degrees-of-freedom associated with the lumped unsprung mass at front and rear wheel centres, respectively.

The vehicle simulation parameters are listed in Table 6.1. The force-deflection and force-velocity characteristics for the pillar suspension units, as shown in Figure 6.3, are input as look-up tables. The undamped natural frequencies and associated deflection modes, predicted based on the converged stiffness matrix (equation 2.88) corresponding to vehicle's static equilibrium configuration, are listed in Table 6.2.

The ride simulation is carried out for the SFAV crossing over a triangular bump (height = 0.25 m, base = 2 m) at 20 km/h. Figure 6.4 shows the animation snapshots, where the ride harshness is clearly visible as the SFAV frequently lost contact with the ground. The simulated acceleration traces are shown in Figures 6.5 and 6.6, where the trends are well-explained by the animation. The shock performance of SFAV for the simulated condition is unacceptable as the peak value of ride bounce acceleration (4.3 g) is much higher than the limiting value of 2.5 g. The shock-limiting speed (the speed at which the peak value $\leq$ 2.5 g) can thus be established based on repeated simulation runs with gradually-reduced vehicle speed. Similarly, the vehicle suspension system can be optimized in an effort to reduce the peak level transmitted at desired vehicle speed.

Table 6.1 Parameters of SFAV [72].

Description	*Symbol*	*Value*
Sprung mass/inertia:		
Mass, kg	m_h	512
Mass moment of inertia, $kg.m^2$	I_h	449
Unsprung mass/inertia:		
Front wheel/axle, kg	m_{w1}	41.7
Rear wheel/axle, kg	m_{w2}	69.4
Horizontal distance from c.g. to:		
Suspension # 1, m	a_1	1.791
Suspension # 2, m	a_2	-0.775
Driver's seat, m	a_o	0.254
Vehicle's front end, m	a_F	2.159
Vehicle's rear end, m	a_R	-1.524
C.G. height, m	h_{cg}	0.587
Vertical distance from c.g. to:		
Suspension # i, m (i=1,2)	b_i	-0.204
Driver's seat, m	b_o	-0.178
Vehicle's top end, m	b_T	0.304
Vehicle's bottom end, m	b_B	-0.204
Radius:		
Front wheel, m	R_{w1}	0.356
Rear wheel, m	R_{w2}	0.389
Radial Spring Constant:		
Front wheel, N/m/rad	K^1_{rw}	622 193
Rear wheel, N/m/rad	K^2_{rw}	1 272 748
Damping Constant:		
Front wheel, N.s/m	C^1_{rw}	0.0
Rear wheel, N.s/m	C^2_{rw}	0.0

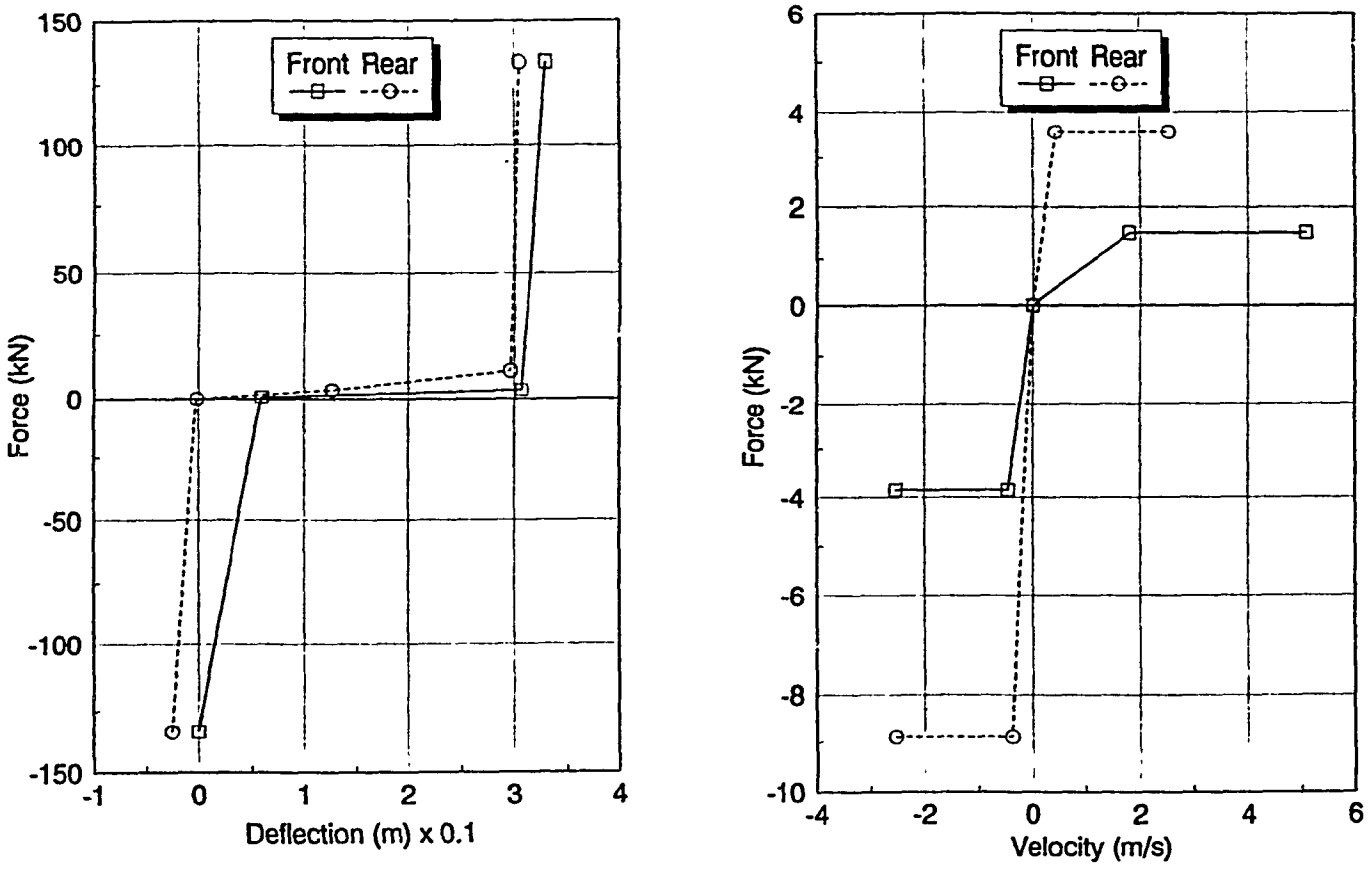

Figure 6.3 Suspension characteristics for SFAV [72].

Table 6.2 Predicted natural frequencies & deflection modes for SFAV.

Undamped Natural Frequency (Hz)	*Dominant Deflection Mode*
1.37	y_h
1.71	θ_h
11.2	y_{w1}
12.5	y_{w2}

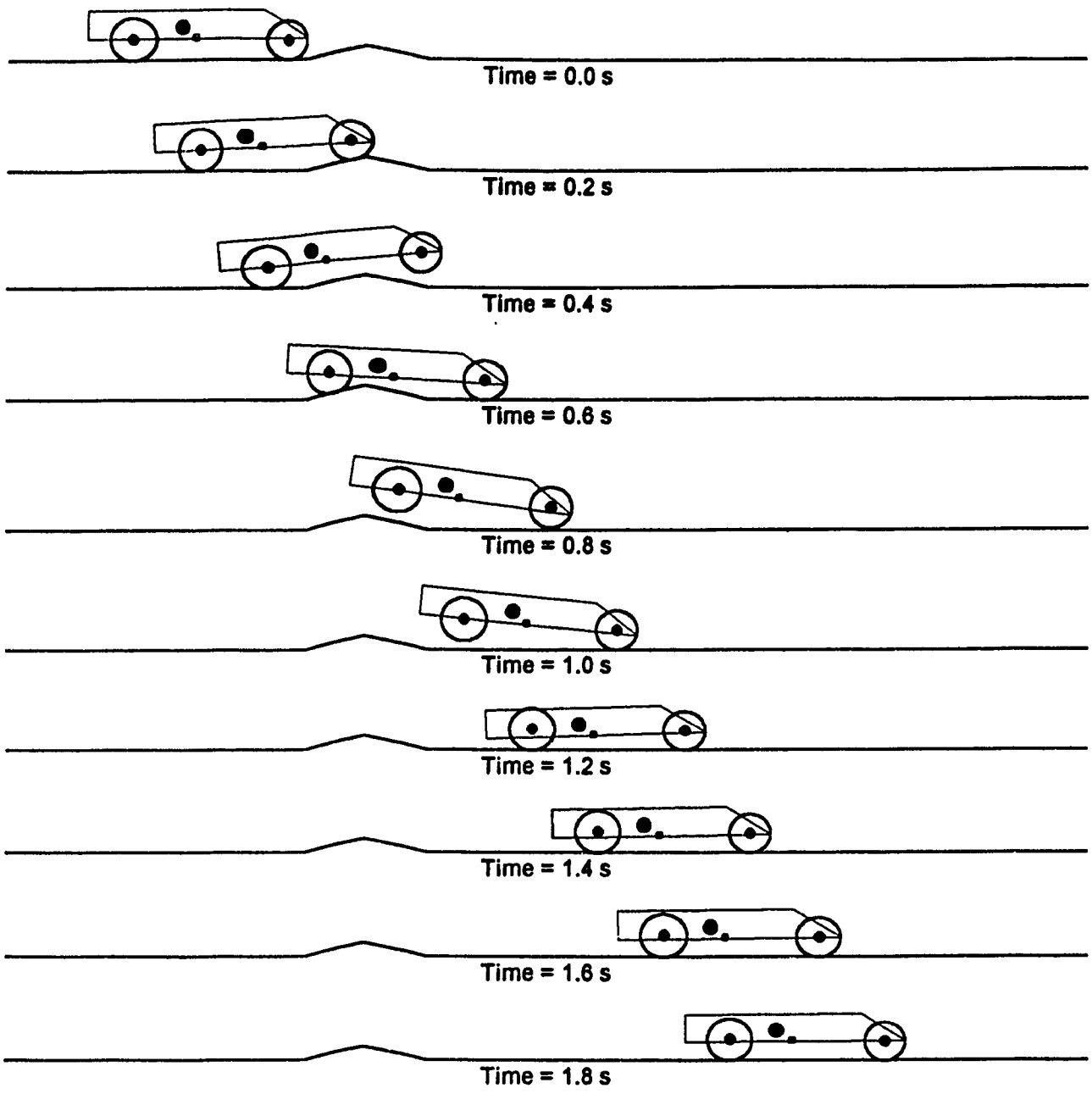

Figure 6.4 Animated snapshots of SFAV crossing triangular bump at 20 km/h.

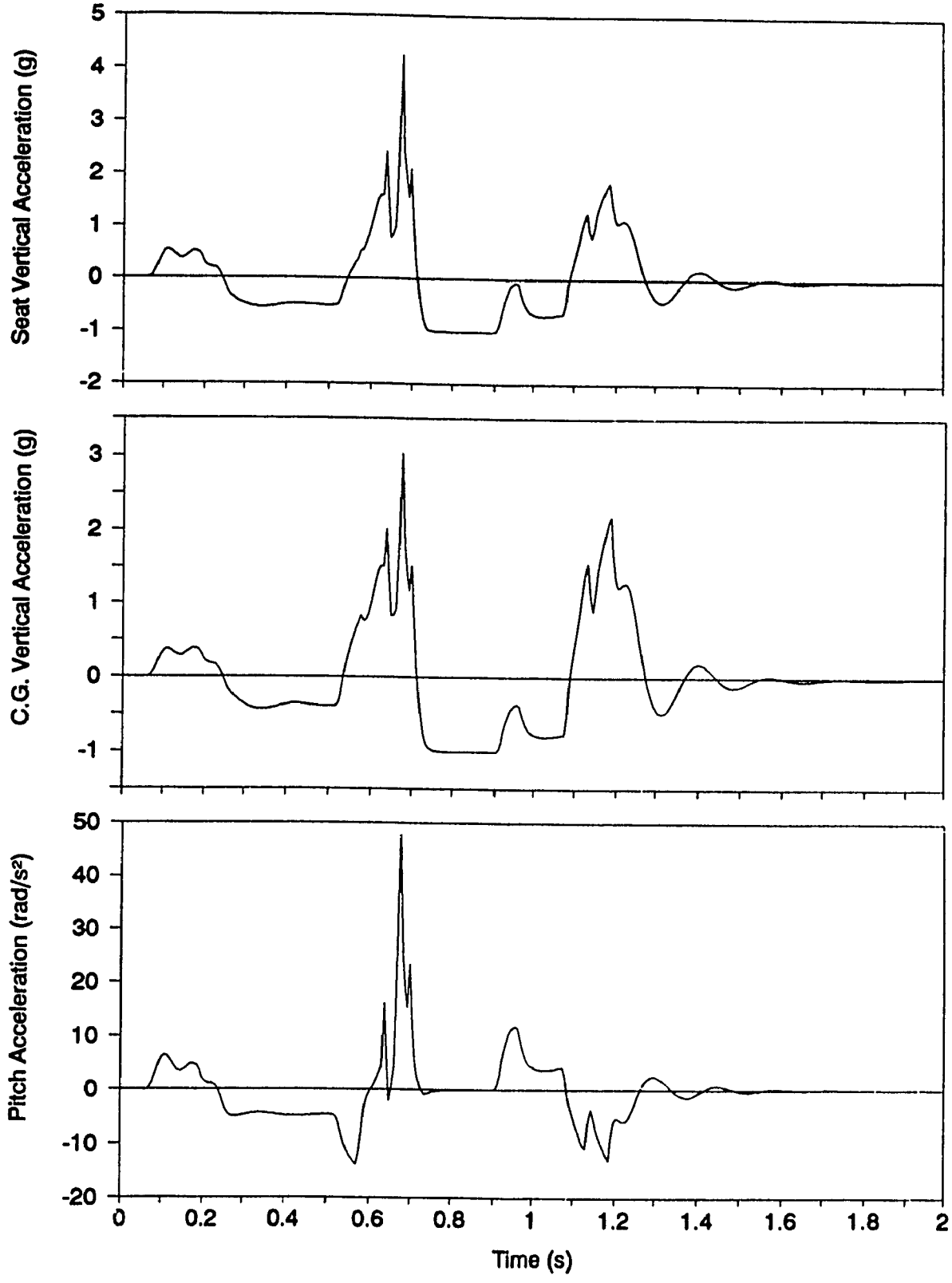

Figure 6.5 Ride acceleration traces for SFAV crossing triangular bump at 20 km/h.

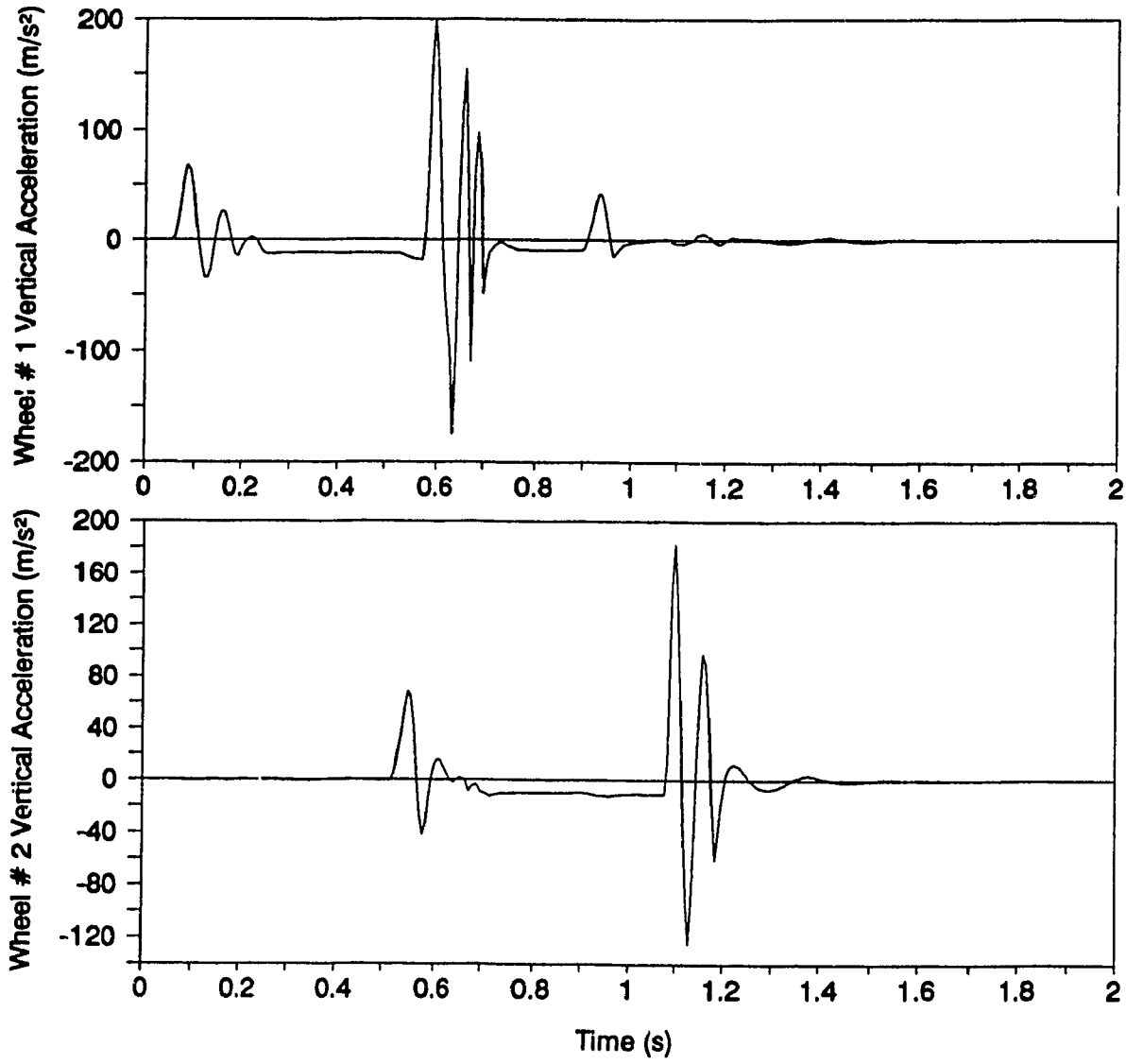

Figure 6.6 Wheel acceleration traces for SFAV crossing triangular bump at 20 km//h.

6.4.2 M923, 5 Ton Cargo Truck

The second example involves a military truck which looks similar to the dump truck shown in Figure 1.2(b). This vehicle has mixed suspension systems including pillar and bogie suspensions. The pillar suspension is fitted to the single-wheel station in the front, whereas the bogie suspension in the rear incorporates a pair of dual-wheel set. The truck ride model is then formulated as a 6 degrees-of-freedom dynamical system considering independent suspension model in the front and bogie suspension model in the rear. The equation of motion are compiled based on the generalized coordinate vector given as:

$$\{ q \} = \{ y_h, \theta_h, y_{w1}, y_{w12}, y_{w22}, \theta_{w2} \}' \qquad (6.2)$$

where, y_{w1} is the vertical degree-of-freedom associated with the independent suspension. y_{w12}, y_{w22}, and θ_{w2} are the three degrees-of-freedom required to describe the kinematic associated with bogie suspension, where y_{w1} and y_{w2} represent the vertical degrees-of-freedom for front and rear bogie wheels, and θ_{w2} is the rotational degree-of-freedom for the bogie beam. It should be noted that the driver's seat computations are excluded in the simulation due to the lack of parameters.

The vehicle simulation parameters are listed in Table 6.3. The force-deflection and force-velocity characteristics for the independent and bogie suspension units are illustrated in Figure 6.7, where the linear damping rate represent the dampers associated with both independent as well as bogie suspensions. Table 6.4 lists the natural frequencies and dominant deflection modes predicted in conjunction with the vehicle's static equilibrium configuration.

Table 6.3 Parameters of M923 truck [72,30].

Description	*Symbol*	*Value*
Sprung mass/inertia:		
Mass, kg	m_h	5 568
Mass moment of inertia, $kg.m^2$	I_h	20 765
Unsprung mass/inertia:		
Wheel/axle mass, kg	m_{wi} (i=1..3)	619
Beam inertia, $kg.m^2$	I_{w2}	19.4
Horizontal distance from c.g. to:		
Independent susp., m	a_1	2.972
Bogie suspension's		
Pivot point (C), m	a_2	-1.575
Front damper (A), m	a_{12}	-0.889
Rear damper (B), m	a_{22}	-2.261
Vehicle's front end, m	a_F	4.064
Vehicle's rear end, m	a_R	-3.632
C.G. height, m	h_{cg}	1.346
Vertical distance from c.g. to:		
Independent susp., m	b_1	-0.432
Bogie suspension's		
Pivot point (C), m	b_2	-0.819
Front damper (A), m	b_{12}	-0.432
Rear damper (B), m	b_{22}	-0.432
Vehicle's top end, m	b_T	0.813
Vehicle's bottom end, m	b_B	-0.432
Wheel radius, m	R_{wi} (i=...3)	0.643
Bogie beam length, m	l_{12}	0.686
	l_{22}	-0.686

(Table 6.3 - continued)

Table 6.3 Parameters of M923 truck [72,30].

Description	*Symbol*	*Value*
Bogie pivot point:		
Torsional spring rate, N.m/rad	K_{T2}	0.0
Equivalent torsional spring rate for bump stops, N.m/rad	K^{U}_{T2}, K^{L}_{T2}	412 374
Radial clearance for upper bump stop, deg	θ^{U}_{w2}	20.0
Radial clearance for lower bump stop, deg	θ^{L}_{w2}	-20.0
Radial spring constant:		
Wheel # 1, N/m/rad	K^{1}_{rw}	1 148 730
Wheel # 2, N/m/rad	K^{2}_{rw}	3 324 143
Wheel # 3, N/m/rad	K^{3}_{rw}	3 361 732
Damping constant:		
Wheel # 1, N.s/m	C^{1}_{rw}	462
Wheel # 2, N.s/m	C^{2}_{rw}	924
Wheel # 3, N.s/m	C^{3}_{rw}	924

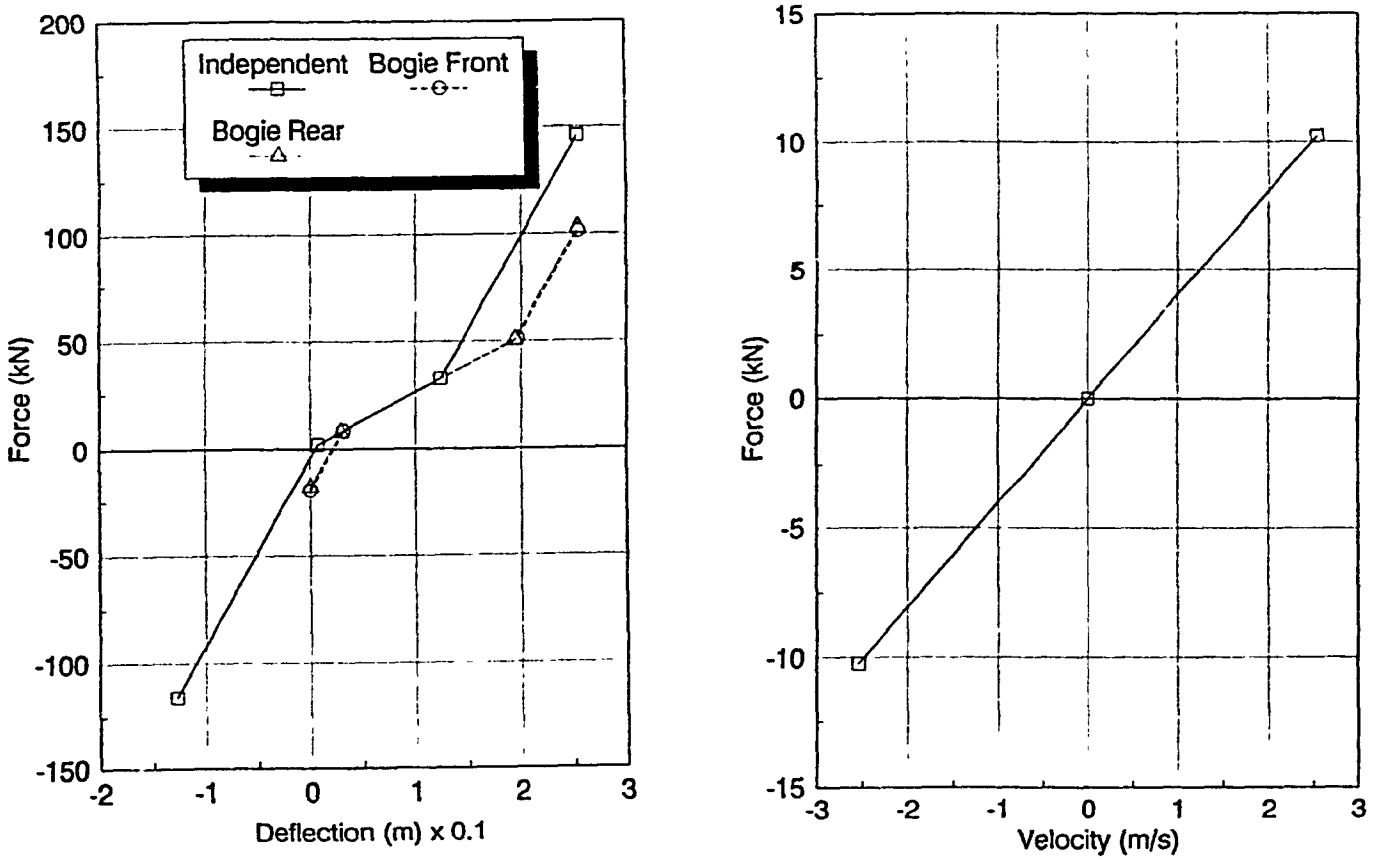

Figure 6.7 Suspension characteristics for M923 cargo truck [72].

Table 6.4 Predicted natural frequencies & deflection modes for M923 truck.

Undamped Natural Frequency (Hz)	*Dominant Deflection Mode*
1.58	y_h, θ_h, y_{w1}
1.82	y_h, θ_h, y_{w1}
5.94	y_{w1}
6.70	y_{w12}, y_{w22}, θ_{w2}
7.62	y_{w12}, y_{w22}
18.0	θ_{w2}

The ride simulations are performed for M923 truck traversing over the triangular bump and the LETE48 random course at 15 km/h. Figures 6.8 and 6.9 show the acceleration traces for M923 truck crossing the bump. The animated snapshots illustrated in Figure 6.10 assist in understanding the vehicle dynamic responses shown in Figures 6.8 and 6.9. The beam angular acceleration trace in Figure 6.9 exhibits high frequency fluctuations. The beam rotation within the specified permissible range is only constrained by suspension units at each end, and corresponding natural frequency is 18.0 Hz (Table 6.4). The beam's natural frequency is, however, increased to 30 Hz beyond the permissible limits, where the bump stops are engaged. Figures 6.11 and 6.12 show the acceleration spectra for M923 truck traversing LETE48 random course. The bounce acceleration spectra for all three wheels exhibit primary peaks occuring at slightly higher frequencies than the one listed in Table 6.4. These frequencies correspond to the bump stops incorporated in the suspension spring characteristics (Figure 6.7).

6.5 SUMMARY

In this Chapter, a multi-purpose ride dynamic simulation model (RIDSIM) is developed considering sub-models for primary suspension systems which are commonly employed for wheeled/tracked off-road vehicles. RIDSIM is formulated based on a modular or building-block approach, where equations of motion are written considering individually each of the basic suspension sub-models. Thus, RIDSIM can be conveniently employed to simulate ride dynamics of wheeled and tracked vehicle configurations with any mixture of suspension types. The dynamic wheel-track-terrain interaction is formulated based on the proposed wheel and

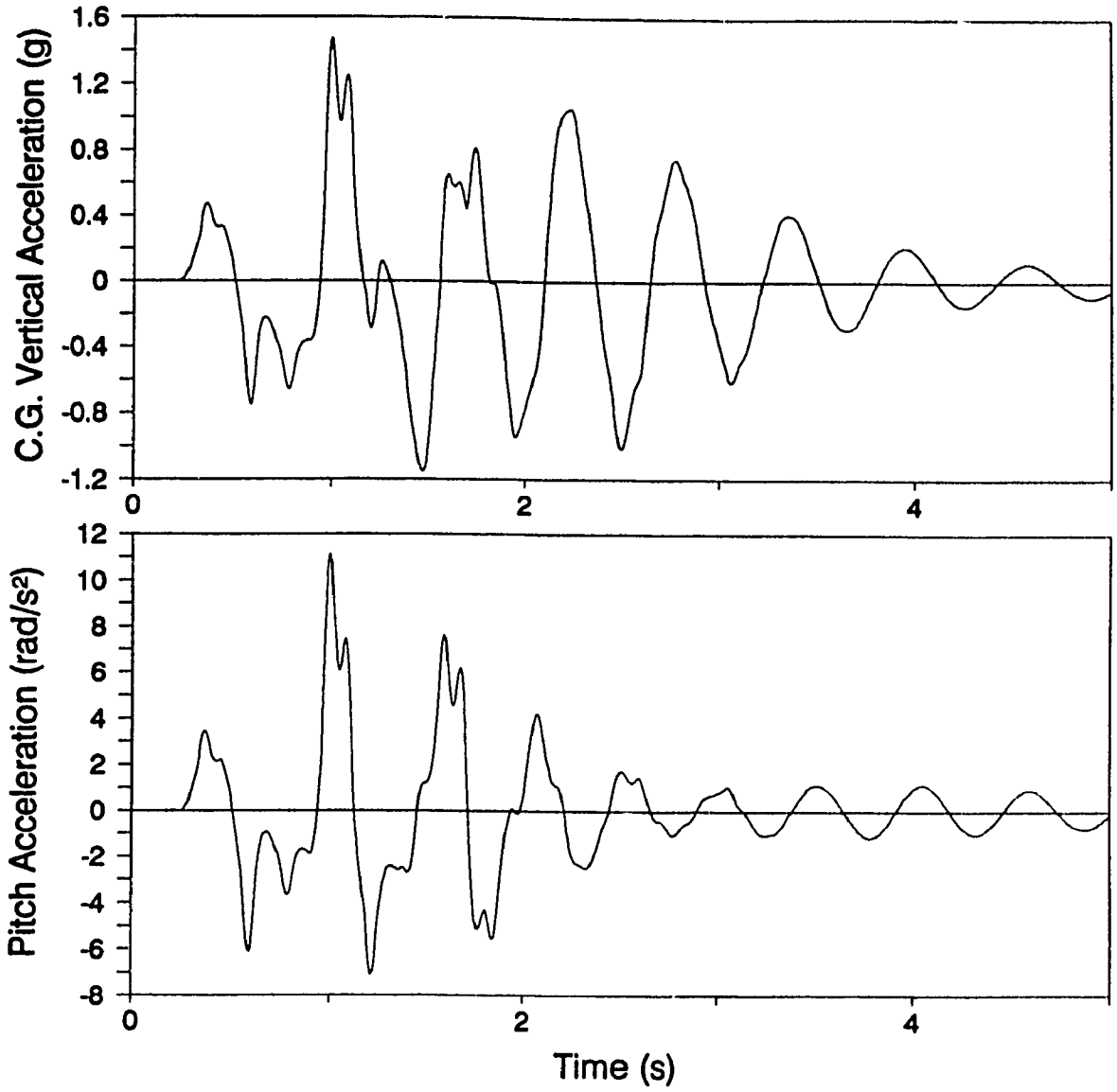

Figure 6.8 Ride acceleration traces for M923 truck crossing triangular bump at 15 km/h.

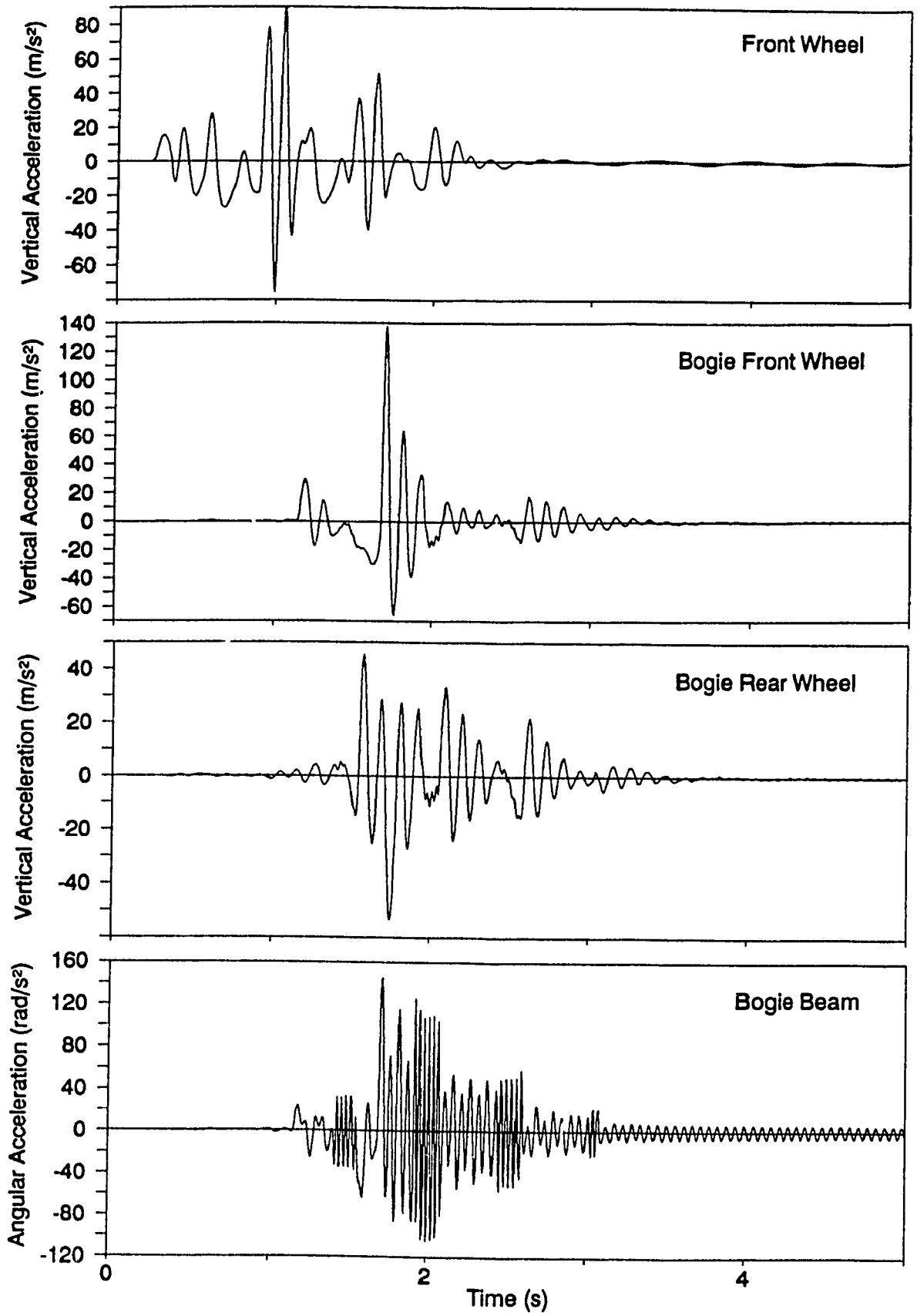

Figure 6.9 Wheel/beam acceleration traces for M923 truck crossing triangular bump at 15 km/h.

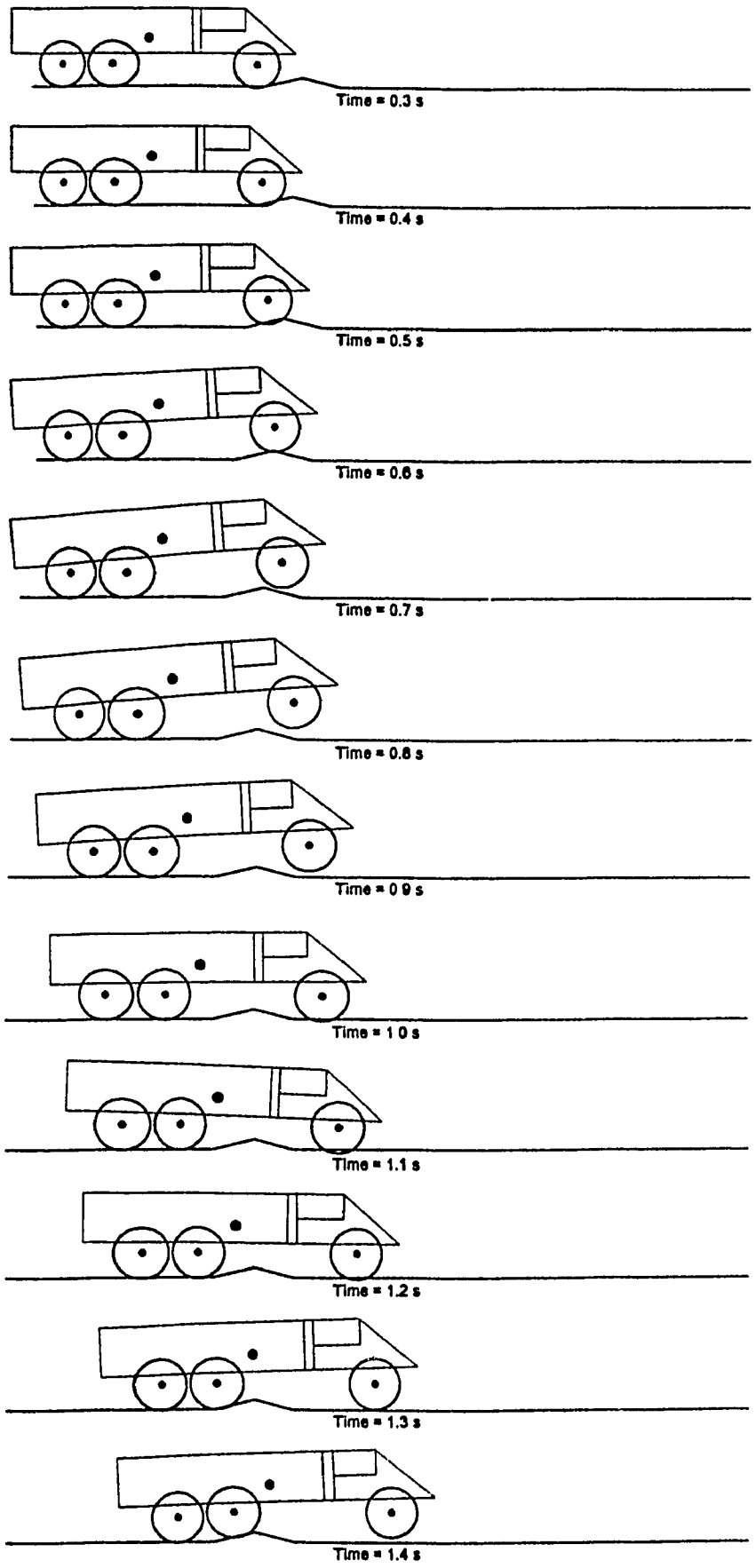

Figure 6.10 Animated snapshots of M923 truck crossing triangular bump at 15 km/h.

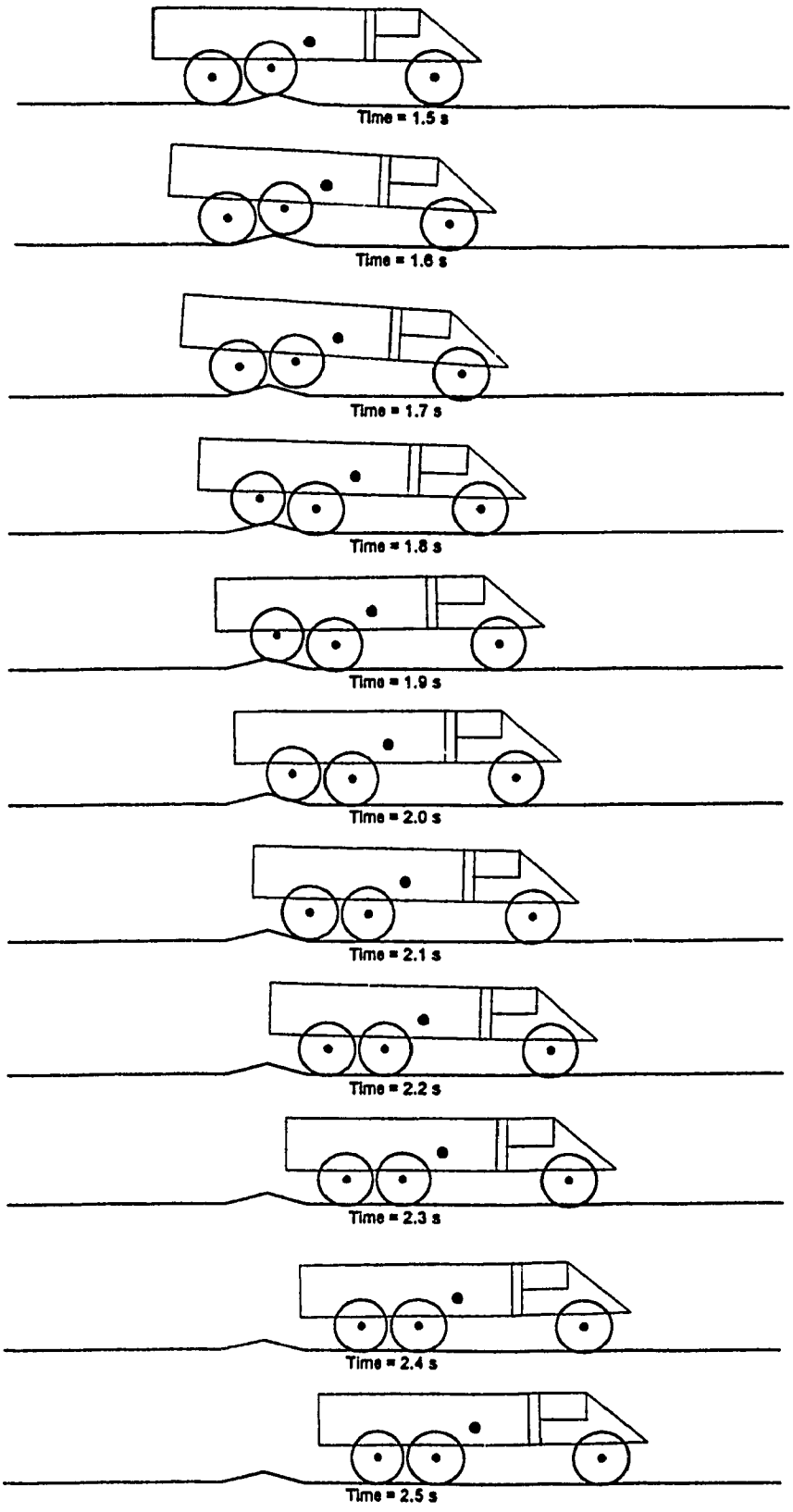

Figure 6.10 (continued) Animated snapshots of M923 truck crossing triangular bump at 15 km/h.

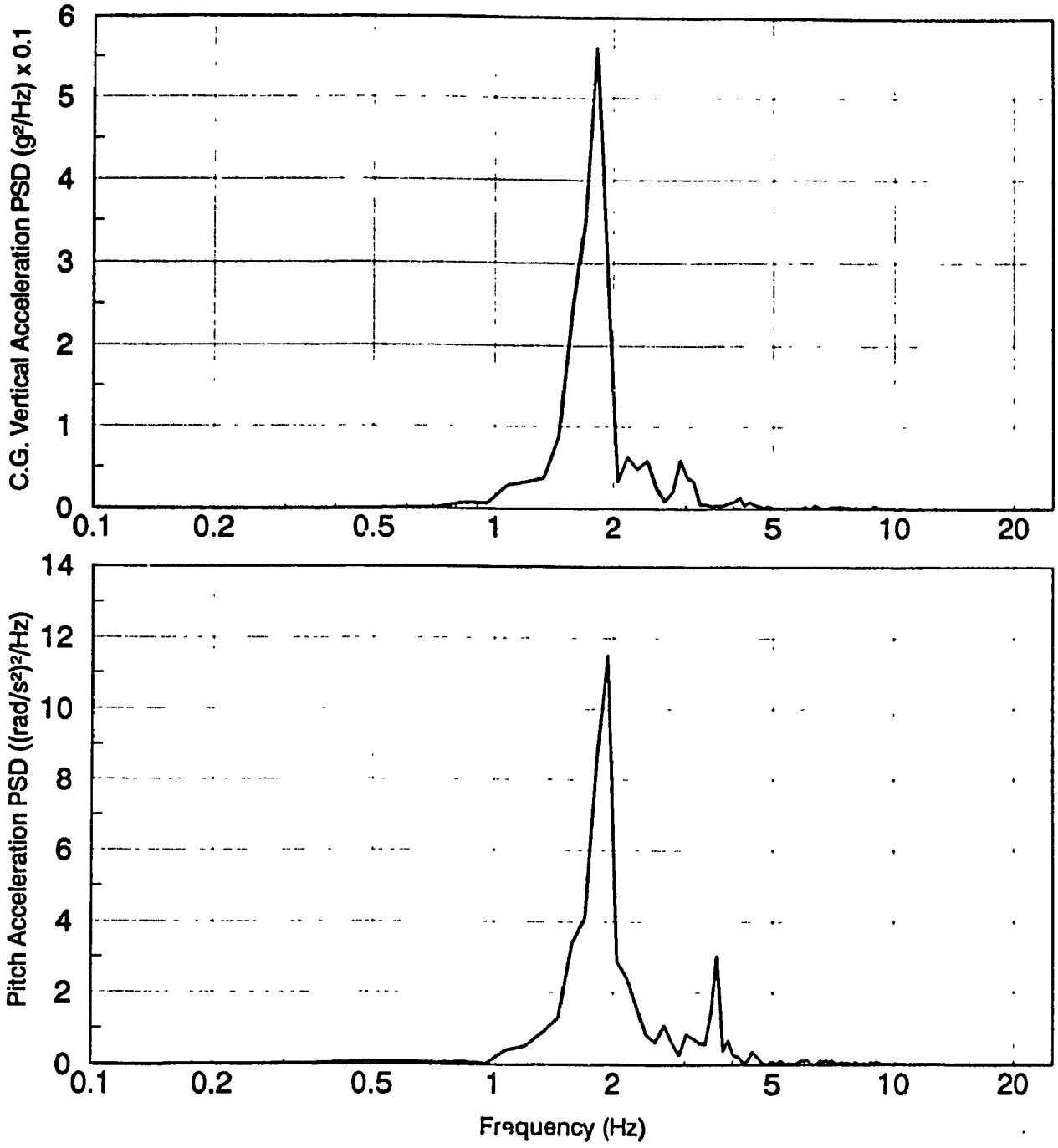

Figure 6.11 Ride acceleration spectra for M923 truck traversing LETE48 random course at 15 km/h.

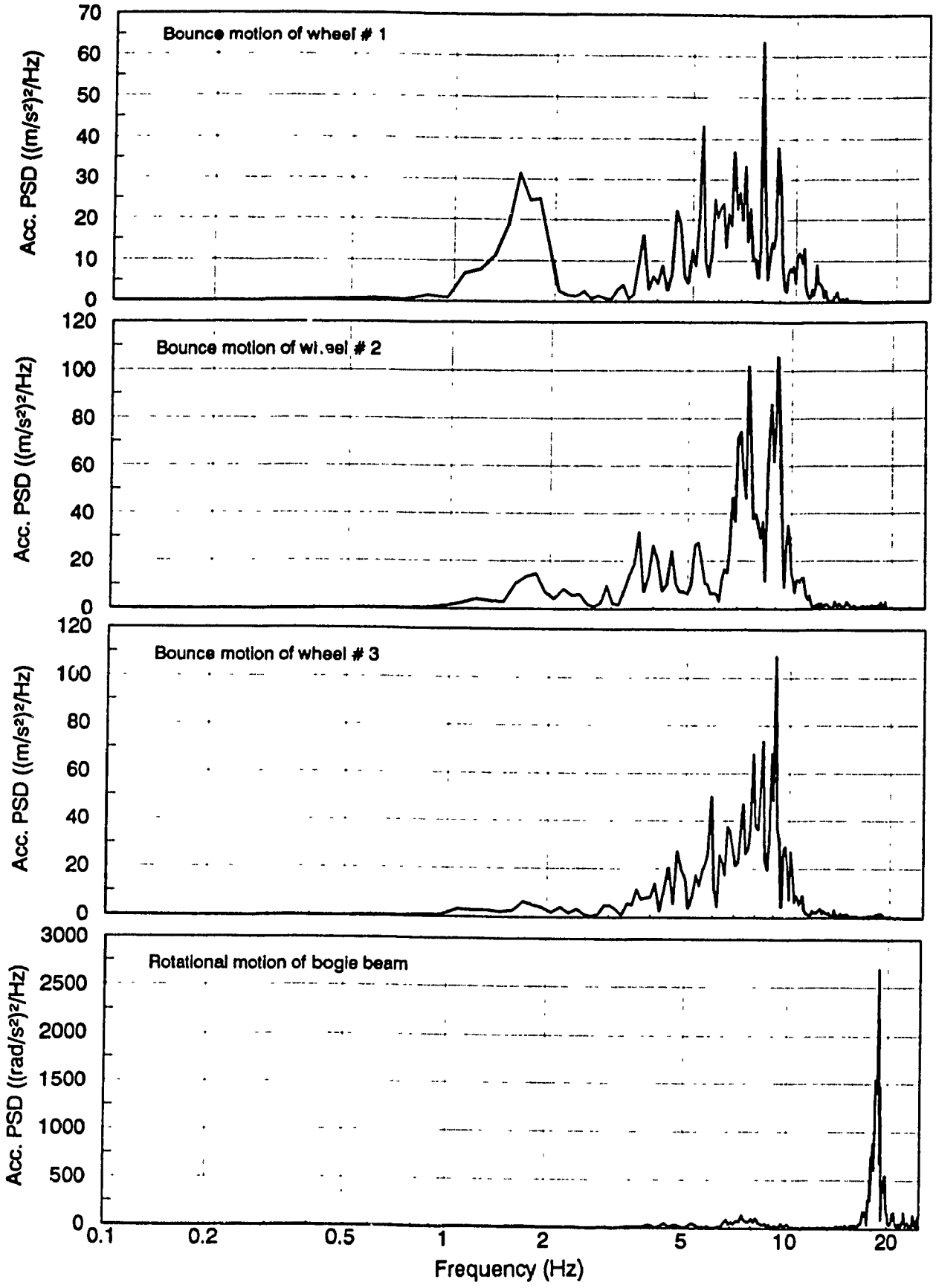

Figure 6.12 Wheel/beam acceleration spectra for M923 truck traversing LETE48 random course at 15 km/h.

track sub-models as well as ones proposed in previous studies. Subsequently, RIDSIM permits vehicle model formulation based on a varying degrees of complexity, where the user specifies the sub-models of choice. Applications of RIDSIM are demonstrated with examples involving two different wheeled off-road vehicles.

Chapter 7

CONCLUSIONS AND RECOMMENDATIONS FOR FUTURE WORK

As set out in Chapter 1, the overall objectives of this research program have been (a) to develop a computer simulation model for ride analysis of high mobility wheeled/tracked off-road vehicles, (b) to carry out an extensive field testing of a typical off-road wheeled/tracked vehicle, and (c) to validate and refine the computer simulation model. The computer model, thus evolved, could be employed as an effective and precise design tool to study and improve ride, and thus mobility performances of off-road vehicles. These objectives have been accomplished as presented in the preceeding chapters. In the present chapter, highlights of the work and main findings are summarized. Also, some recommendations for future work based on the present research are presented.

7.1 HIGHLIGHTS OF THE PRESENT WORK

The proposed computer model, referred to as RIDSIM, is a time-domain ride simulation model formulated considering an in-plane analytical representation of the vehicle traversing over an arbitrary non-deformable terrain profile at constant forward speed. The sub-systems of the basic vehicle-terrain dynamical system, such as primary suspension, wheel and track, are formulated considering common suspension types, and dynamic wheel-track-terrain interaction sub-models of varying complexities. RIDSIM thus permits a convenient vehicle model formulation based on user-specified sub-models of choice. The input information required to operate RIDSIM is basically minimal. The output data from RIDSIM constitute an input to the post-processor, which is developed for data reduction and conditioning to assess ride quality, and vehicle animation.

The development of RIDSIM has been primarily based on the modeling strategies adopted for the ride model formulation of a conventional armoured personnel carrier - M113 APC. The M113 APC, a high mobility tracked vehicle, was selected as a candidate vehicle for present research since it is a more complex dynamical system in view of analytical modeling and validation. Subsequently, the main focus of this study has been to carry out analytical and experimental ride investigations of the candidate vehicle.

The M113 APC in its A1 version was tested at LETE (Land Engineering Test Establishment, Ottawa) for various test conditions: vehicle configurations (loading conditions and track pre-tension settings), field courses (discrete half round obstacles, sine course, and random courses), and vehicle speeds. Prior to field testing, a test plan indicating appropriate instrumentation/equipment, their locations and mounting methods, and a detailed outline of test runs in view of specified test conditions was prepared. The large amount of test data acquired during the course of field testing was conditioned and reduced for the purpose of ride quality assessment and ride model validation.

The ride dynamic model for candidate vehicle is conceived based on three formalism of varying complexities: MODEL I, MODEL II, and MODEL III The equations of motion written for these models are expressed from the vehicle's free or zero-force position in order to incorporate the influence of gravity in simulating the vehicle-terrain contact loss. A procedure is devised for establishing the vehicle's zero-force configuration, which estimates initial static wheel and suspension loads, and associated generalized deflections for shifting the vehicle upward based on the calculated defelections. A further step was taken in order

to assure the static equilibrium of the vehicle when settled under its own weight from the zero-force reference. A procedure based on an iterative stiffness approach is developed to compute the initial generalized displacement vector characterizing the vehicle's static equilibrium, and associated undamped natural frequencies and mode shapes.

The preliminary ride dynamic model (MODEL I) was developed prior to the field testing of M113A1 APC as a tool for devising appropriate test plans. MODEL I incorporates: (i) an *idealized* independent suspension representation of the tracked vehicle's torsion bar/trailing arm suspension system, (ii) an *idealized* continuous radial spring/equivalent damper model for wheel/track-terrain interaction, and (iii) dynamic track loads computed based on track belt extensibility and pre-tension. Effective computational procedures are developed to establish wheel-terrain and track-terrain contact patches, and wheel-track connectivity. MODEL I was employed to carry out ride simulations of the field-tested vehicle, and ride predictions were directly compared against field test data. The MODEL I's ride predictions exhibited generally a good agreement with field measurements. However, MODEL I was considered for further refinements in order to achieve even a closer correlation between simulated and measured responses.

The preliminary ride model, MODEL I, was refined in view of the sub-system modeling strategies, and referred to as MODEL II. The refinements include: (i) an *adaptive* formulation of the idealized continuous radial spring model for the wheel/track-terrain interaction, where the terrain irregularities, if found within the contact patch, are accounted for through the discretized local deformations, (ii) dynamic track loads evaluated based on an improved track model, which in addition to the

track stretching, also incorporates track sag (modeled based on quadratic polynomial approximation of the track segment hanging between hull wheels), and enhanced wheel-track connectivity, track bridging and road wheel-track-terrain separation, and (iii) equations of motion re-derived based on an improved representation of the idealized independent suspension unit. The ride predictions evaluated using MODEL II then showed an improved correlation with the field test data.

In order to assess the relative performance of proposed wheel and track sub-models, various other wheel and track modeling strategies employed in previous studies were considered for simulation of the field-tested vehicle. Previous wheel models [30], and track models [34,38] are formulated in conjunction with MODEL II. Such a comparative analysis has not been presented elsewhere in the literature. This comparative study provided a detailed assessment of individual wheel and track models in view of the accuracy of response predictions, and associated computational time. In comparison, the ride predictions evaluated in conjunction with proposed models exhibited a superior performance.

Finally, the ride model was re-formulated considering a realistic representation of the vehicle's trailing arm/torsion bar suspension system. The new ride model, MODEL III, incorporates the detailed kinematics of trailing arm and shock absorber linkages in addition to the refined wheel and track sub-models used in MODEL II. The relative performance of MODEL III was assessed based on an extensive field validation of its ride predictions. In comparison with MODEL II, the MODEL III's predictions generally exhibited a smoother ride and closer correlation with the field-measured data. The field-validated MODEL III was then employed to carry out a parametric sensitivity analyses for

studying the influence of suspension parameters on the ride performance of the test vehicle. In addition, the ride performance potentials of a hydrogas suspension system exclusively developed for application with M113 APC's were investigated.

7.2 GENERAL CONCLUSIONS

The present research work has demonstrated an effective use of a *modular building-block* approach in formulating ride dynamic models of varying complexities for off-road vehicle systems. It has been shown that a simplified yet credible mathematical formulation of a complex tracked vehicle-terrain dynamical system yields fairly accurate ride predictions. There are two types of conclusions which can be drawn from the ride dynamic study of the candidate vehicle (field-tested M113A1 APC). The first set of conclusions are from the analytical modeling strategies and their assessment based on the field validation of associated ride predictions. The second set of conclusions comment on the ride dynamic behaviour of the candidate vehicle in view of operational and system parameters.

The first set of conclusions are:

- The two-dimensional ride model formalism, while ignoring roll degree-of-freedom, yields fairly accurate ride performance predictions as it has been demonstrated based on the field validation.
- The idealized representation of the torsion bar/trailing arm suspension system in the ride model formulation is convenient and sufficient for routine and repeated simulations. However, the ride model in conjunction with the detailed suspension representation yields relatively accurate predictions, and can be used as a design-

oriented tool for detailed analysis of the suspension components.

- Based on the comparative study of wheel models, following observations are made:

  (a) The proposed *idealized continuous spring model* requires the least computational time in comparison with other models, and yields ride predictions which exhibit a generally good agreement with the field test data.

  (b) The ride predictions evaluated in conjunction with the proposed *adaptive continuous spring model* show even a closer correlation with field test data. This model performs generally well in comparison with other models. For instance, for the discrete obstacle-crossing analysis, this model is as fast as the *idealized* version, yet predicts very close in comparison with other wheel models.

  (c) The point contact wheel model over-estimates the ride acceleration levels for rougher profiles such as discrete half round obstacles and sine course. However, for terrain profiles (LETE48 random course and Belgian pavé), where the changes in the elevation are gradual, the point contact model predicts as well as other high resolution models.

  (d) The adaptive foot-print, which is of highest resolution among the different wheel models considered in this thesis, yields ride predictions similar to those of the proposed adaptive model, but requires large computational time.

  (e) The performance of rigid tread band model is comparable to that of the adaptive foot-print model, whereas the fixed foot-print model yields slightly high ride acceleraion levels.

- Based on the comparative study of track models, following observations are made:

  (a) The proposed track model # 1 requires relatively simpler modeling considerations in comparison with the proposed track model # 2, however, yields ride predictions which are comparable to those of model # 2.

  (b) In comparison with other models, the ride predictions evaluated in conjunction with track model # 2 generally show a closer correlation with field measurements.

  (c) The quadratic polynomial approach employed in track model # 2 yields similar results as an ideal catenary-based approach [34] used in track model # 3. However, track model # 2 permits direct visualization of the track sag in relation with track tension.

  (d) The ride predictions based on track model # 4 [38] exhibit the least agreement with field test data. Although, this model requires relatively less computer run time, the accuracy of ride predictions obtained with track model # 2 outweighs the increase in computer time.

The second set of conclusions are:

- The vehicle ride deteriorates considerably with rougher terrain profiles and higher vehicle speeds, whereas the vehicle loading conditions as well as track pre-tension settings have little influence on the ride dynamic behaviour.
- The equivalent stiffness of road wheel/track pad has very little influence, whereas lowering the torsion bar stiffness improves the ride performance.
- A reduction in the suspension damping improves the vehicle's

transient response to a half round obstacle, however, the ride performance over a random course is deteriorated.

- The ride performance is considerably improved by mounting shock absorbers at all road wheel stations.
- The ride performance with hydrogas suspension units mounted at 1st, 2nd, and 5th wheel stations is comparable to that of the test vehicle equipped with hydrogas suspensions units at all wheel stations.
- The hydrogas suspension units mounted at 1st and 5th wheel stations alone do not offer significant improvement over the conventional torsion bar suspension configuration.

7.3 RECOMMENDATIONS FOR FUTURE WORK

The present research work yields a computer simulation model which has been shown to be an effective and precise tool to study the ride dynamics of a typical high mobility tracked vehicle. There are a number of recommendations which will enhance the potential usefulness of the computer model, and are summarized as follows:

- A successful field validation of RIDSIM has been carried out for the case of a typical high mobility *tracked* vehicle. It is recommended that the RIDSIM's predictions should also be validated for *wheeled* off-road vehicles similar to the ones studied in Chapter 6 (section 6.4). This will further increase the confidence in both the modeling techniques emloyed in this study and their ability in predicting accurately the ride performance. Also the validation will highlight any shortcomings of the current models and the need for refinements.

- The inclusion of sprung mass horizontal degree-of-freedom in conjunction with an appropriate representation of the vehicle driving

force will make the RIDSIM software to be a comprehensive 2D model. The driving force should be modeled considering vehicle drive unit (drive control, engine power, etc.), and traction forces. The ride model would thus be able to accurately predict fore-aft ride acceleration levels, and could also be employed to assess the power requirements as well as mobility/tractive performance of the vehicle.

- The track representation can be further enhanced by taking into account the track tensioning effects induced by the sprocket driving torque and the track tension compensating linkage between idler and adjacent road wheel.
- Active and semi-active controls are gaining prominence in the suspension systems. Appropriate control algorithms integrated in conjunction with the suspension model will expand the analytical capabilities of RIDSIM.
- The ride model formulation can be extended to study the ride dynamics of multi-unit (i.e. articulated) vehicle configurations.
- RIDSIM should be compiled as a PC-based user-friendly software with menu-driven pre- and post-processors using WINDOWS and computer graphics enhancement.

REFERENCES

1. Alanoly, J., "Computerized Analysis and Design of Vehicle Multi-Body Systems," Ph.D. Thesis, Concordia University, Montreal, Quebec, 1989.

2. Wong, J., *Theory of Ground Vehicles*, Wiley Inter-Science, New York, 1978.

3. Crolla, D.A., "Off-Road Vehicle Dynamics," *Vehicle Systems Dynamics*, Vol. 10, pp. 253-266, 1981.

4. Stikeleather, L.F., "Review of Ride Vibration Standards and Tolerance Criteria," *SAE Transaction Paper No.* 760413, pp. 1460-1467, 1976.

5. Rakheja, S., "Computer-Aided Dynamic Analysis and Optimal Design of Suspension Systems for Off-Road Tractors," Ph.D. Thesis, Concordia University, Montreal, Quebec, 1983.

6. Dupuis, H. and Zerlett, G., "The Effects of Whole-Body Vibration," *Spriger-Verlag*, 162 pp., 1986.

7. Rosegger, R. and Rosegger, S., "Health Effects of Tractor Driving," *J. of Agric. Engng. Res.*, Vol. 5, No. 3, pp.241-275, 1960.

8. Claar II, P.W., Buchele, W.F. and Sheth, P.N., "Off-Road Vehicle Ride: Review of Concepts and Design Evaluation with Computer Simulation," *SAE Paper No.* 801023, 1980.

9. Sankar, S., Rakheja, S. and Venkataraman, K., "Ride Dynamic Model of a Tilt Cab for Off-Road Vehicles," *Proceedings of the SAE Noise and Vibration Conference*, Traverse City, Michigan, May 16-18, Paper No. 891140, 1989.

10. Maclaurin, E.B. and Elder, J.W., "Design of Off-Road Vehicles for Higher Speeds," *IMechE Publications*, London, Paper C208/75, 1975.

11. Horton, D.N.L. and Crolla, D.A., "Theoretical Analysis of a Semi-Active Suspension Fitted to an Off-Road Vehicle," *Vehicle System Dynamics*, Vol. 15, pp. 351-372, 1986.

12. McCormac, A.W., Wilson, J.N. and Klassen, N.D., "Active Seat Suspension Systems for Off-Road Vehicles," *Proceedings of CSME Forum*, Montreal, Quebec, June 1-4, pp. 180-185, 1992.

13. Karnopp, D.C., "Active Damping in Road Vehicle Suspension Systems," *Vehicle System Dynamics*, Vol. 12, pp. 291-316, 1983.

14. Alanoly, J. and Sankar, S., "A New Concept in Semi-Active Vibration Isolation," *ASME Journal of Mechanisms, Transmission, and Automation in Design*, 109(2), pp. 224-247, June 1987.

15. Bryson, R.A., "Quantifying Battle Tank Mobility - A Manufacturer's View," *Journal of Terramechanics*, Vol. 25, No. 1, pp. 57-67, 1988.

16. Grosjean, C., "General Survey on some Technical Problems about Military Tracked Vehicles," *Journal of Terramechanics*, Vol. 21, No. 4, pp. 335-346, 1984.

17. Hohl, G.H., "Torsion-Bar Spring and Damping Systems of Tracked Vehicles," *Journal of Terramechanics*, Vol. 22, No. 4, pp. 195-203, 1986.

18. Eberle, W.R. and Steele, M.M., "Investigation of Fluidically Controlled Suspension Systems for Tracked Vehicles," *TACOM Report No.* 12072, U.S. Army Tank-Automotive Command, Warren, Mich., Sept. 1975.

19. Salemka, R.M. and Beck, R.R., "Feasibility Analysis and Evaluation of an Adaptive Tracked Vehicle Suspension and Control System," *TACOM Report No.* 11893 (LL-146), U.S. Army Tank-Automotive Command, Warren, Mich., June 1975.

20. Joo, F., "Dynamic Analysis of a Hydropneumatic Suspension System," M.Eng. Thesis, Concordia University, Montreal, Quebec, 1991.

21. Maclaurin, B., "Progress in British Tracked Vehicle Suspension Systems," *SAE Technical Series Paper No.* 830442, International Congress and Exposition, Detroit, Mich., Feb. 28 - Mar. 4, 1983.

22. Wehage, R.A., "Vehicle Dynamics," *Journal of Terramechanics*, Vol. 24, No. 4, pp. 295-312, 1987.

23. Eppinger, R.H., King, A.I. and Lee, R.A., "Experimental and Mathematical Simulation of a Multi-Wheeled Vehicle With and Without an Elastic Track," *Proceedings of the 2nd International Conference on Vehicle Mechanics*, Paris, pp. 275-286, 1971.

24. Lessem, A.S. and Murphy Jr., N.R., "Studies of the Dynamics of Tracked Vehicles," *WES Technical Report No.* M-72-1, U.S. Army Engineer Waterways Experiment Station, Vicksburg, Miss., June 1972.

25. Murphy Jr., N.R. and Ahlvin, R.B., "AMC-74 Vehicle Dynamics Module," Technical Report No. M-76-1, US Army Engineer Waterways Experiment Station, Vicksburg, Miss., January 1976.

26. Nutall Jr., C.J., Rula, A.A. and Dugoff, H.J., "Computer Model for Comprehensive Evaluation of Cross-Country Vehicle Mobility," *SAE Paper No.* 740426, 1974.

27. Wheeler, P., "Tracked Vehicle Ride Dynamics Computer Program," *SAE Paper No.* 770048, 1977.

28. Smith, D.W., 1977, " Computer Simulation of Tractor Ride for Design Evaluation," *SAE Paper No.* 770704, 1977.

29. Hoogterp, F.B., "Interactive Vehicle Dynamics and Ride Evaluation Package," *TARADCOM Laboratory Technical Report No.* 12413, U.S. Army Tank-Automotive Research and Development Command, Warren, Mich., Nov. 1978.

30. Captain, K.M., Boghani, A.B. and Wormley, D.N., "Analytical Tire Models for Dynamic Vehicle Simulation," *Vehicle System Dynamics*, Vol. 8, pp. 1-32, 1979.

31. Garnich, M.R. and Grimm, T.R., "Modeling and Simulation of a Tracked Vehicle," ASME *Proceedings of the International Computers in Engineering Conference and Exhibit on Advanced Automation*, Vol. 2, Las Vegas, Nevada, Aug. 12-15, pp. 591-600, 1984.

32. Crolla, D.A., Horton, D.N.L. and Dale, A.K., "Off-Road Vehicle Ride Vibration," *IMechE Publications*, Paper C131/84, 1984.

33. Craighead, I.A. and Brown, P.R., "Vibration and Dynamics of Off-Road Vehicles," *IMechE Publications*, Paper C135/84, 1984.

34. McCullough, M.K. and Haug, E.J., "Dynamics of High Mobility Track Vehicles," *ASME Paper No.* 85-DET-95, 1985.

35. Krupka, R.M., "Mathematical Simulation of the Dynamics of a Military Tank," *SAE Technical Series Paper No.* 850416, International Congress and Exposition, Detroit, Mich., Feb. 25 - Mar. 1, 1985.

36. Bennett, M.D. and Penny, P.H.G., "The Assessment of Tracked Vehicle Suspension Using Computer Simulation Techniques," *IMech Conference Publications*, London, Paper C112/85, 1985.

37. Craighead, I.A., Loo, Y.W., Storey, A., Hislop, J. and Martin, R., "Validation Tests on Computer Simulation Programs Modelling Off-Road Vehicles," *Journal of Terramechanics*, Vol. 23, No. 1, pp. 13-22, 1986.

38. Creighton, D.C., "Revised Vehicle Dynamic Module: User's Guide for Computer Program VEHDYN II," WES Technical Report No. SL-86-9, U.S. Army Engineer Waterways Experiment Station, Vicksburg, Miss., May 1986.

39. Hanna, D.M., "NRMM Predictions for Off-Road Mobility of M113A1 and M113A2 Armoured Personnel Carriers," *Research Note No.* 247, Defence Research Establishment Suffield, Ralston, Alberta, Nov. 1982.

40. Petrick, E.N., Janosi, Z.J., and Haley, P.W., "The Use of the NATO Reference Mobility Model in Military Vehicle Procurement," *SAE Technical Paper Series No.* 810373, International Congress and Exposition, Detroit, Michigan, Feb. 23-27, 1981.

41. Afonso, M.F.R., "Ride Dynamic Analysis of Tracked Vehicles," M.Eng. Thesis, Concordia University, Montreal, Quebec, 1989.

42. Rakheja, S. and Sankar, S., "Local Equivalent Constant Representation of Nonlinear Damping Mechanisms," Engineering Computation, International Journal of Computer-Aided Engineering, Vol. 3, No. 1, pp. 11-17, 1985.

43. Galway, M.C. and Wong, J.Y., "A Computer Simulation Model for Precting the Ride Quality of Off-Road Vehicles," *Proceedings of CSME Forum*, Montreal, Quebec, June 1-4, pp. 15-20, 1992.

44. Vodyanik, I.I., "The Motion of a Tracked Vehicle on Deformable Ground," *Journal of Terramechanics*, Vol. 3, No. 1, pp. 7-11, 1966.

45. Kogure, K., "External Motion Resistance Caused by Rut Sinkage of Tracked Vehicles," *Journal of Terramechanics*, Vol. 13, No. 1, 1976, pp. 1-14.

46. Wong, J.Y., Garber, M. and Preston-Thomas, J., "Theoretical Prediction and Experimental Substantiation of The Ground Pressure Distribution and Tractive Performance of Tracked Vehicles," *Proceedings of the Institution of Mechanical Engineers*, Vol. 198, Part D, No. 15, pp. 265-285, 1984.

47. Barton, J.C. and Hefner, J.C., "Whole Body Vibration Levels: A Realistic Baseline for Standards," *SAE Paper No.* 760415, 1976.

48. Griffin, M.J. and Whitham, E.M., "Individual Variability and Its Effect on Subjective and Biodynamic Response to Whole-Body Vibration," *Journal of Sound and Vibration*, Vol. 58, No. 2, 1978, pp. 239-250.

49. Van Deusen, B.D., "Human Response to Vehicle Vibration," *SAE Paper No.* 680090, 1968.

50. Dieckmann, D., "Einfluss Vertikaler Mechanischer Schwingungen auf den Menschen," *Internationale Zeitschrift Angewandte-Physiologie*, Vol. 16, pp. 519-564, 1947.

51. Goldmann, D.E., "A Review of Subjective Responses to Vibratory Motion of the Human Body in the Frequency Range 1 to 70 cps," *Report No.* 4, Naval Medical Research Institute, Mar. 1948.

52. Janeway, R.N., "Passenger Vibration Limits," *SAE Journal*, Vol. 56, pp. 48-49, Aug. 1948.

53. Butkunas, A.A., "Power Spectral Density and Ride Evaluations," *SAE Paper No.* 660138, 1966.

54. VDI - 2057, "Assessing the Effects of Vibration on Human Beings," *Verein Deutscher Ingenieure*, Translated and Published by Peter Peregrinus Ltd. 1963.

55. Pradko, F., Lee, R. and Kaluza, V., "Theory of Human Vibration Response," *ASME Paper No.* 66-WA/BHF-15, 1966.

56. Lee, R.A. and Pradko F., "Analytical Analysis of Human Vibration," SAE Paper No. 680091, 1968.

57. Stikeleather, L.F., Hall, G.O. and Radke, A.O., "A Study of Vehicle Vibration Spectra as Related to Seating Dynamics," *SAE Paper No.* 720001, 1972.

58. International Organization for Standardization, "Guide for Evaluation of Human Exposure to Whole Body Vibrations," ISO-2631, 1974.

59. Smith, C.C., "On Using the ISO Standard to Evaluate the Ride Quality of Broad-Band Vibration Spectra in Transportation Vehicles," *Transactions ASME, Journal of Dynamic Systems, Measurements, and Control*, pp. 440-443, Dec. 1976.

60. Boileau, P.E., Turcot, D. and Scory, H., "Evaluation of Whole-Body Vibration Exposure Using a Fourth Power Method and Comparison with ISO 2631," *Journal of Sound and Vibration*, Vol. 129, No. 1, pp. 143-154, 1989.

61. Griffin M.J., "Evaluation of Vibration with Respect to Human Response," *SAE Paper No.* 860047, 1986.

62. Sankar, S., Dhir, A., and Shankhla, V.S., "Simulation and Field Testing of Tracked Vehicle Suspension Dynamics," accepted for publication in the *ASME Trans. - Journal of Dynamic Systems, Measurements and Control*; also appeared in the *Proceedings of ASME Winter Annual Meeting*, Atlanta, Georgia, Dec. 1-6, pp. 423-436, 1991.

63. Dhir, A. and Sankar, S., "Ride Dynamics of High Speed Tracked Vehicles: Simulation with Field Validation," accepted for publication in the *Journal of Vehicle System Dynamics.*

64. Dhir, A. and Sankar, S., "Analytical Track Models for Ride Dynamic Simulation of Tracked Vehicles," accepted for publication in the *Journal of Terramechanics.*

65. Dhir, A., Sankar, S., and Shankhla, V.S., "An Adaptive Model of Wheel-Track-Terrain Interaction for Predicting Ride Performance of Tracked Vehicles," accepted for publication in the *CSME Trans.*; also appeared in the *Proceedings of CSME Forum*, Montreal, Quebec, June 1-4, pp. 33-38, 1992.

66. Dhir, A., Sankar, S. and Shankhla, V.S., "An Efficient and Validated Computer Simulation Software Code for Predicting Shock and Vibration Response of High Mobility Off-Road Vehicles," *Proceedings of* 24th *Annual Summer Computer Simulation Conference*, Sparks, Nevada, July 27-30, pp. 741-745, 1992.

67. Sankar, S., Dhir, A., and Shankhla, V.S. "Simulating Shock and Vibration Qualification of Unmanned Ground Vehicles Negotiating Off-Road Terrains," *Proceedings of* 3rd *Conference on Military Robotic Application*, Medicine Hat, Alberta, Sept. 9-12, pp. 280-287, 1991.

68. Galaitsis, A.G., "TRAXION: A Model for Predicting Dynamic Track Loads in Military Vehicles," *ASME Transactions Journal of Vibration, Acoustics, Stress, and Reliability in Design*, Vol. 106, pp. 286-291, 1984.

69. Galway, M.C., "Test - Noise and Vibration Validation of M113 APC," *Letter Report on LETE Task Directive No.* 3190-A066, Dept. of National Defence, Land Engineering Test Establishment, Ottawa, Canada, 1991.

70. Spanski, P., and Ronald, R.B., "XM723/M113 Ride Performance Evaluation," *Technical Report No.* 12356, U.S. Army Tank-Automotive, Research and Development Command, Warren, Michigan, October, 1977.

71. Beer, F.P. and Johnston, E.R. *Mechanics for Engineers - Statics and Dynamics.* McGraw-Hill Book Company, 1976.

72. Creighton, D.C., " A Preprocessor for the Revised Vehicle Dynamic Module: User's Guide for Computer Program PREVDYN2," U.S. Army Engineer Waterways Experiment Station, Vicksburg, Miss., May 1986.

APPENDIX I

WHEEL AND TRACK MODELS

I.1 WHEEL MODELS

Four basic wheel (tire) models, namely, point contact, rigid tread band, fixed foot-print and adaptive foot-print, which have been employed in previous studies [30], are formulated for performing ride simulations of the field-tested vehicle. All four models are conceived based on the assumptions made in the formulation of proposed model (section 2.4.1).

Point Contact Model

As illustrated in Figure I.1, the point contact model is represented as a parallel combination of equivalent vertical spring and dashpot, where the terrain contact occurs at a single point vertically beneath the wheel centre. The net foot-print force resulting from the vertical motion of wheel relative to the terrain, is assumed to act normal to the local terrain surface. Consequently, a horizontal or fore-aft component of net foot-print force is generated whenever the local terrain profile is inclined to the horizontal, and is related to the vertical component through the tangent of local profile angle.

The vertical and horizontal components of net foot-print force acting at the i^{th} road wheel centre are obtained as:

$$F^i_{wy} = K^i_{rw}\,\delta + C^i_{rw}\,\dot{\delta} \quad ; \quad F^i_{wx} = F^i_{wy}\,\tan\gamma_p \tag{I.1}$$

where, K^i_{rw} and C^i_{rw} are the equivalent vertical stiffness and damping values for the i^{th} road wheel. The relative displacement and velocity are computed as:

$$\delta = Y_p - (Y_{wi} - R_{wi}) \tag{I.2}$$

$$\dot{\delta} = V_x \tan \gamma_p - \dot{y}_{w1} \qquad (I.3)$$

where Y_p is the terrain elevation at X_{w1}, and $\tan \gamma_p$ is corresponding local slope of terrain profile.

Rigid-Tread Band Model

The rigid tread band model is a modified point contact model, where the point follower is replaced by a roller follower equal to the wheel or tread band radius. Consequently, the terrain contact is not constrained to lie vertically beneath the wheel centre, but is free to move fore and aft of wheel centre depending on the local profile slope. With this model, the motion transmitted to the wheel centre is in general different from the terrain profile due to the geometrical filtering effects of rolling wheel. Therefore, a rigid tread band model can be referred to as an equivalent point contact model operating over a modified profile. The filtering causes attenuation of rough terrain profile irregularities. However, for gradually varying terrain profile, filtering becomes insignificant, and the rigid tread band and point contact models yield equivalent results.

As illustrated in Figure I.2, the schematic representation of the rigid tread band model is similar to the point contact model. Therefore, the rectangular components of net foot-print force are obtained using equation (I.1), and it is only necessary to find the modified profile (Y_p and $\tan \gamma_p$) and corresponding point of contact in terms of wheel centre coordinate (X_{w1},Y_{w1}) and tread band radius (R_{w1}). The criterion for determining the modified terrain profile is that, at contact point, the slope of the tread band and the terrain profile must be equal. For this, the lower circumference of i^{th} road wheel is divided into a number

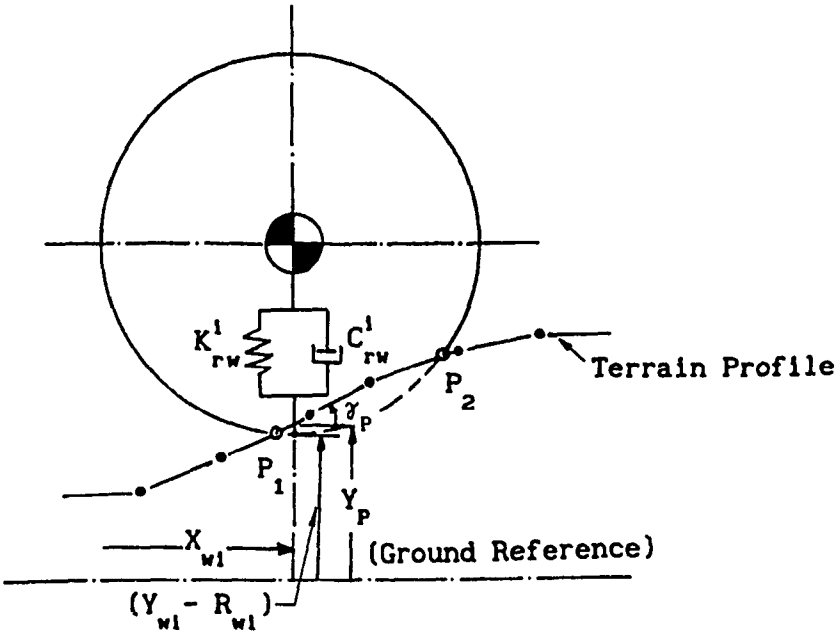

Figure I.1 Point contact model.

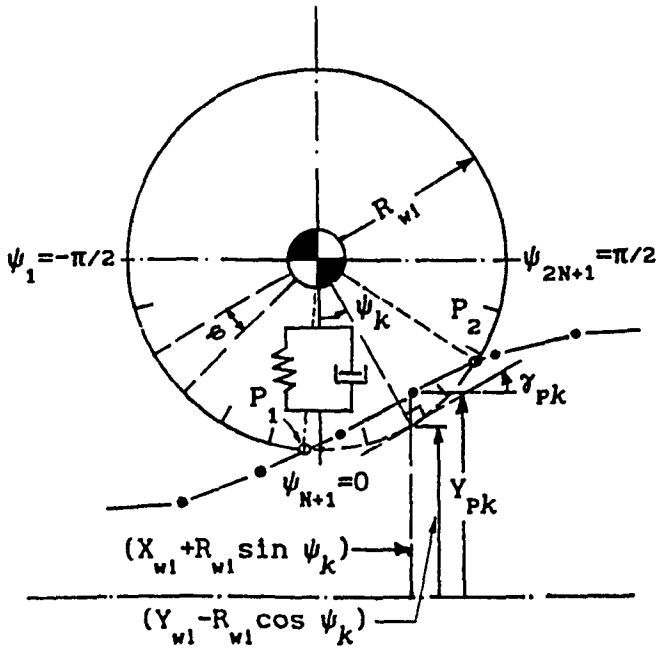

Figure I.2 Rigid tread band model.

of radial segments, whose coordinates are given by $(X_{wl} + R_{wl}\sin\psi_k;$ $Y_{wl} - R_{wl}\cos\psi_k, \quad k = 1\ldots,2N+1; \quad N = \Psi/\varphi; \; \Psi = \pi/2$ and φ = segmentation angle), where ψ_k is the vertical inclination (positive if counter-clockwise). The slope ($\tan\gamma_{Pk}$) and elevation of terrain profile (Y_{Pk}) at each segmented point are computed based on the linear interpolation of the look-up table containing cartesian coordinates of the terrain profile. The modified terrain input (Y_P and $\tan\gamma_P$) is then computed at the point of contact, where the following condition is satisfied,

$$\delta_k = Y_{Pk} - (Y_{wl} - R_{wl}\cos\psi_k) > 0 \quad \text{and} \quad \frac{|\tan\gamma_{Pk} - \tan\psi_k|}{|\tan\psi_k|} \leq \epsilon \qquad (I.4)$$

where ϵ is the specified tolerance. It is possible that the slope condition can be satisfied at several points on the lower half of tread band. In such case, the highest value of δ_k will represent the physically realizable condition. Once the point of contact ($k = \ell$) is established, the relative displacement and velocity are then given as:

$$\delta_\ell = Y_{P\ell} - (Y_{wl} - R_{wl}\cos\psi_\ell) \qquad (I.5)$$

$$\dot{\delta}_\ell = V_x \tan\gamma_{P\ell} - \dot{y}_{wl} \qquad (I.6)$$

This method, as discussed above, requires sufficiently high number of radial segments for an accurate computation of net foot-print force. Consequently, one needs to check for all radial segments, which is quite demanding on computer CPU time. This process can, however, be accelerated if the radial portion of the wheel in contact with terrain (defined by P_1 and P_2) is known such that the segments within the contact patch are only to be checked in order to locate the desired terrain contact point. The computational algorithm developed based on circle-line intersection

(section 2.4.1), is used for computing first and last wheel-terrain contact points.

Fixed or Constant Foot-Print Model

The fixed foot-print model (Figure I.3) represents the wheel-terrain interaction through a foot-print of constant size. This model is represented as a parallel combination of vertical spring and damper elements distributed uniformly over the contact length (L), thus has the ability to envelop terrain irregularities through local deformation within the footprint. With equivalent values of stiffness (K^i_{rw}) and damping (C^i_{rw}), this model is a point contact model, where the local terrain elevation (Y_p) is replaced by an elevation averaged over the contact length. The fixed foot-print model also filters the terrain irregularities like the rigid tread band model, where the filtering is dictated by the the fixed foot-print length rather than the wheel radius.

Like rigid tread band model, the lower circumference of i^{th} road wheel is segmented, as illustrated in Figure I.3. However, the range for segmentation is specified as:

$$\Psi = \sin^{-1}(L/2\ R_{wi}) \tag{I.7}$$

The net horizontal and vertical components of net foot-print force acting at i^{th} road wheel are obtained as:

$$F^i_{wx} = \sum_{k=1}^{N_f} F^i_{vk} \tan \gamma_{pk} \quad ; \quad F^i_{wy} = \sum_{k=1}^{N_f} F^i_{vk} \tag{I.8}$$

where, N_f indicates the total number of discrete vertical spring and damping segments within the wheel-terrain contact patch (defined by P_1 and P_2). F^i_{vk} is the vertical force due to k^{th} segment, obtained as:

$$F^{i}_{vk} = k^{i}_{rw}\,\delta_{k} + c^{i}_{rw}\,\dot{\delta}_{k} \qquad (I.9)$$

where, δ_{k} and $\dot{\delta}_{k}$, the corresponding displacement and velocity, are computed using the mathematical expressions identical to equations (I.5) and (I.6).

k^{i}_{rw} is the vertical spring constant for each discrete segment of i^{th} road wheel, and is established based on the contact patch formed on a flat surface under a specified static load, P.

$$k^{i}_{rw} = P \,/\, \sum_{k=1}^{N_f} \Delta_{k} \qquad (I.10)$$

where, the static vertical deflection, Δ_{k}, is obtained as:

$$\Delta_{k} = R_{wi}(\cos \psi_{k} - 1) + \Delta_{w} \qquad (I.11)$$

where, Δ_{w} is the maximum static deflection directly beneath the wheel centre, given as:

$$\Delta_{w} = P \,/\, K^{i}_{rw} \qquad (I.12)$$

c^{i}_{rw} is the viscous damping coefficient for each discrete vertical segment of i^{th} road wheel, and is estimated based on the assumption of uniform distribution of equivalent damping coefficient, C^{i}_{rw}, over the static contact patch, given as:

$$c^{i}_{rw} = C^{i}_{rw} \,/\, N_{f} \qquad (I.13)$$

Adaptive Foot-Print Model

The adaptive foot-print model (Figure I.4), is represented as parallel combinations of discrete spring and damping elements, which are radially and uniformly distributed over the lower circumference of the

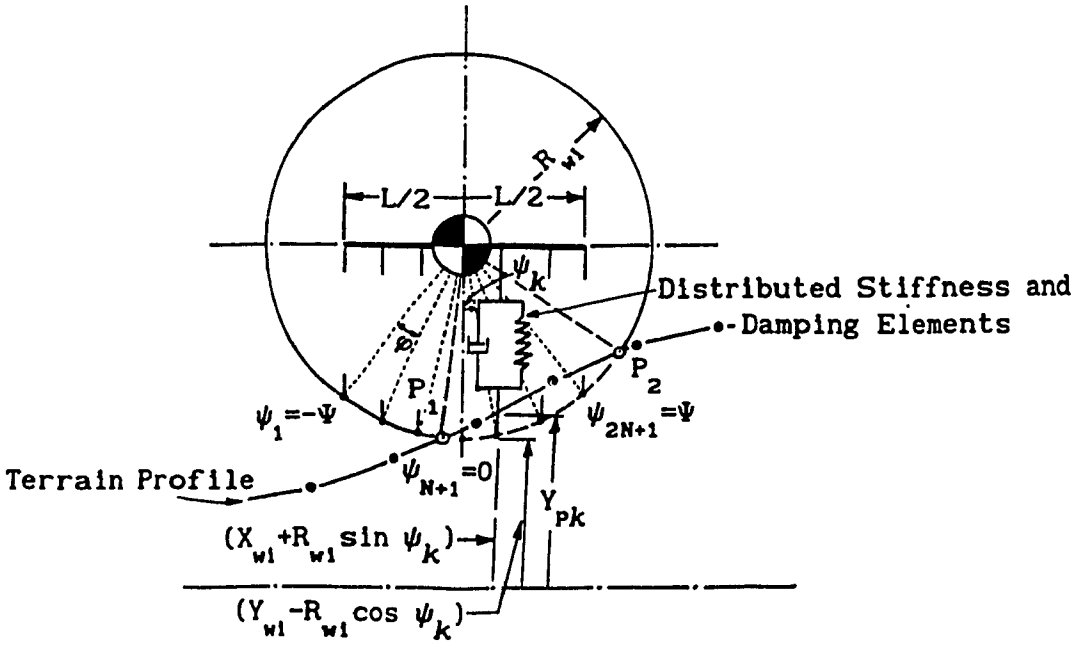

Figure I.3 Fixed foot-print model.

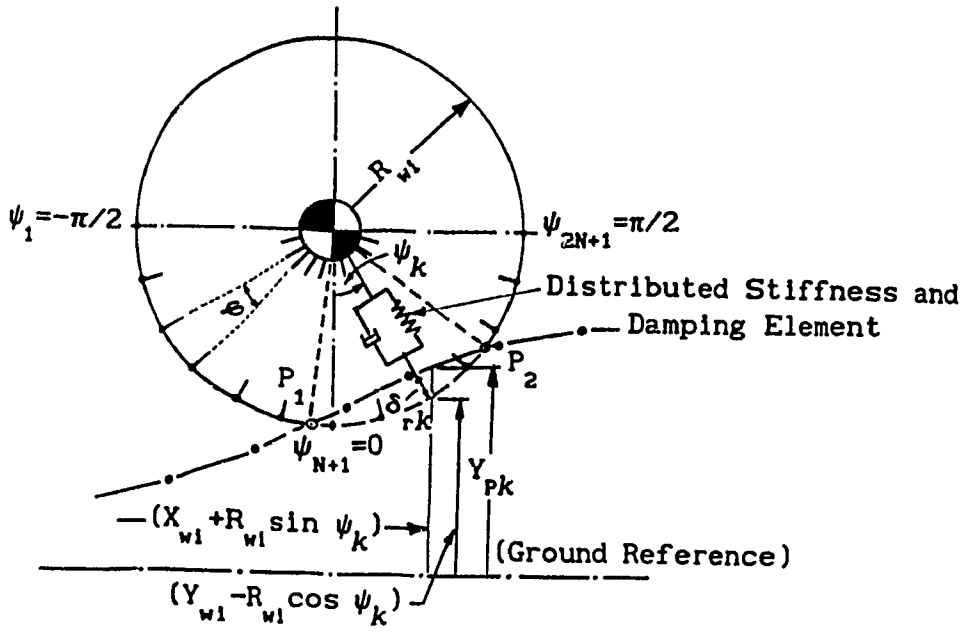

Figure I.4 Adaptive foot-print model.

wheel. Like the fixed foot-print model, this model has the ability to envelop terrain irregularities through local deflections. However, the key features of this model are that: (i) the net foot-print force is not vertical because of the existence of a nonplanar foot-print, and thus fore-aft component is not related to the vertical component through the local profile slope, and (ii) the foot-print size and orientation relative to the wheel centre changes, depending upon the radial portion of wheel in contact with the terrain profile (defined through P_1 and P_2).

As illustrated in Figure I.4, the lower circumference of i^{th} road wheel is segmented like rigid tread band model, and all discrete segments within the contact patch are checked for radial displacements and velocities. The horizontal and vertical components of net foot-print force acting at i^{th} road wheel centre are obtained as:

$$F^i_{wx} = \sum_{k=1}^{N_f} F_{rk} \sin \psi_k \quad ; \quad F^i_{wy} = \sum_{k=1}^{N_f} F_{rk} \cos \psi_k \tag{I.14}$$

where, the radial force along k^{th} segment is computed as:

$$F^i_{rk} = k^i_{rw} \, \delta_{rk} + c^i_{rw} \, \dot{\delta}_{rk} \tag{I.15}$$

where, δ_{rk} and $\dot{\delta}_{rk}$ are the corresponding radial displacement and velocity, given as:

$$\delta_{rk} = \frac{Y_{Pk} - (Y_{wi} - R_{wi} \cos \psi_k)}{\cos \psi_k} \tag{I.16}$$

$$\dot{\delta}_{rk} = \frac{V_x \tan \gamma_{Pk} - \dot{y}_{wi}}{\cos \psi_k} \tag{I.17}$$

k^i_{rw}, the spring constant for each radial segment of i^{th} road wheel, is established based on contact patch formed on a flat surface under a

specified static load, P, given as:

$$k^{i}_{rw} = P \;/\; \sum_{k=1}^{N_f} \Delta_{rk} \qquad (I.18)$$

where, the static radial deflection, Δ_{rk}, is obtained as:

$$\Delta_{rk} = \frac{R_{wl}(\cos \psi_k - 1) + \Delta_w}{\cos \psi_k} \qquad (I.19)$$

Similarly, c^{i}_{rw}, the viscous damping coefficient for each radial suspension segment of i^{th} road wheel, is estimated as:

$$c^{i}_{rw} = C^{i}_{rw} \;/\; \sum_{k=1}^{N_f} \cos \psi_k \qquad (I.20)$$

The wheel models, as discussed above, have been formulated to represent the dynamic wheel/track-terrain interactions. However, these models are also to be incorporated for establishing vehicle's static equilibrium (vehicle settlement). As discussed in section 2.6, the initial generalized displacement vector (equation 2.84) associated with the static equilibrium of the vehicle settled on a flat surface, are established based on an iterative stiffness approach (equation 2.79), where the stiffess matrix (equation 2.80) is updated based on the generalized displacement vector. The structure of the stiffness matrix remains unchanged except the spring constant for i^{th} road wheel, κ_{wl}, is obtained in view of the specified wheel models, given as:

$$K_{wi} = \begin{cases} K^{1}_{rw} & ; \text{ point contact and rigid tread band} \\ \left[\sum_{k=1}^{N_f} k^{1}_{rw}\ \delta_{k}\right] \ / \ \Delta_{wi} & ; \text{ fixed foot-print} \\ \left[\sum_{k=1}^{N_f} k^{1}_{rw}\ \delta_{rk}\right] \ / \ \Delta_{wi} & ; \text{ adaptive foot-print} \end{cases} \qquad (I.21)$$

where, Δ_{wi}, the static deflection of the wheel centre, is given in equation (2.83).

I.2 TRACK MODELS

In this section, two track models, referred to as track model #'s 3 and 4, are developed for ride dynamic simulation of field-tested vehicle. Track model # 3 is identical to the track model employed in MODEL II (track model # 2), however, with the exception of track inextensibility, which is modeled based on an ideal catenary equation as proposed by McCullough *et al* [34]. Track model # 4 is developed based on the track model employed in VEHDYN II [38], where dynamic track tensioning effects are simulated through hypothetical linear springs interconnecting adjacent wheel pairs.

Track Model # 3

McCullough *et al* [34] proposed a catenary-based approach to compute track tension in a hanging track segment between two hull wheels. The proposed method is based on the assumption that the lowermost point, C (Figure 4.2), is located at the mid-point of hanging track, and thus tension at both ends is equal (i.e $T_A = T_B$). To solve catenary equations efficiently, a nondimensional form of catenary (equation 4.6) was proposed, given as [34]:

$$\left(\frac{T}{aw}\right) = \frac{\cosh X}{X} \quad \text{and} \quad \left(\frac{\ell}{a}\right) = \frac{\sinh X}{X} \tag{I.22}$$

where, $X = a/c$

and, T is the maximum tension at hull wheels, ℓ is half of the total track hanging length, L_h, and a is half of the distance between hull wheel centres and is considered to be equal to d/2 for this study. The functional relationship between T/aw and ℓ/a is given in the form of a look-up Table I.1, where intermediate points can be linearly interpolated. Figure I.5 illustrates the linearly-interpolated functional relationship in reference to the actual catenary function, where the track tension for intermediate values of track hanging length is always over-estimated.

The tension based on track inextensibility is computed using the proposed quadratic polynomial approach and the ideal catenary method [34]. Figure I.6 exhibits the relationship between track tension and length for Diehl 213G track hanging between the sprocket and the idler of M113A1 APC, where the data is exhibited from the point of track stretching (L_h^1, T_{tr}^1). For ideal catenary approach [34], the point of track stretching (where $dT/dL = K_{tr}$) is also established, where dT/dL is the absolute value of slope computed based on two consecutive values of track tension, T, and length, ℓ, given in Table I.1 along with appropriate multiplications. Based on quadratic and catenary approaches, the point of track stretching is characterized by similar L_h^1, but relatively different T_{tr}^1, which is computed as 10.5 kN and 12.5 kN, respectively. As shown, the ideal catenary approach [34] yields relatively higher values of track tension for given track hanging length.

The procedure for computing track tension based on track model # 3 is

Table I.1 Ideal nondimensional catenary solutions [34].

$\left(\frac{T}{aw}\right)$	$\left(\frac{\ell}{a}\right)$	$\left(\frac{a}{c}\right)$
1000.00	1.0000001	0.001
100.01	1.00002	0.01
10.05	1.002	0.10
3.48	1.015	0.30
2.26	1.042	0.50
1.976	1.061	0.60
1.793	1.084	0.70
1.672	1.110	0.80
1.592	1.141	0.90
1.54	1.175	1.00
1.52	1.214	1.10
1.51	1.260	1.20
1.52	1.306	1.30
1.54	1.360	1.40

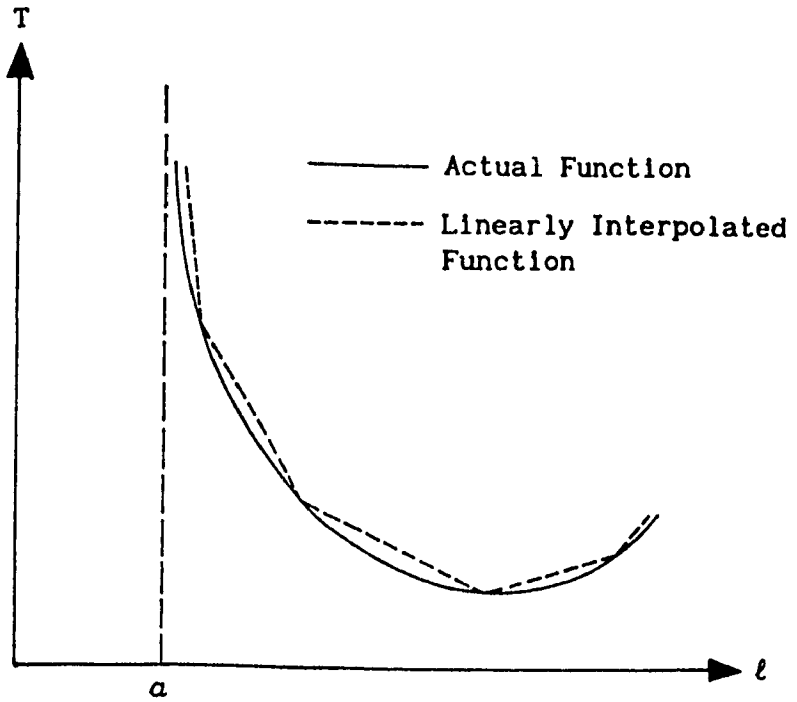

Figure I.5 Catenary approximation of hanging track.

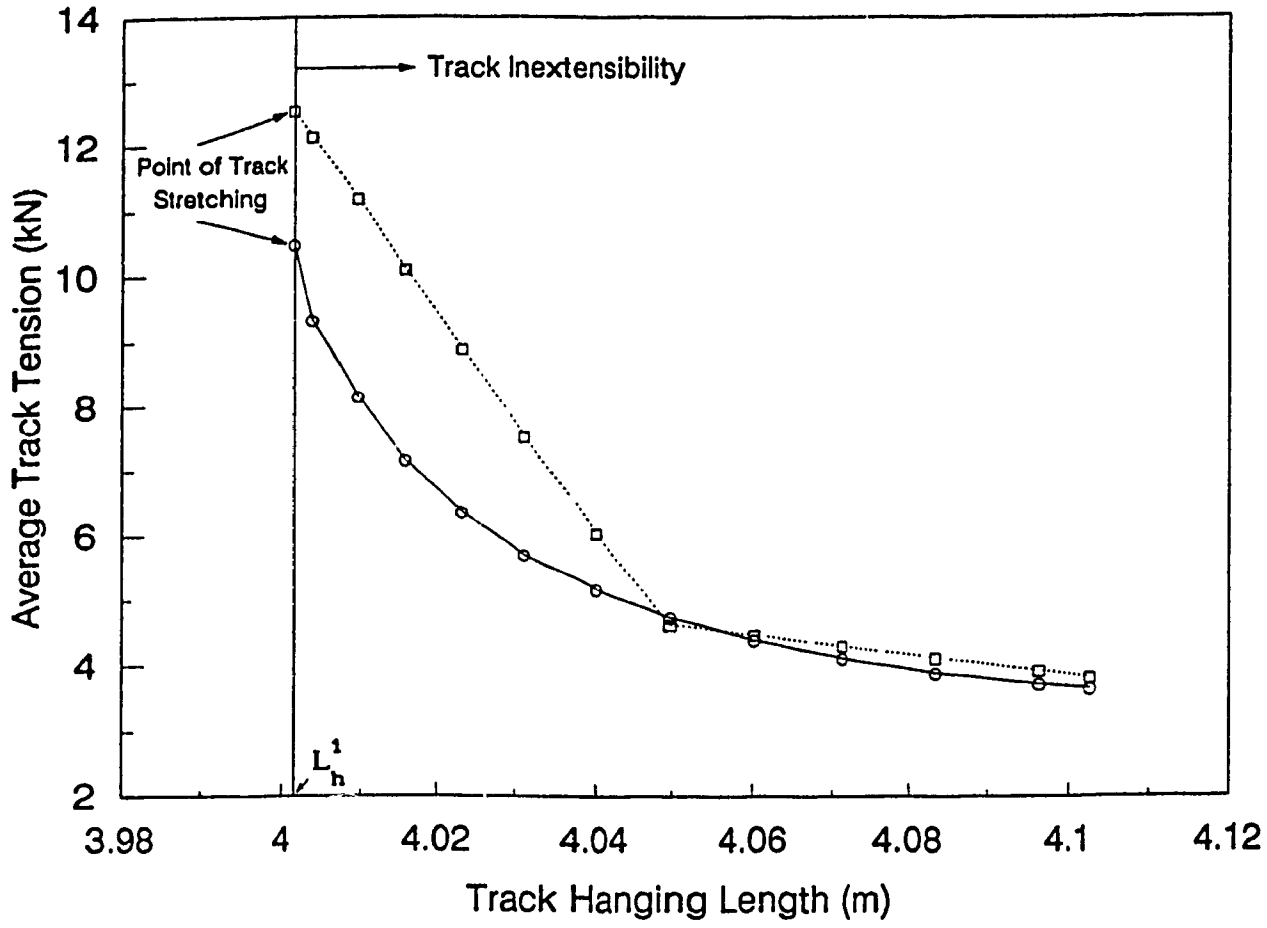

Figure I.6 Track tension characteristics based on track inextensibility (-□—□— Catenary [34], —o—o— Quadratic).

very similar to track model # 2. Prior to simulation, initial track hanging length, L_h^0, corresponding to specified track pre-tension, T_{tr}^0, distance, a, and weight/unit length, w, is obtained from Table I.1. In addition, the point of track stretching (L_h^1, T_{tr}^1) is computed as discussed above. During simulation, the overall track tension is computed as:

$$T_{tr} = \begin{cases} T \text{ @ } \ell = L_h/2 \text{ (Table I.1)} & ; \; L_h > L_h^1 \text{ (Track Inextensibility)} \\ K_{tr}(L_{tr} - L_{tr}^0) + T_0 & ; \; L_h \leq L_h^1 \text{ (Track Extensibility)} \end{cases} \tag{I.23}$$

where, T_0, L_{tr}, and L_h are obtained from equations (4.22), (4.23), and (4.24), respectively. The overall track length, L_{tr}, is obtained from equation (4.26). The horizontal and vertical components of the overall track tension, T_{tr}, acting at the i^{th} road wheel and the k^{th} hull wheel centres are computed using equation (2.14) and (2.18) respectively, where the horizontal inclinations of intermediate track segments, ε_j^j (j=1,2), are computed in view of improved track bridging effects (section 4.2.2.3), and the horizontal inclinations of upper track segment are specified as:

$$\begin{aligned} \Theta_A &= 2\pi + \Theta_h - \theta \\ \Theta_B &= \pi + \Theta_h + \theta \end{aligned} \tag{I.24}$$

where, Θ_h is given in equation (2.49), and θ corresponds to the hanging track inclination with respect to the longitudinal axis assumed to be parallel to the line adjoining the tops of drive sprocket and idler, and is computed from Table I.1 for given value of ℓ (= $L_h/2$) as:

$$\theta = \begin{cases} \tan^{-1}(\ell/c) & ; \; L_h^1 < L_h \\ 0 & ; \; L_h^1 \geq L_h \end{cases} \qquad (I.25)$$

Track Model # 4

The model described in this section is based on the track model employed in VEHDYN II [38], where the dynamic track tensioning effects are modeled as local tensioning effects, while neglecting the overall track tension. The intermediate track segments (between road wheels) are modeled as vertical springs interconnecting each adjacent road wheel pair (Figure I.7), which restricts the relative vertical motion of the road wheels. The springs are linear bi-directional springs, which effectively generate a vertical force proportional to the relative displacement between adjacent road wheel pair. Consequently, when the road wheel centres are all lined-up on the same horizontal axis, there is no force contribution due to the track tension model. Total vertical force acting at the i^{th} road wheel centre due to adjacent track segments, is given as (refer Figure I.7):

$$T_{wy}^{1} = \begin{cases} k_t^j (y_{wi+1} - y_{wi}) & ; \; i = 1 \\ k_t^{j-1}(y_{wi-1} - y_{wi}) + k_t^j (y_{wi+1} - y_{wi}) & ; \; i = 2,..,N-1 \\ k_t^{j-1}(y_{wi-1} - y_{wi}) & ; \; i = N \end{cases} \qquad (I.26)$$

where, $j = i+1$

where, k_t^j, the vertical spring constant of j^{th} intermediate track segment, is determined based on the weight of each road wheel against the track, and is equal for all track segments if road wheels are equally spaced.

The interaction of the track feeler with the terrain profile is

modeled by a linear spring placed perpendicular to the undeflected feeler at the *point of maximum deflection*, δ_{max}. Consequently, a normal froce proportional to δ_{max} is imparted to the feeler by the terrain profile, which increases the tension in the feeler to balance this force. Subsequently, the track feeler tension is applied to both hull wheel and the nearest road wheel. Figure I.8 illustrates the front and the rear track feeler-terrain interactions. The magnitude of track feeler tension is thus obtained as:

Front Track Feeler (j=1):

$$T_1 = \frac{k_t^1 . \delta^1_{max}}{\sin \lambda_1^1 + \sin \lambda_2^1} \tag{I.27}$$

where, $\lambda_1^1 = \varepsilon_1^1 - \Theta_1 + \pi$ and $\lambda_2^1 = \Theta_1 - \varepsilon_2^1$

Rear Track Feeler (j=N+1):

$$T_{N+1} = \frac{k_t^{N+1} . \delta^{N+1}_{max}}{\sin \lambda_1^{N+1} + \sin \lambda_2^{N+1}} \tag{I.28}$$

where, $\lambda_1^{N+1} = \varepsilon_1^{N+1} - \Theta_2$ and $\lambda_2^{N+1} = \Theta_2 - \pi - \varepsilon_2^{N+1}$

where k_t^j (j = 1 and N+1) is the perpendicular spring constant, and δ^j_{max} is computed using equation (2.53).

The horizontal and vertical components of dynamic track load acting at i^{th} road wheel and k^{th} hull wheel are obtained as:

$$T^i_{wx} = \begin{cases} T_j \cos \varepsilon_j^j \\ 0 \end{cases} ; \; T^i_{wy} = \begin{cases} T^i_{wy} + T_j \sin \varepsilon_j^j & \text{for } i=1,N \\ T^i_{wy} & \text{for } i=2,..,N-1 \end{cases} \tag{I.29}$$

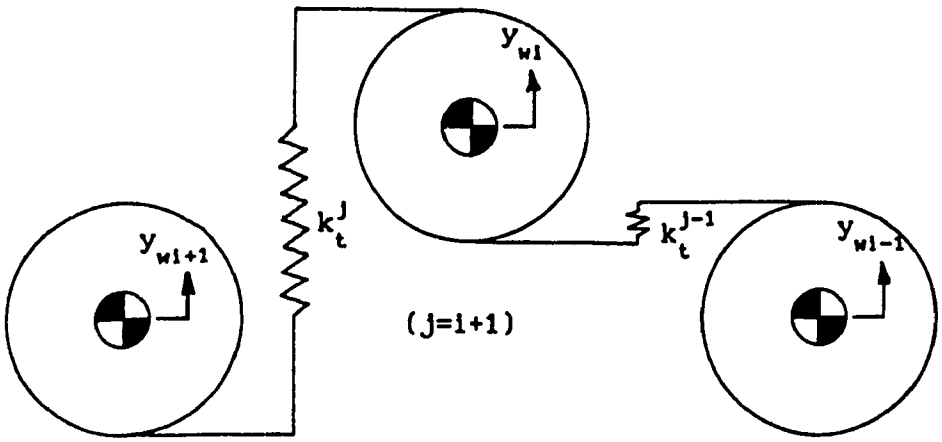

Figure I.7 Tension model for track segments between road wheels.

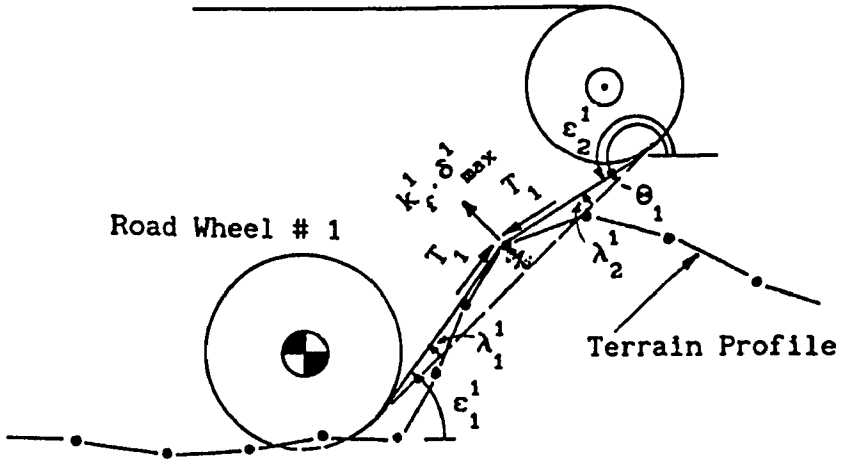

(a) Front track feeler

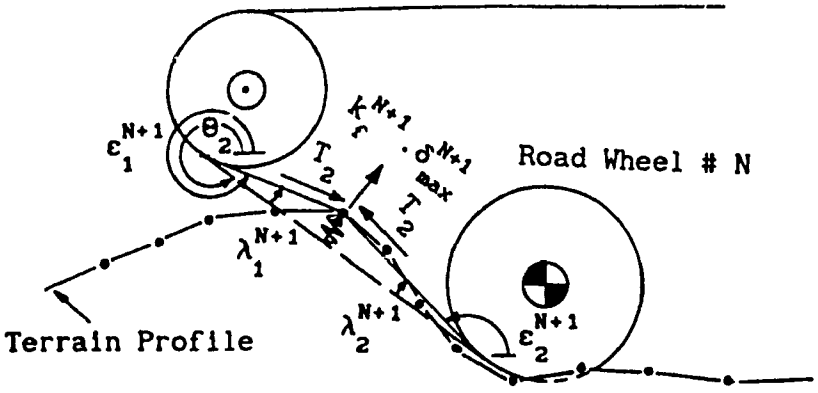

(b) Rear track feeler

Figure I.8 Tension model for track feelers.

where, $$j = \begin{cases} 1 \\ \\ N+1 \end{cases} \text{ and } j = \begin{cases} 1 & \text{for } i = 1 \\ \\ 2 & \text{for } i = N \end{cases}$$

$$T^k_{hx} = T_j \cos \varepsilon^j_j \quad ; \quad T^k_{hy} = T_j \sin \varepsilon^j_j \tag{I.30}$$

where, $$j = \begin{cases} 1 \\ \\ N+1 \end{cases} \text{ and } j = \begin{cases} 2 & \text{for } k = 1 \\ \\ 1 & \text{for } k = 2 \end{cases}$$

APPENDIX II

RIDSIM: EQUATIONS OF MOTION

RIDSIM is a time-domain ride simulation model formulated as a non-linear, in-plane dynamical system having "3+ND" degrees-of-freedom, where "3" accounts for the bounce and pitch motions (y_h, θ_h) of vehicle sprung body and an optional bounce motion (y_o) of the suspended driver/seat system, and "ND" indicates total number of degrees-of-freedom associated with the specified suspension types, computed as:

$$ND = NI + NT + 2\,NW + 3\,NB \qquad (II.1)$$

where, NI, NT, NW, and NB indicates the user-specified numbers of independent suspensions, torsion bar/trailing arm suspensions, walking beam suspensions, and bogie suspensions, respectively. The unsprung/rigid suspension (NU) is not included in equation (II.1) since it has no degree-of-freedom.

The equations of motion are expressed in its general form as:

$$[\,M\,]\{\,\ddot{q}\,\} = \{\,F\,\} \qquad (II.2)$$

where,

$[\,M\,]$ = the mass/inertia matrix of size (3+ND x 3+ND),

$\{\,F\,\}$ = the generalized force vector of size (3+ND x 1), and

$\{\,q\,\}$ = the generalized coordinate vector of size (3+ND x 1), specified as

$$\{\,q\,\} = \{\,y_h,\ \theta_h,\ \ldots y_{wi},\ \theta_{wi},\ \ldots,\ y_o\,\}' \qquad (II.3)$$

where, y_{wi} and θ_{wi} indicate translational (vertical) and rotational degrees-of-freedom associated with the general description of an i^{th} suspension unit, and are compiled in an order based on the specified

suspension type which are indexed from front to back of the vehicle. For instance, the independent suspension model (Figure 2.4) requires vertical degree-of-freedom (y_{wi}) only; the torsion bar/trailing arm suspension model (Figure 5.2) requires rotational degree-of-freedom (θ_{wi}) only; the walking beam suspension model requires both y_{wi} and θ_{wi}; and, the bogie suspension model requires three degrees-of-freedom ($y_{w1i}, y_{w2i}, \theta_{wi}$).

The equations of motion are written considering individually each of the specified suspension type. Similarly, the vehicle's zero-force configuration (section 2.5) and static equilibrium (section 2.6) are established in view of each suspension type. The suspension forces, in general, are modeled using the nonlinear spring characteristics, Coulomb friction damping to account for loading-unloading hysteresis loop, bump stops, and nonlinear force-velocity characteristics of shock absorber. It should be noted that, a common set of description variables are used in the modeling of each suspension type. As mentioned earlier in Chapter 6, the wheel and track are represented based on the user-specified sub-models, which are selected among the ones proposed in this study and previous studies.

Unsprung/Rigid Suspension

This suspension type is conceived as a simple rigid link between the wheel centre and the vehicle frame as illustrated in Figure II.1(a). Consequently, the wheel or unsprung body is the main suspension medium. This suspension has no degree-of-freedom, and is assumed to remain perpendicular to the vehicle frame. The equations of motion are written as (refer to Figure II.1(b)):

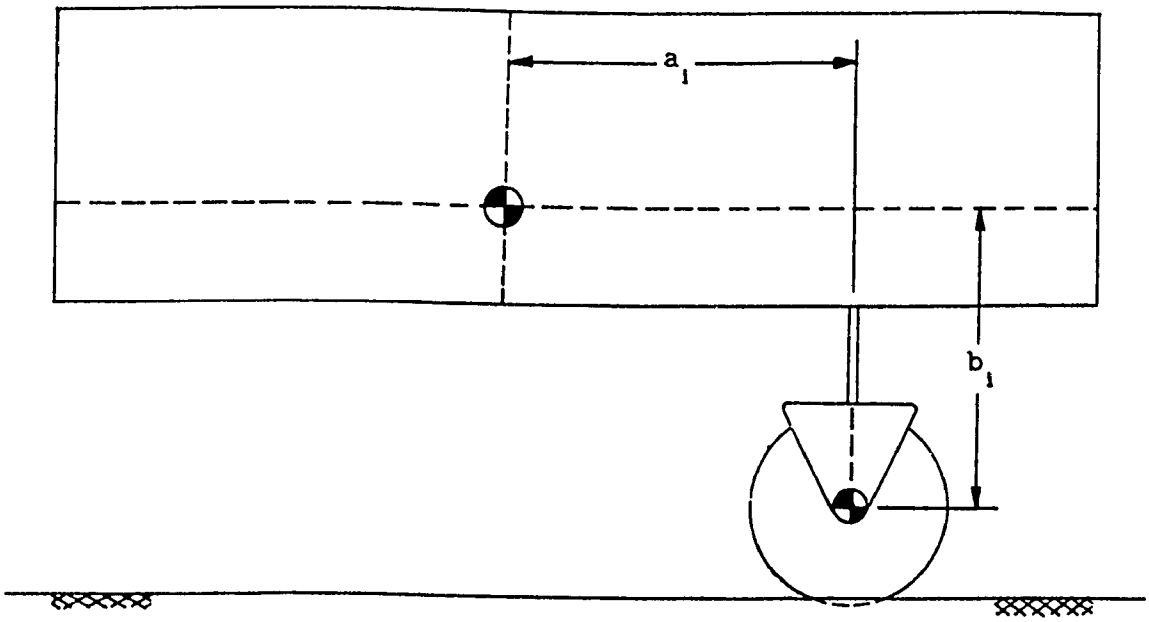

(a) Geometry

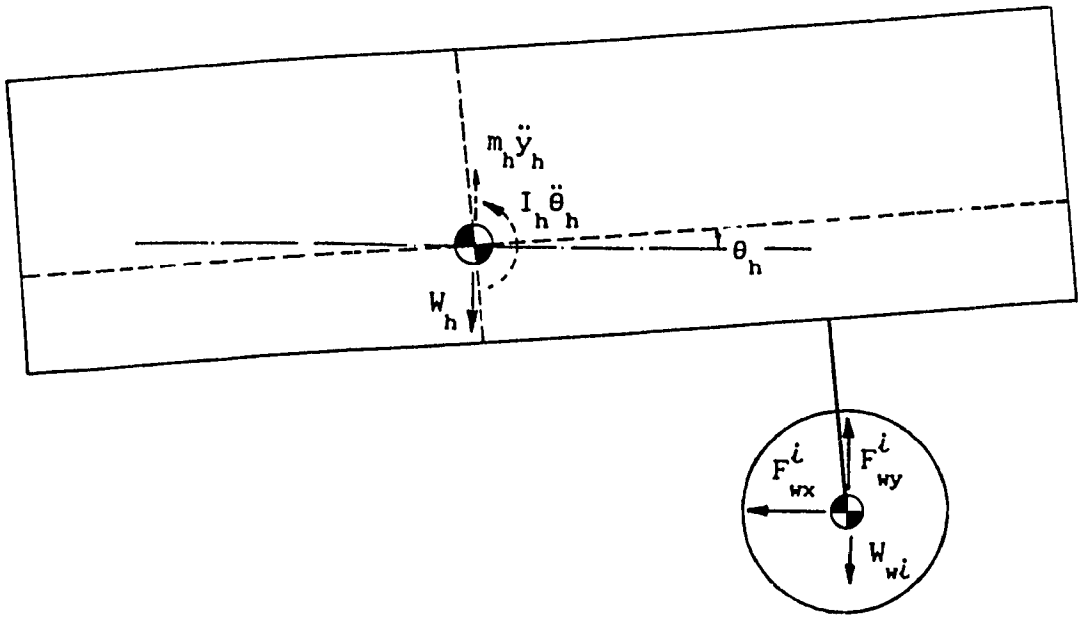

(b) Forces and moments

Figure II.1 Unsprung/rigid suspension.

Vehicle Bounce:

$$m_h \ddot{y}_h = \sum_{i=1}^{NU} \left[F_{wy}^{i} - W_{wi} \right] - W_h \qquad (II.4)$$

Vehicle Pitch:

$$I_h \ddot{\theta}_h = \sum_{i=1}^{NU} a_i \left[F_{wx}^{i} S_\theta + (F_{wy}^{i} - W_{wi}) C_\theta \right] + b_i \left[F_{wx}^{i} C_\theta - (F_{wy}^{i} - W_{wi}) S_\theta \right] + M_{HW} \qquad (II.5)$$

where, the net moment due to the forces acting at the centre of hull wheels (only for tracked vehicles) is given as:

$$M_{HW} = \sum_{k=1}^{M} a_{hk} \left[F_{hx}^{k} S_\theta + F_{hy}^{k} C_\theta \right] + b_{hk} \left[F_{hx}^{k} C_\theta - F_{hy}^{k} S_\theta \right] \qquad (II.6)$$

It should be noted that the sub-script " i " is the *identification* of the road wheel associated with the i^{th} unsprung suspension, and is consistent with other suspension models. The net horizontal and vertical forces acting at the road wheel centre are expressed based on equations (2.11) and (2.12) as:

$$F_{wx}^{i} = \begin{cases} \mathbb{F}_{wx}^{i} \\ \mathbb{F}_{wx}^{i} - T_{wx}^{i} \end{cases} ; \quad F_{wy}^{i} = \begin{cases} \mathbb{F}_{wy}^{i} & ; \text{ Wheeled} \\ \mathbb{F}_{wy}^{i} + T_{wy}^{i} & ; \text{ Tracked} \end{cases} \qquad (II.7)$$

As mentioned earlier, the wheel forces ($\mathbb{F}_{wx}^{i}, \mathbb{F}_{wy}^{i}, \mathbb{F}_{hx}^{k}, \mathbb{F}_{hy}^{k}$), and the track forces ($T_{wx}^{i}, T_{wy}^{i}, T_{hx}^{k}, T_{hy}^{k}$) are evaluated based on the user-specified wheel and track sub-models.

The instantaneous location of the road wheel centre associated with the unsprung suspension is simply computed as·

$$P_{wi} = \begin{Bmatrix} X_{wi} \\ \\ Y_{wi} \end{Bmatrix} = \begin{Bmatrix} a_1 C_\theta - b_1 S_\theta + X_{cg} \\ \\ a_1 S_\theta + b_1 C_\theta + Y_{cg} \end{Bmatrix} \qquad (II.8)$$

The suspension deflection, Δ_1^0, required for evaluating initial vertical deflection, δ_h^0 (equation 2.73) and pitch angle, θ_h^0 (equation 2.74), and thus establishing vehicle's zero-force configuration, is expressed as:

$$\Delta_1^0 = R_{wi} - h_{wi} \qquad (II.9)$$

The initial generalized displacement vector characterizing the vehicle's static equilibrium configuration is computed based on the iterative stiffness method (equation 2.79), where:

$$[\, K_{i-1} \,] = \begin{bmatrix} -\sum_{1=1}^{NU} K_{wi} & -\sum_{1=1}^{NU} K_{wi} a_1 \\ \\ & -\sum_{1=1}^{NU} K_{wi} a_1^2 \end{bmatrix} \qquad (II.10)$$

$$\{\, u_i \,\} = \{\, \delta_h,\ \theta_h \,\}' \qquad (II.11)$$

and,
$$\{\, F_a \,\} = \begin{Bmatrix} W_h + \sum_{1=1}^{NU} [W_{wi} + K_{wi}(Y_{wi}^0 - R_{wi}) - T_{wy}^i] - \sum_{k=1}^{M} T_{hy}^k \\ \\ -M_a + \sum_{1=1}^{NU} [W_{wi} + K_{wi}(Y_{wi}^0 - R_{wi})] a_1 \end{Bmatrix} \qquad (II.12)$$

where, K_{wi} , the spring constant for the road wheel, is evaluated in conjunction with the specified wheel sub-model (equations 2.83 and I.21), where the vertical deflection of the wheel centre is computed as:

$$\Delta_{wi} = R_{wi} - (Y_h^0 + b_1 + \delta_h + a_1 \theta_h) \qquad (II.13)$$

The applied moment vector due to the static track forces is computed as:

$$M_a = \sum_{i=1}^{NU} a_i \left[T_{wx}^i S_\theta + T_{wy}^i C_\theta \right] + b_i \left[T_{wx}^i C_\theta - T_{wy}^i S_\theta \right] + M_{tr} \qquad (II.14)$$

where, the net moment due to the static track forces acting at the centre of hull wheels is given as:

$$M_{tr} = \sum_{k=1}^{M} a_{hk} \left[T_{hx}^k S_\theta + T_{hy}^k C_\theta \right] + b_{hk} \left[T_{hx}^k C_\theta - T_{hy}^k S_\theta \right] \qquad (II.15)$$

Independent Suspension

This suspension type, as illustrated in Figure 2.4, is employed as an idealized representation of the torsion bar/trailing arm suspension system of the candidate vehicle (MODEL I & II). The equations of motion written for MODEL II incorporate a realistic representation of the independent suspension, where it is considered to remain perpendicular to the vehicle frame underside with no flexure (section 4.2.3). Consequently, this model representation is employed for RIDSIM, and the equations of motion are summarized as below.

Vehicle Bounce:

$$m_h \ddot{y}_h = \sum_{i=1}^{NI} \left[F_{si} + F_{di} \right] C_\theta + \sum_{k=1}^{M} F_{hy}^k - W_h \qquad (II.16)$$

Vehicle Pitch:

$$I_h \ddot{\theta}_h = \sum_{i=1}^{NI} \left[[F_{si} + F_{di}] a_i + b_{wi} [F_{wx}^i C_\theta - (F_{wy}^i - W_{wi}) S_\theta] \right] + M_{HW} \qquad (II.17)$$

Road Wheel Bounce:

$$m_{wi} \ddot{y}_{wi} = (F_{wy}^i - W_{wi}) - (F_{si} + F_{di}) C_\theta \qquad (II.18)$$

The procedure for establishing vehicle's zero-force and static equilibrium configurations in conjunction with the independent suspension is discussed in Chapter 2 (sections 2.5 and 2.6). The governing equation for establishing the vehicle's static equilibrium (equation 2.79) is, however, summarized as below.

$$[\,K_{i-1}\,] = \begin{bmatrix} -\sum_{1=1}^{NI} K_1 & -\sum_{1=1}^{NI} K_1 a_1 & K_1 \\ & -\sum_{1=1}^{NI} K_1 a_1^2 & K_1 a_1 \\ & & -(K_1 + K_{wi}) \end{bmatrix} \qquad \text{(II.19)}$$

$$\{\,u_i\,\} = \{\,\delta_h,\ \theta_h,\ \delta_{w1}\,\}' \qquad \text{(II.20)}$$

and,
$$\{\,F_a\,\} = \begin{Bmatrix} W_h - \sum_{k=1}^{M} T_{hy}^k \\ -M_a \\ W_{wi} + K_{wi}(Y_{wi}^o - R_{wi}) - T_{wy}^i \end{Bmatrix} \qquad \text{(II.21)}$$

where,

$$M_a = \sum_{1=1}^{NI} b_{w1}\left[T_{wx}^i C_\theta - T_{wy}^i S_\theta\right] + M_{tr} \qquad \text{(II.22)}$$

Torsion Bar/Trailing Arm Suspension

This suspension model has been already formulated, and details are given in Chapter 5 (section 5.2). The governing equations are, however, summarized here. The dynamic equations are given as:

Vehicle Bounce:

$$[m_h + \sum_{1=1}^{NT} m_{wi}]\ddot{y}_h + [\sum_{1=1}^{NT} m_{wi}(a_1 C_\theta - b_1 S_\theta + d_{x1})]\ddot{\theta}_h + \sum_{1=1}^{NT} [m_{wi} d_{x1}]\ddot{\theta}_{w1} = \sum_{1=1}^{NT} [(F_{wy}^i -$$

$$W_{wi}) + m_{wi}[(a_1 S_\theta + b_1 C_\theta)\dot{\theta}_h^2 + d_{y1}(\dot{\theta}_h + \dot{\theta}_{w1}^2)]\Big] + \sum_{k=1}^{M} F_{hy}^k - W_h \qquad (II.23)$$

Vehicle Pitch:

$$[\sum_{i=1}^{NT} m_{wi}(a_1 C_\theta - b_1 S_\theta + d_{x1})]\ddot{y}_h + [I_h + \sum_{i=1}^{NT}\{I_{w1} + m_{wi}(a_1^2 + b_1^2 + R_{a1}(R_{a1} - 2c_1))\}]\ddot{\theta}_h +$$

$$\sum_{i=1}^{NT}[I_{w1} + m_{wi}(R_{a1}(R_{a1} - c_1))]\ddot{\theta}_{w1} = \sum_{i=1}^{NT}\Big[F_{wx}^i(a_1 S_\theta + b_1 C_\theta + d_{y1}) + (F_{wy}^i - W_{wi})$$

$$(a_1 C_\theta - b_1 S_\theta + d_{x1}) - m_{wi} R_{a1}(a_1 S_\theta^1 - b_1 C_\theta^1)(2\dot{\theta}_h + \dot{\theta}_{w1})\dot{\theta}_{w1}\Big] + M_{HW} \qquad (II.24)$$

Road Arm-Road Wheel Rotation:

$$[m_{wi} d_{x1}]\ddot{y}_h + [I_{w1} + m_{wi}(R_{a1}(R_{a1} - c_1))]\ddot{\theta}_h + [I_{w1} + m_{wi} R_{a1}^2]\ddot{\theta}_{w1} = F_{wx}^i d_{y1} +$$

$$[F_{wy}^i - W_{wi}]d_{x1} + F_S^1 d_1 + M_T^1 + m_{wi} R_{a1}(a_1 S_\theta^1 - b_1 C_\theta^1)\dot{\theta}_h^2 \qquad (II.25)$$

The governing equation for establishing the vehicle's static equilibrium (equation 2.79) is summarized as:

$$[K_{i-1}] = \begin{bmatrix} -\sum_{i=1}^{NT} K_{wi} & -\sum_{i=1}^{NT} K_{wi} a_{wi} & -K_{wi} V_1 \\ -\sum_{i=1}^{NT} K_{wi} a_{wi} & -\sum_{i=1}^{NT} K_{wi} a_{wi}^2 & -K_{wi} V_1 a_{wi} \\ -K_{wi} d_{x1} & -K_{wi} d_{x1} a_{wi} & K_{wi} V_1 d_{x1} - K_{T1} - K_1 S_{a1} d_1 \end{bmatrix} \qquad (II.26)$$

$$\{u_i\} = \{\delta_h,\ \theta_h,\ \theta_{w1}\}' \qquad (II.27)$$

and,

$$\{F_a\} = \begin{Bmatrix} W_h - \sum_{k=1}^{M} F_{hy}^k - \sum_{i=1}^{NT}[W_{wi} - T_{wy}^i + K_{wi}(Y_{cg}^o + b_1 - R_{wi})] \\ -M_{tr} + \sum_{i=1}^{NT}[\{W_{wi} - T_{wy}^i + K_{wi}(Y_{cg}^o + b_1 - R_{wi})\}d_{x1} - T_{wx}^i d_{y1}] \\ -T_{wx}^i d_{y1} + [W_{wi} - T_{wy}^i + K_{wi}(Y_{cg}^o + b_1 - R_{wi})]d_{x1} - K_{T1}\theta_{w1}^0 - K_1 S_{a1} d_1 \theta_{w1}^0 \end{Bmatrix} \qquad (II.28)$$

Walking Beam Suspension

This suspension type, as illustrated in Figure II.2(a), comprises of a parallel spring-damper combination rigidly connected to the frame underside in a perpendicular manner (like independent suspension), a rigid beam with wheel set mounted at each end, and optional outboard shock absorbers mounted between beam and frame. The beam is usually free to rotate about the pivot point C within certain permissible range, and bump stops are mounted to restrict the rotation beyond the specified radial clearance. The walking beam suspension has two degrees-of-freedom: vertical displacement of the pivot point C (y_{wl}), and the rotation of the beam about the pivot point (θ_{wl}).

The equations of motion for a vehicle fitted with walking beam suspension system are expressed as (refer to Figure II.2(b)):

Vehicle Bounce:

$$m_h \ddot{y}_h = \sum_{i=1}^{NW} \left[(F_{si} + F_{di}) C_\theta + \sum_{n=1}^{2} F_{dni} \sin \zeta_{ni} \right] - W_h \qquad \text{(II.29)}$$

Vehicle Pitch:

$$I_h \ddot{\theta}_h = \sum_{i=1}^{NW} \left[(F_{si} + F_{di}) a_i + b_{wi} \sum_{j=i}^{i+1} [F^j_{wx} C_\theta - (F^j_{wy} - W_{wj}) S_\theta] - \sum_{n=1}^{2} F_{dni} [a_{ni} \sin(\theta_h - \zeta_{ni}) - b_{wi} \cos(\theta_h - \zeta_{ni})] + M^i_T \right] \qquad \text{(II.30)}$$

Pivot Point Bounce:

$$m^{\bullet}_{wi} \ddot{y}_{wi} = \sum_{j=i}^{i+1} [F^j_{wy} - W_{wj}] - (F_{si} + F_{di}) C_\theta - \sum_{n=1}^{2} [F_{dni} \sin \zeta_{ni}] \qquad \text{(II.31)}$$

where, $$m^{\bullet}_{wi} = m_{wi} + m_{wi+1}$$

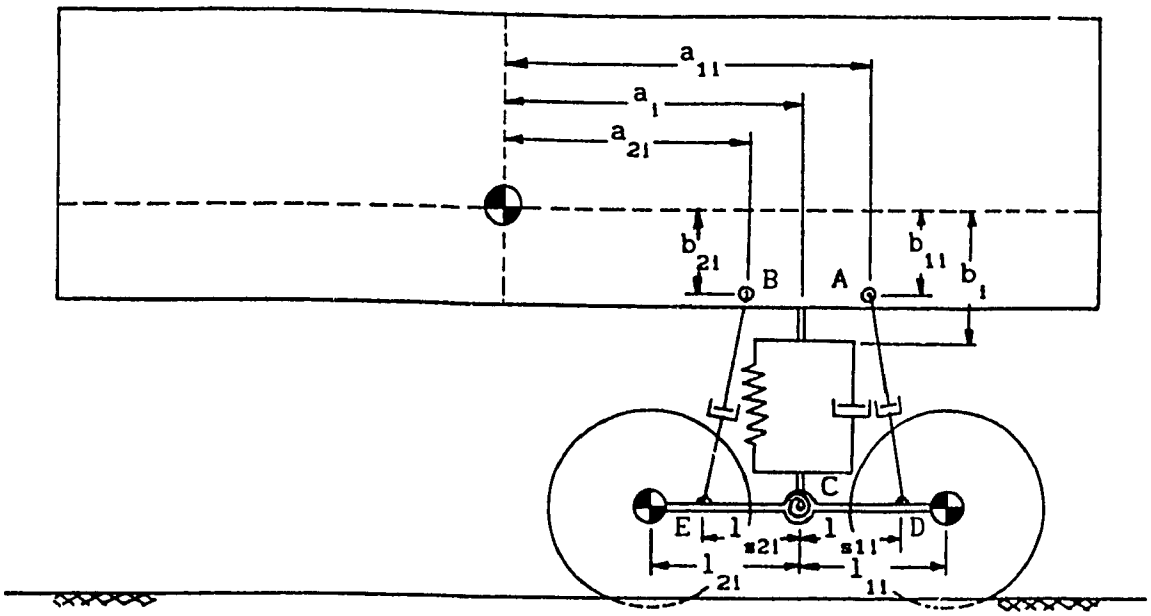

(a) Geometry

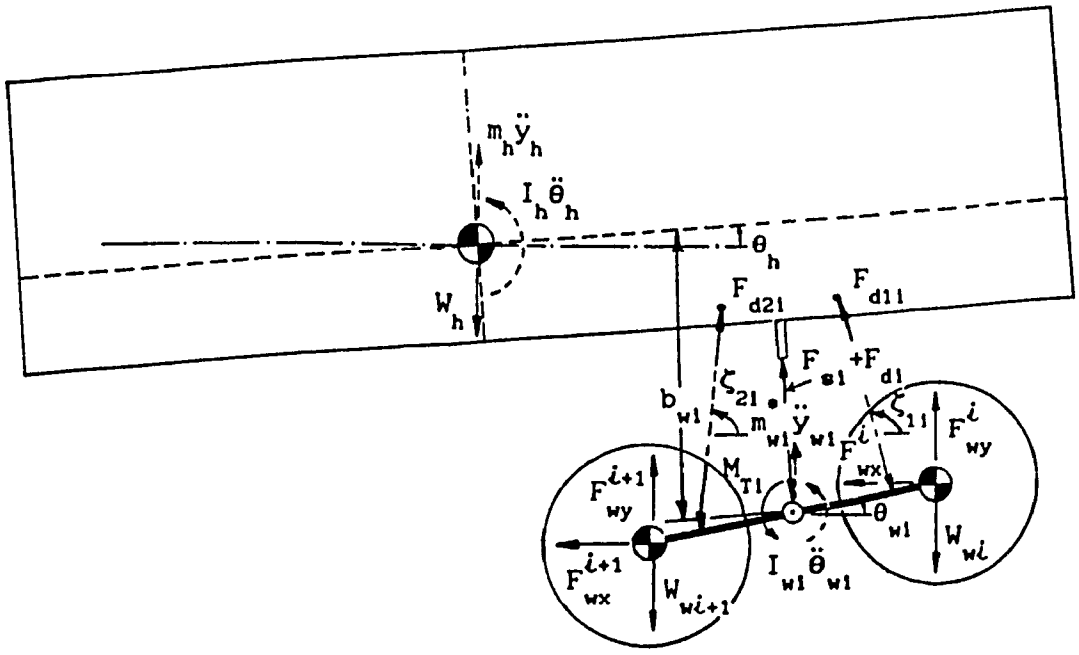

(b) Forces and moments

Figure II.2 Walking beam suspension.

Walking Beam Rotation:

$$I_{wi}\ddot{\theta}_{wi} = \sum_{j=i,\,n=1}^{i+1,2} [F_{wx}^{j} S_{\theta}^{i} + (F_{wy}^{j} - W_{wj}) C_{\theta}^{i}] l_{ni} + \sum_{n=1}^{2} [F_{dni} \sin(\theta_{wi} - \zeta_{ni})] l_{sni} - M_{T}^{i} \tag{II.32}$$

where, F_{si} and F_{di}, spring and damping forces due to the suspension unit between pivot point C and frame, are evaluated based on instantaneous values of relative displacement and velocity computed using equations, which are identical to (4.34). Similarly, F_{dni} (n=1,2) is the damping force due to the outboard shock absorber evaluated based on the relative velocity, given as:

$$\dot{r}_{ni} = [\dot{y}_{wi} - \dot{y}_{h} + l_{sni}\dot{\theta}_{wi} C_{\theta}^{i} - a_{ni}\dot{\theta}_{h} C_{\theta}] \sin \zeta_{ni} + [b_{ni}\dot{\theta}_{h} C_{\theta}] \cos \zeta_{ni} \tag{II.33}$$

The resistive moment, M_{T}^{i}, due to the beam rotation, is computed based on the nonlinear torsional stiffness and frictional damping characteristics. Similar to the torsion bar/trailing arm suspension (Figure 5.4), piece-wise linear spring characteristics are incorporated in the computation of M_{T}^{i}, which is then expressed as (refer to Figure II.3):

$$M_{T}^{i} = \begin{cases} K_{Ti}(\theta_{wi}^{U} - \theta_{h}) + K_{Ti}^{U}(\theta_{wi} - \theta_{h}) & ; \quad \theta_{wi} > \theta_{wi}^{U} \\ K_{Ti}(\theta_{wi} - \theta_{h}) & ; \quad \theta_{wi}^{L} \leq \theta_{wi} \leq \theta_{wi}^{U} \\ K_{Ti}(\theta_{wi}^{L} - \theta_{h}) + K_{Ti}^{L}(\theta_{wi} - \theta_{h}) & ; \quad \theta_{wi} < \theta_{wi}^{L} \end{cases} \tag{II.34}$$

The instantaneous location of the pivot point C with respect to the global reference system is given by:

$$P_{Ci} = \begin{Bmatrix} X_{Ci} \\ Y_{Ci} \end{Bmatrix} = \begin{Bmatrix} a_{i} C_{\theta} - b_{wi} S_{\theta} + X_{cg} \\ Y_{Ci}^{0} + y_{wi} \end{Bmatrix} \tag{II.35}$$

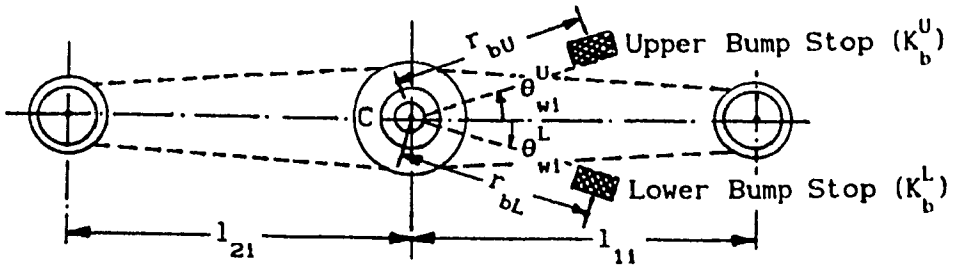

(a) Beam description and bump stops

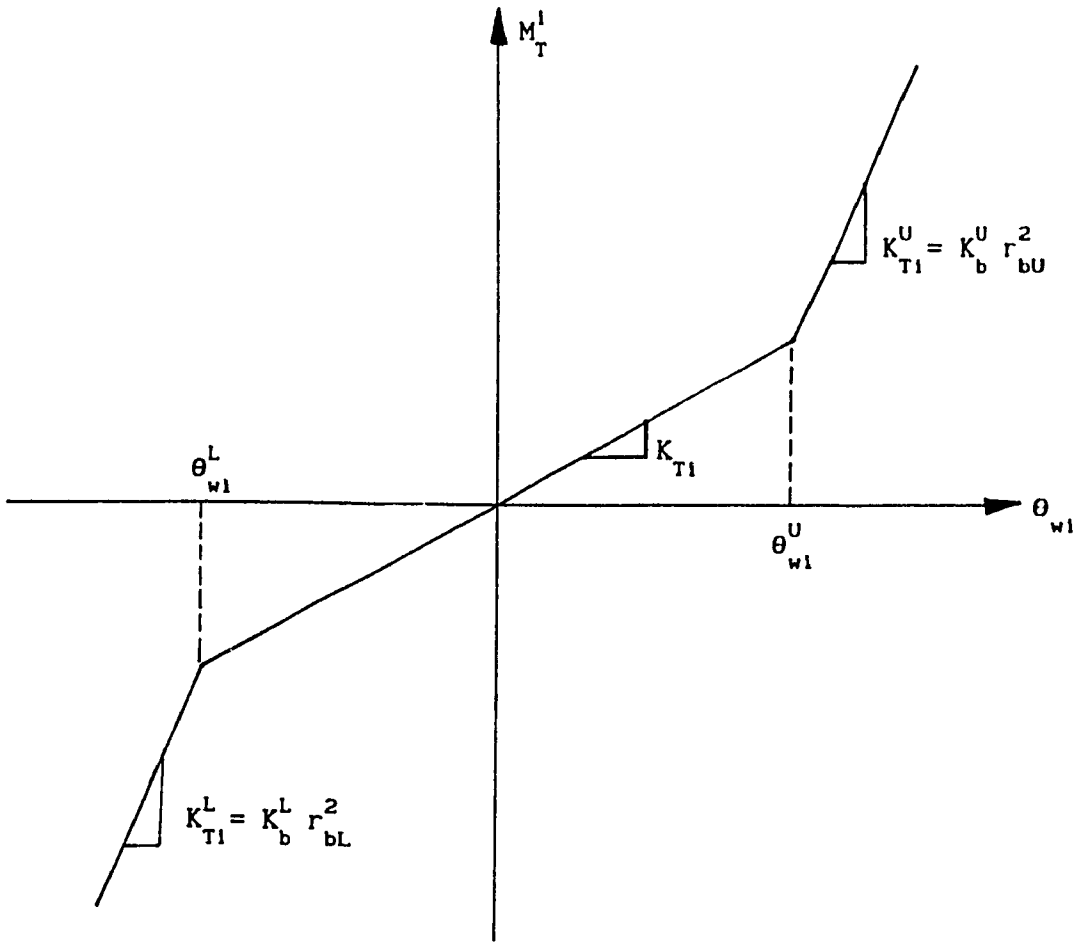

(b) Torsional spring characteristics

Figure II.3 Beam model.

where,

$$b_{wi} = \frac{Y_{Ci} - Y_{cg} - a_i S_\theta}{C_\theta} \tag{II.36}$$

and Y^0_{Ci} indicates the elevation of the pivot point associated with vehicle's zero-force configuration. Similarly, the coordinates of the road wheel centre at each end of the beam is obtained using:

$$P_{wj} = \begin{Bmatrix} X_{wj} \\ \\ Y_{wj} \end{Bmatrix} = \begin{Bmatrix} X_{Ci} + l_{ni} C^i_\theta \\ \\ Y_{Ci} + l_{ni} S^i_\theta \end{Bmatrix} \quad ; \quad j=i, n=1 \;\&\; j=i+1, n=2 \tag{II.37}$$

As illustrated in Figure II.2(b), angles ζ_{1i} and ζ_{2i} indicate the horizontal inclinations of the outboard shock absorbers mounted between points A-D, and B-E, respectively, and are evaluated using:

$$\begin{aligned} \zeta_{1i} &= \text{ATAN3}((Y_{Ai} - Y_{Di}), (X_{Ai} - X_{Di})) \\ \zeta_{2i} &= \text{ATAN3}((Y_{Bi} - Y_{Ei}), (X_{Bi} - X_{Ei})) \end{aligned} \tag{II.38}$$

where, the coordinates of points A, B, D, and E are given as:

$$P_{Ai} = \begin{Bmatrix} X_{Ai} \\ \\ Y_{Ai} \end{Bmatrix} = \begin{Bmatrix} a_{1i} C_\theta - b_{1i} S_\theta + X_{cg} \\ \\ a_{1i} S_\theta + b_{1i} C_\theta + Y_{cg} \end{Bmatrix} \tag{II.39}$$

$$P_{Bi} = \begin{Bmatrix} X_{Bi} \\ \\ Y_{Bi} \end{Bmatrix} = \begin{Bmatrix} a_{2i} C_\theta - b_{2i} S_\theta + X_{cg} \\ \\ a_{2i} S_\theta + b_{2i} C_\theta + Y_{cg} \end{Bmatrix} \tag{II.40}$$

$$P_{Di} = \begin{Bmatrix} X_{Di} \\ \\ Y_{Di} \end{Bmatrix} = \begin{Bmatrix} X_{Ci} + l_{s1i} C^i_\theta \\ \\ Y_{Ci} + l_{s1i} S^i_\theta \end{Bmatrix} \tag{II.41}$$

$$P_{Ei} = \begin{Bmatrix} X_{Ei} \\ \\ Y_{Ei} \end{Bmatrix} = \begin{Bmatrix} X_{Ci} + l_{s2i} C_{\theta}^{i} \\ \\ Y_{Ci} + l_{s2i} S_{\theta}^{i} \end{Bmatrix} \qquad (II.42)$$

The vehicle's zero-force configuration in conjunction with the walking beam suspension is established very similar to the independent suspension except the static suspension force between the pivot point C and the vehicle frame is evaluated using (refer to equation 2.70):

$$F_{si}^{o} = (F_{wi} - W_{wi}) + (F_{wi+1} - W_{wi+1}) + (T_{wy}^{i} + T_{wy}^{i+1}) \qquad (II.43)$$

The spring deflection, Δ_i^0, is then computed based on F_{si}^{o}, and employed to establish the vehicle's zero-force configuration. The elevations of road wheel centres at each end of the beam are considered equal for zero-force reference, which implies that beam is horizontal. Subsequently, the zero-force elevation of the pivot point C is computed equal to that of the road wheel, given as:

$$Y_{Ci}^{0} = h_{wi} + \delta_{wi}^{0} \qquad (II.44)$$

The vehicle's static equilibrium is established based on the iterative stiffness method, where the governing equation (2.79) is expressed via:

$$[\, K_{i-1} \,] = \begin{bmatrix} -\sum_{i=1}^{NW} K_i & -\sum_{i=1}^{NW} K_i a_i & K_i & 0 \\ & -\sum_{i=1}^{NW} (K_i a_i^2 + K_{Ti}) & K_i a_i & K_{Ti} \\ & & -(K_i + \sum_{j=i}^{i+1} K_{wj}) & -\sum_{j=i,\, n=1}^{i+1,\, 2} K_{wj} l_{ni} \\ & & & -\sum_{j=i,\, n=1}^{i+1,\, 2} K_{wj} l_{ni}^2 \end{bmatrix} \qquad (II.45)$$

$$\{ u_i \} = \{ \delta_h, \theta_h, \delta_{wi}, \theta_{wi} \}' \qquad \text{(II.46)}$$

and,
$$\{ F_a \} = \begin{Bmatrix} W_h - \sum_{k=1}^{M} T_{hy}^k \\ -M_a \\ \sum_{j=i}^{i+1} W_{wj} + \kappa_{wj}(Y_{Ci}^0 - R_{wj}) - T_{wy}^j \\ \sum_{j=i,\, n=1}^{i+1,\, 2} [W_{wj} + \kappa_{wj}(Y_{Ci}^0 - R_{wj}) - T_{wy}^j] l_{ni} \end{Bmatrix} \qquad \text{(II.47)}$$

where, κ_i, the spring constant for i^{th} walking beam suspension, is evaluated using equation (2.82). κ_{wj}, the spring constant for the attached road wheels, is computed based on:

$$\Delta_{wj} = R_{wj} - (Y_{Ci}^0 + \delta_{wi} + l_{ni}\theta_{wi}) \quad ; \quad j=i, n=1 \;\&\; j=i+1, n=2 \qquad \text{(II.46)}$$

The torsional spring constant, κ_{Ti}, is given by:

$$\kappa_{Ti} = M_T^i \;/\; (\theta_{wi} - \theta_h) \qquad \text{(II.47)}$$

and,

$$M_a = M_{tr} + \sum_{i=1}^{NW} b_{wi} \left[\sum_{j=i}^{i+1} [T_{wx}^j C_\theta - T_{wy}^j S_\theta] \right] \qquad \text{(II.48)}$$

Bogie Suspension

The schematic of a bogie suspension unit is illustrated in Figure II.4(a). Like walking beam suspension, the bogie suspension system involves a set of wheel pair and a rigid beam. However, the road wheels are connected to the beam through springs, where springs deflect along the lines which remain perpendicular to the beam. The bogie beam itself is directly pivoted to the vehicle frame, and is modeled identical to the walking beam (Figure II.3). The outboard shock absorbers are directly

linking the road wheels to the vehicle frame. The kinematics of bogie suspension involves three degrees-of-freedom: bounce motion of front bogie wheel (y_{w1i}), bounce motion of rear bogie wheel (y_{w2i}), and rotation of bogie beam about the pivot point, C (θ_{wi}).

The equations of motion for a vehicle fitted with bogie suspension system are expressed as (refer to Figure II.4(b)):

Vehicle Bounce:

$$m_h \ddot{y}_h = \sum_{i=1}^{NB} \left[\sum_{n=1}^{2} [F_{sni} C_\theta^i + F_{dni} \sin \zeta_{ni}] \right] - W_h \qquad (II.49)$$

Vehicle Pitch:

$$I_h \ddot{\theta}_h = \sum_{i=1}^{NB} \left[\sum_{n=1}^{2} [F_{sni} \cos(\theta_{wi} - \theta_h) a_i - F_{dni} \sin(\theta_h - \zeta_{ni}) a_{ni}] + M_T^i \right] \qquad (II.50)$$

Front/Rear Bogie Wheel Bounce:

$$m_{wj} \ddot{y}_{wni} = F_{wy}^j - F_{sni} C_\theta^i - F_{dni} \sin \zeta_{ni} - W_{wj} \qquad (II.51)$$

where, $j=i, n=1$ & $j=i+1, n=2$

Bogie Beam Rotation:

$$I_{wi} \ddot{\theta}_{wi} = \sum_{j=i,\, n=1}^{i+1,2} \left[F_{sni} l_{ni} + b_{wni} [F_{wx}^j C_\theta^i - (F_{wy}^j - W_{wj}) S_\theta^i] \right] - M_T^i \qquad (II.52)$$

where, the spring and damping forces, F_{sni} and F_{dni} (n=1,2), are evaluated based on:

$$r_{ni} = (y_{wj} - y_h - a_i S_\theta - l_{ni} S_\theta^i) C_\theta^i - b_i S_\theta S_\theta^i \qquad (II.53)$$

$$\dot{r}_{ni} = (\dot{y}_{wj} - \dot{y}_h - a_{ni} \dot{\theta}_h C_\theta) \sin \zeta_{ni} + (b_{ni} \dot{\theta}_h C_\theta) \cos \zeta_{ni} \qquad (II.54)$$

where, $n=1, j=i$ & $n=2, j=i+1$

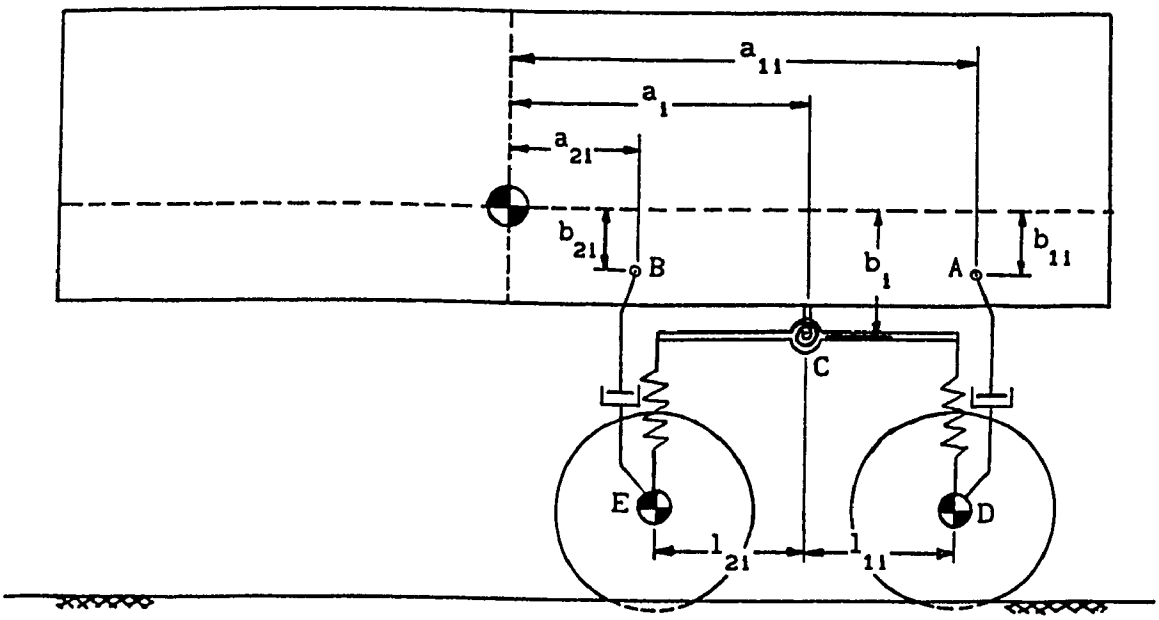

(a) Geometry

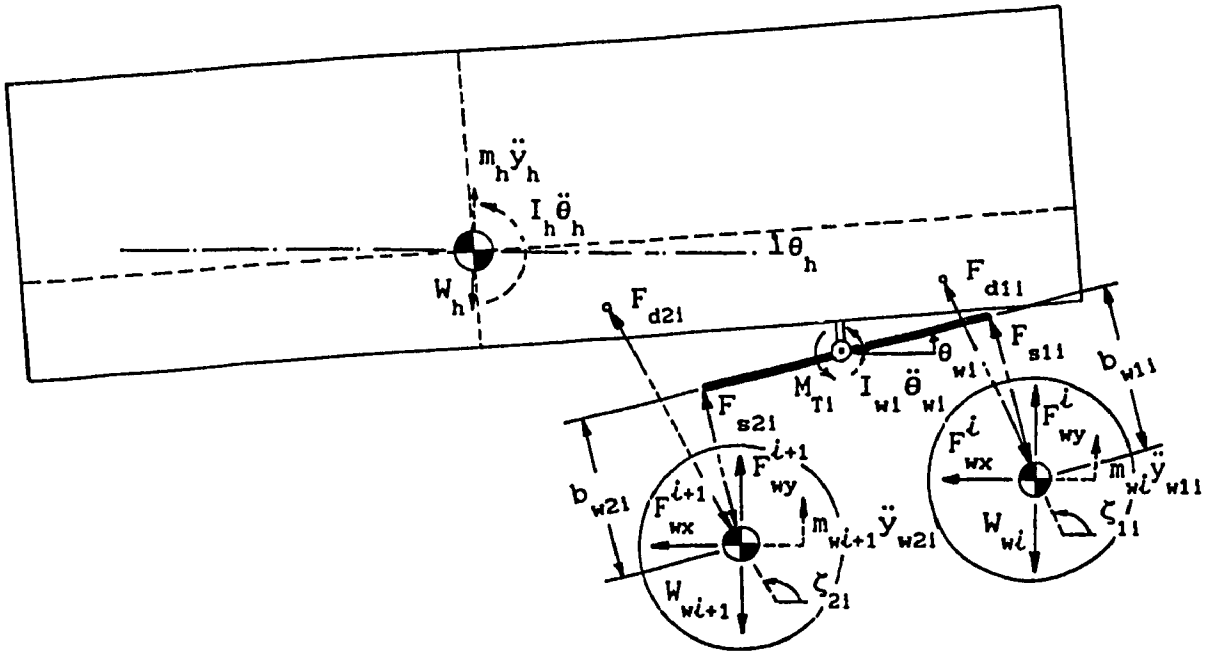

(b) Forces and moments

Figure II.4 Bogie suspension.

and, the resistive moment, M_T^i, is computed using equation (II.34). The perpendicular distance between the road wheel centre and the beam is given by:

$$b_{wni} = \frac{Y_{Ci} - Y_{wj} - l_{ni} S_\theta^i}{C_\theta^i} \quad ; \quad n=1, j=i \;\&\; n=2, j=i+1 \tag{II.55}$$

where, the coordinates of pivot point C, and road wheel centre are given as:

$$P_{Ci} = \begin{Bmatrix} X_{Ci} \\ \\ Y_{Ci} \end{Bmatrix} = \begin{Bmatrix} a_i C_\theta - b_i S_\theta + X_{cg} \\ \\ a_i S_\theta + b_i C_\theta + Y_{cg} \end{Bmatrix} \tag{II.56}$$

$$P_{wj} = \begin{Bmatrix} X_{wj} \\ \\ Y_{wj} \end{Bmatrix} = \begin{Bmatrix} X_{Ci} + l_{ni} C_\theta^i - b_{wni} S_\theta^i \\ \\ Y_{wj}^0 + y_{wni} \end{Bmatrix} ; \; j=i, n=1 \;\&\; j=i+1, n=2 \tag{II.57}$$

The horizontal inclinations of outboard shock absorbers, ζ_{1i} and ζ_{2i}, are computed using equation (II.38), where the coordinates of point A and B are given by equations (II.39) and (II.40), and the coordinates of points D and E which coincide with bogie wheel centres, are thus given by equation (II.57).

The zero-force configuration of a vehicle fitted with bogie suspension is established based on the static deflection of pivot point C, given by:

$$\Delta_i^0 = \Delta_{1i}^0 - l_{1i}\left[\frac{\Delta_{1i}^0 - \Delta_{2i}^0}{l_{1i} - l_{2i}}\right] \tag{II.58}$$

where, Δ_{1i}^0 and Δ_{2i}^0, deflection of front and rear spring units, correspond to the static suspension loads, given as:

$$F^{o}_{s1i} = -\frac{F^{o}_{s1}\, l_{2i}}{(l_{1i} - l_{2i})} \quad \text{and} \quad F^{o}_{s2i} = F^{o}_{s1} - F^{o}_{s1i} \tag{II.59}$$

where, F^{o}_{s1} is the combined suspension load given by equation (II.43). The zero-force elevation of bogie wheels is then computed considering a horizontal orientation of the beam, as:

$$Y^{o}_{wj} = h_{wj} + \delta^{o}_{wni} \tag{II.60}$$

where, $\delta^{o}_{wni} = \delta^{o}_{h} - \Delta^{o}_{ni}$ and $j=i, n=1$ & $j=i+1, n=2$

The vehicle's static equilibrium is established based on (equation 2.79):

$$[K_{i-1}] = \begin{bmatrix} -\sum_{i=1}^{NB}(K_{1i}+K_{2i}) & -\sum_{i=1}^{NB}(K_{1i}+K_{2i})a_i & K_{1i} & K_{2i} & -\sum_{n=1}^{2}K_{ni}l_{ni} \\ & -\sum_{i=1}^{NB}[(K_{1i}+K_{2i})a_i^2 + K_{Ti}] & K_{1i}a_i & K_{2i}a_i & -[\sum_{n=1}^{2}K_{ni}l_{ni}]a_i + K_{Ti} \\ & & -(K_{wi}+K_{1i}) & 0 & K_{1i}l_{1i} \\ & & & -(K_{wi+1}+K_{2i}) & K_{2i}l_{2i} \\ & & & & -\sum_{n=1}^{2}K_{ni}l_{ni}^2 - K_{Ti} \end{bmatrix} \tag{II.61}$$

$$\{ u_i \} = \{ \delta_h,\ \theta_h,\ \delta_{w1i},\ \delta_{w2i},\ \theta_{wi} \}' \tag{II.62}$$

and,

$$\{ F_a \} = \begin{Bmatrix} W_h - \sum_{k=1}^{M} T_{hy}^k \\ -M_{tr} \\ W_{wi} + \kappa_{wi}(Y_{wi}^o - R_{wi}) - T_{wy}^i \\ W_{wi+1} + \kappa_{wi+1}(Y_{wi+1}^o - R_{wi+1}) - T_{wy}^{i+1} \\ -\sum_{j=i,n=1}^{i+1,2} [T_{wx}^j C_\theta^i - T_{wy}^j S_\theta^i] b_{wni} \end{Bmatrix} \qquad (II.63)$$

where, the spring constant, κ_{ni} (n=1,2), for the front and rear spring units is computed based on:

$$\Delta_{ni} = \delta_{wni} - \theta_{wi} l_{ni} - \delta_h - \theta_h a_i \quad ; \quad n=1,2 \qquad (II.64)$$

The torsional spring constant is given by equation (II.47). The spring constant for bogie wheels is computed based on:

$$\Delta_{wj} = R_{wj} - (Y_{wj}^o + \delta_{wn1}) \quad ; \quad j=i, n=1 \ \& \ j=i+1, n=2 \qquad (II.65)$$

Driver's Seat Suspension

There are three user-specified options concerning the type of driver's seat computations:

(a) no computations at all, or

(b) computations without driver/seat dynamics, or

(c) computations with dynamics.

The option (b) means that the driver's seat is rigidly connected to the vehicle sprung body, and the ride motion is thus computed based on the kinematic relationship (equation 2.5). The option (c) implies that the driver is sitting on a suspended seat, which is modeled as a dynamical system having vertical degree-of-freedom (Figure 6.1). The seat/secondary

suspension is modeled as an independent suspension unit. The dynamic and static equations for the suspended driver's seat have been already written in conjunction with the models developed for the candidate vehicle, and are summarized here. The dynamic equations are given as (see section 4.2.3):

Vehicle Bounce:

$$m_h \ddot{y}_h = -(F_{so} + F_{do})C_\theta - W_h \tag{II.66}$$

Vehicle Pitch:

$$I_h \ddot{\theta}_h = -(F_{so} + F_{do})a_o \tag{II.67}$$

Driver's Seat Bounce:

$$m_o \ddot{y}_o = (F_{so} + F_{do})C_\theta - W_o \tag{II.68}$$

The instantaneous location of the suspended driver's seat is given by

$$P_{ds} = \begin{Bmatrix} X_{ds} \\ \\ Y_{ds} \end{Bmatrix} = \begin{Bmatrix} a_o C_\theta - (b_o + b_{ds})S_\theta + X_{cg} \\ \\ Y^0_{ds} + y_o \end{Bmatrix} \tag{II.69}$$

where,

$$b_{ds} = \frac{Y_{ds} - Y_{cg} - a_o S_\theta}{C_\theta} - b_o \tag{II.70}$$

and Y^0_{ds}, the zero-force elevation, is given by equation (2.78).

The vehicle's static equilibrium in conjunction with suspended driver's seat is established based on (refer to equations 2.79 and 2.81):

$$[\, K_{i-1} \,] = \begin{bmatrix} -\kappa_o & -\kappa_o a_o & \kappa_o \\ & -\kappa_o a_o^2 & \kappa_o a_o \\ & & -\kappa_o \end{bmatrix} \tag{II.69}$$

$$\{\, u_i \,\} = \{\, \delta_h,\ \theta_h,\ \delta_o \,\}' \tag{II.70}$$

and,

$$\{\, F_a \,\} = \{\, W_h,\ 0,\ W_o \,\}' \tag{II.71}$$